DTIC FILE COPY

②

AD-A225 058

Final Report

to

U.S. Army Strategic Defense Command

HYPERSONIC AERODYNAMICS AND CONTROL

TITLE ON COVER AND TITLE PAGE SHOULD READ:
"HYPERVELOCITY AERODYNAMICS AND CONTROL"
per letter Dr. Thomas Adamson, College of
Engineering, University of Michigan, Ann
Arbor, MI 48109-2140

DTIC
ELECTE
AUG 07 1990
D
E

June 6, 1990

College of Engineering

DEPARTMENT OF AEROSPACE ENGINEERING

The University of Michigan
Ann Arbor, Michigan 48109

DISTRIBUTION STATEMENT A
Approved for public release;
Distribution Unlimited

DEPARTMENT OF AEROSPACE ENGINEERING

College of Engineering
The University of Michigan
Aerospace Engineering Building
Ann Arbor, Michigan 48109-2140
313/764-3310 FAX 763-0578

25 September 1990

Defense Technical Information Center
Attn: DTIC-FDAC (Virginia Guidi)
Cameron Station
Alexandria, VA 22304-6145

Acquisition No. A-225058

Dear Ms. Guidi:

✓ I have enclosed the errata sheets for our final report, Hypervelocity Aerodynamics and Control.

As per our conversation, please change the title of the report, on the cover, to Hypervelocity Aerodynamics and Control. The title on the DD Form 1473 is correct.

Sincerely yours,

T. C. Adamson Jr.

Thomas C. Adamson, Jr.
Professor and Chairman

TCA:cr

Enclosure

SECURITY CLASSIFICATION OF THIS PAGE

REPORT DOCUMENTATION PAGE

1a. REPORT SECURITY CLASSIFICATION Unclassified	1b. RESTRICTIVE MARKINGS
2a. SECURITY CLASSIFICATION AUTHORITY BMD Classification Guide Dated 4/1/85	3. DISTRIBUTION/AVAILABILITY OF REPORT Unlimited
2b. DECLASSIFICATION/DOWNGRADING SCHEDULE	
4. PERFORMING ORGANIZATION REPORT NUMBER(S) Final Report	5. MONITORING ORGANIZATION REPORT NUMBER(S)

6a. NAME OF PERFORMING ORGANIZATION The University of Michigan	6b. OFFICE SYMBOL *(If applicable)*	7a. NAME OF MONITORING ORGANIZATION U.S. Army Strategic Defense Command
6c. ADDRESS *(City, State, and ZIP Code)* Department of Aerospace Engineering 2508 Patterson Place Ann Arbor, MI 48109-2140		7b. ADDRESS *(City, State, and ZIP Code)* P. O. Box 1500 Huntsville, Alabama 35807-3801
8a. NAME OF FUNDING/SPONSORING ORGANIZATION SDIO/T/1S	8b. OFFICE SYMBOL *(If applicable)*	9. PROCUREMENT INSTRUMENT IDENTIFICATION NUMBER DASG60-88-C-0037
8c. ADDRESS *(City, State, and ZIP Code)* Washington, D. C. 20301-7100		10. SOURCE OF FUNDING NUMBERS

PROGRAM ELEMENT NO.	PROJECT NO.	TASK NO.	WORK UNIT ACCESSION NO

11. TITLE *(Include Security Classification)*
Final Report: Hypervelocity Aerodynamics and Control

12. PERSONAL AUTHOR(S)
T. C. Adamson, Jr. and R. M. Howe

13a. TYPE OF REPORT	13b. TIME COVERED	14. DATE OF REPORT *(Year, Month, Day)*	15. PAGE COUNT
Final	FROM 4/4/88 TO 6/3/90	1990, June, 6	288

16. SUPPLEMENTARY NOTATION

17. COSATI CODES			18. SUBJECT TERMS *(Continue on reverse if necessary and identify by block number)*
FIELD	GROUP	SUB-GROUP	

19. ABSTRACT *(Continue on reverse if necessary and identify by block number)*

Two different but related research studies were supported by this contract and are discussed in this report. The first is concerned with the use of gas injection from the surface of a hypervelocity vehicle such that the effective shape of the body is changed to obtain desired aerodynamic forces and thus desired vehicle control; this type of aerodynamic control represents a gas injection scheme which might possibly be used for control both inside and outside the atmosphere. The second study is concerned with determining optimal trajectories and control of multi-stage surface-launched interceptors with ranges of several thousand miles and flight times of a few minutes; both propulsive and aerodynamic controls have been considered, and trajectory optimization has been based on minimizing the total interceptor mass ratio.

In the aerodynamic control work, studies were made of gas injection into the boundary layer on one side of a thin wedge in steady hypersonic flow, as proposed. In order to ascertain the magnitudes of the largest force changes available with blowing, gas injection rates large enough to cause the boundary layer to be blown off the body were considered. Conditions for the desired flight envelope are such that laminar flows could be

20. DISTRIBUTION/AVAILABILITY OF ABSTRACT ☐ UNCLASSIFIED/UNLIMITED ☐ SAME AS RPT ☐ DTIC USERS	21. ABSTRACT SECURITY CLASSIFICATION	
22a. NAME OF RESPONSIBLE INDIVIDUAL	22b. TELEPHONE *(Include Area Code)*	22c. OFFICE SYMBOL

DD FORM 1473, 84 MAR

83 APR edition may be used until exhausted.
All other editions are obsolete.

SECURITY CLASSIFICATION OF THIS PAGE

19. (Cont'd)

considered. Both analytical and numerical approaches were employed. A fundamental conclusion reached is that relatively large aerodynamic force changes can be obtained with relatively small rates of gas injection.

Analytical work concentrated on providing, for a simple flow field with gas injection, solutions from which the results of changes in parameters could be ascertained and which would provide example test cases for the numerical codes. The case considered is one for which the shear layer, which lies between the shock layer and the blown gas layer, has a thickness of the same order of magnitude as the other layers. Similarity solutions for a specific form of distributed gas injection were derived and used to provide pressure distributions; changes in force due to blowing and the dependence of these forces on various parameters were illustrated. Special methods necessary to compute the shear layer solutions were developed. An indication of the effects to be expected due to chemical reactions was found by consideration of oxygen dissociation with chemical equilibrium.

In the numerical studies, two different codes were developed. In the first, an inviscid flow field was considered, and problems associated with a crisp reproduction of the shock wave in hypersonic flow and the accurate representation of the desired blowing velocity at the body surface were considered. In the absence of experimental data, the code was validated by comparing results with available analytical results. It is valid for those cases where the boundary layer is blown off and is very thin compared to the shock layer and blown gas layer. A Navier-Stokes code was also developed. Solutions for a boundary layer on a flat plate and for a non-separated flow in a compression corner compared well with those found by others. Solutions attempted for a parameter set for which analytical results are known were unstable; i.e. a shear layer instability resulted. There is a possibility that this is a physical instability. Consideration of a very hot blown gas allowed stable solutions to be found, but they did not show a satisfactory comparison with corresponding analytical results; a fundamental difference between the flows is that the flow field found numerically shows a slightly detached shock wave, whereas it is assumed to be attached in the analytical study. Some computations for flow fields with strip blowing were carried out.

The second study has been motivated by the concept of surface-launched rather than space-launched kinetic-energy weapons for intercepting ICBM's during their ascent trajectory. Because this requires final interceptor velocities that are several times circular-orbit velocity, takeoff to payload mass ratios must be very large when using conventional rocket engines. Thus minimization of overall interceptor mass ratio is a natural goal in trajectory optimization. The high centrifugal acceleration associated with supercircular speeds means that sizeable down forces, corresponding to many g's of acceleration, are required to maintain the desired intercept trajectory. A key result of the research has been the determination of the important gains associated with the use of aerodynamic forces versus propulsive forces for achieving the required down force.

Specific contributions of the research include: a good understanding of the basic form of the optimum trajectories including the midcourse aeroassisted phase; the nature of the optimal stage design; the effect of target parameters, time of flight, number of stages, specific impulse of rocket engines and trajectory constraints on the optimum launch mass; effective tools for implementing reliably and efficiently the numerical optimizations; development of fast, efficient methods for numerical integration of the trajectory equations; approximate analytical characterizations of the separate phases of the optimal trajectories; development of a new scheme for overcoming the poor conditioning of the optimization problem by (indirectly) parameterizing the angle of attack through specification of the flight path angle. In addition, a simple method of attitude control for a final spinning guided stage has been developed, based on thrust modulation of a single side-thrusting control jet. This simple control scheme produces minimum-time attitude control maneuvers and realizes the required complex feedback control law by a simple on-board computer implementation.

Details of analyses from both studies are contained in published papers, copies of which are contained in Appendix A of this report.

Suggestions for further work include:

I) Aerodynamic Control Using Gas Injection Into the Boundary Layer

1) Inclusion of equilibrium chemistry (dissociation and reaction) in the Navier-Stokes code. The stability of the shear layer is sensitive to the temperature distribution in this layer, which is affected by chemical

reactions which may occur. Frozen and equilibrium flow calculations allow these effects to be bracketed.

2) Improvement of numerical code efficiency so as to handle separated flows economically, in terms of computer time. This will involve implementation of implicit time-marching or multi-grid relaxation, or both.

3) Definitive study of strip blowing, including both analytical and numerical studies, and including cases of simple and multiple strips.

4) Study of shear-layer stability in hypersonic flows, both analytically and numerically. Little previous work has been done on this problem, which must be understood before extensive practical use can be made of the injection of gases in the boundary layer for aerodynamic control.

5) Numerical study of temporal effects associated with stopping and starting blowing. Steady state examples give satisfactory results. Any problems associated with the unsteady processes when starting or stopping the blowing bear upon the feasibility of using surface blowing for control purposes, especially if a rotating vehicle with a control which is on only during part of the rotation is considered. This study will involve extending the temporal accuracy of the codes.

6) Study of effects of increasing altitude, to a point where free molecule flow exists; calcuation of jet forces needed for vacuum conditions (no boundary layer). It is not possible to cover the whole range from continuum to vacuum conditions computationally.

7) Consideration of three-dimensional, axially symmetric body in hypersonic flow at an angle of attack.

II) Combined Atmospheric and Exo-atmospheric Attitude and Trajectory Control

1) Extension of the research on attitude control out of the atmosphere to integrate it with the research on generation of aerodynamic forces at hypersonic speeds using boundary-layer injection (Part I).

2) Extension of the time-optimal control laws developed for a spinning missile with an on-off thruster to the continuously-thrusting case, where hot gas is switched back and forth from one nozzle to another. This single control scheme has the advantage that it can be utilized both for attitude control in the atmosphere, using boundary-layer injection, and for control out of the atmosphere.

3) Modification of the thrust-switching scheme to provide high-resolution attitude control by means of pulse-width modulation of the control-jet switch.

4) Implementation of closed-loop control with high sample rates by storing only one-bit switch position data in the multivariable function table for the time-optimal control law, based on the desired attitude and current measurements of missile attitude and attitude rate. The multivariable function scheme for storing control-jet switch times, as developed in the research to date, uses on-line table lookup with linear interpolation to determine thruster turn-on and turnoff times. The proposed new scheme offers possible advantages over the table-lookup scheme. It is potentially simpler from a hardware point of view and achieves direct closed loop control rather than partially open loop control.

5) Develop minimum-fuel thruster control laws.

6) Extend the parametric studies of trajectory optimization with the support of the simplified trajectory optimization program developed during the last six months. This research would be used to provide performance requirements for the attitude control schemes described above.

HYPERSONIC AERODYNAMICS AND CONTROL

FINAL REPORT

April 4, 1988 - June 3, 1990

U.S. ARMY STRATEGIC DEFENSE COMMAND
CONTRACT NO. DASG60-88-C-0037

T.C. Adamson, Jr. Principal Investigator
R.M. Howe Principal Investigator

Department of Aerospace Engineering
The University of Michigan
Ann Arbor, Michigan 48109-2140

June 6, 1990

Accession For
NTIS GRA&I ☒
DTIC TAB ☐
Unannounced ☐
Justification
By
Distribution/
Availability Codes
Dist Avail and/or Special
A-1

Funded by Strategic Defense Initiative Organization
Innovative Science and Technology

Managed by U.S. Army Strategic Defense Command
Advanced Technology Directorate

The views, opinions, and/or findings contained in this report are those of the author(s) and should not be construed as an official Department of the Army position, policy, or decision, unless so designated by other official documentation.

Table of Contents

I. Introduction....1

II. Review of Work Accomplished....4

Part I Study of Gas Injection into the Boundary Layer on a Wedge at Hypersonic Velocities....4
  1. Introduction....4
  2. Analytical Approach....6
  3. Numerical Approach....11
  4. Summary and Conclusions....18

Part II Optimal Aerodynamic and Propulsion Control of Intercept Trajectories at Supercircular Speeds....21
  1. Introduction....21
  2. Modeling the Multi-Stage Interceptor....23
  3. The Optimization Problems and its Solution....25
  4. Numerical Methods for Integrating Equations of Motion....27
  5. Results of the Trajectory Optimization Studies....28
  6. The Mid-Course Universal Curve....30
  7. Performance of Multi-Stage Rocket (Semi Analytical Approach)....31
  8. The Attitude Control Scheme....32
  9. Minimum Fuel Interception with Time Constraint....34
  10. Reachable Domain for Interception at Hyperbolic Speeds....35

III Suggested Future Work....36
IV. References....38
V. Table....41
VI. Figures....42
VII. Appendix A Copies of Publications and Conference Papers Resulting from this Contract....66
VIII. Appendix B Bibliography of Papers Dealing with Boundary Layer Control....284

HYPERSONIC AERODYNAMICS AND CONTROL

Contract No. DASG 60-88-C-0037

Principal Investigators	T. C. Adamson, Jr. R. M. Howe
Co-Principal Investigators	E. G. Gilbert N. X. Vinh A. F. Messiter B. van Leer

FINAL REPORT

I. Introduction

This final report covers work supported by Contract No. DASG60-88-C-0037 for a two year period beginning on April 15, 1988. A two-month no-cost extension was granted so that the writing of this report would not conflict with end of the academic year duties.

Aside from the faculty members listed as principal or co-investigators, five graduate students working on their PhD degrees, one post-doctoral fellow, and one undergraduate student worked on this project. One of the graduate students has completed his work and has graduated, two are well along in their research and should be finished within a year, and two are in the initial phases of their research.

The research work to be described here actually began with a 13 month SDIO contract monitored by AFOSR (No. F49620-86-C-0138; September 15, 1986 to October 14, 1987). Due to a unique option clause which was not noticed by the original contract monitor, the original contract lapsed during the period when the management of this and other contracts was being transferred from AFOSR to the Army Strategic Defense Command; a new contract, the present one, was submitted and awarded. The net effect was a six-month hiatus in research support, although some graduate student work continued.

Two different but related studies were supported by this contract and thus are discussed in this report. The first involves the use of gas injection from the surface of a hypervelocity vehicle such that the effective shape of the body is changed so as to obtain desired aerodynamic forces, and thus desired vehicle control. The second has to do with the attainment of optimal trajectories for trans-atmospheric vehicles to achieve minimum vehicle mass and minimum transit time, or minimum energy expenditure for a given transit time. Both thrust and aerodynamic control were considered in the second study. The application of either study is to any hypervelocity vehicle which spends at least part of its time in the atmosphere, including ground based kinetic energy weapons. The type of aerodynamic control analyzed in the first study allows for consideration of a gas injection scheme which might possibly be used both within and outside of the atmosphere.

The type of aerodynamic control analyzed in the first study allows for consideration of a gas injection scheme which might possibly be used both within and outside of the atmosphere. That is, one could imagine a conical vehicle with four regions of gas injection, each extending from nose to base over a 20° to 30° circumferential arc, with each region centered about lines 90° apart. In addition, valving would allow changing the gas flow to four jets with equal circumferential spacing near the nose and four more near the vehicle base. In the atmosphere, control is attained through changing the displacement thickness of the boundary layer asymmetrically by blowing. Outside the atmosphere, control is maintained through the jet thrust applied asymmetrically. Mass flow requirements will probably be different in the two limiting cases. Preliminary indications are that strip blowing, rather than the distributed blowing just described, may provide a more flexible and efficient control system in the atmosphere; in that case, the valving needed to change to jets will be quite simple. In any event, the fundamental idea of control by gas injection would be the same for flight in and outside of the atmosphere and the general mechanical devices required would be the same. It should be noted that such a control system would then be useful both for earth-launched vehicles which either remain in the atmosphere or go into space, and for space-launched vehicles which either remain in space or enter the atmosphere.

An important consideration for any control system is its scaleability. In order to address this problem, using the best available information from the studies made so far, an estimate of the mass rate of flow of injected gas has been made for a vehicle of 500 gms mass and volume of 500 cc, configured as a 10° cone traveling at a Mach number of 25 at 200,000 ft. The injected gas is taken to be helium. Currently solutions are available only for a two-dimensional wedge, not a cone. Even if it is assumed that gas is injected over a 20° arc on the cone, there may be significant 3-D effects. Nevertheless, the solutions obtained for the wedge should be representative of what would be found for flow over a cone. Calculations indicate that in order to achieve a 2-g transverse acceleration, a gas flow rate of roughly 0.6 gms/sec is required. Thus, even if it were necessary to maintain 2-g's over two to three minutes, only 70 to 110 gms of helium would be required. (Less hydrogen would be needed; here helium was chosen so that no chemical reactions need be considered.) Although this result gives only the required mass of injected gas, with no account taken of the necessary gas generator and valving weights, the estimate appears low enough to give good indication that the control system can be scaled down for quite small vehicles.

It appears, then, that a control system employing gas injection is scaleable and has the possibility of being used for both endo- and exo-atmospheric vehicles. Further study would seem warranted. In particular, the behavior of the injected gas as altitude increases and vacuum conditions are approached requires analysis, as does the effect of unsteadiness. Finally, three-dimensional flow fields will have to be considered.

Quarterly progress reports [1 - 7] have been submitted, as required. Publications and conference papers resulting from this work are referred to in the following text and reproduced in Appendix A.

II. Review of Work Accomplished

Part 1. Study of gas injection into the boundary layer on a wedge at hypersonic velocities

1. Introduction

The first effect of gas injection at a low rate from the surface of a body in a flow field is a thickening of the boundary layer (weak blowing). As the mass flux of injected gas increases, the boundary layer eventually is blown off the wall, so that a three layer flow structure is obtained (strong blowing). The blown-gas layer is adjacent to the wall; above this are first the shear layer and then the shock layer, which is immediately downstream of the shock wave. In Figure 1 (from Reference 8) are shown sketches illustrating both weak and strong blowing, the speckled regions corresponding to the boundary layer and shear layer, and weak and strong interactions, in flow over a thin wedge. Here, the term weak interaction refers to the fact that solutions for the boundary layer (weak blowing), or the shear and blown-gas layers (strong blowing) may be found independently of the solutions in the shock layer; solutions from the shock layer merely provide boundary conditions. When the interaction is strong, on the other hand, solutions in the shock layer and inner layers must be found simultaneously; they affect each other strongly. Weak interaction occurs when the thickness of the inner layers (boundary layer in weak blowing, and shear plus blown-gas layer in strong blowing) is small compared to the thickness of the wedge, and strong interaction when the thickness of the inner layers is large compared to the wedge thickness. In order to quantify these ideas, X_r is defined as the distance from the vertex of the wedge to the point where the boundary layer is of the same thickness as the wedge. The thickness of the boundary layer increases more slowly than does that of the wedge, so that for $X/X_r >> 1$ (X is the distance from the wedge vertex) the interaction is weak and for $X/X_r << 1$ it is strong. When the blowing becomes strong and the boundary layer is blown off the wedge, the cases considered are those where the thickness of the shear layer is at most of the same order of magnitude as the thickness of the blown-gas layer, so that the definition of X_r may still be used to order weak and strong interactions. It may be noted that as $x = X/X_r \rightarrow 0$, separate layers cannot be defined and the entire region of disturbed flow near the leading edge is referred to as a merged layer. In Figure 1, this region is shown to occur for $x = 0(\alpha^4)$ where α is the semi-vertex angle of the wedge; since the wedge is thin, $\alpha << 1$.

In the event the blowing is weak and the boundary layer remains attached, the distributions of velocity and temperature are those typical of boundary layers. When the blowing is strong, the distributions of pressure P, temperature T, flow velocity u, and relative mass concentration of blown gas Y_b are sketched in Figure 2, again from Reference 8. Of particular importance is the large spike in temperature caused by the transfer of ordered to thermal energy as the flow is decelerated in the shear layer.

The fundamental goal of the work described here was to ascertain the viability of boundary layer blowing as an aerodynamic control. The first point at issue was the magnitude of the mass flux of injected gas for realistic forces. To that end, it was decided early to consider strong blowing first so that the largest possible forces would be achieved, and to assess the corresponding mass rate of flow of blown gas. Next, the distribution of pressure forces was clearly an important point and so it was clear that both distributed and strip blowing cases had to be analyzed. Third, because injected gases other than air are of considerable importance in terms of both cooling efficiency and force obtained per unit mass flux of blown gas, and since the effects of dissociation and chemical reaction had to be assessed, it was decided that at least a simple gas mixture and chemical equilibrium had to be included. These points will be discussed in varying detail in what follows.

One important point which has not been addressed is the effect of turbulence. It is common practice to employ the Reynolds averaged equations of motion with some closure model for the turbulent eddy viscosity, in solving flow problems involving turbulent boundary layers. These models consist of the use of an algebraic equation in the simplest case to two partial differential equations in complex cases. It is known that as Mach number and altitude increase, transition to turbulent flow occurs at higher and higher Reynolds numbers and thus becomes less and less of a problem. In Figure 3 (Reference 9) are shown experimental, flight and wind tunnel data giving the transition Reynolds number as a function of the Mach number and the mean Reynolds number per foot. Superimposed on this plot are curves showing the actual Reynolds number for a body that is ten feet long, at various altitudes, and at the indicated Mach numbers. It is seen that above 25,000 feet, a very low altitude, the actual Reynolds number is considerably less than the transition Reynolds number, so the flow is laminar. Hence, in all that follows, laminar flow is considered. It should be noted that the method of blowing, e.g., using a finite number of holes rather than a completely distributed injection over a surface, could cause local areas of turbulent flow. This level of detail was not considered in the present study.

Because this was in large measure a feasibility study, the simplest possible geometry for a body in hypervelocity flow was employed. Thus, a thin wedge in a two-dimensional hypersonic flow field was chosen, with gas being injected from one side wall. Since the pressure which occurs with inviscid flow is easily calculated, the force difference induced by blowing was found by consideration of only the flow field over the side with blowing. Two methods of analysis were used, one essentially analytical in nature and the other numerical. The analytical studies, confined to very simple sub-problems in the main, provided much needed information on the scaling of various regions, to be used in setting up numerical algorithms, as well as solutions which gave insight to the problem and examples to which numerical solutions could be compared as checks of the algorithms. Because there are few if any experimental results available for comparison, these checks are very important. The numerical analysis provides two codes. In the first, which holds for inviscid flows, a number of flow fields can be studied as long as the boundary layer has been blown off the body and conditions are such that the shear layer is thin compared to the other two layers; with the inviscid flow code, such studies can be made relatively easily and inexpensively. The other code is a full Navier-Stokes code. When strip blowing, or blowing which does not start at the vertex, is considered, for example, this code must be used because the existence of separated flow and recirculating regions means that viscous terms are required.

In the following, the analytical and numerical studies are discussed separately, for convenience, although the work was carried out in one cooperative effort. It may be noted that the first task carried out in the original contract was a literature search. In Appendix B is given a list of relevant references which may be useful to others working in this field. In particular, some references are presented from thirty years ago, when there was considerable interest in hypersonic flow and some flows with blowing were considered.

2. Analytical Approach

As noted above, a major goal of this study has been to estimate the size of the aerodynamic forces available as a result of surface blowing. The force changes are caused by the distortion of the flow field that results from gas injection, and so a detailed study of the flow is required for a calculation of the modified pressure distributions. We wished to have at least one analytical formulation which would provide insight into the manner in which various parameters of the problem will affect the resulting aerodynamic forces, as well as a means of validating computer codes developed to handle more complicated cases. Moreover, in such an analytical formulation most of the parameters can be absorbed through rescaling of the variables, so that the solutions depend on a relatively small number of dimensionless parameters. The simplest example appears to be two-dimensional flow past a wedge with a continuous distribution of blowing velocity in a power-law form, such that the problem requires study of ordinary rather than partial differential equations. Later of course one would wish to consider more complicated geometries with more general blowing distributions.

For sufficiently strong blowing the boundary layer is blown away from the surface as a free shear layer. If the blowing rate is large enough (but still for low subsonic values of the injection velocity), for fixed values of the other parameters, the shear layer will be very thin relative to the total displacement of the outer flow, and may be neglected in a first approximation. The pressure force causes the injected gas to move downstream, still at a speed much lower than the speed of the undisturbed flow. The displacement effect is then caused entirely by the layer of blown gas and is described by the inviscid-flow approximation of Cole and Aroesty [10]. Our first calculations focused on application of this theory to determine force changes resulting from various blowing distributions with various chemically inert injectants.

In hypersonic flow, however, viscous layers are hotter and therefore substantially thicker than at lower speeds. It was thus anticipated that significant flight regimes exist where the viscous shear layer may not be neglected, and an extension of viscous-interaction theory to include strong blowing was derived. As explained earlier, sufficiently far downstream from the leading edge the interaction remains weak, since flow disturbances caused by the blown gas and the shear layer are small. At points closer to the leading edge, however, the shear-layer thickness is as large as, or larger than, the wedge thickness and the interaction with the external flow is strong. The analytical ideas are discussed in a paper [11] (Appendix A) which has been accepted for publication in the Journal of Fluid Mechanics. The shear layer has been assumed laminar, since, as already discussed, for typical values of Mach number and Reynolds number transition to turbulence is not expected to occur on the wedge. The temperature of the blown gas is considered to be much lower than the high temperature in the shear layer.

In the limiting cases considered, solutions can be obtained for the thin layer of blown gas adjacent to the surface, for the thin viscous shear layer, and for the outer inviscid-flow region between the shear layer and the shock wave. Certain constants are obtained by suitable matching conditions, and the end results are surface pressure distributions for both the strong- and weak-interaction regions. The introduction of an interpolation formula then provides an approximate description of the surface pressure over the entire length of the wedge and allows integration to give a relation between the blowing rate and the change in the pressure force.

A numerical solution was required for the system of equations describing the shear layer. The desired solutions proved difficult to compute since they exhibit singular behavior at the lower boundary (closest to the wedge) of the shear layer where the temperature and velocity are low, a property which was understood only after a substantial amount of numerical experimentation; once the behavior of neighboring solutions was known, a suitable numerical procedure could be developed. The two-point boundary-value problem to be solved was one in which the location of the lower boundary is not known a priori and may only be determined after it is further specified that the numerical solution must have the proper asymptotic behavior as the lower boundary is approached (the velocity and temperature must vary as specific powers of the coordinate). As an additional complication, it was found that the required behavior, based on the asymptotic solutions that were derived analytically, occurs in an extremely small neighborhood of the lower boundary, typically between 10^{-4} and 10^{-3} times the size of the overall computational domain. Numerically this requires an exceptionally high level of resolution near the lower boundary. Initial attempts at solving the problem using a shooting method, together with asymptotic solutions and certain invariance properties of the system, were unsuccessful. A Newton-based finite-difference scheme utilizing continuation, with the location of the lower boundary treated as the free parameter, was ultimately found to be successful. A complete description is given in a paper [12] submitted to the Journal of Computational Physics (Appendix A). In Fig. 4 (similar to Fig. 2 from Ref. 12) typical computed solutions for the scaled velocity and temperature profiles in the shear layer are shown and a comparison is made with the asymptotic solutions near the lower boundary. It may be seen that the agreement between the numerical and analytical solutions is very good, and thus provides a validation of the numerical computations.

Initially, asymptotic solutions were obtained for the case of air injection at constant wall density, with air treated as an ideal gas (constant specific heats and no dissociation). The formulation was then extended to include injection of a chemically inert foreign gas with either constant wall density or constant wall temperature. Finally, to provide a measure of the extent to which ideal-gas results are changed, the analysis for the weak-interaction region was repeated for injected air using equilibrium chemistry, with the effects of variable specific heats and dissociation of oxygen included (the first deviations from ideal-gas behavior as temperature increases). Numerical results have been obtained for a range of Mach numbers and altitudes, for different wedge angles and lengths, for different blowing intensities and surface temperatures, and for various injected gases. The results are contained in a paper presented at the AIAA Aerospace Sciences Meeting in Jan. 1990; an extended version [8] (Appendix A) including a calculation with oxygen dissociation has been submitted for publication in the AIAA Journal .

In Fig. 5 (Fig. 3 from Ref. 8) the scaled surface pressure distribution (measured relative to the undisturbed surface pressure) is shown for a wedge with three different values of a scaled blowing rate. (See Ref. 8 for complete definitions of these quantities.) For each blowing rate, the asymptotic solutions for the weak and strong interaction regions are indicated by dashed lines, and the interpolated solution by a solid line. The pressure variation in Fig. 5 results from strong blowing normal to the wall, with the injected mass flux varying as a particular power of the coordinate x, a choice made, as pointed out previously, to allow reduction of the partial differential equations to ordinary differential equations.

Note that, as would be expected, the pressure increases as the blowing rate increases. Note also that, for a given blowing rate, the surface pressure decreases monotonically in the streamwise direction, a feature to be expected since a favorable pressure gradient must be present to drive the injected gas downstream. To achieve a more general pressure distribution, one would probably require injection through discrete strips.

A principal result of the analytical work is shown in Fig. 6 (Fig. 5, Ref. 8), where a scaled change in force on a wedge of length L with vertex half-angle α is plotted against a scaled mass-flow rate for various cases, all with constant wall temperature. In general, the scaled force change depends not only on the scaled blowing rate, but also on the type of injectant, the ratio of wedge length L to the reference length X_r (where X_r gives the approximate boundary between strong and weak viscous interaction), and the hypersonic similarity parameter $M_\infty\alpha$ (which equals the component of the free-stream Mach number M_∞ normal to the wedge surface, for small α). Three limiting cases are shown for air injection. For $L/X_r \rightarrow 0$, strong interaction occurs over most of the wedge, and the solution is independent of $M_\infty\alpha$ in a first approximation, since the total displacement thickness is large in comparison with the wedge thickness. For $L/X_r \rightarrow \infty$, weak interaction occurs over most of the wedge, and for a fixed scaled blowing rate a larger force change is found for $M_\infty\alpha \rightarrow \infty$ than for $M_\infty\alpha \rightarrow 0$, as might be expected since the latter case can be interpreted as describing a wedge thickness which tends to zero in comparison with the total thickness of the region of disturbed flow. It appears worthwhile to note that all other cases for air injection will lie in the region of the figure bounded above and below by the two curves for $L/X_r \rightarrow \infty$.

Also shown in Fig. 6 is a comparison between air and helium as injectants, for $L/X_r=1$ and $M_\infty\alpha=1$. As in the inviscid-flow case considered by Cole and Aroesty [10], it is seen that strong blowing of a gas lighter than air, in this case helium, yields higher surface pressures and thus larger force changes for a fixed mass flow than would be found when air (or a gas heavier than air) is used as the injectant. Interestingly, this trend appears to become reversed when the strength of the blowing decreases. It is found that the high specific heats of light injectants cause substantial cooling of the viscous layer, thereby reducing its thickness. At quite low injection rates, where the viscous layer provides a large fraction of the total displacement thickness, this can lead to a reduction in force on the wedge. The curves for air and helium would therefore be expected to cross if they were extended to smaller values of mass flow. (Curves are not plotted near zero scaled blowing rate since it has been assumed that the blowing is sufficiently high to cause an inviscid blown layer with thickness at least of the same order as that of the shear layer; this condition is violated if the blowing rate is taken too small.)

To establish numerical orders of magnitude, dimensional values of the change ΔF in force (per unit span) and the total mass-flow rate $\dot{m}$ of injected gas (per unit span) have been computed for a range of parameter values and for various injectants, using the properties of the standard atmosphere. The solutions depend on several parameters, which can be divided conveniently into three groups. Parameters related to flight regime are M_∞ and altitude z; those characterizing wedge geometry are α and L; and those representing properties of the injected mass are $\dot{m}$, the wall temperature T_w, the ratio σ_b of the injectant molecular mass to that of air, and the ratio γ_b of specific heats of the injectant. In Ref. 8 air injection on a wedge having length 3m and half-angle 6 deg, for Mach number M_∞=15 and altitude z=30km, was selected as a baseline case. For this case it was found that rather large changes in force per unit span, of the order of 1000N/m (68.5lb/ft), are achieved with seemingly moderate injection rates per unit span, of the order of 0.1kg/m-sec (0.067lbm/ft-sec). The parameters were systematically varied and a typical result is illustrated in Fig. 7 (Fig. 6a of Ref. 8), where ΔF is plotted against $\dot{m}$ for various flight regimes, with air injection. (Also shown are results from the real-gas analysis, to be discussed later.) As may be seen, for given injectant rates the force changes increase with increasing Mach number and decrease with increasing altitude. In Ref. 8 it is shown that, for a given Mach number and altitude, the force changes increase with wedge angle and wedge length. Overall trends with changes in the parameters are about as expected.

For the higher injection rates, if a simple isothermal model for the atmosphere is adopted, and certain relatively small variations are ignored, a rough approximation showing the primary dependence on parameters is given by (Ref. 8)

$$\Delta F = \text{const.}\ (M_\infty^{\ 2}\, e^{-z/H}\, L\, \dot{m}^2\, T_w/\sigma_b)^{1/3}$$

where H is the atmospheric scale height and the other parameters have already been defined. This simple expression shows most of the major trends, although not the proper quantitative values. It is seen that the force change increases with increasing $M_\infty^{\ 2}e^{-z/H}$, a factor proportional to the free-stream dynamic pressure. Increasing the ratio T_w/σ_b of the injectant temperature to its molecular mass will cause greater displacement of the outer flow and thus also increase the force change. The dependence on wedge length L implies that it would be most efficient to distribute a given amount of blown mass over a large surface area.

At higher temperatures, real-gas effects must also be taken into account. For air, the specific heats begin to vary when $T \gtrsim 600$ K, and O_2 begins to dissociate when $T \gtrsim 2000$-2500 K, for $p \approx 0.01$-1 atm. In the real-gas analysis the temperature was assumed low enough that, to a good approximation, only the dissociation of oxygen occurs. (For pressures of the order of 0.1 atm, this assumption limits the temperature to values below about 4000 K; the limit increases with increasing pressure.) Air is then composed of N_2, O_2, and O. The real-gas analysis leads to values of the maximum temperature in the shear layer that are lower than the ideal-gas values, as would be expected. The shear-layer thickness is likewise reduced, but only by a relatively small amount; for a 6 deg wedge at 30 km altitude with M_∞=20, there is about a 5% decrease in shear-layer thickness, and a still smaller fractional change in the excess pressure force. For the two cases illustrated in Fig. 7, real-gas effects are seen to give only small changes in the force change corresponding to a given blowing rate. The differences would of course be greater if higher Mach numbers and temperatures had been considered.

Currently some of the issues relevant to strip blowing are being considered. Boundary-layer separation will occur ahead of the point where blowing is first introduced. At supersonic speeds, the flow near separation can be described by a local interaction of the viscous boundary layer with the external inviscid flow. In a recent paper [13], this kind of local flow description has been shown to remain possible at high Mach number, with certain modifications, provided that the wall is cooled and the wall temperature is well below the stagnation temperature of the external flow. We have been able to simplify the results of this work, with the intention of using these results to provide initial conditions for a study of strip blowing at hypersonic speeds. With this added information, an existing theoretical description of strip blowing at supersonic speeds [14] can be extended to higher Mach numbers. Work on the separated region downstream of a strip is in progress with consideration of a simple case where the blowing velocity at the trailing edge of the strip is small but finite.

As noted elsewhere in this report, numerical solutions have indicated an instability of the free shear layer that appears to be a genuine physical effect rather than a consequence of the computational method. Others have also encountered such an instability in numerical calculations [15]. Following a few investigations of the stability of hypersonic boundary layers, a recent analytical study considers linear instability at high Mach number for a free shear layer with a prescribed velocity profile [16]. An analytical study of vortex-sheet instability at supersonic speeds includes nonlinear effects [17], but neglects shear-layer thickness, and finds "kink" modes, with a shock wave on one side and an expansion wave on the other side. Much more needs to be done, to gain a full understanding of the conditions under which instability should be expected and to consider ways in which instability might be avoided. In particular, the nonlinear theory should be extended to hypersonic speeds, both for a vortex sheet with zero thickness and for a shear layer with nonzero thickness.

3. Numerical Approach

The computation of hypersonic flows, in the Mach-number range 8-30, puts before the computational fluid dynamists a number of problems not encountered for lower Mach numbers. Most serious is the loss of accuracy of conventional finite-volume methods when capturing strongly oblique discontinuities. In the initial research period, preceding the period covered by this final report, an attempt was made to develop a finite-volume code that would be more nearly isotropic in its treatment of oblique discontinuities. This was to be accomplished by computing inviscid fluxes in a frame locally aligned with the most prominent physical feature, for example, a shock wave.

It turned out that the development of a robust technique of this kind was far less trivial than expected. To avoid stagnation of the research, this approach was abandoned for the more standard one of generating a grid more or less aligned with the most important shock and shear waves, and cluster the grid points near those waves. (The formulation of inviscid fluxes in a frame rotated with respect to the grid is currently the subject of two thesis projects in the Department of Aerospace Engineering).

A general strategy adopted in developing the more conventional computational code was to validate the code as often as possible as greater degrees of complexity were added. For lack of experimental results, the code was benchmarked against analytically obtained flow solutions. Two decades ago Cole and Aroesty [10], and Wallace and Kemp [18], and recently Messiter and Matarrese [8, 11, and in Appendix A] were able to obtain similarity solutions for inviscid hypersonic flows over flat plates and wedges in the presence of strong surface blowing. These solutions all involve blowing distributions which are singular at the leading edge and therefore are harder to match than experimental data, thus putting strong demands on code accuracy and robustness.

Initially, an Euler code was written and used to reproduce such solutions. The code is based on a higher-order Godunov-type [19] finite-volume discretization of the inviscid Euler equations. Higher-order accuracy is obtained by reconstructing interface values of the state quantities using a monotone interpolation technique suggested by Koren [20], based on Van Leer's "*kappa*" scheme [21] [22]. The interface fluxes are computed using Roe's upwind-biased flux-difference splitting technique [23]. Standard characteristic boundary procedures are applied along the leading edge and top of the computational domain (Fig. 8). Proper treatment of the wall and exit boundaries proved to be the first real challenge in developing the code.

Wall boundary conditions were initially implemented through a combination of a characteristic boundary condition and a ghost cell approach. The desired blowing distribution was achieved by specifying the velocity magnitude, direction and either the density or temperature in the ghost cells just "below" the wall. The pressure in these cells was then determined by extrapolating an incremental form of the Riemann invariant to the wall in a characteristic boundary procedure. The incremental form of the Riemann invariant was, and still is, used, since the flow may not be locally isentropic near the wall. This method, though very robust, did not enable precise specification of the mass flux along the wall. The actual mass flux resulted from the application of Roe's approximate Riemann solver at the cell interfaces along the wall boundary. It was determined that in order to accurately reproduce the types of injection distributions used in the analytical solutions, a more exact method of specifying the inflow boundary conditions was required. Instead of specifying the flow values in the ghost cells, the same extrapolating methods are used to specify the flow values at the boundary itself. From these quantities, the exact inflow fluxes may be derived. This provides a greater degree of control over the injection distribution, but it also results in a less robust boundary procedure.

Along the rear portion of the grid where the flow exits the computational domain, both supersonic and subsonic outflow conditions exist. For the subsonic exit flow region, a characteristic boundary procedure requires the specification of some flow parameter, such as the pressure, along the boundary of the grid. Since little is known about the solution a priori, this is not possible. An order-of-magnitude analysis of the governing equations shows that the pressure is nearly constant across the blown layer which contains the subsonic region. Initially, a pressure was extrapolated from the supersonic exit region down to the subsonic region assuming a zero pressure gradient normal to the wall. This enabled the use of a standard characteristic boundary procedure. Unfortunately, such a scheme delays, or even prevents, convergence of the solution.

A time-dependent non-reflecting characteristic boundary condition developed by Hedstrom [24] of the form

$$\frac{\partial p}{\partial t} - \rho a \frac{\partial u}{\partial t} = 0$$

was considered, but was found to produce a steady state which was dependent upon the initial conditions. It was noted, however, that by introducing the pressure gradient normal to the wall as a source term in Hedstrom's condition, it becomes an effective mechanism for enforcing the proper behavior of the pressure along the exit boundary. This exit boundary condition has the form

$$\frac{\partial p}{\partial t} - \rho a \frac{\partial u}{\partial t} = -K\,(u - a)\,\frac{\partial p}{\partial y}$$

where K is a constant, typically taken to be between 0.1 and 10. If K is taken too small or too large, convergence to a steady state is delayed.

Two different time-marching algorithms were considered during the development of the code. It was first considered to use a block-Gauss/Seidel technique, used by Koren [20]. This algorithm updates while sweeping through the grid in the coordinate directions, updating all flow variables in one cell simultaneously. For two-dimensional flow, this requires the inversion of a local 4 x 4 matrix. This method turned out to be less robust than was anticipated.

Especially in the initial phases of the calculation, when strong transients are present, severe under-relaxation was needed to prevent loss of positivity, i.e. temperatures becoming negative, which considerably reduced the efficiency of the method. In the later stages of convergence, time-steps corresponding to Courant numbers of the order of 10 could be maintained.

A well-known disadvantage of sweeping algorithms such as Gauss/Seidel, is that they do not lend themselves very well to vectorization. When CPU time on the Cray machines at the National Aerodynamic Simulator facility became available, it became desirable to select a method more compatible with vector processing.

The answer was found in certain multi-stage explicit marching methods concurrently developed [25] at the Aerospace Engineering Department. These methods, when applied to a scalar convection equation, achieve optimal damping of high spatial frequencies in the instantaneous error (the deviation from the steady solution). The more stages the method includes, the better the short-wave damping becomes; since strong transients usually contain strong spatial high-frequency components, methods with good short-wave damping are expected to be robust. The experience in using these methods for the full nonlinear Euler equations in the hypersonic flow regime indicates that the two-stage method performs as well as any of the more-stage methods, and is more robust. The reason probably is that using many stages leads to a larger time-step for the multi-stage method than is warranted by the linear analysis on which the scheme's coefficients are based.

The two-stage scheme is a simple predictor-corrector method for solving the equation

$$\frac{\partial U}{\partial t} = L(U) ,$$

namely,

$$\begin{aligned} \tilde{U}^{n+\alpha} &= U^n + \alpha \, \Delta t \, L(U^n) \\ U^{n+1} &= U^n + \Delta t \, L(\tilde{U}^{n+\alpha}) \end{aligned}$$

where n indicates the iteration number. The parameter α is adjusted such that the overall method is most dissipative for the high-frequency part of the spectrum for the spatial differencing operator L(U). For example, if L(U) is the first-order upwind differencing operator, the optimal value of α is 1/3, and is associated with a time step Δt corresponding to a Courant number of 1/2 (half the maximum allowed by stability for this operator). For the third-order spatial differencing scheme adopted in the code, the value of α becomes 0.6612 and the associated Δt corresponds to a Courant number of 0.8276.

Proper construction of a computational grid proved crucial in obtaining accurate solutions of flow fields for which analytical solutions exist. Strong blowing distributions which extend up to the nose of a wedge result in strong, highly curved shocks. Blowing distributions which are singular at the nose (x=0) require a great deal of refinement at the nose in order to adequately resolve the singularity. To keep the total number of grid points down to a manageable level, the grid point spacing increases away from the nose (by about 10% per cell typically). Representation of a strong curved shock on a grid with uneven spacing in the x and y direction can result in solution inaccuracies and even non-convergence.

As the shock changes its orientation relative to the grid, its numerical "structure" changes. For example, if the shock is aligned with the grid in one direction, the shock can be resolved to within a single cell, whereas when the shock passes through the grid at an oblique angle, it can be smeared over 4 to 5 cells. The difference between these two representations of the shock is also manifested in different post shock entropies or densities. This was one of the main motives behind the early work in calculating interface fluxes in a frame locally aligned with the shock instead of the grid. Fig. 9 shows a carpet plot of the density for a case in which this effect is very prominent. Notice that the post shock density varies non-smoothly along the shock as it changes its orientation to the grid. These density variations are then convected back into the flow.

Rapid variations in the numerical representation of the flow can also lead to non-convergence of the flow solution. After decreasing several orders of magnitude, the residual becomes nearly constant in the distorted region, and is convected back with the flow. The exact mechanisms behind this phenomena are not clear, but the problem can be eliminated by better alignment of the grid with the flow.

The code was used to calculate solutions for three different comparison cases for which analytical solutions exist. The cases considered were for an inverse-square-root injection-velocity distribution along a flat plate in both the strong and weak interaction regions and along a wedge in the weak interaction region. In each comparison case, good agreement was obtained between the analytical and numerical solutions. This validation study was developed into a paper entitled "Euler Computations of Hypersonic Flow with Strong Blowing" and presented at the AIAA 28th Aerospace Sciences Meeting in Reno, Nevada (26, and in Appendix A).

With the completion of the inviscid code validation study, viscous terms were added to the code in order to model the Navier Stokes equations. The discretization of the diffusion terms is done by second-order-accurate central differencing [27]. This preserves the second-order spatial accuracy of the entire scheme.

Validation of the Navier Stokes code began with a calculation of a subsonic boundary layer on a flat plate. Fig. 10 shows good agreement between the scaled numerical velocity profiles and a Blasius profile. The code also compared well with numerical solutions generated at NASA Langley [28] for high Mach number flows in a nonseparated compression corner. Next, a comparison with an analytical similarity solution derived by Messiter, Matarrese, and Adamson [8, and in Appendix A] was attempted for flow over a wedge in the strong interaction limit in which the shear-layer thickness is of the same order as the blown layer thickness. The case of constant-temperature air injection was chosen, with the temperature of the injected air equal to that of the free-stream air, and injection velocity specified proportional to $x^{1/4}$. Free-stream flow parameters were;

$M_\infty=25$,
$Re_\infty=50{,}000$,
$Pr_\infty=0.72$,
$\alpha=5°$.

where α is the wedge half angle. A power-law viscosity-temperature relation $\mu=T^{0.75}$, was used to be consistent with the analytical work. It was found that for this case, the resulting shear wave was unstable and oscillated back and forth (Fig. 11). The instability can be eliminated by increasing the temperature, and hence, the viscosity coefficient of the injected gas. Fig. 12 shows a converged case in which the injected air temperature was equal to four times that of the free-stream air. Unfortunately, such a case compares poorly with the similarity solutions. The analytical work predicts a wall pressure distribution of the form

$$\frac{P}{\rho_\infty U_\infty^2} = \frac{\alpha^2}{\gamma}\, P_1^{(s)} \left(\frac{L}{X_R}\right)^{-1/2} (x)^{-1/2}$$

where the ratio of the plate length L to the viscous interaction length X_R is equal to 0.0232 and $P_1^{(s)}$ is equal to 0.74476. Fig. 13 shows a comparison between the numerically determined pressure distribution along the wall and the analytical prediction. The reason for the discrepancy is not completely clear. The numerical solution predicts that the shock will be detached from the leading edge of the wedge whereas the analytical solution assumes that it is attached. Also, as the temperature is increased in the blown layer, viscous effects become more important yet are assumed negligible in the analytical blown layer.

The exact nature of the instability, namely, whether it is purely physical, or partly numerical, is not clear at present. There certainly is a physical basis to the unsteady wave-forms, but it is also clear that truncation error present in the code may influence or even trigger the instability. From a physical point of view, it is not clear whether the instability of these layers is linear, i.e., comparable to the inviscid Helmholtz instability, or nonlinear. Numerical experiments indicate it can be removed by increasing the physical viscosity. In the inviscid case, where the instability was also observed [26, and in Appendix A], it can be removed by maintaining the proper level of artificial viscosity, namely by downward limiting of the computational cell size. It is conjectured that numerical "noise", generated at the leading edge, where the flow gradients are very large, especially for the singular blowing distributions considered, may seed the instability and cause it to appear as a severe disturbance in flow cases where it otherwise would become visible much farther downstream. This explanation is due to Woodward [15], who encountered a similar shear instability in supersonic channel flow.

The case of constant-density air injection was also considered. The same free-stream parameters were retained from the previous cases, and the injection parameters were chosen so that the blown layer and shear layer thicknesses would again be equal. With an injected air density equal to 25 times free-stream density and an injection velocity specified proportional to $x^{1/2}$, a stable solution was obtained. Unfortunately the numerical and analytical predictions of the wall pressure do not agree (Fig. 14). As before, the shock in the numerical solution stands off ahead of the leading edge of the wedge. Also, for the constant density case, the temperature distribution of the injected gas varies as $x^{1/2}$ (Fig. 15). With such high temperatures near the leading edge, it is not clear that viscous effects would be negligible everywhere in the blown layer as assumed in the analytical model. This would indicate that the constant-temperature injectant case, while not only more physically realistic, should provide the best comparison.

In an attempt to obtain a stable constant-temperature injectant solution which compares well with the analytical predictions, the code was modified to handle injection of a gas different from the free-stream gas. This modification required the addition of a species conservation equation to the computational code. Diffusion coefficients are calculated using proportionality factors which are consistent with the analytical work [8, and in Appendix A]. It was anticipated that injecting a gas with a lower molecular weight would decrease the Mach number in the blown gas layer, and help to stabilize the shear layer. In practice, it was found that with the same free-stream conditions and apparent body shape as in the previous cases, but with helium injected at free-stream temperature, the shear layer was again unstable. If the temperature of the injected helium is raised to twice that of the free-stream air, the shear layer can be stabilized, whereas air injection required a blown gas temperature of four times the free-stream temperature before a stable solution was obtained. This indicates that use of a lighter gas as an injectant not only provides greater net body force for a given mass flow rate, but may also help to stabilize the flow. However, the comparison with analytical results, although better, is not considered satisfactory as yet; again, this may be due to some assumptions made in the derivation of the analytical results. More research is required in the area of hypersonic shear layer stability before the relationship between temperature and molecular weight variation across the layer and the stability of the layer can be completely understood.

Calculations were also performed involving more practical blowing distributions such as blowing in discrete strips. Fig. 16 shows Mach number contours for a case in which helium was blown from a 10° half angle wedge in two strips from $0.2 < X < 0.4$, and $0.6 < X < 0.8$ with uniform velocity and temperature along each strip. Free-stream conditions for this case were

$$M_\infty = 25\ ,$$
$$Re_\infty = 50{,}000\ ,$$
$$Pr_\infty = 0.72\ .$$

Of particular interest in this solution are the two regions of separated flow which result from the discrete blowing pattern. Fig. 17 shows velocity vectors in the separated flow region created just ahead of the first blowing strip. The size of this region is not geometrically defined in that the length of this region is dependent upon the blowing strength. In numerically generated 2-D representations of such flows, we and others [28] have found that the length of the separation region is also dependent upon grid resolution of the flow. This makes accurate calculations of such flows very difficult. Adding to the difficulty of such calculations is the fact that free separated regions tend to develop very slowly numerically, resulting in high computational costs. Due to the frequent occurrence of such separated regions in flows with discrete strong blowing, more research is warranted to find ways to rapidly and accurately resolve free separated flows. Fig. 18 shows velocity vectors for the recirculation regions which occur between the two blowing strips. The length of such a region is geometrically defined by the spacing of the strips, but the effect of grid resolution on the resulting flow pattern is not yet known.

4. Summary and Conclusions

Based on the work completed to date, it seems clear that it is possible to obtain significant aerodynamic forces by injecting gas from the surface of a hypersonic vehicle at relatively low rates of mass flow. For example, if one imagines a 1000 lb vehicle, say 10 feet long with a span of 2 feet at an altitude of 30 km and a Mach number of 15, then a one-g maneuver would require a force per unit span of 1000/2 = 500 #/ft = 7300 N/m. From Figure 6c of Reference 8 (in Appendix A) it is seen that an injection rate of roughly 0.40 lbm/sec of hydrogen is required. This injection rate is evidently enough to cause the boundary layer to leave the surface, thus causing a considerable change in equivalent body shape and hence pressure distribution and body force. Thus, this type of aerodynamic control appears feasible.

The general pressure distribution obtained with distributed injection is, as seen for example in Fig. 5 is one in which the pressure and thus the body force, decreases along the body. This must be the case, of course, if the fluid is to flow along the body. Such a force distribution may not be the one desired for a given maneuver; in that event, a series of strips from which gas is injected at differing rates is needed. Hence, strip blowing must be considered as an important part of this study. Moreover, because it may be necessary, for practical reasons, to begin gas injection somewhat downstream of the foremost point of the body, the flow field near the nose will be similar to that at the beginning of a strip. In this event, separated flow regions of varying size will occur at the beginning and the end of the strip. As mentioned previously, an inability to reproduce numerically a separated flow region in the same number of iterations as required for the rest of the flowfield is a problem common to all known codes for supersonic and hypersonic flows; in general, the separated flow regions require three to ten times the computer time needed when no separation occurs. Because there are so many separated flow regions when strip blowing is considered it is necessary that more efficient methods of calculation be found. Some work on this problem has been done during the latter part of this contract year. More remains to be done and is mentioned later in the section on suggestions for new work. Analytical work on the strip blowing problem has also been initiated, is also incomplete, and is mentioned later in suggestions for new work.

The inclusion of the effects of chemistry, through consideration of dissociation of oxygen in a simple example solved analytically, indicates that the expected decrease in maximum temperature occurs; that is, some of the thermal energy is used to dissociate the oxygen molecules. The net effect on the force change is shown to be minimal, in the example considered. However, this cannot be taken to be a general result as yet. More cases, including those involving the more complex issues associated with the injection of a reactive gas such as hydrogen, must be considered. Again, the inclusion into the numerical code of the ability to handle enough mixture components and the calculation of equilibrium concentrations such that hydrogen injection may be considered has been begun, but is not completed as of the end of the contractual period; inclusion of this capability is mentioned in suggestions for future work.

It should be noted that the studies proposed and carried out under this contract are for steady state flow fields. This is certainly a proper condition to consider for the first step. However, there are cases for which a control would be actuated intermittently, rather than on a steady basis. In that event, it is necessary to analyze the unsteady flow field structure and thus the time dependence of the force distribution, for various starting and stopping control procedures. Such studies are proposed in future work.

In summary the essential contributions of the research have been the establishment of the viability of gas injection as a possible aerodynamic control, solutions for several benchmark example cases, the development of a code valid for conditions under which the flow may be considered to be inviscid, the development of a Navier-Stokes code for cases where viscous effects are important, and the initiation of definitive studies of strip blowing and the effects of chemical reaction, all at hypersonic flow velocities; the body shape considered was a thin wedge. It should also be mentioned that two graduate students, Michael Matarrese and Nelson Carter, have been supported through a large part of their advanced graduate work by this contract, their thesis work being on the analytical and numerical approaches described above. In approximately one year, they should graduate and be in a position to join the professional community in gasdynamics.

Part II. Optimal Aerodynamic and Propulsion Control of Intercept Trajectories at Supercircular Speeds

1. Introduction

The primary goal of the research in Part II has been to investigate trajectories and basic design parameters for high-performance, multistage, earth-based interceptors with ranges of several thousands of miles and flight times of a few minutes. Such interceptors offer a possible alternative to the space-based interceptors which are currently being considered in the U. S. Strategic Defense Initiative. While the earth-based interceptors have many obvious advantages, they impose severe requirements on the propulsion system; both the stage accelerations and ratio of launch mass to payload mass must be very large. Solid propellent engines offer the capability of producing the required accelerations and small guided warheads can contribute greatly to the reduction of the payload mass. However, even with relatively small payloads, the high launch mass remains a critical concern. This has led us to base our research on the minimization of the mass ratio with respect to the trajectory and the design parameters. A key result of the research is the importance of using aerodynamic forces. When they are properly exploited during the midcourse phase of the trajectory, a sizable reduction in the launch mass is achieved.

Specific contributions of the research include: a good understanding of the basic form of the optimum trajectories including the midcourse aeroassisted phase, the nature of the optimal stage design, the effect of target parameters and trajectory constraints on the optimum launch mass, effective tools for implementing reliably and efficiently the numerical optimizations, approximate analytical characterizations of the separate phases of the optimal trajectories, simple methods for attitude control which may help to minimize the mass of the final guided stage, and methods for evaluating the targeting capabilities of the final stage. In the remaining paragraphs of this section, these contributions are reviewed briefly along with some comments on how the research has evolved. Subsequent sections go into greater detail and make connections with with material in prior progress reports [1-7] and technical papers [29-37, and in Appendix A] which have been written under the contract.

Because of their very short flight times and long ranges the ground-based interceptors require terminal speeds significantly greater than circular orbital speeds. At the onset of the research activity little was known about the effect of such speeds on the design of the stages and the ascent and intercept trajectory. It was clear that a down-force would be needed on the final stage (or stages) to keep the trajectory from escaping to altitudes far above target altitudes.

Since it does not consume engine fuel, an obvious candidate for generating the down-force was negative aerodynamic lift. However, little was known about when and where in the trajectory that such aeroassisted forces should be applied.

Answers to the stage-design and trajectory questions were sought by minimizing the overall vehicle mass ratio with respect to variables such as: stage size parameters, engine burn times, coasting times between stages, and the angle-of-attack program. This is a formidable numerical optimization problem and much of the research activity was devoted to its formulation and solution. The formulation involved models of: the aerodynamic forces, atmospheric density, vehicle structure, engine performance, and equations of motion [Section 2] Other concerns were: approximate finite dimensional parameterizations of the infinite dimensional control function (angle of attack) [Section 3], fast methods for accurate integration of the equations of motion (thousands of solutions were needed to compute each optimal trajectory)[Section 4], and the choice of an optimization algorithm [Section 3]. In the beginning relatively simple optimization problems were solved and most of the effort was put into the integration algorithms. As problems of greater difficulty were considered the optimization problems became poorly conditioned, seriously affecting the reliability of the optimization algorithms. The poor conditioning was overcome by a new scheme for (indirectly) parameterizing the angle of attack through the flight path angle [Section 3].

As the numerical work proceeded it became possible to generate optimal trajectories for a wide variety of target conditions. A general pattern emerged [Section 5]. The optimal ascent trajectories consisted of three phases: a boost phase, in the atmosphere, to an altitude of approximately 65 km.; an aeroassisted, coasting phase near the 65 km. altitude; an essentially out-of-the-atmosphere coasting phase where the trajectory rises to intercept the target. The details of an example optimal solution for a five-stage interceptor are shown in Fig. 19. The three phase character of the optimal trajectory is evident. The flight time is six minutes; the range is 3100 miles; the mass ratio is 1,900. Later, more extensive parametric studies were performed. They show [Section 5] the effect on launch mass of such parameters as the time of flight, the intercept altitude, the number of stages, the specific impulse of the engines. They also show that eliminating the aerodynamic lift or imposing certain altitude constraints on the ascent trajectory can increase significantly the optimal mass ratio.

Based on the results of the general optimization studies it has been possible to develop simplified models for each of the three trajectory phases. These models give insight into the form of the optimum trajectories and lead to faster, reasonably accurate, approximate solutions of the optimization problem. The model for the aeroassisted, mid-course phase assumes that speed and altitude are connected by a function (called the universal curve) that is determined by balancing the difference between centrifugal and gravity forces by negative aerodynamic lift at the maximum lift-to-drag ratio [Section 6]. On the universal curve all flight motions are defined by simple formulas. The final ascent phase is essentially Keplerian and for a fixed target it can be determined by a solution of the Lambert problem. The boost phase is represented by a simplified modelling of the staging parameters and simple functional representation of the flight path angle [Section 7].

Another series of investigations explored questions concerning possible maneuvering of the final stage when it is out of the sensible atmosphere. As has been indicated, it is essential to reduce as much as possible the mass of the final stage. If attitude control is needed, this places a premium on the simplicity of the control scheme. An implementation for a spinning stage, which uses thrust modulation of a single side-thrusting control jet has been developed [Section 8]. It produces minimum-time attitude control maneuvers and realizes the required complex feedback control law by a simple on-board computer implementation. Still another investigation concerns out-of-the-atmosphere, fuel-optimal interception. Suppose, during the ascent of the final stage, data on a specified target is transmitted to the stage and it is desired to intercept the target within a given time and to minimize the mass of the fuel required to achieve the interception. When the available engine thrust is large, a method for computing the required thrusting program has been obtained [Section 9]. Finally, suppose the thrusting capability of the final stage is given and its initial state as it leaves the atmosphere is known. What is the set of targets that may be intercepted by all possible maneuvers of the final stage? This question may be answered if the reachable domain of the stage (the set of positions which can be reached in a given time) is known. Considerable progress in characterizing the reachable domain has been made, both for intermittent thrusting of high-thrust engines and for continuously thrusting engines [Section 10].

2. Modelling the Multistage Interceptor

When the launch and target points have been specified, they determine a plane passing through the center of the earth. Motion out of this plane consumes additional engine fuel. Thus, to minimize the launch mass it is sufficient to describe the motion of the interceptor in the plane. Specifically, there is no great loss of accuracy if it is assumed that all stages of the interceptor are modelled as a point mass moving in a plane which contains the center of a spherical, non-rotating earth with an inverse-square gravitational field. In dimensionless form the equations of motion have the form

$$\frac{dR}{d\tau} = V \sin\gamma , \quad \frac{d\theta}{d\tau} = \frac{V \cos\gamma}{R}$$

$$\frac{d\gamma}{d\tau} = \frac{1}{V}\left[\frac{A \sin\alpha + L}{M} + \left(\frac{V^2}{R} - \frac{1}{R^2}\right)\cos\gamma \right],$$

$$\frac{dV}{d\tau} = \frac{A\cos\alpha - D}{M} - \frac{\sin\gamma}{R^2}, \quad \frac{dM}{d\tau} = -\frac{A}{I_{SP}}. \tag{1}$$

where: τ is dimensionless time, R is proportional to the distance of the stage from the center of the earth, θ is its polar angle, V is proportional to its speed, γ is its flight path angle, M is proportional to its mass, α is its angle of attack, A is a dimensionless thrust, and I_{SP} is the specific impulse of the engine. The dimensionless lift and drag forces are given in terms of the dimensionless altitude $H = R$-1 and V by

$$L = \frac{1}{2}\eta P(H) V^2 C_L, \quad D = \frac{1}{2}\eta P(H) V^2 C_D. \tag{2}$$

where η is a constant, P is proportional to atmospheric density, and C_L and C_D are, respectively, the lift and drag coefficients. These equations are highly nonlinear and illustrate the complexity of the dynamics for each stage.

In the early phases of the research a variety of models of varying complexity were considered for the functions P, C_L and C_D. See the progress reports [1-7] and papers [29, 30, and in Appendix A]. Smoothness of the functions is vital to the proper functioning of the minimization algorithms, so table-look-up schemes cause problems. It was learned through experience that relatively simple models (exponential density and Jorgensen's formulas for lift and drag) affected little the accuracy of the optimal solutions.

The control variables are the angle of attack $\alpha(\tau)$ and the engine thrust magnitude A. The angle of attack generates the ascent program and is a function of time. For solid propellent engines, the engine is either off or at full thrust. Thus, its time dependence can be represented by two parameters: a coast time and a burn time. The thrust magnitude for each stage is determined indirectly by the burn time and fuel mass for the stage. By making some simplifying assumptions concerning the structural efficiencies of the stages, it is in turn possible to obtain the initial stage masses and the fuel masses from the initial launch mass of the interceptor and parameters σ_i which denote the ratio of the payload mass to initial mass for each stage. Finally, the physical dimensions of each stage, which are necessary for computing the lift L and drag D, are determined from the stage masses and some sizing assumptions. Thus, the complete trajectory and vehicle design data are determined by the angle-of-attack program for each stage, the initial launch mass of the entire interceptor, the burn and coast times, and stage mass ratios σ_i. See the quarterly progress reports [1-7] and paper [33, and in Appendix A] for full details.

Given the angle-of-attack programs and the indicated data, it is possible by using the equations of motion to determine the entire trajectory of the interceptor. At launch the initial conditions of the interceptor are known: $R(0) = 1$ and $\theta(0)$ specify the launch position in the plane of motion (without loss of generality it is possible to set $\theta(0) = 0$), $\gamma(0) = 90$ degrees (vertical launch), $V(0) = 0$, $M(0) =$ initial launch mass. Thus, the first stage equations of motion can be integrated to generate the motion of the first stage. After staging, the parameters of the second stage, including its initial mass, are determined as has been described in the previous paragraph. The variables R, θ, V, and γ are continuous across staging. Thus, their initial values are known at the beginning of second-stage flight and again the equations of motion may be integrated. Similarly, the entire trajectory is determined.

3. The Optimization Problem and Its Solution

The optimal interception problem is stated in terms of the model of the previous section. The required data of the problem are: the total flight time of the interceptor from launch to interception, the target range angle = θ_f, the target altitude = h_f and the payload mass. The optimization objective is to minimize the total launch mass. The free variables in the interception are: the angle-of-attack programs for each stage, the coasting and burn times for each stage, and the mass-ratio parameters. Thus, there are equality conditions which must be met (final conditions on the interceptor altitude, range angle and mass) and a cost function to be minimized (the launch mass). In addition, there may be constraints on the free variables, such as upper and lower limits on coast and burn times and the stage mass ratios.

The above optimization problem is actually an optimal control problem with parameters, where the control function is the angle-of-attack program $\alpha(\tau)$. Many approaches for solving such problems (particularly single stage problems) have been discussed in the literature. See, e.g., the discussion in papers [32, 33, and in Appendix A]. The difficulty in solving optimal control problems is that the control function belongs to an infinite dimensional space and computations must take place in a finite dimensional space.

Our initial approach to numerical solutions was to approximate $\alpha(\tau)$ by simple finite-dimensional representations such as piecewise linear functions [5]. Thus, the optimal control problem is approximated by an optimization problem with a finite number of parameters (the original free parameters plus the parameters which determine the representation for $\alpha(\tau)$). While this approach is simple and very flexible and produced good results on certain problems, it proved to have a fatal shortcoming. It often produced optimization problems which were very poorly conditioned. For example, small changes in the angle of attack at the beginning of the flight produced very large changes in the variables at the end of the flight. This sensitivity caused the minimization algorithm to fail or have very slow convergence. These difficulties are well documented in our earlier progress reports [1-7].

The poor conditioning was eventually overcome by parameterizing $\alpha(\tau)$ indirectly through a direct parameterization of the flight path angle $\gamma(\tau)$. In this approach, $d\gamma/d\tau$ is computed from the parameterized $\gamma(\tau)$ and then substituted, together with R, γ, V and M, into the third equation of (1). This equation then becomes through $\sin\alpha$ and L an implicit equation in α. The indirect parameterization of α is obtained by solving the implicit equation. Note that this eliminates the need to integrate the differential equation for $d\gamma/d\tau$. Of course, the remaining differential equations in (1) must be integrated as usual. When the indirect parameterization is used, the entire trajectory is under more direct control. Changes in $\gamma(\tau)$ near the beginning of the trajectory have very little effect on the terminal portions of the trajectory. Thus, the sensitivity of the terminal constraints to the parameterization is greatly reduced. Another advantage, perhaps less important, is evident at launch. Here, the differential equation for $d\gamma/d\tau$ has a singularity because $V = 0$. With the γ parameterization the differential equation is not integrated and the normally troublesome singularity is circumvented. Other issues involving the indirect parameterization such as imposing various smoothness conditions on the angle of attack and pitch angle are discussed in the progress reports [1-7] and [32, 33, and in Appendix A].

A good deal of effort and experience was involved in setting up the numerical optimization algorithms which were used to solve the finite dimensional problems resulting from the γ parameterization. The following is a brief review. The basic approach was an augmented Lagrangian method. This method addressed directly the equality constraints. The various inequality constraints on the problem parameters were handled indirectly by nonlinear transformations, a technique which proved to be simple and reliable. The iterative descent algorithm was of the BFGS type. At each iteration it requires the numerical evaluation of the errors in meeting the terminal conditions and their partial derivatives with respect to all of the parameters. Because of the highly nonlinear character of the optimization problem it was necessary to compute these partial derivatives by finite differences. This process introduces appreciable rounding errors, which at times affected the reliability of the optimization procedure. Such difficulties were overcome by careful attention to numerical details, e.g., in the integration of the differential equations at the staging times and in the use of smooth functions to represent problem nonlinearities. Because of the finite-difference derivatives, each solution of a typical optimization problem involved over 4000 solutions of the differential equations. The corresponding computational time was about 2 hours on an Apollo DN 4000. Again, further details are available in the progress reports [1-7] and [32, 33, and in Appendix A].

4. Numerical Methods for Integrating Equations of Motion

It has already been pointed out that thousands of individual trajectory solutions are needed to compute each optimal trajectory solution. For this reason there is a great deal of leverage on selecting accurate and efficient numerical integration algorithms. Early in the research program it was demonstrated that a single-pass, fifth-order Adams-Moulton (SPAM-5) predictor-corrector algorithm provides much better computational performance than the traditional fourth-order Runge Kutta (RK-4) algorithm [30, and in Appendix A]. Conventional AM predictor methods consist of two integration passes per overall integration step, a predictor pass and a corrector pass. In the single-pass version all state-variable derivatives are based on the predicted values of each state variable. For this reason only one derivative evaluation is required per integration step. Therefore the method runs approximately twice as fast as conventional AM-5 integration and four times faster than conventional RK-4 integration. This, combined with the dependence of dynamic errors on h^5 rather than h^4, where h is the integration step size, accounts for the improved efficiency of SPAM-5 versus RK-4. There is, however, a startup problem associated with predictor algorithms because of their dependence on past as well as current state-varianle derivatives. For the SPAM-5 method this problem was solved by using a special Gear RK-4 startup algorithm [30, and in Appendix A]. It was necessary to use this startup algorithm whenever staging took place as well as initially when integrating the trajectory equations.

Another major improvement in trajectory integration efficiency was obtained by using an analytic formula rather than numerical integration to compute the velocity gained each integration step due to engine thrusting. Only the much smaller effects of gravity, Coriolis, centrifugal and gravity accelerations need to be integrated numerically. This also results in a substantial improvement in computational accuracy.

The overall effects of the improvements in integration methods as described above can be seen in Fig. 20, which shows the error in burnout position versus dimensionless integration step size for a typical 4-stage ascent trajectory. The step size for the RK-4 data points in the figure has been decreased by a factor of four over the step size actually used to take into account the four passes per RK-4 integration step. Thus the reciprocal of the step sizes shown in the figure is a true measure of the relative computational speed associated with each method. Plots 1 and 2 in the figure compare the accuracy of RK-4 and SPAM-5 integration when the angle of attack α is used as the control variable in the optimization program. Clearly the SPAM-5 is roughly an order of magnitude more accurate for a given step size. Conversely, for a given accuracy, the SPAM-5 runs approximately twice as fast. Plots 3, 4, 5 and 6 compare the accuracy of RK-4 and SPAM-5 integration when the flight-path angle γ is used as the control variable in the optimization program. Switching from α to γ control provides an additional three orders of magnitude of accuracy improvement for the same step size. This is mainly due to the fact that $d\gamma/dt$ is no longer integrated. The figure also shows that analytic integration of the thrust term produces an additional accuracy improvement of one to two orders of magnitude for the same integration step size. In summary, the control and integration methods developed for use in the trajectory optimization program have increased the speed and hence lowered computational costs by more than an order of magnitude for a given trajectory accuracy.

5. Results of the Trajectory Optimization Studies

Many optimal intercept problems have been solved using the methods and models reviewed in the preceding sections. In this section we present some of the results. The angle of attack is parameterized indirectly through the flight path angle γ as described in Section 3. For each stage the parametric representation of $\gamma(\tau)$ is a linear function plus two exponential functions. The pitch angle is constrained to have a continuous derivative; this guarantees that the required pitching moment is bounded. A variety of problems have been solved where coasting of the stages is allowed. In these problems the optimal coasting times are either zero or so small that they have little effect on the optimal launch mass. For all the problems considered here the coasting times have been set to zero. The minimum burn time for each stage is 10 seconds and the payload mass is 10 kg. Except for the results in Fig. 24, the specific impulse is fixed at 300 seconds. Except for the results shown in Fig. 23, there are five stages.

Trajectory details for an example optimal aeroassisted trajectory are shown in Fig. 19. The problem data are: time of flight = 360 seconds, target range angle = 45 degrees (approximately 3100 miles), target altitude = 400 km.(approximately 250 miles), payload mass = 10kg.. The staging times are apparent. With the exception of the fifth stage, the optimal burn times are at their lower limits of 10 seconds. The resulting vehicle acceleration A/M is quite high, ranging from about 20 to 70 g's. If the minimum burn time is reduced below 10 seconds, even higher accelerations are obtained. The aeroassisted midcourse coasting phase begins at burn out of the final stage and runs from about 53 seconds to 194 seconds. The slight drop in V is due to the drag loss. There is little loss in speed after the exit from the midcourse phase. The reason is obvious: the trajectory leaves the atmosphere quickly, so there is little aerodynamic drag. Close inspection of $\gamma(\tau)$ for $0 < \tau < 60$ shows its linear-exponential parameterization. If the smoothness constraint on the pitch angle is removed and $\alpha(\tau)$ is allowed to be discontinuous at the staging points, the overall character of the trajectory is essentially the same and the launch mass is reduced by about 0.5 %. Thus, the smoothness of the pitch angle does not seem to be a very stringent constraint.

Operational considerations may add further constraints to the interception problem. We have, for example, considered two constrained versions of the problem in Fig. 15. They differ only in the assumptions placed on the motion of the final stage after engine burn out; the models for the earlier stages of the trajectory remain the same. The altitude vs. range angle plots are shown in Fig. 21. Plot B is the optimal aeroassisted trajectory described in the previous paragraph. In plot A, the final payload is constrained to move essentially outside the atmosphere. Thus, after burn out, the trajectory for the final stage is a Keplerian transfer to target interception. The out-of-the-atmosphere constraint is imposed by requiring the minimum altitude of the Keplerian segment to exceed a specified altitude (100 km.). In plot C, the payload is allowed to move through the atmosphere, but it is not aeroassisted, i. e., the angle of attack is zero and there is no aerodynamic down lift. This avoids any increase in drag and heating which may result from lift.

Table 1 gives numerical results for the three problems. As expected, the launch mass is least for the aeroassisted case. For the zero-lift, atmospheric case negative aerodynamic lift is also exploited, but because of the no-lift constraint on the payload it occurs together with engine thrust in the final stage. This accounts for the long burn-time of this stage; it allows more time for the negative aerodynamic lift to act. In the Keplerian case, the altitude constraint leads to a very large launch mass because it essentially eliminates any effective utilization of negative aerodynamic lift. The Keplerian solution does have a potential operational advantage. Since the trajectory is essentially outside the atmosphere, communication with the payload is not blocked by atmospheric ionization.

Figs. 22 through 24 illustrate the effect of key parameters on optimal launch mass. Each point on the curves is the result of an optimal solution. Except for the results in Fig. 22 the trajectories are aeroassisted. Note that the target altitude is 200 km.; this a more demanding intercept condition than the 400 km. of the preceding problem. Fig. 22 shows the relative performance of optimal aeroassisted trajectories and optimal trajectories where aerodynamic lift is not allowed during the coasting of the final stage. The advantage of the aeroassisted trajectories is greater for shorter intercept times. For both types of trajectories the launch mass grows very rapidly as the flight time approaches 320 seconds. As explained in the preceding paragraph, aerodynamic lift is actually used in the midcourse phase. It is just used less efficiently because it must occur while the engine is thrusting. Fig. 23 shows the difference between 5 and 6 stage aeroassisted interceptors. The 6 stage interceptor has a decided advantage for the shorter flight times. Fig. 24 shows the affect of reducing the specific impulse. The 10 second reduction increases the launch mass by over 40 % for the shorter flight times.

Additional solution results for the aeroassisted case suggest other trends. If all other parameters are fixed, the optimal launch mass varies little if the range angle and intercept time of the target vary in direct proportion. Increasing the axial drag coefficient, C_A, by 0.02 increases the launch mass by about 10 %. Increasing the mass density of the stages by 50 % decreases the launch mass by about 6 %. More accurate models of atmospheric density have very little effect on the launch mass.

6. The Mid-course Universal Curve

The aeroassisted trajectory in Fig. 19 has an obvious mid-course segment on which the final payload coasts for an extended period of time until it begins its rise to the target. On the segment there is a negative aerodynamic lift and the path is nearly horizontal. Such segments have been observed on all optimal aeroassisted trajectories where performance requirements are high, i.e., the time of flight is small, the target range angle is large and the target altitude is small. It has been possible to model these mid-course phases accurately by a single ***universal curve*** which relates altitude and speed. This unique relationship is obtained by balancing the difference between centrifugal and gravity forces with negative aerodynamic lift and minimizing the drag losses by choosing the angle of attack which maximizes the lift-to-drag ratio. It also follows that the time-dependent motion of the payload on the universal curve has a universal character.

The full derivation of the universal curve and its consequences is quite lengthy. Papers [32, 33, and in Appendix A] contain the details. Here we indicate the main results. The required balance of forces on the nearly horizontal trajectory is achieved by setting the normal acceleration, $V d\gamma / d\tau$, and γ equal to zero in (1). The result is the universal curve, an expression which relates the altitude and speed:

$$V = (1+H)^{-1/2}\ [1 - \tfrac{3}{4}(1+H)\,P(H)]^{-1/2}. \tag{13}$$

By using a local exponential representation for the density and making a very accurate approximation a simple formula for the universal curve is obtained:

$$V = G(H) = (1 - \tfrac{3}{4}\, e^{-\mu H})^{-1/2}. \tag{14}$$

Along this universal curve there are drag losses and V must decrease. This in turn causes H, θ, γ and α to depend on τ. By using the equations of motion (1) and going through some further approximations it is possible to integrate them and obtain simple formulas for the dependencies. Nondimensional plots of the functions are shown in Fig. 25. The variable x is given by a linear transformation of τ. The ranges of variables which are shown are adequate for any reasonable target conditions.

The accuracy of the formulas has been found to be extremely high. The formulas have been used in many of our numerical solutions of the minimum launch mass problem. This reduces the number of parameters needed to represent the angle of attack program and improves the conditioning of the optimization problem. The result is a considerable saving in computer time. Moreover, the normalized functions in Fig. 25 give a clear picture of how H, θ, γ and V vary during the mid-course phase.

7. Performance of Multi-stage Rocket (Semi-analytical Approach)

For a system of n stages, if the specific impulse I_{sp} and the structural efficiency ratio k_s are the same for all stages, then a known optimal property is that the staging ratios are the same. In this case it can be shown that the ratio of the payload mass to the initial mass is

$$\frac{m_p}{m_0} = \left[(1+k_s)\exp\left(- \frac{V_{total}}{n I_{sp} g_0 \cos\alpha} \right) - k_s \right]^n \tag{15}$$

where α is the average angle of attack during the ascent and the total velocity is

$$V_{total} = V_{burnout} + \Delta V_g + \Delta V_D \tag{16}$$

Here

$$\Delta V_g = \int_0^{t_f} g \sin\gamma \, dt, \qquad \Delta V_D = \int_0^{t_f} (D/m) \, dt \tag{17}$$

are the velocity losses due to gravity and drag acceleration, respectively. The following procedure is used to obtain ΔV_g and ΔV_D:

Based on a typical variation of the flight path angle γ as discussed in [32, 33, and in Appendix A], we assume that

$$\sin\gamma = e^{-t/\tau} \tag{18}$$

where the time constant τ is to be selected to satisfy the final altitude. Then ΔV_g is obtained by a simple quadrature, while we have an integral relation for the current velocity

$$V(t) = f(t) - \int_0^t (D/m)\, dt \tag{19}$$

where $f(t)$ is a known function. We start the computation with $D = 0$ to generate the elements of the trajectory in altitude and velocity. These elements are used to evaluate ΔV_D for the next iteration. Usually ΔV_D tends to its final value after 4 or 5 iterations.

This scheme has been used to compute the boost phase. Compared to the exact optimal solution it provides excellent agreement.

For the overall aeroassisted interception trajectory, we assume that the coasting phase is strictly at constant altitude and the last phase for ascent to intercept is strictly in the vacuum. Explicit solutions for these phases are available. Together with the simplified program for the boost phase, the intercept trajectories have been computed using the data in [32, 33, and in Appendix A] and the accuracy obtained is such that the error is between 5 and 15%. These results are shown in Figs. 26 and 27. They can be compared with the exact results in Figs. 23 and 24.

8. The Attitude Control Scheme

Another portion of the research study has been concerned with the investigation of simple, innovative means of attitude control of the final homing interceptor stage when it is out of the atmosphere. To minimize weight and complexity, a time-optimal attitude control method which uses only a single small control jet has been studied. The method assumes that the final stage is spinning about its x body axis, the axis of axial symmetry. The main rocket engine is also aligned along the x body axis and is continuously thrusting. Through control of the attitude, the main-engine thrust is pointed in the direction required to bring the trajectory onto a collision course with the target. The single control thruster is aligned along the direction of the z body axis and therefore at right angles to the spin axis x. This small control jet can then provide a pitching moment about the y body axis. Attitude control is achieved by turning on this thruster for only a fraction of each roll revolution of the spinning missile. Since no moment is applied about the x axis and since the inertia $I_y = I_z$ due to axial symmetry, ω_x, the x component of missile angular velocity, remains constant and equal to its initial spin rate.

Each discrete change in attitude requires at least two thrusting pulses from the control jet. In the two-pulse case, the first pulse produces an increment in angular momentum perpendicular to the spin axis x. The second control-jet pulse is applied half a role period later to cancel the angular momentum increment perpendicular to the spin axis, which has now been changed in direction by the desired attitude angle increment. The size of the incremental change in attitude angle can be varied by changing the duration of each control-jet pulse.

The attitude control problem is described by a set of five nonlinear state equations involving the rates of change of two transverse angular velocity components, ω_y and ω_z, and three Euler angles ψ, θ and ϕ. It turns out to be more convenient to define transformed Euler angles such that the final desired pointing angle is represented by $\theta = \psi = 0$. Solution of the time-optimal control problem requires the integration of ten nonlinear differential equations (five state equations and five costate equations) with trial initial conditions on the costate variables. The polarity of one of the costates determines whether the control thruster is turned on or off. Thus the solution consists of the control thruster turn-on and turn-off times which take the spinning missile from its initial state to its desired final state (the prescribed pointing direction as given by $\theta = 0$ and $\psi = 0$, with $\omega_y = \omega_z = 0$) at the final time T_f. To avoid the difficulties inherent in the many iterations needed to solve each case for this type of optimal control problem, two alternative approaches have been successfully developed. For details see references [35, 36, 37, and in Appendix A].

The first approach is limited to the case where only two control thruster firings are needed. As noted above, the first thruster firing is used to accelerate the rocket toward the desired final state, the second to brake the motion so that the stage arrives at the desired pointing direction with zero transverse angular velocity. T_1, T_2, T_3 and T_4 ($= T_f$) are defined as the first turn-on, first turn-off, second turn-on and second turn-off times, respectively. Starting with given initial conditions, the five state equations of motion are integrated numerically for trial values of T_1 and T_2. It turns out that T_3 and T_4 can be expressed as analytic functions of the state at T_2 such that the final transverse angular velocity will be zero. A gradient-type algorithm is developed which iterates on T_1 and T_2 until the final Euler angles θ and ψ at T_4 ($= T_f$) are equal to zero within a prescribed ε. This approach does not require integration of the costate equations and has the further advantage of only requiring iterations on two parameters (T_1 and T_2). Based on this approach a table of two four-variable functions, one for the first turn-on time T_1, the second for the first turn-off time T_2, can be constructed. Starting with arbitrary initial conditions as entries to the table, T_1 and T_2 are determined by table lookup and linear interpolation. For times greater than T_2 the missile states become new initial conditions for the same control law, as defined by the table entries. Then the newly determined T_1 and T_2 values are in fact equivalent to the original T_3 and T_4 values associated with the two-thrust maneuver. Simulation runs of an interceptor stage using a control law based on this function-generation scheme have demonstrated near time-optimal performance. This function-generation method is especially suitable for on-board microprocessor implementation using current and projected VLSI memory chips.

In the second approach the state and costate equations are solved backwards in time from the final time T_f using numerical integration. Each backward integration is started with the prescribed final states and trial initial conditions for the five costates. Since one of the costates can arbitrarily be set equal to 1, this is equivalent to four adjustable initial conditions. Every numerical solution generates an optimal control law. From each backward-time solution the set of initial conditions for which the observed on-off control law is optimal can be determined. Time-optimal switching times which span the entire required space of initial states in forward time can be generated by repeating the backward-time solution for different values of the four costate initial conditions. These results can in turn be used to generate the same type of four-variable function tables for turn-on and turn-off times T_1 and T_2, as described above in the first approach. But in this case we are no longer restricted to the two-thrust solution, as in the first approach. Here the time-optimal control law can consist of any number of thruster firings, as needed to reach the final pointing state. Thus an arbitrarily large set of initial states can be handled by the function tables.

To summarize, a practical scheme has been developed for time-optimal control of a spinning interceptor which uses only one control thruster and is particularly compatible with VLSI memory technology. Although developed for attitude control of an interceptor rocket out of the atmosphere, the method has the potential of being combined with the boundary-layer injection scheme for control at hypersonic speeds in the atmosphere, which has been the subject of Part I of this final research report.

9. Minimum Fuel Interception with Time Constraint

This analysis applies to both the case of ground-launched interceptor and space-based interceptor. We assume that at a certain time t_0, called the acquisition time, the trajectory of the target as defined by the position vector $\mathbf{r}_T(t)$ is known. Let $\mathbf{r}_0(t)$ be the current position vector of the interceptor. It is proposed to make the necessary correction to $\mathbf{r}(t)$ with minimum fuel consumption such that $\mathbf{r}(t_f) = \mathbf{r}_T(t_f)$ for a certain final time t_f such that $t_0 < t_f \leq t_{max}$, where t_{max} is a prescribed upper limit, (Fig. 28).

We consider the general case of three dimensional flight in the vacuum about a spherical earth. The engine thrust is assumed to be sufficiently high such that the velocity change is impulsive. Then by the maximum principle, the impulse ΔV is parallel to the primer vector $\mathbf{p}_V$ which is the adjoint vector associated to the velocity vector. Since the function $\mathbf{p}_V(t)$ can be expressed explicitly in terms of elementary integrals, we can write the set of necessary conditions for optimality. They consist of:

- The kinematic relations for transfer between orbits, including the Lambert solution for prescribed time of flight.

- The optimality conditions: $\mathbf{p}_V$ parallel to $\Delta \mathbf{V}$, and $p_V = \|\mathbf{p}_V\| = 1$ at the time of application of the impulse.

- The transversality condition which expresses the fact that the final velocity is free in the case of pure interception. This condition is

$$\mathbf{p}_{r_f} \cdot (\mathbf{V}_{T_f} - \mathbf{V}_f) = 0 \tag{20}$$

and it shows that at the final time the relative velocity is orthogonal to the adjoint vector $\mathbf{p}_r$ associated to the position vector.

Finally, there is the condition

$$p_V(t) \leq 1, \qquad t \in [t_0, t_f] \ . \tag{21}$$

The procedure for the computation is as follows:

Use one impulse applied at the initial time t_0 to find the solution satisfying all the boundary conditions, including equation (20). Then we check condition (21). If it is satisfied, then the trajectory computed is optimal. If condition (21) is not satisfied and if $\dot{p}_V(t_0) > 0$, the unique impulse must be applied at a certain time $t_1 > t_0$ after an initial coasting phase to bring the interceptor to a more appropriate position to initiate the change in the trajectory. This time t_1 is computed with the additional condition $\dot{p}_V(t_1) = 0$. If the condition (21) is not satisfied during a time interval (t_1, t_2) where $t_0 < t_1 < t_2 < t_f$, then a mid-course impulse, applied at a time t_m should be applied. The trajectory must be recomputed using two impulses ΔV_1 and ΔV_2, will all conditions satisfied.

All the equations involved as presented in [31, and in Appendix A] are given in explicit form and several numerical examples are presented.

10. Reachable Domain for Interception at Hyperbolic Speeds

As discussed in previous sections, for a short time interception of an ICBM at low altitude a multi-stage earth-based interceptor must accelerate to hyperbolic speed. In practice, at a time t_0 , about 2 to 3 minutes before the intended interception time t_f, revised information about the trajectory of the target $\mathbf{r}_T(t)$, may dictate a correction in the trajectory of the interceptor, from the reference nominal trajectory $\mathbf{r}_0(t)$ to the actual trajectory $\mathbf{r}(t)$. Then, for a given fuel potential for the last interceptor stage it is necessary to assess the possibility of a successful interception. This fuel potential is conveniently expressed in terms of the total characteristic velocity ΔV, available for the maneuver.

By definition, the reachable domain at the time t is the set of all points P attainable by the interceptor, using all the available ΔV_0. From [31, and in Appendix A], it is known that the largest set for the points P is obtained by applying the maximum impulse at the acquisition time t_0. For any point P inside this domain, interception can be achieved with a smaller impulse.

We have derived the exact equations for the computation of the reachable surface $S(\Delta V,t)$ which is the boundary of the reachable domain for a given ΔV. For small ΔV the equations which generate $S(\Delta V,t)$ can be linearized. It is then seen that the reachable surface is an ellipsoid and it is approximately a sphere for short time of flight, (Fig. 29). Properties of this surface and its mathematical characterization were presented in [35, and in Appendix A].

The condition for interception may be expressed in terms of a capture function F, for which an explicit formula has been derived. Let $\Delta\mathbf{r}_T(t) = \mathbf{r}_T - \mathbf{r}_{P_0} - (\Delta x_T, \Delta y_T, \Delta z_T)$ be the relative position between the reference point P_0 of the interceptor on its nominal trajectory (without correction) and the target T. Suppose

$$F\ (\Delta x_T, \Delta y_T, \Delta z_T, t) \leq \|\Delta V\|^2$$

is satisfied for all $t \in [t_1, t_2]$, where $\|\Delta V\|$ is the characteristic velocity available. Then interception is possible for any t in $[t_1, t_2]$.

The concept of reachable domain can also be used to determine the requirements for defense of an area on the surface of the earth which may be the intended target of ICBMs.

III. Suggested Future Work

Based on the work done under this contract, the following extensions to the work completed and new studies are suggested as areas of future work.

I) Aerodynamic Control Using Gas Injection Into the Boundary Layer

1) Inclusion of equilibrium chemistry (dissociation and reaction) in the Navier-Stokes code. The stability of the shear layer is sensitive to the temperature distribution in this layer, which is affected by chemical reactions which may occur. Frozen and equilibrium flow calculations allow these effects to be bracketed.

2) Improvement of numerical code efficiency so as to handle separated flows economically, in terms of computer time. This will involve implementation of implicit time-marching or multi-grid relaxation, or both.

3) Definitive study of strip blowing, including both analytical and numerical studies, and including cases of simple and multiple strips.

4) Study of shear-layer stability in hypersonic flows, both analytically and numerically. Little previous work has been done on this problem, which must be understood before extensive practical use can be made of the injection of gases in the boundary layer for aerodynamic control.

5) Numerical study of temporal effects associated with stopping and starting blowing. Steady state examples give satisfactory results. Any problems associated with the unsteady processes when starting or stopping the blowing bear upon the feasibility of using surface blowing for control purposes, especially if a rotating vehicle with a control which is on only during part of the rotation is considered. This study will involve extending the temporal accuracy of the codes.

6) Study of effects of increasing altitude, to a point where free molecule flow exists; calcuation of jet forces needed for vacuum conditions (no boundary layer). It is not possible to cover the whole range from continuum to vacuum conditions computationally.

7) Consideration of three-dimensional, axially symmetric body in hypersonic flow at an angle of attack.

II) Combined Atmospheric and Exo-atmospheric Attitude and Trajectory Control

1) Extension of the research on attitude control out of the atmosphere to integrate it with the research on generation of aerodynamic forces at hypersonic speeds using boundary-layer injection (Part I).

2) Extension of the time-optimal control laws developed for a spinning missile with an on-off thruster to the continuously-thrusting case, where hot gas is switched back and forth from one nozzle to another. This single control scheme has the advantage that it can be utilized both for attitude control in the atmosphere, using boundary-layer injection, and for control out of the atmosphere.

3) Modification of the thrust-switching scheme to provide high-resolution attitude control by means of pulse-width modulation of the control-jet switch.

4) Implementation of closed-loop control with high sample rates by storing only one-bit switch position data in the multivariable function table for the time-optimal control law, based on the desired attitude and current measurements of missile attitude and attitude rate. The multivariable function scheme for storing control-jet switch times, as developed in the research to date, uses on-line table lookup with linear interpolation to determine thruster turn-on and turnoff times. The proposed new scheme offers possible advantages over the table-lookup scheme. It is potentially simpler from a hardware point of view and achieves direct closed loop control rather than partially open loop control.

5) Develop minimum-fuel thruster control laws.

6) Extend the parametric studies of trajectory optimization with the support of the simplified trajectory optimization program developed during the last six months. This research would be used to provide performance requirements for the attitude control schemes described above.

References

1. Quarterly Progress Report, April 1, 1988-June 30, 1988, July 20, 1988.
2. Quarterly Progress Report, July 1, 1988-September 30, 1988, November 4, 1988.
3. Quarterly Progress Report, October 1, 1988-December 31, 1988, March 10, 1988.
4. Quarterly Progress Report, January 1, 1989-Spril 3, 1989, May 23, 1989.
5. Quarterly Progress Report, April 3, 1989-July 3, 1989, August 10, 1989.
6. Quarterly Progress Report, July 4, 1989-October 3, 1989, November 17, 1989.
7. Quarterly Progress Report, October 4, 1989-December 31, 1989, February 15, 1990.
8. M. D. Matarrese, A. F. Messiter, & T. C. Adamson, Jr., "Control of Hypersonic Aerodynamic Forces with Surface Blowing," AIAA Paper 90-0602, presented at 28th Aerospace Sciences Meeting, Jan. 1990; submitted to *AIAA J.*, 1990.
9. K. F. Stetson, "On Predicting Hypersonic Boundary Layer Transition," Air Force Wright Aeronautical Laboratories Technical Memorandum AFWAL-TM-87-160-FIMG, March 1987.

10. J. D. Cole & J. Aroesty, "The Blowhard Problem - Inviscid Flows with Surface Injection," *International Journal of Heat and Mass Transfer,* Vol. 11, 1968, pp. 1167-1183.

11. A. F. Messiter & M. D. Matarrese, "Hypersonic Viscous Interaction with Strong Blowing," to appear in *J. Fluid Mech.*, 1990.

12. M. D. Matarrese & A. F. Messiter, "A Numerical Method for the Self-Similar Hypersonic Viscous Shear Layer," submitted as note to *J. Comp. Phys.*, 1990.

13. S. N. Brown, H. K. Cheng, & C. J. Lee, "Inviscid-Viscous Interaction on Triple-Deck Scales in a Hypersonic Flow with Strong Wall Cooling," to appear in *J. Fluid Mech.*

14. F. T. Smith & K. Stewartson, "On Slot Injection into a Supersonic Laminar Boundary Layer," *Proceedings of the Royal Society of London,* Series A, Vol. 332, 1973, pp. 1-22.

15. P. Woodward & P. Colella, "The Numerical Simulation of Two-dimensional Fluid Flow with Strong Shocks," *J. Comp. Phys.*, Vol. 54, 1984, pp. 115-173.

16. M. Artola & A. J. Majda, "Nonlinear Development of Instabilities in Supersonic Vortex Sheets," *Physica D*, Vol. 28, 1987, pp. 253-281.

17. T. F. Balsa & M. E. Goldstein, "On the Instabilities of Supersonic Mixing Layers: A High Mach Number Asymptotic Theory," to appear in *J. Fluid Mech.*

18. J. Wallace and N. Kemp, “Similarity Solutions to The Massive Blowing Problem”, AIAA Journal, vol. 7, 1969.

19. B. van Leer, “Towards the Ultimate Conservation Difference Scheme. V. A Second-Order Sequel to Godunov’s Method”. Journal of Computational Physics, vol.32, 1979.

20. B. Koren, “Multi-grid and Defect Correction for the Navier-Stokes Equations.” PhD thesis, Delft University, 1989.

21. B. van Leer, “Upwind-Difference Methods for Aerodynamic Problems Governed by the Euler Equations”, in Large-Scale Computations in Fluid Mechanics, Lectures in Applied Mathematics, vol. 22, 1985.

22. W. K. Anderson, J. L. Thomas, and B. van Leer, “Comparison of Finite Volume Flux Vector Splittings for the Euler Equations”, AIAA Journal, vol. 24, no. 9, 1986.

23. P. L. Roe, “Approximate Riemann Solvers, Parameter Vectors, and Difference Schemes,” Journal of Computational Physics, vol. 43, 1981.

24. G. A. Hedstrom, “Nonreflecting Boundary Conditions for Nonlinear Hyperbolic Systems,” Journal of Computational Physics, vol. 30, 1970.

25. B. van Leer, C. H. Tai, and K. G.Powell, "Design of Optimally-Smoothing Mulllti-Stage Schemes for the Euler Equations," in AIAA 9th Computational Fluid Dynamics Conference, 1989.

26. N. Carter and B. van Leer, "Euler Computations of Hypersonic Flow with Strong Blowing", AIAA 90-0603, presented at the 28th Aerospace Sciences Meeting, Jan. 1990.

27. J. L. Thomas, and R. W. Walters, "Upwind Relaxation Algorithms for the Navier Stokes Equations," AIAA-85-1501, pp. 117-128, AIAA Collection of Technical Papers CP854, 1985.

28. D. H. Rudy, J. L. Thomas, A. Kumar, P. A. Gnoffo, S. R. Chakravarthy, "A Validation Study of Four Navier-Stokes Codes for High-Speed Flows," AIAA Paper 89-1838, presented at the 20th Fluid Dynamics, Plasma Dynamics and Lasers Conference, June 1989.

29. Gilbert, E.G., R.M. Howe, P. Lu, and N.X. Vinh, "Trajectory Optimization of Earth-launched Interceptors at Supercircular Speeds,"*Proc. of the International Society for Optical Engineering*, Vol. 872, 1988, pp. 12-18.

30. Howe, R.M., E.G. Gilbert, G. Shorr, and N.X. Vinh, "Computation of Optimal Trajectories Using State-of-the-art Simulation Technology,"*Proc. of the Conference on Aerospace Simulation III*, Feb. 3-5, 1988, pp. 263-274.

31. Vinh, N.X., P. Lu, R.M. Howe, and E.G. Gilbert, "Optimal Interception with Time Constraint," to appear in *Journal of Optimization Theory and Applications*, Sept., 1990.

32. Gilbert, E.G., R.M. Howe, P. Lu, and N.X. Vinh, "Optimal Aeroassisted Trajectories at Hyperbolic Speeds, *Proc. of the 1989 AIAA Guidance, Navigation and Control Conf.*, Aug. 14-16, 1989.

33. Gilbert, E.G., R.M. Howe, P. Lu, and N.X. Vinh, "Optimal Aeroassisted Trajectories at Hyperbolic Speeds," accepted for publication in the *Journal of Guidance, Control & Dynamics*.

34. Howe, R.M., and E. Jahangir, "A Two-pulse Scheme for Time-optimal Control of a Spinning Missile," to be presented at the *AIAA Guidance, Navigation and Control Conference*, Portland, Oregon, Aug. 20-22, 1990.

35. Vinh, N.X., E.G. Gilbert, R.M. Howe and P. Lu, "Reachable Domain for Interception at Hypersonic Speeds," to be presented at the *AIAA Astrodynamics Conference*, Portland, Oregon, Aug. 20-22, 1990.

36. Jahangir, E., "Time-optimal Control of a Spinning Missile," PhD Thesis, Department of Aerospace Engineering, The University of Michigan, Ann Arbor, MI 48109, 1990.

37. Jahangir, E., and R.M. Howe, "A Scheme to Generate Thruster Firing Times for the Time-optimal Reorientation of a Spinning Missile," submitted for presentation at the 29th Aerospace Sciences Meeting, Reno, Nevada, January 7-10, 1991.

Table 1. Numerical Data for Optimal Trajectories in Figure 1

				Burnout conditions for 4th stage		
Type of Solution	Launch Mass (kg)	h (km)	V	θ(deg)	γ (deg)	t (sec)
Aeroassisted	18,990	58.3	1.68	2.2	3.2	40.6
Zero Lift Atmospheric	23,070	57.0	1.89	2.5	3.5	42.5
Keplerian	50,720	64.6	1.82	5.8	-1.6	75.2

				Burnout conditions for 5th stage		
Type of Solution	Coasting time between 4th and 5th stage	h (km)	V	θ(Deg)	γ (deg)	t (sec)
Aeroassisted	0	63.7	2.11	3.7	0	52.6
Zero Lift Atmospheric	0	66.5	1.96	24.0	0.005	201.9
Keplerian	90.6	127.8	2.10	19.5	-4.7	182.0

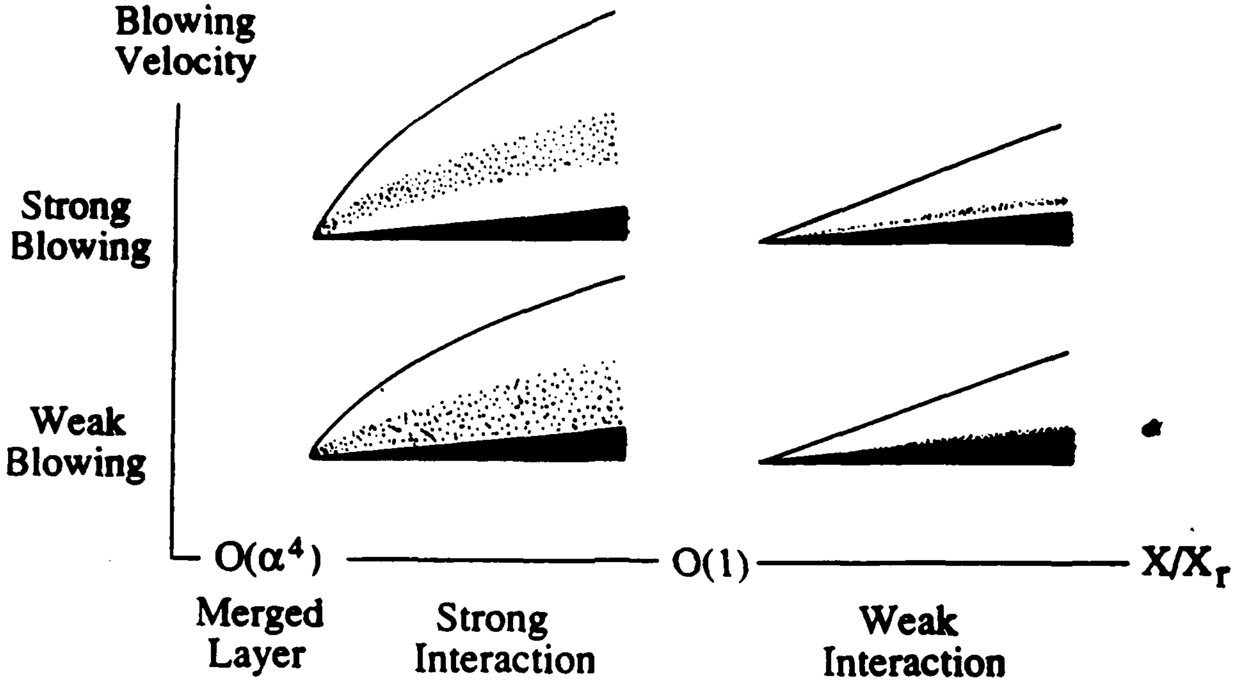
Blowing Velocity
Strong Blowing
Weak Blowing
O(α⁴)
O(1)
X/Xr
Merged Layer
Strong Interaction
Weak Interaction

Fig. 1 Qualitative sketch of wedge flow field with weak or strong blowing and weak or strong interaction. (Speckled regions are viscous layers.)

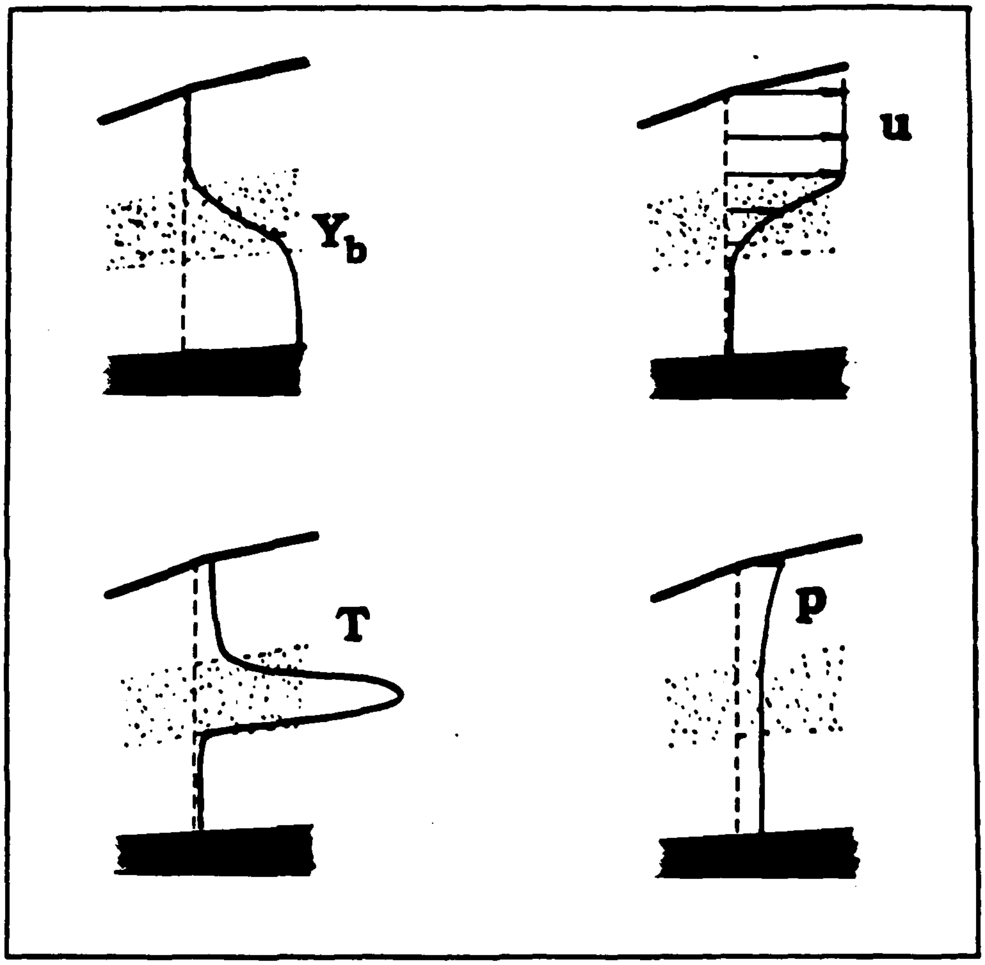

Fig. 2 Qualitative profiles of blown-gas mass fraction Y_b, velocity component u, temperature T, and pressure p.

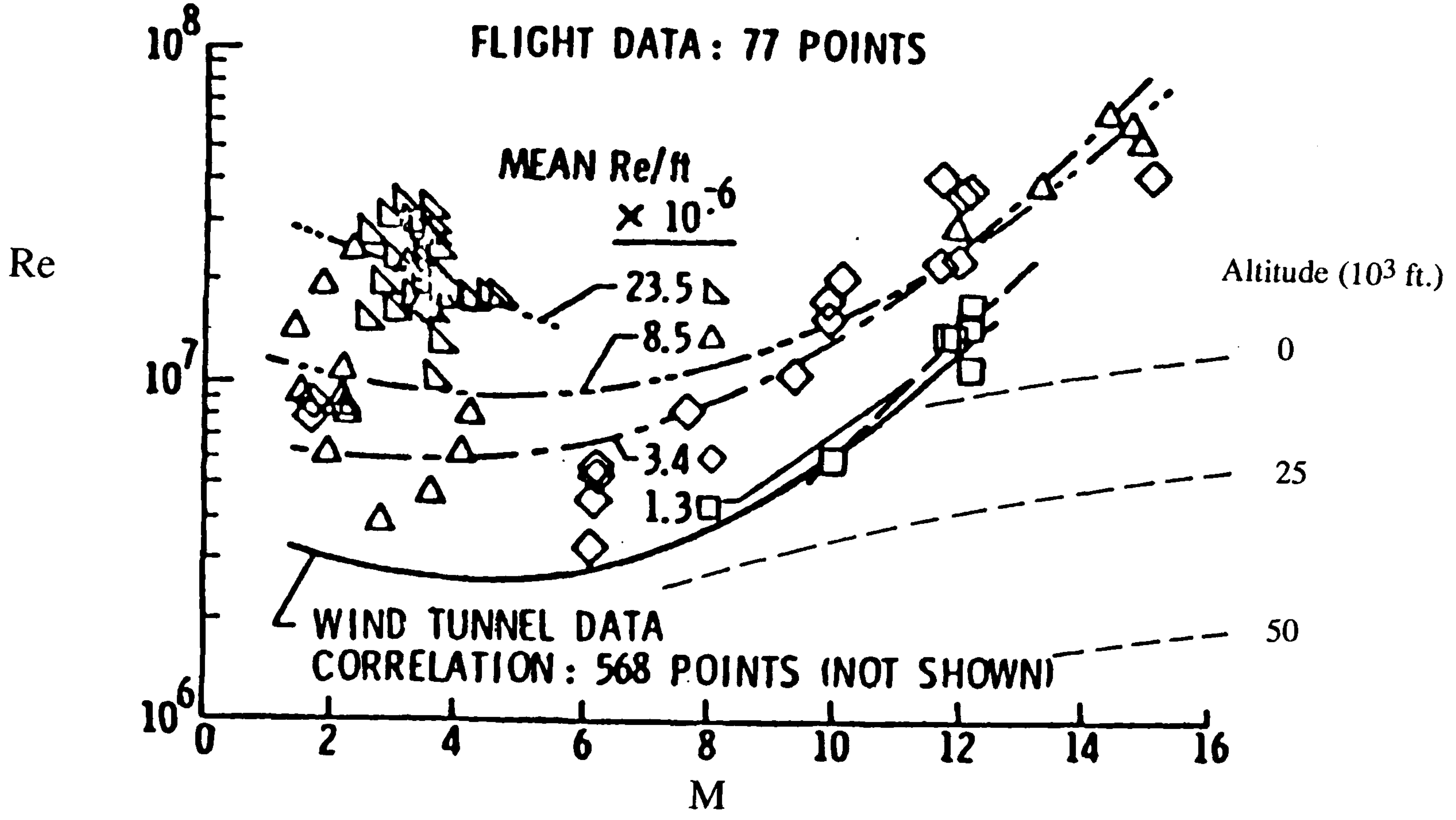

Fig. 3 Free-stream Reynolds-number for a 10' body at various altitudes (– – – –) and transition Reynolds-number data for sharp cones in wind tunnels and in flight (all other symbols and curves) vs. Mach number. (From Ref. 9)

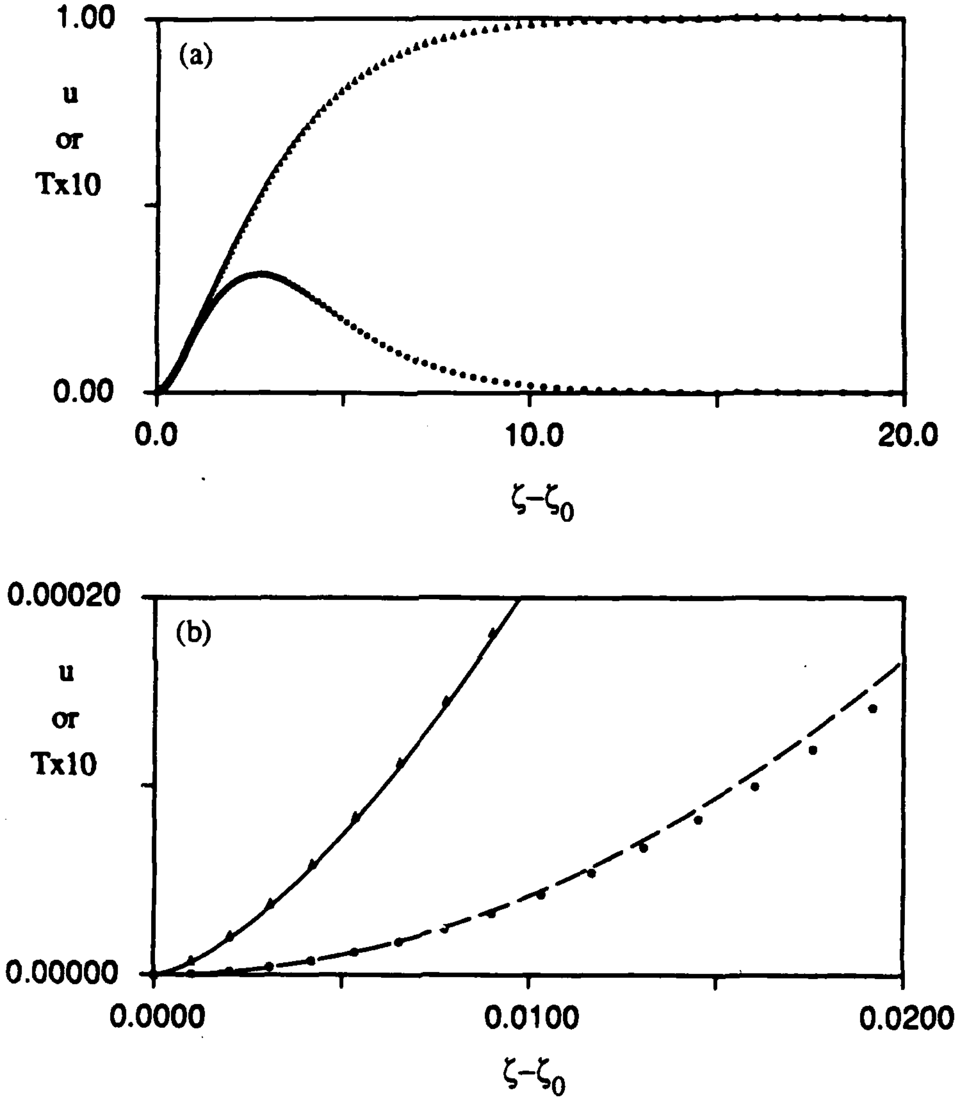

Fig. 4 (a): profiles of scaled velocity component u (Δ) and scaled temperature Tx10 (○) in viscous shear-layer; (b): comparison with second-order asymptotic solutions for u (——) and T (— —) near lower boundary $\zeta=\zeta_0$ (blow-up of region near origin in part (a)).

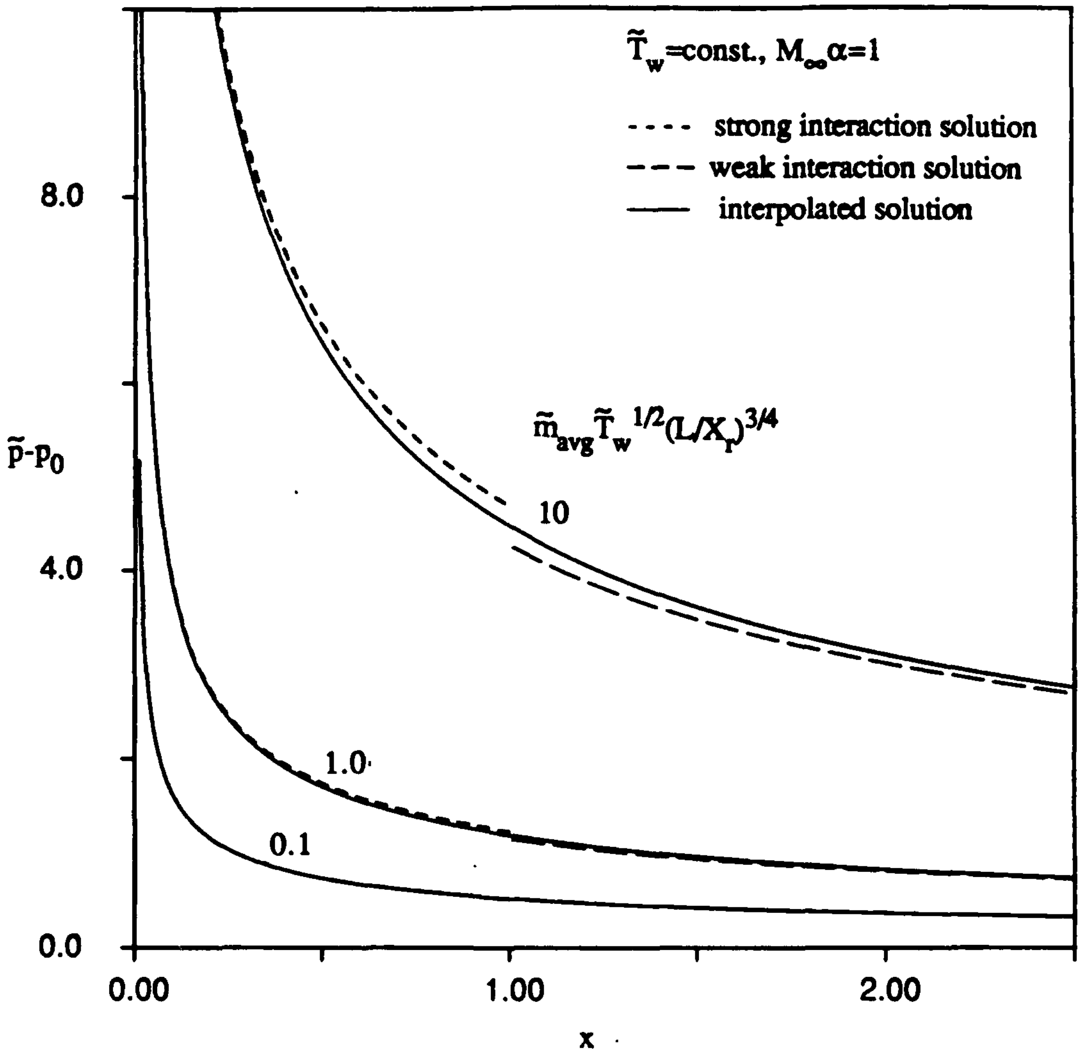

Fig. 5 Surface pressure $\tilde{p}-p_0$ vs. x for various rates of air injection.

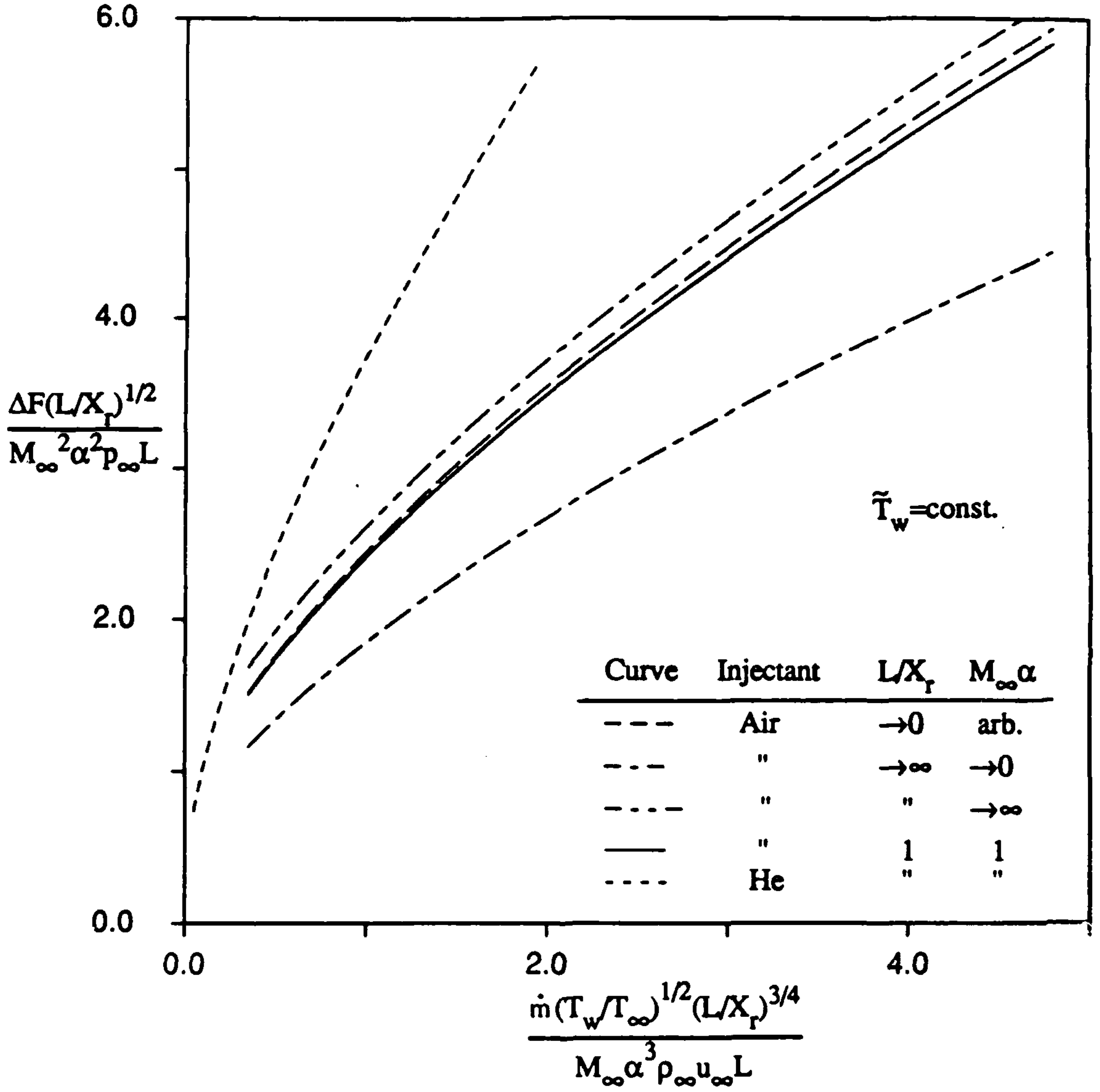

Fig. 6 Scaled force-change $\Delta F(L/X_r)^{1/2}/(M_\infty^2\alpha^2 p_\infty L)$ vs. scaled mass flow-rate $\dot{m}(T_w/T_\infty)^{1/2}(L/X_r)^{3/4}/(M_\infty\alpha^3\rho_\infty u_\infty L)$ for various cases.

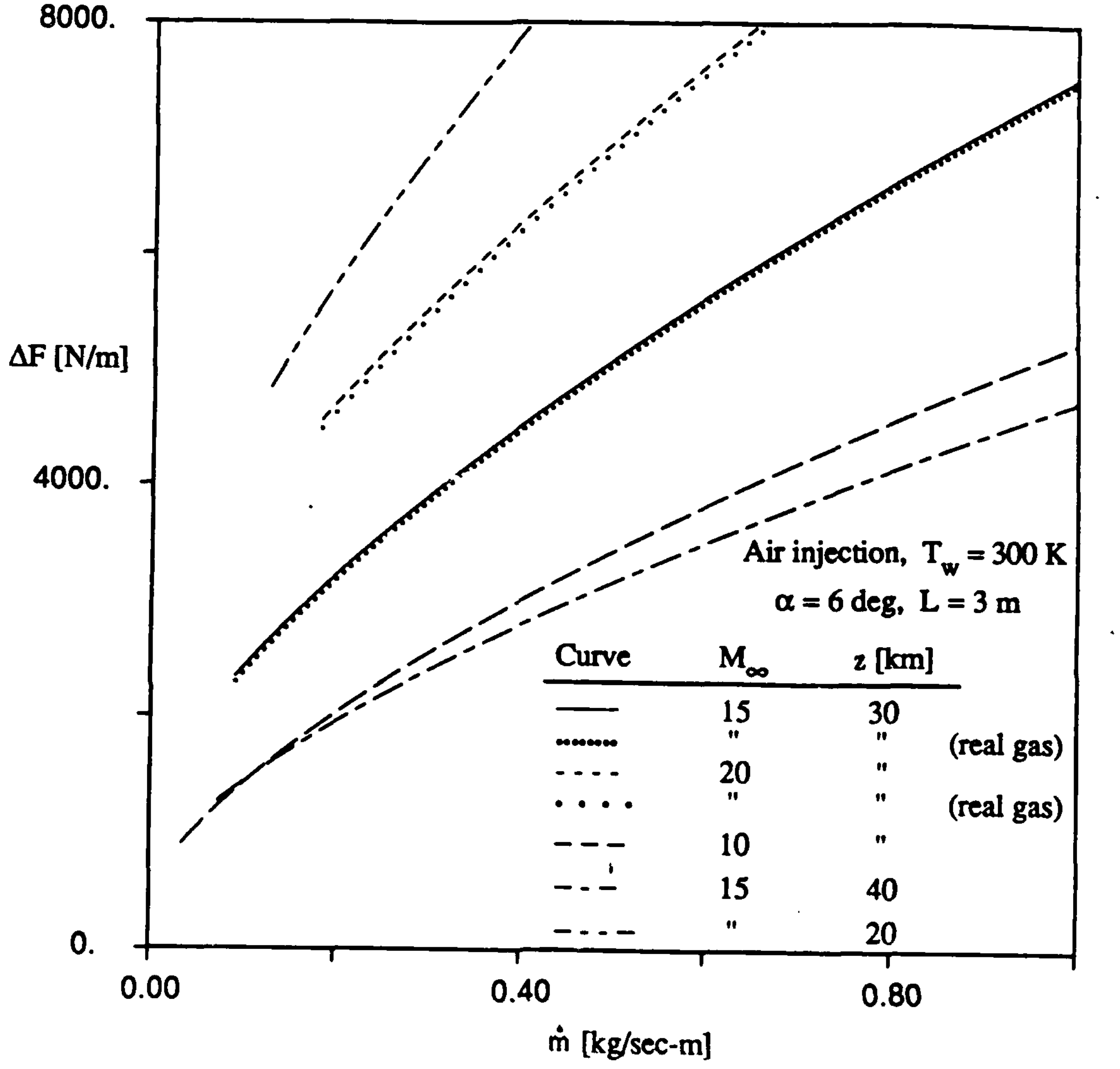

Fig. 7 ΔF vs. ṁ for various flight regimes.

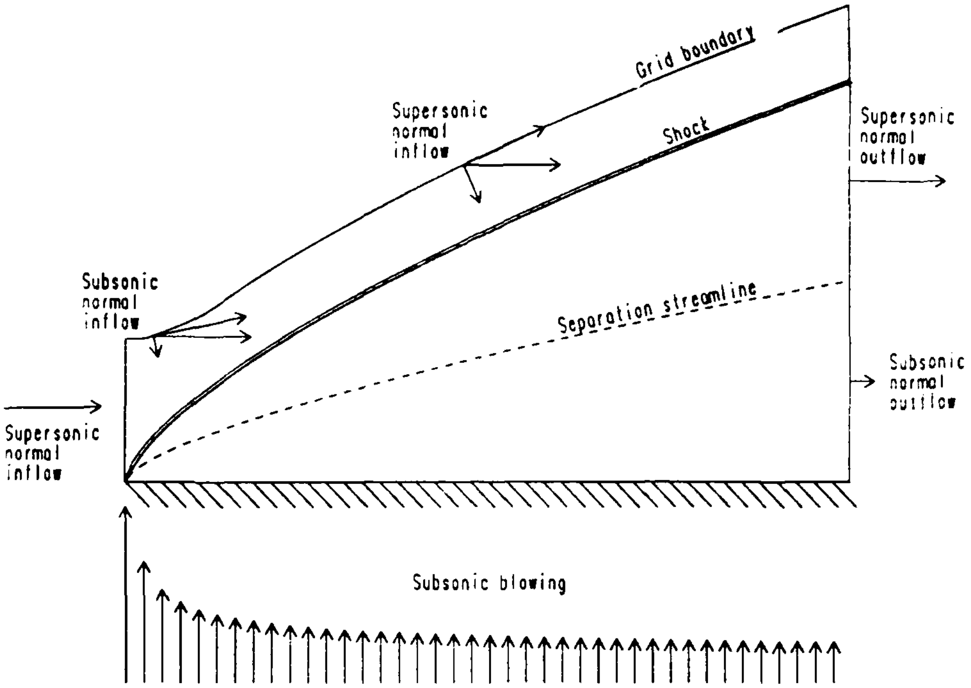
Grid boundary
Supersonic normal inflow
Shock
Supersonic normal outflow
Subsonic normal inflow
Separation streamline
Subsonic normal outflow
Supersonic normal inflow
Subsonic blowing

Fig. 8: Schematic indicating the various types of boundary conditions encountered.

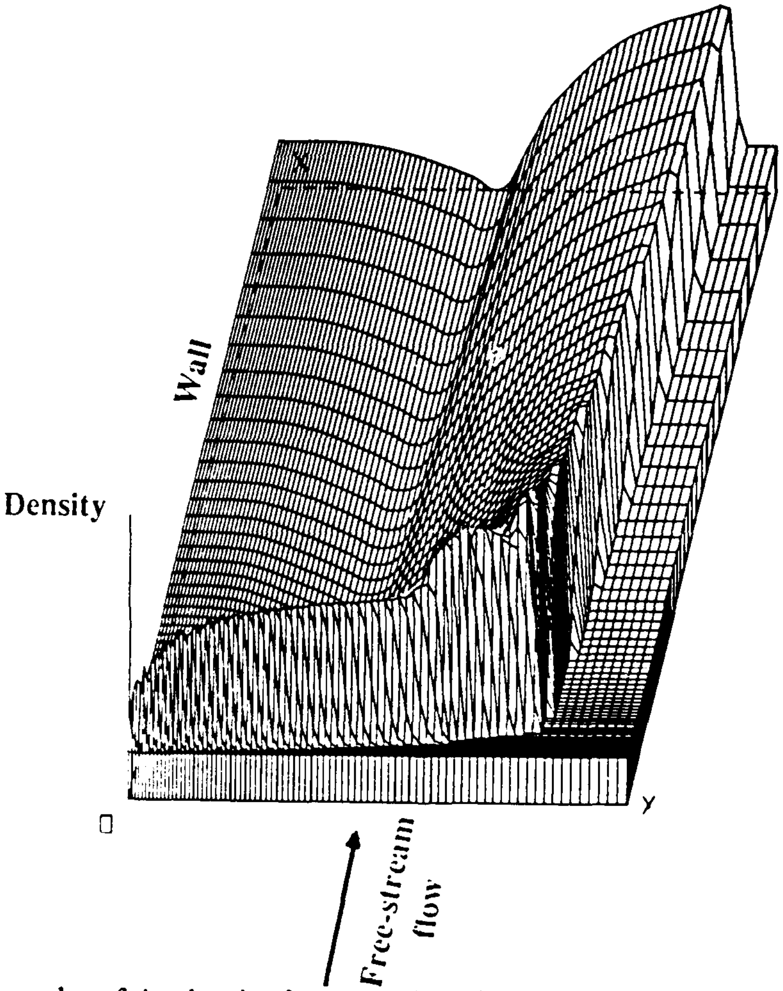

Fig. 9: Carpet plot of the density for strong blowing along a flat plate in Mach 20 flow. A smoothly curving shock in physical space becomes kinked in computational space when the grid is improperly alined.

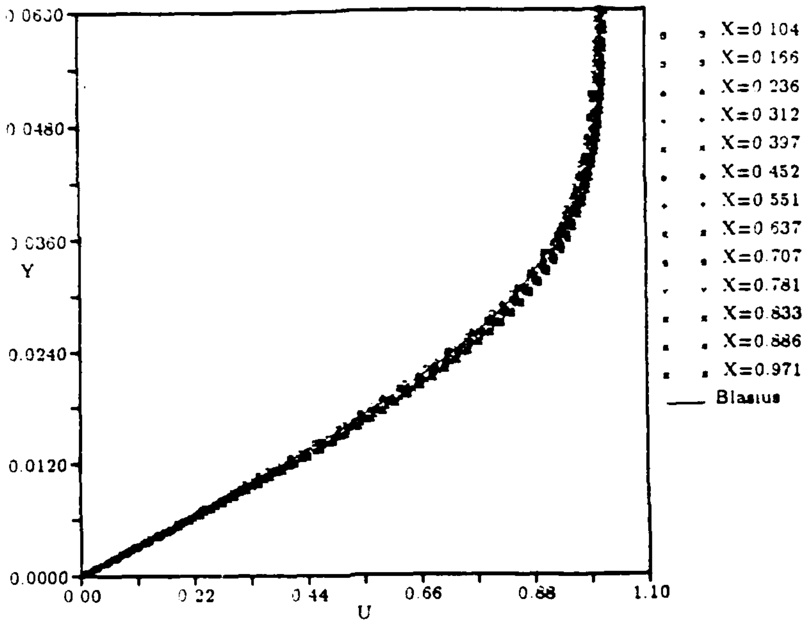

Fig. 10: Velocity profiles for a Blasius boundary layer.

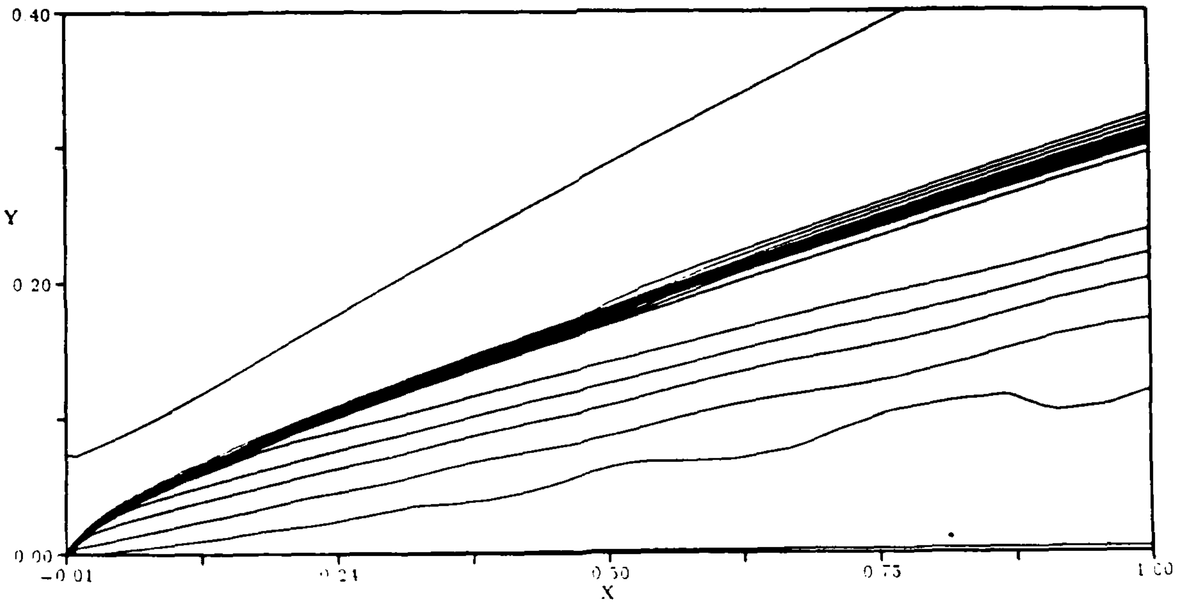

Fig. 11: Mach number contour plots for strong interaction on a wedge with constant temperature air injection. The injected air temperature is equal to the free-stream air temperature.

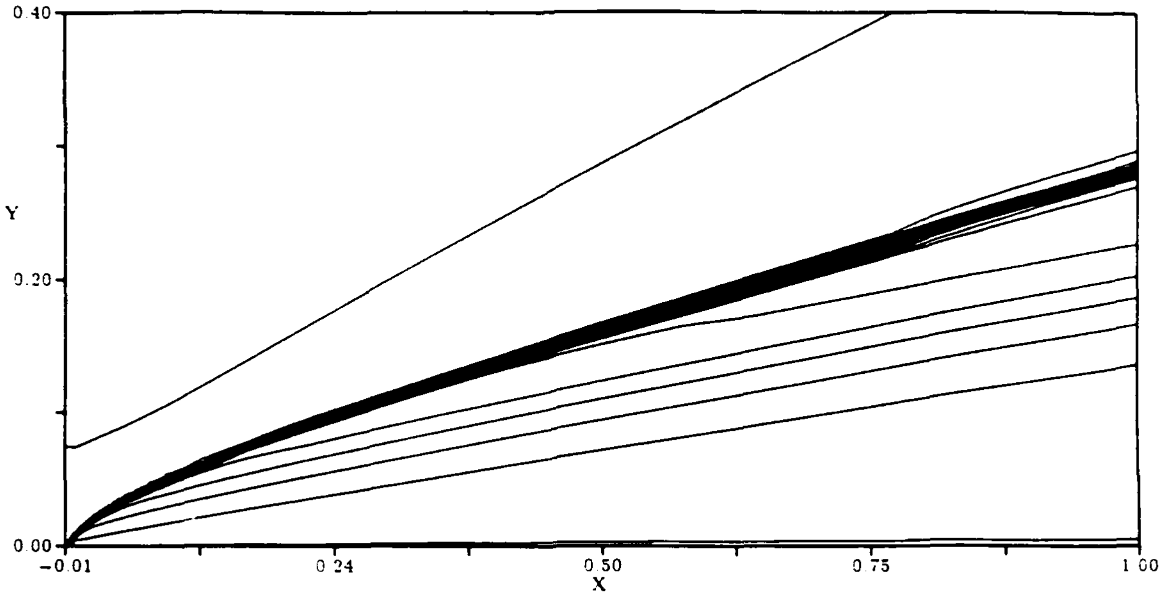

Fig. 12: Mach number contour plot for strong interaction on a wedge with constant temperature air injection. The injected air temperature is equal to four times the free-stream air temperature.

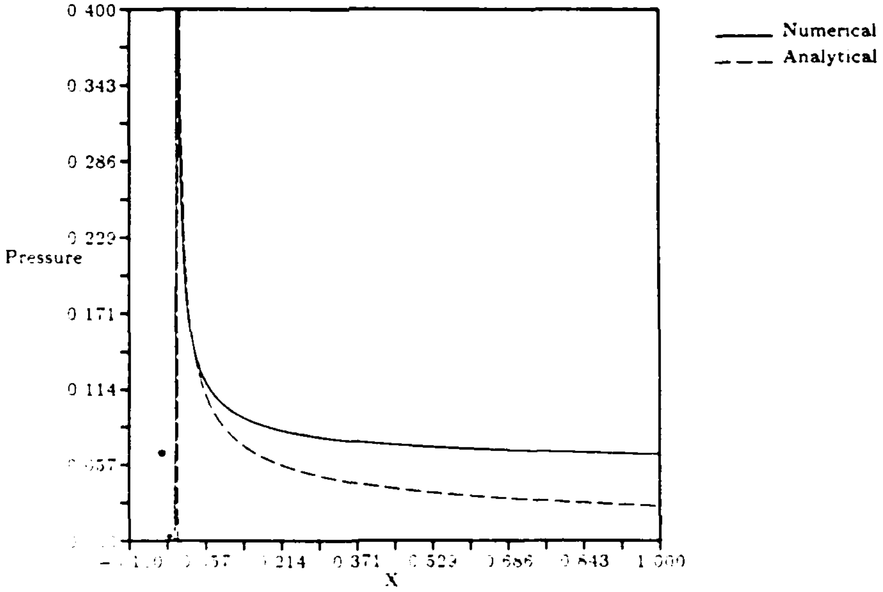

Fig. 13: Wall pressure profiles for constant temperature air injection with the injected air temperature equal to four times the free-stream air temperature.

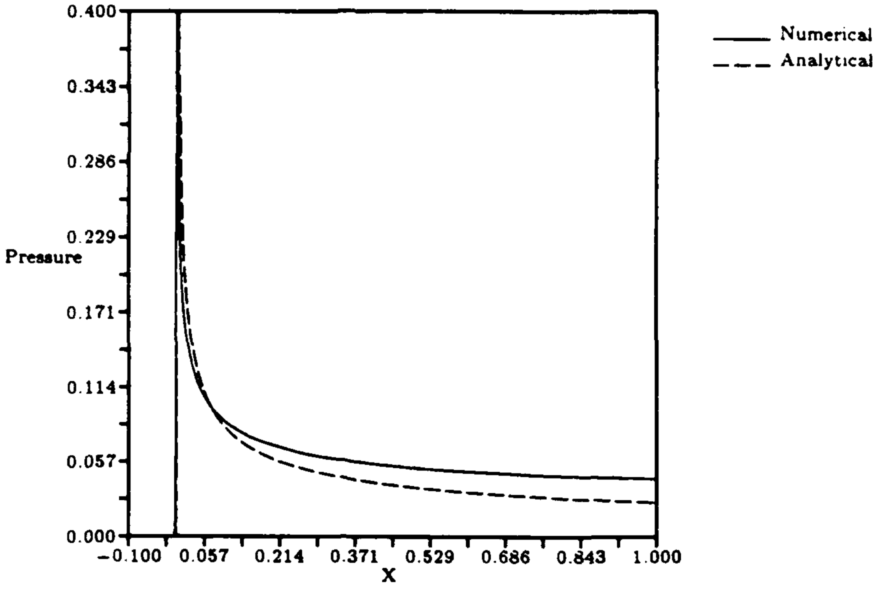

Fig. 14: Wall pressure profiles for constant density air injection with the injected air density equal to twenty-five times the free-stream air density.

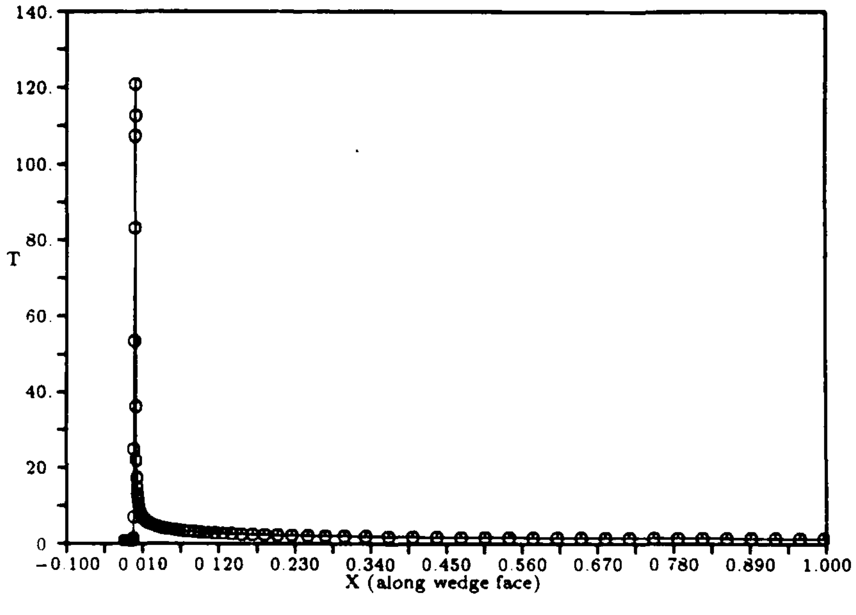

Fig. 15: Temperature distribution along the wall for the constant-density injection case. (temperature is referenced to tree-stream temperature)

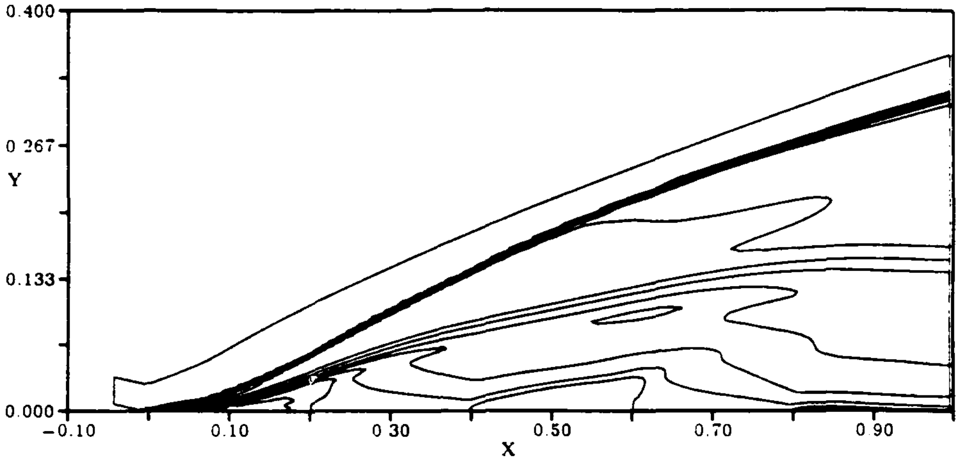

Fig. 16: Mach number contour plots for strip blowing along a wedge. Blowing is from 0.2 to 0.4, and from 0.6 to 0.8.

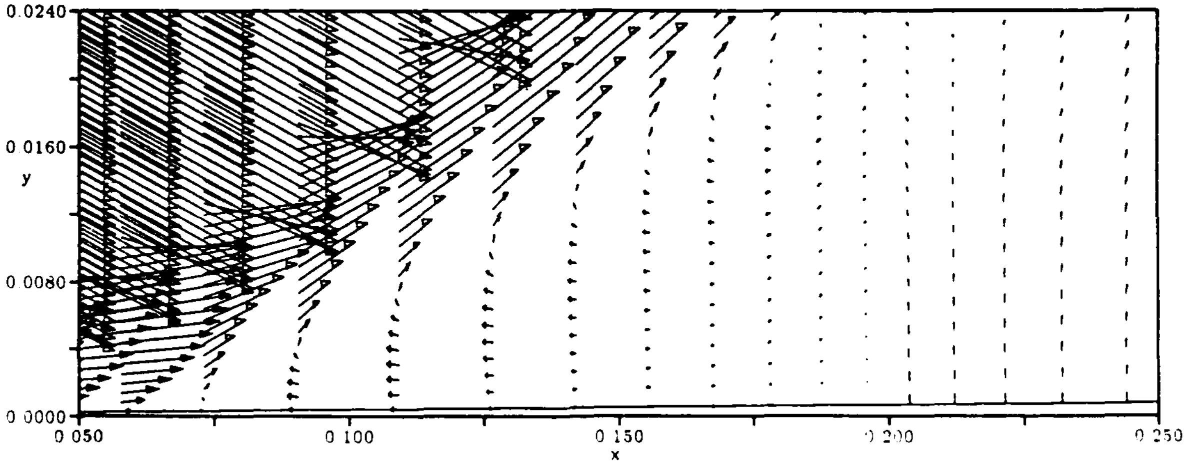

Fig. 17: Velocity vectors in the separated flow region just ahead of the first strip.

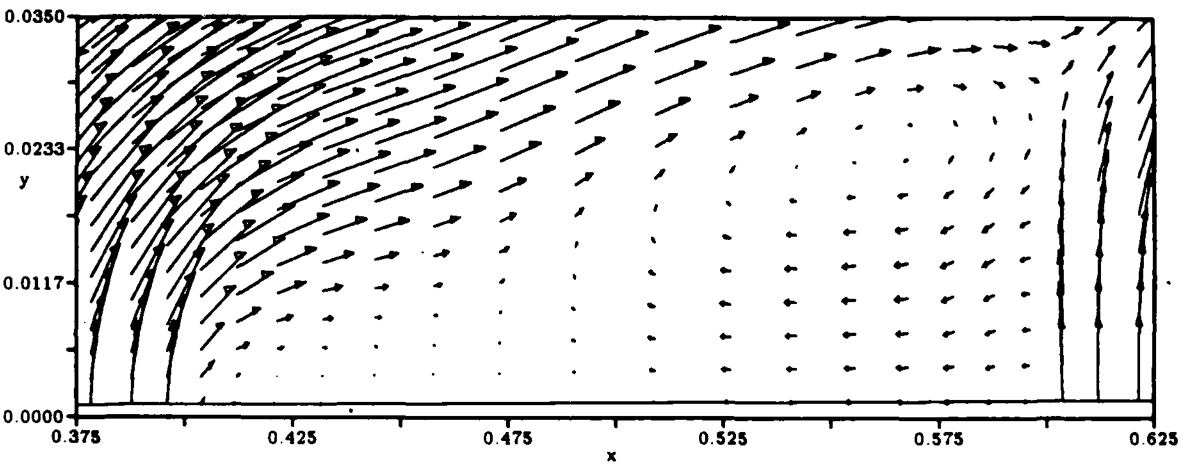

Fig. 18: Velocity vectors in the separated flow region between the two blowing strips.

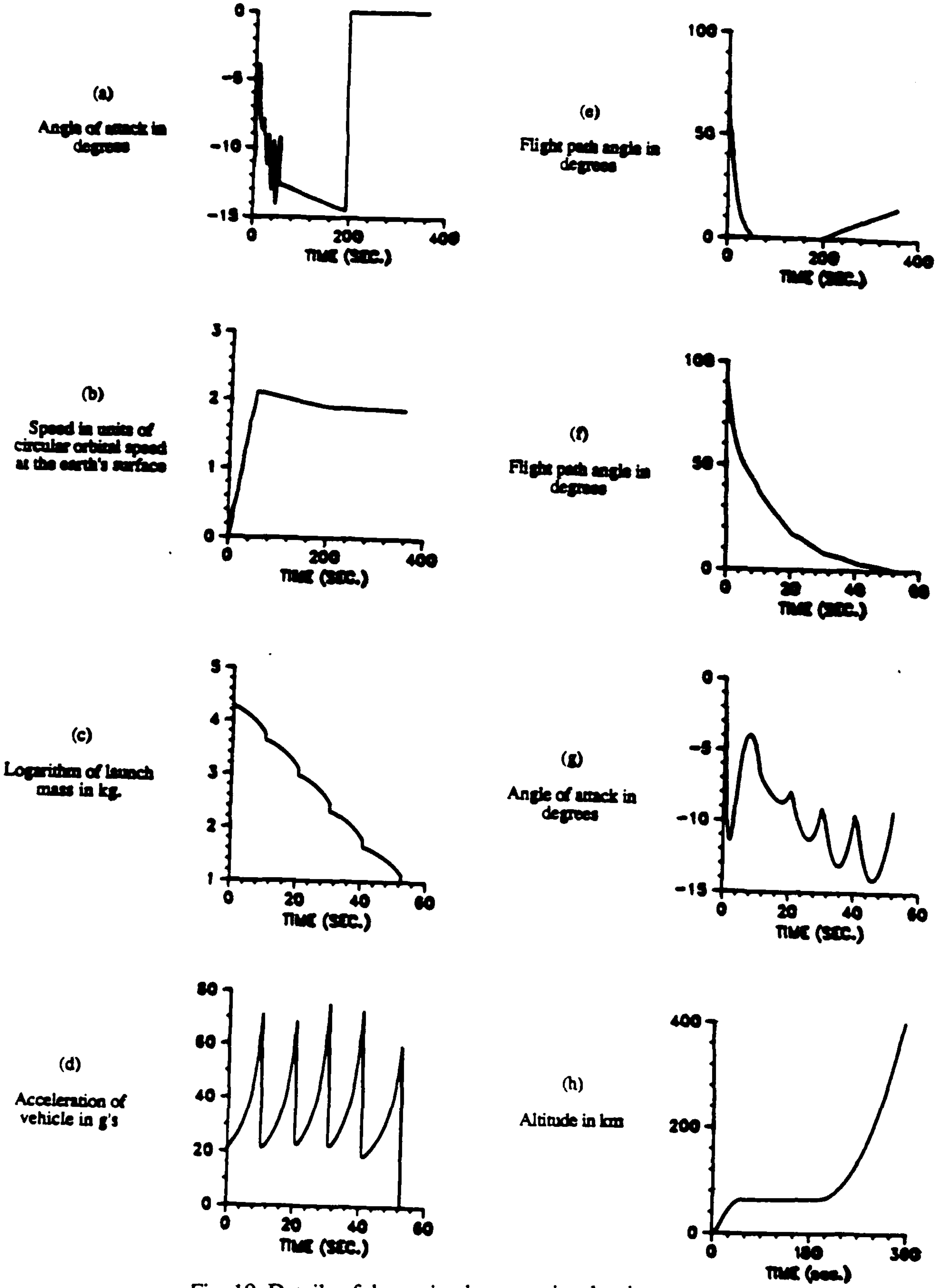

Fig. 19 Details of the optimal aero assisted trajectory.

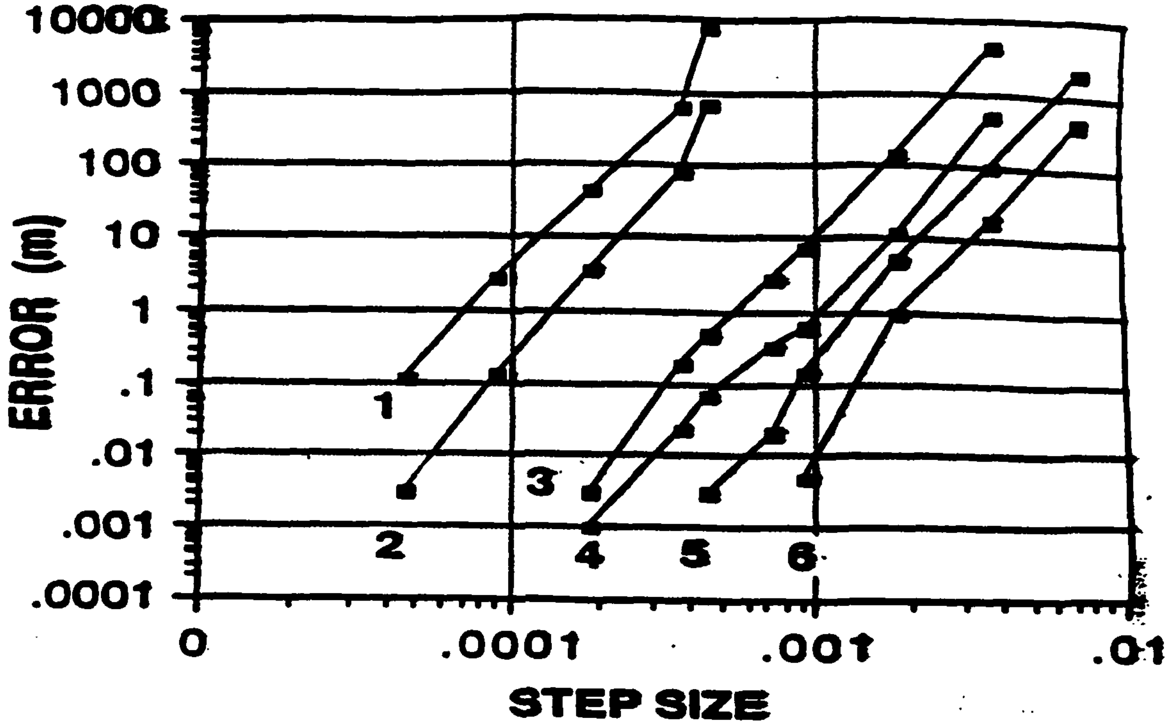

NO.	INTEGRATION METHOD	CONTROL
1	RK-4	ALPHA
2	SPAM-5	ALPHA
3	RK-4	GAMMA
4	SPAM-5	GAMMA
5	RK-4 + ANALYTIC THRUST TERM	GAMMA
6	SPAM-5 + ANALYTIC THRUST TERM	GAMMA

Fig. 20 The final time position error for the various integration methods and controls.

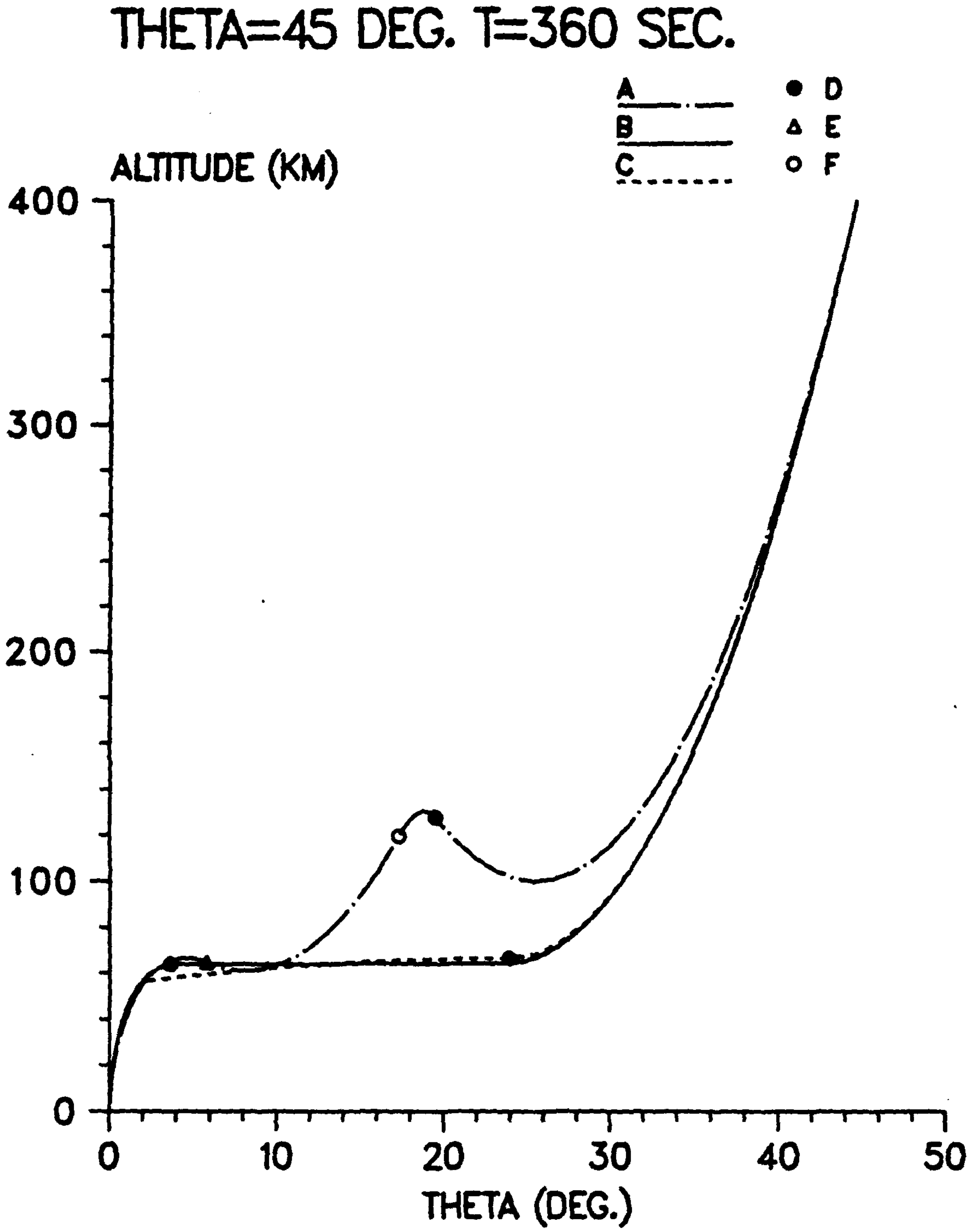

Fig. 21 Optimal trajectories for minimum launch mass: A-Keplerian, B-aeroassisted, C-zero-lift atmospheric, D-burnout of fifth stage, E-burnout of fourth stage, F-end of coast for fifth stage. Payload = 10 kg.; range angle = 45 deg.; target altitude = 400 km.; flight time = 360 sec.

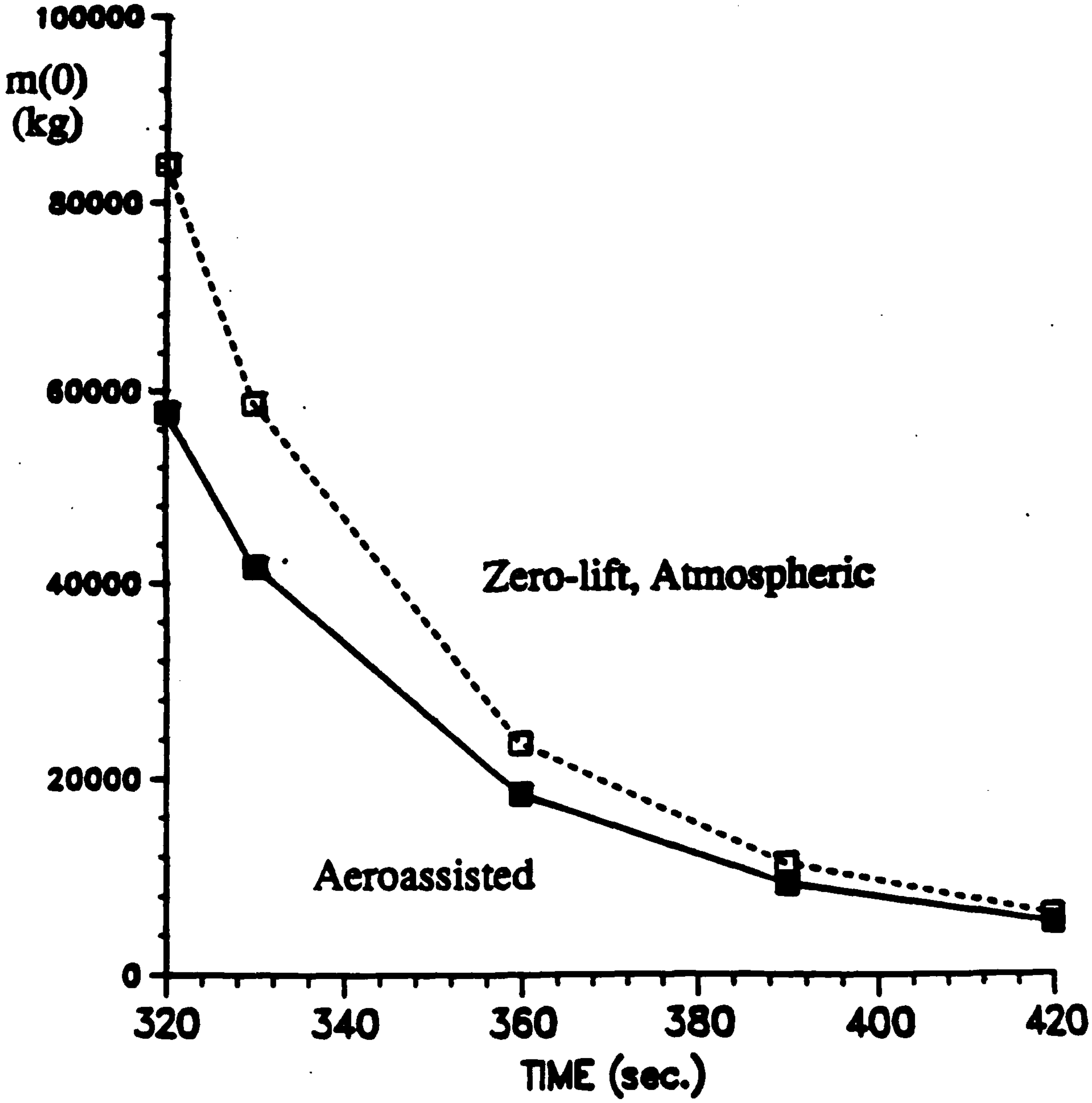

Fig. 22 Optimal launch mass as a function of flight time. Number of stages = 5; payload = 10 kg.; range angle = 45 deg.; target altitude = 200 km.; specific impulse = 300 sec.

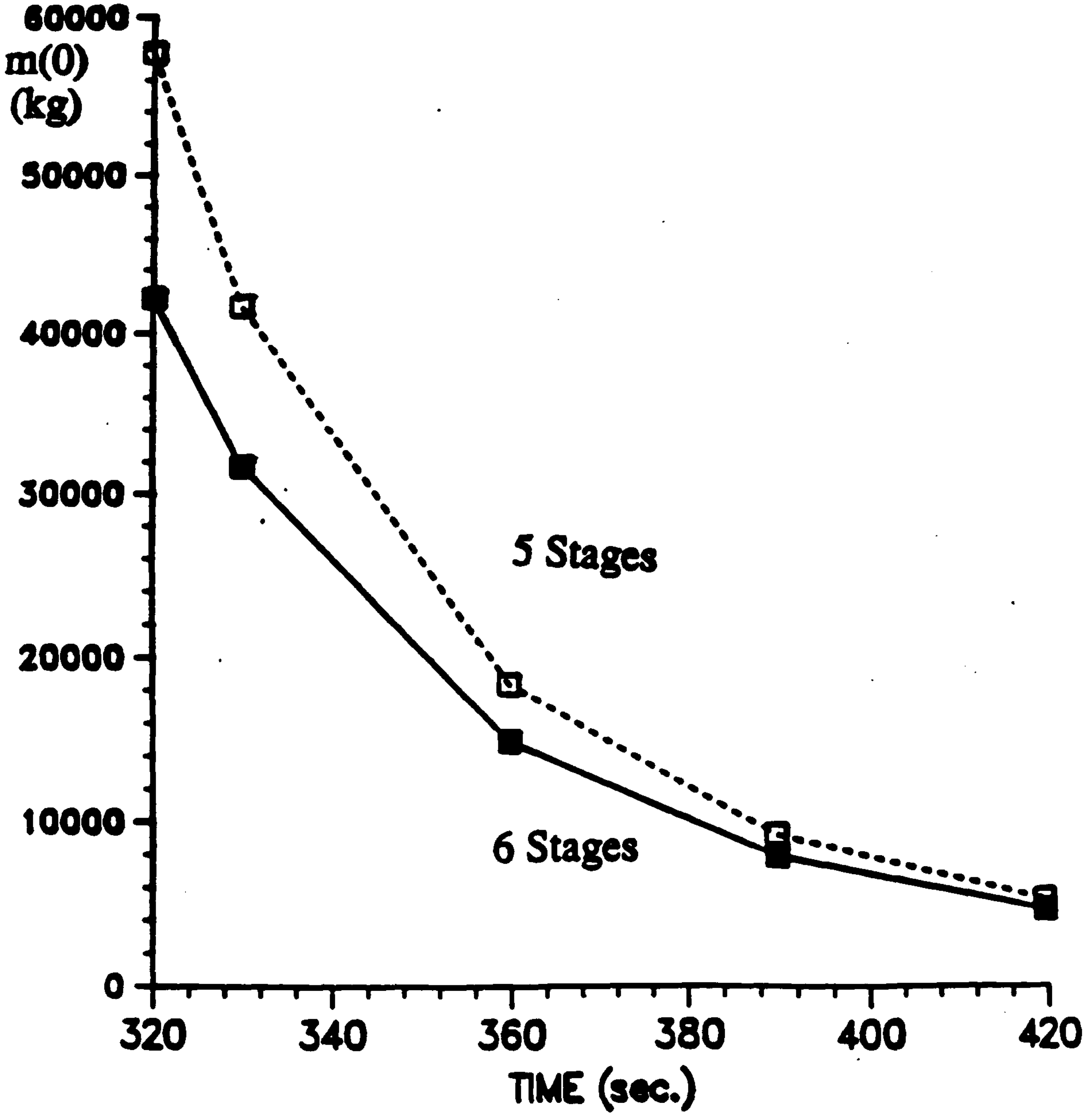

Fig. 23 Optimal launch mass as a function of flight time for aeroassisted trajectories.
Payload = 10 kg.; range angle = 45 deg.; target altitude = 200 km.;
specific impulse = 300 sec.

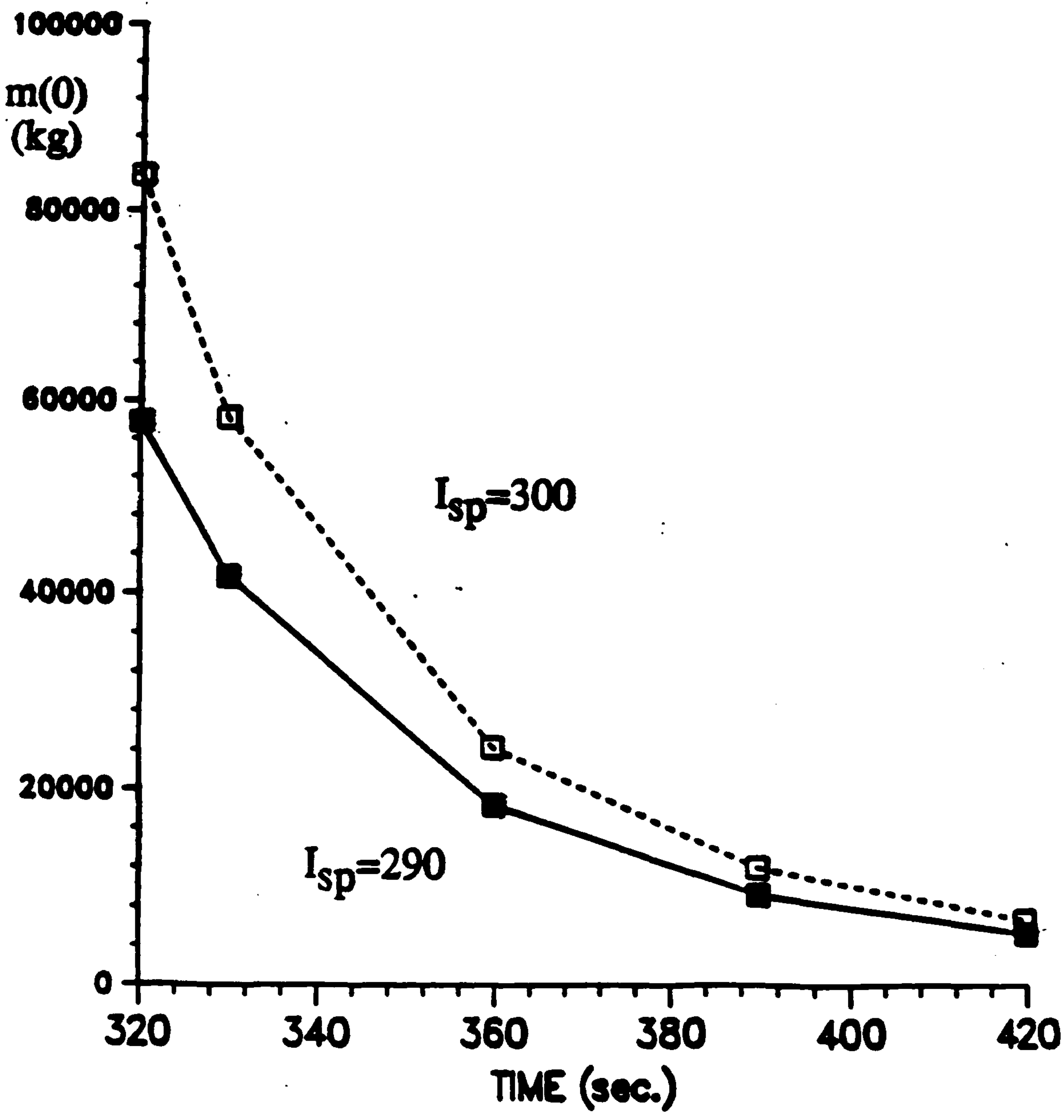

Fig. 24 Optimal launch mass as a function of flight time for aeroassisted trajectories. Number of stages = 5; payload = 10 kg.; range angle = 45 deg.; target altitude = 200 km.

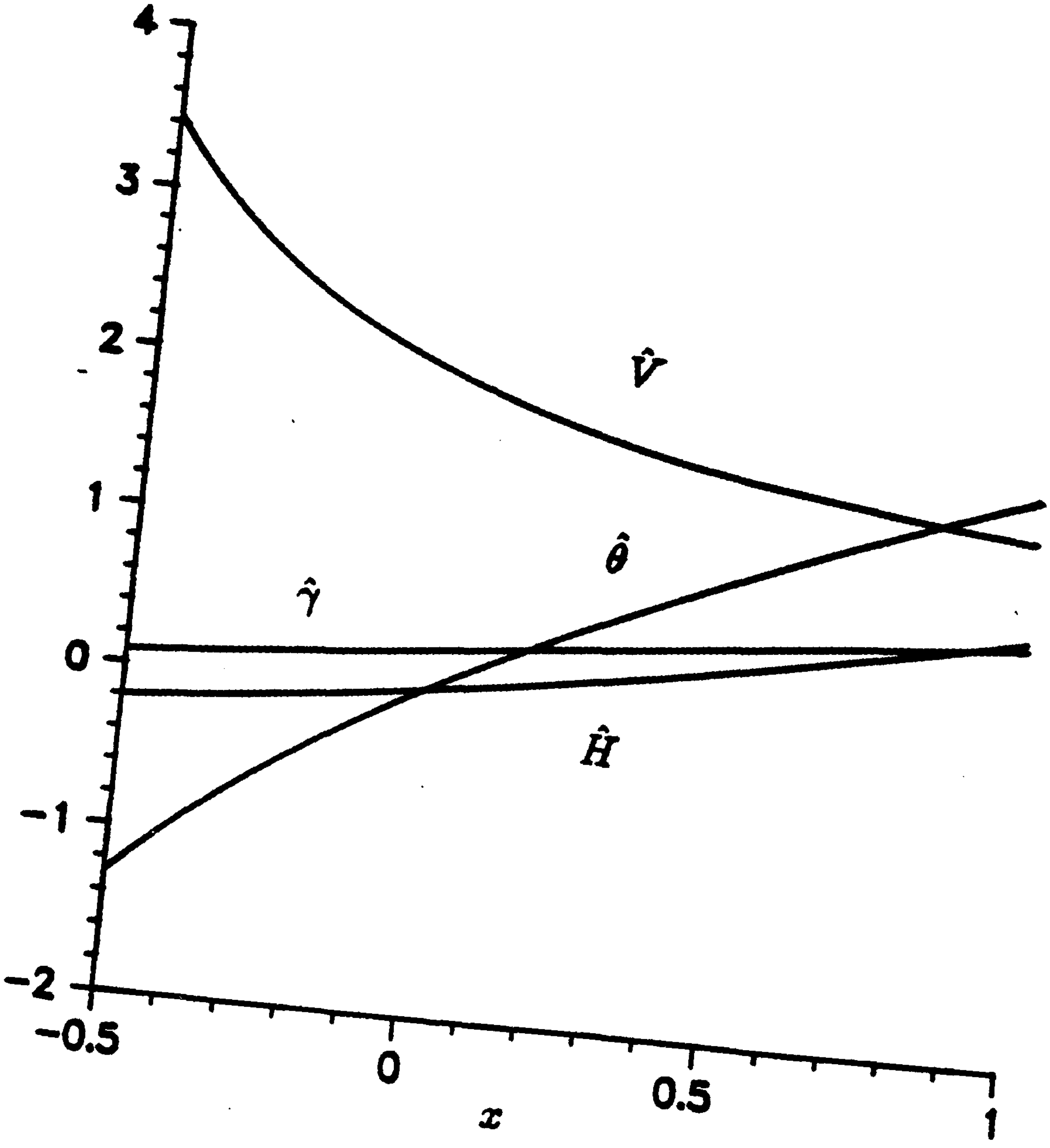

Fig. 25 Functions describing motion on the universal curve.

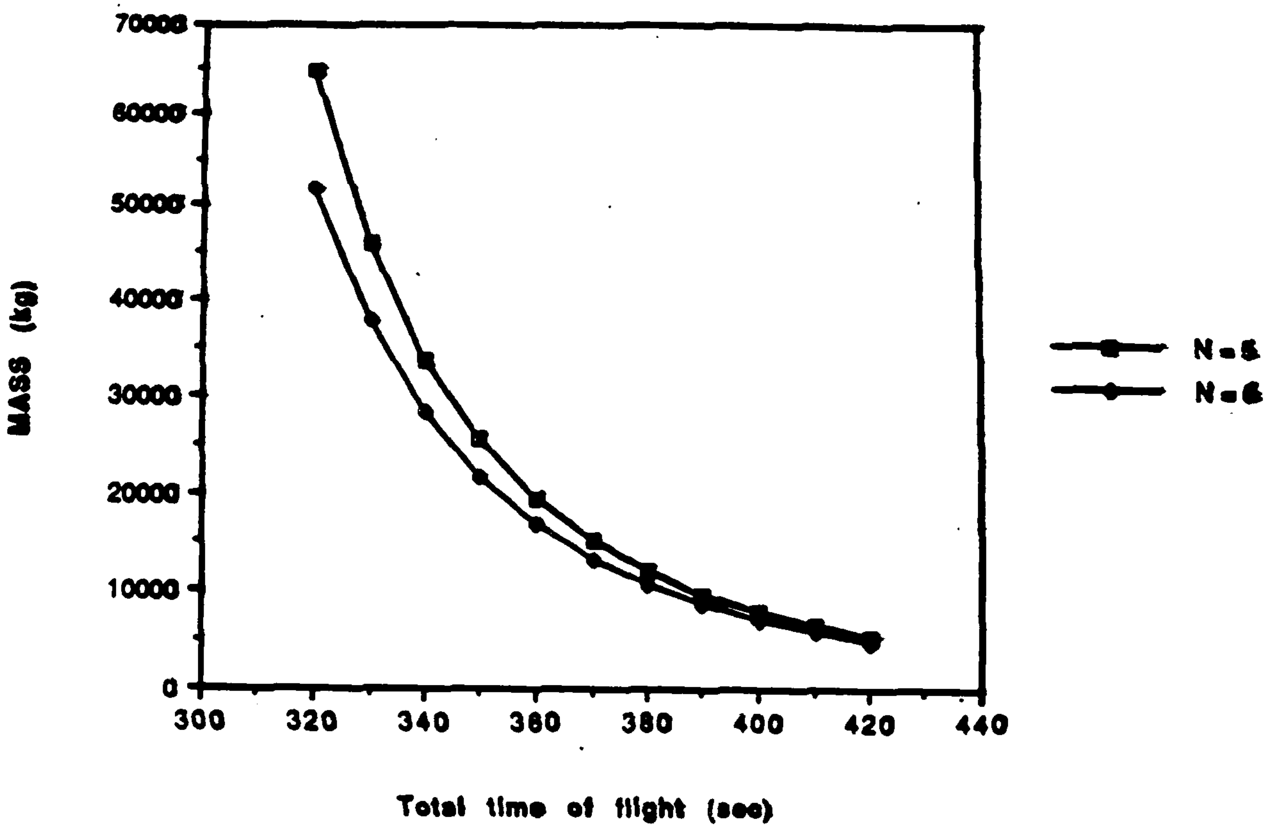

Fig. 26 Optimal solutions based on semi-analytic approach.

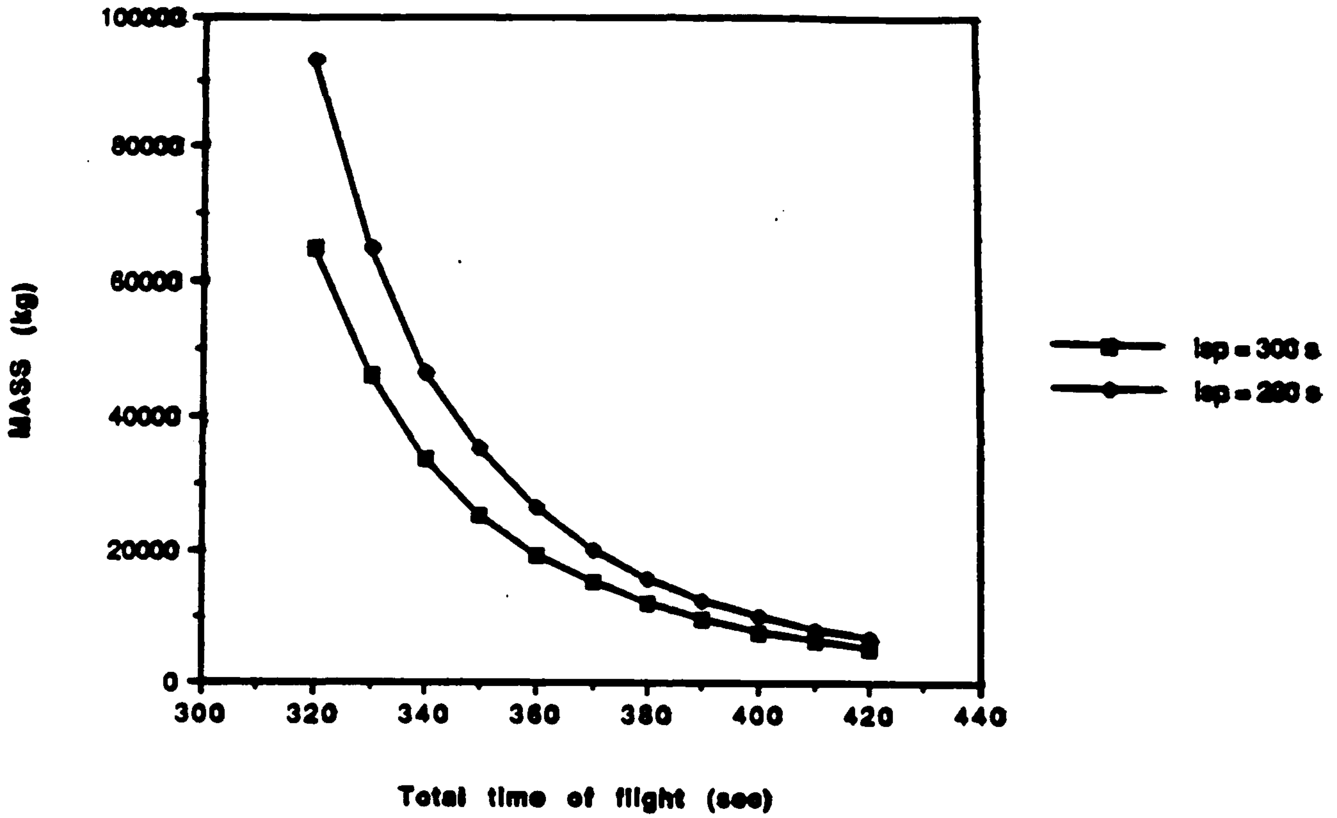

Fig. 27 Optimal solutions based on semi-analytic approach.

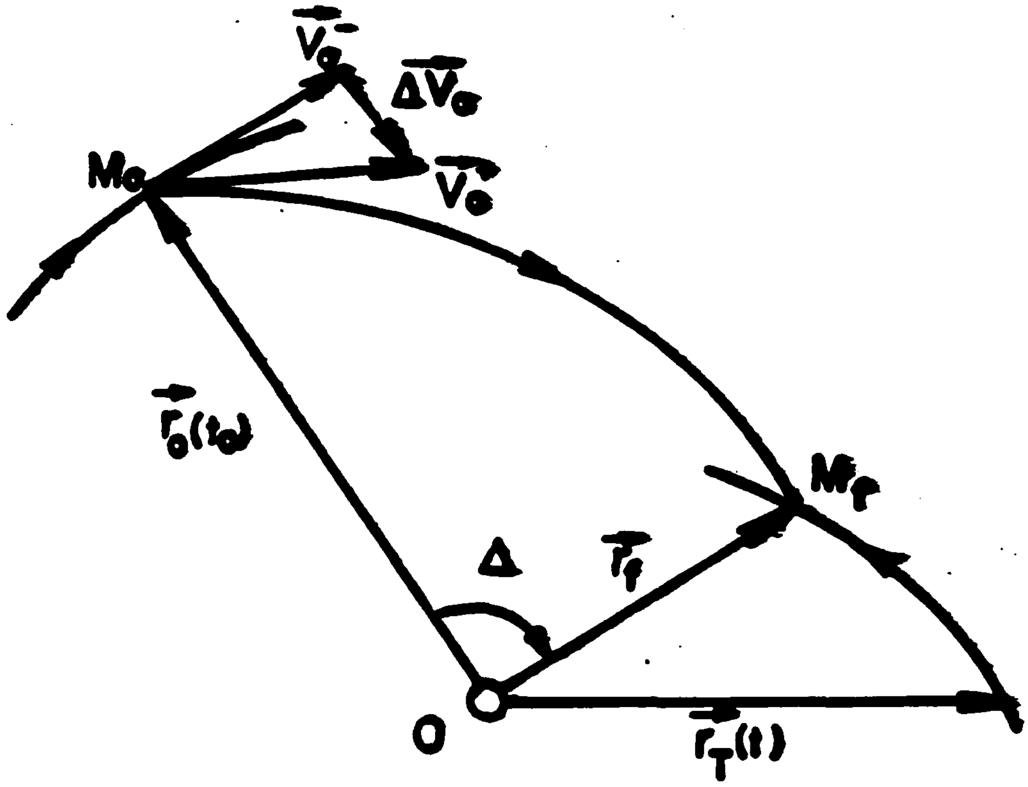
$\vec{V}_0^-$
$\Delta\vec{V}_0$
M_0
$\vec{V}_0$
$\vec{r}_0(t_0)$
M_f
Δ
$\vec{r}_f$
O
$\vec{r}_T(t)$

Fig. 28 Intercept trajectory.

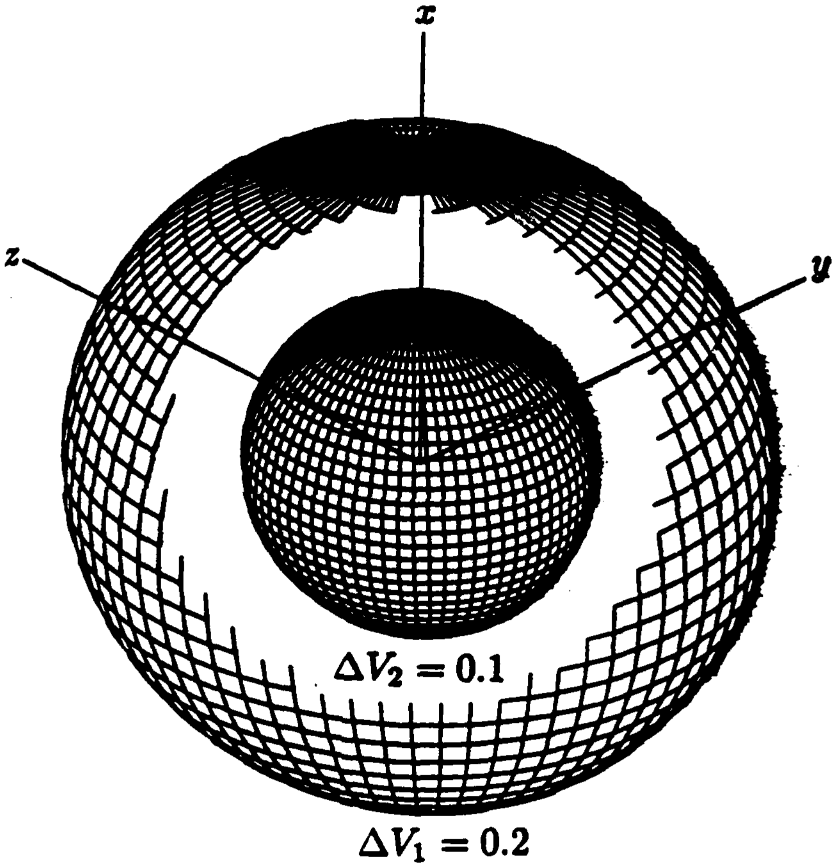
x
z
y
$\Delta V_2 = 0.1$
$\Delta V_1 = 0.2$

Fig. 29 The reachable surface with $\Delta V_1 > \Delta V_2$.

Appendix A

Copies of Publications and Conference Papers Resulting from Work Done for this Contract

Hypersonic viscous interaction with strong blowing

By A. F. MESSITER AND M. D. MATARRESE

Department of Aerospace Engineering, The University of Michigan,
Ann Arbor, MI 48109-2140, USA

Solutions are obtained for hypersonic viscous interaction along a flat plate in the presence of strong boundary-layer blowing, with inverse-square-root injection velocity, for laminar flow over a cold wall and with a power-law viscosity-temperature relation. In the strong-interaction region, self-similarity is preserved if the blowing is such that the thicknesses of the inviscid shock layer, viscous shear layer, and inviscid blown layer all have the same order of magnitude. The weak-interaction region is also considered, and an approximate interpolation is used to join the solutions for the surface pressure. Certain difficulties in asymptotic matching are discussed, and the extension to flow past a thin wedge is shown.

---

1. Introduction

Drastic changes in the pressure variation along a boundary layer can occur in the presence of strong surface blowing, especially if the blowing velocity is large enough that the boundary layer is completely "blown off" from the surface. In that event a region of nearly inviscid injected fluid is present between the thin viscous layer and the wall, with the pressure distribution determined through an interaction with the external flow. For subsonic or for incompressible laminar flow asymptotic solutions beyond blowoff were given by Kassoy (1971) and by Klemp & Acrivos (1972). For supersonic speeds Cole & Aroesty (1968) considered strong blowing in limiting cases such that the thickness of the blown-off shear layer could be neglected.

Among other studies, only a few were primarily concerned with obtaining asymptotic solutions for strong blowing. Kubota & Fernandez (1968) solved the boundary-layer equations for compressible laminar flow in the limit of large mass injection. Wallace & Kemp (1969) followed Cole & Aroesty (1968) in considering examples for which the shear-layer thickness can be neglected. Smith & Stewartson (1973b) treated a supersonic boundary layer with uniform blowing that starts at a point downstream of the leading edge, choosing the velocity to have an order of magnitude consistent with triple-deck scaling. A good summary of this and other earlier work was given by Smith & Stewartson (1973a).

At hypersonic speeds interaction effects are present even in the absence of blowing. If a flat plate is placed in a uniform hypersonic flow, the boundary-layer displacement effect causes the appearance of a shock wave. Far enough downstream the pressure change across the shock wave is small ("weak interaction") but in a region further forward the pressure ratio across the shock becomes large ("strong interaction"). At points still closer to the leading edge, all relevant distances are of the same order of magnitude, so that the boundary-layer approximation fails, and the distinction between boundary layer, inviscid shock layer, and shock wave disappears ("merged-layer regime"). These effects have been discussed in the books by Hayes & Probstein (1959) and by Stewartson (1964); additional details concerning asymptotic matching of the strong-interaction solutions have been given by Bush (1966) and by Lee & Cheng (1969).

Self-similarity for hypersonic strong interaction is preserved for surface blowing of a power-law form consistent with the usual interaction solutions. Li & Gross (1961) gave numerical results for the strong-interaction problem with weak blowing such that the boundary layer is not yet blown off. Of interest in the present work is the case of larger blowing velocity such that the injected gas occupies a "blown layer" having thickness of the same order as the thickness of the viscous shear layer and the inviscid "shock layer" between the viscous layer and the shock wave. The shock layer is described by hypersonic small-disturbance theory (Van Dyke 1954), the blown layer by "inviscid boundary-layer equations" and the viscous layer by the usual boundary-layer equations, all in self-similar form. In the case considered here, the injected gas is taken to have density of the same order as the density in the undisturbed external flow, whereas the density in the high-temperature viscous layer is much lower. Solutions are described for each of the three layers, weak interaction further downstream is discussed for the same wall conditions, and the extension to wedge flow is shown.

2. Formulation

A semi-infinite flat plate is placed in a uniform hypersonic flow with velocity u_∞, pressure p_∞, density ρ_∞, temperature T_∞, Mach number M_∞, and viscosity coefficient μ_∞. Coordinates X and Y are measured along and normal to the plate, respectively, with origin at the leading edge. The nondimensional velocity $\mathbf{u}=(u,v)$, pressure p, density ρ, temperature T, and viscosity coeffient μ are all referred to their undisturbed values. The viscosity is assumed to depend on the temperature through the power-law relation $\mu=T^\omega$, where $1/2<\omega<1$; the case $\omega=1$ is also considered briefly.

The nondimensional continuity, momentum, and energy equations for steady flow can be written

$$\operatorname{div} \rho\mathbf{u} = 0, \tag{2.1}$$

$$\rho\mathbf{u}\cdot\nabla\mathbf{u} + (\gamma M_\infty^2)^{-1}\nabla p = Re^{-1} \operatorname{div} \tau, \tag{2.2}$$

$$\rho\mathbf{u}\cdot\nabla(H/2) = Re^{-1} \operatorname{div} (\tau\,\mathbf{u} - \mathbf{q}), \tag{2.3}$$

where $\gamma=c_p/c_v$ is the ratio of specific heats; H is the total enthalpy, nondimensional with $u_\infty^2/2$; the coordinates are $x=X/X_r$ and $y=Y/X_r$, with X_r a reference length still to be defined; and $Re=u_\infty X_r/\nu_\infty$ is the Reynolds number, with $\nu_\infty=\mu_\infty/\rho_\infty$. The stress tensor is $\tau = 2\mu\varepsilon + \lambda I \operatorname{div} \mathbf{u}$, where λ is the second viscosity coefficient, nondimensional with μ_∞; ε is the rate-of-strain tensor; and I is the identity tensor. The heat conduction vector is $\mathbf{q} = -\mu\nabla T/\{(\gamma-1)M_\infty^2 Pr\}$, where Pr is the Prandtl number. For simplicity the specific heats are taken to be constant; the injected gas is considered to be air; a perfect gas is assumed, so that $p=\rho T$; and the Prandtl number is taken equal to one.

The reference length X_r is chosen such that for $X \gg X_r$ the boundary layer has only a small effect on the external flow ("weak interaction") whereas for $X \ll X_r$ the changes in pressure are large in comparison with the undisturbed pressure ("strong interaction"); that is, the shock wave is very weak for $X \gg X_r$ but very strong for $X \ll X_r$. For weak interaction the shock wave has slope $\approx 1/M_\infty$, whereas the streamline inclination resulting from the boundary-layer displacement effect is $O\{(M_\infty^{1+\omega}/\sqrt{Re})(X_r/X)^{1/2}\}$. Requiring the latter expression to be much smaller than $1/M_\infty$ when $X \gg X_r$ leads to the choice $X_r=M_\infty^{4+2\omega}\nu_\infty/u_\infty$, and so the two large parameters M_∞ and Re are related by $Re= M_\infty^{4+2\omega}$. The coordinates then are defined by

$$x = X/X_r, \qquad y=Y/X_r, \qquad X_r=M_\infty^{4+2\omega}\nu_\infty/u_\infty. \tag{2.4}$$

The usual hypersonic viscous interaction parameter χ, based on a distance X, is proportional to $x^{-1/2}$. Solutions for the strong- and weak-interaction regions are found by considering limits of equations (2.1) through (2.3) as $M_\infty \to \infty$ and $x \to 0$ or $x \to \infty$ respectively.

It is convenient to think first in terms of the dividing case, represented by equations obtained in the limit as $M_\infty \rightarrow \infty$ with x fixed. In this case the Mach number based on velocity normal to the shock wave is neither close to one nor large. With strong blowing the boundary layer is blown off the wall as a viscous free shear layer, again described in the limit by the boundary-layer equations. An inviscid shock layer between the shock wave and the shear layer is described in a first approximation by the hypersonic-small-disturbance equations. The injected gas in a low-speed region below the shear layer is also described asymptotically by inviscid-flow equations. Solutions in adjacent regions are to be joined by appropriate asymptotic matching.

The nondimensional stream function ψ (referred to $\rho_\infty u_\infty X_r$) is defined by

$$\psi_y = \rho u, \qquad \psi_x = -\rho v. \tag{2.5}$$

It can be seen that the mass flow ψ will have different orders of magnitude in different parts of the flow. For $x=O(1)$, the shock wave is located at $y=O(1/M_\infty)$ and has slope $O(1/M_\infty)$; the mass flow crossing the shock wave is $\psi=O(1/M_\infty)$; and in the inviscid flow behind the shock wave $p-1=O(1)$, $\rho=O(1)$, and $T=O(1)$. The viscous shear layer has high temperature $T=O(M_\infty^2)$, because some of the kinetic energy is converted to thermal energy, and low density $\rho=O(1/M_\infty^2)$, because $p=\rho T$. If diffusion and convection terms are required to be of the same order for $X=O(X_r)$, where X_r is defined by (2.4), the shear-layer thickness is $O(1/M_\infty)$, and since $u=O(1)$ the mass flow in the shear layer is $\psi=O(1/M_\infty^3)$. In the blown layer adjacent to the wall, the density ρ is $O(1)$ for the case to be considered, and for $p-1=O(1)$ the momentum equation then gives $u=O(1/M_\infty)$. If the blown-layer thickness is also to be $O(1/M_\infty)$, the mass flow must be $\psi=O(1/M_\infty^2)$. The reference streamline is chosen such that $\psi>0$ for air from the free stream and $\psi<0$ for the blown gas; the streamline $\psi=0$ lies within the shear layer.

It appears helpful to introduce notation which takes into account the different orders of magnitude in the different flow regions. For this purpose a hat, bar and tilde will denote variables in the inviscid shock layer, the viscous shear layer, and the inviscid blown layer, respectively. The corresponding stream-function coordinates are, respectively,

$$\hat{\psi}=M_\infty\psi, \qquad \bar{\psi}=M_\infty^3\psi, \qquad \tilde{\psi}=M_\infty^2\psi. \tag{2.6}$$

In the shock layer, the dependent variables are expanded in the form

$$v=M_\infty^{-1}\hat{v}(x,\hat{\psi}) + \ldots, \tag{2.7}$$

$$p=\hat{p}(x,\hat{\psi}) + \ldots, \tag{2.8}$$

$$\rho=\hat{\rho}(x,\hat{\psi}) + \ldots, \tag{2.9}$$

$$y=M_\infty^{-1}\hat{y}(x,\hat{\psi}) + \ldots, \tag{2.10}$$

for $0<\hat{\psi}<\hat{\psi}_s$, where $\hat{\psi}_s$ is the value of $\hat{\psi}$ at the shock wave; also $u=1+\ldots$, and $\hat{T}=\hat{p}/\hat{\rho}$. In the shear layer,

$$u=\bar{u}(x,\bar{\psi}) + \ldots, \tag{2.11}$$

$$\rho=M_\infty^{-2}\bar{\rho}(x,\bar{\psi}) + \ldots, \tag{2.12}$$

$$T=M_\infty^{2}\,\bar{T}(x,\bar{\psi}) + \ldots, \tag{2.13}$$

$$y=M_\infty^{-1}\bar{y}(x,\bar{\psi}) + \ldots, \tag{2.14}$$

and $\bar{p} = \bar{\rho}\,\bar{T}$. The range for $\bar{\psi}$ is $\bar{\psi}_0(x)<\bar{\psi}<\infty$, where $\bar{\psi}_0(x)<0$ is to be determined. In the blown layer,

$$u=M_\infty^{-1}\tilde{u}(x,\tilde{\psi}) + \ldots, \tag{2.15}$$

$$v=M_\infty^{-2}\tilde{v}(x,\tilde{\psi}) + \ldots, \tag{2.16}$$

$$\rho=\tilde{\rho}(x,\tilde{\psi}) + \ldots, \tag{2.17}$$

$$T=\tilde{T}(x,\tilde{\psi}) + \ldots, \tag{2.18}$$

$$y=M_\infty^{-1}\tilde{y}(x,\tilde{\psi}) + \ldots, \tag{2.19}$$

and $\tilde{p}=\tilde{\rho}\tilde{T}$. The range for $\tilde{\psi}$ is $\tilde{\psi}_w(x)<\tilde{\psi}<0$, where $\tilde{\psi}_w(x)$ is the value of $\tilde{\psi}$ at the wall and is specified. The combined displacement effect of the viscous layer and blown layer implies an effective thin body shape

$$y=M_\infty^{-1}\Delta(x), \qquad \Delta(x)=\bar{\Delta}(x)+\tilde{\Delta}(x), \tag{2.20}$$

where the functions $\bar{\Delta}(x)$ and $\tilde{\Delta}(x)$ represent, respectively, the contributions of the viscous and blown layers, to be determined. When M_∞ is large, omitted terms are small in comparison with terms retained in each of the expansions (2.7)-(2.19). Formulations for the strong- and weak-interaction problems are obtained by further expansion of (2.7) through (2.20) as $x\to 0$ or $x\to\infty$ respectively.

In the strong-interaction limit $x \rightarrow 0$, the hypersonic small-disturbance equations possess a family of self-similar solutions corresponding to flows past thin power-law bodies. The viscous-layer equations likewise possess a family of self-similar solutions. If the solutions in the two regions are required to match correctly, it is found that the similarity variable (for y) must be $M_\infty y/x^{3/4}$ and the pressure in the viscous layer is $\bar{p} \sim \bar{p}_1 x^{-1/2}$ (e. g., Stewartson 1964). In the presence of surface blowing the self-similarity is preserved if the blowing velocity and wall temperature are such that the thickness of the blown layer is also $O(M_\infty^{-1} x^{3/4})$. The effective body shape $\Delta(x)$ then has the form

$$\Delta(x) \sim \Delta_1 x^{3/4}, \qquad \Delta_1 = \bar{\Delta}_1 + \tilde{\Delta}_1, \tag{2.21}$$

where $\bar{\Delta}_1$ and $\tilde{\Delta}_1$ are constants to be determined, and the contributions of the viscous and blown layers are $\bar{\Delta}(x) \sim \bar{\Delta}_1 x^{3/4}$ and $\tilde{\Delta}(x) \sim \tilde{\Delta}_1 x^{3/4}$. It also follows that the shock-wave slope dY/dX is no longer small when $x = O(M_\infty^{-4})$, i. e., when $X = O(M_\infty^{2\omega} \nu_\infty / u_\infty)$; a strong-interaction solution thus describes the flow region $M_\infty^{-4} \ll x \ll 1$. The various flow regions are indicated in figure 1.

For strong interaction it is seen, with the help of the shock-wave jump conditions, that the mass flow in the inviscid shock layer is $\psi = M_\infty^{-1} \hat{\psi} = O(M_\infty^{-1} x^{3/4})$. In the shear layer, the temperature is $T \sim M_\infty^2 \bar{T} = O(M_\infty^2)$ and the density (from the perfect-gas law) is $\rho \sim M_\infty^{-2} \bar{\rho} = O(M_\infty^{-2} x^{-1/2})$; the velocity is $u = O(1)$, and so the mass flow is much smaller, namely $\psi = M_\infty^{-3} \bar{\psi} = O(M_\infty^{-3} x^{1/4})$. In the case to be considered here, the wall density is taken to be $\rho_w \sim \tilde{\rho}_w = O(1)$, and the Bernoulli equation for compressible flow gives $u \sim M_\infty^{-1} \tilde{u} = O(M_\infty^{-1} x^{-1/4})$ for the injected gas; the required mass flow $\psi = M_\infty^{-2} \tilde{\psi} = O(M_\infty^{-2} x^{1/2})$ in the blown layer is therefore provided by a blowing velocity $v_w \sim M_\infty^{-2} \tilde{v}_w = O(M_\infty^{-2} x^{-1/2})$. It follows, for example, that the mass flow $\rho_w v_w$ at the wall is smaller than the mass flow $\rho_\infty u_\infty d(\Delta/M_\infty)/dx$ through the shock wave by a factor $O(1/M_\infty)$, and that the wall shear stress $(\mu \partial u/\partial y)_w$ is smaller than the momentum flux $\rho_w v_w^2$ at the surface by a factor $O(M_\infty^{-2\omega})$. The three different mass flows suggest the three similarity variables (for ψ) needed for the inviscid shock layer, the viscous shear layer, and the inviscid blown layer:

$$\hat{\zeta} = \hat{\psi}/x^{3/4}, \qquad \bar{\zeta} = \bar{\psi}/x^{1/4}, \qquad \tilde{\zeta} = \tilde{\psi}/x^{1/2}. \tag{2.22}$$

The choices for the blown layer are, however, not unique. The required conditions (mass conservation, perfect-gas law, Bernoulli equation) are found to be satisfied if $M_w=(\text{const.})\, M_\infty^{-1}x^{-1/2}$, where $M_w=M_\infty v_w T_w^{-1/2}$ is the Mach number of the injected gas at the surface. Another possible choice that would satisfy this requirement is T_w=const. and $v_w=M_\infty^{-2}\,\tilde{v}_{1w}\,x^{-1/4}$, giving a mass flow $\tilde{\psi}=O(M_\infty^{-2}x^{1/4})$ that has the same x-dependence as the mass flow in the shear layer. This case corresponds more closely to the flows considered by Kubota & Fernandez (1968) and Li & Gross (1961). Although the wall temperature then would not match directly with the higher temperature in the merged-layer regime, the solution methods are otherwise the same, with some different details for the blown layer and for the final result relating surface pressure and blowing velocity.

The layer thicknesses and mass flows for strong interaction corresponding to (2.21) and (2.22) are summarized in figure 2. Solutions for the three regions can be obtained separately, each leading to a relation between pressure and a layer thickness, as shown in §3. First-order matching conditions then allow the results to be combined so as to determine the relation between surface pressure and blowing velocity. Some numerical results are described in §4.

3. Solutions

3.1 *Inviscid shock layer*

In a first approximation the inviscid flow at high Mach number past a thin two-dimensional body is equivalent to one-dimensional unsteady flow in a plane slab of fluid passing over the body at the undisturbed speed, and is described by the hypersonic small-disturbance equations (Van Dyke 1954). In terms of independent variables x and $\hat{\psi}$ the continuity, momentum, entropy, and streamline equations become, respectively,

$$(1/\hat{\rho})_x - \hat{v}_{\hat{\psi}} + \ldots = 0, \tag{3.1}$$

$$\hat{v}_x + \gamma^{-1}\hat{p}_{\hat{\psi}} + \ldots = 0, \tag{3.2}$$

$$\hat{p}_x - (\gamma\hat{p}/\hat{\rho})\hat{\rho}_x + \ldots = 0, \tag{3.3}$$

$$\hat{y}_{\hat{\psi}} - (1/\hat{\rho}) + \ldots = 0. \tag{3.4}$$

If the shock wave $\hat{\psi}=\hat{\psi}_s(x)$ is very strong, so that $\hat{\psi}_s' \gg 1$, the corresponding jump conditions across the shock are

$$\hat{\rho}_s = (\gamma+1)/(\gamma-1) + \ldots, \tag{3.5}$$

$$\hat{p}_s = 2\gamma\, \hat{\psi}_s'^2/(\gamma+1) + \ldots, \tag{3.6}$$

$$\hat{v}_s = 2\hat{\psi}_s'/(\gamma+1) + \ldots, \tag{3.7}$$

$$\hat{y}_s = \hat{\psi}_s, \tag{3.8}$$

where $\hat{\rho}_s=\hat{\rho}(x, \hat{\psi}_s)$, etc. As $\hat{\psi}\rightarrow 0$, at the inner "edge" of the shock layer, $\hat{y}\rightarrow\Delta(x)$ and $\hat{v}\rightarrow\Delta'(x)$.

In the limit as $M_\infty\rightarrow\infty$, $x\rightarrow 0$, and $\hat{\psi}\rightarrow 0$ such that $M_\infty{}^4x\rightarrow\infty$ and $\hat{\zeta} = \hat{\psi}/x^{3/4}$ is held fixed, the functions appearing in (2.7) through (2.10) can be expressed in self-similar form by

$$\hat{v} = x^{-1/4}\, \hat{v}_1(\hat{\zeta}) + \ldots, \tag{3.9}$$

$$\hat{p} = x^{-1/2}\, \hat{p}_1(\hat{\zeta}) + \ldots, \tag{3.10}$$

$$\hat{\rho} = \hat{\rho}_1(\hat{\zeta}) + \ldots, \tag{3.11}$$

$$\hat{y} = x^{3/4}\, \hat{y}_1(\hat{\zeta}) + \ldots. \tag{3.12}$$

Substitution into (3.1) through (3.4) then provides a system of first-order nonlinear ordinary differential equations, subject to boundary conditions found from the shock relations (3.5) through (3.8). The entropy equation can be integrated to give a relation between $\hat{p}_1$ and $\hat{\rho}_1$:

$$\hat{\rho}_1{}^\gamma = \left(\frac{\gamma+1}{\gamma-1}\right)^\gamma \frac{\gamma+1}{2\gamma}\left(\frac{4}{3}\right)^2\left(\frac{\Delta_1}{\hat{y}_{1s}}\right)^2\left(\frac{\hat{p}_1}{\Delta_1{}^2}\right)\left(\frac{\hat{\zeta}}{\hat{y}_{1s}}\right)^{2/3}. \tag{3.13}$$

Numerical integration of the remaining equations for $\gamma=1.4$, with $\hat{y}_1\rightarrow\Delta_1$ and $\hat{v}_1\rightarrow 3\Delta_1/4$ as $\hat{\zeta}\rightarrow 0$, leads to the values

$$\hat{p}_1(0)/\Delta_1{}^2 = 1.1194, \qquad \Delta_1/\hat{y}_{1s} = 0.5912, \tag{3.14}$$

which agree with values given by Brown & Stewartson (1975) and by Li and Gross (1961). Since $\hat{p}_1 \sim$ constant as $\hat{\zeta}\to 0$, (3.13) shows that $\hat{\rho}_1 = O(\hat{\zeta}^{2/(3\gamma)})$ as $\hat{\zeta}\to 0$. Solutions for the viscous and blown layers are now needed to determine Δ_1 in terms of the blowing velocity at the surface.

3.2 *Inviscid blown layer*

Solutions for the blown layer follow directly from the results of Cole and Aroesty (1968). Since the layer is thin, in a first approximation the pressure is a function only of x and the differential equations are "inviscid boundary-layer equations":

$$\tilde{\rho}\tilde{u}\tilde{u}_x + \gamma^{-1}\tilde{p}_x + \ldots = 0, \tag{3.15}$$

$$\tilde{p}_{\tilde{\psi}} + \ldots = 0, \tag{3.16}$$

$$\tilde{p}_x - (\gamma\tilde{p}/\tilde{\rho})\tilde{\rho}_x + \ldots = 0, \tag{3.17}$$

$$\tilde{y}_{\tilde{\psi}} - (\tilde{\rho}\tilde{u})^{-1} = 0, \tag{3.18}$$

where $\tilde{p}=\tilde{p}(x)$. The mass flow at the wall is $\tilde{\psi}=\tilde{\psi}_w(x)$, where $d\tilde{\psi}_w=-\tilde{\rho}_w\tilde{v}_w dx$; the inverse relationship $x=x_w(\tilde{\psi})$, where $dx_w=-(\tilde{\rho}_w\tilde{v}_w)^{-1}d\tilde{\psi}$, identifies a streamline by the location at which it leaves the wall. At the wall the density $\tilde{\rho}_w$ and the blowing velocity $\tilde{v}_w$ are to be specified, and can be expressed by evaluating $\tilde{\rho}$ and $\tilde{v}$ either at x and $\tilde{\psi}_w(x)$ or at x_w and $\tilde{\psi}(x_w)$. The latter interpretation is needed in most of the following, so $\tilde{\rho}_w$ and $\tilde{v}_w$ will denote quantities which are constant along streamlines. Integration of the entropy and momentum equations leads to solutions for $\tilde{\rho}$ and $\tilde{u}$ in terms of x and x_w:

$$\tilde{\rho} = \left(\frac{\tilde{p}}{\tilde{p}_w}\right)^{1/\gamma}\tilde{\rho}_w + \ldots, \tag{3.19}$$

$$\tilde{u}^2 = \frac{2}{\gamma-1}\tilde{T}_w\left\{1-\left(\frac{\tilde{p}}{\tilde{p}_w}\right)^{(\gamma-1)/\gamma}\right\} + \ldots, \tag{3.20}$$

where $\tilde{p}=\tilde{p}(x)$ and $\tilde{p}_w=\tilde{p}(x_w)$; $\tilde{T}_w=\tilde{p}_w/\tilde{\rho}_w$ is the wall temperature, as a function of x_w.

If now $x\to 0$ with $\tilde{\zeta}=\tilde{\psi}/x^{1/2}$ fixed, where $\tilde{\zeta}_w<\tilde{\zeta}<0$, the solutions can be expanded in the form

$$\tilde{u} = x^{-1/4}\,\tilde{u}_1(\tilde{\zeta}) + \ldots, \tag{3.21}$$

$$\tilde{v} = x^{-1/2}\,\tilde{v}_1(\tilde{\zeta}) + \ldots, \tag{3.22}$$

$$\tilde{\rho} = \tilde{\rho}_1(\tilde{\zeta}) + \ldots, \tag{3.23}$$

$$\tilde{p} = x^{-1/2}\,\tilde{p}_1 + \ldots, \tag{3.24}$$

$$\tilde{y} = x^{3/4}\,\tilde{y}_1(\tilde{\zeta}) + \ldots, \tag{3.25}$$

where $\tilde{p}_1$ is a constant to be determined, the blowing velocity is $\tilde{v}_w = x_w^{-1/2}\tilde{v}_{1w}$, and $\zeta_w = -2\tilde{\rho}_{1w}\tilde{v}_{1w}$ is a specified constant. With $\tilde{p}_w \sim \tilde{p}_1 x_w^{-1/2}$ and $\xi = x_w/x$, the streamline shapes are found by substituting the expansions of (3.19) and (3.20) in (3.18):

$$d\tilde{y}_1 = -\left(\frac{\gamma-1}{2\tilde{T}_{1w}}\right)^{1/2} \tilde{v}_{1w}\, \xi^{-(\gamma+2)/(4\gamma)} \left(1-\xi^{(\gamma-1)/(2\gamma)}\right)^{-1/2} d\xi, \tag{3.26}$$

where $\tilde{T}_1 = \tilde{p}_1/\tilde{\rho}_1$, $\tilde{T}_{1w} = \tilde{T}_1(\zeta_w)$, etc. The effective layer thickness $\tilde{\Delta}_1 x^{3/4}$ is found by integration between 0 and 1. After a change of variable $\eta = \xi^{(\gamma-1)/(2\gamma)}$,

$$\tilde{\Delta}_1 = \left(\frac{2\tilde{\rho}_{1w}}{(\gamma-1)\tilde{p}_1}\right)^{1/2} \gamma\, \tilde{v}_{1w} \int_0^1 \eta^{(\gamma/2)/(\gamma-1)}\,(1-\eta)^{-1/2}\, d\eta$$

$$= \{2\pi(\gamma-1)\}^{1/2}\, \frac{2\gamma^2}{2\gamma-1} \left(\frac{\tilde{\rho}_{1w}\tilde{v}_{1w}^{\,2}}{\tilde{p}_1}\right)^{1/2} \Gamma\left(\frac{\gamma}{2(\gamma-1)}\right) \Big/ \Gamma\left(\frac{1}{2(\gamma-1)}\right), \tag{3.27}$$

in agreement with a result of Cole & Aroesty (1968). For $\gamma = 1.4$, $\tilde{\Delta}_1 = 3.501 \cdot (\tilde{\rho}_{1w}\tilde{v}_{1w}^{\,2}/\tilde{p}_1)^{1/2}$. If the shear-layer thickness were negligible, i. e., if $\bar{\Delta}_1 \ll \tilde{\Delta}_1$, then $\Delta_1 \approx \tilde{\Delta}_1$ and the surface pressure would be found by substituting this result in (3.14), with $\tilde{p}_1 = \hat{p}_1(0)$. In the case of primary interest here, however, $\bar{\Delta}_1$ can not be neglected; the required shear-layer solution is given in the next subsection.

In the weak-interaction region downstream, for $x \gg 1$, the form of solution is different because pressure changes are small rather than large. If the blowing velocity remains $v_w(x) = M_\infty^{-2}\tilde{v}_{1w}x^{-1/2} = M_\infty^{\omega}\tilde{v}_{1w}(u_\infty X/\nu_\infty)^{-1/2}$ for $x \gg 1$, the mass flow in the blown layer is again $\tilde{\psi} = O(x^{1/2})$. The pressure perturbation $\tilde{p}-1$, in a first approximation, is now proportional to the slope $d\Delta/dx$ of the equivalent body. From the Bernoulli equation, the velocity $\tilde{u}$ is $O((\tilde{p}-1)^{1/2})$. A mass-flow balance for the blown layer then shows that, for $x \gg 1$,

$$\tilde{p} - 1 = x^{-1/3}\,\tilde{\tilde{p}}_1 + \dots, \tag{3.28}$$

$$\tilde{u} = x^{-1/6}\,\tilde{\tilde{u}}_1(\tilde{\zeta}) + \dots, \tag{3.29}$$

$$\tilde{y} = x^{2/3}\,\tilde{\tilde{y}}_1(\tilde{\zeta}) + \dots, \tag{3.30}$$

where a double tilde is used to distinguish where necessary from the symbols introduced for $x \ll 1$. The solutions are found in the same way as for $x \ll 1$, but are simpler in form because the density $\tilde{\rho} \sim \tilde{\rho}_{1w}$ is nearly constant for $x \gg 1$:

$$\tilde{\tilde{u}}_1{}^2 = \frac{2\tilde{\tilde{p}}_1}{\gamma\tilde{\rho}_{1w}}\left\{\left(\frac{2\tilde{\rho}_{1w}\tilde{v}_{1w}}{-\tilde{\psi}}\right)^{2/3} x^{1/3} - 1\right\}, \tag{3.31}$$

$$\tilde{\tilde{p}}_1 = 2\gamma\tilde{\tilde{\Delta}}_1/3 = 2(2/3)^{2/3}\gamma(\tilde{\rho}_{1w}\tilde{v}_{1w}{}^2)^{1/3}, \tag{3.32}$$

where the effective thickness is $\tilde{\tilde{\Delta}}(x)=\tilde{\tilde{\Delta}}_1 x^{2/3}$. The constant-pressure shear layer for $x \gg 1$ has only a higher-order effect since its thickness $\bar{\Delta}(x)=O(x^{1/2})$ is small in comparison with the blown-layer thickness $\tilde{\Delta}(x)$. The air that has passed through the strong shock wave further upstream, and therefore has higher entropy, contributes still another higher-order displacement effect that likewise can be neglected in a first approximation. The value (3.32) is consistent with the results of Cole & Aroesty (1968).

3.3 *Viscous shear layer*

The viscous shear layer is described in a first approximation as a mixing layer between air moving with uniform speed at zero temperature and another gas, here taken also to be air, at rest with zero temperature. In terms of independent variables x and $\bar{\psi}$ the boundary-layer approximations to the momentum, total-enthalpy, and streamline equations are

$$\bar{u}_x + \frac{\bar{T}}{\gamma\bar{p}\bar{u}}\,\bar{p}_x = \bar{p}\,(\bar{T}^{\omega-1}\,\bar{u}\bar{u}_{\bar{\psi}})_{\bar{\psi}} + \dots, \tag{3.33}$$

$$\bar{H}_x = \bar{p}\,(\bar{T}^{\omega-1}\,\bar{u}\bar{H}_{\bar{\psi}})_{\bar{\psi}} + \dots, \tag{3.34}$$

$$\bar{y}_{\bar{\psi}} = (\bar{\rho}\bar{u})^{-1}, \tag{3.35}$$

where $\bar H = \bar u^2 + 2\bar T/(\gamma-1)$.

Asymptotic representations of the solutions as x→0 are expressed in terms of the similarity variable $\bar\zeta = \bar\psi/x^{1/4}$, for $\bar\zeta_0 < \bar\zeta < \infty$, in the form

$$\bar u = \bar u_1(\bar\zeta) + \dots, \tag{3.36}$$

$$\bar T = \bar T_1(\bar\zeta) + \dots, \tag{3.37}$$

$$\bar p = x^{-1/2}\,\bar p_1 + \dots, \tag{3.38}$$

$$\bar y = x^{3/4}\,\bar y_1(\bar\zeta) + \dots, \tag{3.39}$$

where $\bar\zeta_0 < 0$ and $\bar p_1$=constant; also $\bar\rho = \bar p/\bar T$. The value of $\bar\zeta_0$, which characterizes the amount of mass entrained in the lower part of the shear layer, is to be determined. Substitution gives the ordinary differential equations

$$-\frac{1}{4}\bar\zeta\,\bar u_1' - \frac{\bar T_1}{2\gamma\bar u_1} = \bar p_1\,(\bar T_1^{\omega-1}\,\bar u_1\bar u_1')', \tag{3.40}$$

$$-\frac{1}{4}\bar\zeta\,\bar T_1' + \frac{\gamma-1}{2\gamma}\bar T_1 = \bar p_1(\bar T_1^{\omega-1}\,\bar u_1\bar T_1')' + (\gamma-1)\bar p_1\bar T_1^{\omega-1}\,\bar u_1\bar u_1'^2\,, \tag{3.41}$$

$$\bar y_1' = \frac{\bar T_1}{\bar p_1\bar u_1}\,. \tag{3.42}$$

The solutions should match with the shock-layer solutions as $\bar\zeta\to\infty$ and with the blown-layer solutions as $\bar\zeta\to\bar\zeta_0$. Thus it is required that $\bar u_1\to 1$, $\bar T_1\to 0$ as $\bar\zeta\to\infty$ and $\bar u_1\to 0$, $\bar T_1\to 0$ as $\bar\zeta\to\bar\zeta_0$. The effective layer thickness is $\bar\Delta_1 x^{3/4}$, where $\bar\Delta_1$ is the integral of (3.42) from $\bar\zeta_0$ to ∞; the integral is finite because the temperature decreases sufficiently rapidly as $\bar\zeta\to\bar\zeta_0$. The numerical solution is carried out in terms of a rescaled independent variable $\bar p_1^{-1/2}\bar\zeta$, and $\bar p_1$ is to be found later from the appropriate matching conditions.

The differential equations (3.40) and (3.41) are singular at $\bar\zeta=\bar\zeta_0$. For $1/2<\omega<1$, the range of particular interest, the solutions as $\bar\zeta\to\bar\zeta_0$ have the form $\bar u_1=(\bar\zeta-\bar\zeta_0)^{\alpha}u^{\dagger}$ and $\bar T_1=(\bar\zeta-\bar\zeta_0)^{\beta}T^{\dagger}$, where $u^{\dagger}$ and $T^{\dagger}$ are analytic, and the exponents are $\alpha=\omega/(2\omega-1)$ and

$\beta=1/(2\omega-1)$. The coefficients $\bar{T}_1^{\omega-1}\,\bar{u}_1$ of the second derivatives in (3.40) and (3.41) are therefore $O(\bar{\zeta}-\bar{\zeta}_0)$ as $\bar{\zeta}\to\bar{\zeta}_0$. The numerical integration, described in detail elsewhere (Matarrese and Messiter 1989), is based on a Newton iteration scheme, starting from simple assumed distributions for $\bar{u}_1$ and $\bar{T}_1$ over a range $\bar{\zeta}_L<\bar{\zeta}<\infty$. Initially the lower limit $\bar{\zeta}_L$ is chosen large enough to ensure that $\bar{\zeta}_L>\bar{\zeta}_0$. However, the solutions thus obtained for $\bar{u}_1$ and $\bar{T}_1$ do not have the correct asymptotic behavior when $\bar{\zeta}\to\bar{\zeta}_L$. Next $\bar{\zeta}_L$ is decreased until the numerical and asymptotic solutions are seen to agree closely for small $\bar{u}_1$ and $\bar{T}_1$; the value found for $\bar{p}^{-1/2}\bar{\zeta}_0$ is believed to be accurate to within less than 0.1%. The results for $\gamma=1.4$ and $\omega=0.75$ are

$$\bar{p}_1^{-1/2}\bar{\zeta}_0=-3.683, \qquad \bar{p}_1^{1/2}\bar{\Delta}_1=0.3518. \tag{3.43}$$

The corresponding velocity and temperature functions $\bar{u}_1$ and $\bar{T}_1$ are plotted against $\bar{p}_1^{-1/2}\bar{\zeta}$ in figure 3, for $\bar{p}_1^{-1/2}\bar{\zeta}_0<\bar{p}_1^{-1/2}\bar{\zeta}<\infty$; $\bar{T}_1$ has been normalized with its maximum value $\bar{T}_{1m}$.

Calculation of the pressure is completed by matching $\bar{p}_1$ as $\bar{\zeta}\to\infty$ with the shock-layer pressure $\hat{p}_1$ evaluated as $\hat{\zeta}\to 0$ and matching $\bar{p}_1$ as $\bar{\zeta}\to\bar{\zeta}_0$ with the blown-layer pressure $\tilde{p}_1$ as $\tilde{\zeta}\to 0$. Thus

$$\tilde{p}_1=\bar{p}_1=\hat{p}_1(0). \tag{3.44}$$

Now (3.14), (3.27), and (3.43) can be combined to eliminate the layer thicknesses, as shown in §4 below.

If $\omega\to 1/2$, the exponents α and β obtained above in the solutions for $\bar{\zeta}\to\bar{\zeta}_0$ will both become infinite, and clearly a different kind of asymptotic form is required. Numerical solutions for $\omega=0.7$ and $\omega=0.6$, not shown here, suggest that the lower limit $\bar{\zeta}_0\to-\infty$ as $\omega\to 1/2$. When $\omega=1/2$, it then follows from (3.40) and (3.41) that $\bar{u}_1$ and $\bar{T}_1$ become exponentially small as $\bar{\zeta}\to-\infty$.

For $\omega=1$ the asymptotic behavior as $\bar{\zeta}\to\bar{\zeta}_0$ seems easier to understand in terms of Howarth variables defined by $dY=\bar{\rho}d\bar{y}$, $dX=\bar{p}dx$ and the similarity variable $\eta=Y/(2X)^{1/2}$. The stream function and total enthalpy are $\bar{\psi}=(2X)^{1/2}F(\eta)+\ldots$ and $\bar{H}=G(\eta)+\ldots$ respectively, where F and G satisfy the ordinary differential equations $F'''+FF''=\gamma^{-1}(\gamma-1)\cdot(F'^2-G)$ and $G''+FG'=0$. As $\eta\to-\infty$, $G=O(e^{\eta})$ and $F-F_0=O(\eta e^{\eta})$, with F_0 (corresponding to $\bar{\zeta}_0$) to be determined; the fact that $G=O\{(F-F_0)/\ln(F-F_0)\}$ as $\eta\to-\infty$ implies the presence of a logarithm in $\bar{T}_1$ as $\bar{\zeta}\to\bar{\zeta}_0$. The numerical solution when $\omega=1$ can be obtained by a shooting method to give

$$\bar{p}_1^{-1/2}\bar{\zeta}_0 = -2.066, \qquad \bar{p}_1^{1/2}\bar{\Delta}_1 = 0.2100. \tag{3.45}$$

3.4 *Higher-order matching*

Matching of the shock-layer and shear-layer solutions requires for each variable that the solutions evaluated as $\hat{\zeta}\to0$ and $\bar{\zeta}\to\infty$ agree term by term. As $\hat{\zeta}\to0$, the inner edge of the shock layer is approached from above and the hypersonic-small-disturbance solutions (3.13) and (3.14) show that the temperature has the form $T\sim\hat{T}=\hat{p}/\hat{\rho}=x^{-1/2}\hat{p}_1/\hat{\rho}_1+\ldots=O(x^{-1/2}\hat{\zeta}^{-2/(3\gamma)})$ as $x\to0$ and $\hat{\zeta}\to0$. However, as $\bar{\zeta}\to\infty$, the outer edge of the shear layer is approached from below and it follows from (3.41) that $T\sim M_\infty^2\bar{T}=M_\infty^2\bar{p}/\bar{\rho}=O(\bar{\zeta}^{-2/(1-\omega)})$. Since these two representations for T are not the same, the matching is not complete. Bush (1966) has shown that an additional "layer" is required between the shock layer and the shear layer. A solution for T in terms of a variable $\zeta_B=M_\infty^A\psi/x^C$, for proper choices of the exponents A and C, allows matching in a first approximation with $\hat{T}$ as $\zeta_B\to\infty$ and with $M_\infty^2\bar{T}$ as $\zeta_B\to0$. When $\omega=1$, the solution for $\bar{T}$ decays exponentially as $\bar{\zeta}\to\infty$; Lee & Cheng (1969) have shown that the matching difficulty is resolved not by adding another layer but by including higher-order terms in the shock-layer and shear-layer solutions.

Another difficulty arises with respect to matching of the shear-layer and blown-layer solutions. As $\bar{\zeta}\to\bar{\zeta}_0$, the inner edge of the shear layer is approached from above with $u\sim\bar{u}=O\{(\bar{\zeta}-\bar{\zeta}_0)^{\omega/(2\omega-1)}\}$ and $T\sim M_\infty^2\bar{T}=O\{M_\infty^2(\bar{\zeta}-\bar{\zeta}_0)^{1/(2\omega-1)}\}$. As $\tilde{\zeta}\to0$, the outer edge of the blown layer is approached from below with $u\sim M_\infty^{-1}\tilde{u}=O\{M_\infty^{-1}x^{-1/4}(-\tilde{\zeta})^{-1/2}\}$ and

$T \sim \tilde{T} = \tilde{p}/\tilde{\rho} = O\{x^{-1/2}(-\tilde{\zeta})^{-1/\gamma}\}$. The matching again is not complete, and it is not entirely clear how to proceed. For a first attempt, one might think that an additional solution is needed in a region between the shear layer and the blown layer, for $\bar{\psi}$ close to $x^{1/4}\bar{\zeta}_0$ and $\tilde{\psi}$ close to $M_\infty^{-1}x^{1/4}\bar{\zeta}_0$. The blown-layer and viscous-layer solutions for u would then be required to match with this new solution. If the matching for u is considered first, one is led to introduce a similarity variable

$$\zeta^* = (M_\infty x^{1/4})^{-1/(2\omega)} M_\infty(\bar{\psi} - x^{1/4}\bar{\zeta}_0), \tag{3.46}$$

and to try representations

$$\bar{u} = (M_\infty x^{1/4})^{-1/2} u_1^*(\zeta^*) + \dots, \tag{3.47}$$

$$\bar{T} = (M_\infty x^{1/4})^{-1/(2\omega)} T_1^*(\zeta^*) + \dots, \tag{3.48}$$

for $-\infty < \zeta^* < \infty$. However, this procedure leads to approximate equations that are just simplified versions of (3.40) and (3.41), with $\bar{\zeta} \approx \bar{\zeta}_0$ and $\bar{u}_1^2 << \bar{T}_1$. Except for additive integration constants, the solutions are already contained within the solutions to (3.40) and (3.41), and are not sufficient to allow the proper functional forms for both $\zeta^* \to -\infty$ and $\zeta^* \to \infty$. It is probably necessary both to include higher-order terms and to consider still other limit processes for a complete description of the local asymptotic structure. These details are not needed if only a first approximation to the pressure is desired.

If instead $\omega = 1$ the definition (3.46) for ζ^* again is appropriate, as is the representation (3.47) for u, but T has the modified form

$$\bar{T} = \{(M_\infty x^{1/4})^{1/2} \ln (M_\infty x^{1/4})\}^{-1} T_1^*(\zeta^*) + \dots. \tag{3.49}$$

The presence of the logarithm is associated with the exponential forms of u and T in terms of the Howarth variables noted at the end of the preceding subsection. As a result, the pressure-gradient term is absent from the momentum equation and two integrations can be carried out directly to give

$$(u_1^* - u_{10}^*) + u_{10}^* \ln (u_1^* - u_{10}^*) = -\bar{\zeta}_0\zeta^*/(4\,\bar{p}_1), \tag{3.50}$$

where $u_{10}^* = 2(\bar{p}_1\tilde{v}_{1w})^{1/2}/\{(\gamma-1)(-\bar{\zeta}_0)\}^{1/2}$, for matching with (3.20). It follows also that

$$T_1^* = (\text{const.})\,(u_1^* - u_{10}^*). \qquad (3.51)$$

The representations for u and T match properly as $\zeta^* \to \infty$, and u approaches a small constant value as $\zeta^* \to -\infty$, but T_1^* is exponentially small as $\zeta^* \to -\infty$ and higher-order terms would be needed for completeness, as at the outer edge of the shear layer (Lee & Cheng 1969).

These considerations indicate some of the difficulties encountered in attempting to derive higher-order terms and thus to obtain estimates of the largest neglected effects. For $x = O(1)$, it is fairly easy to see that the relative errors in the differential equations obtained in each of the three limits (shock layer, viscous layer, blown layer) are all $O(M_\infty^{-2})$. The expansions of the flow variables as $M_\infty \to \infty$ would then seem to proceed in integer powers of M_∞^{-2}. But the higher-order terms not yet matched will evidently require larger correction terms, probably in all three flow regions. It is therefore not possible to assess the error without further consideration of the next terms in each of the expansions. Moreover, in the strong-interaction limit $x \to 0$ the solutions will have expansions in positive powers of $x^{1/4}$ and $(M_\infty x^{1/4})^{-1}$, and in the weak-interaction limit $x \to \infty$ the solutions will be found as series expansions in negative powers of x, so that still other higher-order terms would have to be considered.

An additional question concerns the behavior of the flow for weaker blowing. If the blowing velocity is decreased by taking $\tilde{v}_{1w} \ll 1$, the injected mass $\psi = 2M_\infty^{-2}\tilde{\rho}_{1w}\tilde{v}_{1w}x^{1/2}$ remains large in comparison with the mass flow $M_\infty^{-3}x^{1/4}|\zeta_0|$ in the lower part of the shear layer for values of x such that $M_\infty x^{1/4} \gg \tilde{v}_{1w}^{-1}$. The location of blowoff is at $x = O(M_\infty \tilde{v}_{1w})^{-4}$ and moves downstream as $\tilde{v}_{1w}$ decreases from $O(1)$ to $O(M_\infty^{-1})$. When $\tilde{v}_{1w} = O(M_\infty^{-1})$, the boundary layer is attached throughout the strong-interaction region $x \ll 1$, and in the weak-interaction region $x \gg 1$ the injected mass is of the same order as the mass flow $O(M_\infty^{-3}x^{1/2})$ required for the constant-pressure free shear layer. A special solution is needed for a narrow range of $M_\infty \tilde{v}_{1w}$ close to a dividing value, as for incompressible flow (Kassoy 1971, Klemp & Acrivos 1972).

3.5 *Wedge flow*

Inviscid hypersonic flow past a thin wedge is easily described with the help of suitable approximations to the shock-wave jump conditions. If the wedge half-angle is $\alpha \ll 1$, and

$M_\infty\alpha \gg 1$, (3.5) gives $\rho \sim (\gamma+1)/(\gamma-1)$ and (3.6) with the shock slope $M_\infty \hat{y}_s' \sim (\gamma+1)M_\infty\alpha/2$ gives $p \sim \gamma(\gamma+1)M_\infty^2\alpha^2/2$ in the uniform flow between the shock wave and the wedge surface; the Mach number there is $M \sim \{\gamma(\gamma-1)/2\}^{-1/2}\alpha^{-1}$. If now a boundary layer is considered, its temperature is again $T=O(M_\infty^2)$, but the density $\rho=p/T$ is $O(\alpha^2)$. For weak interaction the boundary-layer thickness is $O\{M_\infty^\omega\alpha^{-1}(\nu_\infty X/u_\infty)^{1/2}\}$, smaller by a factor $O(M_\infty^{-1}\alpha^{-1})$ than for a flat plate. This thickness is small in comparison with the distance $(\gamma-1)\alpha X/2$ between wedge surface and shock wave, and the shock wave is therefore weak, only if $X \gg M_\infty^{2\omega}\alpha^{-4}\nu_\infty/u_\infty$. The reference length X_r should therefore be $X_r=M_\infty^{2\omega}\alpha^{-4} \cdot \nu_\infty/u_\infty$ for the wedge, smaller by a factor $(M_\infty\alpha)^{-4}$ than for a flat plate. The nondimensional coordinates x, y and ψ are now defined in terms of this new X_r. The scaled y-coordinates, however, are measured relative to the surface, with M_∞^{-1} replaced by α, so that

$$\tilde{y} = \hat{y} = (y - \alpha x)/\alpha. \tag{3.52}$$

With the new X_r the wedge flow is identical to flow past a flat plate in the first approximation when $X \ll X_r$. That is, the wedge thickness is small in comparison with the thickness of the disturbed-flow region when $X \ll X_r$. Since the merged-layer regime again is present for $X=O(M_\infty^{2\omega}\nu_\infty/u_\infty)$, i. e., for $x=O(\alpha^4)$, the strong-interaction description given above now applies to the region $\alpha^4 \ll x \ll 1$, a region which is shorter than for a flat plate in view of the revised definition for X_r.

In the weak-interaction region for $x \gg 1$, the flow between the shear layer and the strong shock wave from the wedge vertex is, however, described in a different way, in terms of small perturbations about the uniform flow behind the shock wave. A linearized flow description is again appropriate, but both families of waves are present because outgoing waves are reflected from the shock wave; the reflected waves are weak in a numerical sense, but not in an asymptotic sense, since the ratio of reflected-wave strength to incident-wave strength does not vanish under the limit processes considered here. In the blown layer the density is nearly constant, and so the incompressible form of the Bernoulli equation is appropriate in the first approximation.

The required solution in the blown layer was given by Cole and Aroesty (1968). The blowing velocity is taken to be $v_w=\alpha^2\tilde{v}_{1w}x^{-1/2}=M_\infty^\omega\tilde{v}_{1w}(u_\infty X/\nu_\infty)^{-1/2}$, the same as chosen for the flat plate. For $x\to\infty$, the pressure perturbation is related to u by the Bernoulli equation for incompressible flow and, for matching with the perturbed wedge flow, has the same order of magnitude as the product of $(M_\infty \alpha)^2$ and the ratio of a typical perturbation in streamline slope to the wedge angle. In the blown layer (3.19) and (3.20) are replaced by

$$\rho \sim \tilde{\rho}_{1w} = \text{constant}, \qquad u^2 \sim \frac{2}{\gamma M_\infty{}^2 \tilde{\rho}_{1w}} \{p(x_w) - p(x)\}, \tag{3.53}$$

where again the value of x_w defines a streamline. The solutions for u and p when $x \gg 1$ are expanded in terms of $\tilde{\zeta} = \tilde{\psi}/x^{1/2}$ as

$$u = \alpha\, x^{-1/6}\, \tilde{\tilde{u}}_1(\tilde{\zeta}) + \ldots, \qquad p = M_\infty{}^2 \alpha^2 \{\gamma(\gamma+1)/2 + x^{-1/3}\, \tilde{\tilde{p}}_1 + \ldots\}, \tag{3.54}$$

where $\tilde{\tilde{u}}_1$ is found in terms of $\tilde{\tilde{p}}_1$ from (3.53) and $\tilde{\tilde{p}}_1$ is a constant to be determined later. Again the double tilde is used where necessary to distinguish from quantities defined for $x \ll 1$. The streamline shapes are found, again using $\psi_y = \rho u$ and $\xi = x_w/x$, from

$$\tilde{y} = x^{2/3} \tilde{\tilde{y}}_1(\tilde{\zeta}) + \ldots, \qquad d\tilde{\tilde{y}}_1 = -\left(\frac{\gamma \tilde{\rho}_{1w}}{2 \tilde{\tilde{p}}_1}\right)^{1/2} \tilde{v}_{1w}\, \xi^{-1/3} (1 - \xi^{1/3})^{-1/2}\, d\xi. \tag{3.55}$$

The blown layer has the shape of an effective body

$$\tilde{y} \sim \tilde{\tilde{\Delta}}_1 x^{2/3}, \qquad \tilde{\tilde{\Delta}}_1 = 4\{\gamma \tilde{\rho}_{1w} \tilde{v}_{1w}{}^2 / (2 \tilde{\tilde{p}}_1)\}^{1/2}, \tag{3.56}$$

where $\tilde{\tilde{\Delta}}_1$ is found by integration of (3.55).

In the region between the shear layer and the shock wave the flow is nearly uniform with the flow variables equal to the values obtained from the shock-wave relations. As $x \to \infty$,

$$v = \alpha\{1 + v_1(x, \hat{y}) + \ldots\}, \tag{3.57}$$

$$p = M_\infty{}^2 \alpha^2 \{\gamma(\gamma+1)/2 + p_1(x, \hat{y}) + \ldots\}, \tag{3.58}$$

$$\rho = \frac{\gamma+1}{\gamma-1} + \rho_1(x, \hat{y}) + \ldots, \tag{3.59}$$

where $|v_1| \ll 1$, $|p_1| \ll 1$, and $|\rho_1| \ll 1$. The perturbations in v, p, and ρ are described by the linearized form of the hypersonic small-disturbance equations (3.1) through (3.3):

$$\rho_{1x} + \frac{\gamma+1}{\gamma-1} v_{1\hat{y}} = 0, \qquad \frac{\gamma+1}{\gamma-1} v_{1x} + \frac{1}{\gamma} p_{1\hat{y}} = 0, \qquad p_{1x} - \tfrac{1}{2}\gamma^2(\gamma-1)\rho_{1x} = 0, \tag{3.60}$$

where ρ_1 is easily eliminated. Linearized boundary conditions are given at the wedge surface $\vartheta=0$ and at the undisturbed shock-wave position $\vartheta=(\gamma-1)x/2$:

$$v_1(x,0) = d\bar{\Delta}(x)/dx, \qquad p_1(x,\tfrac{\gamma-1}{2}x) = \gamma(\gamma+1)\, v_1(x,\tfrac{\gamma-1}{2}x), \tag{3.61}$$

where $\bar{\Delta}(x)=\bar{\Delta}_1 x^{2/3}$.

The differential equations (3.60) and boundary conditions (3.61) are satisfied by solutions in the self-similar form $x^{-1/3}\mathrm{fn}(\vartheta/x)$. Since p_1 and v_1 must each satisfy a wave equation, the solutions are known moreover to be functions only of $x\pm M_0\vartheta$, where $M_0=\{\gamma(\gamma-1)/2\}^{-1/2}$. It follows that

$$\frac{1}{\gamma}p_1 = c_1\{x+M_0\vartheta\}^{-1/3} + c_2\{x-M_0\vartheta\}^{-1/3}, \tag{3.62}$$

$$-\frac{\gamma+1}{(\gamma-1)M_0}v_1 = c_1\{x+M_0\vartheta\}^{-1/3} - c_2\{x-M_0\vartheta\}^{-1/3}. \tag{3.63}$$

The integration constants c_1 and c_2 are found from the boundary conditions to be

$$c_2 = \frac{k^{1/3}}{\lambda}c_1 = \frac{2(\gamma+1)\bar{\Delta}_1 k^{1/3}}{3(\gamma-1)M_0(k^{1/3}-\lambda)}, \tag{3.64}$$

where

$$k = \frac{2-(\gamma-1)M_0}{2+(\gamma-1)M_0}, \qquad \lambda = \frac{(\gamma-1)M_0-1}{(\gamma-1)M_0+1}, \qquad M_0 = \left(\frac{2}{\gamma(\gamma-1)}\right)^{1/2}. \tag{3.65}$$

The solution to (3.60) and (3.61) for arbitrary $\bar{\Delta}(x)$ has been discussed by Chernyi (1961). The result is found as an infinite series, since a disturbance reaching the surface contains the effects of infinitely many wave reflections. Chernyi (1961) and Cole and Aroesty (1968) also specialized this solution for a power-law form of $\bar{\Delta}(x)$; eqns. (3.62)-(3.65) duplicate their results.

Setting $\vartheta = 0$ in (3.62) gives $\bar{p}_1$ in terms of $\bar{\Delta}_1$:

$$\bar{p}_1 = x^{1/3}p_1(x,0) = \frac{2\gamma(\gamma+1)\bar{\Delta}_1(\lambda+k^{1/3})}{3(\gamma-1)M_0(k^{1/3}-\lambda)}. \tag{3.66}$$

A second relation between $\tilde{\bar{p}}_1$ and $\tilde{\bar{\Delta}}_1$ is found from the blown-layer solution (3.56). Eliminating $\tilde{\bar{\Delta}}_1$,

$$\tilde{\bar{p}}_1=2\,(\gamma\,\tilde{\rho}_{1w}\tilde{v}_{1w}{}^2)^{1/3}\left(\frac{2\gamma(\gamma+1)(\lambda+k^{1/3})}{3(\gamma-1)M_0(k^{1/3}-\lambda)}\right)^{2/3}. \tag{3.67}$$

For $\gamma=1.4$, $\tilde{\bar{p}}_1= 3.615\,(\tilde{\rho}_{1w}\tilde{v}_{1w}{}^2)^{1/3}$.

4. Numerical Results

The strong-interaction solutions are obtained in the limit as $x\rightarrow 0$ and $M_\infty x^{1/4}\rightarrow\infty$, with $M_\infty y/x^{3/4}$ held fixed. In this limit the nondimensional velocity u is zero in the blown layer, increases from zero to one across the viscous layer, and is equal to one in the shock layer. The scaled temperature $M_\infty{}^2T$ is zero, in the limit, in the blown layer and in the shock layer, and is O(1) in the viscous layer. For finite but large $M_\infty x^{1/4}$, the first corrections to the zero values of u and $M_\infty{}^2T$ in the blown layer are proportional to powers of $(M_\infty x^{1/4})^{-1}$. The remaining parameters are the ratio of specific heats γ, here taken equal to 1.4; the exponent ω in the viscosity law $\mu=T^\omega$; and a blowing parameter $\tilde{\rho}_{1w}\tilde{v}_{1w}{}^2$, related to the momentum flux normal to the surface.

In the first approximation for the strong-interaction region, the pressures (3.24) and (3.38) in the blown layer and viscous layer are functions of x only and are equal to the pressure (3.10) evaluated at the inner edge of the shock layer. The result (3.44) is $\tilde{p}_1 = \bar{p}_1 = \hat{p}_1(0)$. The quantities $\hat{p}_1(0)/\Delta_1{}^2$, $\tilde{p}_1{}^{1/2}\tilde{\Delta}_1$, and $\bar{p}_1{}^{1/2}\bar{\Delta}_1$ are given by (3.14), (3.27), and (3.43) respectively. With $\Delta_1=\bar{\Delta}_1+\tilde{\Delta}_1$ according to (2.21), the pressure p_w at the surface is found for $\gamma=1.4$ and $\omega=0.75$ as

$$p_w = \{0.3721+3.703(\tilde{\rho}_{1w}\tilde{v}_{1w}{}^2)^{1/2}\}x^{-1/2} + \ldots. \tag{4.1}$$

If instead $\omega=1$, the surface pressure becomes

$$p_w = \{0.2221+3.703(\tilde{\rho}_{1w}\tilde{v}_{1w}{}^2)^{1/2}\}x^{-1/2} + \ldots. \tag{4.2}$$

The ratio of the shear-layer thickness $\bar{\Delta}_1$ to the blown-layer thickness $\tilde{\Delta}_1$ is found from (3.27), (3.43), and (3.44), and is seen to decrease as $\tilde{\rho}_{1w}\tilde{v}_{1w}^2$ increases. When $\omega=0.75$, the ratio is

$$\bar{\Delta}_1/\tilde{\Delta}_1 = 0.119/(\tilde{\rho}_{1w}\tilde{v}_{1w}^2)^{1/2}, \tag{4.3}$$

and when $\omega=1.0$, the constant is replaced by 0.071. Thus the two layer thicknesses are equal when the value of $(\tilde{\rho}_{1w}\tilde{v}_{1w}^2)^{1/2}$ is about 0.1; in the numerical calculations this parameter is taken equal to 0.1 or 0.2. The shock-wave shape for $\omega=0.75$ is then found from (2.20), (2.21), and (3.14) to be

$$y_s = M_\infty^{-1}\{0.9515 + 9.469(\tilde{\rho}_{1w}\tilde{v}_{1w}^2)^{1/2}\}^{1/2}x^{3/4} + \dots \tag{4.4}$$

If $\omega=1$, the constant 0.9515 is replaced by 0.5680.

The shear-layer velocity and temperature profiles of figure 3 are replotted in figure 4 as functions of $M_\infty y/x^{3/4}$, instead of $\bar{p}_1^{-1/2}M_\infty^3\psi/x^{1/4}$, for two values of the exponent ω and for $\tilde{\rho}_{1w}\tilde{v}_{1w}^2=0.01$, i. e., for nearly equal blown-layer and shear-layer thicknesses. The hot low-density shear layer occupies the region $\tilde{\Delta}_1< M_\infty y/x^{3/4}< \tilde{\Delta}_1+\bar{\Delta}_1$ and thus has a clearly defined thickness, as shown both by the figure and by the integral of (3.42). The blown layer is defined to be the region $0<M_\infty y/x^{3/4}<\tilde{\Delta}_1$ between the shear layer and the wall and contains almost all of the blown gas, with the exception of an amount smaller by a factor $O\{(M_\infty x^{1/4})^{-1}\}$ that is entrained in the lower part of the shear layer. The streamline separating free-stream air from the blown gas thus lies within the shear layer. Since the scaled viscosity coefficient in (3.33) and (3.34) is proportional to $\bar{T}^\omega$, and $\bar{T}<1$, an increase in ω decreases the diffusion rate and therefore decreases the shear-layer thickness $\bar{\Delta}_1$. In figure 4 a change in ω from $\omega=0.75$ to $\omega=1.0$ is seen to decrease $\bar{\Delta}_1$ by a factor of about 2/3, and also, because of coupling through the pressure, to give a small increase in the blown-layer thickness $\tilde{\Delta}_1$, such that the sum $\Delta_1= \bar{\Delta}_1+\tilde{\Delta}_1$ decreases. Since the shock-wave position $\hat{y}_{1s}$ is proportional to Δ_1, as seen in (3.14), the shock-wave slope then decreases, and the pressure also decreases, as shown by (4.1) and (4.2).

In figure 5 the shear-layer velocity u is plotted against $M_\infty y/x^{3/4}$ for $\omega=0.75$ and for three values of the blowing parameter, $\tilde{\rho}_{1w}\tilde{v}_{1w}^2=0.01$, 0.02, and 0.04. Stronger blowing of course moves the shear layer further from the wall and also decreases its thickness slightly. The velocity in the blown layer, smaller by a factor $O\{(M_\infty x^{1/4})^{-1}\}$, is shown for $M_\infty x^{1/4}=10$, $\tilde{\rho}_{1w}\tilde{v}_{1w}^2=0.01$, and $\tilde{v}_{1w}=0.05$. An inverse composite solution is also shown, obtained by adding the blown-layer and shear-layer solutions for $M_\infty y/x^{3/4}$ in terms of u, for $0<u<1$, and subtracting the common part, namely $\tilde{\Delta}_1$. This composite is uniformly valid to O(1) in $M_\infty y/x^{3/4}$, since the shear-layer and blown-layer solutions are recovered by taking limits with u fixed and with $M_\infty x^{1/4}u$ fixed, respectively. It would also be possible to obtain a shock-layer solution for u-1 and to use the results of Bush (1966) to show a smooth joining with the shear-layer solution.

Profiles of the scaled temperature M_∞^2T are shown in figure 6 for two of the cases, $\tilde{\rho}_{1w}\tilde{v}_{1w}^2=0.01$ and 0.04, shown in figure 5. The maximum temperature T_m is seen to be about $T_m= 0.0315\ M_\infty^2T_\infty$, for the selected values $\gamma=1.4$ and $\omega=0.75$. This value of T_m is less than 1/6 of the isentropic stagnation temperature T_0, and so real-gas effects are delayed to a somewhat higher Mach number than if the full T_0 were reached. A composite solution for $M_\infty y/x^{3/4}$ in terms of M_∞^2T, $0<T<T_m$, is shown for the same numerical values as in figure 5. To allow the correct T_1 at $y=0$, the curve has been displaced downward by a small (higher-order) amount; the correction is chosen to decrease linearly with T_1 and disappears at $T_1=T_m$.

Figure 7 shows the strong-interaction pressure for three values of the blowing parameter $\tilde{\rho}_{1w}\tilde{v}_{1w}^2$, for $\omega=0.75$ and for $\omega=1.0$. As predicted by (4.1) and (4.2), the pressure is linear in $(\tilde{\rho}_{1w}\tilde{v}_{1w}^2)^{1/2}$ and decreases as ω increases.

The weak-interaction pressure, for $X \gg X_r$, differs from a constant value by $O(x^{-1/3})$, as in the solutions (3.28) for a flat plate and (3.62) for a wedge. A calculation for $X=O(X_r)$, however, would require numerical solution of partial differential equations in the shock layer and shear layer. Nevertheless, since the extensions (unwarranted, to be sure) of the asymptotic solutions toward $X=X_r$ do not lie very far apart, a reasonable idea of the approximate surface pressure in this region can be found quite easily by interpolating in some simple arbitrary way between the strong-interaction and weak-interaction results. The interpolation formula adopted here is

$$p_w - 1 = r\{p_w^{(\text{strong})} - 1\} + (1-r)\{p_w^{(\text{weak})} - 1\}$$

$$= r\,\tilde{p}_1 x^{-1/2} + (1-r)\tilde{\tilde{p}}_1 x^{-1/3}, \qquad (4.6)$$

where $\tilde{\tilde{\bar{p}}}_1$ is given by (3.32), and

$$r = \frac{1}{\cosh \beta x}, \qquad \beta = \cosh^{-1} 2, \tag{4.7}$$

so that r decreases from 1 to 0 as x increases from 0 to ∞. The free parameter β in the interpolation formula has been chosen so that $r=1/2$ when $x=1$. That is, at $x=1$ the interpolated solution is chosen to lie halfway between the pressures that would be predicted if the strong-interaction and weak-interaction solutions were evaluated there (beyond their respective regions of validity $x \ll 1$ and $x \gg 1$). For a thin wedge, the required rescaling gives

$$\frac{p_w}{(M_\infty \alpha)^2} - \frac{\gamma(\gamma+1)}{2} = r\,\tilde{p}_1 x^{-1/2} + (1-r)\tilde{\tilde{\bar{p}}}_1 x^{-1/3}, \tag{4.8}$$

where now $x = X/\{M_\infty{}^{2\omega}\alpha^{-4}\nu_\infty/u_\infty\}$ and $\tilde{\tilde{\bar{p}}}_1$ is given by (3.67). Interpolated surface pressures for a wedge are shown in figure 8. Although the error appears to be small, it should be remembered that the value (4.7) for β is arbitrary, and a change in β would shift the location of the interpolated curve. The function r is likewise arbitrary, and there is no theoretical basis for the suggested choice; the accuracy of the interpolated curve in figure 8 remains uncertain in the absence of a numerical solution for $X=O(X_r)$.

Additional numerical results for a wedge in the case of uniform surface temperature, including the integrated force change as a function of blowing rate and other parameters, have been given by Matarrese *et al.* (1990).

5. Concluding remarks

The extension of hypersonic viscous strong-interaction theory to permit large surface blowing velocity requires that choices be made among several possibilities for the surface boundary conditions. Two constraints have been imposed: the perfect-gas law must be satisfied, and the blown-layer thickness is taken to be of the same order of magnitude as the viscous- and shock-layer thicknesses. Here the density of the blown gas has been chosen to be of the same order as the undisturbed air density and to be constant at the wall; the corresponding form for the blowing velocity is then fixed. Other choices can be made, leading to differences in the blown-layer solution and in some cases differences in the conditions at the lower "edge" of the shear layer.

Even a first approximation is found to introduce some subtleties. Although the three appropriate limit processes have been successfully applied to give self-consistent asymptotic flow representations in the three layers, the matching of solutions in adjacent layers is not complete, and would have to be refined if higher approximations, presumably proceeding in powers of x and $(M_\infty x^{-1/4})^{-1}$, were desired. Moreover, the results do not reduce in a simple way to the solutions for weak blowing. As for incompressible flow, a special limiting case would have to be considered in the neighborhood of blowoff, when the amount of injected mass is close to the mass entrained in the lower part of the free shear layer. Finally, numerical solution of the shear-layer equations for $\omega \neq 1$ was not successful with a straightforward shooting technique, and ultimately was carried out by an approach to the desired result through neighboring solutions.

In the present formulation the scaled results contain only a single blowing parameter which measures the normal momentum flux at the surface. (The ratio of specific heats and the exponent in the viscosity law of course appear as well.) As an obvious extension it is planned to consider the injected gas as different from air, so that in general one more differential equation is required, with one or more additional nondimensional parameters. Further numerical studies will then be carried out. It is also anticipated that the present formulation will serve as a useful test case for comparison with numerical Euler and Navier-Stokes codes.

This research was supported in part by the U. S. Army Strategic Defense Command.

REFERENCES

BROWN, S. N. & STEWARTSON, K. 1975 A nonuniqueness of the hypersonic boundary layer. *Q. J. Mech. & Appl. Math.* **28**, 75-90.

BUSH, W. B. 1966 Hypersonic strong-interaction similarity solutions for flow past a flat plate. *J. Fluid Mech.* **25**, 51-64.

CHERNYI, G. G. 1961 *Introduction to Hypersonic Flow.* Academic Press.

COLE, J. D. & AROESTY, J. 1968 The blowhard problem - inviscid flows with surface injection. *Int. J. Heat & Mass Transfer* **11**, 1167-1183.

HAYES, W. D. & PROBSTEIN, R. F. 1959 *Hypersonic Flow Theory*. Academic Press.

KASSOY, D. R. 1971 On laminar boundary-layer blowoff. Part 2. *J. Fluid Mech.* **48**, 209-228.

KLEMP, J. B. & ACRIVOS, A. 1972 High Reynolds number flow past a flat plate with strong blowing. *J. Fluid Mech.* **51**, 337-356.

KUBOTA, T. & FERNANDEZ, F. L. 1968 Boundary-layer flows with large injection and heat transfer. *A.I.A.A. J.* **6**, 22-28.

LEE, R. S. & CHENG, H. K. 1969 On the outer-edge problem of a hypersonic boundary layer. *J. Fluid Mech.* **38**, 161-179.

LI, T.-Y. & GROSS, J. F. 1961 Hypersonic strong viscous interaction on a flat plate with surface mass transfer. *Proc. 1961 Heat Transf. & Fluid Mech. Inst.*, 146-160.

MATARRESE. M. D. & MESSITER, A. F. 1990 A numerical method for the self-similar hypersonic viscous shear layer, submitted to *J. Comp. Phys.*

MATARRESE. M. D., MESSITER, A. F., & ADAMSON, T. C, JR. 1990 Control of hypersonic aerodynamic forces with surface blowing. *AIAA Paper* 90-0602.

SMITH, F. T. & STEWARTSON, K. 1973a On slot injection into a supersonic laminar boundary layer. *Proc. Roy Soc.* A **332**, 1-22.

SMITH, F. T. & STEWARTSON, K. 1973b Plate-injection into a separated supersonic boundary layer. *J. Fluid Mech.* **58**, 143-159.

STEWARTSON, K. 1964 *The Theory of Laminar Boundary Layers in Compressible Fluids*. Oxford University Press.

VAN DYKE, M. D. 1954 A study of hypersonic small-disturbance theory. *N.A.C.A. Rep.* no. 1194 (supersedes *TN* no. 3173, 1954).

WALLACE, J. & KEMP, N. 1969 Similarity solutions to the massive blowing problem. *A.I.A.A. J.* 7, 1517-1523.

Figure captions

1. Flow regions for viscous interaction in hypersonic flow past a flat plate with strong blowing.

2. Orders of magnitude for layer thicknesses and mass flows in strong-interaction region.

3. Scaled shear-layer solutions in strong-interaction limit, as functions of the stream-function variable $\bar{p}_1^{-1/2}\bar{\zeta} = \bar{p}_1^{-1/2}M_\infty^3\bar{\psi}/x^{1/4}$, for $\omega=0.75$: ——, velocity $\bar{u}_1$; – – –, temperature $\bar{T}_1/\bar{T}_{1m}$.

4. Scaled shear-layer solutions in strong-interaction limit, as functions of $M_\infty y/x^{3/4} \sim \bar{y}_1$, for $\tilde{\rho}_{1w}\tilde{v}_{1w}^2=0.01$: ——, velocity $\bar{u}_1$ for $\omega=0.75$; — - —, velocity $\bar{u}_1$ for $\omega=1.0$; – – –, temperature $\bar{T}_1/\bar{T}_{1m}$ for $\omega=0.75$; - - - -, temperature $\bar{T}_1/\bar{T}_{1m}$ for $\omega=1.0$.

5. Velocity profiles u vs. $M_\infty y/x^{3/4}$ in strong-interaction region, for $\omega=0.75$: – – –, shear layer for $\tilde{\rho}_{1w}\tilde{v}_{1w}^2=0.01$; - - - -, blown layer for $\tilde{\rho}_{1w}\tilde{v}_{1w}^2=0.01$, $M_\infty x^{1/4}=10$, $\tilde{\rho}_{1w}=4$; ——, composite for $\tilde{\rho}_{1w}\tilde{v}_{1w}^2=0.01$, $M_\infty x^{1/4}=10$, $\tilde{\rho}_{1w}=4$; — - —, shear layer for $\tilde{\rho}_{1w}\tilde{v}_{1w}^2=0.02$; — - - —, shear layer for $\tilde{\rho}_{1w}\tilde{v}_{1w}^2=0.04$.

6. Temperature profiles M_∞^2T vs. $M_\infty y/x^{3/4}$ in strong-interaction region, for $\omega=0.75$: – – –, shear layer for $\tilde{\rho}_{1w}\tilde{v}_{1w}^2=0.01$; - - - -, blown layer for $\tilde{\rho}_{1w}\tilde{v}_{1w}^2=0.01$, $M_\infty x^{1/4}=10$, $\tilde{\rho}_{1w}=4$; ——, composite for $\tilde{\rho}_{1w}\tilde{v}_{1w}^2=0.01$, $M_\infty x^{1/4}=10$, $\tilde{\rho}_{1w}=4$; — - - —, shear layer for $\tilde{\rho}_{1w}\tilde{v}_{1w}^2=0.04$.

7. Surface pressure distribution p_w vs. x, in strong-interaction region: ——, for $\tilde{\rho}_{1w}\tilde{v}_{1w}^2=0.01$ and $\omega=0.75$; – – –, for $\tilde{\rho}_{1w}\tilde{v}_{1w}^2=0.01$ and $\omega=1.0$; — - —, for $\tilde{\rho}_{1w}\tilde{v}_{1w}^2=0.04$ and $\omega=0.75$; - - - -, for $\tilde{\rho}_{1w}\tilde{v}_{1w}^2=0.04$ and $\omega=1.0$; — - - —, for $\tilde{\rho}_{1w}\tilde{v}_{1w}^2=0.16$ and $\omega=0.75$; · · · · ·, for $\tilde{\rho}_{1w}\tilde{v}_{1w}^2=0.16$ and $\omega=1.0$.

8. Surface pressure $\Delta p_w = \{p_w - \frac{\gamma(\gamma+1)}{2}(M_\infty \alpha)^2\}/(M_\infty \alpha)^2$ vs. $x = X/\{M_\infty{}^{2\omega}\alpha^{-4}\nu_\infty/u_\infty\}$ for thin wedge, for $\tilde{\rho}_{1w}\tilde{v}_{1w}{}^2 = 0.01$ and $\omega = 0.75$: – – –, strong-interaction solution; - - - -, weak- interaction solution; ——, interpolated solution.

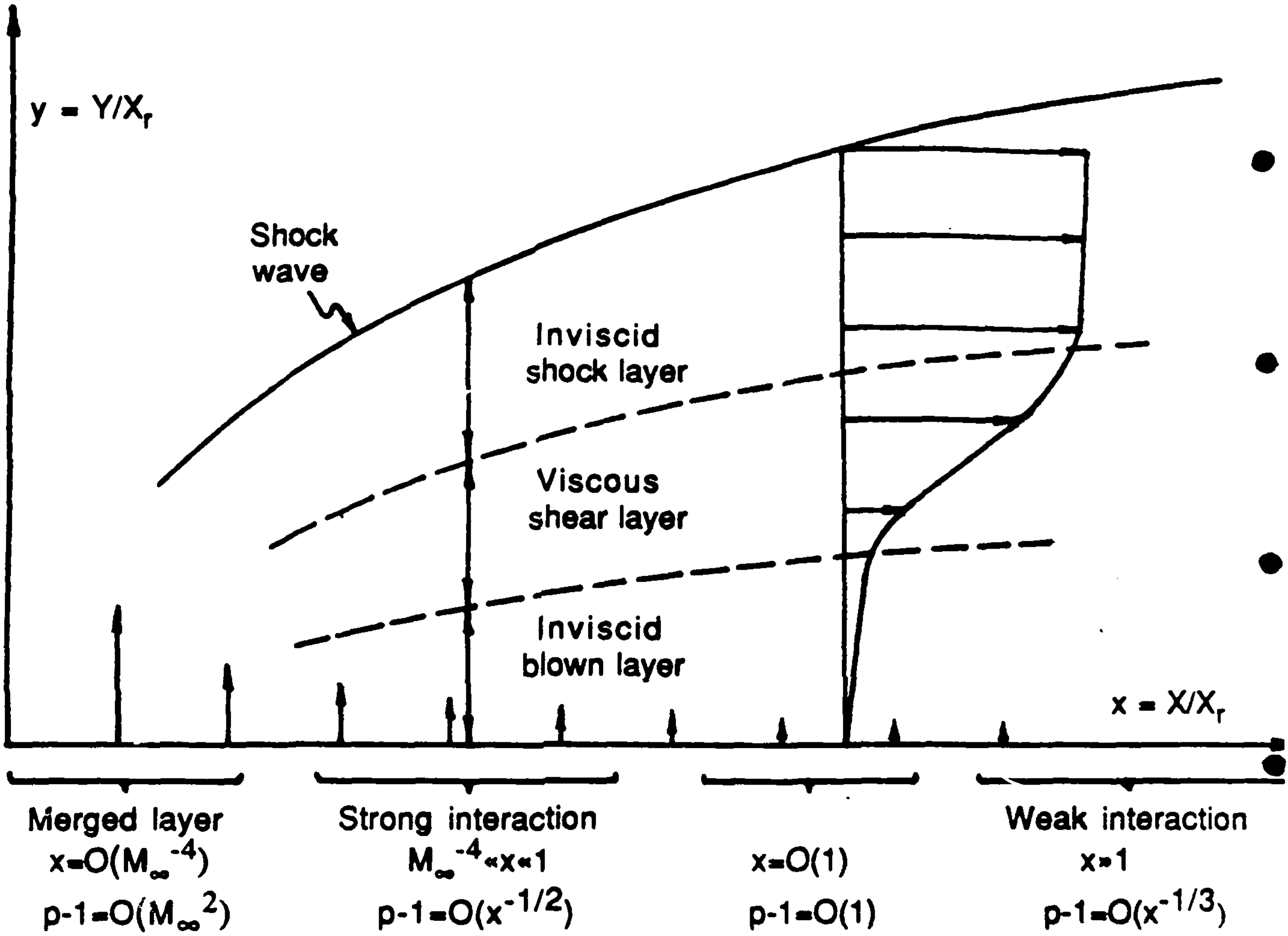
y = Y/X_r
Shock wave
Inviscid shock layer
Viscous shear layer
Inviscid blown layer
x = X/X_r
Merged layer
x=O(M_∞^-4)
p-1=O(M_∞^2)
Strong interaction
M_∞^-4«x«1
p-1=O(x^-1/2)
x=O(1)
p-1=O(1)
Weak interaction
x»1
p-1=O(x^-1/3)

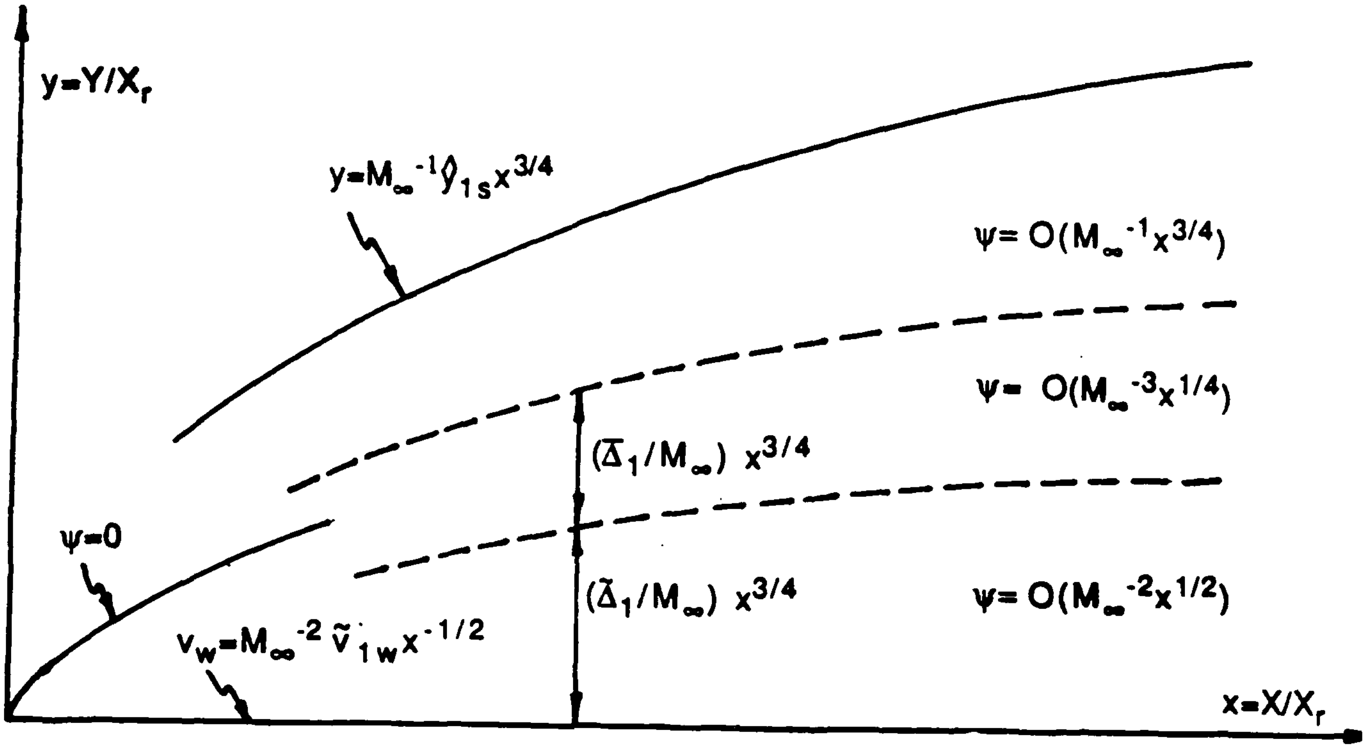
$y=Y/X_r$
$y=M_\infty^{-1}\hat{y}_{1s}x^{3/4}$
$\psi= O(M_\infty^{-1}x^{3/4})$
$\psi= O(M_\infty^{-3}x^{1/4})$
$(\bar{\Delta}_1/M_\infty)\ x^{3/4}$
$\psi=0$
$(\tilde{\Delta}_1/M_\infty)\ x^{3/4}$
$\psi= O(M_\infty^{-2}x^{1/2})$
$v_w=M_\infty^{-2}\,\tilde{v}_{1w}x^{-1/2}$
$x=X/X_r$

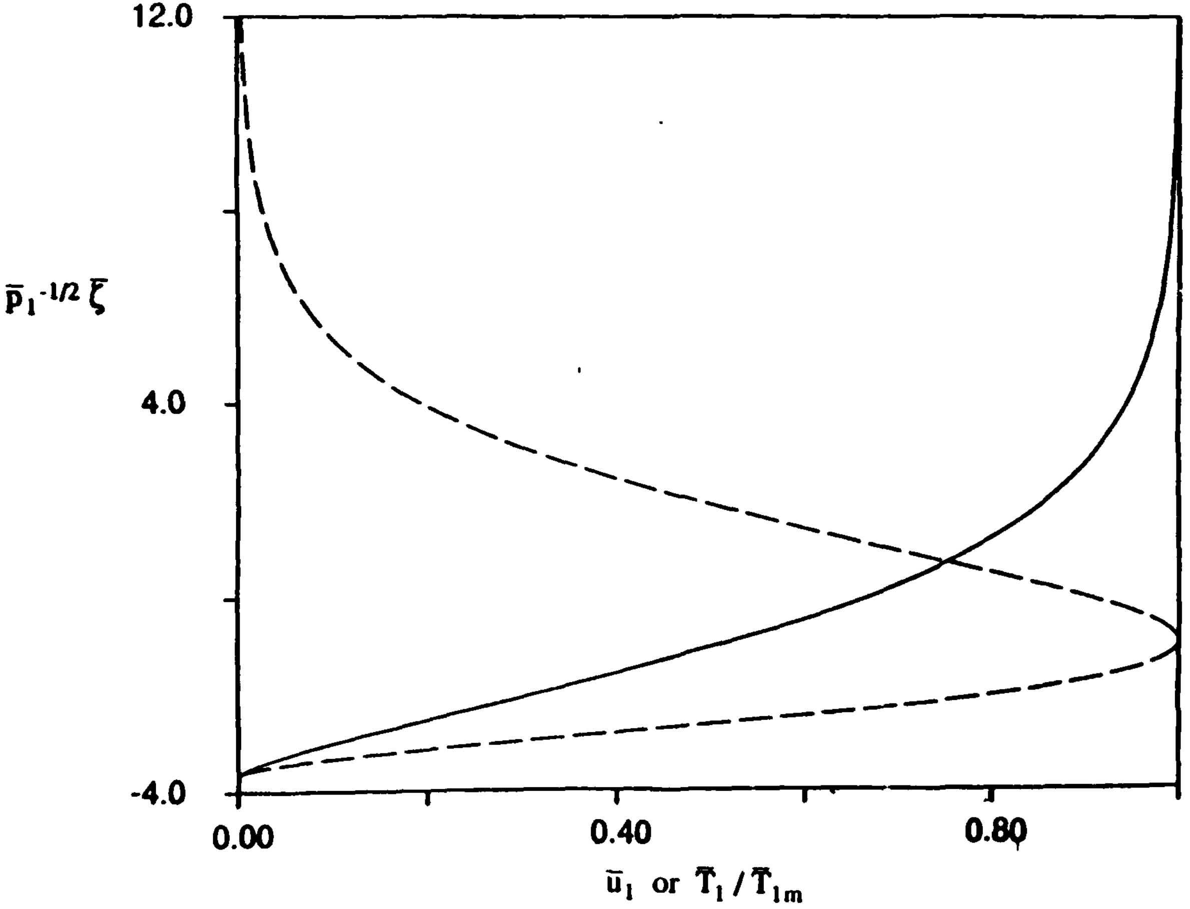
12.0
4.0
-4.0
$\bar{p}_1^{-1/2}\bar{\zeta}$
0.00
0.40
0.80
$\tilde{u}_1$ or $\bar{T}_1/\bar{T}_{1m}$

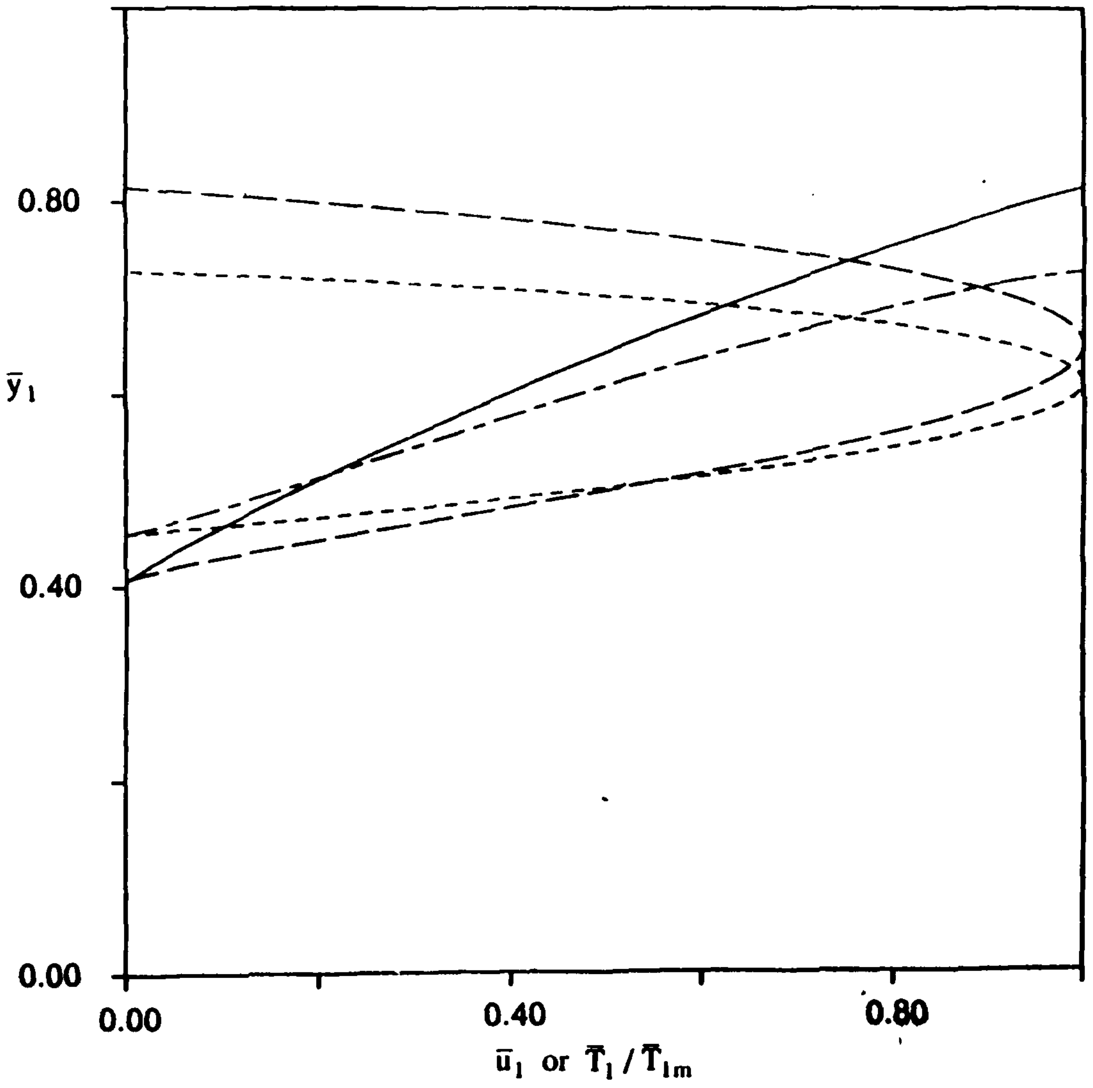
0.80
0.40
0.00
$\bar{y}_1$
0.00
0.40
0.80
$\bar{u}_1$ or $\bar{T}_1/\bar{T}_{1m}$

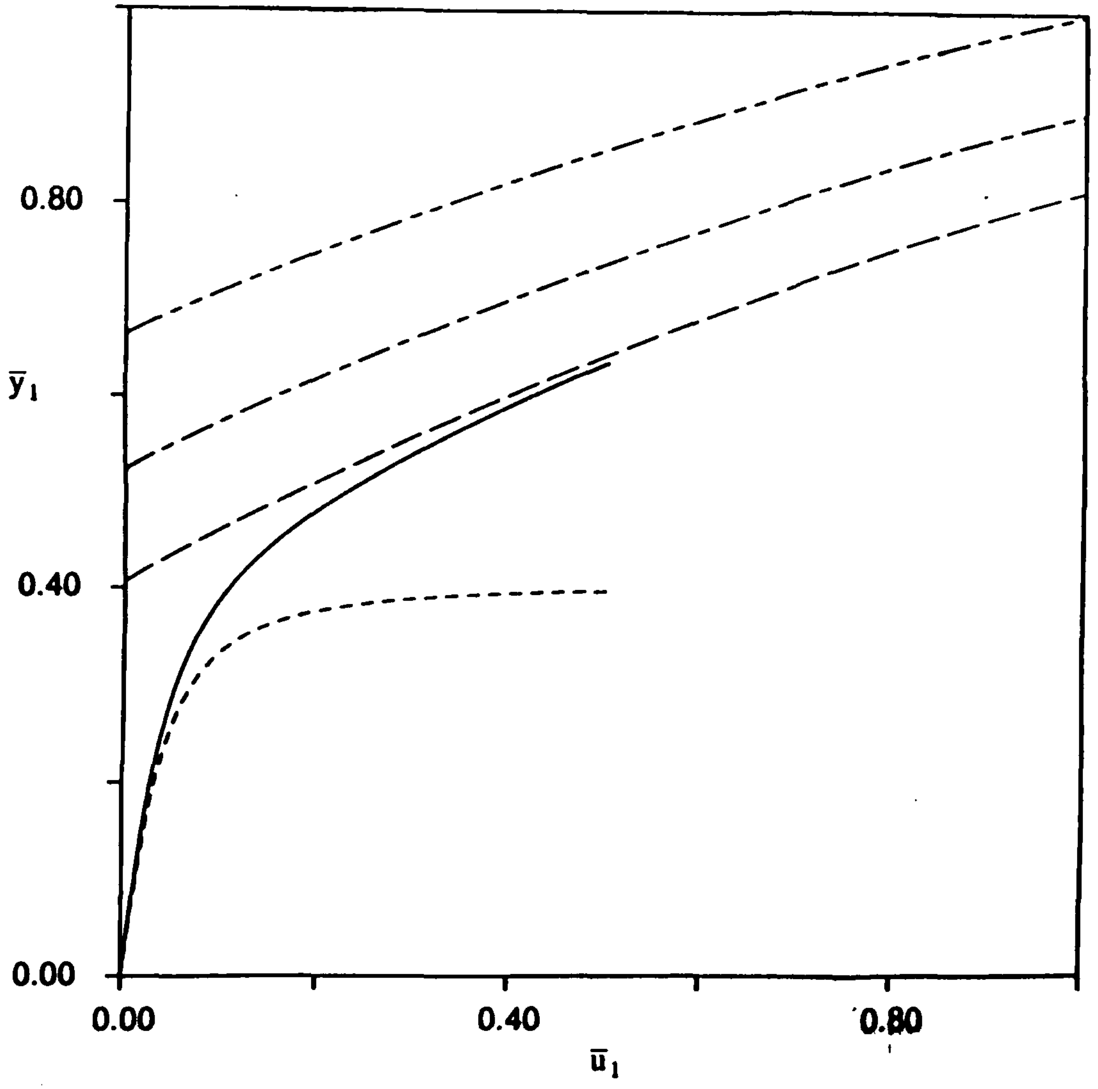
0.80
$\bar{y}_1$
0.40
0.00
0.00
0.40
0.80
$\bar{u}_1$

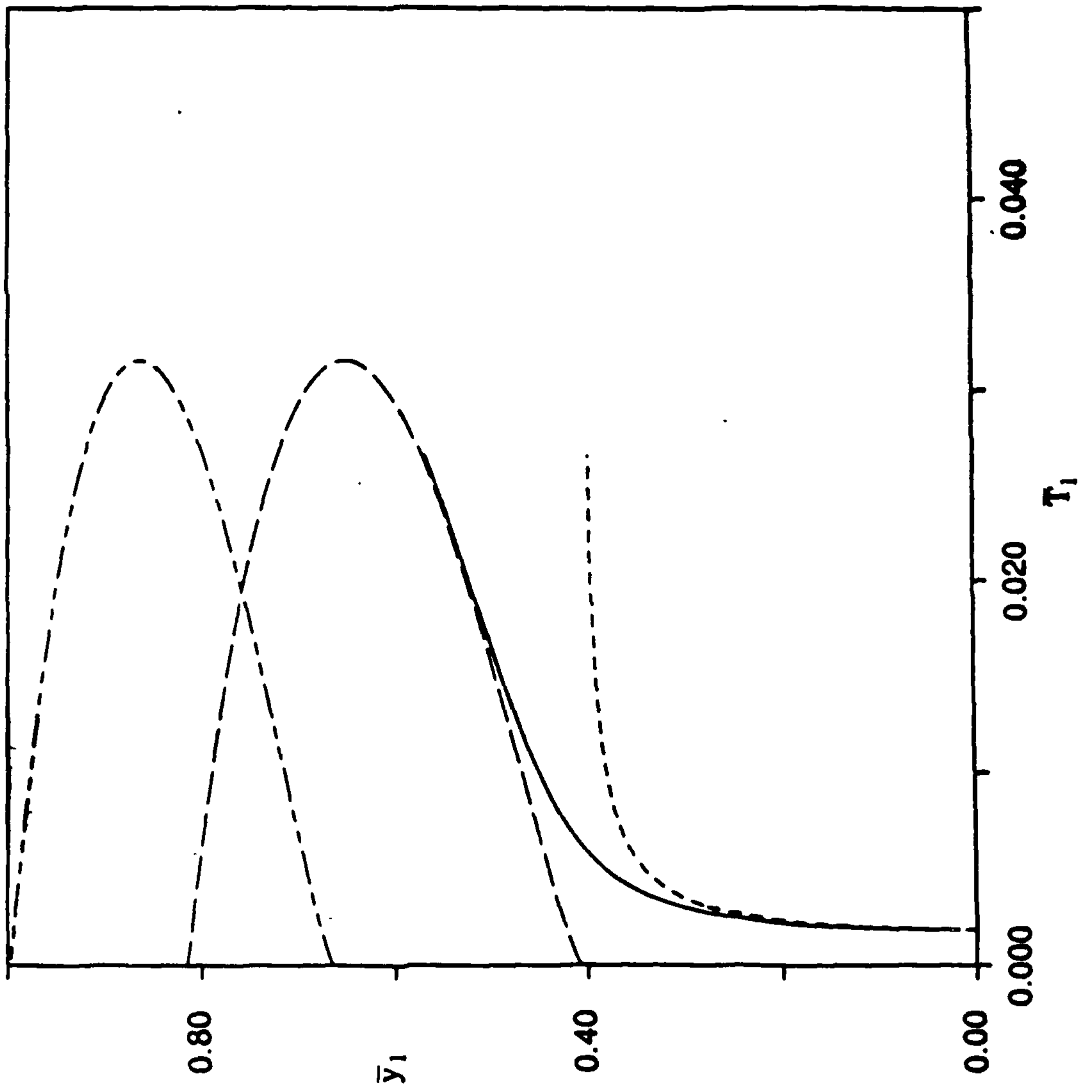
0.80
$\bar{y}_1$
0.40
0.00
0.000
0.020
0.040
T_1

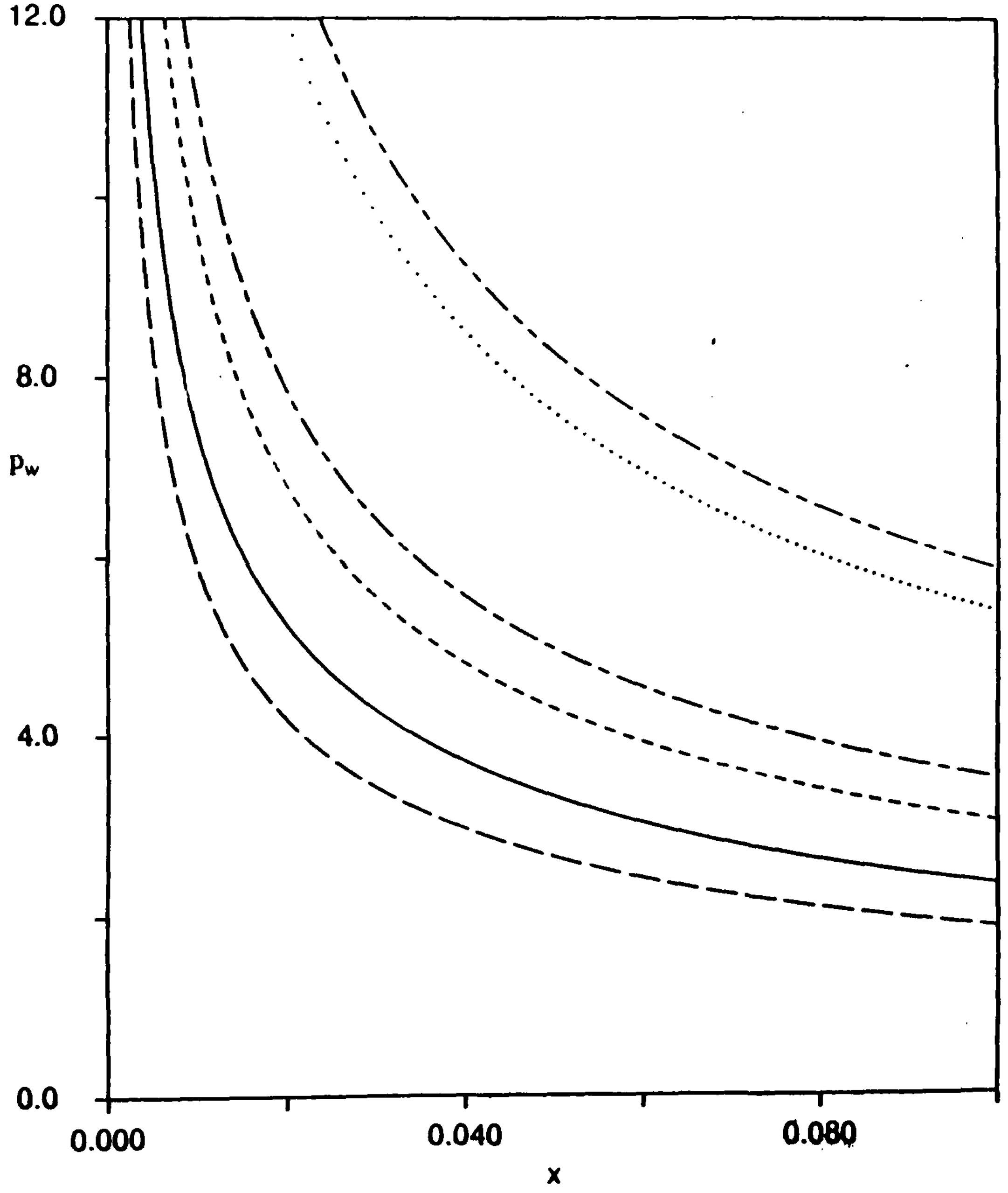
12.0
8.0
p_w
4.0
0.0
0.000
0.040
0.080
x

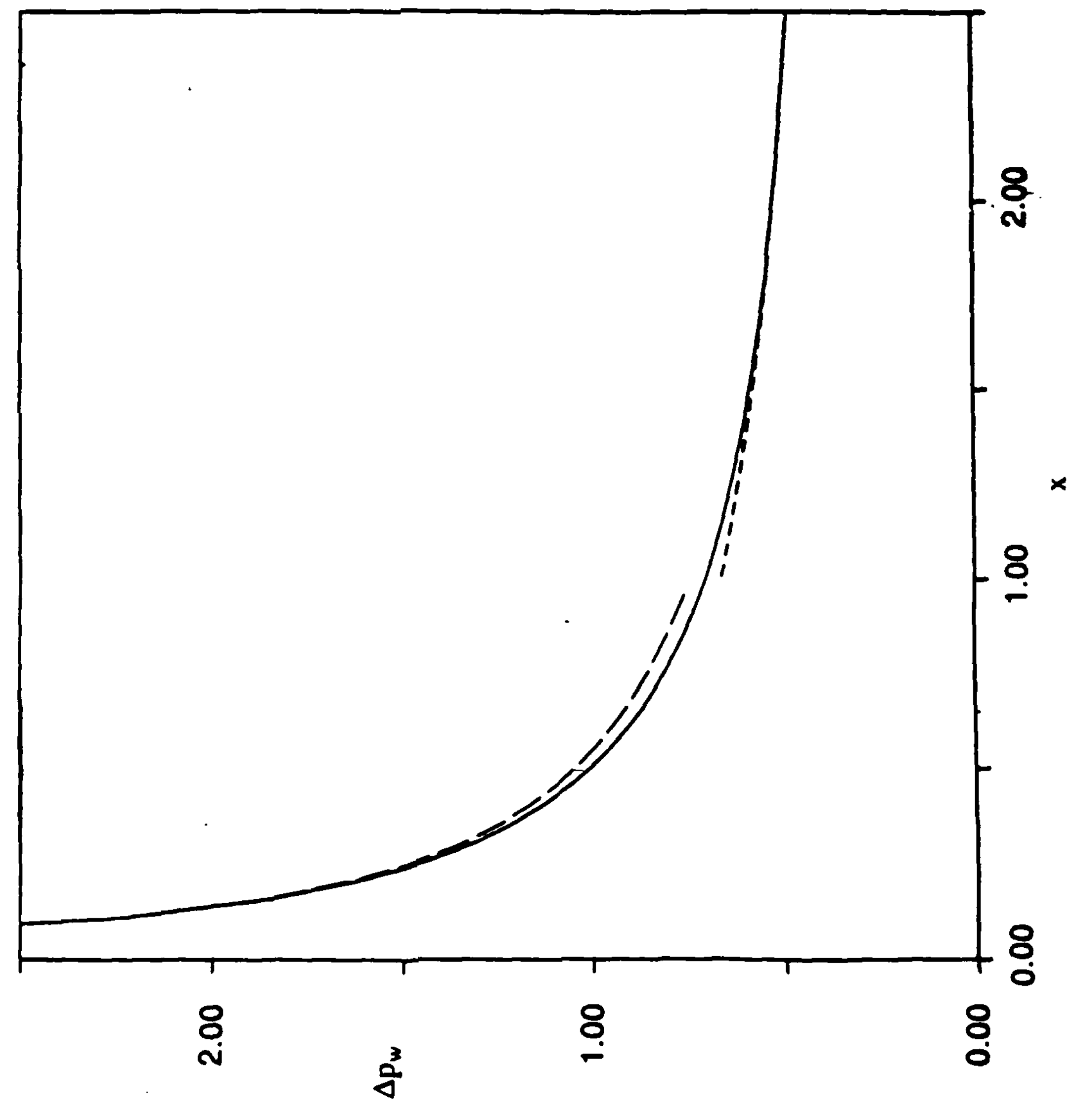
Δp_w
2.00
1.00
0.00
x
0.00
1.00
2.00

Note

A Numerical Method for the Self-similar Hypersonic Viscous Shear Layer

M. D. Matarrese
Graduate Student

and

A. F. Messiter
Professor

Department of Aerospace Engineering
The University of Michigan
Ann Arbor, MI 48109-2140

CLASSIFICATION:

65L110 -- Boundary value problems
76K05 -- Hypersonic flows
76N05 -- Boundary layer theory

PROPOSED RUNNING HEAD:

Hypersonic Shear Layer

PROOFS MAY BE SENT TO:

Michael D. Matarrese
Department of Aerospace Engineering
College of Engineering
The University of Michigan
Aerospace Engineering Building
Ann Arbor, MI 48109-2140

Note

A Numerical Method for the Self-similar Hypersonic Viscous Shear Layer

1. INTRODUCTION

In laminar fluid motion at high Reynolds numbers, viscous forces are important primarily in thin layers described by the boundary-layer approximation to the Navier-Stokes equations. For the special case in which the pressure varies as a power of the distance x along such a shear layer, the solutions have a self-similar form. If the stream function ψ is chosen as the independent variable, and the pressure is $p=(\text{const.})x^b$, the similarity variable is $\zeta=(\text{const.})\psi/x^{(1+b)/2}$. The nondimensional boundary-layer equations may then be written as

$$(T^{\omega-1}uu')' + \frac{(1+b)}{2}\zeta u' - \frac{b}{\gamma}\frac{T}{u} = 0 \qquad (1)$$

$$(T^{\omega-1}uT')' + \frac{(1+b)}{2}\zeta T' + \frac{(\gamma-1)b}{\gamma}T + (\gamma-1)T^{\omega-1}uu'^2 = 0 \qquad (2)$$

where $u=u(\zeta)$ is the fluid velocity; $T=T(\zeta)$ is the temperature; γ is the ratio of specific heats; the Prandtl number has been taken equal to one; the viscosity coefficient has been assumed proportional to T^{ω}, with $1/2<\omega<1$; and the Mach number has been absorbed in the temperature and density.

The boundary conditions for (1) and (2) will typically be given at two values of ζ, say $\zeta=\infty$ and $\zeta=\zeta_0$, where the value of ζ_0 depends on the problem considered. For a boundary layer along an impermeable surface, $\zeta_0=0$; for a free shear layer, ζ_0 is a negative constant to be determined as part of the solution. If the Mach number in the inviscid flow above the shear layer is very large (hypersonic), the temperature on one or both sides of the layer will be low relative to the very high peak temperature in the layer, and in a first approximation T→0 on one or both boundaries. The example to be considered here is concerned with "hypersonic strong viscous interaction" in the presence of large surface injection. The viscous boundary layer is blown away from the surface to form a free shear layer, and the interaction with inviscid flow behind a strong shock wave leads to a pressure variation with $b=-1/2$; details are discussed in [1].

In the limiting case of interest here, both u and T are zero at $\zeta=\zeta_0$, and so the coefficients of u" and T" in (1) and (2) also vanish at that point. The asymptotic behavior as $\zeta\to\zeta_0$ is given by $u=O\{(\zeta-\zeta_0)^{\omega/(2\omega-1)}\}$ and $T=O\{(\zeta-\zeta_0)^{1/(2\omega-1)}\}$; if $\omega\to1$, a logarithm also appears, whereas if $\omega\to1/2$, then $\zeta_0\to-\infty$ and the behavior is exponential rather than algebraic. The boundary conditions to be used for (1)-(2) when $1/2<\omega<1$ are then

$$\zeta\to\zeta_0: \qquad u\sim(\text{const.})(\zeta-\zeta_0)^{\omega/(2\omega-1)}, \qquad T\sim(\text{const.})(\zeta-\zeta_0)^{1/(2\omega-1)} \tag{3}$$

$$\zeta\to\infty: \qquad u\to1, \qquad T\to0 \tag{4}$$

The system (1)-(2) with boundary conditions (3)-(4) thus forms a two-point boundary-value problem in which the location of one boundary, at which the solution is singular, is unknown a priori and must be determined as part of the solution. Knowledge of the asymptotic forms (3) is found to be necessary for obtaining a numerical solution; specifying $u=T=0$, for example, is not sufficient. (The asymptotic behavior as $\zeta\to\infty$ is also known but will not be needed.)

Several numerical techniques have been used to solve the compressible laminar boundary-layer equations. Early solutions with $\zeta_0 = 0$ were computed by Cohen and Reshotko [2] using a successive-approximation scheme. For the case $\zeta_0 << -1$ (with ζ_0 specified explicitly), shooting from the interior was found successful by Nachtsheim and

Green [3] as was the Newton-iteration finite-difference method described by Liu and Chiu [4]. Nachtsheim and Swigert [5] developed a shooting method to handle asymptotic boundary conditions. For the current problem, a Newton-based finite-difference method utilizing continuation has been successful and is described below.

2. NUMERICAL METHOD

To handle the difficulties at the lower boundary, a continuation method is employed with the location ζ_L of this boundary treated as a free parameter. (ζ_0 denotes the value of ζ_L for which (3) is satisfied.) Trial numerical calculations show that if the boundary condition $u(\zeta_L)=T(\zeta_L)=0$ is adopted, then for $\zeta_L>\zeta_0$ solutions are found which do not satisfy the requirement (3) as $\zeta\to\zeta_L$, whereas if $\zeta_L<\zeta_0$ the trivial solution $u=T=0$ is found for $\zeta_L<\zeta<\zeta_0$, with the desired behavior (3) occurring for $0<\zeta-\zeta_0<<1$. Figure 1 provides an illustration of such behavior for the case $\gamma=1.4$, $\omega=3/4$, and $b=-1/2$ with the trial solutions satisfying the boundary conditions $u(\zeta_L)=0$, $T(\zeta_L)=T_L$, $u(24)=1$, $T(24)=0$. The two curves to the left are typical of solutions with $T_L>0$, $\zeta_L<\zeta_0$, and the two curves to the right are typical of solutions with $T_L=0$, $\zeta_L>\zeta_0$; note that as $T_L\to0$, $u\to0$ and $T\to0$ for $\zeta_L<\zeta<\zeta_0$. Thus the second and all higher derivatives of u and T are discontinuous at $\zeta=\zeta_0$, and one may expect computational difficulties if an assumed location for the lower boundary in some iterative numerical scheme is less than ζ_0 (that is, if ζ_0 lies within the computational domain).

The problem is now reformulated as follows. The new independent variable

$$x \equiv \zeta - \zeta_L \tag{5}$$

is introduced, and solutions are considered on the truncated domain $0\le x\le x_U$, where x_U is chosen large enough that (4) is satisfied within a specified tolerance (both 1-u and T are

$O(x^{-2/(1-\omega)})$ as $x \to \infty$). The system (1)-(2) will be written in terms of x as a two-element vector equation in the form

$$r(s; \zeta_L) = 0 \tag{6}$$

where $s^T \equiv (u(x;\zeta_L), T(x;\zeta_L))$, and r is the appropriate vector differential expression. The boundary conditions

$$x=0: \qquad u=0, \qquad T=0 \tag{7}$$

$$x=x_U: \qquad u=1, \qquad T=0 \tag{8}$$

are now adopted, together with the additional condition

$$g(\zeta_L)|_{\zeta_L=\zeta_0} = 0 \tag{9}$$

where g is a function designed to monitor the solution behavior near the lower boundary, vanishing only when (3) is satisfied. Starting with an initial guess $\zeta_L^{(0)} > \zeta_0$, the numerical procedure is to march in ζ_L, solving (6)-(8) at each step, and approaching ζ_0 from above so that the singularity at ζ_0 lies outside the computational domain. Marching is terminated when (9) is satisfied within some desired level of accuracy.

To solve the boundary-value problem (6)-(8) at each iteration level in ζ_L, a Newton-based method is adopted, utilizing second-order finite differences and a nonuniform computational grid . Based upon the first two terms in the asymptotic expansions for u and T as $\zeta \to \zeta_0$, it is found that (3) is an accurate representation of the solution with maximum fractional error of order 10^{-3} over the small interval $0<\zeta-\zeta_0 \le \varepsilon_a$, where ε_a is of order 10^{-3} for $\omega=3/4$. To resolve the solution in this small region without requiring an excessive number of grid points, the "exponential" grid

$$x_j = x_0 + \frac{(\alpha^j-1)}{(\alpha-1)} \Delta x_0 \qquad j = 1, \ldots, N \tag{10}$$

is employed, where $x_0 = 0$; $\Delta x_0 \equiv x_1 - x_0$ is specified (typically of order 10^{-4} to 10^{-3}); and the constant $\alpha \equiv (x_{j+1}-x_j)/(x_j-x_{j-1}) > 1$ (≈ 1.03 for example) satisfies

$$\frac{\alpha^N-1}{\alpha-1} = \frac{x_N}{\Delta x_0} \tag{11}$$

with $x_N = x_U$ specified (≈ 24 typically).

The system (6) may be written in a form suitable for numerical solution: the diffusion terms are expanded and all negative powers of u and T are factored away to avoid possible floating-point overflow during iteration and inaccuracies associated with computing ratios of terms that vanish near ζ_o; first and second derivatives are then replaced with three-point central-difference formulas appropriate for the grid (10), e.g.,

$$du/dx \,\Big|_{x = x_j} \approx u_{x_j} \equiv \frac{u_{j+1} + (\alpha^2-1)u_j - \alpha^2 u_{j-1}}{\Delta x_{j-1}\alpha(1+\alpha)} \tag{12}$$

$$d^2u/dx^2 \,\Big|_{x = x_j} \approx u_{xx_j} \equiv \frac{u_{j+1} - (\alpha+1)u_j + \alpha u_{j-1}}{(\Delta x_{j-1})^2 \alpha(1+\alpha)/2} \tag{13}$$

where $\Delta x_{j-1} \equiv x_j - x_{j-1}$. The errors are $O((\Delta x_j)^2)$ in (12), and if $\alpha = 1 + O(\Delta x_j)$, in (13) as well. The numerical approximation to system (6) thus reads

$$\mathbf{r}_j = \mathbf{r}_j(\mathbf{s}_{j-1}, \mathbf{s}_j, \mathbf{s}_{j+1}; \zeta_L) = O((\Delta x_j)^2) \tag{14}$$

where the first element of $\mathbf{r}_j$ is given by

$$r_{1_j} \equiv T_j u_j^2 \, u_{xx_j} + \{(\omega-1)T_{x_j}u_j + T_j u_{x_j} + \frac{(1+b)}{2}(x_j+\zeta_L)T_j^{(2-\omega)}\} \, u_j u_{x_j} - \frac{b}{\gamma} T_j^{(3-\omega)} \tag{15}$$

and the second by

$$r_{2_j} \equiv T_j u_j T_{xx_j} + \{(\omega-1)T_{x_j}u_j + T_j u_{x_j} + \frac{(1+b)}{2}(x_j+\zeta_L)T_j^{(2-\omega)}\}\, T_{x_j} + \frac{(\gamma-1)b}{\gamma} T_j^{(3-\omega)} + (\gamma-1)T_j u_j u_{x_j}^{\;2} \tag{16}$$

with the subscript j denoting evaluation at x_j. Requiring (14) to vanish at the N-1 interior grid points and using the boundary conditions (7)-(8), one obtains the nonlinear algebraic system

$$\mathbf{R}(\mathbf{S}; \zeta_L) = \mathbf{0} \tag{17}$$

$$s_0^T = (0, 0), \qquad s_N^T = (1, 0) \tag{18}$$

where $\mathbf{S}^T = \mathbf{S}^T(\zeta_L) \equiv (\mathbf{s}_1, \mathbf{s}_2, ..., \mathbf{s}_{N-1})$, and the "residual vector" $\mathbf{R}^T \equiv (\mathbf{r}_1, \mathbf{r}_2, ..., \mathbf{r}_{N-1})$.

Given a value of ζ_L and an initial distribution $\mathbf{S}^{(0)}$, the system (17)-(18) may be solved using a variant of Newton's method which reads at the kth iteration level (as denoted by superscript k)

$$(\partial\mathbf{R}/\partial\mathbf{S})^{(k)}\, \Delta^{(k)} = -\,\mathbf{R}^{(k)} \tag{19}$$

$$\mathbf{S}^{(k+1)} = \mathbf{S}^{(k)} + \sigma_1^{(k)}\Delta^{(k)} \tag{20}$$

where $(\partial\mathbf{R}/\partial\mathbf{S})^{(k)}$ is the 2(N-1)x2(N-1) Jacobian matrix associated with $\mathbf{R}^{(k)}$, and $\Delta^{(k)}$ is the solution of the linear system (19) (the estimated required change in $\mathbf{S}^{(k)}$ to give $\mathbf{R}^{(k+1)} = \mathbf{0}$). The "relaxation factor" $\sigma_1^{(k)}$ which limits the maximum fractional change in any element of $\mathbf{S}^{(k)}$ over one iteration cycle, is defined by

$$\sigma_1^{(k)} \equiv \min\,(1,\, \delta \,/\, \max_i\, |\Delta_i^{(k)}/S_i^{(k)}|\,) \tag{21}$$

where δ is a specified constant (≈ 0.3 typically), and $\Delta_i^{(k)}$ and $S_i^{(k)}$ are the ith elements of $\Delta^{(k)}$ and $\mathbf{S}^{(k)}$ respectively. The iterate $\mathbf{S}^{(k)}$ is considered converged when

$$\max_i\, |\Delta_i^{(k+1)}/S_i^{(k+1)}| \le \varepsilon_1 << 1 \tag{22}$$

where ε_1 is specified (typically $\approx 10^{-4}$). The matrix $\partial R/\partial S$ is of block-tridiagonal form with the jth 2x2 subdiagonal, diagonal, and superdiagonal blocks given by $\partial r_j/\partial s_{j-1}$, $\partial r_j/\partial s_j$, and $\partial r_j/\partial s_{j+1}$ respectively; system (19) may thus be solved efficiently using a routine such as listed in [6].

Given the start-up values $\zeta_L^{(0)}$ and $\zeta_L^{(1)}$ (both $> \zeta_0$, e.g., 0.01 and 0), the (m+1)th iterate $\zeta_L^{(m+1)}$ is computed using a variant of the secant method

$$\zeta_L^{(m+1)} = \zeta_L^{(m)} - \sigma_2^{(m)} \frac{g^{(m)}}{(g^{(m)} - g^{(m-1)}) / (\zeta_L^{(m)} - \zeta_L^{(m-1)})} \tag{23}$$

where $g^{(m)} \equiv g(\zeta_L^{(m)})$ is evaluated from $S(\zeta_L^{(m)})$, the solution of (17)-(18) computed by solving (19)-(20) with $\zeta_L = \zeta_L^{(m)}$ and the initial distribution $S(\zeta_L^{(m-1)})$. The relaxation factor, $0 < \sigma_2^{(m)} < 1$, is included to avoid overshooting ζ_0 and is adjusted during marching based on the number of iterations required to solve (17)-(18); specifically, if (23) gives a value of $\zeta_L^{(m+1)}$ for which (19)-(20) does not converge within a specified number of iterations, $\sigma_2^{(m)}$ is replaced with a lower value such as $(\sigma_2^{(m)})^2$, (23) is then re-evaluated, and the (m+1)th iteration restarted. It is found numerically that (19)-(20) will not converge in the sense (22) when $\zeta_L < \zeta_0$; thus the inclusion of $\sigma_2^{(m)}$ in (23) is a necessity. The iterate $\zeta_L^{(m)}$ is considered converged when

$$\left| \zeta_L^{(m+1)} - \zeta_L^{(m)} \right| / \left| \zeta_L^{(m)} \right| \leq \varepsilon_2 << 1 \tag{24}$$

where ε_2 is specified (typically $\approx 10^{-5}$).

To compute $S(\zeta_L^{(0)})$, (19)-(20) may be solved starting with the simple piecewise linear distributions $u=x/6$ for $x \leq 6$, $u=1$ for $x \geq 6$, and $T=T_L(1-x/x_U)$; continuation is then applied as the lower boundary temperature T_L is incrementally reduced from an initial value .02 (say) to 0, thus providing an initial distribution to begin marching in ζ_L.

The choice of the "monitor function" g is arbitrary and need only provide a sufficient condition for satisfying (3). One might for example select $g(\zeta_L) = dE/d\zeta_L$ where E is the square of the L_2-norm of the relative error between the asymptotic and numerical solution evaluated over the small interval $0 \leq x \leq \varepsilon_a$; g vanishes when E is a minimum, i.e., when $\zeta_L = \zeta_0$. Since (19)-(20) will not converge when $\zeta_L < \zeta_0$, one may define a simpler criterion on $\zeta_L \geq \zeta_0$ alone. A possibility which works well for ω near 3/4 is

$$g(\zeta_L) \equiv \frac{T_1(1+\alpha)^2 - T_2}{\Delta x_0 \alpha(1+\alpha)}, \qquad \zeta_L \geq \zeta_0 \tag{25}$$

which is a second-order forward-difference representation of $dT/dx(0; \zeta_L)$ with $T_0 = 0$; this expression is particularly well suited for the case $\omega = 3/4$ since (3) gives $T = O(x^2)$ for $0 \leq x << 1$ when $\zeta_L = \zeta_0$, and such quadratic behavior may be computed exactly by (25).

3. RESULTS

A typical solution computed using (25) is illustrated in figure 2 for γ=1.4, ω=3/4, b=-1/2, N=200, $\Delta x_0 = 10^{-3}$ and $x_U = 24$ ($\alpha \approx 1.034$). Both u and T versus x are plotted with most of the computational domain shown in part (a), and a blow-up of the region $0 \leq x \leq 0.02$ shown in part (b). For comparison, second-order asymptotic solutions are also plotted in part (b) where relative errors between the numerical and asymptotic solutions are seen to be of order 2% for $0 \leq x \leq 0.01$. For the case shown, solutions computed with larger N indicate that N=200 (which required approximately 3 minutes to compute on an Apollo DN 4000) gives an accuracy of approximately 4 significant figures over regions where the solution is of order 1, falling to approximately 2 significant figures near x=0; the computed location of the lower boundary, ζ_0=-3.683, is believed to be accurate to within less than 0.1%.

The rather large value of N required for reasonable accuracy, even with the use of grid (10), is dictated by the need to resolve the solution near x=0. When the grid was overly stretched (α too large), accuracy was degraded and it proved difficult to obtain converged solutions; the allowable amount of stretch is therefore limited and since Δx_0 must be quite small, N must be large. If ζ_0 were known a priori, then the required resolution near x=0 would not be as great, and $N \approx 50$ with the same x_U and α (but larger Δx_0) would have provided an equivalent level of accuracy over most of the grid for the case illustrated in figure 2.

The replacement of asymptotic boundary conditions with numerical boundary conditions plus a sufficient condition g=0, e.g., the replacement of (3) with (7) plus (25), appears to offer a useful general technique. In the example presented here, a particularly simple function g could be defined since the behavior of neighboring solutions was well understood after computation of several trial solutions. Possibly the general case might best be handled with g based on some least-square error measure, similar to the ideas presented in [5].

ACKNOWLEDGMENTS

Thanks are extended to Prof. Bram van Leer and Prof. Thomas C. Adamson, Jr. for their helpful suggestions. This work was supported in part by the U. S. Army Strategic Defense Command.

M. D. MATARRESE and A. F. MESSITER
Department of Aerospace Engineering
The University of Michigan
Ann Arbor, MI 48109-2140

REFERENCES

1. A. F. MESSITER AND M. D. MATARRESE, Hypersonic viscous interaction with strong blowing, submitted to *J. Fluid Mech.*
2. C. B. COHEN AND E. RESHOTKO, *NA.CA. Rep.* no. 1293 (1956).
3. P. R. NACHTSHEIM AND M. J. GREEN, *AIAA. J.* 9, 3 (1971).
4. T.-M. LIU AND H. H. CHIU, *AIAA. J.* 14, 1 (1976).
5. P. R. NACHTSHEIM AND P. SWIGERT, *NASA. TN* no. D-3004 (1965).
6. D. A. ANDERSON, J. C. TANNEHILL, AND R. H. PLETCHER, *Computational Fluid Mechanics and Heat Transfer* (Hemisphere, 1984), p. 551.

FIGURE CAPTIONS

1. Trial numerical solutions (broken lines) and the desired solution (solid line) for u (a) and T (b) near $\zeta=\zeta_0$. With $T_L=0$: $\zeta_L=-3.2$ (— —); $\zeta_L=-3.4$ (- - - -). With $\zeta_L=-5$: $T_L=10^{-4}$ (— - - - —); $T_L=10^{-5}$ (— - —).

2. (a): profiles of u (▵) and Tx10 (∘); (b): comparison with second-order asymptotic solutions for u (——) and T (— —) near x=0.

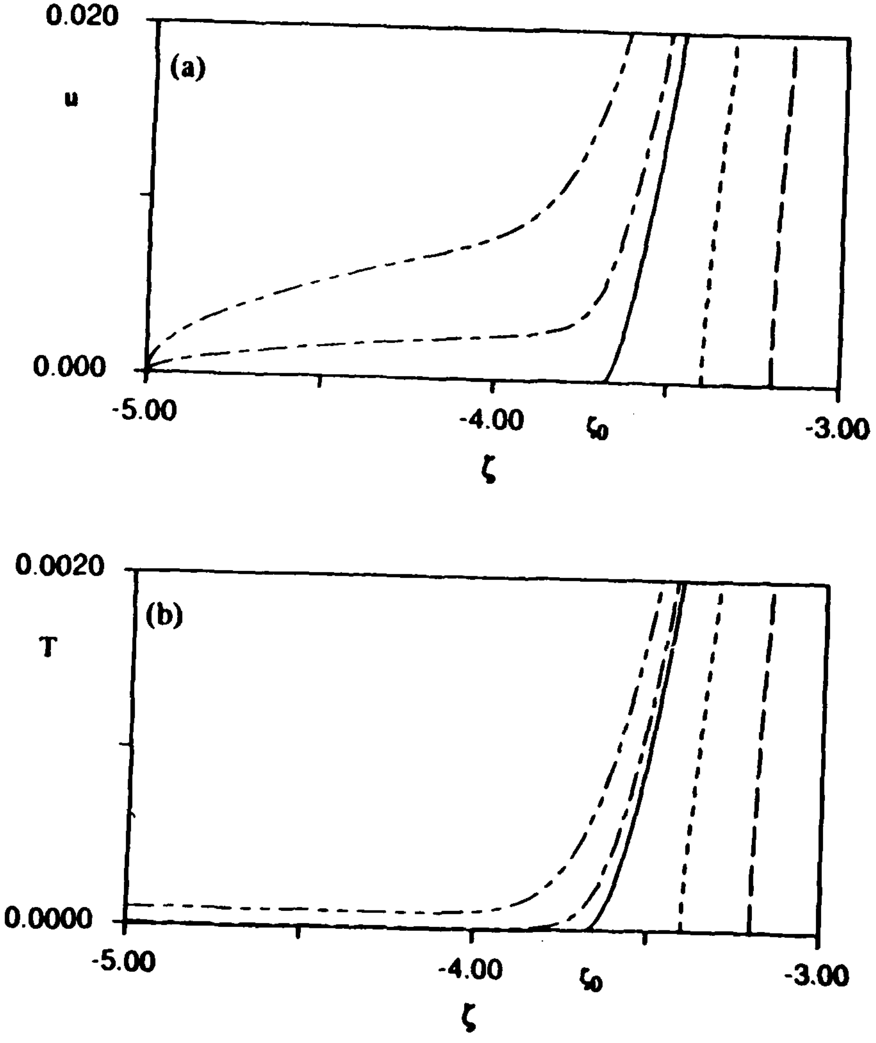

Fig. 1.

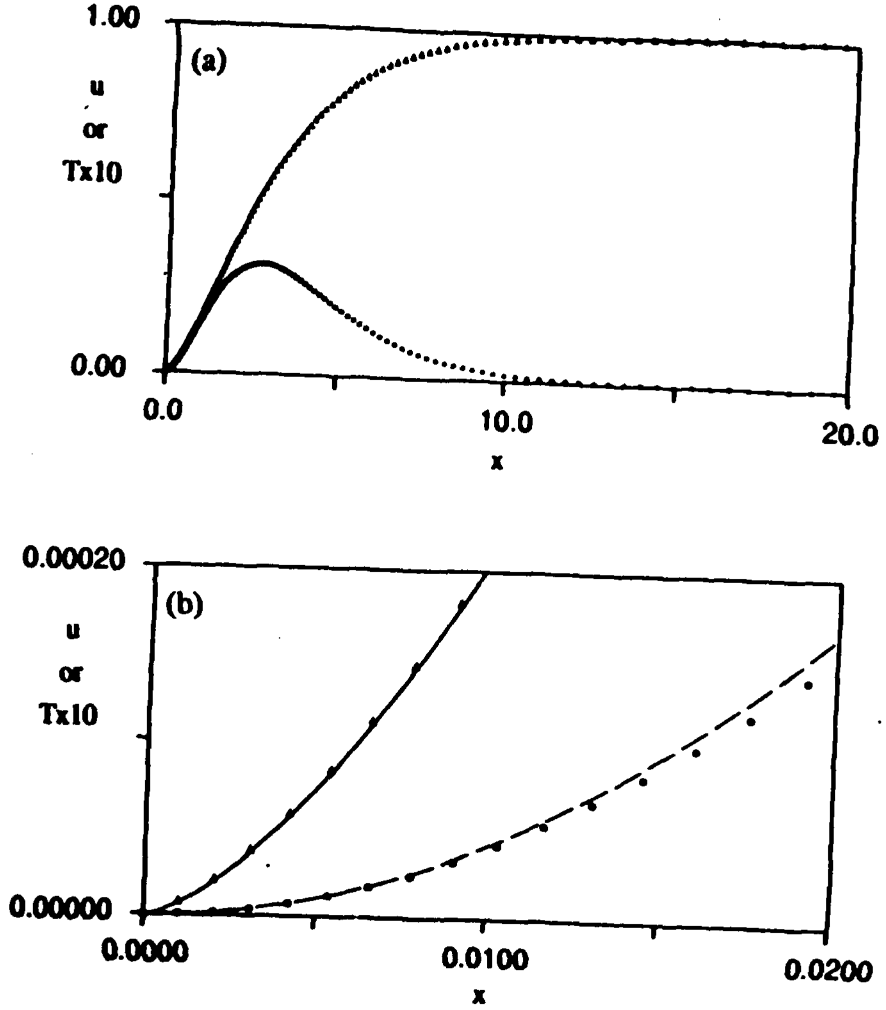

Fig 2.

Journal of Computational Physics

Control of Hypersonic Aerodynamic Forces with Surface Blowing

M. D. Matarrese,* A. F. Messiter,† and T. C., Adamson, Jr.‡
University of Michigan, Ann Arbor, Michigan

Pressure forces are derived for laminar flow past a thin wedge at high Mach number and high Reynolds number, with mass added at the surface according to a power-law velocity distribution strong enough that the boundary layer is blown away from the wall as a free shear layer. Self-similar solutions are obtained for the thin layer of blown gas adjacent to the surface, for the thin viscous shear layer, and for the outer inviscid-flow region between the shear layer and the shock wave. Pressures obtained in the strong- and weak-interaction regions are joined by a simple interpolation formula. Integrated pressure forces are shown for a range of Mach numbers and altitudes, for various wedge lengths and vertex angles, and for different injected gases. Equilibrium dissociation of oxygen in the shear layer is found to have only a small effect on the pressure forces.

Nomenclature

A = constant defined in Eq. (3.12)
C = constant defined in Eq. (2.13)
c_p = specific heat at constant pressure
D = coefficient in expression for layer thickness
D_∞ = self-diffusion coefficient for undisturbed air
G = constant defined in Eq. (2.40)
h = enthalpy
H = atmospheric scale height
I_n = integral defined in Eq. (3.15)
j = exponent in Eq. (2.24)
J = defined following Eq. (2.42)
k = constant defined in Eq. (2.13)
K_D = proportionality constant for mass diffusion, Eq. (2.40)

Copyright © 1989 by authors. Published by American Institute of Aeronautics and Astronautics, Inc., with permission.

* Graduate Student, Department of Aerospace Engineering. Student Member AIAA.

† Professor, Department of Aerospace Engineering. Associate Fellow AIAA.

‡ Professor, Department of Aerospace Engineering. Fellow AIAA.

K_p = equilibrium constant for $\frac{1}{2}O_2 \rightleftarrows O$, Eq. (2.51)
K_λ = proportionality constant for diffusion of heat, Eq. (2.42)
$K_{\lambda D}$ = proportionality constant for energy transfer by mass diffusion, Eq. (2.54)
K_μ = proportionality constant in viscosity law, Eq. (2.41)
L = wedge length
$\dot{m}$ = total mass flow of injected gas, per unit span, defined in Eq. (2.24)
$\tilde{m}$ = scaled mass flow of injected gas per unit area, defined in Eq. (2.20)
$\tilde{m}_{avg}$ = scaled total mass flow of injected gas, per unit span, defined in Eq. (2.24)
M = Mach number
n = exponent in Eq. (2.9)
p = pressure
P = scaled pressure perturbation defined in Eqs. (3.7), (3.8)
Pr = Prandtl number, $c_{p_\infty}\mu_\infty/\lambda_\infty$, defined following Eq. (2.39)
q = exponent in Eq. (2.43)
Q = scaled mass flow defined in Eqs. (3.7), (3.8)
r = function of x defined in Eq. (3.12)
R = nondimensional gas constant for mixture, defined in Eq. (2.35)
Re = Reynolds number, $u_\infty L/\nu_\infty$
Sc = Schmidt number, $\mu_\infty/(\rho_\infty D_\infty)$, defined following Eq (2.39)
T = temperature
u = x-component of velocity
v = y-component of velocity
x = nondimensional coordinate in direction of undisturbed flow
X = coordinate in direction of undisturbed flow
X_r = reference length defined in Eq. (2.1)
y = nondimensional coordinate normal to undisturbed flow
Y = coordinate normal to undisturbed flow
Y_b = mass fraction of blown gas
Y_O = mass fraction of atomic oxygen
z = altitude
α = wedge vertex half-angle

β = shock-wave inclination angle

γ = ratio of specific heats

Δ = layer thickness

ΔF = increase in normal force on wedge, above inviscid-flow value

ε = fraction of molecules which dissociate into oxygen atoms, Eq. (2.50)

ζ = similarity variable defined in Eq. (2.43)

ζ_ℓ = lower limit for ζ

λ = thermal conductivity

μ = viscosity coefficient

ν = kinematic viscosity

ρ = density

σ_b = ratio of molecular weight of blown gas to that of air

ϕ = defined in Eq. (3.9)

χ = defined in Eq. (3.10)

ψ = nondimensional stream function

$\overline{\psi}_\ell, \overline{\psi}_u$ = lower and upper limits of $\overline{\psi}$ in Eq. (3.1)

ω = exponent in viscosity law

Subscripts

0 = (scaled) quantity in inviscid wedge flow

1 = coefficient in perturbation quantity

∞ = undisturbed-flow value

a = air

b = blown gas

s = value at shock wave

w = value at wall

Superscripts

(s) = strong-interaction region

(w) = weak-interaction region

^ = nondimensional quantity in outer inviscid-flow region

~ = nondimensional quantity in blown-gas layer

– = nondimensional quantity in viscous shear layer

Introduction

Control of flight vehicles at hypersonic speeds has usually been achieved by means of moving control surfaces and/or by changing the magnitude and direction of the thrust vector. As a possible alternative method of control, it might be of interest to consider the use of boundary-layer blowing to introduce desired modifications in pressure distributions over the surface and thus to provide control forces on a specified part of a vehicle. Different injection patterns would be possible, including distributed or strip blowing. In the present study a simple blowing distribution is considered for the simplest possible geometry, a thin wedge in two-dimensional hypersonic flow. If the mass rate of flow of injected gas is sufficiently large, the boundary layer is completely blown off from the surface; this is the case considered here. The solutions can be useful in several contexts. First, they provide a measure of the magnitudes of forces to be expected for a given blowing rate at given flight conditions; second, they can be used to check computer codes developed to handle more complex flow problems;[1] finally, they may have some application in the related problems of cooling hypersonic vehicles by boundary-layer blowing, and of the introduction of fuel into the combustion region of a SCRAMJET.

Hypersonic flows of a perfect gas past simple shapes have been studied extensively using inviscid-flow theory, and viscous interaction effects are also well understood. For a thin wedge the effects of small perturbations in surface shape require solution of linearized equations.[2] If the perturbations are caused by the displacement thickness of a laminar boundary layer, the equations for a constant-pressure boundary layer at high Mach number allow a complete description of the flow at points far enough from the leading edge. In a region closer to the vertex where the boundary-layer thickness is large compared to the wedge thickness (but streamline slopes are still small), a self-similar solution is available,[3,4] based on the hypersonic small-disturbance equations[5] for the shock layer and boundary-layer equations for the viscous layer. The interactions of the boundary layer with the external inviscid flow in these two regions are, respectively, "weak" and "strong" interactions.

Surface injection of a gas in the strong-interaction region, for a suitable power-law velocity variation, still allows a self-similar formulation but with modified boundary conditions. Li and Gross[6] obtained numerical results for strong interaction using boundary-layer solutions with a nonzero normal velocity component at the surface, over a range of prescribed surface temperatures. If the blowing is strong enough, however, the boundary layer is blown away from the surface. Kubota and Fernandez[7] considered a compressible free shear layer, with prescribed power-law pressure gradient, and an additional thin layer of inviscid flow adjacent to the wall. For still stronger blowing velocities the layer of blown gas is much thicker than the free shear layer and the shear layer can be regarded as a surface of discontinuity. Cole and Aroesty[8] described the blown gas by "inviscid boundary-layer equations" and the shock layer again by hypersonic small-disturbance equations. A useful summary of this and earlier related work was given by Smith and Stewartson.[9]

When the blowing velocity has suitable strength, as well as an appropriate power-law variation, in the strong-interaction region, the displacement effects of the blown gas and of the shear layer are of the same order of magnitude.[10] Solutions in the strong-interaction limit can then be obtained independently for the thin layer of blown gas, the viscous free shear layer, and the inviscid shock layer, with certain constants to be found by proper asymptotic matching. The shock layer is described by the hypersonic small-disturbance equations,[5] the viscous layer by the usual boundary-layer equations, and the blown gas by inviscid boundary-layer equations.[8] The derivations of Ref. 10 were given primarily for a flat plate, with an application to a thin wedge mentioned relatively briefly. Since the temperature in the shear layer is high, the scaled temperature in the shear layer should approach zero both above and below. Numerical solution of the shear-layer equations was carried out by a continuation method in which the mass flow entrained in the lower part of the shear layer is varied until the proper asymptotic behavior is observed.[11] The weak-interaction region can also be described by self-similar solutions; an approximate interpolation formula was proposed in Ref. 10 for joining the surface pressures found from the strong- and weak-interaction solutions.

The present study is concerned with pressure forces acting on a thin wedge in the presence of mass injection at the surface having a power-law dependence on distance from the vertex. The derivations of Ref. 10 are extended in several ways: to allow constant surface temperature rather than constant surface density, as assumed in Ref. 10 to achieve some minor simplifications; to allow arbitrary values of the hypersonic similarity parameter instead of requiring that the normal Mach number at the shock wave be large; to allow an injected gas different from air; to allow for variable specific heats and oxygen dissociation in the viscous shear layer; and to provide a variety of numerical results for pressure forces caused by blowing.

The main objective is to relate the pressure distribution at the wedge surface to the prescribed surface conditions, expressed by the specified distribution of injected mass and either a constant wall density or a constant wall temperature. Solutions for the inviscid outer flow provide the relation between the surface pressure and the effective body shape; solutions for the inviscid layer of blown gas give an expression for the thickness of this layer in terms of the surface pressure and the Mach number at the wall, here expressed in terms of the surface mass flux and the temperature or density at the wall; the solution for the viscous shear layer provides a relation between the shear-layer thickness and the surface pressure. Combining these results with the help of first-order matching conditions then yields the desired results.

The following section summarizes the analysis, with emphasis on the new aspects. Numerical results for integrated forces are then shown and discussed for a range of Mach numbers and altitudes, for various wedge lengths and vertex angles, and for different injected gases at different values of surface temperature.

Analysis

A thin wedge having length L and small vertex half-angle $\alpha<<1$ is placed at zero incidence in a uniform hypersonic flow with speed u_∞, pressure p_∞, density ρ_∞, temperature T_∞, enthalpy h_∞, Mach number $M_\infty>>1$, and viscosity coefficient μ_∞. Local values of the velocity vector, pressure, density, temperature, enthalpy, and viscosity coefficient are denoted, respectively, by (u,v), p, ρ, T, h, and μ. A power-law viscosity-temperature relation $\mu/\mu_\infty=(T/T_\infty)^\omega$ is assumed for air; if a different gas is injected at the wedge surface, μ also depends on the mass fraction Y_b of the blown gas.

Coordinates X and Y are measured along and normal to the free-stream direction, respectively, with origin at the vertex of the wedge. In the absence of surface blowing, an effective body shape is found by adding the boundary-layer displacement thickness to the location of the wedge surface $Y \sim \alpha X$. At points sufficiently far from the vertex (when L is large enough) the boundary-layer thickness $O\{M_\infty^{\omega}\alpha^{-1}(\nu_\infty X/u_\infty)^{1/2}\}$, where $\nu_\infty=\mu_\infty/\rho_\infty$, is small in comparison with one-half the wedge thickness αX, and the pressure is nearly the same as for inviscid flow. At points closer to the leading edge, however, this is no longer true. A reference length X_r is defined by equating the two thicknesses, so that for $X \gg X_r$ the boundary layer has only a small effect on the external flow, and the interaction is "weak," whereas for $X \ll X_r$ the boundary-layer displacement effect is dominant, and the interaction is "strong."[3,4] Nondimensional coordinates are then defined by

$$x=\frac{X}{X_r}, \qquad y=\frac{Y-\alpha X}{\alpha X_r}, \qquad X_r=M_\infty^{2\omega}\alpha^{-4}\nu_\infty/u_\infty \tag{2.1}$$

where $\alpha \ll 1$; $y=0$ at the wedge surface (in the small-angle approximation); and at the shock wave $y=O(1)$ when $x=O(1)$. The ratio L/X_r is proportional to the Reynolds number $Re=u_\infty L/\nu_\infty$ based on wedge length and free-stream quantities. For constant Mach number and an isothermal atmosphere, the length X_r increases exponentially with altitude; a weaker dependence on temperature can be introduced by assuming a standard atmosphere. At low altitudes X_r might be small in comparison with L; at sufficiently high altitudes $X_r \gg L$. The stream function, nondimensional with $\alpha\rho_\infty u_\infty X_r$, is defined by

$$\rho_\infty u_\infty \psi_y=\rho u \tag{2.2}$$

with $\psi=0$ along the streamline from the vertex of the wedge.

If mass is added to the flow by surface blowing, here taken as directed normal to the surface, the effective body thickness is increased further, and for sufficiently strong injection the boundary layer is blown away from the surface as a free shear layer. The equivalent body now includes the effects of both blowing and viscous diffusion. The sketches in Fig. 1 suggest the qualitative features of the flow in the strong- and weak-interaction regions, for weak blowing when the boundary layer is still attached and for strong blowing; in each case, the speckled region is the viscous layer. For the "strong" blowing considered here, three thin flow layers can be distinguished. Qualitative sketches of the mass-fraction, velocity, temperature, and pressure profiles for $x=O(1)$ are shown in Fig. 2 for the entire region of disturbed flow between the wedge surface and the shock wave. A tilde will be used to indicate quantities in the nearly inviscid thin layer of blown gas; an overbar will denote variables in the viscous free shear layer where mixing (assumed laminar) of the blown gas and free-stream gas takes place; and a caret will denote solutions for the outer inviscid flow between the shear layer and the shock wave. Superscripts s and w will denote strong and weak interaction, for $x<<1$ and $x>>1$, respectively. In general, the flow variables will have different orders of magnitude in the different flow regions. The surface temperature will be taken to have the same order of magnitude (other choices of course are possible) as the temperature in the undisturbed air, whereas the temperature in the viscous layer is larger by a factor $O(M_\infty^2)$. The mass flow in the blown layer is small because the flow velocities are small there, and in the viscous layer the mass flow is still smaller because the density is low; the first approximation to the pressure is a function only of x in both regions. The amount of injected mass is chosen such that the blown-layer thickness is of the same order of magnitude as the wedge thickness when $x=O(1)$. The thickness of the viscous layer is likewise of this order when $x=O(1)$; if, however, the mass flow is increased further, the viscous-layer thickness can be neglected.

Inviscid Outer Flow

The location $y = \Delta(x)$ of the equivalent body surface, flow variables in the region between this surface and the shock wave, and the stream function can be written as

$$\Delta(x) = \tilde{\Delta}(x) + \bar{\Delta}(x), \qquad p/p_\infty = M_\infty^2\alpha^2\,\hat{p}(x,y) + \dots ,$$
$$\rho/\rho_\infty = \hat{\rho}(x,y) + \dots , \qquad u/u_\infty = 1 + \dots , \qquad \psi = \hat{\psi} \tag{2.3}$$

where $\tilde{\Delta}(x)$ and $\bar{\Delta}(x)$ describe the contributions of the blown gas and the shear layer respectively. The pressure at the displacement surface $y = \Delta(x)$ can be found in terms of $\Delta(x)$ in both the strong- and weak-interaction limits, for suitably specified mass injection rates.

For $x<<1$, a self-similar solution describes strong viscous interaction. The surface of the equivalent body and the pressure at this surface have the form

$$\Delta(x) = \Delta_1^{(s)}x^{3/4} + \dots , \qquad \hat{p}^{(s)}(x,\Delta(x)) = p_1^{(s)}x^{-1/2} + \dots \tag{2.4}$$

where the superscript "s" indicates "strong" interaction and $p_1^{(s)}$ is a constant to be determined; the required form for surface blowing is shown below. The flow in the inviscid shock layer is described by the self-similar form of the hypersonic small-disturbance equations, with appropriate exponents. Numerical solution of these equations, for $\gamma_\infty=1.4$, gives a relation[10] between the coefficients in Eq. (2.4):

$$\Delta_1^{(s)} = \hat{D}^{(s)}(p_1^{(s)})^{1/2}, \qquad \hat{D}^{(s)} = 0.945 \tag{2.5}$$

The numerical value agrees with that of Ref. 6. The representation given by Eqs. (2.4) requires that streamline slopes be small and that the pressure be small in comparison with the dynamic pressure in the undisturbed flow. Thus the solution fails for very small x, in the "merged-layer regime" for $x=O(\alpha^4)$, or $X=O(M_\infty^{2\omega}\nu_\infty/u_\infty)$; boundary-layer approximations fail here as well, as noted below.

If $X_T<<L$, the strong interaction is confined to a small fraction of the wedge length. Further downstream, for the portion of the wedge where $x>>1$, the boundary layer causes only small disturbances to the outer inviscid flow. In the hypersonic small-disturbance approximation, the shock-wave jump conditions can be combined in the form

$$\frac{v_s}{\beta u_\infty} = 1 - \frac{\rho_\infty}{\rho_s} = \frac{p_s - p_\infty}{\gamma_\infty M_\infty^2 \beta^2 p_\infty} = \frac{2}{\gamma_\infty+1}\left(1 - \frac{1}{M_\infty^2\beta^2}\right) \tag{2.6}$$

where β is the shock-wave inclination angle, γ_∞ is the ratio of specific heats in the undisturbed flow, and the subscript s indicates that a quantity is evaluated immediately downstream of the shock wave. The flow variables for $x>>1$ have the form

$$p/p_\infty = M_\infty^2\alpha^2\{p_0 + \hat{p}_1^{(w)}(x,y) + \ldots\}, \qquad \rho/\rho_\infty = \rho_0 + \ldots$$

$$v/u_\infty = \alpha\{1 + \hat{v}_1^{(w)}(x,y) + \ldots\}, \qquad \beta = \alpha\beta_0 + \ldots, \qquad M = \alpha^{-1}M_0 + \ldots \tag{2.7}$$

where M is the local Mach number, the subscript "0" denotes solutions for inviscid wedge flow, and the superscript "w" refers to "weak" interaction. The values for turning through a small angle α are given by

$$\beta_0 = \frac{\gamma_\infty+1}{4} + \left\{\left(\frac{\gamma_\infty+1}{4}\right)^2 + \frac{1}{M_\infty^2\alpha^2}\right\}^{1/2}, \qquad \rho_0 = \frac{\beta_0}{\beta_0-1}$$

$$p_0 = \gamma_\infty\beta_0 + \frac{1}{M_\infty^2\alpha^2}, \qquad M_0^2 = \frac{\rho_0}{p_0} \tag{2.8}$$

The product $M_\infty\alpha$ is the usual similarity parameter of hypersonic small-disturbance theory.

For the weak-interaction region x>>1, the surface $y=\Delta(x)$ of the equivalent body lies very close to the wedge surface. The body shape and the linearized boundary condition are

$$\Delta(x) = \Delta_1^{(w)} x^n + \dots, \qquad \hat{v}_1^{(w)}(x,0) = n\Delta_1^{(w)} x^{n-1} + \dots \tag{2.9}$$

where the value of $n<1$ depends on the choice of prescribed conditions at the surface. The shock-wave jump conditions given by Eqs. (2.6) provide a relation between the perturbations $\hat{p}_1^{(w)}$ and $\hat{v}_1^{(w)}$ at the linearized shock position $Y=\alpha\beta_0 X$ or $y=(\beta_0-1)x$:

$$\gamma_\infty^{-1}\hat{p}_1^{(w)}(x,(\beta_0-1)x) = \frac{\beta_0^2}{\beta_0 - \frac{\gamma_\infty+1}{4}}\,\hat{v}_1^{(w)}(x,(\beta_0-1)x) \tag{2.10}$$

Each of the functions $\hat{p}_1^{(w)}$ and $\hat{v}_1^{(w)}$ must satisfy a wave equation in the x, y coordinates, and the boundary conditions require that each have a self-similar form. The solutions satisfying these conditions are

$$\gamma_\infty^{-1}\hat{p}_1^{(w)} = c_1(x+M_0 y)^{n-1} + c_2(x-M_0 y)^{n-1} \tag{2.11}$$

$$-\frac{\rho_0}{M_0}\hat{v}_1^{(w)} = c_1(x+M_0 y)^{n-1} - c_2(x-M_0 y)^{n-1} \tag{2.12}$$

where the constants are defined by

$$\frac{c_1}{C} = \frac{c_2}{k^{1-n}} = \frac{\rho_0 n\Delta_1^{(w)}}{(k^{1-n} - C)M_0},$$

$$k = \frac{1-M_0(\beta_0-1)}{1+M_0(\beta_0-1)}, \qquad C = \frac{M_0\beta_0(\beta_0-1) - (\beta_0 - \frac{\gamma_\infty+1}{4})}{M_0\beta_0(\beta_0-1) + (\beta_0 - \frac{\gamma_\infty+1}{4})} \tag{2.13}$$

The pressure at the surface of the equivalent body and the shape of the body are related by

$$\Delta_1^{(w)} = \hat{D}^{(w)} p_1^{(w)} = x^{1-n}\hat{D}^{(w)}\hat{p}_1^{(w)}(x,0), \qquad \hat{D}^{(w)} = \frac{M_0(k^{1-n} - C)}{\gamma_\infty n\rho_0(k^{1-n} + C)} \tag{2.14}$$

Thus $\hat{D}^{(w)}$ depends on γ_∞, n, and $M_\infty\alpha$. The results are equivalent to those of Ref. 2.

Inviscid Blown-Gas Layer

At the wedge surface, gas is injected in a direction normal to the wall at a low Mach number $M_w = O(\alpha)$. For the blowing rates considered here, most of the injected gas occupies a thin layer adjacent to the surface; the flow in this blown-gas layer is nearly inviscid, and only a small fraction of the injected mass is entrained in the mixing layer. In the layer of blown gas the scalings for the flow variables are essentially the same as suggested by Cole and Aroesty,[8] and are found from the boundary and matching conditions, thermodynamic relations, and the conservation laws to have the form

$$p/p_\infty = M_\infty^2\alpha^2\,\tilde{p}(x) + \dots, \quad \rho/\rho_\infty = M_\infty^2\alpha^2\,\sigma_b\,\tilde{\rho}(x,y) + \dots, \quad T/T_\infty = \tilde{T}(x,y) + \dots \tag{2.15}$$

$$u/u_\infty = \frac{1}{M_\infty}\left(\frac{\gamma_b}{\sigma_b\gamma_\infty}\right)^{1/2}\tilde{u}(x,y) + \dots, \quad v/u_\infty = \frac{\alpha}{M_\infty}\left(\frac{\gamma_b}{\sigma_b\gamma_\infty}\right)^{1/2}\tilde{v}(x,y) + \dots \tag{2.16}$$

where γ_b and γ_∞ are the ratios of specific heats for the blown gas and for the undisturbed stream, respectively, and σ_b is the ratio of the molecular weight of the blown gas to that of air. The pressure is a function of x in the first approximation since the layer is thin and the gas velocity is low. The stream function ψ is then

$$\psi = M_\infty\alpha^2\left(\frac{\sigma_b\gamma_b}{\gamma_\infty}\right)^{1/2}\tilde{\psi} \tag{2.17}$$

The streamline, total-enthalpy, entropy, and state equations become

$$y_{\tilde{\psi}} = \frac{1}{\tilde{\rho}\tilde{u}}, \qquad \frac{1}{2}\tilde{u}^2 + \frac{\tilde{T}}{\gamma_b - 1} = \frac{\tilde{T}_w}{\gamma_b - 1}, \qquad \tilde{\rho} = \left(\frac{\tilde{p}}{\tilde{p}_w}\right)^{1/\gamma_b}\tilde{\rho}_w, \qquad \tilde{p} = \tilde{\rho}\tilde{T} \tag{2.18}$$

where the subscript w indicates conditions at the wall. This is the set of equations studied by Cole and Aroesty.[8] The wall values $\tilde{\rho}_w$, $\tilde{v}_w$, $\tilde{T}_w$, and $\tilde{p}_w$ are understood to be functions of $\tilde{\psi}$ and can be expressed instead in terms of a coordinate x_w that identifies the location at which a streamline leaves the surface. Thus

$$\tilde{\rho}_w = \tilde{\rho}(x_w,0), \qquad \tilde{v}_w = \tilde{v}(x_w,0), \qquad \tilde{p}_w = \tilde{p}(x_w) \tag{2.19}$$

where $x_w(\tilde{\psi})$ is defined by

$$d\tilde{\psi} = -\,\tilde{m}\,dx_w, \qquad \tilde{m} = \tilde{\rho}_w\tilde{v}_w \tag{2.20}$$

and $\tilde{m}$ is the scaled nondimensional mass flow of injected gas per unit area. The Mach number of the injected gas is also expressed as a function of x_w:

$$M_w = \alpha\tilde{M}_w(x_w) \tag{2.21}$$

From Eqs. (2.18) and (2.20), the streamline equation can be written as

$$dy = -\left(\frac{\gamma_b - 1}{2}\right)^{1/2}\tilde{M}_w\left(\frac{\tilde{p}}{\tilde{p}_w}\right)^{-1/\gamma_b}\left\{1 - \left(\frac{\tilde{p}}{\tilde{p}_w}\right)^{(\gamma_b - 1)/\gamma_b}\right\}^{-1/2}dx_w \tag{2.22}$$

The contribution $\tilde{\Delta}(x)$ to the shape of the equivalent body is found by integration over x_w, at a given x, from a point on the surface up to the zero streamline:

$$\tilde{\Delta}(x) = \int_{\tilde{\psi}_w}^{0} \frac{d\tilde{\psi}}{\tilde{\rho}\tilde{u}} = -\int_{0}^{x} \frac{\partial y}{\partial x_w} dx_w \tag{2.23}$$

where $\tilde{\psi}=\tilde{\psi}_w(x)$, the stream function at the wall, is the inverse of $x=x_w(\tilde{\psi})$. The choice $M_w = O(\alpha)$ gives $\tilde{\Delta}=O(1)$; i. e., for this choice the thickness of the blown-gas layer is of the same order of magnitude as the wedge thickness when $x=O(1)$.

The average mass flow per unit area equals the integral of $\rho_w v_w$ divided by the length L. If $\rho_w v_w$ is proportional to a power of x, the scaled mass flow $\tilde{m}$ can then be written in terms of a scaled average $\tilde{m}_{avg}$, which is proportional to the integrated dimensional mass flow $\dot{m}$ per unit span:

$$\tilde{m} = \tilde{m}_{avg}\left(\frac{X_r}{L}\right)^{-j}(1-j)\,x^{-j}, \qquad \tilde{m}_{avg} = \frac{X_r}{L}\int_{0}^{L/X_r} \tilde{m}(x)\,dx$$

$$\dot{m} = \rho_\infty u_\infty L\, M_\infty \alpha^3 \left(\frac{\sigma_b \gamma_b}{\gamma_\infty}\right)^{1/2} \tilde{m}_{avg} \tag{2.24}$$

The mass flow $\tilde{m}$ is taken to have the same form for all x. In the strong-interaction region, for $x<<1$, self-similarity requires that the pressure and the blowing Mach number have the form

$$\tilde{p} = p_1^{(s)}x^{-1/2}, \qquad \tilde{M}_w = \tilde{M}_{w1}^{(s)}x^{-1/4} \tag{2.25}$$

These conditions can be achieved, for example, if either the wall density $\tilde{\rho}_w$ or the wall temperature $\tilde{T}_w$ is constant, with the other of these quantities following a power-law variation found from the equation of state. In the weak-interaction region, the scaled pressure and the blowing Mach number are

$$\tilde{p} = p_0 + p_1^{(w)}x^{n-1} + \ldots, \qquad \tilde{M}_w = \tilde{M}_{w1}^{(w)}\,x^{-j} + \ldots \tag{2.26}$$

It is then found from Eq. (2.22) that the contributions of the blown-gas layer to equivalent body shapes for the strong- and weak-interaction regions are, respectively,

$$\tilde{\Delta}^{(s)} = \tilde{\Delta}_1^{(s)}x^{3/4} + \ldots, \qquad \tilde{\Delta}_1^{(s)} = \tilde{D}^{(s)}\tilde{M}_{w1}^{(s)} \tag{2.27}$$

$$\tilde{\Delta}^{(w)} = \tilde{\Delta}_1^{(w)}\,x^{(3-2j)/3} + \ldots, \qquad \tilde{\Delta}_1^{(w)} = \tilde{D}^{(w)}(p_0/p_1^{(w)})^{1/2}\tilde{M}_{w1}^{(w)} \tag{2.28}$$

and the exponents j, n are related by n=(3-2j)/3.

If the wall temperature $\tilde{T}_w$ is specified to be constant, the density $\tilde{\rho}_w$ and velocity $\tilde{v}_w$ at the surface are $O(x^{-1/2})$ and $O(x^{-1/4})$, respectively, for x<<1. The exponent j appearing in $\tilde{m} = \tilde{v}_w \tilde{p}/\tilde{T}_w$ is 3/4, and the injected mass flux is proportional to $x^{-3/4}$. The coefficient for the blowing Mach number in Eq. (2.25) is

$$\tilde{M}_{w1}^{(s)} = \frac{\tilde{T}_w^{\,1/2}}{4p_1^{(s)}}\, \tilde{m}_{avg}\left(\frac{L}{X_r}\right)^{3/4} \tag{2.29}$$

Substitution in Eq. (2.27) then provides a relation between $p_1^{(s)}$ and $\tilde{\Delta}_1^{(s)}$. Integration of Eq. (2.22) gives the constant $\tilde{D}^{(s)}$ for the streamline shape in the strong-interaction region as

$$\tilde{D}^{(s)} = \{2\pi(\gamma_b-1)\}^{1/2} \frac{2\gamma_b^{\,2}\,\Gamma\left(\frac{1}{2}\gamma_b/(\gamma_b-1)\right)}{(2\gamma_b-1)\Gamma\left(\frac{1}{2}/(\gamma_b-1)\right)} \tag{2.30}$$

In the weak-interaction region, again for constant wall temperature, the density and the coefficient in the blowing Mach number are

$$\tilde{\rho}_w = \frac{p_0}{\tilde{T}_w} + \dots, \qquad \tilde{M}_{w1}^{(w)} = \frac{\tilde{T}_w^{\,1/2}}{4p_0}\, \tilde{m}_{avg}\left(\frac{L}{X_r}\right)^{3/4} \tag{2.31}$$

Since pressure changes are small for x>>1, the Mach number remains small throughout the blown-gas layer, and the streamline shape is found from the incompressible form of Eq. (2.22). Integration then gives the constant $\tilde{D}^{(w)}$ in Eq. (2.28) for the thickness of this layer:

$$dy = -\left(\frac{\gamma_b p_0}{2(\tilde{p}_w - \tilde{p})}\right)^{1/2} \tilde{M}_w\, dx_w, \qquad \tilde{D}^{(w)} = 2(2\gamma_b)^{1/2} \tag{2.32}$$

If instead the surface density $\tilde{\rho}_w$ is taken to be constant,[10] the exponent in $\tilde{m} = \tilde{\rho}_w \tilde{v}_w$ is j=1/2 and the mass flux is proportional to $x^{-1/2}$. It is shown in Ref. 10 that the expressions obtained for $\tilde{D}^{(s)}$ and $\tilde{D}^{(w)}$ are the same as those given by Eqs. (2.30) and (2.32).

Viscous Shear Layer

In the high-temperature separated free-shear layer, the velocity and the thermodynamic variables have the form

$$u/u_\infty = \bar{u}(x,\bar{\psi}) + \dots, \qquad p/p_\infty = M_\infty^{\,2}\alpha^2\,\bar{p}(x) + \dots, \qquad \rho/\rho_\infty = \alpha^2\,\bar{\rho}(x,\bar{\psi}) + \dots,$$
$$T/T_\infty = M_\infty^{\,2}\bar{T}(x,\bar{\psi}) + \dots, \qquad h/h_\infty = M_\infty^{\,2}\bar{h}(x,\bar{\psi}) + \dots \tag{2.33}$$

where the stream function and the streamline equation are

$$\psi = \alpha^2\bar{\psi}, \qquad y_{\bar{\psi}} = \frac{1}{\bar{\rho}\bar{u}} + \ldots \tag{2.34}$$

If the shear layer is treated as a binary mixture of ideal gases, the equation of state is

$$\bar{p} = \bar{\rho}R\bar{T}, \qquad R = 1 - Y_b + \sigma_b^{-1}Y_b \tag{2.35}$$

where Y_b is the mass fraction of blown gas and $1-Y_b$ is the mass fraction of air; real-gas effects will be considered later. With each constituent modeled by the same "point-center-of-repulsion" potential-energy function, the transport coefficients for mass, momentum, and heat are all proportional to $\bar{T}^{\omega}$.[12] For a chemically inert mixture with negligible thermal diffusion, the concentration, momentum, and energy equations are then (e. g., Ref. 13)

$$Y_{b_x} = \frac{1}{Sc}(K_D\bar{T}^{\omega}\bar{\rho}\bar{u}\,Y_{b_{\bar{\psi}}})_{\bar{\psi}} \tag{2.36}$$

$$\bar{u}_x + \frac{1}{\gamma_\infty\bar{\rho}\bar{u}}\frac{d\bar{p}}{dx} = (K_\mu\bar{T}^{\omega}\bar{\rho}\bar{u}\bar{u}_{\bar{\psi}})_{\bar{\psi}} \tag{2.37}$$

$$\begin{aligned}\bar{c}_p\bar{T}_x - \frac{1}{\bar{\rho}}\frac{d\bar{p}}{dx} &= \gamma_\infty K_\mu\bar{T}^{\omega}\bar{\rho}\bar{u}\bar{u}_{\bar{\psi}}^{2}\\ &+ \frac{\gamma_\infty}{(\gamma_\infty-1)Pr}(K_\lambda\bar{T}^{\omega}\bar{\rho}\bar{u}\bar{T}_{\bar{\psi}})_{\bar{\psi}} + \frac{1}{Sc}K_D\bar{T}^{\omega}(\bar{c}_{p_b} - \bar{c}_{p_\infty})\bar{\rho}\bar{u}Y_{b_{\bar{\psi}}}\bar{T}_{\bar{\psi}}\end{aligned} \tag{2.38}$$

The specific heats appearing in (2.38) are

$$\bar{c}_p = \bar{c}_{p_b}Y_b + \bar{c}_{p_\infty}(1-Y_b), \qquad \bar{c}_{p_b} = \frac{\sigma_b^{-1}\gamma_b}{\gamma_b-1}, \qquad \bar{c}_{p_\infty} = \frac{\gamma_\infty}{\gamma_\infty-1} \tag{2.39}$$

where $\bar{c}_p$ has been made nondimensional with the gas constant for undisturbed air, and the (dimensional) species specific heats c_{p_b} and c_{p_∞} have been assumed independent of temperature. The Prandtl number Pr and Schmidt number Sc are defined by $Pr = c_{p_\infty}\mu_\infty/\lambda_\infty$ and $Sc = \mu_\infty/(\rho_\infty D_\infty)$, where λ_∞ is the thermal conductivity and D_∞ is the self-diffusion coefficient, for undisturbed air. The proportionality factors in the diffusion coefficients are given by[14]

$$K_D = \frac{G^{-1}}{\sigma_b R}, \qquad G = \left(\frac{2}{\sigma_b(1+\sigma_b)}\right)^{1/2} \tag{2.40}$$

$$K_\mu = \frac{1-Y_b}{1-Y_b+GY_b} + \frac{\sigma_b^{1/2}Y_b}{Y_b+G\sigma_b^{3/2}(1-Y_b)} \tag{2.41}$$

$$K_\lambda = \frac{1-Y_b}{1-Y_b+GY_b}\frac{Eu_a}{Eu_\infty} + \frac{\sigma_b^{-1/2}JY_b}{Y_b+G\sigma_b^{3/2}(1-Y_b)} \tag{2.42}$$

where $J=1$ or $J=(Eu_\infty)^{-1}$ for an injected diatomic or monatomic gas, respectively. The Eucken correction Eu is approximated[15] by $Eu_{a,\infty}= 0.115 + 0.354\,\bar{c}_{p_{a,\infty}}$. With the specific heat of air assumed constant, $Eu_a=Eu_\infty$; otherwise c_{p_a} is the specific heat of air evaluated at the local temperature.

If the pressure is proportional to a power of x, the equations have self-similar solutions and can be reduced to ordinary differential equations. The pressure $\bar{p}$ and the similarity variable ζ are

$$\bar{p} = p_1 x^{q-1} + \dots, \qquad \zeta = \frac{\bar{\Psi}}{{p_1}^{1/2} x^{q/2}} \tag{2.43}$$

For strong interaction $q=1/2$, in agreement with Eq. (2.4) for the shock layer and Eq. (2.25) for the blown layer, and $p_1={p_1}^{(s)}$; for weak interaction the pressure is nearly constant, and so $q=1$ and $p_1=p_0$. Now $\bar{u}$, $\bar{T}$, and Y_b are functions only of ζ. The differential equations, Eqs. (2.36)-(2.38), become

$$\frac{1}{2} q\zeta Y_b' = -\frac{1}{Sc}\left(K_D R^{-1} \bar{T}^{\omega-1} \bar{u} Y_b'\right)' \tag{2.44}$$

$$\frac{1}{2} q\zeta \bar{u}' - \frac{q-1}{\gamma_\infty}\frac{R\bar{T}}{\bar{u}} = -\left(K_\mu R^{-1} \bar{T}^{\omega-1} \bar{u}\bar{u}'\right)' \tag{2.45}$$

$$\begin{aligned} \frac{\bar{c}_p}{2\gamma_\infty} q\zeta \bar{T}' + \frac{q-1}{\gamma_\infty} R\bar{T} &= -K_\mu R^{-1} \bar{T}^{\omega-1} \bar{u}\bar{u}'^2 \\ &\quad - \frac{1}{(\gamma_\infty-1)Pr}\left(K_\lambda R^{-1} \bar{T}^{\omega-1} \bar{u}\bar{T}'\right)' - \frac{1}{\gamma_\infty Sc} K_D R^{-1} \bar{T}^{\omega-1} \bar{u}\left(\bar{c}_{p_b} - \bar{c}_{p_\infty}\right) Y_b' \bar{T}' \end{aligned} \tag{2.46}$$

Numerical integration of these equations is carried out for $\zeta_\ell<\zeta<\infty$, where $\zeta_\ell<0$ and $|\zeta_\ell| {p_1}^{1/2} x^{q/2}$ is the (scaled) amount of mass entrained in the part of the shear layer below the zero streamline. The boundary conditions as $\zeta\to\infty$ require that $\bar{u}\to1$, $\bar{T}\to0$, and $Y_b\to0$, and as $\zeta\to\zeta_\ell$ it is required that $\bar{u}\to0$, $\bar{T}\to0$, and $Y_b\to1$; moreover, the asymptotic form as $\zeta\to\zeta_\ell$ is known, and the solutions for $\bar{u}$ and $\bar{T}$ must approach zero in the proper way. The computational scheme is a continuation method in which the value of ζ at the lower boundary is taken to be a small negative number that is gradually increased in magnitude until the correct asymptotic behavior is achieved.[11] Since the numerical scheme in Ref. 11 does not appear to converge for $q=1$, the weak-interaction solutions are found by linear extrapolation from solutions computed for q close to 1 (e. g., $q=0.98$ and 0.99).

The streamline equation is found from Eq. (2.34) as

$$y_\zeta = p_1^{-1/2} x^{1-q/2} R\bar{T}/\bar{u} \tag{2.47}$$

For strong and weak interaction, respectively, the shear-layer thicknesses are

$$\bar{\Delta}^{(s)}(x) = \bar{\Delta}_1^{(s)} x^{3/4} + \ldots, \qquad \bar{\Delta}_1^{(s)} = (p_1^{(s)})^{-1/2}\,\bar{D}^{(s)} \tag{2.48}$$

$$\bar{\Delta}^{(w)}(x) = \bar{\Delta}_1^{(w)} x^{1/2} + \ldots, \qquad \bar{\Delta}_1^{(w)} = p_0^{-1/2}\,\bar{D}^{(w)} \tag{2.49}$$

where $\bar{D}^{(s)}$ and $\bar{D}^{(w)}$ are numbers found by integrating the appropriate solutions for $R\bar{T}/\bar{u}$ from ζ_ℓ to ∞. These integrals exist since $\bar{T} \to 0$ sufficiently rapidly as $\zeta \to \infty$, as can be seen by deriving the asymptotic form for $\bar{T}$. For strong interaction $\alpha\bar{\Delta}^{(s)}(x) = O(\alpha x^{3/4})$, and the shear-layer thickness remains small in comparison with x when $x \gg \alpha^4$; i. e., as anticipated, the boundary-layer approximation fails in the merged-layer régime $x = O(\alpha^4)$.

The analysis may be extended to include real-gas effects which occur at high temperatures. For air, the specific heats begin to vary when $T \gtrsim 600$ K, and O_2 begins to dissociate when $T \gtrsim 2000$-2500 K, for $p \sim 0.01$-1 atm. Self-similar solutions may still be computed when the gas is chemically reactive provided the pressure is nearly constant, as in the weak-interaction region, and chemical equilibrium will be closely approached sufficiently far downstream.

To provide a measure of the extent by which the ideal-gas results will change, the analysis of the weak-interaction region is repeated for the case of air injection, with air treated as a real gas in chemical equilibrium. Following Hansen's analysis,[16] it is assumed that, for a given pressure, the peak temperature remains low enough that, to a good approximation, only the dissociation of oxygen occurs. (For pressures of the order of 0.1 atm, this assumption limits the temperature to values below approximately 4000 K; the limit increases with increasing pressure.) Air is then composed of N_2, O_2, and O, with the mass fraction of O given by $Y_O = 2(16/29)\varepsilon$, where 16/29 is the approximate ratio of the molecular mass of O to that of undissociated air. The fraction ε of molecules which dissociate into oxygen atoms may be written[16]

$$\varepsilon = \{-0.8 + [0.64 + 0.8(1+4p/K_p^2)]^{1/2}\} \,/\, (1+4p/K_p^2) \tag{2.50}$$

The equilibrium constant K_p for $\frac{1}{2}O_2 \rightleftarrows O$ is given to within 4% of the values listed in Ref. 17 over the temperature range 1500-4000 K (with K_p^2 and p expressed in atmospheres) by

$$K_p = 40.68\,T^{1/2} \exp\{-29685/T\} \tag{2.51}$$

where T is expressed in degrees Kelvin; the quantity 29685 is, in degrees Kelvin, the formation enthalpy of O at absolute zero divided by the universal gas constant. With $R=1+\varepsilon$, the equation of state remains as written in Eq. (2.35),[16] and the scaled enthalpy $\bar{h}$ is approximately related to the temperature by

$$\bar{h} = \bar{T}\left(1 + \frac{2}{7}\,\frac{3390/T}{\exp(3390/T) - 1} + \frac{4}{7}\varepsilon\,\frac{29685}{T}\right) \qquad (2.52)$$

where the sensible enthalpy of O_2 has been equated with that of N_2, and sensible enthalpies in the term proportional to ε have been neglected in comparison with the formation enthalpy of O. Since only air injection is considered, the species conservation equation (2.44) may be dropped. If dissociated air is approximated as a binary mixture of "air molecules" and O atoms in evaluating the viscous fluxes, then treatment of the transport properties as before leaves the momentum equation (with $q = 1$) unchanged, and the energy equation may be written more conveniently in the form

$$-\frac{1}{2}\zeta\bar{h}' = (\gamma_\infty - 1)\,K_\mu \bar{T}^{\omega-1} R^{-1} \bar{u}\bar{u}'^2 + \frac{1}{Pr}\{(K_\lambda + K_{\lambda D})\bar{T}^{\omega-1} R^{-1} \bar{u}\bar{T}'\}' \qquad (2.53)$$

The proportionality factor $K_{\lambda D}$ for energy transfer by mass diffusion is given by

$$K_{\lambda D} = \frac{\gamma_\infty - 1}{\gamma_\infty}\,\frac{Pr}{Sc}\,K_D\,\frac{29685}{T}\left(\frac{2\,(1/2 + 29685/T)}{1/\varepsilon + 0.5/(0.2-\varepsilon) - 0.5/(1+\varepsilon)}\right) \qquad (2.54)$$

where sensible enthalpies have been neglected, and the term in brackets (similar to Hansen's[16] Eq. (43a)) is proportional to $T\partial Y_O/\partial T$. The quantity K_μ is taken to be unity (considering the current level of approximation), and K_λ, K_D are given by Eqs. (2.40), (2.42), respectively, with $\sigma_b=16/29$, $Y_b=Y_O$, and $J=1$; the Eucken correction Eu_a for "air molecules" is evaluated with $\bar{c}_{p_a} = 7/2 + \{3390/(2T)\}/\sinh^2\{3390/(2T)\}$, the nondimensional specific heat of N_2.[16] The boundary conditions remain the same as before, and Eqs. (2.45), (2.53) are solved following the same numerical procedure as described above; the pressure-gradient term, $-\{(\gamma_\infty-1)/\gamma_\infty\}(q-1)R\bar{T}$, is added to the left hand side of Eq. (2.53) for computational purposes, with q approaching 1. Unlike the ideal-gas case, the free-stream conditions and wedge angle must be specified before computing a solution since real-gas behavior is explicitly dependent on dimensional temperature and pressure.

Results

The location of a streamline in the shock layer can be expressed by writing the integral of the streamline equation in three parts:

$$y = \rho_\infty u_\infty \int_{\psi_w}^{\alpha^2\bar{\psi}_\ell} \frac{d\psi}{\rho u} + \rho_\infty u_\infty \int_{\alpha^2\bar{\psi}_\ell}^{\alpha^2\bar{\psi}_u} \frac{d\psi}{\rho u} + \rho_\infty u_\infty \int_{\alpha^2\bar{\psi}_u}^{\psi} \frac{d\psi}{\rho u} \qquad (3.1)$$

where u becomes small as $\bar{\psi}$ decreases toward $\bar{\psi}_\ell$; $\psi_w=O(M_\infty\alpha^2)$ is the value of ψ at the wall; and $\bar{\psi}_u$ is still arbitrary. Then

$$y = \int_{\tilde{\psi}_w}^{b\bar{\psi}_\ell/M_\infty} \frac{d\tilde{\psi}}{\tilde{\rho}\tilde{u}} + \int_{\bar{\psi}_\ell}^{\bar{\psi}_u} \frac{d\bar{\psi}}{\bar{\rho}\bar{u}} + \int_{\alpha^2\bar{\psi}_u}^{\hat{\psi}} \frac{d\hat{\psi}}{\hat{\rho}\hat{u}} \qquad (3.2)$$

where $b=(\sigma_b\gamma_b/\gamma_\infty)^{-1/2}$. For $\alpha<<1$ and $\bar{\psi}_u>>1$ such that $\alpha^2\bar{\psi}_u<<1$, the first integral approaches $\tilde{\Delta}(x)$ as defined by Eq. (2.23); the second integral approaches a finite value $\bar{\Delta}(x)$ since $\bar{\rho}\to\infty$ rapidly enough as $\bar{\psi}\to\infty$; and the third integral approaches zero if also $\hat{\psi}\to 0$. Then the left-hand side approaches the equivalent body shape $y=\Delta(x)$, and so Eq. (3.2) approaches the first of Eqs. (2.3). For strong and weak interaction respectively, the coefficients in the equivalent body shapes defined by Eqs. (2.4) and (2.9) include contributions from both the thin layer of blown gas and the viscous free shear layer:

$$\Delta_1^{(s)} = \tilde{\Delta}_1^{(s)} + \bar{\Delta}_1^{(s)}, \qquad \Delta_1^{(w)} = \tilde{\Delta}_1^{(w)} + \bar{\Delta}_1^{(w)} \qquad (3.3)$$

The pressures are found in terms of these quantities from Eqs. (2.5), (2.27), and (2.48) for strong interaction, and from Eqs. (2.14), (2.28), and (2.49) for weak interaction. As indicated by the notation, the pressures in the blown-gas layer and the viscous layer are equal to the pressure in the outer inviscid flow evaluated at $y=\Delta(x)$ if $x<<1$ and at $y=0$ if $x>>1$.

The constants $\hat{D}^{(s)}$ and $\hat{D}^{(w)}$ introduced in Eqs. (2.5) and (2.14) are given in Table 1 for $\gamma_\infty=1.4$ and, in the case of $\hat{D}^{(w)}$, for $n=1/2$ ($\tilde{T}_w$=constant) or $n=2/3$ ($\tilde{\rho}_w$=constant) and a representative value $M_\infty\alpha=1$. The constants $\tilde{D}^{(s)}$ and $\tilde{D}^{(w)}$ defined for the blown-gas layer in Eqs. (2.27) and (2.28) are functions only of γ_b; the values for $\gamma_b=7/5$ and $\gamma_b=5/3$ found from the solutions in Eqs. (2.30) and (2.32) are shown in Table 2. Some ideal-gas results for the viscous shear layer are listed in Table 3 for injected gases having a wide range of molecular weights. The constants $\bar{D}^{(s)}$ and $\bar{D}^{(w)}$ defined in Eqs. (2.48) and (2.49) are shown, along with the lower limit ζ_ℓ for the similarity variable in both the strong- and weak-interaction solutions. The scaled maximum temperature $\bar{T}_{max}$ is seen to be a small number in each case; to find the actual maximum temperature in the shear layer, the value of $\bar{T}_{max}$ is to be multiplied by $M_\infty{}^2 T_\infty$. For example, with air injection the maximum in the strong-interaction region is about $0.03 M_\infty{}^2 T_\infty$, implying that significant levels of O_2 dissociation (which, as noted earlier, begin when the local temperature is about 2000-2500 K for $p \gtrsim 0.01$-1 atm) will not occur until $M_\infty \gtrsim 15$-17 if $T_\infty \approx 300$ K; for helium injection, cooling of the viscous layer increases this Mach number to $M_\infty \gtrsim 26$-29. The ideal-gas results are understood to be applicable when the Mach number is low enough (or the shear layer thin enough) that dissociation effects are not appreciable. A comparison between the ideal- and real-gas results for the shear layer is presented in Table 4 for the case of air injection on a 6-degree wedge at an altitude of 30 km with $M_\infty = 15$ or 20. It may be seen that the real-gas analysis yields values for the maximum temperature T_{max} that are lower than the ideal-gas values, as would be expected; the values of $\bar{D}^{(w)}$, which is proportional to the layer thickness, are likewise reduced. For the conditions considered, however, real-gas effects do not greatly alter the values of $\bar{D}^{(w)}$ and ζ_ℓ; for example, there is only a 5% decrease in $\bar{D}^{(w)}$ when $M_\infty = 20$. The differences would of course be greater if higher Mach numbers and temperatures had been considered.

If the density of the gas at the wall is constant, the pressures are found, using the definitions of M_w and $\tilde{m}_{avg}$, in an explicit form equivalent to the results of Ref. 10:

$$p_1{}^{(s)} = \frac{\bar{D}^{(s)}}{\hat{D}^{(s)}} + \frac{\tilde{D}^{(s)}}{\hat{D}^{(s)}} \frac{1}{2\tilde{\rho}_w{}^{1/2}} \tilde{m}_{avg} \left(\frac{L}{X_T}\right)^{1/2} \tag{3.4}$$

$$p_1{}^{(w)} = \left(\frac{\tilde{D}^{(w)}}{2\hat{D}^{(w)}} \tilde{m}_{avg}\right)^{2/3} \frac{1}{\tilde{\rho}_w{}^{1/3}} \left(\frac{L}{X_T}\right)^{1/3} \tag{3.5}$$

In this case the viscous shear layer for $x \gg 1$ has thickness $O(x^{1/2})$ that is of higher order than the blown-layer thickness, which is $O(x^{2/3})$, and so the shear layer does not affect the first approximation for the pressure. If instead the temperature of the gas at the wall is constant, the thicknesses of the viscous and blown layers are of the same order of magnitude for weak interaction as well as for strong interaction. Now the pressures are obtained from solution of the cubic equation

$$(P^{1/2})^3 - 3(P^{1/2}) - 2Q = 0 \tag{3.6}$$

where P and Q are defined for strong interaction by

$$p_1{}^{(s)} = \frac{1}{3}\frac{\bar{D}^{(s)}}{\hat{D}^{(s)}}P, \qquad \frac{\tilde{D}^{(s)}}{\hat{D}^{(s)}}\frac{\tilde{T}_w{}^{1/2}}{4}\left(\frac{L}{X_r}\right)^{3/4}\tilde{m}_{avg} = 2\left(\frac{\bar{D}^{(s)}}{3\hat{D}^{(s)}}\right)^{3/2}Q \quad . \tag{3.7}$$

and for weak interaction by

$$p_1{}^{(w)} = \frac{1}{3p_0{}^{1/2}}\frac{\bar{D}^{(w)}}{\hat{D}^{(w)}}P, \qquad \frac{\tilde{D}^{(w)}}{p_0{}^{1/2}\hat{D}^{(w)}}\frac{\tilde{T}_w{}^{1/2}}{4}\left(\frac{L}{X_r}\right)^{3/4}\tilde{m}_{avg} = 2\left(\frac{\bar{D}^{(w)}}{3p_0{}^{1/2}\hat{D}^{(w)}}\right)^{3/2}Q \tag{3.8}$$

The relevant root of the cubic equation is found from

$$Q \le 1: \qquad P^{1/2} = 2\cos\phi, \qquad \cos 3\phi = Q, \qquad 0 \le \phi \le \pi/2 \tag{3.9}$$

$$Q \ge 1: \qquad P^{1/2} = 2\cosh\chi, \qquad \cosh 3\chi = Q \tag{3.10}$$

It is seen that P=3 when Q=0 and that P increases monotonically as Q increases. For Q sufficiently large ($\ge$16 for less than 10% fractional error), $P \approx (2Q)^{2/3}$. This may be regarded as an inviscid-flow limit, since Q is proportional to $(L/X_r)^{3/4}\tilde{m}_{avg}$ and L/X_r is proportional to the Reynolds number $Re = u_\infty L/\nu_\infty$; thus, for fixed values of the other parameters, large Q implies that Re and/or the blowing rate $\tilde{m}_{avg}$ are large, and that the viscous-layer thickness may therefore be neglected.

The pressures for x>>1 and x<<1 have the forms given by Eqs. (2.25) and (2.26) respectively. Because of self-similarity, these require solving only ordinary differential equations, whereas a solution for x=O(1) would be much more difficult to obtain and is not attempted here. Instead, since the numerical values of $p_1{}^{(s)}$ and $p_1{}^{(w)}$ are not greatly different, interpolation between the strong- and weak-interaction results would be expected to provide an approximate representation that is fairly accurate. The interpolation formula chosen is

$$\tilde{p} - p_0 = r(x)p_1{}^{(s)}x^{-1/2} + \{1 - r(x)\}p_1{}^{(w)}x^{n-1} \tag{3.11}$$

$$r(x) = \frac{1}{\cosh(Ax^{1/2})}, \qquad A = \cosh^{-1}2 \tag{3.12}$$

For x<<1, $r(x) \approx 1$ and Eq. (2.25) for strong interaction is recovered; for x>>1, $r(x) \approx 0$ and Eq. (2.26) for weak interaction is recovered; and A is defined such that r(x)=1/2 when x=1. (The definition of r(x) differs slightly from that in Ref. 10.) The interpolated pressure is shown by the solid curves in Fig. 3 for air injection at three different blowing rates with T_w=constant. The differences from the asymptotic solutions derived for x>>1 and x<<1 are seen to remain small, even if the asymptotic solutions are used (incorrectly) at x=1.

The increase ΔF in the (dimensional) normal force above the inviscid-flow value is found by integration of Eq. (3.11):

$$\frac{\Delta F}{(M_\infty \alpha)^2 p_\infty L} = 2\frac{X_r}{L}\left\{p_1^{(s)} I_{1/2} + p_1^{(w)}\left[\frac{1}{2n}\left(\frac{L}{X_r}\right)^n - I_n\right]\right\} + \ldots \tag{3.13}$$

$$I_{1/2} = \frac{1}{A}\tan^{-1}\{\sinh(A(L/X_r)^{1/2})\} \tag{3.14}$$

$$I_n = \int_0^{(L/X_r)^{1/2}} s^{2n-1}\,\mathrm{sech}(As)\,ds \tag{3.15}$$

where n=2/3 if $\tilde{p}_w$ is constant and n=1/2 if $\tilde{T}_w$ is constant.

When the blowing rate is sufficiently large, for given values of the other parameters, the viscous-layer thickness is small relative to the total displacement thickness and can be neglected in a first approximation. The displacement effect is then caused entirely by the layer of blown gas, and is described by the inviscid-flow model of Cole and Aroesty.[8] The approach to this limiting case is illustrated in Fig. 4a, where the scaled total displacement thickness $\Delta_1^{(s)}$, scaled blown-layer thickness $\tilde{\Delta}_1^{(s)}$, and the ratio of viscous-layer to total displacement thickness $\bar{\Delta}_1^{(s)}/\Delta_1^{(s)}$ are plotted against the scaled blowing rate $\tilde{m}_{avg}(L/X_r)^{3/4}\tilde{T}_w^{1/2}$ for air injection at constant wall temperature. As the blowing rate increases, it is seen that $\bar{\Delta}_1^{(s)}/\Delta_1^{(s)}$ decreases, falling to less than 10% for $\tilde{m}_{avg}(L/X_r)^{3/4}\tilde{T}_w^{1/2} \gtrsim 7.2$. The domain of parameter values for which the flow is nearly inviscid may be defined arbitrarily as that for which the force change ΔF_{inv} computed neglecting the shear layer underestimates ΔF by less than, say, 10%, where again the force change is measured relative to the force on a thin wedge in inviscid flow. This arbitrary choice is illustrated in Fig. 4b by plots of $\log(\tilde{m}_{avg}\tilde{T}_w^{1/2})$ versus $\log(L/X_r)$ for $\Delta F_{inv}=0.9\Delta F$, with $M_\infty \alpha=1$.

It should also be noted in Fig. 4a that the solutions do not remain valid if $\tilde{m}_{avg}(L/X_r)^{3/4}\tilde{T}_w^{1/2}$ is taken to be too small. It is assumed in the present theory that the blowing rate is large enough to generate an inviscid blown layer with a thickness at least of the same order of magnitude as that of the viscous free shear layer, a condition that is not met if $\tilde{m}_{avg}(L/X_r)^{3/4}\tilde{T}_w^{1/2} \rightarrow 0$. (A somewhat weaker assumption can be shown to suffice, namely that the amount of injected mass is large in comparison with the mass in the viscous layer.) In Fig. 4b the dashed curves, for both strong and weak interaction, indicate the case where the thicknesses of the viscous layer and the blown layer are exactly the same, to give a qualitative sense of the range in which the theory is applicable. For the results presented below, the blowing rate has been chosen arbitrarily to be large enough that $\tilde{\Delta}^{(s)} \gtrsim \bar{\Delta}^{(s)}$; for air injection this implies $\tilde{m}_{avg}(L/X_r)^{3/4}\tilde{T}_w^{1/2} \gtrsim 0.34$.

In Fig. 5, the scaled change in force $\Delta F(L/X_r)^{1/2}/(M_\infty^2 \alpha^2 p_\infty L)$ is plotted versus the scaled total mass-flow rate $\dot{m}(T_w/T_\infty)^{1/2}(L/X_r)^{3/4}/(M_\infty \alpha^3 \rho_\infty u_\infty L)$ for various cases, all with constant wall temperature. Two limiting cases are shown for air as the injectant. For $L/X_r \rightarrow 0$, the strong-interaction limit, the viscous-layer thickness is so large compared to the wedge thickness that the magnitude of $M_\infty \alpha$ is irrelevant, and the force change depends on $p_1^{(s)}$. For $L/X_r \rightarrow \infty$ and either $M_\infty \alpha \rightarrow 0$ or $M_\infty \alpha \rightarrow \infty$, the force change depends on $p_1^{(w)}$; the larger force change is found for $M_\infty \alpha \rightarrow \infty$ and the smaller for $M_\infty \alpha \rightarrow 0$, as might be expected since for $M_\infty \alpha \rightarrow 0$ the wedge thickness tends to zero in comparison with the total thickness of the region of disturbed flow between the wedge surface and the shock wave.

Also shown in Fig. 5 is a comparison between air and helium as injectants, for $L/X_r=1$ and $M_\infty \alpha=1$, again for $\tilde{T}_w$=constant. As in the inviscid-flow case considered by Cole and Aroesty,[8] it is seen that strong blowing of a gas lighter than air, in this case helium, yields higher induced surface pressures and thus larger force changes for a fixed mass flow than when air (or a gas heavier than air) is the injectant. Interestingly, this trend appears to become reversed when the strength of the blowing decreases. Introduction of a light gas increases the specific heat for the mixture and thus cools the viscous layer, as indicated by the maximum temperatures listed in Table 3. The average density is therefore increased and the transport coefficients are decreased. As a result the thickness of the viscous layer is reduced and thus the force changes are also reduced. The curves for air and helium in Fig. 5 would therefore be expected to cross if they were extended to smaller values of mass flow.

To establish numerical orders of magnitude for the change in force and the associated mass-flow rate of the injected gas, dimensional values of ΔF and $\dot{m}$ for T_w=constant have been computed for a range of parameter values and for various injectants, using the properties of the standard atmosphere. The solutions depend on several parameters which may be divided conveniently into three groups. Parameters related to flight régime are M_∞ and altitude z; those characterizing wedge geometry are α and L; and those representing properties of the injected mass are $\dot{m}$, T_w, σ_b, and γ_b. (The solutions also depend on ω, the exponent in the viscosity law, taken here as 3/4.) Air injection on a wedge having length L=3 m and half-angle α=6 deg, for M_∞=15 and z=30 km, is selected as a baseline case and is indicated by the solid line in each part of Fig. 6, where M_∞ and z (Fig. 6a), α and L (Fig. 6b), and injectant type (Fig. 6c) have been varied. Note that large changes in force per unit span of order 1000 N/m (68.5 lb/ft) are achieved with seemingly moderate injection rates per unit span of order 0.1 kg/m-sec (0.067 lbm/ft-sec).

In. Fig. 6a, it is seen that, for given injectant rates, the force changes increase with flight Mach number at a given altitude and decrease with increasing altitude at a given flight Mach number, as expected. Also presented is a comparison between the ideal-gas and real-gas results for Mach 15 and 20, where differences between the solutions are seen to be small. (Since the real-gas analysis was for weak interaction only, the real-gas curves were computed using the ideal-gas results for the strong-interaction region, which extends over a negligibly small portion of the wedge for the conditions considered.) As shown in Fig. 6b, at a given flight Mach number and altitude, the force changes increase with wedge angle for a given length and increase with length for a given wedge angle. Finally, in Fig. 6c, it is shown that the force change increases with decreasing molecular weight of the injected gas, at higher injectant mass-flow rates. At lower injection rates the opposite effect occurs and the crossover of the curves anticipated above is seen for argon, air, and neon. It is also observed that the crossover occurs at lower injectant rates as the molecular weight of the injectant decreases. For all the calculations in Fig. 6 the wall temperature T_w is constant.

If a simple isothermal model for the atmosphere is adopted and the weak dependence on γ_b is neglected, then the force change for injection with completely inviscid flow over a wedge with predominantly strong or weak interaction (for $M_\infty\alpha\rightarrow\infty$), and constant wall temperature, may be written in the form

$$\Delta F = \text{const.}\ (M_\infty^{\ 2}\, e^{-z/H}\, L\, \dot{m}^2\, T_w / \sigma_b\,)^{1/3} \tag{3.16}$$

where H is the atmospheric scale height. This simple expression shows the trends indicated in Fig. 6, although not the proper quantitative values. For a fixed mass rate of injected flow it is seen that ΔF increases with increasing $M_\infty^{\ 2}e^{-z/H}$, a factor proportional to free-stream dynamic pressure, and also increases as the wedge length L increases; the dependence on L implies that it would be most efficient to distribute a given amount of blown mass over a large surface area. Increasing the ratio of the injectant temperature T_w to its molecular mass will cause greater displacement of the outer flow and thereby also increase the force change. The dependence on wedge angle α, not present in the above expression, is seen in Fig. 6b to be small for the conditions considered there.

Conclusions

From the results of this analysis, it is concluded that relatively large pressure forces can be achieved with relatively small amounts of gas injected at the surface of a vehicle traveling at hypersonic speeds. Hence it appears that boundary-layer blowing is a possible alternative to the use of moveable surfaces and/or vectored thrust for control of such a vehicle in the atmosphere, and should be investigated further. Although only the very simple case of two-dimensional wedge flow with a power-law distribution of injected mass is considered in this study, the magnitudes of the surface forces found for relatively small mass-flow rates of the blown gas indicate that it is worthwhile to analyze more complex blowing patterns with various injectant gases, in order to obtain desired force distributions, and finally to consider more complex geometries. A numerical code presently under development will be used to accomplish the first of the above extensions to this work.

Acknowledgment

Support for this research was provided in part by the U. S. Army Strategic Defense Command.

References

[1] Carter, N. D., and van Leer, B., "Euler Computations of Hypersonic Flow with Strong Blowing," AIAA Paper 90-0603, Jan. 1990.

[2] Chernyi, G. G., *Introduction to Hypersonic Flow*. Academic Press, 1961.

[3] Stewartson, K., *The Theory of Laminar Boundary Layers in Compressible Fluids*. Oxford University Press, 1964.

[4] Hayes, W. D. and Probstein, R. F., *Hypersonic Flow Theory*. Academic Press, 1959.

[5] Van Dyke, M. D., "A Study of Hypersonic Small-Disturbance Theory," NACA Rept. 1194, 1954 (supersedes TN 3173, 1954).

[6] Li, T.-Y. and Gross, J. F., "Hypersonic Strong Viscous Interaction on a Flat Plate with Surface Mass Transfer," *Proceedings of the 1961 Heat Transfer and Fluid Mechanics Institute*, pp. 146-160.

[7] Kubota, T. and Fernandez, F. L., "Boundary-Layer Flows with Large Injection and Heat Transfer," *AIAA Journal*, Vol. 6, 1968, pp. 22-28.

[8] Cole, J. D. and Aroesty, J., "The Blowhard Problem - Inviscid Flows with Surface Injection," *International Journal of Heat and Mass Transfer*, Vol. 11, 1968, pp. 1167-1183.

[9] Smith, F. T. and Stewartson, K., "On slot injection into a supersonic laminar boundary layer," *Proceedings of the Royal Society of London, Series A*, Vol. 332, 1973, pp. 1-22.

[10] Messiter, A. F. and Matarrese, M. D., "Hypersonic Viscous Interaction with Strong Blowing," to appear in *Journal of Fluid Mechanics*.

[11] Matarrese, M. D. and Messiter, A. F., "A Numerical Method for the Self-Similar Hypersonic Viscous Shear Layer," submitted to *Journal of Computational Physics*.

[12] Hirschfelder, J. O., Curtiss, C. F., and Bird, R. B., *Molecular Theory of Gases and Liquids*. Wiley, 1954.

[13] Anderson, J. D., Jr., *Hypersonic and High Temperature Gas Dynamics*. McGraw-Hill, 1989.

[14] Bird, R. B., Stewart, W. E., and Lightfoot, E. N., *Transport Phenomena*, Wiley, 1960.

[15] Hirschfelder, J. O., "Heat Conductivity in Polyatomic or Electronically Excited Gases. II," *Journal of Chemical Physics*, Vol. 26, 1957, pp. 282-285.

[16] Hansen, C. F., "Approximations for the Thermodynamic and Transport Properties of High-Temperature Air," NASA TR R-50, 1959.

[17] JANAF Thermochemical Tables, 2nd ed., U. S. Standard Reference Data System NSRDS-NBS 37, 1971.

Table 1 Shock-Layer Data

Case	$\hat{D}^{(s)}$	$\hat{D}^{(w)\,a}$
T_w = const.[b]	0.945	0.5675
ρ_w = const.[c]	"	0.4150

[a] Eq. (2.14) with $M_\infty \alpha = 1$, [b] $n=1/2$, [c] $n=2/3$

Table 2 Data for Blown-Gas Layer [a]

γ_b	$\tilde{D}^{(s)\,b}$	$\tilde{D}^{(w)\,c}$
7/5	3.501	3.347
5/3	3.604	3.651

[a] Either T_w or ρ_w const., [b] Eq. (2.30), [c] Eq. (2.32)

Table 3 Shear-Layer Data[a]

Inj.	γ_b	σ_b	Strong Interaction (q = 1/2)			Weak Interaction (q = 1)		
			$\bar{D}^{(s)}$	$-\zeta_\ell$	$\bar{T}_{max}$	$\bar{D}^{(w)}$	$-\zeta_\ell$	$\bar{T}_{max}$
H_2	7/5	0.0690	0.1103	0.9623	0.0047	0.1259	0.6107	0.0079
He	5/3	0.1379	0.1796	1.4262	0.0098	0.2157	0.8101	0.0168
Ne	5/3	0.6897	0.3515	3.2133	0.0258	0.4384	1.6391	0.0437
Air	7/5	1.0000	0.3669	3.8154	0.0280	0.4331	1.9665	0.0447
Ar	5/3	1.3793	0.4604	4.5670	0.0356	0.5896	2.1818	0.0594

[a] $\gamma_\infty = 1.4$, $\omega = 0.75$, $Pr = 0.72$, $Sc = 0.74$

Table 4 Comparison Between Ideal- and Real-Gas Results for Shear Layer[a]

M_∞	Ideal			Real		
	$\bar{D}^{(w)}$	$-\zeta_\ell$	T_{max} [K]	$\bar{D}^{(w)}$	$-\zeta_\ell$	T_{max} [K]
15[b]	0.4331	1.9665	2,326	0.4099	1.9825	2,082
20[c]	"	"	4,135	0.4131	1.9949	3,662

[a] γ_∞=1.4, ω=0.75, Pr=0.72, Sc=0.74, α=6 deg, z=30 km (T_∞=231.2 K, p_∞=0.1174 atm)

[b] $M_\infty{}^2T_\infty$ = 52,020 K, p = 0.07131 atm, [c] $M_\infty{}^2T_\infty$ = 92,480 K, p = 0.10991 atm

Figure Captions

Fig. 1 Qualitative sketch of wedge flow field with weak or strong blowing and weak or strong interaction. (Speckled regions are viscous layers.)

Fig. 2 Qualitative profiles of blown-gas mass fraction Y_b, velocity component u, temperature T, and pressure p.

Fig. 3 Surface pressure $\tilde{p}-p_0$ vs. x for various rates of air injection.

Fig. 4a Strong-interaction solutions for scaled total displacement thickness $\Delta_1^{(s)}$, thickness $\tilde{\Delta}_1^{(s)}$ of blown-gas layer , and the ratio of shear-layer to total displacement thickness $\bar{\Delta}_1^{(s)}/\Delta_1^{(s)}$ vs. blowing-rate parameter $\tilde{m}_{avg}\tilde{T}_w^{1/2}(L/X_r)^{3/4}$ for air injection with constant wall temperature.

Fig. 4b Parameter ranges where flow may be treated as inviscid and where present theory does not apply.

Fig. 5 Scaled force-change $\Delta F(L/X_r)^{1/2}/(M_\infty^2\alpha^2 p_\infty L)$ vs. scaled mass flow-rate $\dot{m}(T_w/T_\infty)^{1/2}(L/X_r)^{3/4}/(M_\infty\alpha^3\rho_\infty u_\infty L)$ for various cases.

Fig. 6a ΔF vs. $\dot{m}$ for various flight regimes.

Fig. 6b ΔF vs. $\dot{m}$ for various wedge geometries.

Fig. 6c ΔF vs. $\dot{m}$ for various injectants.

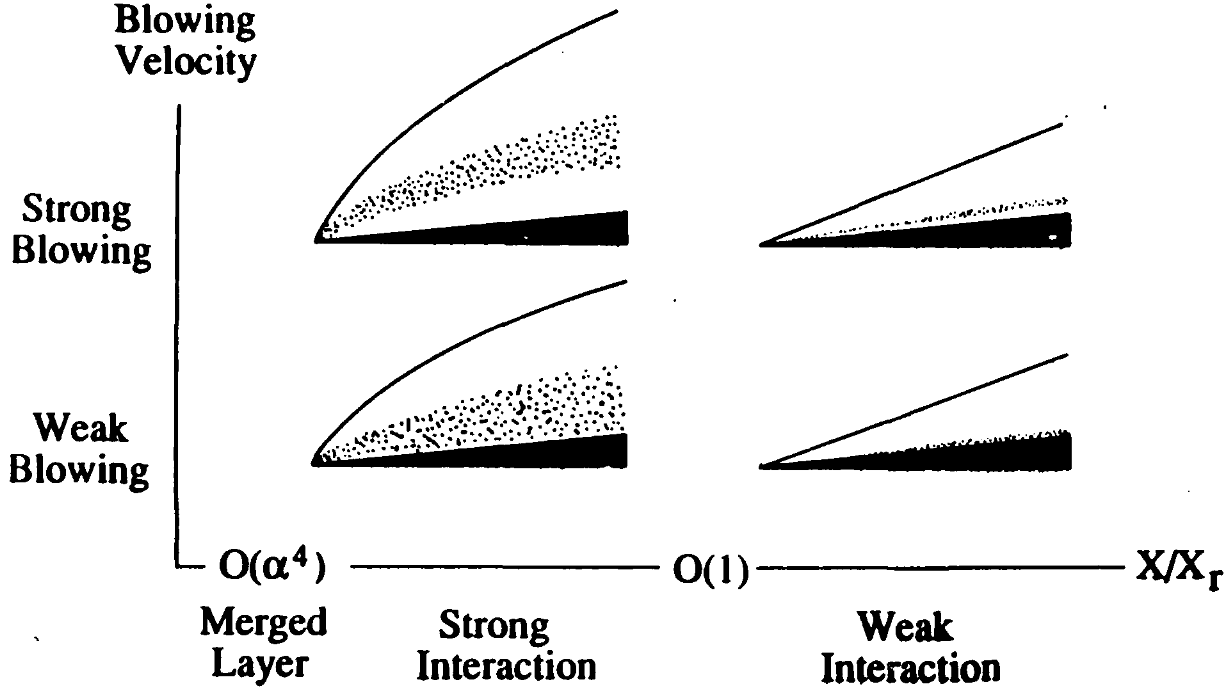
Blowing Velocity
Strong Blowing
Weak Blowing
O(α^4)
O(1)
X/X$_r$
Merged Layer
Strong Interaction
Weak Interaction

Fig. 2

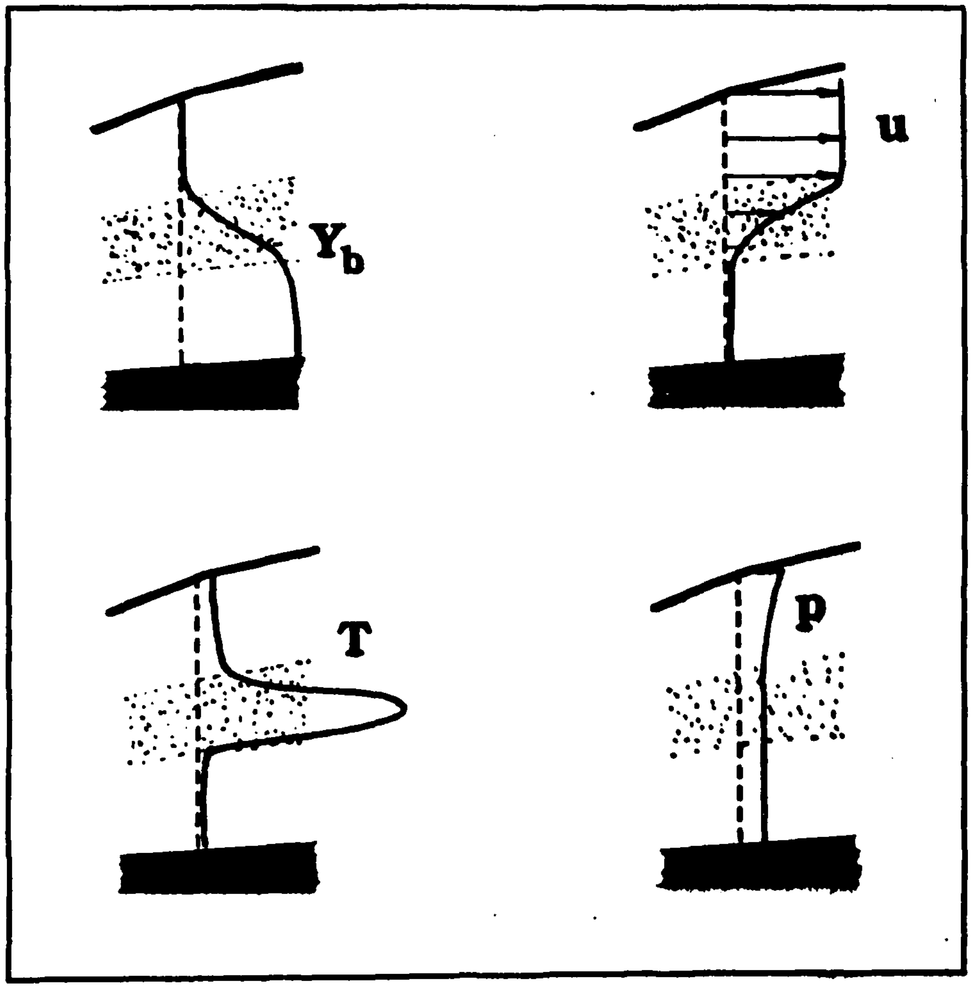

Fig. 2

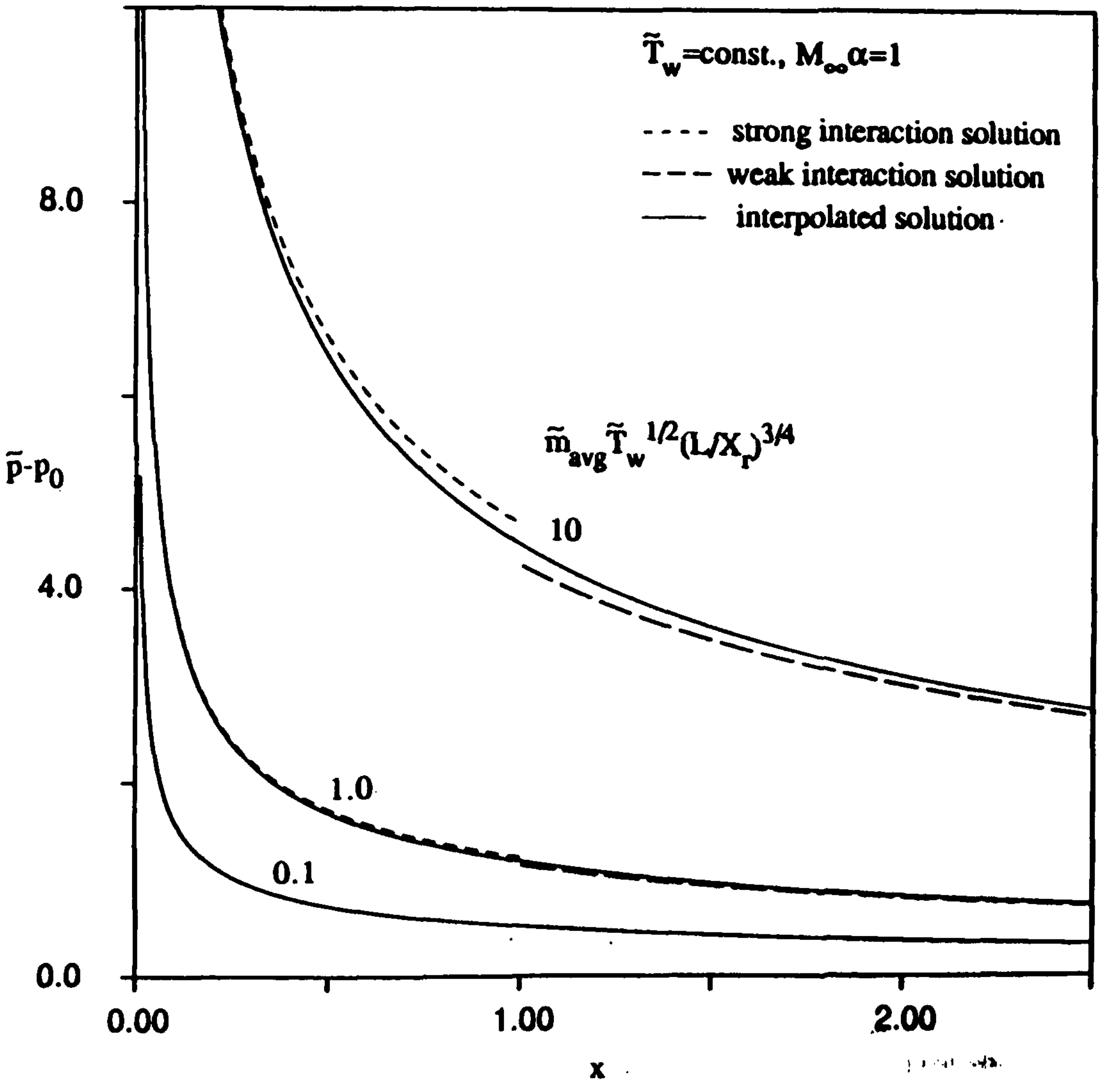
$\tilde{T}_w$=const., $M_\infty\alpha=1$
strong interaction solution
weak interaction solution
interpolated solution
$\tilde{m}_{avg}\tilde{T}_w^{1/2}(L/X_r)^{3/4}$
10
1.0
0.1
8.0
4.0
0.0
$\tilde{p}-p_0$
0.00
1.00
2.00
x

Fig. 3

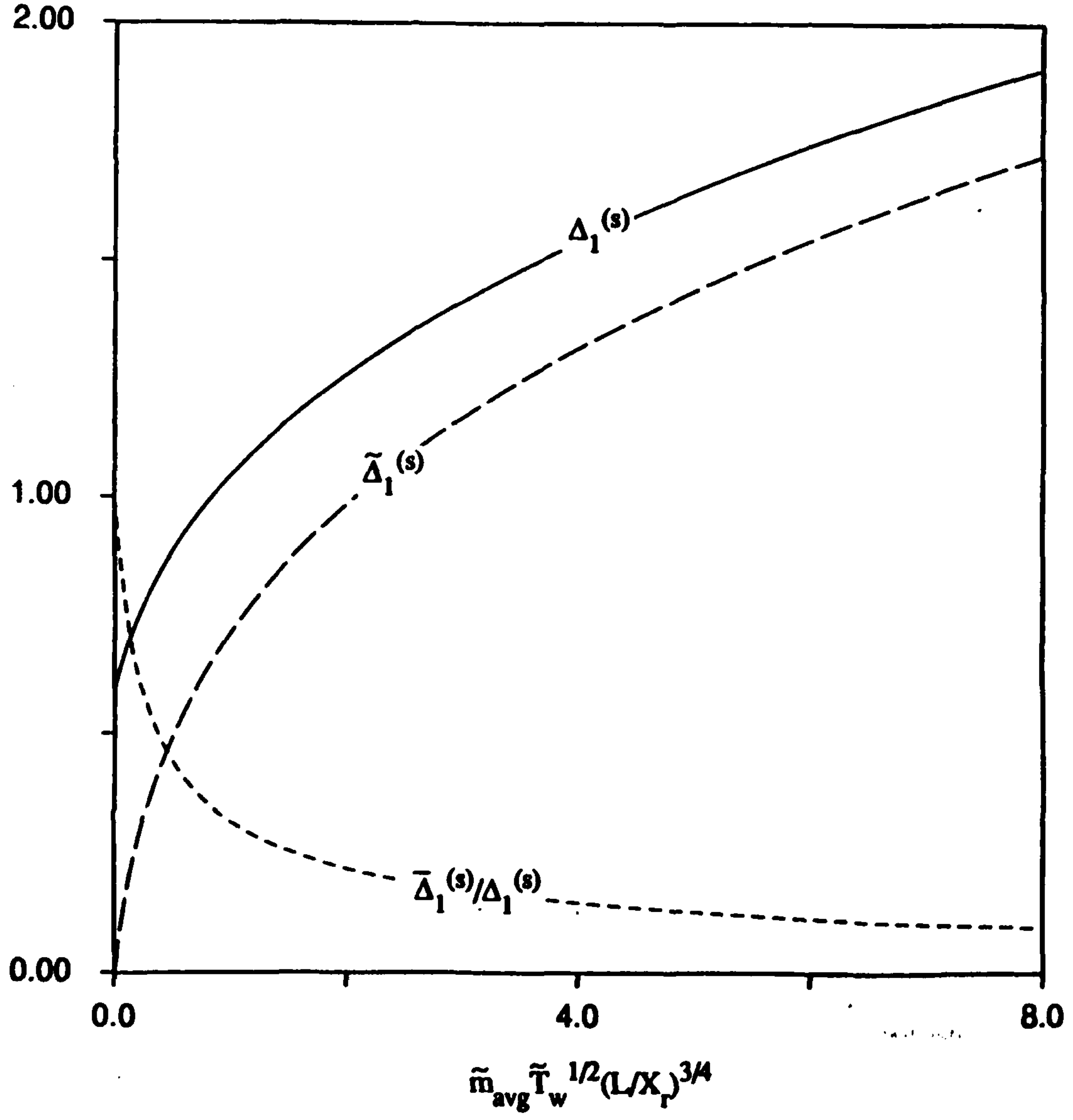
2.00
1.00
0.00
0.0
4.0
8.0
$\tilde{m}_{avg}\tilde{T}_w^{1/2}(L/X_r)^{3/4}$
$\Delta_1^{(s)}$
$\tilde{\Delta}_1^{(s)}$
$\bar{\Delta}_1^{(s)}/\Delta_1^{(s)}$

Fig. 7a

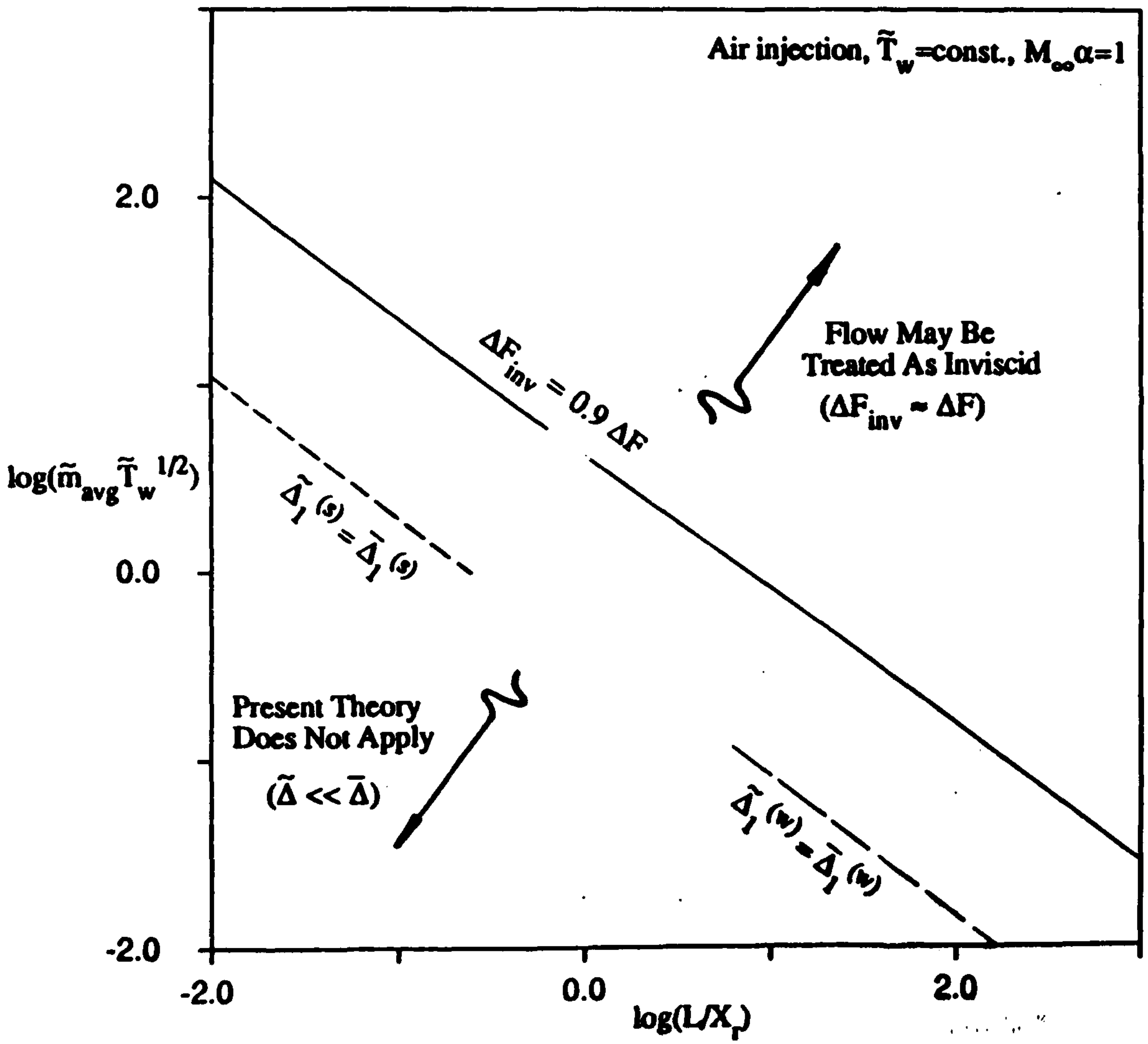
Air injection, $\tilde{T}_w$=const., $M_\infty\alpha$=1
Flow May Be Treated As Inviscid ($\Delta F_{inv} \approx \Delta F$)
$\Delta F_{inv} = 0.9\,\Delta F$
$\tilde{\Delta}_l(s) = \bar{\Delta}_l(s)$
$\tilde{\Delta}_l(w) = \bar{\Delta}_l(w)$
Present Theory Does Not Apply ($\tilde{\Delta} << \bar{\Delta}$)
$\log(\tilde{m}_{avg}\tilde{T}_w^{\;1/2})$
2.0
0.0
-2.0
-2.0
0.0
2.0
$\log(L/X_r)$

Fig. 7b

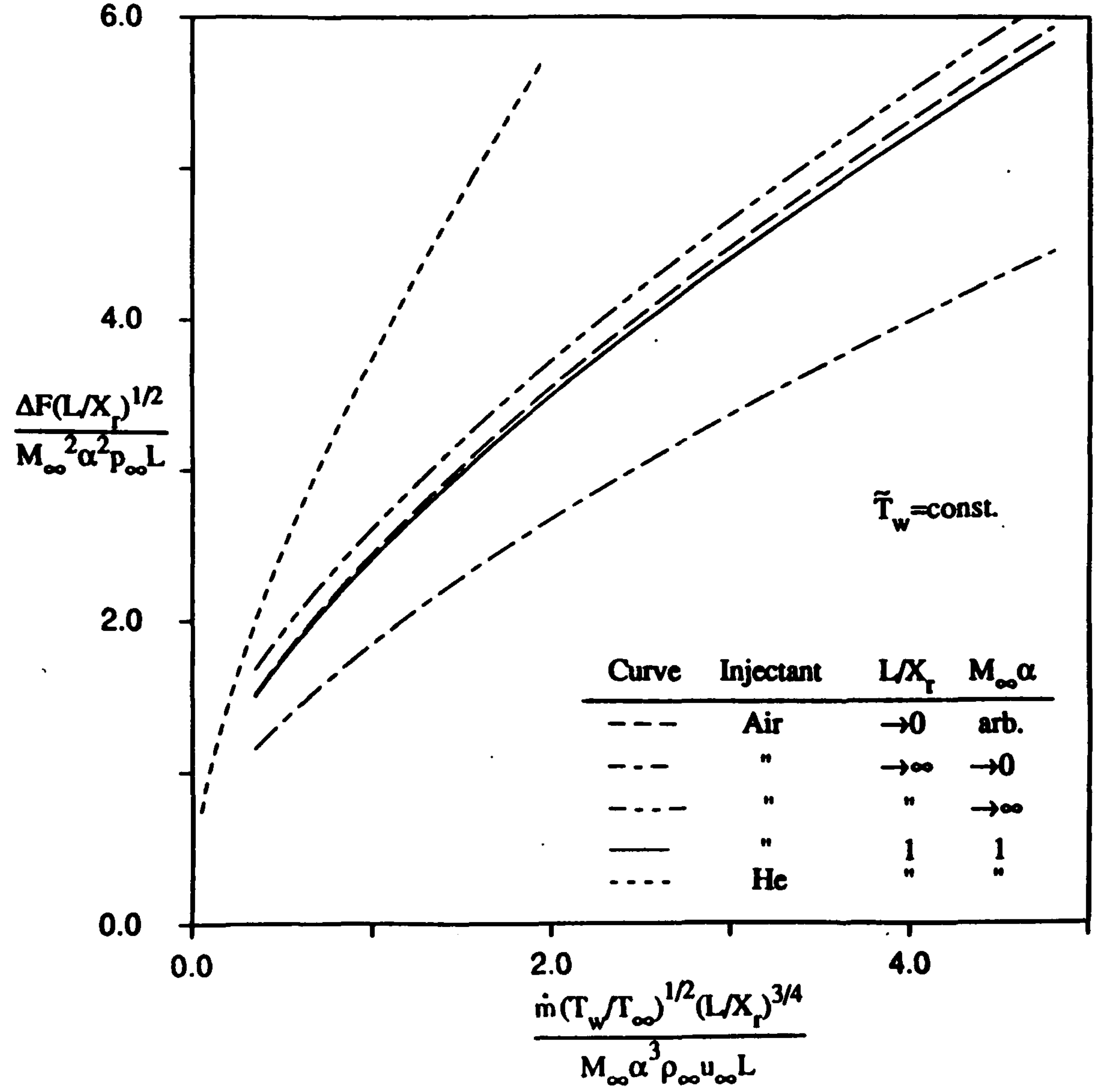

$\frac{\Delta F (L/X_r)^{1/2}}{M_\infty{}^2 \alpha^2 p_\infty L}$
6.0
4.0
2.0
0.0
0.0
2.0
4.0
$\frac{\dot{m} (T_w/T_\infty)^{1/2} (L/X_r)^{3/4}}{M_\infty \alpha^3 \rho_\infty u_\infty L}$
$\tilde{T}_w$=const.
Curve Injectant L/X_r $M_\infty \alpha$
Air →0 arb.
" →∞ →0
" " →∞
" 1 1
He " "

Fig. 5

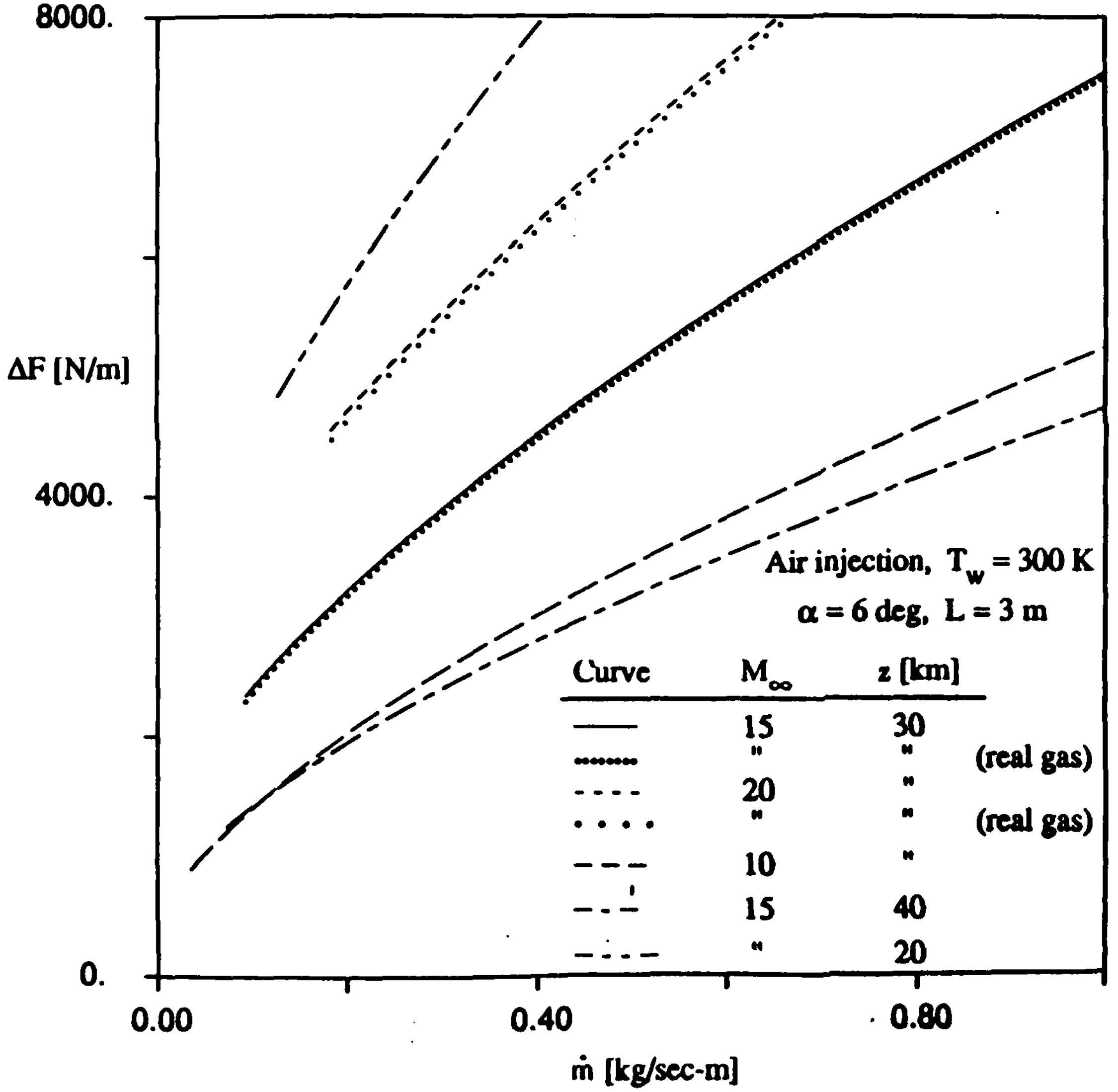
8000.
4000.
0.
ΔF [N/m]
0.00
0.40
0.80
ṁ [kg/sec-m]
Air injection, T_w = 300 K
α = 6 deg, L = 3 m
Curve
M_∞
z [km]
15 30
" " (real gas)
20 "
" " (real gas)
10 "
15 40
" 20

Fig. 6a

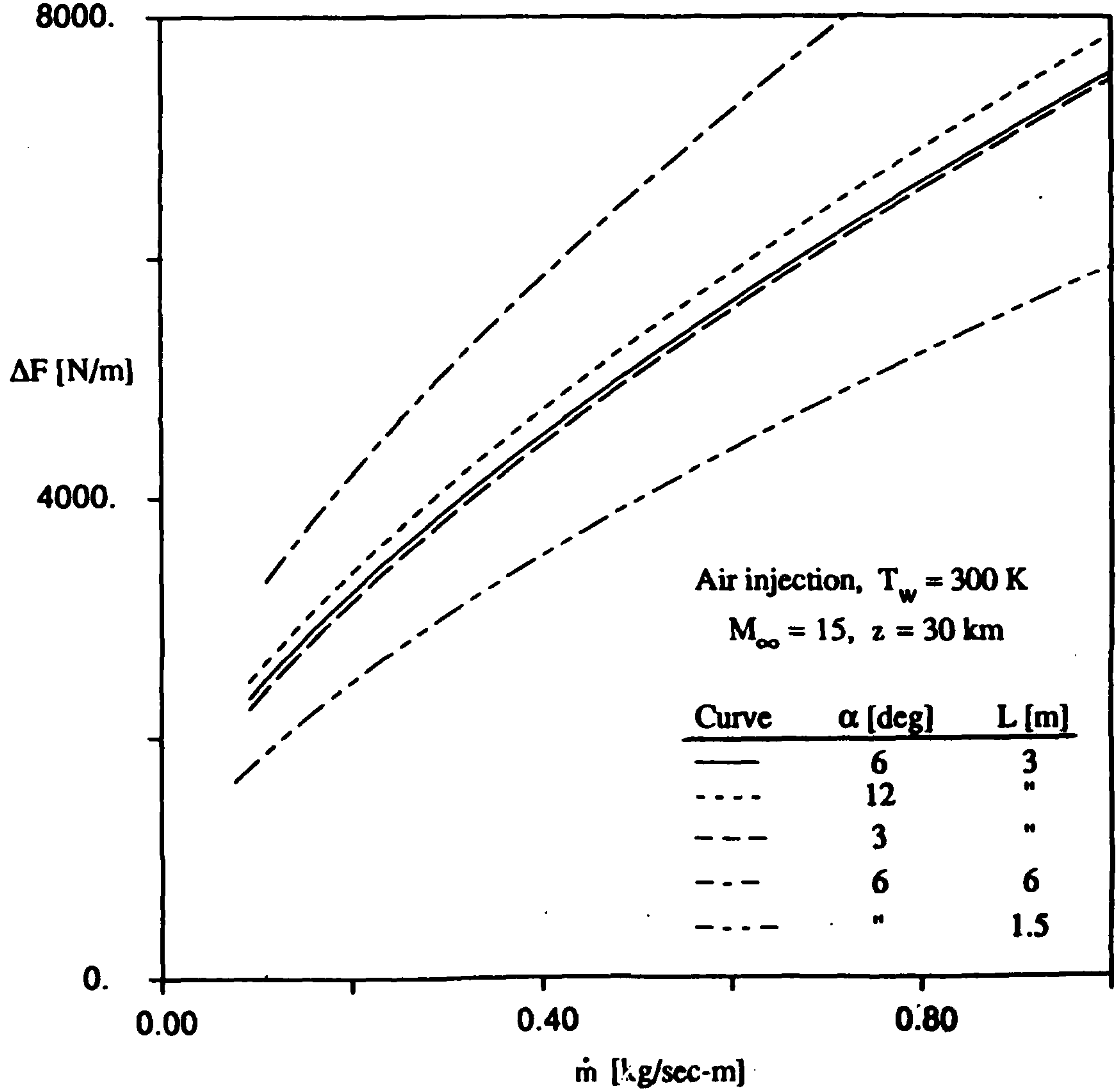
8000.
4000.
0.
ΔF [N/m]
0.00
0.40
0.80
ṁ [kg/sec-m]
Air injection, $T_w = 300$ K
$M_\infty = 15$, $z = 30$ km
Curve α [deg] L [m]
6 3
12 "
3 "
6 6
" 1.5

Fig. 6b

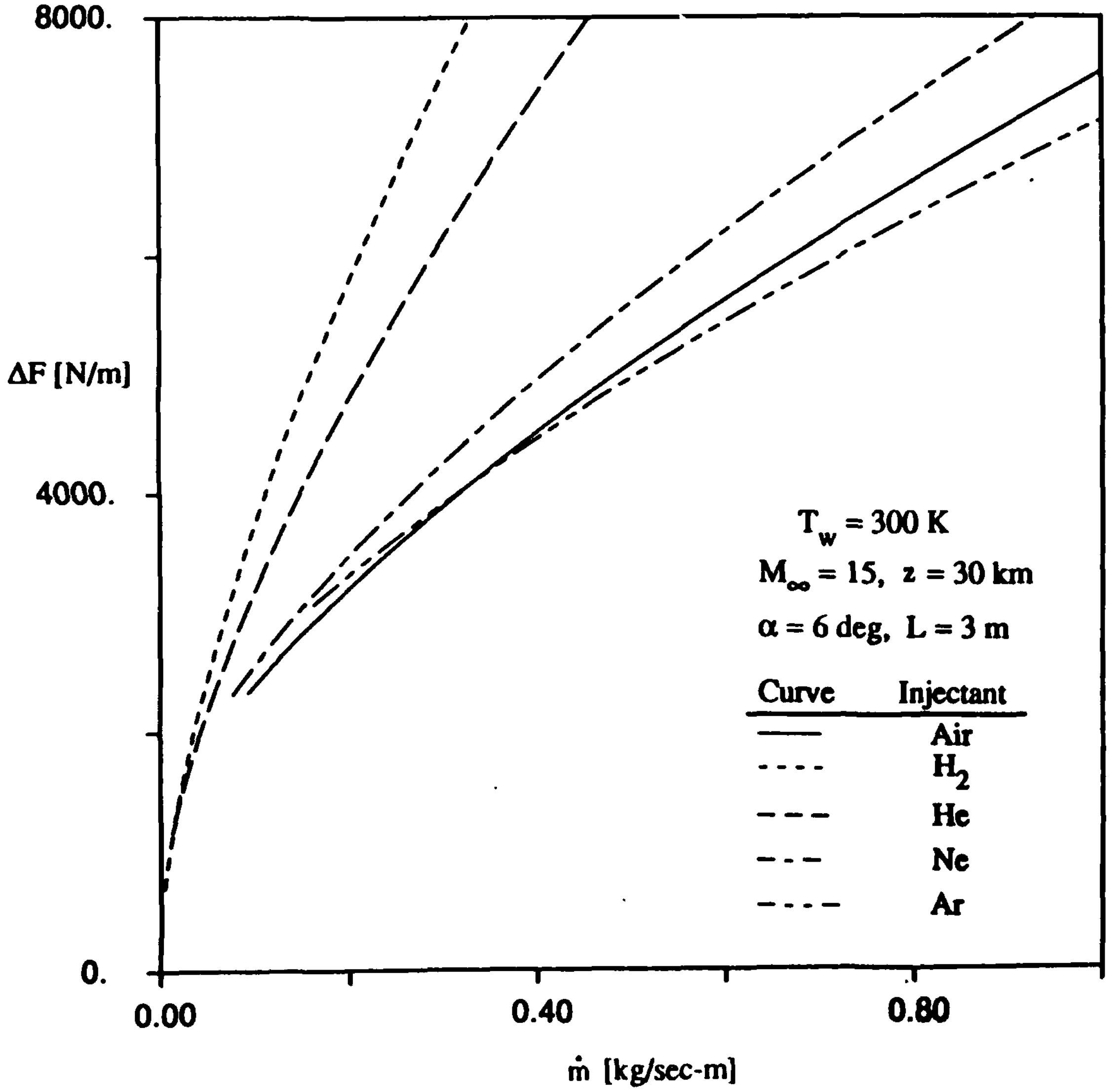
8000.
4000.
0.
ΔF [N/m]
0.00
0.40
0.80
ṁ [kg/sec-m]
$T_w = 300$ K
$M_\infty = 15$, $z = 30$ km
$\alpha = 6$ deg, $L = 3$ m
Curve Injectant
Air
H_2
He
Ne
Ar

Fig. 6c

AIAA-90-0603

Euler Computations of Hypersonic Flow with Strong Blowing

Nelson Carter
Bram van Leer

Department of Aerospace Engineering
The University of Michigan
Ann Arbor, MI

28th Aerospace Sciences Meeting
January 8-11, 1990/Reno, Nevada

For permission to copy or republish, contact the American Institute of Aeronautics and Astronautics
370 L'Enfant Promenade, S.W., Washington, D.C. 20024

Euler Computations of Hypersonic Flow with Strong Blowing

Nelson Carter [*]
Bram van Leer [†]

The University of Michigan
Department of Aerospace Engineering
Ann Arbor, MI 48109-2146

Abstract

A validation study is presented for a numerical code which calculates a two-dimensional steady-state solution for inviscid hypersonic flows in the presence of strong surface blowing. A higher-order Godunov-type finite-volume approach is used to discretize the inviscid Euler equations. Interface values of the state quantities are reconstructed using a monotone interpolation technique suggested by Koren, based on Van Leer's *kappa* scheme. The interface fluxes are computed using Roe's upwind-biased flux-difference splitting technique. The time-differencing algorithms used are a locally implicit, linearized Gauss-Seidel iteration scheme and an explicit multi-stage scheme with optimized short-wave damping. The results of the numerical calculations are compared with analytical solutions obtained for strong blowing along a flat plate and a wedge with an inverse-square-root injection-velocity distribution.

Introduction

The recent revival of interest in hypersonic vehicles has renewed interest in the study of hypersonic flow. One subject of study is the use of surface blowing to influence an external hypersonic flow field. Understanding of the interaction between the injected gas and the high-speed outer flow is critical to applications of blowing in propulsion, surface cooling, and control-force generation. Experiments in hypersonic flows, however, are difficult to perform; thus a heavy reliance on computational predictions has resulted. In the absence of experimental results, the only recourse is to validate the computational codes on the basis of flow cases for which analytical solutions exist. This can help to distinguish between physical and numerical effects in cases where only numerical results are available.

A generic problem is that of hypersonic flow over a flat plate with distributed blowing off the surface. The displacement effect of the blowing causes a shock wave to form ahead of the blowing region. If the blowing is of sufficient strength, the boundary layer is blown off; this is called "strong blowing". It results in a viscous free shear layer separating an essentially inviscid rotational blown layer next to the wall from an inviscid shock layer extending from the shear layer to the shock (Figure 1). For sufficiently high Reynolds numbers, the free shear layer can be assumed to have negligible thickness and be regarded as a slip-stream. This fully inviscid limiting case was considered two decades ago by Cole and Aroesty [1], and by Wallace and Kemp [2]. Recently, Messiter and Matarrese [3] have obtained similarity solutions that take into account the viscous interaction for an inverse-square-root distribution of the injection velocity along a flat plate and along a thin wedge, in two dimensions.

The present paper is a validation study for an Euler code for hypersonic flow with surface blowing developed by the authors. Numerical solutions obtained with a discretization of the Euler equations are compared with analytical solutions for the inviscid strong-blowing case. The numerical method used is a finite-volume technique for finding steady solutions to the two-dimensional Euler equations with boundary conditions consistent with the assumptions made in the analytical work. Comparisons for blowing off a flat plate and a wedge are presented.

Summary of Analytical Work

In the inviscid case to be considered, the flow field over a flat plate or a wedge in the presence of strong blowing can be separated into two different layers:

1. The blown layer next to the wall, made up of the injected gas.
2. The shock layer between the blown layer and the shock, made up of free-stream gas that has passed through the shock.

---

[*] Graduate Research Student, Member AIAA
[†] Professor, Member AIAA

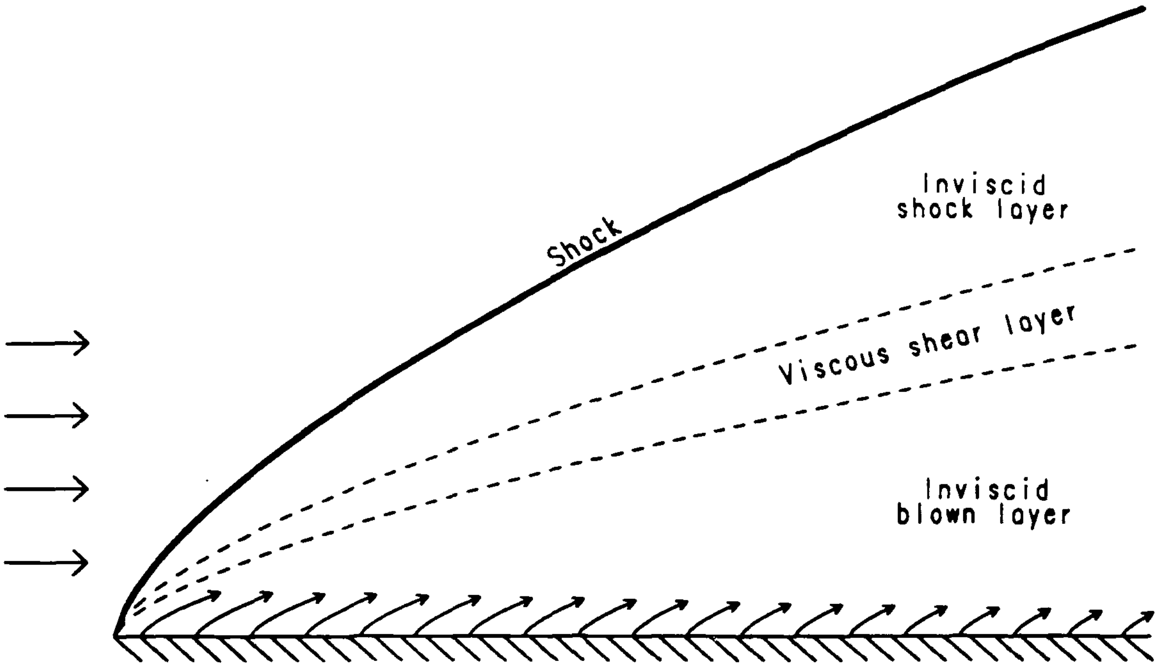
Shock
Inviscid shock layer
Viscous shear layer
Inviscid blown layer

Figure 1: Schematic of the various layers present for strong blowing off a flat plate.

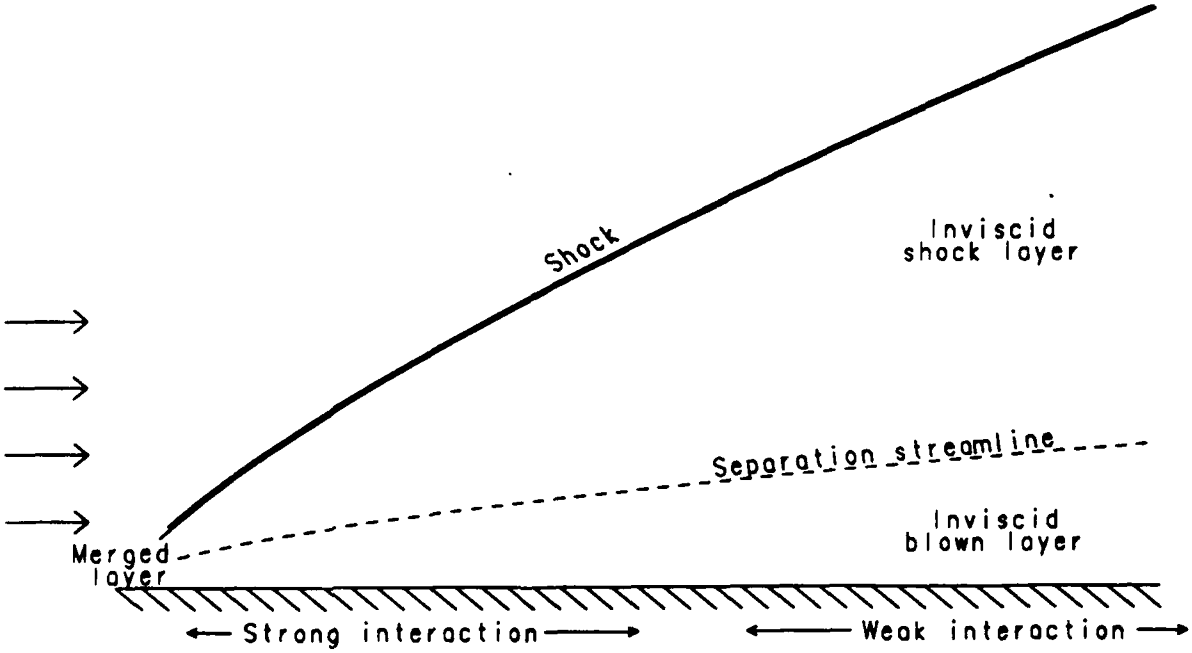
Shock
Inviscid shock layer
Separation streamline
Inviscid blown layer
Merged layer
Strong interaction
Weak interaction

Figure 2: Schematic showing the inviscid case. The inviscid blown layer and the inviscid shock layer meet in a slip-stream along the separation streamline.

The two layers meet in a slip-stream along the separating streamline (Figure 2). Flow in these layers can be characterized by three different regions along the plate or wedge. Far enough downstream, the relative pressure changes are small, and the interaction between the blown layer and the shock is described as weak (weak-interaction region). Further upstream, the curvature of the shock increases, and the relative pressure changes become large; here the interaction between the blown layer and shock is described as strong (strong-interaction region). Still further upstream, the thickness of the shock layer, blown layer, and free shear layer (whose thickness has been considered negligible up to this point) all become of the same order and no real distinction between them can be made. This region is referred to as the merged-layer regime. Similar flow classifications have been defined for viscous hypersonic flow in the absence of blowing and are discussed in books by Hayes and Probstein [4] and by Stewartson [5].

In the strong-interaction region, the flow in the shock layer is described by hypersonic small-disturbance theory. The flow in the blown layer is compressible, and is described by the so-called "inviscid boundary-layer equations". For flow on a flat plate, the results of Cole and Aroesty [1] and Messiter and Matarrese [3] may be used to show that an inverse square-root injection velocity distribution of the form

$$\frac{v_w}{U_\infty} = 0.3022 \frac{\delta^2}{\sqrt{\tilde{\rho}_{1w}}} x^{-\frac{1}{2}},$$

for $\gamma = 1.4$, results in a separating streamline of the shape

$$y_{ss} = \delta x^{\frac{3}{4}};$$

the corresponding pressure distribution along the plate is

$$\frac{p_w}{p_\infty} = 1.119 M_\infty^2 \delta^2 x^{-\frac{1}{2}}.$$

Here $\delta << 1$ is the blown-layer thickness at $x = 1$, and $\tilde{\rho}_{1w}$ is the ratio of the blown-gas density to the free-stream density, assumed to be constant with a magnitude of $O(1)$. The coordinates x and y and thickness δ are non-dimensionalized with respect to the length of the plate. The strong-interaction results are appropriate for regions in which the parameter $M_\infty^2 \delta^2$ is large $(\rightarrow \infty)$.

In the weak-interaction region, pressure changes are small and linearized supersonic flow theory can be applied. The pressure perturbations $\left(\frac{p - p_\infty}{p_\infty}\right)$ are proportional to the local slope of the effective body created by the blown layer (y'_{ss}). The flow inside the blown layer is assumed incompressible. Again, for a flat plate with an inverse square-root blowing distribution of the form

$$\frac{v_w}{U_\infty} = \frac{\delta^{\frac{3}{2}}}{3.464} (M_\infty \tilde{\rho}_{1w})^{-\frac{1}{2}} x^{-\frac{1}{2}},$$

[1] and [3] show that the resulting separating streamline has the form

$$y_{ss} = \delta x^{\frac{2}{3}};$$

the pressure distribution along the plate is

$$\frac{p_w}{p_\infty} = 1 + \frac{2}{3} \gamma M_\infty \delta x^{-\frac{1}{3}}.$$

These results are valid in regions where the parameters y_{ss} and M_∞ are such that

$$y_{ss} << \frac{x}{M_\infty}$$

i.e., the thickness of the blown layer (y_{ss}) is small in comparison with the thickness of the shock layer, so that linearized supersonic flow theory is applicable.

These results have been extended in [1] and [3] to blowing along a slender wedge in hypersonic flow. In the strong- interaction region, the solution is the same as that for a flat plate since the wedge thickness is assumed to be small in comparison with the blown-layer thickness in this region. This requires that $y_{ss} >> x\alpha$, where α is the wedge half-angle.

The solution for the weak-interaction region is different for wedge flow. For the case of an inverse square-root injection velocity distribution of the form

$$\frac{v_w}{U_\infty} = \alpha^2 \tilde{\rho}_{1w}^{\frac{1}{2}} \left(\frac{\frac{\delta}{\alpha}}{1.7601} \right)^{\frac{3}{2}} x^{-\frac{1}{2}},$$

the separating streamline retains its shape, i.e.,

$$y_{ss} = \delta x^{\frac{2}{3}},$$

but the pressure along the wedge becomes

$$\frac{p_w}{P_\infty} = M_\infty^2 \alpha^2 \left(\frac{\gamma(\gamma+1)}{2} + 2.0541 \frac{\delta}{\alpha} x^{-\frac{1}{3}} + \ldots \right).$$

The key parameter in this region is the ratio of the blown-layer thickness δ to the wedge half-angle α. This ratio is assumed to be small. Also, as for the flat plate, the thickness of the blown layer is assumed to be small in comparison with the thickness of the shock layer.

Numerical Strategy

A higher-order Godunov-type [6] finite-volume approach was used to discretize the inviscid Euler equations. This requires a spacial interpolation routine, a numerical flux function, and a time-marching technique.

- State quantities in cell centers were interpolated at cell interfaces using a formula introduced by Van Leer [7][8]:

$$\begin{aligned} q_{i+\frac{1}{2},j} = q_{i,j} &+ \frac{1+\kappa}{4}(q_{i+1,j} - q_{i,j}) \\ &+ \frac{1-\kappa}{4}(q_{i,j} - q_{i-1,j}). \end{aligned}$$

This type of interpolation is at most second order accurate (for $\kappa = \frac{1}{3}$), and may lead to spurious oscilations in the solution in the neighborhood of flow discontinuities. To avoid this while maintaining the high order of accuracy in smooth flow regions, a limiter may be employed (Sweby [9]); the limiter adopted was one introduced by Koren [10] which is consistent with $\kappa = \frac{1}{3}$. It has the form

$$q_{i+\frac{1}{2},j} = q_{i,j} + \frac{1}{2}\frac{2R^2+R}{2R^2-R+2}\left(q_{i,j} - q_{i-1,j}\right),$$

$$R = \frac{(q_{i+1,j} - q_{i,j})}{(q_{i,j} - q_{i-1,j})}.$$

In order to apply Koren's interpolation formula uniformly, state quantities at the boundary were calculated first using an appropriate boundary proceedure, as explained below. The finite differences across the boundary were then replaced by twice the finite difference from the cell center to the boundary.

- Roe's approximate Riemann solver [11] was used to calculate the flux across each cell interface.

- Two different marching procedures were employed to reach the steady state solution.

  1. On scalar machines, a locally implicit, linearized Gauss-Seidel iteration scheme was used. In order to avoid non-physical states (i.e. negative pressure) in the evolving flow, the time-step used was based on the ratio of the magnitude of the state vector to the magnitude of its rate of change. This is the Switched Evolution/Relaxation approach of Van Leer and Mulder [12].
  2. On vector machines it appeared advantageous to use an explicit time-marching scheme. Multi-stage schemes developed by Van Leer, Tai, and Powell [13] with optimized short-wave damping vectorize well and are effective in avoiding non-physical transient states.

In order to make accurate comparisons with the analytical solutions, it is crucial to implement numerical boundary conditions that are consistent with the analytical ones (Figure 3).

- Along the inflow boundary of the grid, the flow normal to the boundary is supersonic inward, so there are no out-going characteristics. Thus, the flux into the cells along this boundary can be specified explicitly according to the free-stream state.

- Depending upon the shape of the grid chosen, the flux normal to the top boundary may be either supersonic or subsonic inward. If the flow is subsonic inward, disturbances from inside the computational domain must be allowed to propagate outward through the boundary. Along this upper boundary the flow is nearly uniform, so that the entropy is locally constant and derivatives along the boundary can be neglected. In a coordinate frame normal to the boundary one can define the Riemann invariants

  $$R^{\pm} = u_{\perp} \pm \frac{2a}{\gamma - 1}$$

  transported normal to the boundary along characteristics with speed

  $$u_{\perp} \pm a$$

  Here $u_{\perp}$ is the component of the flow velocity normal to the boundary, and a is the local sound speed. Since the flow is subsonic inward, information from the interior propagates out along the $u_{\perp} + a$ characteristic. Thus the value of the R^+ Riemann invariant should be extrapolated toward the boundary in a manner consistent with the order of the spacial discretization. The inward flux is then completely determined by the R^+ Riemann invariant and three other flow quantities specified on the boundary according to the free-stream state.

- Along the boundary where the flow exits the grid, both supersonic and subsonic outflow exists. For the supersonic exit flow, no information can propagate in from outside the computional domain, thus the flux across the boundary is completely determined by the state quantities in the interior. For boundary cells where the flow is subsonic outward, information from outside can propagate in along the $u_{\perp} - a$ characteristic. Thus, some value of the R^- Riemann invariant should be specified; the problem is that the exterior flow conditions are not known here. Values from a known exact solution could be specified, but this would be incorrect when considering arbitrary blowing distributions. Hedstrom [14] proposed the time-dependent non-reflecting characteristic boundary condition

  $$\frac{\partial p}{\partial t} - \rho a \frac{\partial u_{\perp}}{\partial t} = 0$$

  This type of boundary condition has the disadvantage that it produces a steady state dependent upon the initial conditions. An order-of-magnitude analysis of the governing equations shows that the pressure is constant across the blown layer; this condition can be enforced at the exit by using Hedstrom's boundary condition with the pressure gradient as a source term. The exit boundary condition then becomes

  $$\frac{\partial p}{\partial t} - \rho a \frac{\partial u_{\perp}}{\partial t} = -K\left(u_{\perp} - a\right)\frac{\partial p}{\partial y}, K > 0.$$

  This enforces the correct behavior of the pressure along the subsonic part of the outflow boundary.

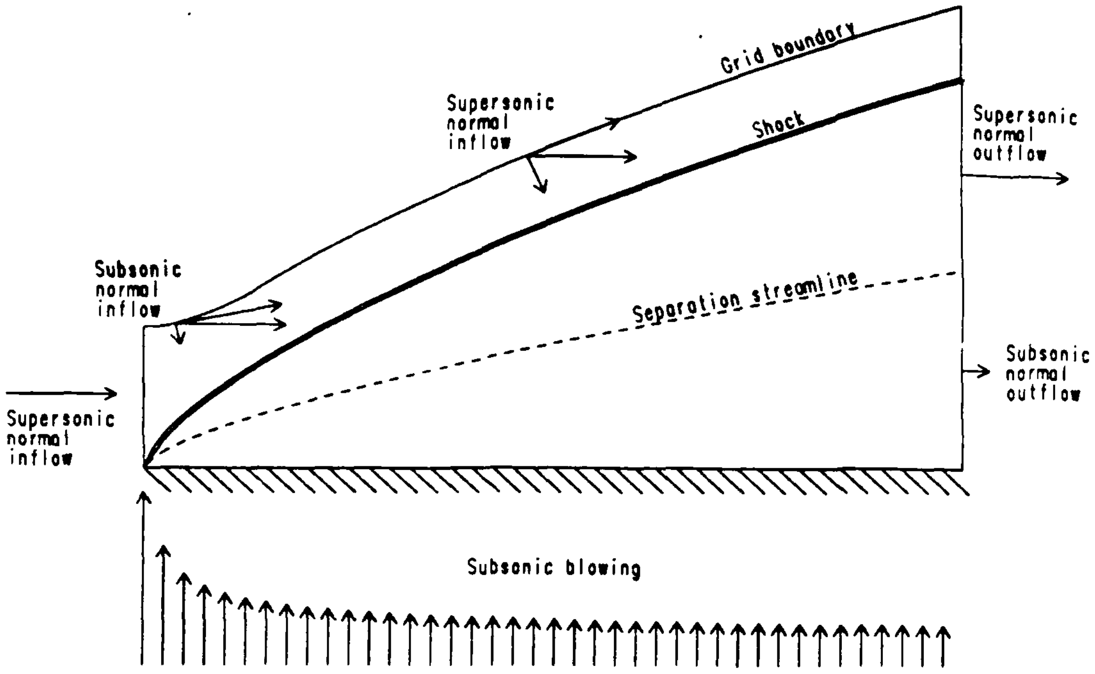

Figure 3: Schematic indicating the various types of boundary conditions encountered.

Typically values of K between 0.1 and 1.0 were used. If K is taken too small or too large, convergence to a steady state is delayed.

- Along the plate or wedge, the injected flow is subsonic inward, except very close to the nose where the flow can become supersonic for an $x^{-\frac{1}{2}}$ blowing distribution. Thus one can specify the normal velocity v_w, the tangential velocity (equal to zero for the cases considered), and the ratio of the injection density to the free-stream density $\tilde{\rho}_{1w}$ (assumed constant along the wall). The wall pressure can then be determined by the R^- Riemann invariant extrapolated from the interior back toward the wall with the proper order of accuracy. Near the wall, the flow may not be locally isentropic; therefore, the approximate incremental form of the Riemann invariant

  $$\Delta p - \bar{\rho}\bar{a}\Delta u_\perp$$

  should be used for extrapolation; barred quantities refer to quantities averaged across the cell interfaces. The pressure then follows from

  $$p_w - p_{i,j} - \rho_{i,j} a_{i,j} \left(u_{\perp w} - u_{\perp i,j} \right) =$$

  $$\frac{1}{2} \left(\Delta p - \bar{\rho}\bar{a}\Delta u_\perp \right)_{extrap.}$$

The analytical solutions were employed in generating grids that would adequately resolve regions of interest in the flow field. Using the analytical predictions, grid points were clustered about the wall, the free shear layer and the shock (Figure 4). The clustering was based on an exponential spacing in the y direction, and an algebraic spacing in the x direction. Once a converged solution was obtained, this adaptive procedure was iterated on to achieve an optimal grid-point distribution for the case considered.

Numerical Experiments

Numerical experiments were conducted to obtain finite-volume solutions of the Euler equations for comparison with the analytical predictions for three different cases:

- Strong interaction on a flat plate.
- Predominantly weak interaction on a flat plate
- Predominantly weak interaction on a slender wedge

The case of strong interaction on a wedge was not considered since the theory assumes that the wedge thickness is small in comparison to the blown layer thickness. Thus to lowest order, the solution for strong interaction on a flat plate is recovered.

For the case of strong interaction on a flat plate, good agreement has been obtained. The parameters chosen for this case are;

$$\delta = 0.09,$$

$$M_\infty = 20,$$

$$M_\infty^2 \delta^2 = 3.24,$$

$$\tilde{\rho}_{1w} = \frac{\rho_{injected}}{\rho_{free-stream}} = 1.$$

Early results on a rectangular grid showed poor agreement with the analytical solution. Cross-sectional profiles of the flow varibles indicated the presence of a viscous-like shear layer where the numerical code was

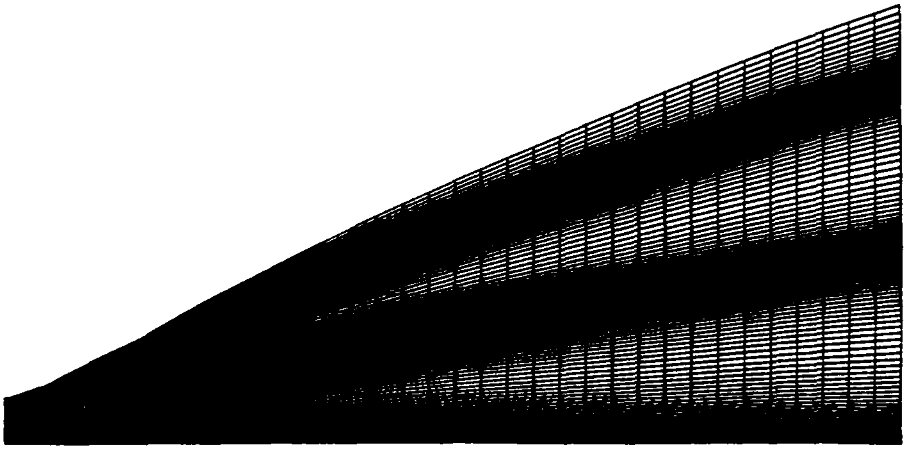

Figure 4: Computational grid.

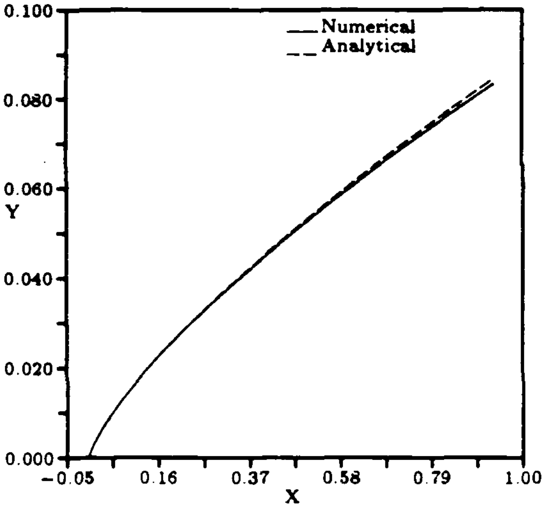

Figure 5: Seperating streamline shapes for strong interaction on a flat plate.

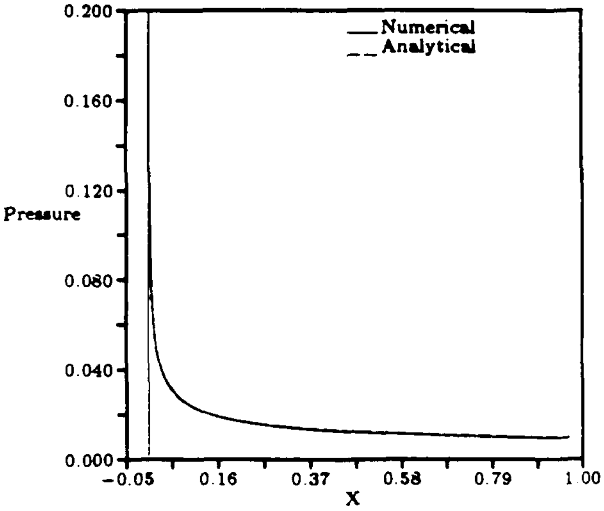

Figure 6: Strong interaction pressure distribution along a flat plate.

trying to model the free slip-stream. This is due to the artificial dissipation associated with the numerical scheme. Restructuring the grid to better fit the flow field, and clustering grid points near the numerical shear layer resulted in a reduction in the thickness of this layer. As the thickness of the layer decreased, the numerical solution approached the analytical solution.

A converged second-order solution on a (83x91) grid shows good agreement between the numerically determined blown-layer shape and the analytical prediction (Figure 5). The pressure distributions along the plate

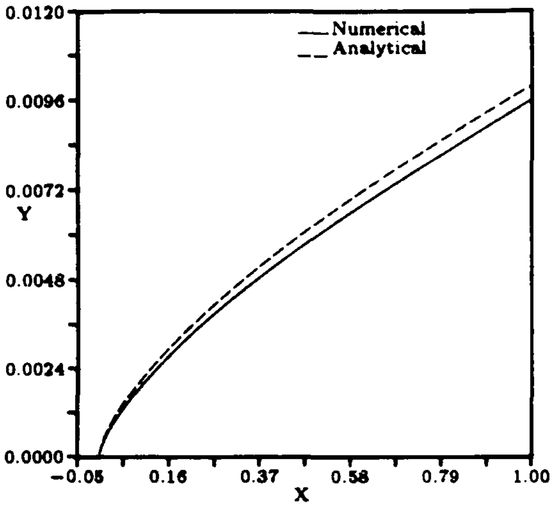

Figure 7: Separating streamline shapes for weak interaction on a flat plate.

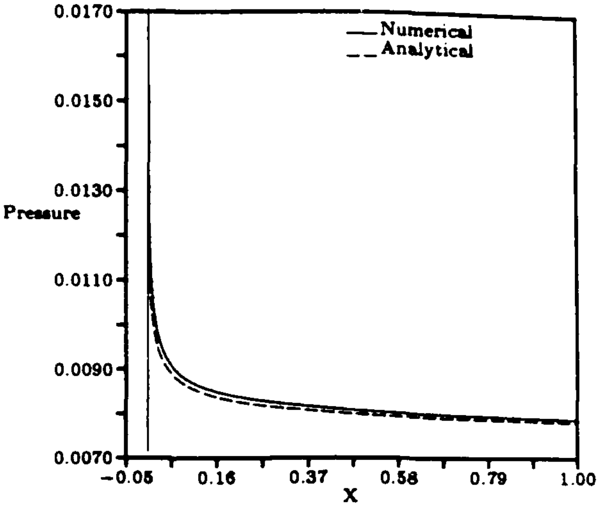

Figure 8: Weak interaction pressure distribution along a flat plate.

also compare well with each other (Figure 6). Further grid refinements were attempted to verify that the numerical solution continued to approach the analytical solution as the mesh spacing decreased. It was found, however, that by refining the grid too far, the numerical dissipation can become so small that the solution becomes unstable and exhibits features similar to those of a physically unstable shear layer (Figure 12).

Fair agreement with the analytical solution was obtained for the case of weak interaction on a flat plate. In this case, the blown layer thickness is thin in comparison with the shock layer. The shock is very weak, and lies roughly along the Mach lines. This case presents two difficulties. The magnitude of the blowing is much smaller so high resolution of the singular blowing distribution and flow features at the nose is even more important. Also, the thinness of the blown layer makes the solution more sensitive to the existence of a numerical shear layer whose thickness is grid dependent. The parameters chosen for this case are;

$$\delta = 0.01,$$

$$M_\infty = 10,$$

$$\tilde{\rho}_{1w} = 1.$$

A comparison between the analytical and the computational separating streamline shapes shows shows a discrepency of about five percent in the thickness of the blown layer (Figure 7). This discrepancy is also apparent in the pressure profiles along the plate (Figure 8).

The last case considered was that of weak interaction on a wedge. For this case the parameters were chosen to be;

$$\frac{\delta}{\alpha} = 0.1,$$

$$\alpha = 8^\circ,$$

$$M_\infty = 20,$$

$$\tilde{\rho}_{1w} = 1.$$

Figure 9 shows good agreement between the analytical and numerical separation streamline shapes, but Figure 10 shows that the numerically calculated pressure is higher than that predicted analytically. The analytical work assumes an infinite value of $(M_\infty \alpha)^2$. If large but finite values of $M_\infty \alpha$ are considered in the analysis, the resulting analytical pressure distribution,

$$\frac{p_w}{P_\infty} = M_\infty^2 \alpha^2 \left(1.946 + 2.084\,\frac{\delta}{\alpha}\,x^{-\frac{1}{3}} + \ldots\right),$$

compares well with the numerically determined values (Figure 11).

Further Work

With the validation study completed, the code will be used to obtain flow solutions in cases where no analytical predictions exist. Of particular interest is strip blowing as a practical means to control the pressure distribution along the surface. The code has been expanded to include the effects of physical viscosity and heat conduction, i.e. to approximate the Navier-Stokes equations. For validation of the code in viscous cases, analytical solutions are again avaiable [3]. A future paper will include some comparisons in the viscous regime.

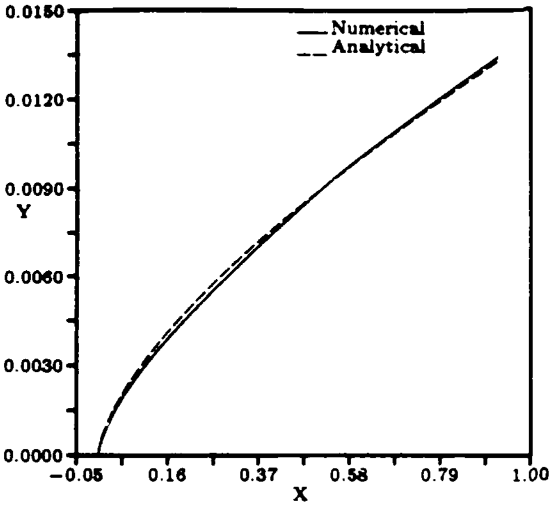

Figure 9: Separating streamline shapes for weak interaction on a wedge.

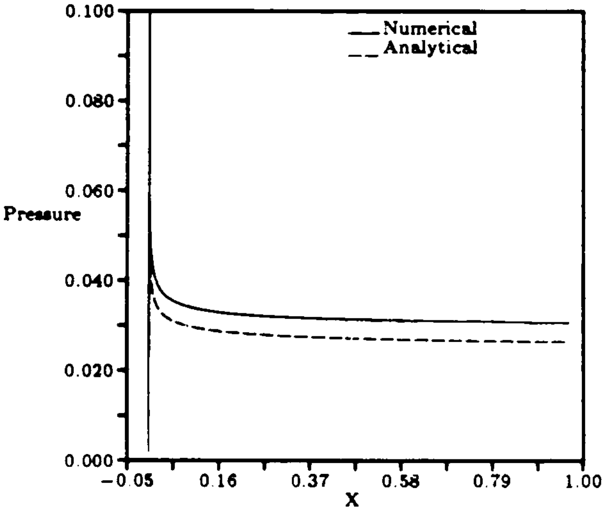

Figure 10: Weak interaction pressure distributions along a wedge.

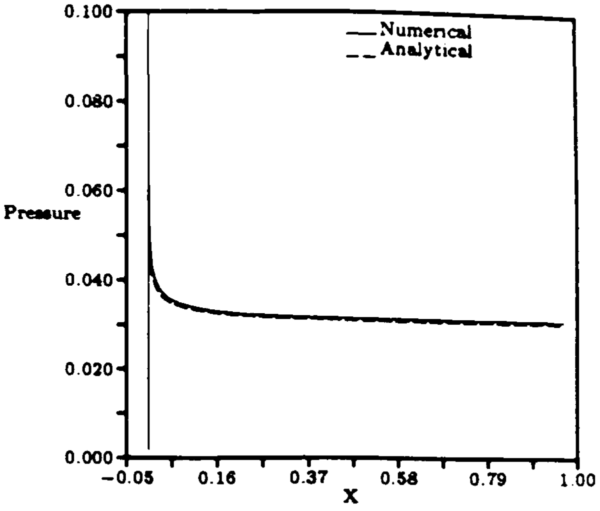

Figure 11: Weak interaction pressure distribution comparison with finite $M_\infty \alpha$ correction.

Acknowledgement

Supported in part by the U. S. Army Strategic Defence Command.

References

[1] J. D. Cole and J. Aroesty, "The blowhard problem-inviscid flows with surface blowing," *Journal of Heat and Mass Transfer*, vol. 11, 1967.

[2] J. Wallace and N. Kemp, "Similarity solutions to the massive blowing problem," *AIAA Journal*, vol. 7, 1969.

[3] A. F. Messiter and M. Matarrese, "Hypersonic viscous interaction with strong blowing," in preparation, 1989.

[4] W. D. Hayes and R. F. Probstein, *Hypersonic Flow Theory*. Academic Press, 1959.

[5] K. Stewartson, *The Theory of Laminar Boundary Layers in Compressible Fluids*. Oxford University Press, 1964.

[6] B. van Leer, "Towards the ultimate conservative difference scheme. V. A second-order sequel to Godunov's method," *Journal of Computational Physics*, vol. 32, 1979.

[7] B. van Leer, "Upwind-difference methods for aerodynamic problems governed by the Euler equations," in *Large-Scale Computations in Fluid Mechanics, Lectures in Applied Mathematics*, vol. 22, 1985.

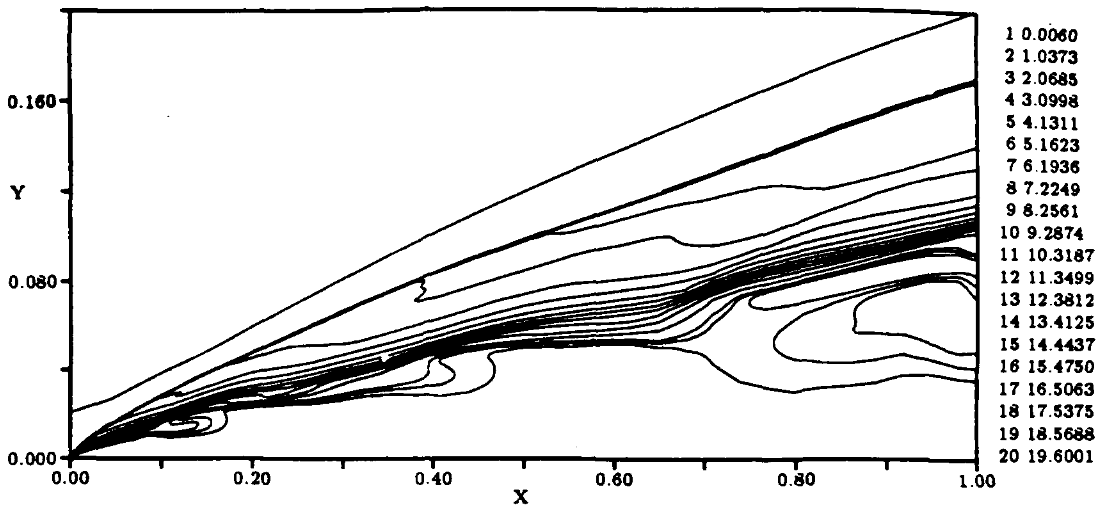

Figure 12: Example of an unstable shear layer encountered in a higher-order calculation on a refined grid.

[8] W. K. Anderson, J. L. Thomas, and B. van Leer, "Comparison of finite volume flux vector splittings for the Euler equations," *AIAA Journal*, vol. 24, no. 9, 1986.

[9] P. K. Sweby, "High resolution schemes using flux limiters for hyperbolic conservation laws," *SIAM Journal on Numerical Analysis*, vol. 21, 1984.

[10] B. Koren, *Multigrid and Defect Correction for the Navier-Stokes equations*. PhD thesis, Delft University, 1989.

[11] P. L. Roe, "Approximate Riemann solvers, parameter vectors, and difference schemes," *Journal of Computational Physics*, vol. 43, 1981.

[12] B. van Leer and W. A. Mulder, "Relaxation methods for hyperbolic equations," in *Numerical Methods for the Euler Equations of Fluid Dynamics*, 1985.

[13] B. van Leer, C. H. Tai, and K. G. Powell, "Design of optimally-smoothing multi-stage schemes for the Euler equations," in *AIAA 9th Computational Fluid Dynamics Conference*, 1989.

[14] G. W. Hedstrom, "Nonreflecting boundary conditions for nonlinear hyperbolic systems," *Journal of Computational Physics*, vol. 30, 1970.

Trajectory Optimization of Earth-Launched Interceptors at Supercircular Speeds

R.M. Howe, E.G. Gilbert, Ping Lu, N.X. Vinh
The University of Michigan, Ann Arbor, Michigan 48109

ABSTRACT

An alternative to satellite-based kinetic energy weapons for intercepting ballistic missiles early in their trajectories is the use of earth-based hyper-velocity rockets. Simple calculations show that with existing solid-propellant technology, rockets can be accelerated to more than twice circular-orbit speeds with mass ratios of several thousand to one. For intercept distances ranging from 2000 to 5000 miles this translates into flight times of between 4 and 10 minutes. This permits interception of hostile ballistic missiles during their ascent trajectory when vulnerability remains high. The use of miniature guided warheads in the defensive weapon reduces the interceptor takeoff weight to within reasonable bounds. Parameters to be optimized include the mass ratios and thrusting time for each stage, the coasting time between powered stages, and the parameters used to represent the time history of angle of attack. A quasi-Newton minimization algorithm is utilized with penalty functions to implement the terminal constraints, as well as any other constraints. The necessary gradients are computed numerically using finite differences. The multiple stage trajectories are calculated many thousands of times faster than real time using an AD 100 multiprocessor computer. A VAX host computer implements the optimization algorithm and inputs new parameters to the multiprocessor for each successive trajectory run. In this way the total required time for an overall trajectory optimization consisting of several thousand trajectories is reduced from several hours to several minutes.

1. INTRODUCTION

The study of satellite-based kinetic-energy weapons for intercepting intercontinental ballistic missiles during their ascent trajectory represents one of the major efforts in the current U.S. Strategic Defense Initiative program. In this paper we consider an alternative to space-based weapons, namely, the use of land or sea-based kinetic energy interceptors. When such interceptors are based on the U.S. continent, ranges of up to 5000 miles are needed. If the interceptors are sea launched, for example from submarines, the required interceptor range may be reduced to as little as 2000 miles or less. In either case the interceptor must accelerate to very high speeds, typically twice circular orbit velocity, in order to reach a target at these distances within several minutes.

In order to achieve these velocities, a rocket powered interceptor requires an overall mass ratio of several thousand to one. Even so, the interceptor takeoff weight can be held within reasonable bounds by the use of miniature guided warheads. It is clear that such large mass ratios can only be achieved by using between 4 and 7 rocket boost stages. In this paper we consider the problem of optimizing a number of stage parameters and the angle of attack control in order to minimize the overall required mass ratio. The time history of angle of attack is parameterized by letting the angle of attack for each thrusting stage vary linearly with time. Additional parameters to be optimized include the thrust burn times for each stage and the coast times between stage burns. Although rockets of this type would normally be launched straight up, we also include the initial launch flight-path angle as a parameter. This is based on the assumption that a fairly rapid pitchover manuever can be performed immediately after launch to achieve the desired initial flight path angle.

Once the trajectory optimization problem is converted to a parameter optimization problem, a quasi-Newton minimization algorithm is utilized with penalty functions to implement the terminal constraints required for intercept, as well as any additional constraints. The necessary gradients of the cost function with respect to the parameters are computed numerically using finite differences. A complete multi-stage trajectory must be run using numerical integration for every evaluation of the cost function. For each set of N parameters this means that N+1 complete trajectories must be computed, one to evaluate the cost function for the given parameter settings, and N to evaluate the gradient of the cost function with respect to each of the N parameters. For the trajectory optimization problems we have considered thus far, between 10 and 20 parameters have been used. Thus between 11 and 21 complete 4 to 7-stage trajectories must be computed numerically for a single iteration of the optimization procedure. Also, each iteration utilizes a line search which requires several additional trajectory computations. It has been found that between 200 and 400 iterations are needed until satisfactory convergence to an optimal solution is achieved. It follows that several thousand trajectories must be computed for each optimization case considered.

In the next section scalar equations of motion for the interceptor trajectory are presented. Subsequent sections discuss the optimization problem, its numerical solution, and results for a typical 4-stage trajectory optimization.

2. EQUATIONS OF MOTION

In order to reduce the trajectory computation times we will only consider the two dimensional equations of motion of the interceptor. As a further simplification, we will neglect the effect of earth's rotation. We feel that neither of these simplifications alter the overall nature of the optimization problem. More comprehensive equations of motion can always be incorporated into the optimization problem at a later time to improve the accuracy for those cases which may turn out to be of practical interest. Thus we consider the interceptor rocket to be a point mass m moving in a plane which contains the center of a spherical, non-rotating earth with inverse square gravitational field. A convenient and efficient method for representing the velocity state of the interceptor is in terms of the total velocity and the flight path angle with repect to the local horizontal [1]. This leads to the following two-dimensional equations of motion:

$$\dot{r} = V \sin\gamma \tag{1}$$

$$\dot{\theta} = \frac{V}{r}\cos\gamma \tag{2}$$

$$\dot{V} = \frac{T}{m}\cos\alpha - \frac{D}{m} - \frac{g_0 r_0^2}{r^2}\sin\gamma \tag{3}$$

$$\gamma = \frac{1}{V}\left[\frac{T}{m}\sin\alpha + \frac{L}{m} - \frac{g_0 r_0^2}{r^2}\cos\gamma + \frac{V^2}{r}\cos\gamma\right] \tag{4}$$

$$\dot{m} = \frac{T}{I_{sp} g_0} \tag{5}$$

where

r = radial distance from center of earth
V = total velocity
m = interceptor mass
α = angle of attack
L = aerodynamic lift
g_0 = gravity acceleration at $r = r_0$

θ = polar angle
γ = flight path angle
T = rocket thrust
D = aerodynamic drag
r_0 = reference radius
I_{sp} = specific impulse of rocket motor

The aerodynamic lift, L, and drag, D, are given by the following formulas:

$$L = \frac{1}{2}\rho V^2 A C_L, \quad D = \frac{1}{2}\rho V^2 A C_D \tag{6}$$

$$C_L = C_N \cos\alpha - C_A \sin\alpha, \quad C_D = C_N \sin\alpha + C_A \cos\alpha \tag{7}$$

where

ρ = atmospheric density
C_L = lift coefficient
C_N normal force coefficient

A = interceptor cross-sectional area
C_D = drag coefficient
C_A = axial force coefficient

C_N and C_A, which represent aerodynamic normal and axial force coefficients in body axes, can be approximated for slender bodies by the following formulas [2]:

$$C_N = \sin 2\alpha \cos\frac{\alpha}{2} + \frac{5}{\pi}\frac{\lambda}{d}\sin\alpha\,|\sin\alpha|, \quad C_A = 0.15 \tag{8}$$

where

λ = rocket length
d = rocket diameter

The atmospheric density, ρ, in Eq. (6) is a function of the rocket altitude h, which is given by the equation

$$h = (R - 1)\, r_0 \tag{9}$$

We have considered three different methods for approximating the variation of ρ with h. The first utilizes table lookup with linear interpolation based on a tabulated standard atmosphere. This method introduces into the simulation a function with discontinuous slopes, which has the potential of causing numerical difficulties in the descent algorithm (see Section 4). The second method uses the following exponential approximation:

$$\rho = \rho_0 e^{-\beta h} \tag{10}$$

where $1/\beta$ = 23,500 ft. and ρ_0 is the atmospheric density at sealevel. The third method uses the following analytic approximation [3]:

$$\rho/\rho_0 = [A_0 + A_1 h + A_2 h^2 + \cdots + A_{11} h^{11}]^{\cdot 4} \qquad (11)$$

with

$A_0 = 1.0000000000$ $A_1 = 0.3393495800 \times 10^{-1}$ $A_2 = -0.3433553057 \times 10^{-2}$
$A_3 = 0.5497466428 \times 10^{-3}$ $A_4 = -0.3228358326 \times 10^{-4}$ $A_5 = 0.1106617734 \times 10^{-5}$
$A_6 = -0.2291755793 \times 10^{-7}$ $A_7 = 0.2902146443 \times 10^{-9}$ $A_8 = -0.2230070938 \times 10^{-11}$
$A_9 = 0.1010575266 \times 10^{-13}$ $A_{10} = -0.2482089627 \times 10^{-16}$ $A_{11} = 0.2548769715 \times 10^{-19}$

Eq. (11) is valid from 0 to 200 km. altitude and is accurate to better than 5 percent for altitudes up to 70 km. It is a considerably better approximation than the exponential model in Eq. (10) and takes no longer to execute than the table lookup scheme. Thus it represents our preferred approach.

Dimensionless versions of Eqs. (1) through (9) and Eq. (11) are used for the trajectory simulation of each inteceptor stage while thrusting or coasting ($T = 0$). The state variables r, θ, V and γ are continuous from one stage to the next. On the other hand, the state variable m, which represents the mass of each stage, undergoes a discontinuous decrease each time a stage burns out and is dropped. Note that the mass state m can be made continuous by defining it as the mass of rocket fuel divided by the initial takeoff mass. The total instantaneous mass for each stage is then the sum of the fuel mass and the inert mass. The burn time for each stage, as well as the coast time per stage, constitute parameters to be optimized. For a given stage mass ratio, the stage burn time determines the thrust level for the stage. Thus the parameters representing stage burn times are equivalent to parameters representing stage thrust levels. As noted previously, the time history of angle of attack is parameterized by letting it vary linearly for each stage. Thus an additional parameter per stage is the time-rate-of-change of angle of attack.

3. CONSTRAINTS AND OPTIMIZATION PROBLEM FORMULATION

To complete the statement of the optimization problem it is necessary to introduce certain constraints on the trajectory and its defining parameters. The most obvious of these are the ones required for target interception. After final stage cutoff, the payload must coast in such a manner that at the specified intercept time, t_f, the position variables, $r(t_f)$ and $\theta(t_f)$, match those of the target.

There are several ways to implement the intercept conditions. One way is to impose them at the time of final-stage cutoff, t_c. If $r(t_c)$, $\theta(t_c)$, $r(t_f)$, and $\theta(t_f)$ are known and the coast is an out-of-the-atmosphere conic transfer, the values $\gamma(t_c)$ and $V(t_c)$ required for intercept are determined by solving an appropriate Lambert problem. This can be done numerically by the methods given in [4]. The errors between the required and actual values of $\gamma(t_c)$ and $V(t_c)$ must be zero for intercept and these conditions give two equality constraints on the trajectory at $t = t_c$.

We have found that unconstrained optimal conic coast trajectories re-enter the atmosphere or even pass through the earth's surface. To assure that this doesn't happen, the minimum altitude during the coast is computed (as part of the solution of the Lambert problem) and specified to lie outside the sensible atmosphere. The error between the computed minimum altitude and its specified value constitutes, when set to zero, a third equality constraint.

Another way to implement the intercept condition is to integrate numerically the equations of motion of the final coast trajectory, just as the equations for the previous stages were integrated. In this case the errors between the interceptor coordinates $r(t_f)$, $\theta(t_f)$ and the target coordinates at the final time t_f are set equal to zero to form two equality constraints. As before, a minimum allowable altitude outside the sensible atmosphere can be chosen for the final coast trajectory. This minimum altitude is then the third constraint. Alternatively, the effect of the atmosphere itself, which is included in the trajectory equations, will ensure that a realistic altitude constraint is enforced when the final coast trajectory equations are integrated. Indeed, this is the required approach in the aero-assisted case, where the final coast trajectory actually utilizes aerodynamic down lift to hold the trajectory at near constant altitude in the presence of supercircular velocity. In Section 5 we consider an example of this type.

In addition to the equality constraints on the trajectory, inequality constraints may be imposed on some of the problem parameters. For example, an initial stage acceleration, A^0_T, may have upper and lower limits, A_{max} and A_{min}. To avoid treating these constraints directly in the algorithmic process, we impose them implicitly by introducing a nonlinear transformation of a new parametric variable. In the case just mentioned a suitable transformation is

$$A^0_T = \frac{A_{max} + A_{min}}{2} + \frac{A_{max} - A_{min}}{2} \sin a_T \qquad (12)$$

where a_T is the new unconstrained parameter.

Putting all of the above details together in a compact notation yields a problem of the form

$$\text{minimize } f(z) \text{ subject to } g_i(z) = 0\,, \quad i = 1,2,3. \qquad (13)$$

Here: $f(z)$ is the ratio of the launch mass to the payload mass, the $g_i(z)$ are the errors in meeting the equality constraints, and z is a vector whose components are the "unconstrained" parameters arising from models described in Section 2. Given z, it is clear that $f(z)$

and $g_i(z)$ may be evaluated by integrating the equations of motion, computing $m(t_c)$, $\gamma(t_c)$, $V(t_c)$, $r(t_c)$, and $\theta(t_c)$, and solving the Lambert problem determined by the target specification. When the alternative method involving numerical integration of the final coast trajectory is used to implement the intercept condition, $f(z)$ is still evaluated from $m(t_c)$, but $g_i(z)$ is evaluated from $r(t_f)$ and $\theta(t_f)$.

Our algorithm for the numerical solution of (13) requires the gradient (collection of N first partial derivatives) of functions such as $f(z)$. While it is possible to derive formulas for the partials (they may be written in terms of the differential equations adjoint to the linearized equations of motion), they are exceedingly complex because of the nonlinear functions appearing in Eqs. (1) - (9) and (11). This motivates our desire to use finite differences for the gradient calculations.

4. NUMERICAL SOLUTION OF THE OPTIMIZATION PROBLEM

A variety of numerical approaches have been used to solve trajectory optimization problems with equality constraints. These include: (1) gradient projection methods, (2) Newton-Raphson solution of the necessary conditions, (3) penalty function methods. Approach (1) gives slow convergence; approach (2) requires second derivatives of problem data and good initial estimates; approach (3) leads to badly conditioned (though unconstrained) minimization problems. We have followed approach (3), attacking its disadvantage by using a rapidly convergent quasi-Newton algorithm [5,6] and an augmented Lagrangian for the penalty function.

In the usual penalty function method approximate solutions of (13) are sought by algorithmic minimization of

$$F_P(z) = f(z) + \sum_{i=1}^{3} \mu_i [g_i(z)]^2 \qquad (14)$$

It can be shown [5,6] that the equality conditions can be accurately enforced by choosing the penalty coefficients, $\mu_i > 0$, to be sufficiently large. In practice, numerical hazards, such as slow convergence or convergence to false minima, are reduced by minimizing $F_P(z)$ several times with successively larger values for the penalty coefficients. At each successive stage the starting point for the minimization algorithm is taken as the solution point from the previous stage. Even so, the conditioning of $F_P(z)$ worsens [5,6] as the μ_i increase and there is a practical limit to the accuracy which can be achieved. Numerical errors in the minimization algorithm and the evaluation of $F_P(z)$ and its gradient eventually become limiting.

In the augmented Lagrangian approach $F_P(z)$ is replaced by

$$F_L(z) = f(z) + \sum_{i=1}^{3} \lambda_i g_i(z) \quad \sum_{i=1}^{3} \mu_i [g_i(z)]^2 \qquad (15)$$

where the λ_i are real numbers approximating the Lagrange multipliers for the minimization problem (13). When $F_L(z)$ is minimized, it is possible to satisfy the equality constraints accurately with much smaller values for the penalty coefficients [5,6]. The resulting improved conditioning of $F_L(z)$ reduces the bad effects of the numerical errors. Again, it is advantageous to solve a sequence of minimization problems with successive initializations, where in this case both the λ_i and the μ_i are adjusted. We have used the adjustment scheme proposed by Powell and described on page 134 of [5] with good results. It eliminates the need for human intervention in selecting the parameters λ_i and μ_i and improves accuracy of equality constraints over the simple penalty function approach by at least an order of magnitude.

Because of the highly nonlinear character of $F_L(z)$ and its poor conditioning, it is necessary to pay careful attention to the procedure for its unconstrained minimization. Certainly, the second order properties of $F_L(z)$ must be taken into account. We have found the BFGS, quasi-Newton program of Shanno and Phua [7] to be effective. Its line search has been modified to compute derivatives along the search direction directly by forward differences. This eliminates the need for gradient evaluations during the line search.

The performance of a quasi-Newton algorithm is predicated on the smoothness of the function being minimized. The function should be at least twice continuously differentiable. Here, the representation of empirical data appearing in the equations of motion is important. See, for example, the comments in Section 2 on computing the atmospheric density by table lookup with linear interpolation.

Another concern is the forward difference computation of the partial derivatives of $F_L(z)$. If the step size is too small, the effects of round off errors are exacerbated; if the step size is too large, truncation errors become appreciable. If the machine precision is ε, it can be argued [6] that the step size should be the order of $\varepsilon^{1/2}$. In our case the machine precision $\varepsilon \cong 10^{-12}$ is determined by the AD 100, which has a 40 bit significand. We have found that the step size 10^{-6} is reasonable, but that experimentation with the step size can improve the accuracy noticeably. Even better accuracy has been obtained by using central differences for the partial derivatives. It reduces the effects of round-off errors because a larger step size may be used for the same truncation error [6]. Of course, $2N + 1$ evaluations of $F_L(z)$ are then needed to obtain $F_L(z)$ and its gradient.

It should be mentioned that the trajectory state equations were solved numerically using fourth-order Runge-Kutta integration with a fixed step size. A single-pass predictor method with a Gear RK-4 startup algorithm was found to give better performance in some cases [8] and will be further investigated in later studies.

5. EXAMPLE OPTIMAL TRAJECTORY SOLUTIONS

Two example optimal trajectory solutions are considered in this section. $\theta(t_f) - \theta_0$, the total change in polar angle of each trajectory, is set equal to 30 degrees. This corresponds to an interceptor range of 2094 miles. The total time of interceptor flight is prescribed to be 300 seconds and the target is intercepted at an altitude of 200 km. Stage takeoff weight is equal to 10,000 kg and physical parameters are assumed to be similar to those of a Minuteman III. The specific impulse I_{sp} of the rocket engines is equal to 300 seconds, and the ratio of initial fuel weight to inert weight for the rocket motor of each stage is assumed to be 10. The intercept condition is implemented by two equality constraints that require the interceptor coordinates at the final time t_f to match the target coordinates. Two cases are considered; aeroassisted and non-aeroassisted. In the aeroassisted case the final coasting stage reenters the earth's atmosphere with a controlled angle of attack which can be used to generate downward lift. In the non-aeroassisted case the angle of attack of the final coasting stage is maintained at zero, which means that aerodynamic forces can only cause drag. In each case there are 4 booster stages, with equal mass ratios prescribed for each stage. The common mass ratio is therefore a parameter. As noted earlier, the performance objective is to maximize the final payload weight. The results are summarized in Table 1.

TABLE 1. Optimal Trajectory Data for 4-stage Interceptor

	Aeroassisted	Non-aeroassisted
Final optimal payload weight	9.73 kg	5.63 kg
Mass ratio per stage	3.98	4.33
Minimum altitude in final coast to target	93.82 km	96.82 km
Burnout speed (V_c = circular orbit speed)	1.766 V_c	1.775 V_c
Burnout altitude	98.24 km	155.04 km
Launch flight path angle, γ_0	82.8 deg	60.6 deg
Initial thrust acceleration, stage 1	13.05 g	9.28 g
Burn time, stage 1	17.21 sec	24.86 sec
Coast time between stages 1 and 2	6.49 sec	1.84 sec
Initial thrust acceleration, stage 2	23.37 g	12.93 g
Burn time, stage 2	9.61 sec	17.84 sec
Coast time between stages 2 and 3	5.35 sec	2.41 sec
Initial thrust acceleration, stage 3	31.40 g	23.87 g
Burn time, stage 3	7.15 sec	9.67 sec
Coast time between stages 3 and 4	14.85 sec	56.74 sec
Initial thrust acceleration, stage 4	37.52 g	31.67 g
Burn time, stage 4	5.99 sec	7.29 sec
Final coast time to target	233.67 sec	179.36 sec
Total flight time	300 sec	300 sec
Total distance	2094 miles	2094 miles

From the table it is clear that the optimal aeroassisted trajectory yields a significantly larger payload, 9.73 kg versus 5.63 kg for the non-aeroassisted case. In Figure 1 are shown time history plots of velocity, flight path angle, dynamic pressure and angle of attack for the aeroassisted optimal trajectory. Figure 2 shows altitude versus polar angle plots for both the aeroassisted and non-aeroassisted trajectories. Note how the aeroassisted trajectory is able to maintain an approximately constant altitude of some 95 km over more than half of the final coast to intercept. This is possible despite the supercircular speed because of the aerodynamic down lift, which reaches a maximum of 1.87 g during this portion of the trajectory. The maximum total downward acceleration, including gravity, is therefore 2.87g. Since the centrifugal acceleration in g units is V_c^2 (V_c is the circular-orbit velocity), it follows that constant altitude (i.e., a circular orbit) will, in the presence of 1.87 g of down lift, be maintained at a velocity of $(2.87)^{1/2}$ or $1.694V_c$. Reference to the plot of V versus time in Figure 1 shows that this is indeed the case. On the other hand we see in Figure 2 that the non-aeroassisted trajectory must climb to over 150 km before the final stage burn in order to avoid significant penetration of the atmosphere. This results in a considerable more expensive trajectory in terms of required mass ratio.

The plot of angle of attack α versus time in Figure 1 shows clearly the linear variation of α for each stage. Note that zero angle of attack is assumed during the coast between stage burns. This is based on the assumption that the interceptor is aerodynamically stable during these coasts with no active thrust vector control. Means of active attitude control would be required to maintain the linear angle of attack variation shown for the final coast to intercept. One option for achieving this would be to provide thrust vector control utilizing a low level of thrust during this final portion of the trajectory. Such thrust will probably be required in any event to provide course corrections to intercept the target. When this is included in the overall trajectory optimization, it may very well produce a non-aeroassisted optimal trajectory which is competitive with the aeroassisted case, since now a downward component of thrust can be used to replace the aerodynamic down lift.

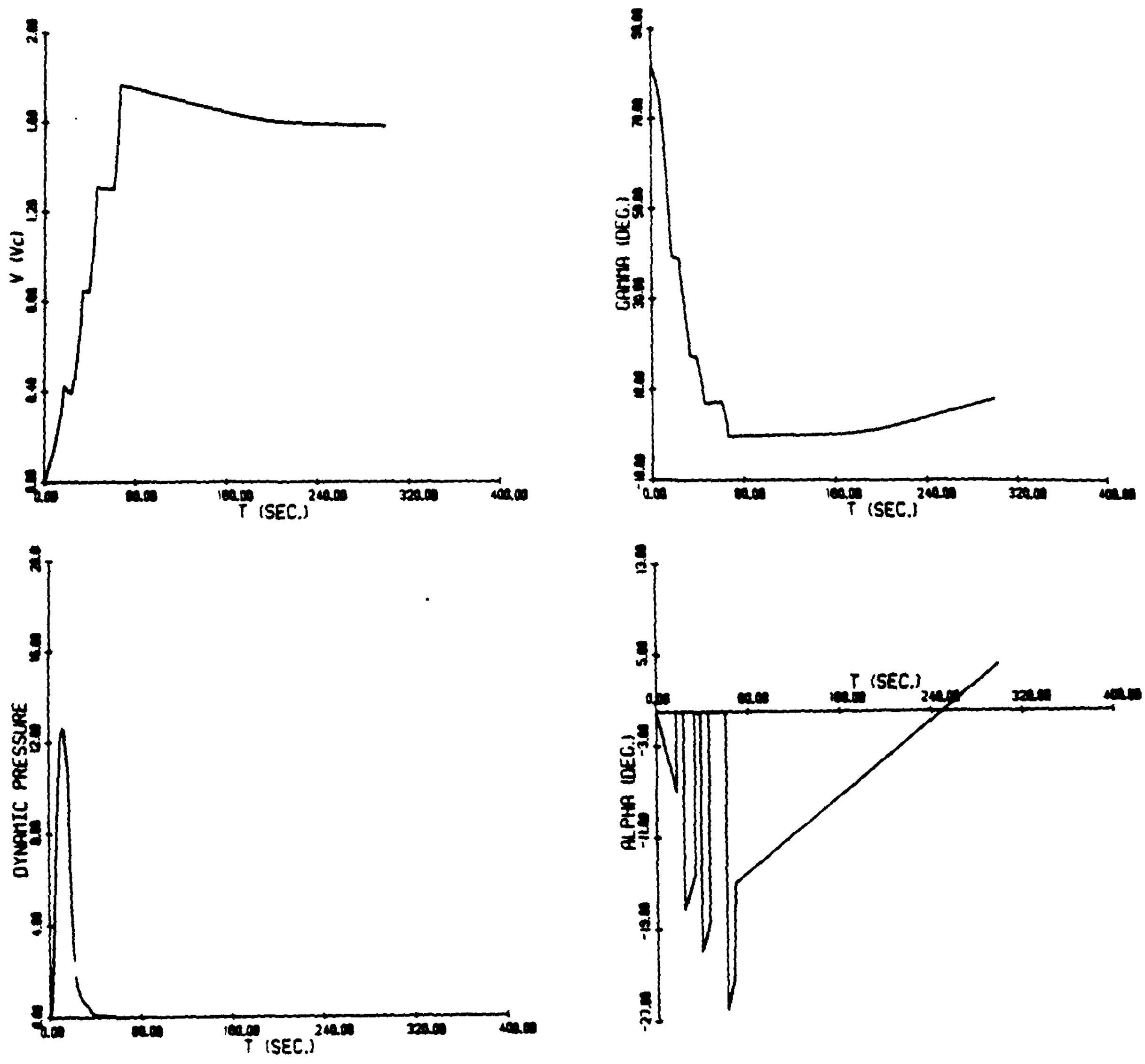

Figure 1. Time history plots for the aeroassisted optimal trajectory.

6. CONCLUSIONS

In this paper we have described techniques for computing the optimal trajectories of earth-launched interceptor rockets which are accelerated to over twice orbital velocity. The objective of the optimization is to maximize the payload with a given interceptor takeoff weight. Terminal constraints have been enforced using penalty functions. The required gradients of the cost functions have been computed numerically using finite differences. Through the use of a special multiprocessor computer, the AD 100, in conjunction with a VAX host computer, we have been able to reduce the time required for each trajectory optimization from hours to minutes.

Preliminary results have been presented for a 4-stage example. It is found that allowing a coast period between booster stages and using an aeroassisted trajectory to generate down lift during the final coast segment improves the optimal payload significantly. Future research efforts will include parametric studies of the effect of different prescribed flight times, target range and altitude, payload mass, and refined aerodynamic and propulsion models.

7. ACKNOWLEDGEMENT

The research reported in this paper has been supported by the Innovative Science and Technology Office, U.S. Strategic Defense Initiative Organization, under contract number DOD-C-F49620-86-C-0138. The authors also acknowledge the support provided by Applied Dynamics International, Ann Arbor, Michigan.

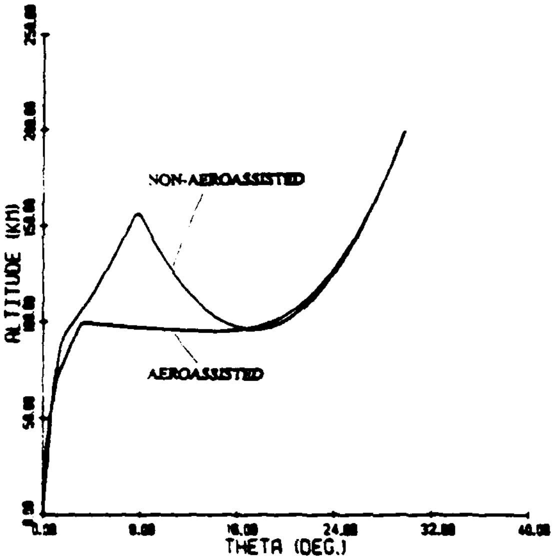

Figure 2. Comparison of optimal tractories with and without aeroassistance.

8. REFERENCES

[1] N.X. Vinh, A. Buseman and R.D. Culp, *Hypersonic and Planet Entry Flight Mechanics*, The University of Michigan Press, Ann Arbor, Michigan, 1980.

[2] L.H. Jorgensen, "Estimation of Aerodynamics for Slender Bodies Alone and with Lifting Surfaces," *AIAA Journal*, Vol. 11, No. 3.

[3] *U.S. Standard Atmosphere Supplements*, 1966, U.S. Government Printing Office, Washington D.C.

[4] R. H. Battin, "An Elegant Lanbert Algorithm," *Journ. Guidance, Control, and Dynamics*, vol. 7, pp. 662-670, 1984.

[5] R. Fletcher, *Practical Methods of Optimization*, vol. 2, Wiley-Interscience, 1981.

[6] P. E. Gill, W. Murray and M. H. Wright, *Practical Optimization*, Adademic Press, 1981.

[7] D. F. Shanno and K.H.Phua, "Minimization of Unconstrained Multivariate Functions, "*ACM Transactions on Mathematical Software*, vol. 6, pp. 618-622, 1980.

[8] R.M. Howe, E.G. Gilbert, Ping Lu, G. Shorr, N.X. Vinh, "Computation of Optimal Trajectories Using State-of-the-art Simulation Technology," to appear in *Proceedings of the Conference on Aerospace Simulation*, no. 3, Feb. 3-5, 1988, San Diego, California.

Computation of Optimal Trajectories Using State-of-the-art Simulation Technology

R.M. Howe, E.G. Gilbert, Ping Lu, G. Shorr, N.X. Vinh
The University of Michigan, Ann Arbor, Michigan 48109

ABSTRACT

Simulation techniques are described for determining the optimal control of earth-launched interceptor rockets which are accelerated to over twice orbital velocity. Each optimization case requires many thousands of trajectory calculations. In order to reduce the overall computational time the multiple stage trajectories are calculated using an AD 100 multiprocessor computer. The VAX host computer implements the optimization algorithm and inputs new parameters to the AD 100 for each successive trajectory run. The necessary derivatives in the optimization process are computed numerically on the AD 100 using finite differences. A quasi-Newton minimization algorithm is used with penalty functions to implement the terminal constraints. For a prescribed intercept time of flight the overall mass ratio is minimized with respect to the time history of angle of attack and the individual stage burn and coast times. A 5th-order single-pass predictor/corrector integration method with a Gear RK-4 startup algorithm for each stage is shown to provide very fast and accurate trajectory solutions. Using the AD 100 for the trajectory calculations reduces the overall time required for each optimization to minutes, compared with hours when the VAX alone is used.

1. Introduction

An alternative to satellite-based kinetic energy weapons for intercepting ballistic missiles early in their trajectories is the use of earth-based hyper-velocity rockets. Simple calculations show that with existing solid-propellant technology, rockets can be accelerated to more than twice circular-orbit speeds with mass ratios of several thousand to one. For intercept distances ranging from 2000 to 5000 miles this translates into flight times of between 3 and 10 minutes. This in turn permits interception of hostile ballistic missiles during their ascent trajectory when vulnerability remains high. The use of miniature guided warheads in the defensive weapon reduces the interceptor takeoff weight to within reasonable bounds.

In order to achieve interceptor velocities of twice circular orbit speed or more, it is necessary to utilize between 4 and 7 rocket boost stages. In this paper we consider the problem of optimizing a number of stage parameters and the angle of attack control to minimize the overall required mass ratio. The time history of angle of attack is parameterized by letting the angle of attack for each thrusting and coasting stage vary linearly with time. Additional parameters to be optimized include the thrust burn times for each stage and the coast times between stage burns. Although rockets of this type would normally be launched straight up, we also include the initial launch flight-path angle as a parameter. This is based on the assumption that a fairly rapid pitchover manuever can be performed immediately after launch to achieve the desired initial flight path angle.

Once the trajectory optimization problem is converted to a parameter optimization problem, a quasi-Newton minimization algorithm is utilized with penalty functions to implement the terminal constraints required for intercept. The necessary gradients of the cost function with respect to the parameters are computed numerically using finite differences. A complete multi-stage trajectory must be run using numerical integration for every evaluation of the cost function. For each set of N parameters this means that N+1 complete trajectories must be computed, one to evaluate the cost function for the given parameter settings, and N to evaluate the gradient of the cost function with respect to each of the N parameters. For the trajectory optimization problems we have considered thus far, between 10 and 20 parameters have been used. Thus between 11 and 21 complete 4 to 7-stage trajectories must be computed numerically for a single iteration of the optimization procedure. Also, each iteration utilizes a line search which requires several additional trajectory computations. It has been found that between 200 and 400 iterations are needed until satisfactory convergence to an optimal solution is achieved. It follows that several thousand trajectories must be computed for each optimization case considered. Typical overall computation times for a single case turn out to require many hours when using general-purpose computers such as a VAX or Apollo. Such long computational times are not only expensive, but also frustrating when one is trying to perform parametric studies which may require many optimization cases to be run. For this reason we have turned to the AD 100 computer for solving the most computationally intensive part of the problem, which is the trajectory calculation associated with the many evaluations of the cost function.

The AD 100 is a multiprocessor with special architecture and software which has been optimized for the solution of ordinary, nonlinear differential equations. The computer uses emitter-coupled (ECL) logic with floating-point word lengths of 53 and 65 bits. It can perform a 53-bit floating-point multiply in 0.075 microseconds and a 65-bit floating-point add in 0.1 microseconds. The equivalent overall instruction rate exceeds 100 MIPS (millions of instructions per second). Because of the short multiply and add times, the AD 100 is extremely fast in the solution of scalar problems. Although the principal application of the AD 100 has been the real-time simulation of complex dynamic systems, such as aircraft and missiles, its overall speed can also be exploited in the sort of optimization problems described in this paper.

In addition to using the AD 100 for the trajectory computations, we have devoted considerable effort to choosing integration algorithms which are both accurate and fast running. We have also attempted to use efficient coordinate systems in which to write the scalar equations of motion for the interceptor trajectory. In the next section these equations are presented. Following this, Section 3 describes the integration methods which were found to be particularly fast and accurate. Subsequent sections discuss the optimization problem, its numerical solution, and results for a typical 4-stage trajectory optimization.

2. Equations of Motion

In order to reduce the trajectory computation times we will only consider the two dimensional equations of motion of the interceptor. As a further simplification, we will neglect the effect of earth's rotation. We feel that neither of these simplifications alter the overall nature of the optimization problem. More comprehensive equations of motion can always be incorporated into the optimization problem at a later time to improve the accuracy for those cases which may turn out to be of practical interest. Thus we consider the interceptor rocket to be a point mass m moving in a plane which contains the center of a spherical, non-rotating earth with inverse square gravitational field. A convenient and efficient method for representing the velocity state of the interceptor is in terms of the total velocity and the flight path angle with repect to the local horizontal [1]. However, at takeoff, when the interceptor velocity is zero, this results in a singularity in the flight-path angle rate which can cause numerical difficulty. We therefore chose to represent the velocity state by means of the horizontal component u and vertical component w of the total interceptor velocity [2]. When polar coordinates are used for the position state variables, this leads to the following two-dimensional equations of motion:

$$\dot{u} = -\frac{uw}{r} + \left[(T-D)\cos(\alpha+\gamma) - L\sin(\alpha+\gamma)\right]\frac{1}{m} \tag{1}$$

$$\dot{w} = \frac{u^2}{r} - \frac{g_0 r_0^2}{r^2} + \left[(T-D)\sin(\alpha+\gamma) + L\cos(\alpha+\gamma)\right]\frac{1}{m} \tag{2}$$

$$\dot{r} = w \tag{3}$$

$$\dot{\theta} = \frac{u}{r} \tag{4}$$

$$\dot{m} = -\frac{T}{I_{sp} g_0} \tag{5}$$

where

u = horizontal velocity component
r = radial distance from the center of earth
m = interceptor mass
$\gamma = \tan^{-1}(w/u)$ = flight path angle
D = aerodynamic drag, body axis
r_0 = radius of earth
I_{sp} = specific impulse of rocket motor

w = vertical velocity component
θ = polar angle
α = angle of attack
T = thrust, constant for each stage
L = aerodynamic lift, body axis
g_0 = gravity acceleration at sea level

For convenience we choose to rewrite Eqs. (1) through (5) in terms of dimensionless state variables U, W, R and M in accordance with the following definitions:

$$U = \frac{u}{\sqrt{g_0 r_0}}, \quad W = \frac{w}{\sqrt{g_0 r_0}}, \quad R = \frac{r}{r_0}, \quad M = \frac{m}{m_0} \tag{6}$$

where $\sqrt{g_0 r_0}$ is the circular orbit velocity at r_0 and m_0 is the initial mass of the stage.

In terms of the dimensionless state variables the equations of motion can be written as

$$\dot{U} = \sqrt{g_0/r_0}\left[-\frac{UW}{R} + (A_T - A_D)\cos(\alpha+\gamma) - A_N \sin(\alpha+\gamma)\right] \tag{7}$$

$$\dot{W} = \sqrt{g_0/r_0}\left[\frac{U^2}{R} - \frac{1}{R^2} + (A_T - A_D)\sin(\alpha+\gamma) + A_N \cos(\alpha+\gamma)\right] \tag{8}$$

$$\dot{R} = \sqrt{g_0/r_0}\, W \tag{9}$$

$$\dot{\theta} = \sqrt{g_0/r_0}\, \frac{U}{R} \tag{10}$$

$$\dot{M} = -\frac{T}{m_0 g_0 I_{sp}} \tag{11}$$

$$A_T = \frac{T}{m_0 g_0 M} \tag{12}$$

$$A_D = \frac{C_A A}{m_0 g_0} \frac{\rho_0}{2} g_0 r_0 (\rho/\rho_0) \frac{V^2}{M} \tag{13}$$

$$A_N = \frac{A_D}{C_A} \left[\sin 2\alpha \cos\frac{\alpha}{2} + \frac{5}{\pi} \frac{\lambda}{d} \sin\alpha \, |\sin\alpha| \right] \tag{14}$$

$$V = \sqrt{U^2 + W^2} \tag{15}$$

$$\gamma = \tan^{-1}\frac{W}{U} \tag{16}$$

where

A_T = thrust acceleration in g_0 units

A_D = body axis drag acceleration in g_0 units

A_N = body axis lift acceleration in g_0 units

C_A = body axis drag coefficient

A = rocket cross-sectional area

ρ = atmospheric density

ρ_0 = sea-level atmospheric density

V = dimensionless total velocity

λ = rocket length

d = rocket diameter

Reference to equations (7), (8), (13) and (14) shows that the aerodynamic drag and normal forces are calculated, respectively, along and perpendicular to the body axes of the rocket. Eqs. (13) and (14) are simple but fairly good approximations for the aerodynamic forces on slender bodies [3].

The atmospheric density ratio ρ/ρ_0 in Eq. (13) is a function of the rocket altitude h, which is given by the equation:

$$h = (R - 1)\, r_0 \tag{17}$$

We have considered three different methods for approximating the variation of ρ/ρ_0 with h. The first utilizes table lookup with linear interpolation based on a tabulated standard atmosphere. This method introduces into the simulation a function with discontinuous slopes, which has the potential of causing numerical difficulties in the descent algorithm (see Section 5). The second method uses the following exponential approximation:

$$\rho/\rho_0 = e^{-\beta h} \tag{18}$$

where $1/\beta$ = 23,500 ft. The third method uses the following analytic approximation [4]:

$$\rho/\rho_0 = [A_0 + A_1 h + A_2 h^2 + \cdots + A_{11} h^{11}]^{-4} \tag{19}$$

with

$A_0 = 1.0000000000$

$A_1 = 0.3393495800 \times 10^{-1}$

$A_2 = -0.3433553057 \times 10^{-2}$

$A_3 = 0.5497466428 \times 10^{-3}$

$A_4 = -0.3228358326 \times 10^{-4}$

$A_5 = 0.1106617734 \times 10^{-5}$

$A_6 = -0.2291755793 \times 10^{-7}$

$A_7 = 0.2902146443 \times 10^{-9}$

$A_8 = -0.2230070938 \times 10^{-11}$

$A_9 = 0.1010575266 \times 10^{-13}$

$A_{10} = -0.2482089627 \times 10^{-16}$

$A_{11} = 0.2548769715 \times 10^{-19}$

Eq. (19) is valid from 0 to 200 km. altitude and is accurate to better than 5 percent for altitudes up to 70 km. It is a considerably better approximation than the exponential model in Eq. (18) and takes no longer to execute than the table lookup scheme. Thus it represents our preferred approach.

Eqs. (7) through (17), along with either (18) or (19), are used for the trajectory simulation of each inteceptor stage while thrusting or coasting ($T = 0$). The state variables R, θ, U and W are continuous from one stage to the next. On the other hand, the state variable M representing the dimensionless mass of each stage is reset to 1 at the initiation of each new stage. From Eq. (12) it follows that A_T represents the thrusting acceleration in g_0 units for each stage at engine ignition. This is an important optimization parameter, since for a given mass ratio it determines the thrusting time for the stage. Note that the dimensionless mass state can be made continuous by defining it as the mass of rocket fuel divided by the initial takeoff mass. The total instantaneous mass for each stage is then the sum of the fuel mass and the inert mass. As noted previously, the time history of angle of attack is parameterized by letting it vary linearly for each stage. Thus a second parameter per stage is the time-rate-of-change of angle of attack.

3. Numerical Integration Method

Since each trajectory optimization requires the computation of many thousands of trajectories, there is a great deal of leverage on selecting accurate and efficient numerical integration algorithms for the trajectory optimization. Based on theoretical considerations and computer experimentation, we decided to select a single-pass 5th-order Adams-Moulton (SPAM-5) predictor-corrector algorithm as our principal method. In the single-pass Adams-Moulton method the derivative of each state is always based on the predicted rather than the corrected value of the state [5]. To illustrate the method we consider the state equation

$$\dot{X} = F[X,U(t)] \tag{20}$$

We define the estimate of the derivative F at the kth integration step based on the estimated state at the kth step by the formula

$$\hat{F}_k = F[\hat{X}_k, U(kh)] \tag{21}$$

where h is the integration step size. From previously computed derivative estimates we compute an estimate for the state X_{n+1} based on X_n with the following Adams-Bashforth 5-th order predictor formula:

$$\hat{X}_{n+1} = X_n + \frac{h}{720}(1901\hat{F}_n - 2774\hat{F}_{n-1} + 2616\hat{F}_{n-2} - 1274\hat{F}_{n-3} + 251\hat{F}_{n-4}) \tag{22}$$

Using $\hat{X}_{n+1}$ from Eq. (22), we compute $\hat{F}_{n+1}$ and then X_{n+1} with the corrector formula

$$X_{n+1} = X_n + \frac{h}{720}(251\hat{F}_{n+1} + 646\hat{F}_n - 264\hat{F}_{n-1} + 106\hat{F}_{n-2} - 19\hat{F}_{n-3}) \tag{23}$$

In the conventional AM-5 integration method, the predictor formula corresponding to Eq. (22) utilizes derivatives based on the actual states X_n rather than the state estimates used here. This requires a first pass through the state equations to compute F_n from X_n, a computation which is avoided in this single-pass method. In the conventional AM-5, then, the derivatives F_n through F_{n-3} are also based on actual states. Only F_{n+1} is based on the estimated state obtained from the predictor pass.

It should be noted that both the predictor formula in Eq. (22) and the corrector formula in Eq. (23) are derived from the area under a quartic time function which passes through each of the five derivatives. The resulting integration algorithm is therefore 5th order. The method of z transforms can be used to determine the characteristic root errors introduced by numerical integration methods [5]. For the SPAM-5 represented by Eqs. (22) and (23), the fractional error in characteristic root is given approximately

$$e_\lambda = \frac{\lambda^* - \lambda}{\lambda} \approx \frac{3}{160}(\lambda h)^5 \;, \quad |\lambda h| << 1 \tag{24}$$

Here λ is the characteristic root of the continuous system being simulated and λ^* is the equivalent characteristic root of the digital system when using the SPAM-5 integration with a step size of h.

Reference to Eq. (22) shows that the 5th-order predictor algorithm presents a startup problem, since at $t = 0$ the previous 4 derivatives are unknown. The same startup problem reappears every time there is a step change in the state-variable derivative, such as will occur in our trajectory simulation during staging. Actually, the 5th-order predictor will in fact only exhibit 5th-order accuracy when state variable derivatives up to order 4 are continuous. Thus it is important to represent the time variation of angle of attack for each stage by functions with appropriate smoothness, such as the linear time function we have assumed here.

One method of solving this startup problem is to use a Runge-Kutta algorithm for the first four integration steps in each stage before switching to the 5th-order predictor-corrector method. Unfortunately, this will add a large number of integration passes to the simulation of each stage and negate much of the speed advantage inherent in the single-pass predictor-corrector method. For example, using RK-4 as the startup method for the first four integration steps requires 16 passes through the state equations, and the resulting states will only be accurate to the 4th power of the step size h. If we use a total of 20 integration steps for each stage (using SPAM-5 we have found that this yields accuracies of the order of one part per million), then the total number of passes through the state equations per stage will be $4 \times 4 + 16 = 32$. Thus standard RK-4, when used for the first 4 steps as a startup method, requires roughly half of the overall computer execution time for the 20-step simulation of each interceptor stage.

A much more efficient startup method which at the same time provides 5th-order accuracy is an RK-4 startup algorithm due to Gear [6]. Here an RK-4 method which requires 5 passes through the state equations is used to compute F_0, F_0', F_0'', and F_0''', i.e., the first four initial derivatives of the state variable X. These derivatives are used in power series formulas to compute the state X_2 two steps in the future, as well as the derivatives F_2, F_1, F_{-1}, and F_{-2}. All the startup derivatives are now available to initiate the SPAM-5 algorithm for subeqent integration steps. For a total of 20 integration steps per stage the total required number of passes through the state equations is now $5 + 18 = 23$. The equations for the Gear RK-4 startup algorithm, when used with a step size H, are the following, where $X_{nH} = X(nH)$, $U_{nH} = U(nH)$:

$$\begin{aligned}
k_1 &= H \cdot F(X_0, U_0) && ; \quad X_H = X_0 + k_1 \\
k_2 &= H \cdot F(X_H, U_H) && ; \quad X_{2H} = X_0 + 2k_2 \\
k_3 &= H \cdot F(X_{2H}, U_{2H}) && ; \quad X_{3H} = X_0 + (3/4)(k_1 + 3k_3) \\
k_4 &= H \cdot F(X_{3H}, U_{3H}) && ; \quad X_{4H} = X_0 + (1/2)(k_1 + 2k_2 + k_3 + 4k_4) \\
k_5 &= H \cdot F(X_{4H}, U_{4H}) && ; \quad X_{5H} = X_0 + (1/12)(k_1 + 24k_2 + 3k_3 + 8k_4 + 24k_5) \\
k_6 &= H \cdot F(X_{5H}, U_{5H})
\end{aligned} \tag{25}$$

The formulas for the derivatives at $t = 0$ are given by

$$\begin{aligned} H \cdot F_0 &= k_1 \\ H^2 \cdot F_0' &= (1/6)(-5k_1 + 3k_3 + 14k_4 - 18k_5 + 6k_6) \\ H^3 \cdot F_0'' &= (1/9)(4k_1 - 4k_3 - 19k_4 + 30k_5 - 11k_6) \\ H^4 \cdot F_0''' &= (1/9)(-k_1 + k_3 + 7k_4 - 12k_5 + 5k_6) \end{aligned} \tag{26}$$

We note that the step size H for these calculations can be chosen completely independently of the step size h that is used for subsequent integration steps. From X_0 and its first four derivatives in Eq. (25) we calculate X_2 and the derivatives F_2, F_1, F_{-1}, and F_{-2} from the following power series formulas:

$$\begin{aligned} X_2 &= X_0 + 2(h/H)(HF_0) + 2(h/H)^2(H^2F_0') + \frac{4}{3}(h/H)^3(H^3F_0'') + \frac{2}{3}(h/H)^4(H^4F_0''') \\ F_2 &= F_0 + 2(h/H^2)(H^2F_0') + 2(h^2/H^3)(H^3F_0'') + \frac{4}{3}(h^3/H^4)(H^4F_0''') \\ F_1 &= F_0 + (h/H^2)(H^2F_0') + \frac{1}{2}(h^2/H^3)(H^3F_0'') + \frac{1}{6}(h^3/H^4)(H^4F_0''') \\ F_0 &= F(X_0, U_0) \\ F_{-1} &= F_0 - (h/H^2)(H^2F_0') + \frac{1}{2}(h^2/H^3)(H^3F_0'') - \frac{1}{6}(h^3/H^4)(H^4F_0''') \\ F_{-2} &= F_0 - 2(h/H^2)(H^2F_0') + 2(h^2/H^3)(H^3F_0'') - \frac{4}{3}(h^3/H^4)(H^4F_0''') \end{aligned} \tag{27}$$

The choice of step size H in the above Gear RK-4 startup equations should be made small enough to ensure that truncation errors are negligible but not so small that roundoff errors predominate. In our trajectory simulations we let $H = h/8$.

Starting with the initial state X_0 at the beginning of each stage, Eqs. (25), (26) and (27) are used to compute X_2 and the derivatives F_2, F_1, F_0, F_{-1}, and F_{-2}. For all subsequent steps in the stage simulation, the SPAM-5 integration algorithm of Eqs. (22) and (23) is used. Since the time derivative of the mass state M is the constant given in Eq. (11), simple Euler integration can be used for that integration.

We recall that the SPAM predictor-corrector method uses a fixed integration step size. Since the acceleration components given by Eqs. (7) and (8) are proportional to the inverse of the dimensionless mass M, it is clear that when M becomes small, the integration truncation errors will become larger for a given integration step size h. However, the optimal solutions are unlikely to permit the final M for each stage to become less than 0.2 to 0.3. Under these conditions the performance improvement which would be achieved by using a smaller step size toward the end of each stage burn is more than offset by the increased computational requirements associated with integration methods suitable for a variable step size.

As noted earlier, we have found that the SPAM-5 method with the Gear RK-4 starter provides accuracies of the order of one part per million when 20 integration steps per stage are used. For a given mass ratio the burn time for each stage is determined by the thrust and hence the initial thrust acceleration. The integration step size h for each stage is therefore equal to the stage burn time divided by 20.

4. Constraints and Final Problem Formulation

To complete the statement of the optimization problem it is necessary to introduce certain constraints on the trajectory and its defining parameters. The most obvious of these are the ones required for target interception. After final stage cutoff, the payload must coast in such a manner that at the specified intercept time, t_f, the position variables, $R(t_f)$ and $\theta(t_f)$, match those of the target.

There are several ways to implement the intercept conditions. We have imposed them at the time of final-stage cutoff, t_c. If $R(t_c)$, $\theta(t_c)$, $R(t_f)$, and $\theta(t_f)$ are known and the coast is an out-of-the-atmosphere conic transfer, the values $\gamma(t_c)$ and $V(t_c)$ required for intercept are determined by solving an appropriate Lambert problem. We do this numerically by the methods given in [7]. The errors between the required and actual values of $\gamma(t_c)$ and $V(t_c)$ must be zero for intercept and these conditions give two equality constraints on the trajectory at $t = t_c$.

We have found that unconstrained optimal conic coast trajectories re-enter the atmosphere or even pass through the earth's surface. To assure that this doesn't happen, the minimum altitude during the coast is computed (as part of the solution of the Lambert problem) and specified to lie outside the sensible atmosphere. The error between the computed minimum altitude and its specified value forms, when set to zero, a third equality constraint.

In addition to the equality constraints on the trajectory, inequality constraints may be imposed on some of the problem parameters. For example, an initial stage acceleration, A°_T, may have upper and lower limits, A_{max} and A_{min}. To avoid treating these constraints directly in the algorithmic process, we impose them implicitly by introducing a nonlinear transformation of a new parametric variable. In the case just mentioned a suitable transformation is

$$A^0_T = \frac{A_{max} + A_{min}}{2} + \frac{A_{max} - A_{min}}{2} \sin a_T \tag{28}$$

where a_T is the new unconstrained parameter.

Putting all of the above details together in a compact notation yields a problem of the form:

$$\text{minimize } f(z) \text{ subject to } g_i(z) = 0\,,\ i = 1,2,3. \tag{29}$$

Here: $f(z)$ is the ratio of the launch mass to the payload mass, the $g_i(z)$ are the errors in meeting the equality constraints, and z is a vector whose components are the "unconstrained" parameters arising from models described in Sections 1 and 2. Given z it is clear that $f(z)$ and $g_i(z)$ may be evaluated by integrating the equations of motion, computing $M(t_c)$, $\gamma(t_c)$, $V(t_c)$, $R(t_c)$, and $\theta(t_c)$, and solving the Lambert problem determined by the target specification.

Our algorithm for the numerical solution of (29) requires the gradient (collection of N first partial derivatives) of functions such as $f(z)$. While it is possible to derive formulas for the partials (they may be written in terms of the differential equations adjoint to the linearized equations of motion), they are exceedingly complex because of the nonlinear functions appearing in Eqs. (7) - (15). This motivates our desire to use finite differences for the gradient calculations.

5. Numerical Solution of the Optimization Problem

A variety of numerical approaches have been used to solve trajectory optimization problems with equality constraints. These included: (1) gradient projection methods, (2) Newton-Raphson solution of the necessary conditions, (3) penalty function methods. Approach (1) gives slow convergence; approach (2) requires second derivatives of problem data and good initial estimates;

approach (3) leads to badly conditioned (though unconstrained) minimization problems. We have followed approach (3), attacking its disadvantage by using a rapidly convergent quasi-Newton algorithm [8,9] and an augmented Lagrangian for the penalty function.

In the usual penalty function method approximate solutions of (29) are sought by algorithmic minimization of

$$F_P(z) = f(z) + \sum_{i=1}^{3} \mu_i [g_i(z)]^2 \tag{30}$$

It can be shown [8,9] that the equality conditions can be accurately enforced by choosing the penalty coefficients, $\mu_i > 0$, to be sufficiently large. In practice, numerical hazards, such as slow convergence or convergence to false minima, are reduced by minimizing $F_P(z)$ several times with successively larger values for the penalty coefficients. At each successive stage the starting point for the minimization algorithm is taken as the solution point from the previous stage. Even so, the conditioning of $F_P(z)$ worsens [8,9] as the μ_i increase and there is a practical limit to the accuracy which can be achieved. Numerical errors in the minimization algorithm and the evaluation of $F_P(z)$ and its gradient eventually become limiting.

In the augmented Lagrangian approach $F_P(z)$ is replaced by

$$F_L(z) = f(z) + \sum_{i=1}^{3} \lambda_i g_i(z) + \sum_{i=1}^{3} \mu_i [g_i(z)^2 \tag{31}$$

where the λ_i are real numbers approximating the Lagrange multipliers for the minimization problem (29). When $F_L(z)$ is minimized it is possible to satisfy the equality constraints accurately with much smaller values for the penalty coefficients [8,9]. The resulting improved conditioning of $F_L(z)$ reduces the bad effects of the numerical errors. Again, it is advantageous to solve a sequence of minimization problems with successive initializations, where in this case both the λ_i and the μ_i are adjusted. We have used the adjustment scheme proposed by Powell and described on page 134 of [8] with good results. It eliminates the need for human intervention in selecting the parameters λ_i and μ_i and improves accuracy of equality constraints over the simple penalty function approach by a factor of at least 10.

Because of the highly nonlinear character of $F_L(z)$ and its poor conditioning it is necessary to pay careful attention to the procedure for its unconstrained minimization. Certainly, the second order properties of $F_L(z)$ must be taken into account. We have found the BFGS, quasi-Newton program of Shanno and Phua [10] to be effective. Its line search has been modified to compute derivatives along the search direction directly by forward differences. This eliminates the need for gradient evaluations during the line search.

The performance of a quasi-Newton algorithm is predicated on the smoothness of the function being minimized. The function should be at least twice continuously differentiable. Here, the representation of empirical data appearing in the equations of motion is important. See, for example, the comments in Section 2 on computing the atmospheric density by table lookup with linear interpolation.

Another concern is the forward difference computation of the partial derivatives of $F_L(z)$. If the step size is too small, the effects of round off errors are exacerbated; if the step size is too large, truncation errors become appreciable. If the machine precision is ε, it can be argued [9] that the step size should be the order of $\varepsilon^{1/2}$. In our case the machine precision $\varepsilon \equiv 10^{-12}$ is determined by the AD 100, which has a 40 bit significand. We have found that the step size 10^{-6} is reasonable, but that experimentation with the step size can improve the accuracy noticeably. Even better accuracy has been obtained by using central differences for the partial derivatives. It reduces the effects of round-off errors because a larger step size may be used for the same truncation error [9]. Of course, 2N + 1 evaluations of $F_L(z)$ are then needed to obtain $F_L(z)$ and its gradient.

6. Example of Optimal Trajectories

In this section we consider the results of a typical optimization case. $\theta(t_f) - \theta_0$, the total change in polar angle of the trajectory, is set equal to 30 degrees. This corresponds to an interceptor range of 2094 miles. The total time of interceptor flight is prescribed to be 300 seconds and the target is intercepted at an altitude of 200 km. Stage takeoff weight is equal to 10,000 kg and physical parameters are assumed to be similar to those of a Minuteman III. The specific impulse I_{sp} of the rocket engines is equal to 300 seconds, and the ratio of initial fuel weight to inert weight for the rocket motor of each stage is assumed to be 10. The constraint on minimum altitude during the final coast to the target is set at 60 km. The number of booster stages is equal to 4, with equal mass ratios prescribed for each stage. The common mass ratio is therefore a parameter. As noted earlier, the performance objective is to maximize the final payload weight. Two cases are considered, one in which there is no coasting between booster stages, and the second in which coasting is allowed. For the two cases the number of parameters to be optimized is 11 and 17, respectively. The results are summarized below.

	No coast between stages	Coast between stages
Final optimal payload weight	7.73 kg	8.7 kg
Mass ratio per stage	4.12	4.05
Minimum altitude in final coast to target	59.52 km	60.06 km
Burnout speed (V_c = circular orbit speed)	1.724 V_c	1.707 V_c
Minimum altitude in final coast to target	59.52 km	60.06 km
Burnout altitude	134.65 km	118.9 km
Burnout time	91.43 sec	98.88 sec
Launch flight path angle, γ_0	64.05 °	64.57 °
Initial acceleration and total burn time, stage 1	11.86 g, 19.16 sec	12.71 g, 18.30 sec
Coast time between stages 1 and 2		8.90 sec
Initial acceleration and total burn time, stage 2	12.49 g, 18.18 sec	25.31 g, 8.80 sec
Coast time between stages 2 and 3		8.85 sec
Initial acceleration and total burn time, stage 3	4.99 g, 45.54 sec	29.08 g, 7.71 sec
Coast time between stages 3 and 4		39.92 sec
Initial acceleration and total burn time, stage 4	26.58 g, 8.55 sec	35.39 g, 6.39 sec
Coast time to target	208.57 sec	201.12 sec

Note that the optimal payload for the case where coasting is allowed between booster stages is somewhat greater than for the no-coast case. In both cases the time for the third stage is much longer than the time for the other stages. For the no-coast case this results in a long burn time; for the coasting case this results in a long post-burn coast time.

The accuracies in meeting the constraints on $\gamma(t_c)$ and $V(t_c)$ in the above two cases were approximately 0.0005 radians and 1 meter/sec, respectively. The differences in the minimum altitude during the final coast to the target for the two cases, compared with the specified constraint altitude of 60 km., can be observed directly. Additional inequality constraints were imposed on many of the parameters using the transformation technique illustrated in Eq. (28). None of these constraints turned out to be active in the example.

On the AD 100 the execution time per 20-step stage integration, thrusting or coasting, is approximately 0.6 milliseconds. To illustrate typical overall AD 100 computational times, consider a 4 stage trajectory with 3 coasts. This requires 17 parameters to be optimized. To compute the cost function and its 17 gradient components takes 18(7)(0.6) = 75.6 milliseconds. Additional trajectories will be needed for each iteration to solve the line search problem, so that 90 milliseconds represents a reasonable value for the average AD 100 time required per iteration. The approximately 200 to 400 iterations needed for satisfactory convergence to an optimal solution then require 18 to 36 seconds of AD 100 time. To these times we must add the time required for the VAX to implement the optimization algorithm for each trial, which in general increases the average overall time per optimization to several minutes.

7. Conclusions

In this paper we have considered techniques for determining the optimal trajectories of earth-launched interceptor rockets which are accelerated to over twice orbital velocity. The objective of the optimization is to maximize the payload with a given interceptor takeoff weight. Terminal constraints have been enforced using penalty functions. The required gradients of the cost functions have been computed numerically using finite differences. We have shown that use of a special multiprocessor computer, the AD 100, in conjunction with a VAX host computer, can reduce very substantially the time required for each trajectory optimization. Utilization of a 5th-order single-pass predictor-corrector integration method with a Gear RK-4 startup algorithm for the trajectory integration also has contributed significantly to the reduction in time. Typical AD 100 computation times for each 5 to 7-stage trajectory range between 3 and 4 milliseconds. For an overall optimization requiring many thousands of trajectory calculations this translates into a total solution time of minutes, compared with hours when the VAX alone is used.

Some preliminary results have been presented for a 4-stage example. It is found that allowing a coast period between booster stages improves the optimal payload significantly. Future research efforts will include parametric studies of the effect of different prescribed flight times, target range and altiitude, payload mass, refined aerodynamic and propulsion models, and aero-assisted midcourse maneuvers.

8. Acknowledgement

The research reported in this paper has been supported by the Innovative Science and Technology Office, U.S. Strategic Defense Initiative Organization, under contract number DOD-C-F49620-86-C-0138. The authors also acknowledge the support provided by Applied Dynamics International, Ann Arbor, Michigan.

References

[1] N.X. Vinh, A. Buseman and R.D. Culp, *Hypersonic and Planet Entry Flight Mechanics*, The University of Michigan Press, Ann Arbor, Michigan, 1980.

[2] L.E. Fogarty and R.M. Howe, "Flight Simulation of Orbital and Reentry Vehicles," *IRE Transactions on Electronic Computers*, Vol. EC-11, Aug., 1962.

[3] L.H. Jorgensen, "Estimation of Aerodynamics for Slender Bodies Alone and with Lifting Surfaces," *AIAA Journal*, Vol. 11, No. 3.

[4] *U.S. Standard Atmosphere Supplements*, 1966, U.S. Government Printing Office, Washington D.C.

[5] R.M. Howe, "Transfer Function and Characteristic Root Errors for Fixed-Step Integration Algorithms," *Transactions of the Society for Computer Simulation*, 2 (4); 293-320.

[6] C.W. Gear, "Runge-Kutta Starters for Multistep Methods," *ACM Transactions on Mathematical Software*, Vol. 6, No. 3, Sept., 1980, pp 263-79.

[7] R. H. Battin, "An Elegant Lanbert Algorithm," *Journ. Guidance, Control, and Dynamics*, vol. 7, pp. 662-670, 1984.

[8] R. Fletcher, *Practical Methods of Optimization*, vol. 2, Wiley-Interscience, 1981.

[9] P. E. Gill, W. Murray and M. H. Wright, *Practical Optimization*, Adademic Press, 1981.

[10] D. F. Shanno and K.H.Phua, "Minimization of Unconstrained Multivariate Functions," *ACM Transactions on Mathematical Software*, vol. 6, pp. 618-622, 1980.

OPTIMAL INTERCEPTION WITH TIME CONSTRAINT[1]

N. X. VINH,[2] P. LU[3], R. M. HOWE[2], and E. G. GILBERT[2]

---

[1] This research was supported by US Army Strategic Defense Command contract No. DASG60-88-C-0037.

[2] Professor of Aerospace Engineering, The University of Michigan, Ann Arbor, Michigan.

[3] Research Associate, The University of Michigan, Ann Arbor, Michigan.

Abstract. This paper considers the problem of minimum-fuel interception with time constraint. The maneuver consists of using impulsive thrust to bring the interceptor from its initial orbit into a callision course with a target which is moving on a well defined trajectory. The intercept time is either prescribed, or is restricted to be less than a upper limit.

The necessary conditions and the transversality conditions for optimality were discussed. The mothed of solution amounted to first solving a set of equations to obtain the primer vector for an initial one-impulse solution. Then based on the information provided by the primer vector, rules were established to search for the optimal solution if the initial one-impulse trajectory was not optimal. The mothed is general in the sense that it allows for solving the problem of three-dimensional interception with arbitrary motion for the target.

Several numerical examples were presented, including orbital interceptions and interception at hyperbolic speeds of a ballistic missile.

Key Words Orbital transfer, optimal interception, primer vector theory, hodograph theory, Lambert's problem, interception of ballistic missile.

1. Introduction

The two problems of interception and rendezvous with time constraint are two fundamental problems in space maneuvering. We shall consider the first problem in this paper. In the following content, the notations with bold faces represent vectors, the notations with plain faces stand for the magnitudes of the corresponding vectors and scalar variables. The product of two vectors is understood as inner product.

The interceptor is initially in a motion defined by its position vector $\mathbf{r}_0(t)$ assumed known. At a certain time t_0, called acquisition time, or sometimes initial time, the target is at the position $\mathbf{r}_T(t_0)$ with velocity $\mathbf{V}_T(t_0)$ assumed known. Hence, if its subsequent motion is uncontrolled and is only subject to a Newtonian gravitational attraction, it is well determined by the two functions $\mathbf{r}_T(t)$ and $\mathbf{V}_T(t)$ which can be computed from the given data. It is proposed to intercept the target at a final time $t_f > t_0$ so that the characteristic velocity required for the transfer is minimum. The specific assumption on t_0 and t_f will be given later when we consider the different types of interception.

It should be noticed that, for the sake of generality, the function $\mathbf{r}_0(t)$ can be completely arbitrary. It may represent an orbital Keplerian motion for the interceptor, or an atmospheric ascent trajectory for a rocket or an airplane which carries the interceptor. Likewise, we can simply assume that the function $\mathbf{r}_T(t)$ defining the motion of the target is known. On the other hand, we shall assume that, in the time interval $[t_1, t_f]$ where t_1, $t_0 \le t_1 < t_f$, is the instant of the first ignition of the control engine, the interceptor is only subject to the inverse-square force field and a controlled action of a propulsive force $\mathbf{F}$.

2. Necessary Conditions for Optimality

We consider the general problem of transfer. A rocket, considered as a mass point with varying mass is governed by the equations

$$\begin{aligned}\dot{\mathbf{r}} &= \mathbf{V},\\ \dot{\mathbf{V}} &= \mathbf{g} + \mathbf{\Gamma},\\ \dot{U} &= \Gamma,\end{aligned} \tag{1}$$

where $\mathbf{g}$ is the acceleration of the gravity, a function of the position, U is the characteristic velocity spent since the initial time

$$U = \int_{t_0}^{t} \Gamma dt, \tag{2}$$

with $\mathbf{\Gamma} = \mathbf{F}/m$ being the thrust acceleration. For a high thrust propulsion system, U is a measure of the fuel consumption.

Consider the Hamiltonian of the system

$$H = \mathbf{p}_r \mathbf{V} + \mathbf{p}_V(\mathbf{\Gamma} + \mathbf{g}) + p_U \Gamma, \tag{3}$$

where the adjoint variables $\mathbf{p}_r$, $\mathbf{p}_V$ and p_U satisfy the equations

$$\begin{aligned}\dot{\mathbf{p}}_r &= -\frac{\partial H}{\partial \mathbf{r}},\\ \dot{\mathbf{p}}_V &= -\frac{\partial H}{\partial \mathbf{V}} = -\mathbf{p}_r,\\ \dot{p}_U &= -\frac{\partial H}{\partial U}.\end{aligned} \tag{4}$$

To maximize H with respect to the control vector $\mathbf{\Gamma}$, we first maximize the product $\mathbf{p}_V \mathbf{\Gamma}$. Then $\mathbf{\Gamma}$ must be selected parallel to $\mathbf{p}_V$ and hence

$$H^* = \mathbf{p}_r \mathbf{V} + \mathbf{p}_V \mathbf{g} + (p_V + p_U)\Gamma, \tag{5}$$

where p_V is the length of $\mathbf{p}_V$.

The thrust acceleration is now linear, subject to

$$0 \leq \Gamma \leq \Gamma_{max}. \tag{6}$$

Consider the switching function

$$\kappa = p_V + p_U. \tag{7}$$

Then, if

$$\kappa > 0, \quad \text{select} \quad \Gamma = \Gamma_{max} \quad \text{(Boost arc)},$$

$$\kappa < 0, \quad \text{select} \quad \Gamma = 0 \quad \text{(Coast arc)},$$

$$\kappa \equiv 0, \quad \text{select} \quad \Gamma = \text{variable} \quad \text{(Sustained arc)}.$$

We have Lawden's optimal law for the thrust control (Refs. 1 and 2):

— Whenever the engine is operating, the thrust direction is parallel to the vector $\mathbf{p}_V$, called the primer vector.

— If $\kappa > 0$, we use $\Gamma = \Gamma_{max}$, while if $\kappa < 0$, we use $\Gamma = 0$. The thrust is switched on and off at $\kappa = 0$.

The problem is solved if we know the time history of $\mathbf{p}_V$ and the switching function κ. For example, if we plot the function κ versus the time, we have the typical variation as in Fig. 1. We use the maximum thrust directed along $\mathbf{p}_V$ between t_1 and t_2 and then between t_3 and t_4. The remaining arcs are coast arcs. Of course, the terminal conditions must be satisfied. For very high thrust, we can use the approximation $\Gamma_{max} \rightarrow \infty$. The time interval Δt for each boost arc tends to zero and we shall have the typical variation of κ in Fig. 2. The thrusting phases are approximated by the impulses I_1 and I_2. For impulsive thrust, by changing the independent variable from t to U, it can be shown that, across an impulse, the functions $\mathbf{r}(t)$, $\mathbf{g}(\mathbf{r})$, $\mathbf{p}_r$ and $\mathbf{p}_V$ are continuous (Ref. 2). On the other hand, we write

$$\frac{d\mathbf{V}}{dU} = \frac{\mathbf{g}}{\Gamma_{max}} + \frac{\mathbf{p}_V}{p_V} \quad \rightarrow \quad \frac{\mathbf{p}_V}{p_V}.$$

Hence, integrating across an impulse, we have the discontinuity in $\mathbf{V}$

$$\Delta\mathbf{V} = \mathbf{V}_2 - \mathbf{V}_1 = (\frac{\mathbf{p}_V}{p_V})\Delta V,$$

where ΔV is the characteristic velocity change across an impulse.

The adjoint p_U satisfies the equation

$$\dot{p_U} = -\frac{\partial H^*}{\partial U} = -\frac{\partial}{\partial U}[\Gamma^* \kappa].$$

On a coast arc, $\Gamma^* = 0$, and on a sustained arc, $\kappa = 0$ and we have p_U =constant. But on a boost arc, with $\Gamma^* = \Gamma_{max}(U)$, we consider the equation for the variation of the mass

$$\frac{dm}{dt} = -\frac{F_{max}}{c} = -\frac{m\Gamma_{max}}{c},$$

where c is the constant exhaust velocity for a high thrust propulsion system. By integrating the equation, we obtain

$$m = m_0 \exp(-\frac{U}{c}).$$

Hence

$$\Gamma_{max}(U) = \frac{F_{max}}{m} = \frac{F_{max}}{m_0} \exp(\frac{U}{c}).$$

The adjoint equation for p_U becomes

$$\dot{p_U} = -\frac{\Gamma_{max}\kappa}{c}.$$

Since $\kappa > 0$ on boost arc, p_U is decreasing along a boost arc. For the case of infinite thrust, since across an impulse, U has a finite variation, we write

$$\frac{dp_U}{dU} = -\frac{\kappa}{c}.$$

Across an impulse, $\kappa = 0$, and hence we also have p_U =constant. We conclude that, in the impulsive case, in the closed interval $[t_0, t_f]$, p_U =constant and from the transversality condition in the next section

$$p_U = p_{Uf} = -1.$$

It is then sufficient to consider $\mathbf{p}_V$ on coast arcs for impulsive thrust since we have $\kappa = p_V + p_U \leq 0$, therefore $p_V \leq 1$ on the interval $[t_0, t_f]$.

The solution for $\mathbf{p}_V$ on a coasting arc has been obtained by Lawden for a Newtonian central force field in Ref. 1 and by Vinh for a general, time invariant force field in Ref. 3.

Along a coasting arc, we consider a rotating coordinate system $MSTW$ with M at the rocket, the $S-$axis along the position vector, positive outward, the $T-$axis in the plane of the motion, orthogonal to the $S-$axis and positive in the direction of motion and the $W-$axis completing a right-handed system as shown in Fig. 3. Notice that θ is the true anomaly measured from the perigee of the osculating orbit.

Let S, T and W be the components of the primer vector $\mathbf{p}_V$. We have (Ref. 1)

$$\begin{aligned} S &= A\cos\theta + Be\sin\theta + CI_1, \\ T &= -A\sin\theta + B(1+e\cos\theta) + \frac{(D - A\sin\theta)}{1+e\cos\theta} + CI_2, \\ W &= \frac{E\cos\theta + F\sin\theta}{1+e\cos\theta}, \end{aligned} \tag{8}$$

where

$$\begin{aligned} I_1 &= \frac{1}{(1-e^2)}[-\cos\theta + \frac{2e}{1+e\cos\theta} - 3\sqrt{\frac{\mu}{p^3}}te^2\sin\theta], \\ I_2 &= \frac{r\cos\theta}{ep\sin\theta} + \frac{p}{er\sin\theta}I_1. \end{aligned} \tag{9}$$

Here μ is the gravitational constant and e is the eccentricity of the ballistic conic with semi-major axis a and semi-latus rectum p

$$\begin{aligned} p &= a(1-e^2) \quad \text{elliptic}, \\ p &= a(e^2-1) \quad \text{hyperbolic}. \end{aligned} \tag{10}$$

It is important to notice that in Eq. (9) t is the time since the passage of the perigee. The coefficients A, B, C, D, E and F are constants of integration to be determined.

For the analysis, we also need the components of the adjoint vector $\mathbf{p}_r = -\dot{\mathbf{p}}_V$. On the rotating axes, we have the components of the derivative of $\mathbf{p}_V$

$$\begin{aligned} \dot{S} &= \frac{\sqrt{\mu p}}{r^2}[\frac{A\sin\theta - D}{1+e\cos\theta} - B + CI_3], \\ \dot{T} &= \sqrt{\frac{\mu}{p^3}}[-A(e+\cos\theta) + De\sin\theta + C\cos\theta], \\ \dot{W} &= \sqrt{\frac{\mu}{p^3}}[F(e+\cos\theta) - E\sin\theta], \end{aligned} \tag{11}$$

where

$$I_3 = \frac{e\sin^2\theta - \cos\theta}{e\sin\theta(1+e\cos\theta)^2} - \frac{I_1}{e\sin\theta}. \tag{12}$$

We conclude this section with a clarification on the constant C. In a time-invariant force field of attraction, the Hamiltonian is constant and we write equation (5)

$$H^* = \mathbf{p}_r\mathbf{V} + \mathbf{p}_V\mathbf{g} + \Gamma^*\kappa = \bar{C}$$

Since the equation is valid over the whole optimal trajectory, it suffices to evaluate the constant on a coast arc with $\Gamma^* = 0$. Lawden's solutions for $\mathbf{p}_V$ and $\mathbf{p}_r = -\dot{\mathbf{p}}_V$ as given in equations (8) and (11) apply separately for each coast arc, with $\theta = 0$ and $t = 0$ at the perigee of the transfer orbit. When connecting several arcs by impulses, the constants of integration A, B, ..., F and the time t have to be accordingly adjusted. In particular, using the equations (8) and (11) for $\mathbf{p}_V$ and $\mathbf{p}_r$, with the components on the *MSTW* system

$$\mathbf{V} = (\sqrt{\frac{\mu}{p}}e\sin\theta,\ \frac{\sqrt{\mu p}}{r},\ 0),$$

$$\mathbf{g} = (-\frac{\mu}{r^2},\ 0,\ 0),$$

by substituting above equations and (8) and (11) into Hamiltonian, we arrive at

$$-\frac{\mu e}{p^2}C = \bar{C},$$

where $\bar{C} = H^*$ is the global constant, and C is the constant on each coasting arc with eccentricity e and semi-latus rectum p. For this reason whenever $H^* = 0$ we simply take $C = 0$.

Across an impulse the term $\Gamma^*\kappa$ has the indeterminate form $\infty \times 0$. But this term is zero before and after an interior impulse since we have then either a coasting arc or a sustained arc. Hence, since $\mathbf{p}_r$ and $\mathbf{p}_V$ are continuous across an impulse

$$H^{*-} = \mathbf{p}_r\mathbf{V}^- + \mathbf{p}_V\mathbf{g} = \mathbf{p}_r\mathbf{V}^+ + \mathbf{p}_V\mathbf{g} = H^{*+}.$$

Because Γ^* is parallel to $\mathbf{p}_V$, so is $\Delta\mathbf{V}$, hence

$$\mathbf{V}^+ = \mathbf{V}^- + \frac{(\mathbf{p}_V)}{p_V}\Delta V.$$

From the two equations above we obtain

$$\mathbf{p}_r \mathbf{p}_V = 0.$$

Hence $p_V \dot{p}_V = \mathbf{p}_V \dot{\mathbf{p}}_V = -\mathbf{p}_V \mathbf{p}_r = 0$. It follows that $\kappa = \dot{\kappa} = 0$ for an interior impulse as shown in Fig. 2. As pointed out by Lawden, this is not necessarily true at the end points t_0 and t_f if an impulse occurs there. This leads to the fact that $\Gamma^* \kappa = 0$ for an interior impulse and $H^* = \mathbf{p}_r \mathbf{V} + \mathbf{p}_V \mathbf{g}$ in the entire open interval (t_0, t_f).

3. Transversality Conditions

In general, the acquisition time and states, the final time and states, may be constrained to satisfy a certain relation of the vector form

$$\mathbf{\Omega}(\mathbf{r}_0, \mathbf{V}_0, t_0, \mathbf{r}_f, \mathbf{V}_f, t_f) = 0. \tag{13}$$

For instance, in the interception problem one of the equations in (13) will be

$$\mathbf{r}_f = \mathbf{r}_T(t_f). \tag{14}$$

Equation (13) leads to a number of transversality conditions which must be satisfied by the states and the adjoint variables at the end points.

In the following application of the maximum principle, we adopt the Pontryagin-Contensou convention of maximizing the Hamiltonian for a minimum of the characteristic velocity. Hence the performance index to minimize is $J = \Gamma_f$, which is equivalent to the maximization of the final mass for impulsive propulsion system. Let I be the augmented function

$$I = J + \int_{t_0}^{t_f} (\mathbf{p}_r \dot{\mathbf{r}} + \mathbf{p}_V \dot{\mathbf{V}} + p_U \dot{U} - H) dt, \tag{15}$$

where H is defined by (3). Then besides the necessary conditions in Section 2, for a stationary value of I, we must have the variation

$$\delta I = \delta J + (\mathbf{p}_r \delta \mathbf{r} + \mathbf{p}_V \delta \mathbf{V} + p_U \delta U - H \delta t)_0^f = 0, \tag{16}$$

with all the variations satisfying $\delta\Omega = 0$. This is called transversality condition. The constraint imposed at the end points in the form (13) renders the problem more difficult, more challenging to solve. We shall examine some realistic and practical situations.

First, since U_f is arbitrary, δU_f in (16) is arbitray and independent. We have $p_{Uf} = -1$ for $\delta J + p_{Uf}\delta U_f = (1 + p_{Uf})\delta U_f = 0$. The transversality condition is reduced to

$$\delta I = (\mathbf{p}_r \delta \mathbf{r} + \mathbf{p}_V \delta \mathbf{V} - H \delta t)_0^f = 0. \tag{17}$$

Following Ref. 2, with some modification, we explicit (17) in the following cases of interest.

Since for an interception problem, the final velocity $\mathbf{V}_f$ is arbitrary, we have the condition $\mathbf{p}_{Vf} = 0$. The last arc is a coasting arc, hence $\Gamma^*(t_f) = 0$. Consequently

$$H_f^* = \mathbf{p}_{rf} \mathbf{V}_f. \tag{18}$$

If the initial time t_0, $\mathbf{r}_0$ and $\mathbf{V}_0$ are fixed, (17) becomes

$$\mathbf{p}_{rf} \delta \mathbf{r}_f - H_f^* \delta t_f = 0.$$

The condition is trivial if t_f is fixed. If t_f is not prescribed, constraint (14) requires that $\delta \mathbf{r}_f = \mathbf{V}_{Tf} \delta t_f$ and we have the orthogonality condition

$$\mathbf{p}_{rf}(\mathbf{V}_{Tf} - \mathbf{V}_f) = 0. \tag{19}$$

It should be noted that from (18) and (19) the Hamiltonian is not necessarily equal to zero because of (14) even if t_f is free in this case.

Another practical constraint is that $t_0 \le t_f \le T$ for some $T > t_0$ with t_0, $\mathbf{r}_0$ and $\mathbf{V}_0$ specified. If an optimal $t_f^* < T$ can be found, (19) remains valid. Otherwise $t_f^* = T$, the transversality condition is modified as (Ref. 4.)

$$\mathbf{p}_{rf}(\mathbf{V}_{Tf} - \mathbf{V}_f) = \alpha, \tag{20}$$

with α being a multiplier.

In the case when t_0 is free and no impulse occurs at t_0, $\delta \mathbf{r}_0 = \mathbf{V}_0^- \delta t_0$, $\delta \mathbf{V}_0 = \mathbf{g}_0 \delta t_0$, the transversality condition is simply

$$H_0^* = \mathbf{p}_{r0} \mathbf{V}_0^- + \mathbf{p}_{V0} \mathbf{g}_0.$$

Suppose an optimal t_0^* is found and the first impulse on the optimal trajectory occurs at $t_1 > t_0^*$. The impulse is an interior one and therefore $\mathbf{p}_r(t_1)\mathbf{p}_V(t_1) = 0$. Apparently any $t \leq t_1$, in particular, t_1, can also be taken as optimal initial time because $[t_0, t_1)$ is a coast period. On the other hand, if $t_0^* = t_1$, any $t < t_1$ can also be optimal initial time provided that the optimal control for the interval $[t, t_1)$ is taken as zero. In conclusion, when t_0 is free, we can always take t_0^* as the point where the first impulse occurs and accordingly $\mathbf{p}_r(t_0^*)\mathbf{p}_V(t_0^*) = 0$. Note that in choosing to do so the relation $\mathbf{p}_r(t_0^*)\mathbf{p}_V(t_0^*) = 0$ replaces $H_0^* = \mathbf{p}_{r0} \mathbf{V}_0^- + \mathbf{p}_{V0} \mathbf{g}_0$.

Finally we consider the situation where $\mathbf{r}_f$ is fixed but not the final time t_f. This amounts to considering the target as fixed. In this case we have trivially $H_f^* = 0$, that is $C = 0$.

4. Method of Solution

From the discussion in the preceeding sections we see that the primer vector $\mathbf{p}_V$ plays an essential role in finding the optimal solution. In this section we shall present an analytic method to obtain the primer vector on a one-impulse trajectory. Based on the information provided by the primer vector, we shall show that if this one-impulse trajectory is not optimal how it can be improved to approach the optimal solution.

We consider the general three dimensional case. Let t_0 be the initial time. We initiate the interception by application of an initial impulse at t_0. The initial position is $\mathbf{r}_0 = \mathbf{r}_0(t_0)$ and the initial velocity is $\mathbf{V}_0^- = \dot{\mathbf{r}}_0(t_0)$. At the final time t_f, let $\mathbf{r}_f = \mathbf{r}_T(t_f)$ be the final position. Notice that for any given t_0 and t_f, we can evaluate $\mathbf{r}_0$ and $\mathbf{r}_f$, and consequently the transfer angle Δ as well as the initial velocity $\mathbf{V}_0^-$ before the application of the impulse. Figure 4. displays the maneuver by one impulse changing $\mathbf{V}_0^-$ into $\mathbf{V}_0^+$. All the elements are now evaluated along the transfer orbit, which is well defined after solving the associated Lambert's problem. In this respect the numerical scheme developed by Battin in Ref. 5. proves very efficient. Since $\mathbf{V}_0^-$ and $\mathbf{V}_0^+$ are known, we can compute the required impulse $\Delta\mathbf{V}_0$ and hence $\mathbf{p}_V(t_0) = \Delta\mathbf{V}_0/\Delta V_0$.

Explicitly, if the initial motion of the interceptor is Keplerian, let e_0 and p_0 be the eccentricity and semi-latus rectum of this orbit and f_0 the true anomaly defining the position $\mathbf{r}_0$ as measured on this orbit. After the impulse we have the corresponding elements e, p and θ_0 of the transfer orbit obtained by solving the Lambert's problem. Let i be the angle between the initial orbital plane and the plane of the transfer orbit. Then, if u, v and w are the components of the impulse $\Delta\mathbf{V}_0$ in the $MSTW$ system attached to the transfer orbit, we have

$$\begin{aligned} u &= \sqrt{\mu}\left(\frac{e}{\sqrt{p}}\sin\theta_0 - \frac{e_0}{\sqrt{p_0}}\sin f_0\right), \\ v &= \frac{\sqrt{\mu}}{r_0}\left(\sqrt{p} - \sqrt{p_0}\cos i\right), \\ w &= \frac{\sqrt{\mu p_0}}{r_0}\sin i. \end{aligned} \tag{21}$$

The characteristic velocity for the transfer is

$$\Delta V_0 = \sqrt{u^2 + v^2 + w^2}. \tag{22}$$

Since $\mathbf{p}_V$ is a unit vector in the direction of $\Delta\mathbf{V}$, its components S, T and W are its direction cosines and we have explicitly

$$S = \frac{u}{\Delta V_0}, \quad T = \frac{v}{\Delta V_0}, \quad W = \frac{w}{\Delta V_0}. \tag{23}$$

By writing Eq. (8) with $t = \tau_0$ and $\theta = \theta_0$, where τ_0 is the time corresponding to θ_0 on the transfer orbit ($\tau = 0$ where $\theta = 0$), we have three linear equations for the six constants A, B, ..., F. For the interception problem the final velocity is free hence $\mathbf{p}_V(t_f) = 0$ as pointed out in Section 3. Then by writing Eq. (8) with $t = \tau_f = \tau_0 + (t_f - t_0)$, $\theta = \theta_f = \theta_0 + \Delta$ and putting $S_f = T_f = W_f = 0$, we have three more linear equations for evaluating the unknown constants. In particular, from the last equation in Eq. (8) we obtain

$$
\begin{aligned}
E &= \frac{pW \sin\theta_f}{r_0 \sin\Delta}, \\
F &= -\frac{pW \cos\theta_f}{r_0 \sin\Delta}.
\end{aligned}
\tag{24}
$$

For the rest of the unknown constants, C is obtained from

$$C = \frac{N}{G}, \tag{25}$$

where

$$
\begin{aligned}
N &= (\frac{p}{r_0})T + S(e\sin\theta_0 - 2\tan\frac{\Delta}{2}), \\
G &= \frac{[1+e^2+2e\cos\theta_0 - 2e\sin\theta_0\tan\Delta/2]}{e\sin\theta_0\sin\theta_f}[I_1(\tau_0)\sin\theta_f - I_1(\tau_f)\sin\theta_0] \\
&\quad + \frac{\sin\Delta}{e\sin\theta_0\sin\theta_f}.
\end{aligned}
\tag{26}
$$

A, B and D then are solved from the following

$$A\sin\Delta = S\sin\theta_f - C[I_1(\tau_0)\sin\theta_f - I_1(\tau_f)\sin\theta_0], \tag{27}$$

$$Be\sin\Delta = -S\cos\theta_f + C[I_1(\tau_0)\cos\theta_f - I_1(\tau_f)\cos\theta_0], \tag{28}$$

$$
\begin{aligned}
De\sin\Delta &= -C(\frac{[2e+(1+e^2)\cos\theta_f]}{\sin\theta_f}[I_1(\tau_0)\sin\theta_f - I_1(\tau_f)\sin\theta_0] + \frac{\cos\theta_f}{\sin\theta_f}\sin\Delta) \\
&\quad + S[2e+(1+e^2)\cos\theta_f].
\end{aligned}
\tag{29}
$$

With the constants evaluated, we can use Eq. (8) to calculate the magnitude of the primer vector along the transfer orbit

$$p_V(t) = \sqrt{S^2+T^2+W^2}. \tag{30}$$

In the computation, the time t can be computed from Kepler's equation

$$\sqrt{\frac{\mu}{a^3}}t = E - e\sin E, \tag{31}$$

where at a little risk of confusion with constant given by (24), here E denotes the eccentric anomaly such that

$$\tan\frac{\theta}{2} = \sqrt{\frac{1+e}{1-e}}\tan\frac{E}{2}. \qquad (32)$$

Once the magnitude of the primer vector is computed by above procedure, three types of typical behaviors of $p_V(t)$ are plotted in Fig. 5. They are representative, if not exhaustive. In the case (a), all necessary conditions are satisfied, the one-impulse solution is thus a candidate of optimal solution. Although in the following sections we shall see that this is the case for many realistic geometrical configurations of interception and reasonable interception time $\Delta t = t_f - t_0$, it is not conclusive so we can not exclude cases (b) and (c). In both of these cases the proposed one-impulse interception is not optimal. However, the following arguments show that for case (b) a coasting arc prior to the application of the impulse will reduce the cost and hence the optimal solution consists of an initial coasting arc. More than one impulse are needed for optimal solution for case (c).

First, from calculus of variations, the first order variational δI of the augmented function (15) is obtained from two neighboring trajectories which satisfy equations of motion (1) and end conditions. But by (15) it is straightforward that if the equations of motion is obeyed the integral in (15) yields zero, thus any variation in I is variation in J, namely $\delta I = \delta J$. By expression (17), only considering the change in cost due to initial variations because they are independent of the final variations in an interception problem, we have the variation in J

$$\delta J = \delta I = -\mathbf{p}_{V0}\delta\mathbf{V}_0 - \mathbf{p}_{r0}\delta\mathbf{r}_0 + H_0^+\delta t_0. \qquad (33)$$

where "+" sign indicates the right limits of involved functions. Since $H_0^+ = \mathbf{p}_{r0}\mathbf{V}_0^+ + \mathbf{p}_{V0}\dot{\mathbf{V}}_0$, $\dot{\mathbf{V}}_0\delta t_0 = \delta\mathbf{V}_0$ and $\delta\mathbf{r}_0 = \mathbf{V}_0^-\delta t_0$, where $\dot{\mathbf{V}}_0^+ = \dot{\mathbf{V}}_0^-$ is assumed, which is generally true if $\mathbf{r}_0(t)$ is Keplerian motion, Eq. (33) leads to

$$\delta J = \mathbf{p}_{r0}(\mathbf{V}_0^+ - \mathbf{V}_0^-)\delta t_0 = \mathbf{p}_{r0}\Delta\mathbf{V}_0\delta t_0 = \Delta V_0\mathbf{p}_{r0}\mathbf{p}_{V0}\delta t_0. \qquad (34)$$

For $\delta t_0 > 0$ we see that $\delta J < 0$ if $-\mathbf{p}_{r0}\mathbf{p}_{V0} = p_{V0}\dot{p}_{V0} = \dot{p}_{V0} > 0$. In other words, if the p_V exceeds unity immediately after t_0 as in case (b) an initial coast will reduce the cost.

As for case (c), suppose that T is the trajectory defined by $\mathbf{r}^*(t)$ with an initial impulse at t_0; T' is a neighboring trajectory, defined by $\mathbf{r}(t)$, which passes through $\mathbf{r}^*(t_0)$ at t_0 and $\mathbf{r}^*(t_f)$ at t_f with one initial impulse at t_0 and a mid-course impulse at some $t_m \in (t_0, t_f)$. According to Ref. 6. such a trajectory can always be constructed provided a nonsingularity condition is satisfied. Along T'

$$\mathbf{r}(t_m) = \mathbf{r}^*_m + \delta\mathbf{r}_m,$$

$$\dot{\mathbf{r}}^-(t_m) = \dot{\mathbf{r}}^*_m + \delta\mathbf{V}^-_m,$$

$$\dot{\mathbf{r}}^+(t_m) = \dot{\mathbf{r}}^*_m + \delta\mathbf{V}^+_m,$$

$$\Delta\mathbf{V}_m = \dot{\mathbf{r}}^+(t_m) - \dot{\mathbf{r}}^-(t_m) = \delta\mathbf{V}^+_m - \delta\mathbf{V}^-_m.$$

Also

$$\dot{\mathbf{r}}^+(t_0) - \dot{\mathbf{r}}^-(t_0) = [\dot{\mathbf{r}}^*(t_0) + \delta\mathbf{V}_0] - \dot{\mathbf{r}}^{*-}(t_0)$$

$$= \Delta\mathbf{V}_0 + \delta\mathbf{V}_0,$$

where δ stands for the small variations from T.

Cost on T

$$J = \Delta V_0.$$

Cost on T'

$$J' = |\Delta\mathbf{V}_0 + \delta\mathbf{V}_0| + |\delta\mathbf{V}^+_m - \delta\mathbf{V}^-_m|.$$

To the first order, the difference is

$$\delta J = J' - J \approx \frac{\Delta\mathbf{V}_0}{\Delta V_0}\delta\mathbf{V}_0 + |\delta\mathbf{V}^+_m - \delta\mathbf{V}^-_m|.$$

Since $\mathbf{p}_V(t_0) = \Delta\mathbf{V}_0/\Delta V_0$,

$$\delta J = \mathbf{p}_V(t_0)\delta\mathbf{V}_0 + |\delta\mathbf{V}^+_m - \delta\mathbf{V}^-_m|. \tag{35}$$

By a property of adjoint variables it is known that along T

$$\mathbf{p}_r\delta\mathbf{r} + \mathbf{p}_V\delta\mathbf{V} = \text{constant}.$$

In particular

$$\begin{aligned} \mathbf{p}_r(t_0)\delta\mathbf{r}_0 + \mathbf{p}_V(t_0)\delta\mathbf{V}_0 &= \mathbf{p}_r(t_m)\delta\mathbf{r}_m + \mathbf{p}_V(t_m)\delta\mathbf{V}_m^-, \\ \mathbf{p}_r(t_f)\delta\mathbf{r}_f + \mathbf{p}_V(t_f)\delta\mathbf{V}_f &= \mathbf{p}_r(t_m)\delta\mathbf{r}_m + \mathbf{p}_V(t_m)\delta\mathbf{V}_m^+. \end{aligned} \tag{36}$$

Noticing that $\mathbf{p}_V(t_f) = 0$ and $\delta\mathbf{r}_0 = \delta\mathbf{r}_f = 0$, we add a vanishing term $-\mathbf{p}_V(t_f)\delta\mathbf{V}_f$ to (35) and with the aid of (36)

$$\begin{aligned} \delta J &= \mathbf{p}_V(t_0)\delta\mathbf{V}_0 - \mathbf{p}_V(t_f)\delta\mathbf{V}_f + |\delta\mathbf{V}_m^+ - \delta\mathbf{V}_m^-| \\ &= -\mathbf{p}_V(t_m)(\delta\mathbf{V}_m^+ - \delta\mathbf{V}_m^-) + |\delta\mathbf{V}_m^+ - \delta\mathbf{V}_m^-| \\ &= -\mathbf{p}_V(t_m)\Delta\mathbf{V}_m + \Delta V_m. \end{aligned}$$

Let $\mathbf{d}$ be the unit vector in the direction of $\Delta\mathbf{V}_m$,

$$\delta J = \Delta V_m(1 - \mathbf{p}_V(t_m)\mathbf{d}). \tag{37}$$

Therefore if there exists a $t_m \in (t_0, t_f)$ such that $p_V(t_m) > 1$, a mid-course impulse can always be selected so that $\delta J < 0$, the greatest descent is when $p_V(t_m)$ is maximum and $\mathbf{d}$ is in the direction of $\mathbf{p}_V(t_m)$.

Note that in Ref. 6. a proof has been given to a two-impulse trajectory which states that if $p_V > 1$ between two impulses a mid-course impulse can reduce the cost, while some modification is adopted in the above treatment for our specific objective of interception. Combining the two results, we have the rule to search for an optimal multi-impulse trajectory, if necessary, by starting with a simple one-impulse solution.

5. Interception at Elliptic Speeds

The necessary conditions in Section 2, and the computation of the primer vector in Section 4 are perfectly general, that is, it is applicable to a minimum-fuel three-dimensional interception problem, for any given pair of arbitrary functions $\mathbf{r}_0(t)$ and

$\mathbf{r}_T(t)$ describing the initial motion of the interceptor and the motion of the target. If $\mathbf{r}_0(t)$ is non-Keplerian, it is sufficient to replace in Eq. (21) $\sqrt{\mu/p_0}e_0 \sin f_0$ and $\sqrt{\mu p_0}/r_0$ by the components on the S and T axes in the initial plane of the current velocity $\mathbf{V}_0^-$. The explicit transversality conditions derived in Section 3, while they allow arbitrary motion of the target, specify that the initial motion of the interceptor is Keplerian. With slight modification, we can derive similar conditions for arbitrary $\mathbf{r}_0(t)$.

To reduce the number of parameters involved in the examples in this section, we consider the initial orbit of the interceptor as circular and take $r_0 = 1$ as the unit distance. By taking the gravitational constant $\mu = 1$, the characteristic velocity is normalized with respect to the circular speed at the distance r_0. Then 2π is the dimensionless orbital period of the interceptor in its initial orbit. Although the dimensionless time and distance are used, to have a physical understanding of the results obtained, from time to time we shall choose some Earth's orbits of particular altitudes in kilometers as reference to interpret.

Problem 1.

The target is in an inner coplanar circular orbit at distance r_f. The initial time is preset, without loss of generality, equal to 0. This is the same as specifying the angular distance ω at the time t_0 (Fig. 6.). The final time t_f is subject to constraint

$$t_f \leq P, \tag{38}$$

where P is the period of the target orbit. Alternatively, it is required to intercept the target before it completes another revolution. By the explicit transversality conditions in Section 3, if an optimal $t_f^* < P$ can be found, Eq. (19) should be met, i.e.

$$\mathbf{p}_{rf}(\mathbf{V}_{Tf} - \mathbf{V}_f) = 0. \tag{39}$$

Otherwise, if $t_f^* = P$, Eq. (20) holds. It should be noted that if (38) is not present, the problem may have an optimal solution with $t_f^* > P$. As we shall see, after (38) is reinforced the constrained optimal solution does not necessarily take $t_f^* = P$, depending on the initial lead angle ω. Of course the unconstrained optimal cost is generally better than the constrained optimal cost.

To solve this problem, we apply the technique disscused in Section 4. An initial impulse is to be applied at t_0. We take the transfer angle Δ between $\mathbf{r}_0$ and a trial $\mathbf{r}_f$ as parameter. For any given Δ we can compute the time of flight from

$$\sqrt{\frac{\mu}{r_f}}t_f = r_f(\omega + \Delta). \tag{40}$$

After solving the associated Lambert's problem, the direction and the magnitude of the corresponding initial impulse are known. We can evaluate the constants in (8) by the method presented in Section 4 and then compute $\mathbf{p}_V$ and $\mathbf{p}_r$ by (8) and (11). To find a solution with $t_f^* < P$, (39) is used for iteration to determine the correct Δ, and hence t_f from (40). Although all transversality conditions $p_V(t_f) = 0$ and (39) are satisfied, for the solution to be optimal $p_V(t)$ must be of case (a) in Fig. 5. Figures 7(a) and 7(b) show the variations of $p_V(t)$ for $\omega = 20°$ and 34.78°, and $p_V(t)$ for $\omega = 50°$ (in solid line) is in Fig. 7(c), with $r_0/r_f = 1.25$. For the first two ω's the one-impulse solution is optimal and the optimal launch time coincides with $t_0 = 0$. Notice that $\dot{p}_V(0) = 0$ for $\omega = 34.78°$. The corresponding Δ angles are 225.76° and 180°. The dimensionless final times are 3.071 and 2.684, the dimensionless characteristic velocities are 0.07139 and 0.05719, which for an initial interceptor orbit with an altitude of 2,000 km, they translate into 62.14 minutes, 54.31 minutes, 0.493 km/sec and 0.394 km/sec respectively, while the period of the inner orbit is $P = 90.97$ minutes. But in the case $\omega = 50°$ the solution is not optimal. By the analysis in Section 4 we know that the behavior of $p_V(t)$ plotted in solid line in Fig. 7(c) suggests a coasting arc prior to the application of the impulse. To have more insight, we look at the case where $\omega = 34.78°$. This lead angle is special in the sense that a tangential retrograde impulse is optimal and the transfer angle Δ is exactly π, i. e. , a Hohmann type transfer. This special lead angle is given by

$$\omega^* = \pi[\sqrt{\frac{1}{8}(1+\frac{r_0}{r_f})^3} - 1]. \tag{41}$$

When the initial ω is greater than ω^*, the optimal strategy for the interceptor is to coast on the initial orbit until ω^* is formed due to relative motion then launch. The coast time is computed from

$$t_1 = \frac{(\omega - \omega^*)}{\Omega}. \tag{42}$$

where Ω is the relative angular speed

$$\Omega = \sqrt{\frac{\mu}{r_f^3}} - \sqrt{\frac{\mu}{r_0^3}}.$$

After such a coast arc is added, the variation of $p_V(t)$ for $\omega = 50°$ is shown in Fig. 7(c) in dashed line. The optimal characteristic velocity is the same as in the case when $\omega = \omega^* = 34.78°$, the final time is 67.83 minutes and the coast time is $t_1 = 13.52$ minutes.

Taking into account the constraint (38) and the fact that the Hohmann type transfer requires $\Delta = \pi$, we can easily have the range of initial lead angle ω within which the Hohmann type optimal interception is possible

$$\omega^* \leq \omega \leq \pi[\sqrt{\frac{1}{8}(1+\frac{1}{n})^3} - \frac{2}{\sqrt{n^3}} + 1], \tag{43}$$

where n is the ratio

$$n = \frac{r_0}{r_f}. \tag{44}$$

Whenever ω is within range given by (43), the optimal characteristic velocity is the same

$$\Delta V = \sqrt{\frac{\mu}{r_0}} - \sqrt{\frac{2\mu r_f}{r_0(r_0+r_f)}}. \tag{45}$$

When $0 \leq \omega < \omega^*$, we found that the initial one-impulse solution is always optimal, and always $t_f < P$. When ω exceeds the upper bound in (43) and is less than about 127°, we found that an initial coast is still needed, but of course is not given by (42) and the impulse is no longer tangential. Morever, $t_f^* = P$, thus condition (20) applies instead of (19). When ω is larger than about 127°, no initial coast is optimal and $t_f^* = P$.

The dimensionless optimal characteristic velocity for different ω ranging from 0° to 180° is plotted in Fig. 8. It is seen that ΔV depends on the lead angle ω and can be prohibitive for large ω. This dependence is due to constraint (38). If t_f is free, the interceptor can always stay on the initial orbit and launch when ω^* is formed no matter what initial configuration at t_0 is. The Hohmann type interception is then performed and the characteristic velocity is always the same, only depending on n. The launch time $0 \leq t_1$ is explicitly

$$t_1 = \begin{cases} (\omega_0 - \omega^*)/\Omega; & \text{if } \omega_0 \geq \omega^*, \\ (2\pi + (\omega_0 - \omega^*))/\Omega; & \text{if } \omega_0 < \omega^*. \end{cases} \tag{46}$$

where ω_0 is the initial lead angle, and ω^* is defined in (41). It is a simple exercise to show that the Hohmann transfer satisfies the conditions

$$\mathbf{p}_r(t_1)\mathbf{p}_V(t_1) = 0, \tag{47}$$

$$\mathbf{p}_r(t_f)(\mathbf{V}_{Tf} - \mathbf{V}_f) = 0. \tag{48}$$

For Hohmann transfer $\mathbf{V}_f$ is parallel to $\mathbf{V}_{Tf}$. Then (48) is equivalent to $H_f^* = \mathbf{p}_{rf}\mathbf{V}_f = 0$, hence $C = 0$. If furthermore

$$\begin{aligned} A &= 0, \\ B &= \frac{1-e}{4e}, \\ D &= -\frac{(1+e)^2(1-e)}{4e}, \end{aligned} \tag{49}$$

where

$$e = \frac{n-1}{n+1},$$

then since $\theta_0 = 180°$ and $\theta_f = 0°$ on the transfer orbit, we see that $p_V(t_f) = 0$ and (47) holds. In addition, $S(t_1) = 0$ and $T(t_1) = -1$, which is the characteristic of Hohmann transfer. But since $C = 0$, from (26) $N = 0$ hence

$$2S \tan\frac{\Delta}{2} = \frac{p}{r_0}T = -\frac{p}{r_0}.$$

From (27)

$$A = -\frac{p}{r_0}\frac{\sin\theta_f}{4\sin^2\Delta/2},$$

$$B = \frac{p}{r_0}\frac{\cos\theta_f}{4e\sin^2\Delta/2},$$

$$D = -\frac{p}{r_0}\frac{[2e + (1+e^2)\cos\theta_f]}{4e\sin^2\Delta/2}.$$

Let $\Delta = 180°$, $\theta_f = 0°$ and $p/r_0 = 1 - e$, we have (49).

Problem 2.

When either or both orbits of the interceptor and the target are elliptic, the basic technique and analysis remain applicable though there may be no explicit relations like in the case of two circular orbits. If the intercept time is constrained by (38) the optimal solution is also expected to show dependence on the initial configuration.

Let us consider the case where the interceptor is still in a circular orbit defined by $r_0 = 1$, but the target is on an inner coplanar elliptic orbit with eccentricity e_T and semi-latus rectum p_T (Fig. 9). It should be noticed that although the orbits are well defined geometrically by the quantities r_0, e_T and p_T, the motion with respect to the time on these orbits can be arbitrary. We assume these motions are known. That is, at t_0, let η be the lead angle of the interceptor with respect to the perigee of the target orbit, ω be the lag angle of the target with respect to the perigee. Both η and ω are known. For a given η, different ω represents different initial configuration.

As for numerical example, we consider a target orbit such that $e_T = 0.2$, $p_T = 0.6$ and select the time t_0 such that $\eta = 30°$. The angle ω is taken as a varying parameter. The method of solution is similar as described in Problem 1, with the flight time $t_f - t_0$ for a transfer angle Δ evaluated by Kepler's equation along the target orbit, instead of (40).

The verification of function $p_V(t)$ against the discussion in Section 4 reveals that for a given η there exists an ω_c, in our case $\omega_c = 101.008°$, such that when $\omega \leq \omega_c$ the initial one-impulse solution is optimal. A coasting arc is needed for optimality when $\omega > \omega_c$. Furthermore, in our case for $148.4° \leq \omega < 176.6°$, $t_f^* = P = 3.1046$ with a coasting prior to the impulse. For $\omega > 176.6°$, $t_f^* = P$ without coasting. Figure 10 gives the variation of optimal ΔV vs ω for $0° \leq \omega \leq 160°$. It should be noted that in the present situation the optimal characteristic velocity shows stronger dependence on ω as in Fig. 10, unlike in Problem 1 where ω in a certain range yields the same ΔV. There exists a overall optimal ΔV corresponding to $\omega^* < \omega_c$, in our case $\omega^* = 98.437°$. The special aspect of the optimal solution for ω^* is that the optimal transfer trajectory tangentially intersects the target orbit at the intercept point. We shall show that this particular trajectory is also the minimum fuel transfer trajectory from the position $\mathbf{r}_0(t_0)$ to the target orbit without considering interception.

Because of the tangency of two orbits, $\mathbf{V}_{Tf}$ is parallel to $\mathbf{V}_f$. Transversality condition (19) is equivalent to $H_f^* = \mathbf{p}_{rf}\mathbf{V}_f = 0$. Hence $C = 0$ and $N = 0$. From (26) we have

$$\frac{p}{r_0}T + S(e\sin\theta_0 - 2\tan\frac{\Delta}{2}) = 0, \tag{50}$$

where S and T are the components of $\mathbf{p}_V(t_0)$ which are proportional to

$$(1 + e\cos\theta_0)^2[1 - \frac{1}{\sqrt{1 + e\cos\theta_0}}] = e\sin\theta_0(2\tan\frac{\Delta}{2} - e\sin\theta_0). \tag{51}$$

In deriving (51) we have used the polar equation

$$\frac{p}{r_0} = 1 + e\cos\theta_0$$

to eliminate p. Next, by writing the condition for collinearity of the two vectors

$$\mathbf{V}_f = (\sqrt{\frac{\mu}{p}}e\sin\theta_f, \frac{\sqrt{\mu p}}{r_f}),$$

$$\mathbf{V}_{Tf} = (\sqrt{\frac{\mu}{p_T}}e_T\sin(\eta + \Delta), \frac{\sqrt{\mu p_T}}{r_f}),$$

we have

$$(\frac{r_0}{p_T})(1 + e\cos\theta_0)e_T\sin(\eta + \Delta) = e\sin(\theta_0 + \Delta). \tag{52}$$

Finally we express the equality of radii on the two orbits at t_f as

$$(\frac{r_0}{p_T})(1 + e\cos\theta_0)[1 + e_T\cos(\eta + \Delta)] = 1 + e\cos(\theta_0 + \Delta). \tag{53}$$

The three equations (51), (52) and (53) can be solved for the unknowns e, θ_0 and Δ^*. The angle ω^* can then be deduced from the Kepler's equation.

The problem of finding a minimum fuel transfer orbit from a given position with one impulse to a given orbit is in the area of parametric optimization. We consider the problem of minimum fuel transfer from the position $\mathbf{r}_0(t_0)$ to the target orbit by following the hodograph theory presented in Ref. 7. We look at the condition required for the velocity $\mathbf{V}(t_0)$ after the impulse for leading the transfer trajectory to a point on the target orbit at the down range angle Δ with radius r_f. Let x and y be the components of the normalized velocity $\mathbf{V}(t_0)/\sqrt{\mu/r_0}$ on the MST system. On the transfer orbit with eccentricity e, semi-latus rectum p and true anomaly θ, we have

$$\begin{aligned} x &= \sqrt{\frac{r_0}{p}}e\sin\theta_0 = \frac{e\sin\theta_0}{\sqrt{1 + e\cos\theta_0}}, \\ y &= \sqrt{\frac{p}{r_0}} = \sqrt{1 + e\cos\theta_0}. \end{aligned} \tag{54}$$

At the final point

$$y_f = \frac{\sqrt{pr_0}}{r_f} = \sqrt{\frac{r_0}{p}}[1 + e\cos(\theta_0 + \Delta)]. \tag{55}$$

Let

$$n = \frac{r_0}{r_f}. \tag{56}$$

From (54)–(56), we have the equation for x and y in the MST system

$$(n - \cos\Delta)y^2 + \sin\Delta xy - (1 - \cos\Delta) = 0. \tag{57}$$

Equation (57) shows that the tip of the velocity $\mathbf{V}(t_0)$ must be on a hyperbola with asymptotes MS and MM_f (Fig. 11). Since the initial normalized velocity has the components $(0, 1)$, the minimum ΔV corresponds to the shortest distance from this point to the hyperbola (57) for prescribed r_f and Δ. When r_f varies as a function of Δ (Fig. 9), we have a family of hyperbolas defined by

$$f(x,y,\Delta) = [\frac{r_0}{p_T}(1+e_T\cos(\eta+\Delta)) - \cos\Delta]y^2 + \sin\Delta xy - (1-\cos\Delta) = 0. \tag{58}$$

This family of hyperbolas has an envelope which is obtained by eliminating Δ between (58) and equation $\partial f/\partial\Delta = 0$

$$[\sin\Delta - \frac{r_0}{p_T}e_T\sin(\eta+\Delta)]y^2 + \cos\Delta xy - \sin\Delta = 0. \tag{59}$$

After elimination of Δ between (58) and (59), we arrive at

$$\alpha y^2 + x^2 + 2\beta xy + \gamma = 0, \tag{60}$$

where

$$\begin{aligned} \alpha &= 1 + (\frac{r_0}{p_T})^2(e_T^2 - 1) - 2\frac{r_0}{p_T}e_T\cos\eta, \\ \beta &= -\frac{r_0}{p_T}e_T\sin\eta, \\ \gamma &= 2[\frac{r_0}{p_T}(1+e_T\cos\eta) - 1]. \end{aligned} \tag{61}$$

Since $\beta^2 - \alpha > 0$, the curve (60) is also a hyperbola. The terminus of the optimal velocity $\mathbf{V}(t_0)$ must be on this envelope. The shortest distance from the point $(0,1)$ to (60) is obtained by solving (60) and the equation for orthogonality

$$\frac{x}{x+\beta y} = \frac{y-1}{\alpha y + \beta x}. \tag{62}$$

If we use an auxiliary variable z

$$z = \frac{x}{y} = \frac{e\sin\theta_0}{1+e\cos\theta_0}, \tag{63}$$

by combining (60), (62) and (63), we obtain a quartic equation in z

$$A_0z^4 + A_1z^3 + A_2z^2 + A_3z + A_4 = 0, \tag{64}$$

where

$$\begin{aligned} A_0 &= 1 + \gamma\beta^2, \\ A_1 &= 4\beta - 2\beta\gamma(1-\alpha), \\ A_2 &= \alpha + 5\beta^2 + \gamma[(1-\alpha)^2 - 2\beta^2], \\ A_3 &= 2\alpha\beta + 2\beta^3 + 2\beta\gamma(1-\alpha), \\ A_4 &= \beta^2(\alpha+\gamma). \end{aligned} \tag{65}$$

Upon solving (64), the components of the optimal $\mathbf{V}(t_0)$ are

$$x = -\frac{(z+\beta)z}{\beta z^2 + (\alpha-1)z - \beta}, \tag{66}$$

$$y = -\frac{(z+\beta)}{\beta z^2 + (\alpha-1)z - \beta}. \tag{67}$$

From (59) and with the aid of (60), (61) and (63) the optimal transfer angle is

$$\tan\frac{\Delta}{2} = -\frac{\gamma}{2(z+\beta)}. \tag{68}$$

To compare the above results with the results from optimal interception, we first notice that using definition (54) to expand (53) leads to (58). Likewise (52) directly yields (59), consequently (60). Finally, using (51) and (52) to eliminate Δ, after some algebraic manipulation, the quartic equation (64) is recovered.

We conclude this section by providing some explicit equations for computing the critical values ω_c where an initial coasting arc starts to appear. This happens when at the time of the impulse $S\dot{S} + T\dot{T} = 0$. Using this relation and noticing that in this case, $H_0^{*-} = H_f^* = -\mu Ce/p^2$, we have a condition

$$\mu\frac{Ce}{p^2} = \sqrt{\frac{\mu}{r_0}}\dot{T} + \frac{\mu}{r_0^2}S. \tag{69}$$

Upon expliciting this equation and simplifying, we have the relation

$$2\left(\frac{p}{r_0}\right)^{3/2}\sin\Delta + \left(\frac{p}{r_0}\right)^3 K - Q\sin\Delta = 0, \tag{70}$$

where

$$\begin{aligned} K &= I_1(r_0)\sin\theta_f - I_1(r_f)\sin\theta_0 \\ &= \frac{1}{(1-e^2)}[-\sin\Delta + 2e(\frac{r_0}{p})\sin\theta_f - 2e(\frac{r_f}{p})\sin\theta_0 + 3\sqrt{\frac{\mu}{p^3}}\Delta t e^2 \sin\theta_0 \sin\theta_f], \\ Q &= 1 + e^2 + 2e\cos\theta_0 - 2e\sin\theta_0 \tan\frac{\Delta}{2}. \end{aligned} \tag{71}$$

In deriving these equations, we have used the simplification of an initial circular orbit. On the other hand if we write the transversality condition (39) we obtain explicitly

$$\begin{aligned} &(\frac{p}{r_f})^2[(\frac{p}{r_0})^{3/2}K + \sin\Delta][e\sqrt{\frac{p_T}{p}}\sin\theta_f - \sqrt{\frac{p}{p_T}}e_T\sin(\eta+\Delta)] \\ &= [Q - (\frac{p}{r_0})^{3/2}][e\sin\theta_f - \sqrt{\frac{p}{p_T}}e_T\sin(\eta+\Delta)]\sin\Delta. \end{aligned} \tag{72}$$

This equation is the general, time free transversality condition for interception from initial circular orbit. In the case of $\omega = \omega_c$, Eq. (70) can be used to eliminate K, and we have the simple relation

$$(\frac{p}{r_f})^2[e\sqrt{\frac{p_T}{p}}\sin\theta_f - \sqrt{\frac{p}{p_T}}e_T\sin(\eta+\Delta)] = (\frac{p}{r_0})^{3/2}[e\sin\theta_f - \sqrt{\frac{p}{p_T}}e_T\sin(\eta+\Delta)]. \tag{73}$$

Now, if we use Eqs. (70) and (73) with $\theta_f = \theta_0 + \Delta$, and the time of flight Δt computed from Kepler's equation along the transfer orbit, and Eq. (53), we have three equations for three unknowns e, θ_0 and Δ. The value ω_c then is computed from Kepler's equation along the target orbit. When $\omega = \omega_1 > \omega_c$, the value $\eta = \eta_1$ which determines the required coasting arc becomes an additional unknown, but we can always solve the inverse problem by fixing η_1 for solving the three equations and then compute the corresponding critical ω for adjustment of η_1

As special cases, we first notice that, for tangential interception, Eq. (52) applies and (72) is reduced to $Q = (p/r_0)^{3/2}$ which is precisely Eq. (51). For both tangential interception and $\omega = \omega_c$, Eq. (73) leads to $\sin\theta_f = 0$. To satisfy all necessary conditions, we must have $\sin\theta_0 = 0$, $\sin\eta = 0$. The transfer is of Hohmann type.

Finally, we notice that, if the target orbit is circular, $e_T = 0$ and the lead angle is irrelevant. Ruling out the very rare case of non-Hohmann type transfer where $e \sin \theta_f = 0$, we obtain from Eq. (72)

$$(\frac{p}{r_f})^{3/2}[(\frac{p}{r_0})^{3/2}K + \sin \Delta] = [Q - (\frac{p}{r_0})^{3/2}] \sin \Delta. \tag{74}$$

Equation (74) is the general transversality used in Problem 1 when $t_f^* < P$.

6. Interception at Hyperbolic Speed

In this section we consider a case of realistic importance when $\mathbf{r}_T(t)$ represents the motion of a ballistic missile. The time t_f is then finite and is usually the time before the missile reaches its maximum altitude. The initial t_0 can not be arbitrary, usually some time after the detection of the motion of a hostile missile. Thus both t_0 and t_f are specified and the intercept time $\Delta t = t_f - t_0$ will be considerably short.

The geometry of interception is shown in Fig. 12. The interceptor is in its initial circular orbit with radius $r_0 = 1$. No extra difficulty will be present if an elliptic orbit is assumed except for more parameters involved. At t_f the target is at the position defined by the polar coordinates r_f, δ and φ with δ being the longitude and φ the latitude as measured from the position of the interceptor at t_0. The initial orbital plane of the interceptor is taken as the reference plane. The inclination angle between the reference plane and the interceptor-target plane at t_0 is

$$\tan i = \frac{\tan \varphi}{\sin \delta}, \tag{75}$$

and the angular distance between the interceptor and the target is

$$\cos \Delta = \cos \varphi \cos \delta. \tag{76}$$

Again the technique presented in Section 4 is applied here. Because all end conditions are given, no transversality condition is involved. When Δt is relatively short, the transfer trajectory is generally hyperbolic. The application of the technique of Section 4 shows that in the hyperbolic region and elliptic region where Δt is not excessively long, the variation of $p_V(t)$ generated by an impulse applied at t_0 always falls into case (a) of Fig. 5, so the initial one-impulse trajectory is optimal provided that the one-impulse transfer trajectory will not intersect the surface of the Earth, which is true for most of practical intercept situations. Only when Δt is quite large we have $p_V(t)$ belonging to case (b) of Fig. 5 where an initial coasting phase is required.

Figure 13 shows the variation of ΔV as function of Δt for a specified down range longitude $\delta = 45°$ using the latitude φ as parameter with 20° increment for an interception of altitude $r_f = 0.95$. To have some physical feeling, an initial orbit of altitude 600 km is chosen, r_f corresponds to an altitude of 251.23 km. The intercept times range from 2 to 15 minutes.

We repeat the experiment with a value $r_f = 1.05$ which corresponds to an altitude of 948.77 km for the same initial orbit. The results are illustrated in Fig. 14.

In each figure, we have plotted a dashed line separating the elliptic and hyperbolic interceptions. This is obtained by solving the equation for parabolic transfer

$$6\sqrt{\mu}\Delta t = (r_0 + r_f + c)^{3/2} - (r_0 + r_f - c)^{3/2}, \tag{77}$$

where c is the chord length

$$c^2 = r_0^2 + r_f^2 - 2r_0 r_f \cos\delta \cos\varphi. \tag{78}$$

For each transfer time Δt and down range longitude δ, it is obvious that as we increase the latitude φ, the transfer angle Δ increases, and the fuel consumption increases.

We notice that for any given δ and φ, or in general for any prescribed transfer angle Δ, there exists an optimal transfer time Δt for overall minimum characteristic velocity. This particular transfer can be obtained as follows.

In the present formulation of the problem, allowing Δt to vary is the same as fixing $\mathbf{r}_0$ and $\mathbf{r}_f$ and letting t_f free. By the final remark in Section 3 this leads to $H_f^* = 0$, hence

$C = 0$. By (50)

$$\left(\frac{r_0}{p}\right)\left(2\tan\frac{\Delta}{2} - e\sin\theta_0\right) = \frac{T}{S} = \frac{v}{u}. \tag{79}$$

It has been shown in Section 5 that, for a velocity $\mathbf{V}_0$ to be such that the trajectory passes through the prescribed final point with radius r_f and down range Δ, its normalized components x and y must satisfy the constraining relation (57). In general, let $\bar{x}$ and $\bar{y}$ be the components, along the S and the T axis, of the velocity $\mathbf{V}_0^- / \sqrt{\mu / r_0}$ before the application of the impulse. We have

$$\begin{aligned} \bar{x} &= \sqrt{\frac{r_0}{p_0}} e_0 \sin f_0, \\ \bar{y} &= \sqrt{\frac{p_0}{r_0}} \cos i. \end{aligned} \tag{80}$$

Notice that $\bar{x}$ and $\bar{y}$ are known quantities. Rewrite (79) by using definitions (21), (54) and (80)

$$\frac{y - \bar{y}}{x - \bar{x}} = \frac{1}{y^2}\left(2\tan\frac{\Delta}{2} - xy\right). \tag{81}$$

The two equations (57) and (81) can be solved for x and y. Explicitly, we solve for x from (57)

$$x = \frac{(1 - \cos\Delta) - (n - \cos\Delta)y^2}{y\sin\Delta}. \tag{82}$$

Upon substituting into (81), we have a quartic equation for y

$$A_0 y^4 + A_1 y^3 + A_2 y^2 + A_3 y + A_4 = 0, \tag{83}$$

where

$$\begin{aligned} A_0 &= 1 + n^2 - 2n\cos\Delta, \\ A_1 &= \sin\Delta[(n - \cos\Delta)\bar{x} - \bar{y}\sin\Delta], \\ A_2 &= 0, \\ A_3 &= \bar{x}(1 - \cos\Delta)\sin\Delta, \\ A_4 &= -(1 - \cos\Delta)^2. \end{aligned} \tag{84}$$

After solving for x and y, we deduce the relevant elements of the transfer orbit from

$$\begin{aligned}
&\frac{p}{r_0} = y^2 = 1 + e\cos\theta_0,\\
&e\sin\theta_0 = xy,\\
&\tan\theta_0 = \frac{xy}{y^2 - 1}, \quad \theta_f = \theta_0 + \Delta,\\
&e^2 = (xy)^2 + (y^2 - 1)^2,\\
&a = \frac{r_0}{2 - (x^2 + y^2)}.
\end{aligned} \tag{85}$$

The minimum overall characteristic velocity is computed from (21) and (22) where now

$$\begin{aligned}
u &= \sqrt{\frac{\mu}{r_0}}(x - \bar{x}),\\
v &= \sqrt{\frac{\mu}{r_0}}(y - \bar{y}).
\end{aligned} \tag{86}$$

The optimal time of flight Δt is obtained from Kepler's equation

$$\sqrt{\frac{\mu}{a^3}}\Delta t = (E_f - E_0) - e(\sin E_f - \sin E_0), \tag{87}$$

where (32) is used to evaluate the eccentric anomalies E_0 and E_f.

The computation using these explicit equations indeed gives the points of minimum ΔV in Figs. 13 and 14.

7. Conclusion

In this paper, we have presented the complete solution of the problem of interception with time constraint for an interceptor with high thrust propulsion system. The necessary conditions and the transversality conditions for optimality were discussed. The method of solution amounted to first solving a set of equations to obtain the primer vector for an initial one-impulse solution. Then based on the information provided by the primer vector, rules were established to search for the optimal solution if the initial one-impulse trajectory was not optimal. The approach is general in the sense that it allows for solving a problem of three dimensional interception with arbitrary motion for the target.

Several numerical examples were presented, including orbital interceptions and ballistic missile interception. Since impulsive thrust is assumed, whenever it is convenient, the results from optimal control theory are verified by parametric optimization using hodograph theory. In the important case of short time interception of a ballistic missile it is found that the intercept trajectory is usually hyperbolic and for a minimum fuel trajectory, a single impulse should be applied immediately at the acquisition time.

References

1. LAWDEN, D. F., Optimal Trajectories for Space Navigation, Butterworth, London, 1963.
2. MAREC, J. P., Optimal Space Trajectories, Elsevier Scientific Publishing Co., Amsterdam, 1979.
3. VINH, N. X., Integration of the Primer Vector in a General Central Force Field, Journal of Optimization Theory and Applications, Vol. 9, No. 1, 1972, pp. 51–58.
4. LEITMAN, G., The Calculus of Variations and Optimal Control, An Introduction, Plenum Press, New York, 1981.
5. BATTIN, R. J. and VAUGHAN, R. M., An Elegant Lambert Algorithm, Journal of Guidance, Control, and Dynamics, Vol. 7, Nov.– Dec., 1984, pp. 662–670.
6. LION, P. M. and HANDELMAN, M., The Primer Vector on Fixed Time Impulsive Trajectories, AIAA Journal, Vol. 6, Jan. 1968, pp. 127–132
7. VINH, N. X., BUSEMANN, A. and CULP, R. D., Hypersonic and Planetary Entry Flight Mechanics, The University of Michigan Press, Ann Arbor, Michigan, 1980.

List of Captions

Fig. 1. Switching function for finite thrust

Fig. 2. Switching function for impulsive thrust

Fig. 3. Rotating coordinate system

Fig. 4. Intercept trajectory

Fig. 5. Typical variations of $p_V(t)$

Fig. 6. Geometry of interception of Problem 1.

Fig. 7. Variations of $p_V(t)$ of Problem 1.

Fig. 8. Optimal characteristic velocity of Problem 1

Fig. 9. Geometry of interception for Problem 2

Fig. 10. Optimal characteristic velocity of Problem 2

Fig. 11. Hodograph of $\mathbf{V}_0$

Fig. 12. Geometry of interception at prescribed t_f

Fig. 13. Optimal characteristic velocity: $r_f/r_0 = 0.95$

Fig. 14. Optimal characteristic velocity: $r_f/r_0 = 1.05$

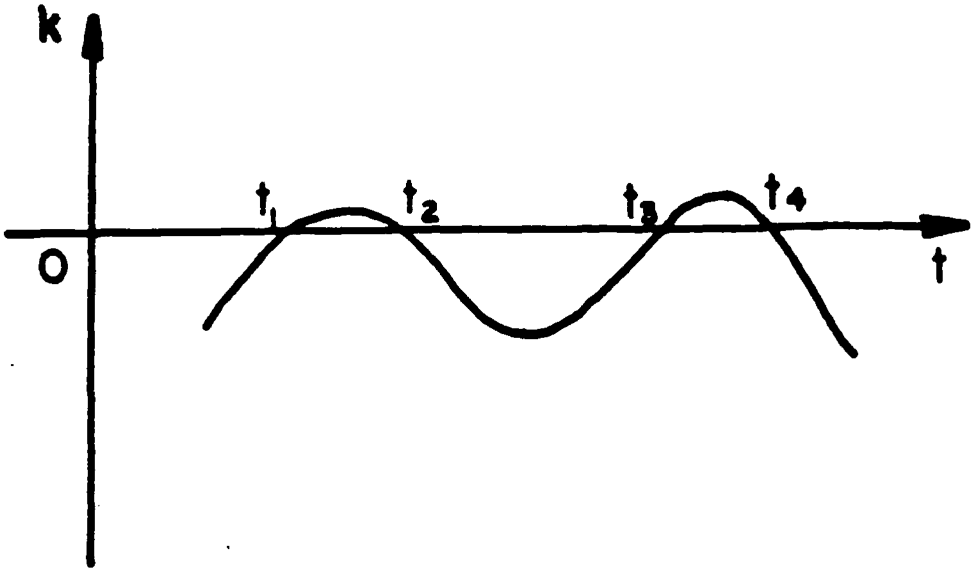

Figure 1— Switching function for finite thrust

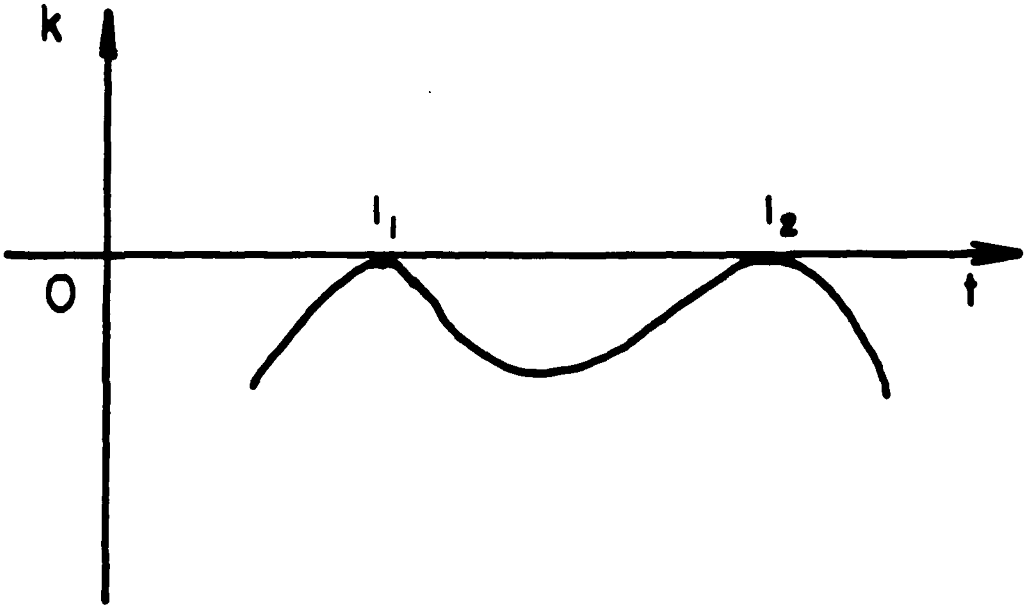

Figure 2— Switching function for impulsive thrust

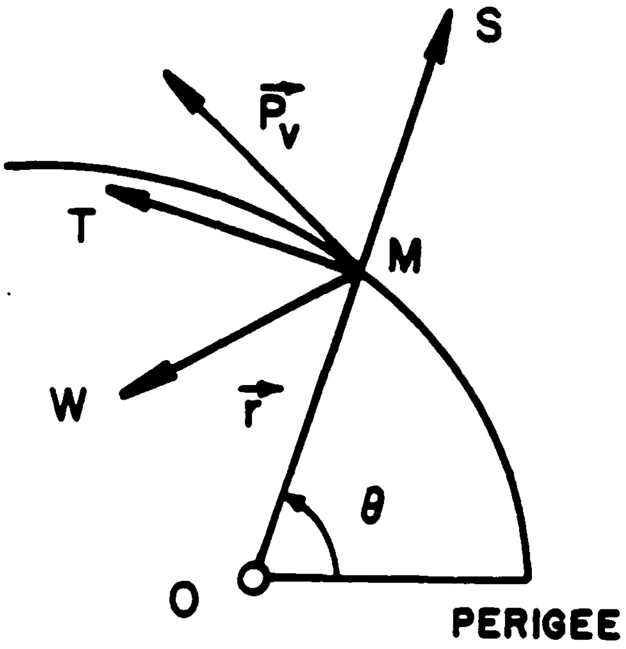
S
$\vec{P}_V$
T
M
W
$\vec{r}$
θ
O
PERIGEE

Figure 3— Rotating coordinate system

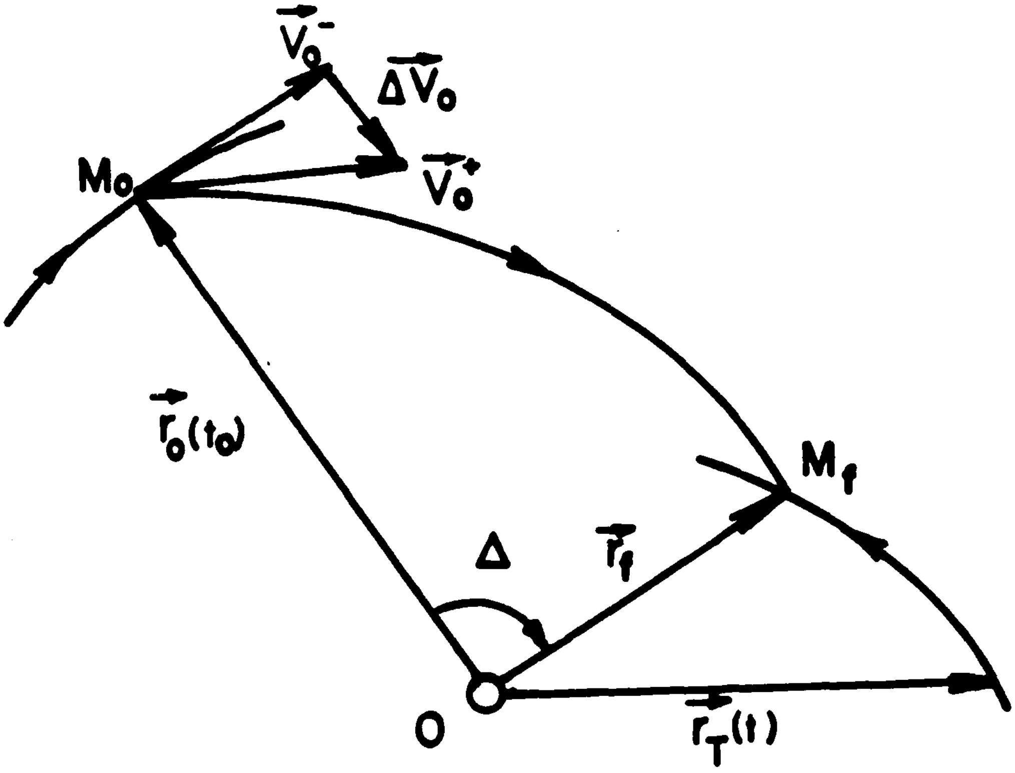

$\vec{V}_0^-$
$\overrightarrow{\Delta V}_0$
$\vec{V}_0^+$
M_0
$\vec{r}_0(t_0)$
M_f
Δ
$\vec{r}_f$
O
$\vec{r}_T(t)$

Figure 4— Intercept trajectory

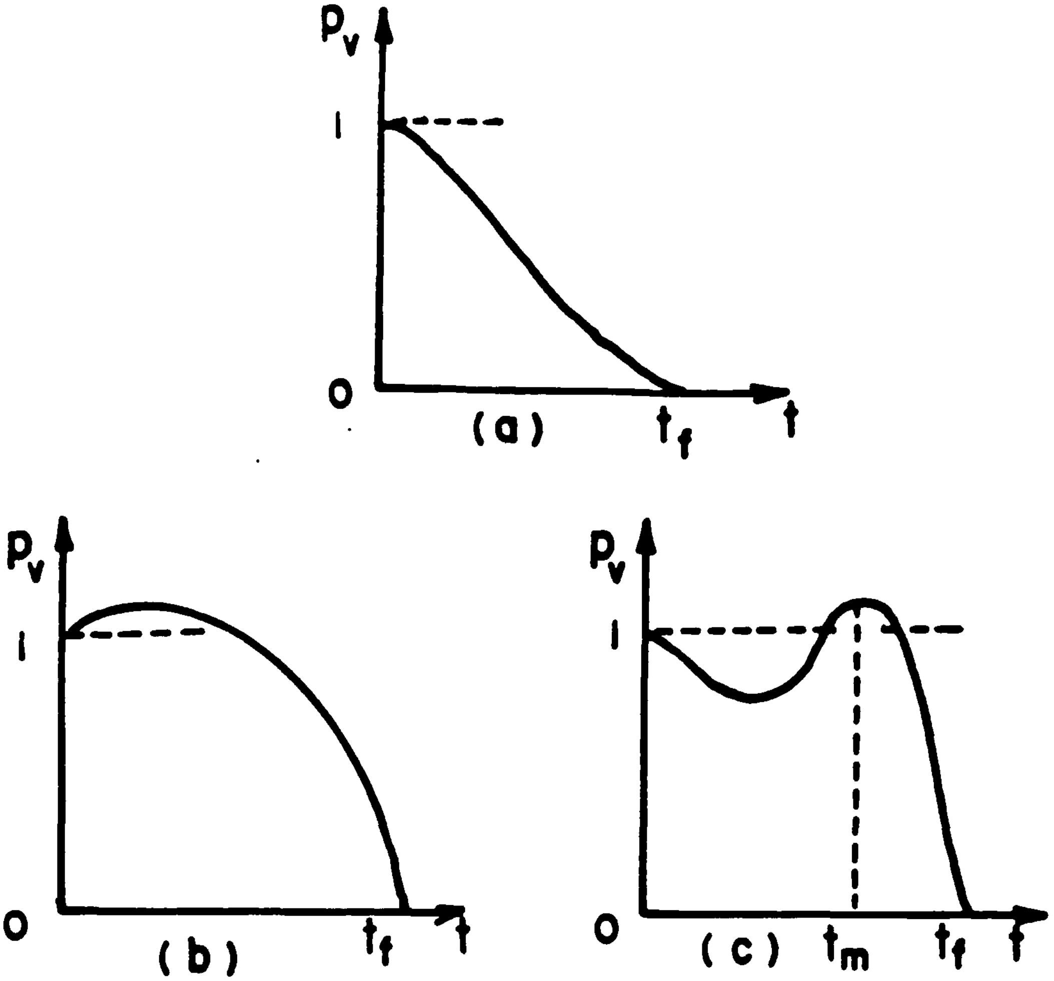

Figure 5— Typical variations of $p_V(t)$

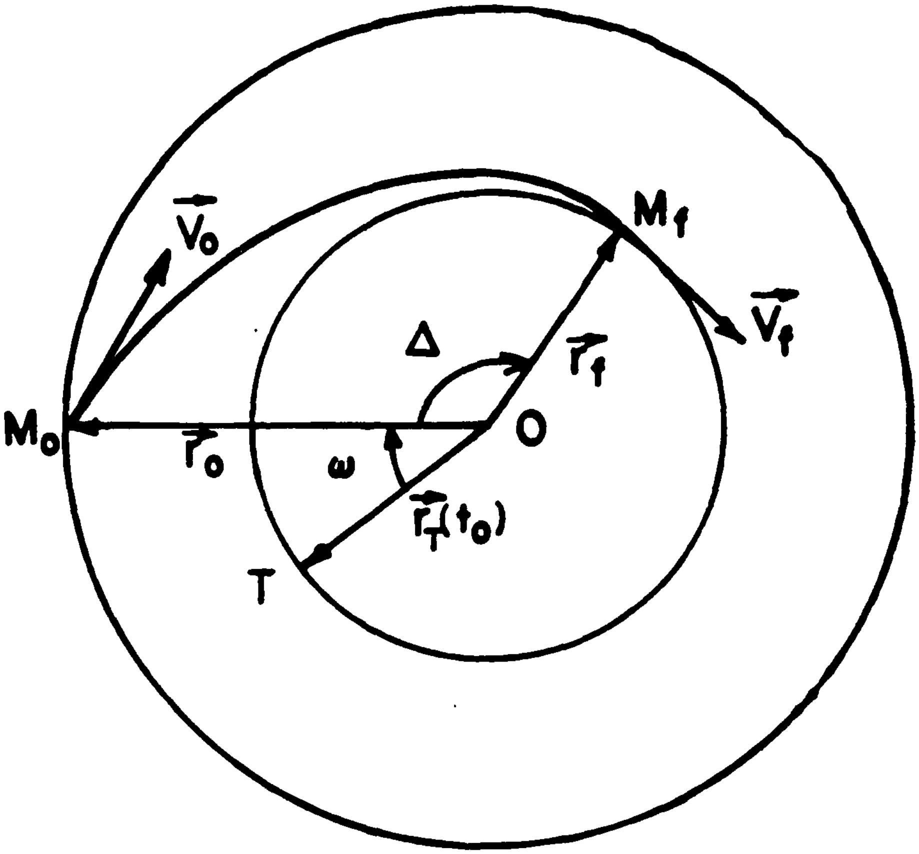
$\vec{V}_0$
M_f
$\vec{V}_f$
Δ
$\vec{r}_f$
M_0
O
$\vec{r}_0$
ω
$\vec{r}_T(t_0)$
T

Figure 6— Geometry of interception for Problem 1

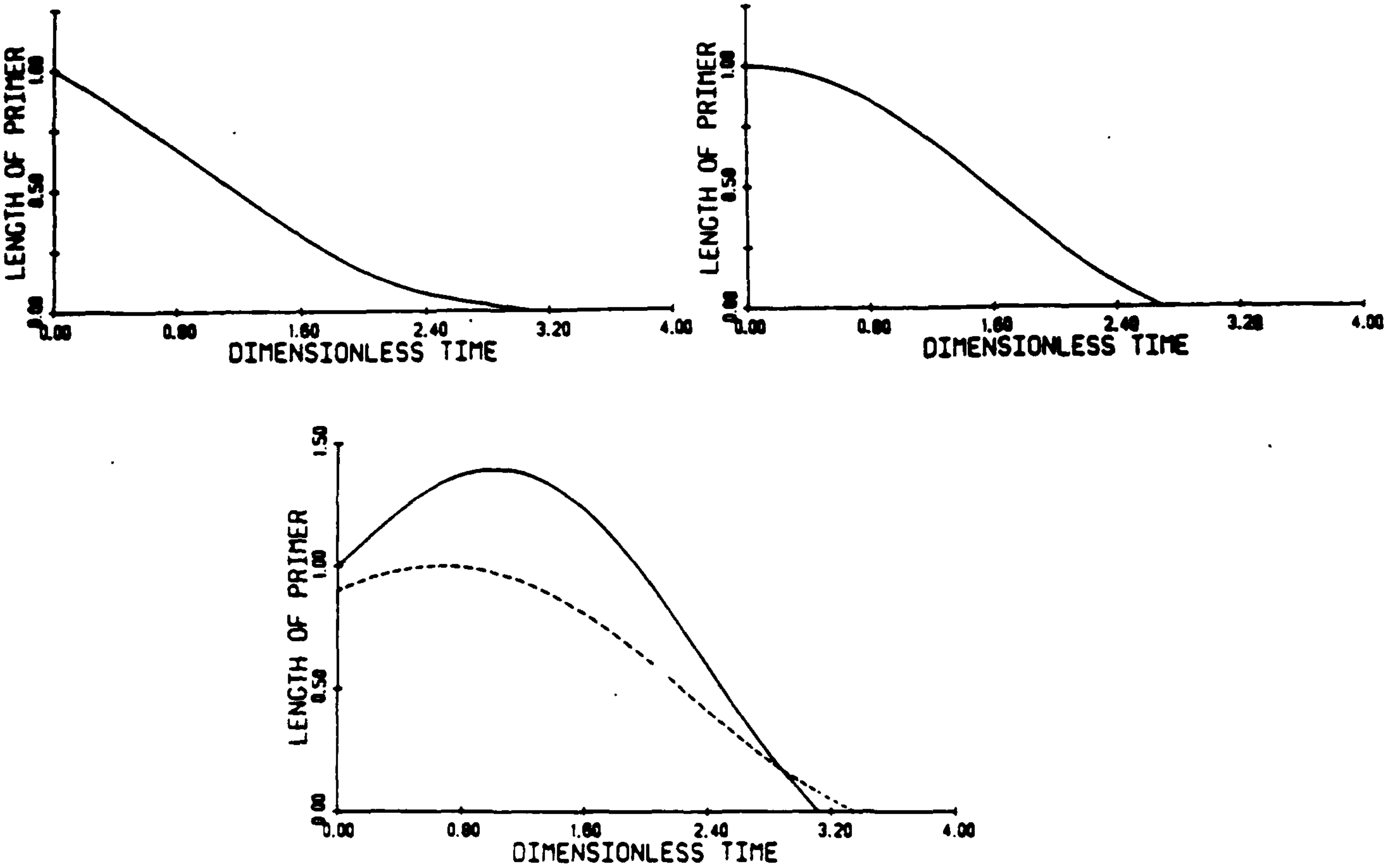

Figure 7— Variations of $p_V(t)$ for Problem 1

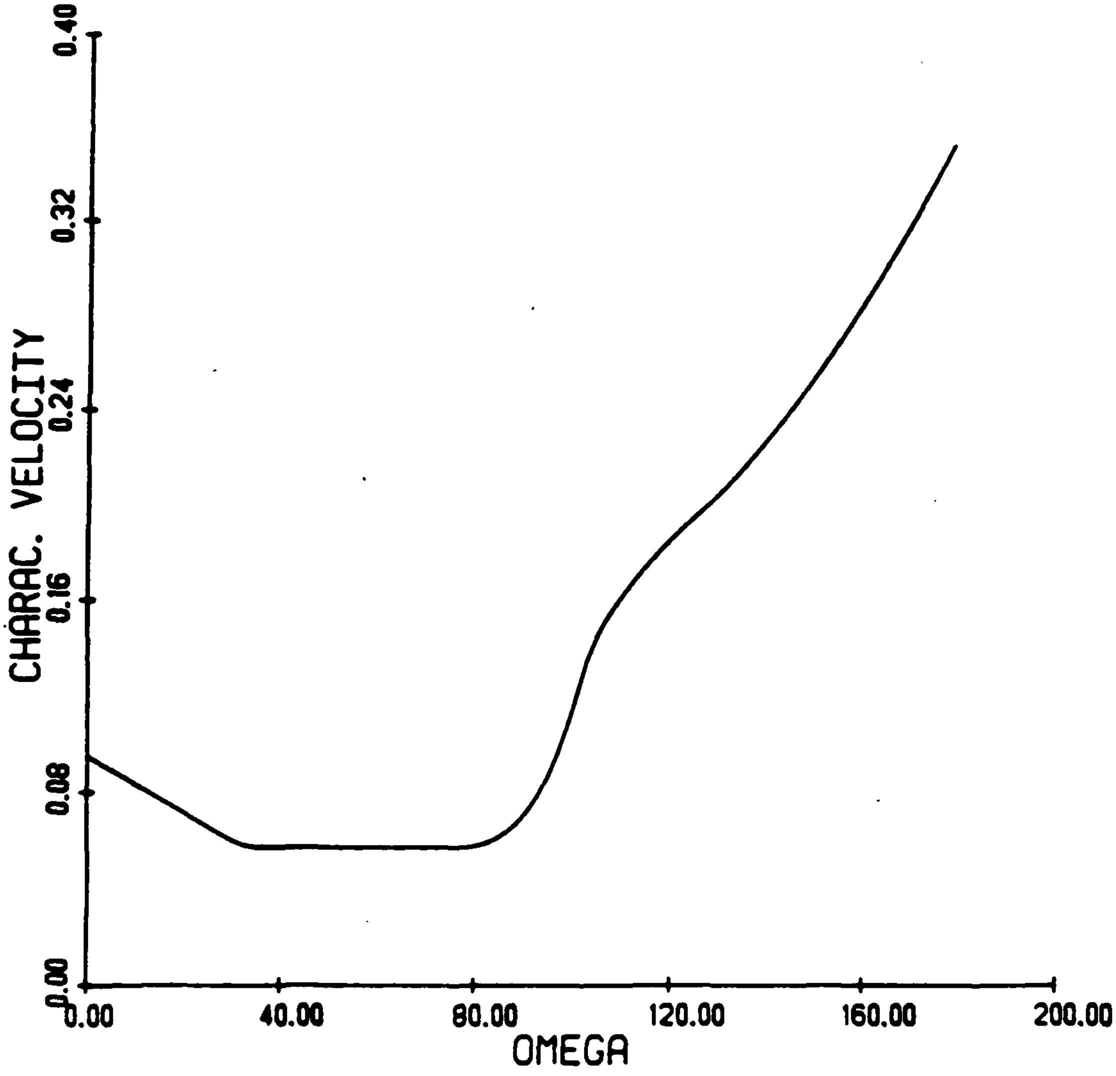

Figure 8— Optimal characteristic velocity of Problem 1

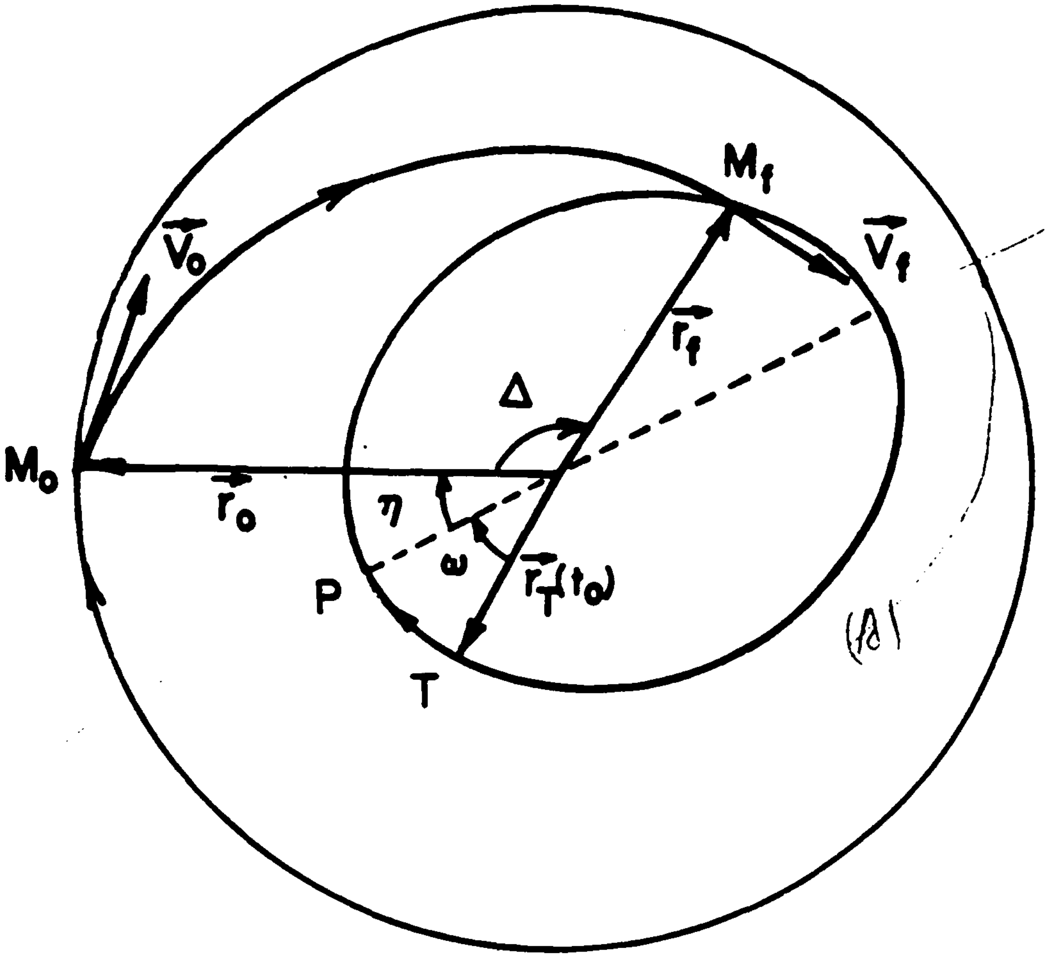
M_f
$\vec{V}_o$
$\vec{V}_f$
$\vec{r}_f$
Δ
M_o
$\vec{r}_o$
η
ω
$\vec{r}_T(t_o)$
P
T
(A)

Figure 9— Geometry of interception of Problem 2

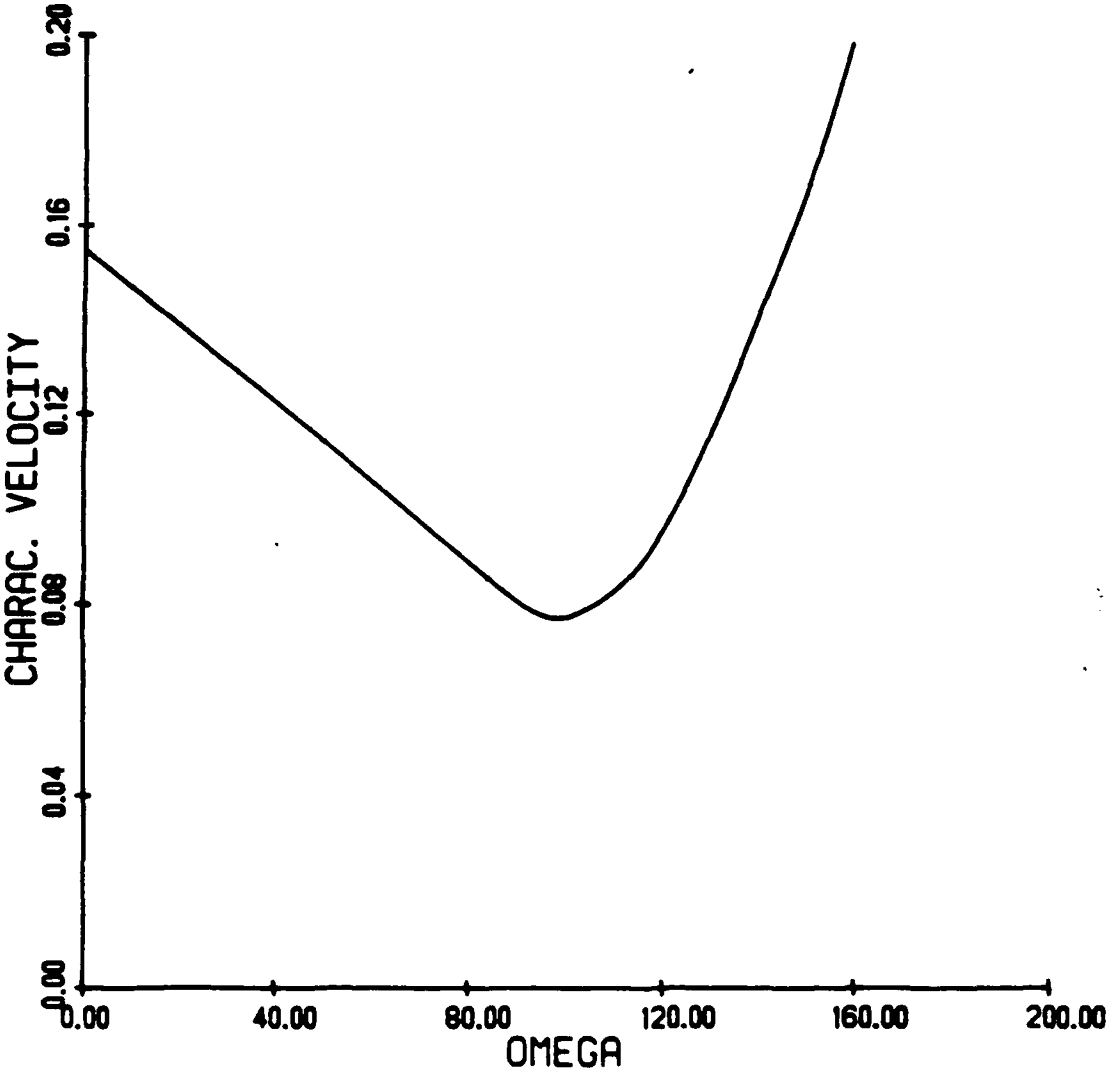

Figure 10— Optimal characteristic velocity for Problem 2

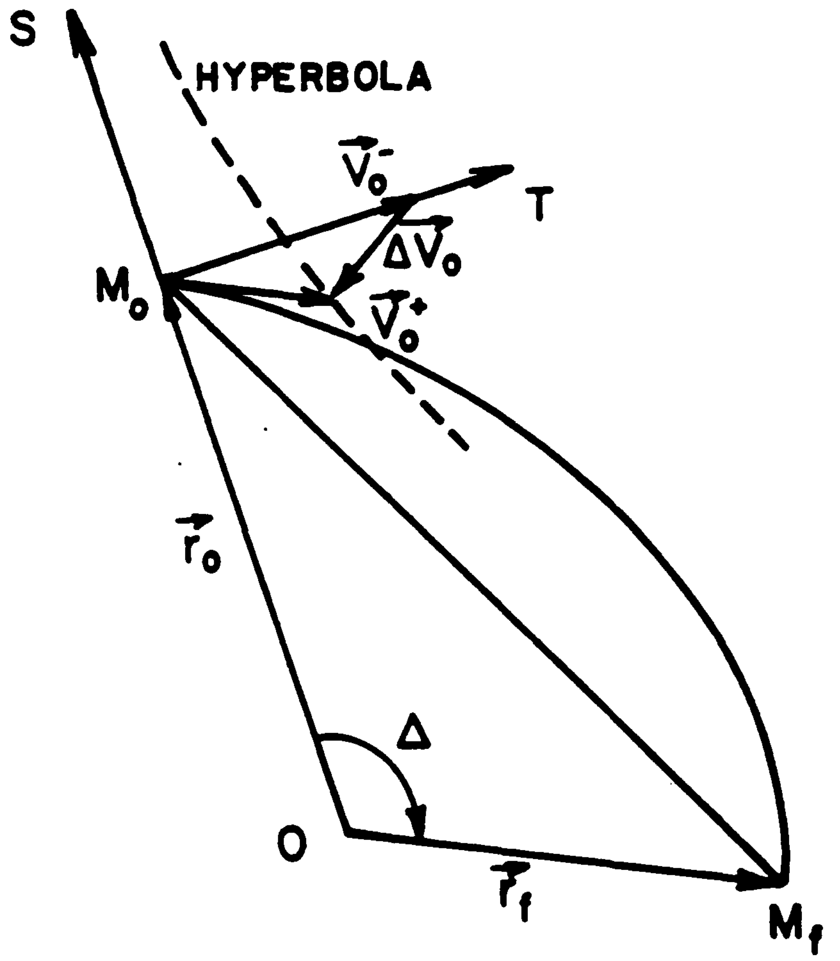
S
HYPERBOLA
$\vec{V}_0^-$
T
$\Delta\vec{V}_0$
M_0
$\vec{V}_0^+$
$\vec{r}_0$
Δ
O
$\vec{r}_f$
M_f

Figure 11— Hodograph of V_0

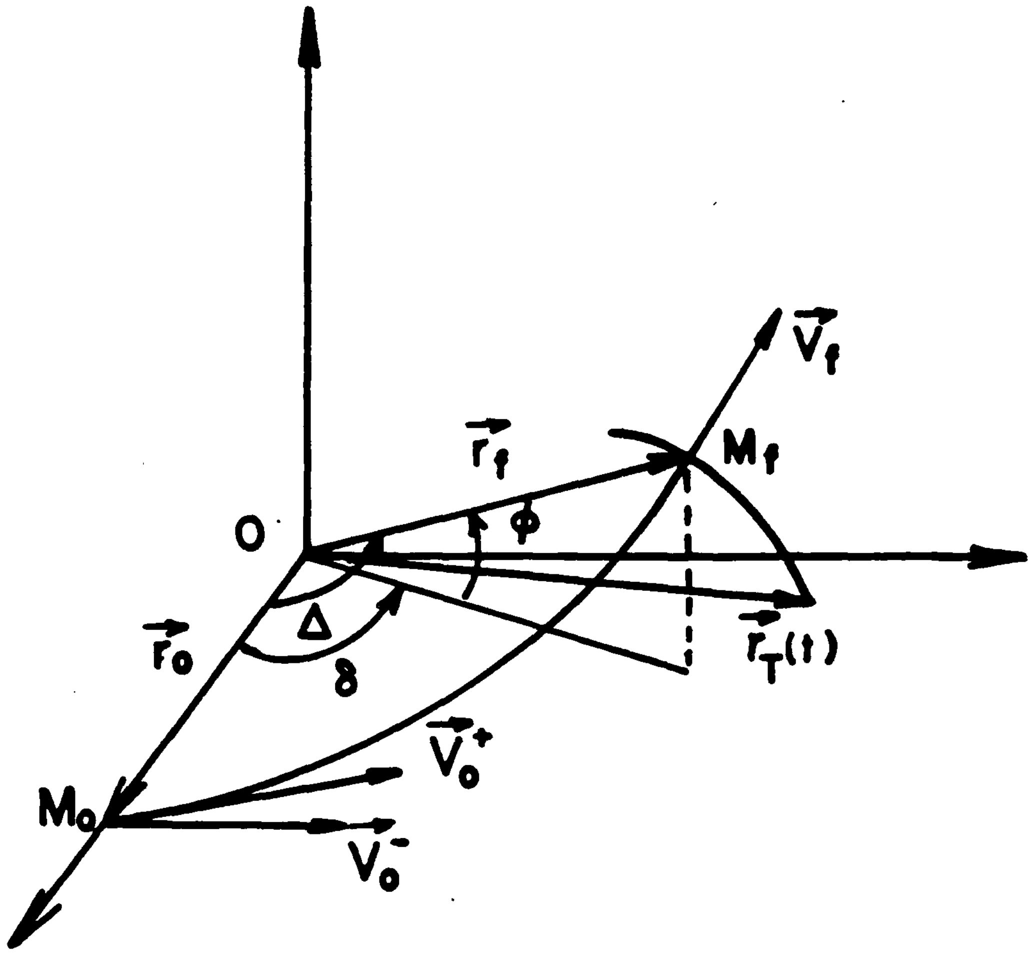
$\vec{V}_f$
$\vec{r}_f$
M_f
O
ϕ
Δ
$\vec{r}_o$
δ
$\vec{r}_T(t)$
$\vec{V}_o^+$
M_o
$\vec{V}_o^-$

Figure 12— Geometry of interception at prescribed t_f

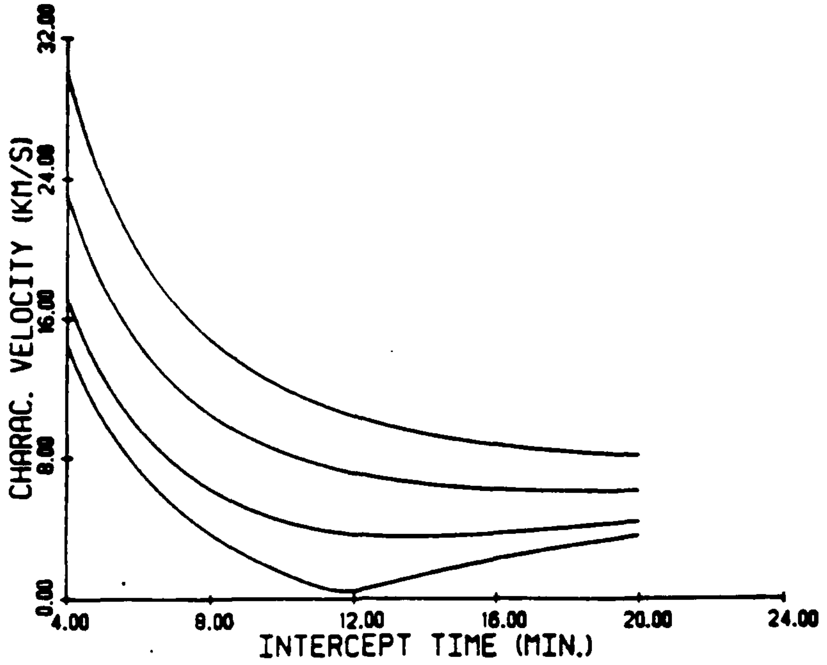

Figure 13— Optimal characteristic velovity: $r_0/r_f = 0.95$

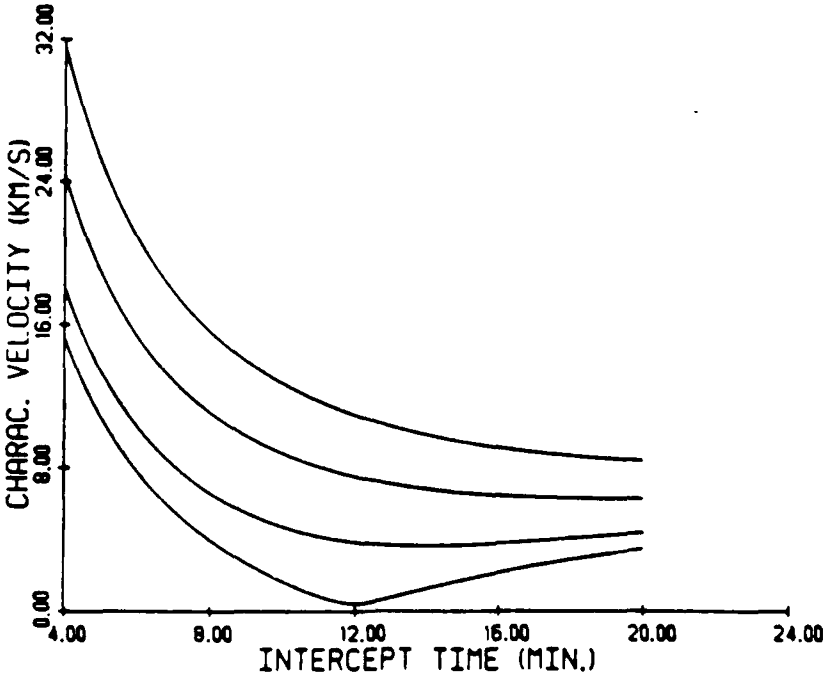

Figure 14— Optimal characteristic velocity: $r_0/r_f = 1.05$

OPTIMAL AEROASSISTED INTERCEPT TRAJECTORIES AT HYPERBOLIC SPEEDS

Elmer G. Gilbert*, Robert M. Howe**, Ping Lu†, Nguyen X. Vinh*

The paper considers the optimization of earth-based multistage rocket interceptors with very short flight times and long ranges. The objective is the minimization of the launch mass as a function of interceptor design variables such as: stage size, engine burn times and the angle-of-attack program. Because of the demanding target conditions the payload reaches hyperbolic speeds and the centrifugal force greatly exceeds the gravity force. The minimization of launch mass shows that the needed down-force on the payload is best provided by negative aerodynamic lift. The description of such negative-lift, aeroassisted optimal trajectories is a principal goal of the paper. Topics treated include: a model for the multistage interceptor, the formulation of the optimization problem, the mathematical derivation of a *universal curve* which provides a simple and accurate model for negative-lift segments of the optimal trajectories, effective procedures for efficient numerical optimization. Results of solution studies are reported. For flight times of six minutes and a range of about 3000 miles, a five-stage interceptor requires a mass ratio of several thousand. The dependence of the optimal mass ratio on key design and target parameters is described.

Presented as Paper No. 89-3444 at the AIAA Guidance, Navigation and Control Conference, August 14-16, 1989, Boston, Massachusetts.

*Professor, Department of Aerospace Engineering, The University of Michigan, Ann Arbor, Michigan 48109-2140

**Professor, Department of Aerospace Engineering,
Associate Fellow, AIAA

†Assistant Research Scientist, Department of Aerospace Engineering

Nomenclature

A	dimensionless thrust in g's = $T/(m_o g_o)$
C_D, C_L	lift and drag coefficients
D	dimensionless drag force = $\frac{1}{2}\rho v^2 S C_D/(m_o g_o)$
g_o	gravity acceleration at r_o
h	altitude = $r - r_o$
h_S	scale height of exponential atmosphere = 7.16 km
H	dimensionless altitude = h/r_o
i_{SP}	specific impulse
I_{SP}	dimensionless specific impulse = $i_{SP}/(r_o/g_o)^{1/2}$
L	dimensionless lift force = $\frac{1}{2}\rho v^2 S C_L/(m_o g_o)$
m	vehicle mass
m_o	reference mass
M	dimensionless mass = m/m_o
N	number of stages
r	distance of vehicle from center of earth
r_o	reference distance
R	dimensionless distance = r/r_o
S	cross sectional reference area
t	real time
T	engine thrust
v	vehicle speed
V	dimensionless speed = $v/(g_o r_o)^{1/2}$
x	dimensionless time for universal curve
α	angle of attack
γ	flight path angle with respect to local horizontal
η	dimensionless force coefficient = $\rho_o r_o S/m_o$
θ	polar angle of vehicle trajectory
λ	fineness ratio = stage length/stage base diameter
μ	dimensionless inverse scale height = r_o/h_S

$\rho(r)$	atmospheric density
ρ_0	reference density = $\rho(r_0)$
$P(H)$	dimensionless density = $\rho(r_0H+r_0)/\rho_0$
σ_i	mass-ratio parameter for ith stage
τ	dimensionless time = $t/(r_0/g_0)^{1/2}$

I. Introduction

The utilization of satellite-based missiles for intercepting ICBM's during their ascent constitutes one of the major efforts in the U.S. Strategic Defense Initiative. Here, an alternative approach is considered: the use of high performance, multistage, earth-based interceptors. The very short flight times and long ranges require hyperbolic speeds and a high ratio of take-off mass to payload mass. A natural objective is the minimization of the mass ratio with respect to interceptor design variables such as: stage size, engine burn times, coasting times between stages and the angle-of-attack program. Using techniques described in this paper, numerical solutions of such minimization problems have been obtained. In addition to giving information on how target parameters affect the optimum launch mass, they show that negative aerodynamic lift plays a crucial role in the midcourse portion of the optimal trajectories. The general physical basis for this key result is easy to understand: the hyperbolic speed generates a centrifugal force far in excess of the gravity force, and the required down-force is generated more efficiently by negative aerodynamic lift than by engine thrust. The primary objectives of this paper are threefold: (1) to summarize the models and methods by which the optimal aeroassisted trajectories are computed, (2) to clarify by analysis the detailed nature of the aeroassisted portion of the optimal trajectories, and (3) to give some insight into how design and target parameters affect the optimal launch mass.

The presentation begins in Section II with the details of the mathematical model for the multistage interceptor. Physically reasonable simplifying assumptions are introduced to keep the complexity of the model within acceptable bounds. The minimum launch mass problem is formulated in Section III. To emphasize the importance of the negative aerodynamic lift, three examples of optimal trajectories are given. They correspond to different assumptions on the trajectory of the payload stage: extra-atmospheric flight, atmospheric flight with zero aerodynamic lift, negative-lift aeroassisted flight. With respect to launch mass the aeroassisted flight offers a clear advantage.

Over a wide range of target conditions it has been observed that the optimal aeroassisted trajectories share a common feature. The atmospheric segments of the payload trajectories follow closely a speed-altitude relationship which we call the *universal curve.* The theory of this universal curve is developed in Section VI. It provides simple formulas which describe accurately the aeroassisted motion of the payload.

Section V reviews techniques used in the computation of the optimal trajectories. The minimum launch mass problem is a nonlinear, multistage, optimal control problem with parameters and constraints. The effect of its inherent complexity on the computations is eased by using a direct method in which the angle-of-attack program is approximated by a finite-dimensional functional representation. The resulting finite-dimensional optimization problem is solved efficiently by the application of an augmented-Lagrangian, quasi-Newton algorithm. Important practical aspects of the overall procedure are discussed. For example, it is shown how the angle-of-attack program can be parameterized indirectly through a direct parameterization of the flight path angle. This step is crucial in obtaining a numerically well-conditioned optimization problem.

Many optimal trajectories have been computed. Some of the results are summarized in Section VI. They show the effect on launch mass of such parameters as the time of flight, the intercept altitude, the number of stages and the specific impulse of the engines. For 5 and 6 stage interceptors mass ratios on the order of several thousand are necessary. Short flight times and low intercept altitudes increase appreciably the launch mass.

II. Model for the Multistage Interceptor

To obtain the equations of motion it is assumed that all stages of the interceptor are modelled as a point mass moving in a plane which contains the center of a spherical, non-rotating earth with an inverse-square gravitational field. Choosing state variables r, θ, v, γ and m and writing the resulting equations[1] in dimensionless form then gives:

$$\frac{dR}{d\tau} = V \sin\gamma \ , \quad \frac{d\theta}{d\tau} = \frac{V\cos\gamma}{R} \ ,$$

$$\frac{d\gamma}{d\tau} = \frac{1}{V}\left[\frac{A\sin\alpha + L}{M} + \left(\frac{V^2}{R} - \frac{1}{R^2}\right)\cos\gamma \right] ,$$

$$\frac{dV}{d\tau} = \frac{A\cos\alpha - D}{M} - \frac{\sin\gamma}{R^2} \ , \quad \frac{dM}{d\tau} = \frac{-A}{I_{SP}} \ . \qquad (1)$$

These equations are well scaled when $r_0 \equiv$ earth radius and $m_0 \equiv$ nominal mass of vehicle. Note $V = 1$ corresponds to the circular orbital speed at r_0 and $\tau = 2\pi$ corresponds to the period of a circular orbit at r_0.

The dimensionless lift and drag forces are given in terms of H and V by

$$L = \frac{1}{2}\,\eta\,P(H)\,V^2 C_L\ ,\quad D = \frac{1}{2}\,\eta\,P(H)\,V^2 C_D\ . \tag{2}$$

For the results reported later in this paper an exponential variation of density with altitude has been used. This approximation simplifies the computations and produces almost the same optimal trajectories as more complex atmospheric models. For the exponential variation,

$$P(H) = e^{-\mu H}\ . \tag{3}$$

Lift and drag coefficients are modelled by the formulas[2]:

$$\begin{aligned} C_L &= C_N \cos\alpha - C_A \sin\alpha\,, \\ C_D &= C_N \sin\alpha + C_A \cos\alpha\,, \\ C_A &= 0.13, \\ C_L &= \sin 2\alpha \cos\frac{1}{2}\alpha + 5\,(\pi)^{-1}\,\lambda \sin\alpha\,|\sin\alpha|. \end{aligned} \tag{4}$$

In addition to choosing an angle-of-attack program, $\alpha(\tau)$, in (1), it is necessary to specify the thrust program and describe parametrically the physical characteristics of the stages. Our model of the thrust program is simple, and is consistent with the requirements of solid-fuel engines. For the i th stage it consists of an initial coasting period, τ_i^C, where $A = 0$, and a single thrusting period, τ_i^B, where $A =$ constant > 0. The first stage has no coasting period ($\tau_1^C = 0$) and there are N powered stages. The final payload stage is unpowered but may generate a controlled aerodynamic lift. Its coasting time from burnout of the Nth stage to target interception is denoted by τ_{N+1}^C.

The stage masses are modelled as follows. For the i th stage, let M_i^P, M_i^F and M_i^S denote, respectively, the masses of the payload, fuel and structure (together with the engine and other jettisoned components). Then

$$M_i^P = M_{i+1}^P + M_{i+1}^F + M_{i+1}^S,\ i = 0, \ldots, N\text{-}1,$$

$$M_0^P = \text{launch mass of entire vehicle},$$

$$M_N^P = \text{mass of final payload.} \qquad (5)$$

Let

$$\sigma_{i+1}\, M_i^P = M_{i+1}^P\,,\ i = 0, \ldots, N\text{-}1. \qquad (6)$$

Here, $0 < \sigma_i < 1$, is a stage mass-ratio parameter. Once $\sigma_1, \ldots, \sigma_N$ and M_N^P are specified, the individual stage-payload masses $M_0^P, \ldots, M_{N-1}^P$ are known. To avoid the need for additional stage-size parameters, a final simplifying assumption is made:

$$M_i^S = 0.1\ M_i^F \quad , \quad i = 1, \ldots, N. \qquad (7)$$

Then from (5) it follows that

$$M_i^F = (1.1)^{-1}\, (M_{i-1}^P - M_i^P),\quad i = 1, \ldots, N. \qquad (8)$$

While (7) neglects many details of the structural design, it is representative of attainable structural efficiencies. Once the fuel masses are determined, the thrust levels A_i can be computed. They are proportional to M_i^F/τ_i^B.

The masses of the stages also affect, through their reference areas, the aerodynamic forces. Let S_i, d_i and λ_i be, respectively, the base area, base diameter and fineness ratio of the i th stage including its payload. Assume that the mass density of each stage prior to the ignition of stage burning is the same. Then, $m_{i-1}^P = (\text{const.}) d_i^3\, \lambda_i$. Since S_i is proportional to d_i^2 this gives

$$\begin{aligned} S_i &= C_S\, (m_{i-1}^P\, \lambda_i^{-1})^{2/3}, \\ &= C_S\, m_0^{2/3}\, (M_{i-1}^P\, \lambda_i^{-1})^{2/3},\ i = 1, \ldots, N + 1. \end{aligned} \qquad (9)$$

We have chosen C_S to make (9) conform closely with the corresponding relation for the Minuteman I vehicle. In our computations $\lambda_i = 10$ for $i = 1, \ldots, N$. Since the final payload is subject to aerodynamic forces during its coast to the target, its reference area, S_{N+1}, and fineness ratio, λ_{N+1}, are needed. This explains $i = N+1$ in (9). In our computations we have chosen $\lambda_{N+1} = 5$.

III. The Optimization Problem

In this section we outline the general features of the optimal interception problem and show by some examples the character of the optimal trajectories. The specified interception data are: the flight time of the interceptor = t_f, the target range angle = θ_f, the target altitude = h_f and the payload mass = m_N^P. The optimization objective is to minimize the total launch mass m_0^P. The free variables in the interception are: the angle-of-attack program, the coasting and thrusting periods t_i^C and t_i^B, and the mass-ratio parameters σ_i.

Once the free variables are given it is clear how the corresponding multistage trajectory is generated. Let r_0 = earth's radius. Then the multistage nondimensional equations of motion can be written. For the first stage: $R(0) = 1$, $\theta(0) = 0$, $\gamma(0) = 90°$, $V(0) = 0$, $M(0) = M_0^P$. Since the free variables determine $A(\tau) = A_1$ (through M_1^F and τ_1^B) and M_0^P, the equations of motion can be integrated for $0 \le \tau \le \tau_1^B$. At $\tau = \tau_1^B$ staging occurs and the equations of motion use data appropriate to the second stage. Specifically, (1) is integrated for $\tau_1^B \le \tau \le \tau_1^B + \tau_2^C + \tau_2^B$ with R, θ, γ and V continuous across staging and with $A(\tau)$ determined by A_2, τ_2^C and τ_2^B in the obvious way. The initial mass of the second stage is $M(\tau_1^B) = M_1^P$. The remaining stages are handled in the same way until $\tau = \tau_f = \tau_1^B + \tau_2^C + \tau_2^B + \ldots + \tau_N^B + \tau_{N+1}^C$. Actually, this equation is used to determine τ_{N+1}^C.

Of course, there are constraints on the free parameters:

$$0 < \sigma_i < 1, \;\; 0 < \bar{\tau}_i^B \le \tau_i^B, 0 \le \tau_i^C, \;\; i = 1, \ldots, N. \tag{10}$$

The lower bounds, $\bar{\tau}_i^B$, provide a means for limiting the maximum thrust or acceleration of each stage; they may, for instance, depend on other parameters such as M_i^F. In addition to these direct parameter constraints, there are the implicit constraints corresponding to target interception: $\theta(\tau_f) = \theta_f$, $r(\tau_f) = r_f$.

Operational considerations may add further constraints to the interception problem. We have, for example, considered three distinct optimization problems. They differ only in the assumptions placed on the motion of the unpowered final stage; the models for the powered ascent stages remain the same. In the first problem, the final payload is constrained to move essentially outside the atmosphere. Thus, the trajectory for the payload is computed easily as a Keplerian transfer from the burnout of stage N to target interception. The constraint is imposed by requiring the minimum altitude of the Keplerian trajectory to exceed a specified altitude. In the second problem, the payload is allowed to move through the atmosphere, but it generates no aerodynamic lift: $\alpha(\tau) = 0$, $\tau_f - \tau_N^C \le \tau \le \tau_f$. This avoids any increase in drag and heating which may result from lift. In the third problem there is no constraint on the payload so that an aeroassisted coasting trajectory is possible.

Figure 1 and Table 1 show typical numerical results for the three problems. The intercept conditions are: $t_f = 360$ sec., $\theta_f = 45°$ (approximately 3100 mi.), $h_f = 400$ km. (approximately 250 mi.), payload mass $= m_N{}^P = 10$ kg., $i_{SP} = 300$ sec. and $N = 5$. In general, the optimal coasting periods for the powered stages turn out to be zero. The only exception is the fifth stage of the Keplerian case.

The launch mass is least for the aeroassisted case. There is a simple physical explanation. The short flight time demands hyperbolic speed ($V > \sqrt{2}$) while simultaneously the trajectory must be kept close to the earth in order to intercept the target. To resolve these conflicting demands, a net down force on the vehicle is needed. This force is supplied, without expensive engine thrusting, by negative aerodynamic lift as the payload begins its coast toward the target.

For the zero-lift atmospheric case negative aerodynamic lift is also exploited, but because of the no-lift constraint on the payload it occurs together with engine thrust in the fifth stage. This accounts for the long burn-time of this stage; it allows more time for the negative aerodynamic lift to act.

In the Keplerian case, the altitude of the payload is constrainted to exceed 100 km. This leads to a very large launch mass because it essentially eliminates effective utilization of negative aerodynamic lift. The Keplerian solution does have a potential operational advantage. Since the trajectory is essentially outside the atmosphere, communication with the payload is not blocked by atmospheric ionization.

IV. The Mid-course Universal Curve

The aeroassisted trajectory in Figure 1 has an obvious mid-course segment on which the final payload coasts for an extended period of time until it begins its rise to the target. On the segment there is a negative aerodynamic lift and the path is nearly horizontal. We have observed such segments on all optimal aeroassisted trajectories where performance requirements are high, i.e., t_f is small, θ_f is large and h_f is small. Moreover, they can be modelled accurately by a single *universal curve* which relates altitude and speed. This unique relationship is obtained by balancing the difference between centrifugal and gravity forces with negative aerodynamic lift and minimizing the drag losses by choosing the angle of attack which maximizes the lift-to-drag ratio. As will be seen, the time-dependent motion of the payload on the universal curve also has a universal character.

Our development begins with some notation and simplifying parametric assumptions. Let $-C_L^*$ and C_D^* be the lift and drag coefficients which maximize $-C_L/C_D$. They are obtained from (4) and depend only on the fineness ratio, $\lambda = \lambda_{N+1}$, of the payload. Recall that the reference area of the payload, S_{N+1}, is given by (9) and is therefore determined by λ_{N+1} and the mass of the payload, m_N^P. A dimensionless coefficient $C_L^*\eta/2$ plays an important role in the equations which we will consider. It is given by

$$\frac{1}{2} C_L^* \eta = \frac{1}{2} C_L^* (m_0)^{-1} \rho(r_0)\, r_0\, S_{N+1} \tag{11}$$

Since C_L^* and S_{N+1} are fixed by λ_{N+1} and m_N^P, $C_L^*\eta/2$ depends only on m_0 and r_0. For the purpose of this section it is convenient to make the following choices for m_0 and r_0:

$$m_0 = m_N^P, \quad \rho(r_0)\, r_0 = \frac{3}{2} m_N^P (C_L^* S_{N+1})^{-1}. \tag{12}$$

This gives $M(\tau) \equiv 1$ in (1) and $\frac{1}{2} C_L^*\eta = \frac{3}{4}$.

The required balance of forces on the nearly horizontal trajectory is achieved by setting the normal acceleration, $V d\gamma/d\tau$, and γ equal to zero in (1) and $C_L = - C_L^*$ in (4). The result is the expression for the universal curve:

$$V = (1+H)^{-1/2} \left[1 - \frac{3}{4}(1+H)\, P(H)\right]^{-1/2}. \tag{13}$$

The reason for choosing r_0 by (12) is now clear: (13) contains only one parameter (μ) and at the reference altitude ($H=0$) the dimensionless speed has a nice nominal value ($V=2$). Now let $P(H)$ be given by (3). Noting that $\mu \cong 10^3$, it is easy to show that $1.3 \leq V \leq 4$ implies $|H| \leq 0.6 \times 10^{-3}$. Since the expected variation of H is so small, (13) is closely approximated by

$$V = G(H) = \left(1 - \frac{3}{4} e^{-\mu H}\right)^{-1/2}. \tag{14}$$

Even for a non-exponential atmosphere this expression is an excellent representation of (13) because the exponential approximation of $P(H)$ only needs to be accurate for $|\mu H| \leq 0.6$, or $|h| \leq 0.6\, h_S$. For the payload described in the previous section, r_0 corresponds to an altitude of 64.0 km. above the earth's surface.

Along the universal curve there are drag losses and V must decrease. This in turn causes H, θ, γ and α to depend on τ. To obtain these dependencies we begin by substituting (14) into (1) with $A = 0$:

$$\frac{dV}{d\tau} = G'(H)\frac{dH}{d\tau} = G'(H)\frac{dR}{d\tau} = G'(H)\,G(H)\sin\gamma = -D - \frac{\sin\gamma}{R^2} \tag{15}$$

Here, $G'(H)$ is the derivative of $G(H)$ so

$$G'(H) = -\frac{3}{8}\mu\, e^{-\mu H}[G(H)]^3. \tag{16}$$

From this expression it is not difficult to verify that $V = G(H) \geq 1.3$ implies $G'(H)\,G(H) > 0.58\,\mu$. Since $\mu \cong 10^3$, $R \cong 1$ and γ is small, the identity on the right side of (15) is closely approximated by

$$D = -G'(H)\,G(H)\sin\gamma. \tag{17}$$

This is the drag required for motion along the universal curve.

By (2) and (4), D defines α and thus C_L. Since the line $C_L = (-C_L^*/C_D^*)C_D$ is the tangent to the lift-drag polar at C_D^*, it is a good approximation for it in the neighborhood of C_D^*. This approximation with D determined by (16) and (17) gives

$$L = -\frac{3}{8}\frac{C_L^*}{C_D^*}\mu\, e^{-\mu H}[G(H)]^4\sin\gamma. \tag{18}$$

Substituting (14) and (18) into (1) yields the equations of motion on the universal curve.

To simplify these equations it is assumed with very little error that $\sin\gamma \cong \gamma$, $\cos\gamma \cong 1$ and $R = 1+H \cong 1$. Then

$$\frac{dH}{d\tau} = \gamma\, G(H)\ , \quad \frac{d\theta}{d\tau} = G(H)\ ,$$

$$\frac{d\gamma}{d\tau} = -\frac{3}{8}\frac{C_L^*}{C_D^*}\mu e^{-\mu H}[G(H)]^3\gamma + G(H) - [G(H)]^{-1}. \tag{19}$$

Because $M(\tau) = 1$ and $V(\tau) = G(H(\tau))$ the order of the original system of equations, (1), has been reduced from five to three. However, the equations (19) are still complicated because they are coupled and nonlinear. Fortunately, the parameter μ is large and this leads to a singularly perturbed system whose solution can be obtained analytically.

The nature of the singularly perturbed problem is revealed more clearly by introducing the scaled variables:

$$\bar{H} = \mu H\ , \quad \bar{\gamma} = \mu\gamma\ , \quad \bar{G}(\bar{H}) = (1 - \tfrac{3}{4}e^{-\bar{H}})^{-1/2}. \tag{20}$$

Then (19) becomes

$$\frac{d\bar{H}}{d\tau} = \bar{\gamma}\bar{G}(\bar{H}) , \quad \frac{d\theta}{d\tau} = \bar{G}(\bar{H})$$

$$\frac{d\bar{\gamma}}{d\tau} = \mu\{-\frac{3}{8}\frac{C_L^*}{C_D^*}e^{-\bar{H}}[\bar{G}(\bar{H})]^3\bar{\gamma} + \bar{G}(\bar{H}) - [\bar{G}(\bar{H})]^{-1}\}. \tag{21}$$

Standard singular perturbation theory can be applied to this system[3] and it shows that the term in the brackets goes to zero quickly and that the remaining, asymptotic, solution satisfies

$$\frac{d\bar{H}_a}{d\tau} = \gamma_a\bar{G}(\bar{H}_a) ,$$

$$\bar{\gamma}_a = \frac{8}{3}\frac{C_D^*}{C_L^*}e^{\bar{H}_a}\{[\bar{G}(\bar{H}_a)]^{-2} - [\bar{G}(\bar{H}_a)]^{-4}\}. \tag{22}$$

This is a first-order system which can be integrated easily when expressed in terms of the variable $y = [\bar{G}(\bar{H}_a)]^{-1}$.

The details of the integration and back substitution to the original problem variables are lengthy and are omitted. They produce the following formulas for the asymptotic motion along the universal curve:

$$H(\tau) = \frac{1}{\mu}\hat{H}(x) , \quad \theta(\tau) - \theta(\tau_o) = \frac{C_L^*}{2C_D^*}[\hat{\theta}(x) - \hat{\theta}(x_o)] ,$$

$$\gamma(\tau) = \frac{2C_D^*}{C_L^*\mu}\hat{\gamma}(x), \quad V(\tau) = \hat{V}(x), \quad x = x_o + \frac{2C_D^*}{C_L^*}(\tau - \tau_o), \tag{23}$$

where

$$\hat{V}(x) = (3e^x - 1)^{-1}(3e^x + 1) , \quad \hat{\gamma}(x) = [\hat{V}(x)]^{-2}$$

$$\hat{H}(x) = -\ln\frac{4}{3}[1 - \hat{\gamma}(x)] , \quad \theta(x) = -x + 2\ln\frac{1}{2}(3e^x - 1) , \tag{24}$$

and x_o is determined by $\hat{V}(x_o) = V(\tau_o)$ or, equivalently, by

$$x_o = \ln\frac{1}{3}[V(\tau_o) - 1]^{-1}(V(\tau_o) + 1). \tag{25}$$

It is easy to confirm that the above formulas cause H and V to lie on the universal curve. Also, using (2), (14), (16), (17) and (24) it follows that

$$C_D = D\left(\frac{1}{2}\eta\, e^{-\mu H} V^2\right)^{-1} \cong -G'(H)\, G(H)\, \gamma \left(\frac{1}{2}\eta e^{-\mu H} V^2\right)^{-1} = C_D^*. \tag{26}$$

Thus, within the accuracy of the approximation $\sin\gamma \cong \gamma$, the motion on the universal curve actually does maximize the lift-to-drag ratio.

The functions $\hat{H}$, $\hat{\theta}$, $\hat{\gamma}$ and $\hat{v}$ are plotted in Figure 2. The ranges of variables which are shown are adequate for any reasonable target conditions. For example, with $C_L^*/C_D^* = 2.5$, the value corresponding to $\lambda = 5$, a unit change in $\hat{\theta}$ corresponds to a 72° change in θ. For the entire range which is shown $|\hat{\gamma}| \leq 0.61$. This implies $|\gamma| \leq 0.61\mu^{-1} \cong 6 \times 10^{-4}$ rad. = 0.034°. The departure of γ from zero is indeed small.

V. The Numerical Optimization Procedure

A. General Discussion

Over the years many procedures have been developed for the numerical solution of problems in optimal control. One approach is to write the necessary conditions and solve the resulting two-point-boundary-value problem by well developed techniques[4,5]. There are difficulties in applying this approach to the interceptor problem. The two-point-boundary-value problem is replaced by a complex multi-point-boundary-value problem and derivatives of the nonlinear functions appearing in the problem statement are needed. Moreover, reasonably good initial estimates of the optimal solution and the corresponding necessary condition multipliers are needed. Various gradient methods[6,7] can be extended with less difficulty to the multistage problem, but at best convergence is slow and terminal conditions cannot be met accurately. Second-order gradient methods[8,9] have better convergence rates, but they require second derivatives of the problem functions which are difficult to obtain because of the complex nonlinear and multistage character of the interceptor problem.

In view of the above mentioned difficulties it seemed most appropriate to use a direct method in which the infinite-dimensional optimal control problem is replaced by a finite-dimensional approximation. Many approaches for doing this have appeared in the literature. See, for example, the review given by Hargraves and Paris[10]. In our approach, the angle-of-attack program, $\alpha(\tau)$, is approximated by a finite-dimensional functional parameterization and the equations of motion with staging conditions are integrated accurately. The details of the overall process, are described in the following subsections. Other direct methods, such as collocation methods[10], could also be applied to the interceptor problem. A possible advantage would be the elimination of special procedures, such as the one described in the next subsection, for improving numerical conditioning. Collocation methods, as well as many other direct methods, do have a have a potential disadvantage. Accurate solution of the differential equations may necessitate a fine collocation grid, which in turn increases the dimension of the finite-dimensional optimization problem.

B. The Indirect Parameterization of $\alpha(\tau)$

In the approximation of the angle-of-attack program several questions arise: the dimension and the form of the functional representation, the accuracy of the corresponding approximate optimum solution, the conditioning of the resulting numerical optimization problem. Our experience shows that relatively low dimensional parameterizations are quite effective, provided the approximating functions are chosen with some care. The dimensionality is important because it has a strong effect on the computational time. Conditioning affects both the speed and reliability of the optimization process.

A direct parameterization of $\alpha(\tau)$ is the most obvious way to proceed. For example, a continuous piecewise linear function, which is parameterized by its values at its joints (points of slope discontinuity), is simple and has flexibility in that the joints may be placed closely where rapid changes in $\alpha(\tau)$ are expected. The fatal shortcoming of direct parameterizations is poor conditioning of the optimization problem. The terminal constraints are very sensitive with respect to small changes in $\alpha(\tau)$, especially when the changes occur early in the flight. This is not surprising in view of the open-ended integrations which occur in solving the equations of motion.

To circumvent this poor conditioning, it is better to parameterize $\alpha(\tau)$ indirectly through a direct parameterization of $\gamma(\tau)$. In this approach, $d\gamma/d\tau$ is computed from the parameterized $\gamma(\tau)$ and substituted, together with $\underset{-}{R}$, γ, V and M, into the third equation of (1). This equation then becomes through $\sin \alpha$ and L an implicit equation in α. The indirect parameterization of α is obtained by solving the implicit equation. Note that this eliminates the need to integrate the differential equation for $d\gamma/d\tau$. Of course, the remaining differential equations in (1) must be integrated as usual. When the indirect parameterization is used, the entire trajectory is under more direct control. Changes in $\gamma(\tau)$ near the beginning of the trajectory have very little effect on the terminal portions of the trajectory. Thus, the sensitivity of the terminal constraints to the parameterization is greatly reduced. Another advantage, perhaps less important, is evident at launch. Here, the differential equation for $d\gamma/d\tau$ has a singularity because $V = 0$. With the γ parameterization the differential equation is not integrated and the normally troublesome singularity is circumvented.

The implicit equation for α presents possible difficulties. An inadmissible $\gamma(\tau)$ may be specified, i. e., one in which the implicit equation has no solution. This corresponds physically to requiring more transverse acceleration than is available. In most of our work inadmissibility has not been a problem, provided the line search in the optimization algorithm has a procedure for reducing step size when it produces an inadmissible $\gamma(\tau)$. Occasionally, when α must be very large, as in the fifth stage of the Keplerian problem of Figure 1, it is better to parameterize $\alpha(\tau)$ directly, keeping the γ parameterization for the other stages. The actual numerical solution of the implicit equation is straightforward. One approach is to use several Newton iterations. Alternatively, L may be approximated by a quadratic function of $\sin \alpha$; then the implicit equation is quadratic in $\sin \alpha$ and it may be solved by formula.

Another issue is the smoothness of $\alpha(\tau)$ and other problem variables. If $\gamma(\tau)$ is continuous but has slope discontinuities, as in the case of a piecewise linear parameterization, the differentiation of $\gamma(\tau)$ causes $\alpha(\tau)$ to be discontinuous. Even for smoother parameterizations the problem is not avoided. At the staging times the vehicle mass, thrust and aerodynamic parameters change discontinuously and this causes discontinuities in $\alpha(\tau)$. Continuity of $\alpha(\tau)$ can be imposed by introducing, through the functional representationof $\gamma(\tau)$, an appropriate jump in $d\gamma/d\tau$ at the staging time. The value of $d\gamma/d\tau$ just after staging, $(d\gamma/d\tau)^+$, is evaluated by using its defining equation, (1), with R, γ, V and α continuous across staging and the changes in M, A and aerodynamic parameters determined by the staging equations of Section II.

It is also possible to introduce other smoothness constraints. For example, consider the pitch angle, $\psi = \alpha + \gamma$. Although ψ does not appear in the point mass equations, it has practical implications because the moment applied to the vehicle is proportional to its second derivative. To avoid an impulsive moment it is necessary to require continuity of $d\psi/d\tau$. This leads to the condition: $(d\alpha/d\tau)^+ - (d\alpha/d\tau)^- = (d\gamma/d\tau)^+ - (d\gamma/d\tau)^-$, where the superscripts give the values immediately before and after staging. In order for the derivatives with respect to α to exist, it is certainly necessary that $\alpha(\tau)$ be continuous. Thus, as in the previous paragraph, both $(d\gamma/d\tau)^+$ and $(d\gamma/d\tau)^-$ are known. The resulting condition on $(d\alpha/d\tau)^+ - (d\alpha/d\tau)^-$ can be obtained by differentiating the $d\gamma/d\tau$ equation once. This in turn defines the value of $(d^2\gamma/d^2\tau)^+$. Thus, conditions on both $(d\gamma/d\tau)^+$ and $(d^2\gamma/d^2\tau)^+$ are obtained.

Our numerical experience has produced some guidlines on the functional form of the γ parameterization. Because of the large changes in γ encountered in the first stage it has been found necessary to use a parameterization with at least three free parameters. Since $\gamma(0) = 90°$, a cubic in τ satisfies this requirement and has been as effective as any other choice. For the remaining stages, one free parameter suffices. When there are no smoothness constraints, a linear function works well. Only one parameter is involved for each stage because $\gamma(\tau)$ must be continuous across staging. When the various continuity constraints are imposed, a more elaborate, one-parameter representation is needed. For instance, when $d\psi/d\tau$ is continuous, we have found it effective to use $\gamma(\tau) = a + b\tau + ce^{-\sigma\tau} + de^{-\nu\tau}$. The parameters c and d allow the matching of the constraints on $(d\gamma/d\tau)^+$ and $(d^2\gamma/d^2\tau)^+$. The values σ and ν are chosen so that the effect of the continuity conditions does not persist for too long a period of time. For a given functional form, the free parameters may be defined in different ways. It has been found that problem conditioning is usually better if values of γ at specified interpolation points are used. For example, when there is one free parameter for a stage, the value of γ at the thrust termination time is a good choice.

C. Formulation of the Finite-dimensional Problem

The variables in the finite-dimensional optimization problem are the parameters in the representation of $\gamma(\tau)$ and the staging parameters: σ_i, $\tau_i{}^B$, and $\tau_i{}^C$, for $i = 1,\ldots,N$. The constraints, (10), on these parameters are implemented by means of nonlinear transformations

$$\sigma_i = (1 - \varepsilon)(0.5 + 0.5 \sin \phi_i), \tag{27}$$

$$\tau_i{}^B = 0.5(\bar{\tau}_i{}^B + \tilde{\tau}_i{}^B) + 0.5(\bar{\tau}_i{}^B - \tilde{\tau}_i{}^B) \sin \upsilon_i , \tag{28}$$

$$\tau_i{}^C = \tilde{\tau}_i{}^C (0.5 + 0.5 \sin \mu_i) . \tag{29}$$

In (27), $\varepsilon > 0$ is a small positive number which implements the strict inequalities on σ_i. The variables ϕ_i, υ_i and μ_i become unconstrained variables in the finite dimensional optimization problem. The parameters $\tilde{\tau}_i{}^B$ and $\tilde{\tau}_i{}^C$ are a scaling parameters which establish upper limits for $\tau_i{}^B$ and $\tau_i{}^C$ and improves the numerical conditioning of the optimization problem. The nonlinearities introduced by the transformations do not appear to affect the speed or reliability of the numerical optimization process. If coasting of the powered stages is not allowed and the guidelines of the preceding subsection are followed, there is a total of 3N +2 variables: N each for (27) and (28), 3 for the parameterization of γ in the first stage and 1 for the parameterization of γ in each of the remaining stages.

The remaining constraints in the optimization problem are the terminal conditions $\theta(\tau_f) = \theta_f$ and $R(\tau_f) = R_f$. Errors in meeting these equality conditions are evaluated by integrating the differential equations of motion, which are fully defined once the variables of the preceding paragraph are specified. The cost to be minimized is $M_o{}^P$, obtained from the σ_i by (6).

D. The Numerical Evaluations

In order to implement the optimization algorithm it is necessary to numerically evaluate $\theta(\tau_f)$, $R(\tau_f)$ and $M_o{}^P$ and their gradients with respect to the variables. To avoid the very complex direct evaluation of the gradients, first order finite differences on $\theta(\tau_f)$, $R(\tau_f)$ and $M_o{}^P$ are used. This is numerically expensive because each evaluation of the gradient requires n + 1 integrations of the differential equations, where n is the number of variables. Techniques for speeding the integrations have been report by Howe et. al.[11]. For the specific results reported here a fixed-step RK-4 procedure was used with approximately 10 steps per stage. Rounding and truncation errors in the computation of the gradients can seriously degrade the performance of the minimization algorithm. In this regard the naturally good scaling of the dimensionless equations (1) is a distinct advantage. Balancing the rounding and truncation errors by a proper choice of the finite difference increment is also important[12].

For those cases where the payload stage follows closely the universal curve it is possible to eliminate for the payload the parameterization of $\gamma(\tau)$ and the numerical integration of the equations of motion. At the time of final-stage burnout, $V(\tau_b)$ is known. By setting $\tau_o = \tau_b$, formulas (23)-(25) define the motion along the universal curve. In general the conditions $V(\tau_b) = G(H(\tau_b))$ and $\gamma(\tau_b) = 0$ (a very accurate approximation since $|\gamma| \leq 6 \times 10^{-4}$ on the universal curve) are not satisfied by the ascent trajectory, so they must be imposed as additional equality constraints. The universal curve is followed until a time $\tau = \tau_d$ is reached. After this time $\alpha(\tau)$ is set to zero.. Because there is no aerodynamic lift and V> 1, the trajectory then departs from the universal curve and rises toward the target. By evaluating this departure trajectory at $\tau = \tau_f$, the errors in the target conditions are determined. Because $\gamma(\tau_b) = 0$ one variable is omitted from the parameterization of $\gamma(\tau)$; this is balanced by the addition of the parameter τ_d.

E. The Optimization Algorithm

The equality constraints are treated by the augmented Lagrangian method, which reduces the constrained problem to a sequence of unconstrained problems. Both the penalty coefficients and the multipliers are updated automatically by a scheme which is described on page 292 of Fletcher[13]. The unconstrained minimization program used in our computations is a variant of the BFGS, quasi-Newton implementation due to Shanno and Phua[14]. It provides superlinear convergence without requiring the evaluation of second derivatives. A reset procedure has been added which greatly reduces the probability that the descent will terminate prematurely due to accumulation of round-off errors in the quasi-Newton update.

Generally, the performance of the overall optimization procedure has been very satisfactory. The number of gradient evaluations required to obtain a solution is between 300 and 400. This is not unreasonable for the typical number of problem variables: 17 for N = 5 and 20 for N = 6. Errors in meeting the specified target conditions are very small: about 1 meter in altitude and about 0.05° in range angle. The computational time for a solution is typically between 60 and 90 minutes on an Apollo DN 4000.

VI. Some Specific Results

Many optimal intercept problems have been solved using the methods and models of the preceding sections. In this section we summarize some of our results for the aeroassisted problem. The pitch angle is constrained to have a continuous derivative except at the entry and exit points of the universal curve, where $\alpha(\tau)$ is allowed to be discontinuous. A variety of problems have been solved where coasting of the stages is allowed. In these problems the optimal coasting times are either zero or so small that they have little effect on the optimal launch mass. For all the problems considered here the coasting times have been set to zero. The minimum burn time for each stage is 10 seconds and the payload mass is 10 kg. Except for the results in Figure 6, the specific impulse is fixed at 300 seconds.

Additional details of the optimal aeroassisted solution described in Section III are shown in Figure 3. The staging times are apparent. With the exception of the fifth stage, the optimal burn times are at their lower limits of 10 seconds. The resulting vehicle acceleration A/M is quite high, ranging from about 20 to 70 g's. If the minimum burn time is reduced below 10 seconds, even higher accelerations are obtained. The universal curve is followed from about 53 seconds to 194 seconds. The slight drop in V predicted by Figure 2 is evident. There is little loss in speed after the exit from the universal curve. The reason is obvious from Figure 1: the trajectory leaves the atmosphere quickly, so there is little aerodynamic drag. Close inspection of $\gamma(\tau)$ for $0 < \tau < 60$ shows its linear-exponential parameterization. If the smoothness constraint on the pitch angle is removed and $\alpha(\tau)$ is allowed to be discontinuous at the staging points, the overall character of the trajectory is essentially the same and the launch mass is reduced by about 0.5 %. Thus, the smoothness of the pitch angle does not seem to be a very stringent constraint.

Figures 4 through 6 illustrate the effect of key parameters on the optimal launch mass. Note that the target altitude is 200 km., a more demanding intercept condition than the 400 km. of the preceding problem. Figure 4 shows the relative performance of optimal aeroassisted trajectories and optimal zero-lift, atmospheric trajectories. The advantage of the aeroassisted trajectories is greater for shorter intercept times. For both types of trajectories the launch mass grows very rapidly as the flight time approaches 320 seconds. Figure 5 shows the difference between 5 and 6 stage aeroassisted interceptors. The 6 stage interceptor has a decided advantage for the shorter flight times. Figure 6 shows the affect of reducing the specific impulse. The 10 second reduction increases the launch mass by over 40 % for the shorter flight times.

Additional solution results for the aeroassisted case suggest other trends. If all other parameters are fixed, the optimal launch mass varies little if the range angle and intercept time of the target vary in direct proportion. Increasing the axial drag coefficient, C_A, by 0.02 increases the launch mass by about 10 %. Increasing the mass density of the stages by 50 % decreases the launch mass by about 6 %. More accurate models of atmospheric density have very little effect on the launch mass.

VII. Conclusions

Models for high-performance, multistage rocket interceptors have been introduced. Efficient numerical procedures for minimizing their launch mass with respect to staging parameters and the angle-of-attack program have been described. These procedures circumvent many of the complexities associated with the nonlinear, multistage character of the minimization problem. Even though the angle-of-attack program is represented approximately, the equations of motion are solved accurately. Inherent ill-conditioning of the procedure is overcome by parameterizing the control variable (angle of attack) indirectly by a direct parameterization of a state variable (flight-path angle). A key aspect of the optimal trajectories is the negative-lift, aeroassisted character of the coasting payload stage. A simple and accurate analytical model of this coasting motion (the universal curve) has been derived. This model may prove useful in other problems where planetary atmospheres are encountered at hyperbolic speeds. The effect of various design parameters and target conditions on the optimal launch mass are described. As the intercept time is reduced the optimal launch mass rises at an ever increasing rate.

Acknowledgement

The research reported in this paper has been supported by the U. S. Army Strategic Defense Command under contract number DASG60-88-C-0037. The authors wish to thank David Parag for his helpful contributions.

References

[1]N. X. Vinh, A. Buseman and R. D. Culp, *Hypersonic and Planetary Entry Flight Mechanics*, The University of Michigan Press, Ann Arbor, Michigan, 1980.

[2]L. H. Jorgensen, "Estimation of Aerodynamics for Slender Bodies Alone and with Lifting Surfaces," *AIAA Journal*, Vol. 11, No. 3, 1975, pp. 409-412.

[3] R. E. O'Malley, Jr., "On Nonlinear Singularly Perturbed Initial Value Problems," ***SIAM Review***, Vol. 30, No. 2, 1988, pp. 193- 212.

[4] **Keller**, H. B., *Numerical Solution of Two Point Boundary Value Problems*, Society for Industrial and Applied Mathematics, Philadephia, Pennsylvania, 1976.

[5] Bulirsch, R. and Stoer, J., *Introduction to Numerical Analysis*, Springer-Verlag, New York, 1980.

[6] Kelly, H. J., "Method of Gradients," *Optimization Techniques*, edited by G. Leitmann, Academic Press, New York, 1962, pp. 205-254.

[7] Bryson, A. E. Jr. and Ho, Y. C., *Applied Optimal Control*, Halsted Press, Washington, D. C., 1975.

[8] Kelly, H. J., Kopp, R.E. and Moyer, H. J., "A Trajectory Optimization Technique Based on the Theory of Second Variation," *Progress in Astronautics and Aeronautics*, Vol 14, Academic Press, New York, 1964, pp. 559-582.

[9] Miele, A., Mangiavacchi, A. and Aggarwal, A.K.,"Modified Quasilinearization Algorithm for Optimal Control Problems with Nondifferential Constraints," *Journal of Optimization Theory and Applications*, Vol. 14, No. 5, 1974, pp. 529-556.

[10] Hargraves, C.R. and Paris, S.W., "Direct Trajectory Optimization Using Nonlinear Programming and Collocation," *AIAA Journal of Guidance, Control and Dynamics*, Vol. 10, No. 4, 1987, pp. 338-342.

[11] R. M. Howe, E. G. Gilbert, Ping Lu and N. X.Vinh, "Trajectory Optimization of Earth-launched Interceptors at Supercircular Speeds," *Proceedings of the International Society for Optical Engineering*, Vol. 872, 1988, pp. 12-18.

[12] P. E. Gill, W. Murray and M. H. Wright, *Practical Optimization*, Academic Press, New York, 1981.

[13] R. Fletcher, *Practical Methods of Optimization*, Second Edition, Wiley-Interscience, New York, 1987.

[14] D. F. Shanno and K.H. Phua, "Minimization of Unconstrained Multivariate Functions," *ACM Transactions on Mathematical Software*, Vol. 6, 1980, pp.618-622.

Table 1. Numerical Data for Optimal Trajectories in Figure 1

		Burnout conditions for 4th stage				
Type of Solution	Launch Mass (kg)	h (km.)	V	θ (deg.)	γ (deg.)	t (sec.)
Aeroassisted	18,990	58.3	1.68	2.2	3.2	40.6
Zero Lift Atmospheric	23,070	57.0	1.89	2.5	3.5	42.5
Keplerian	50,720	64.6	1.82	5.8	-1.6	75.2

		Burnout conditions for 5th stage				
Type of Solution	Coasting Time between 4th and 5th Stage	h (km.)	V	θ (deg.)	γ (deg.)	t (sec.)
Aeroassisted	0	63.7	2.11	3.7	0	52.6
Zero Lift Atmospheric	0	66.5	1.96	24.0	0.005	201.9
Keplerian	90.6	127.8	2.10	19.5	-4.7	182.0

Figure Captions

Fig. 1 Optimal trajectories for minimum launch mass: A- Keplerian, B- aeroassisted, C- zero-lift atmospheric, D- burnout of fifth stage, E- burnout of fourth stage, F- end of coast for fifth stage. Payload = 10 kg.; range angle = 45 deg.; target altitude = 400 km.; flight time = 360 sec..

Fig. 2 Functions describing motion on the universal curve.

Fig. 3 Additional details of the optimal aero assisted trajectory shown in Figure 1.

Fig. 4 Optimal launch mass as a function of flight time. Number of stages = 5; payload = 10 kg.; range angle = 45 deg.; target altitude = 200 km.; specific impulse = 300 sec..

Fig. 5 Optimal launch mass as a function of flight time for aeroassisted trajectories. Payload = 10 kg.; range angle = 45 deg.; target altitude = 200 km.; specific impulse = 300 sec..

Fig. 6 Optimal launch mass as a function of flight time for aeroassisted trajectories. Number of stages = 5; payload = 10 kg.; range angle = 45 deg.; target altitude = 200 km..

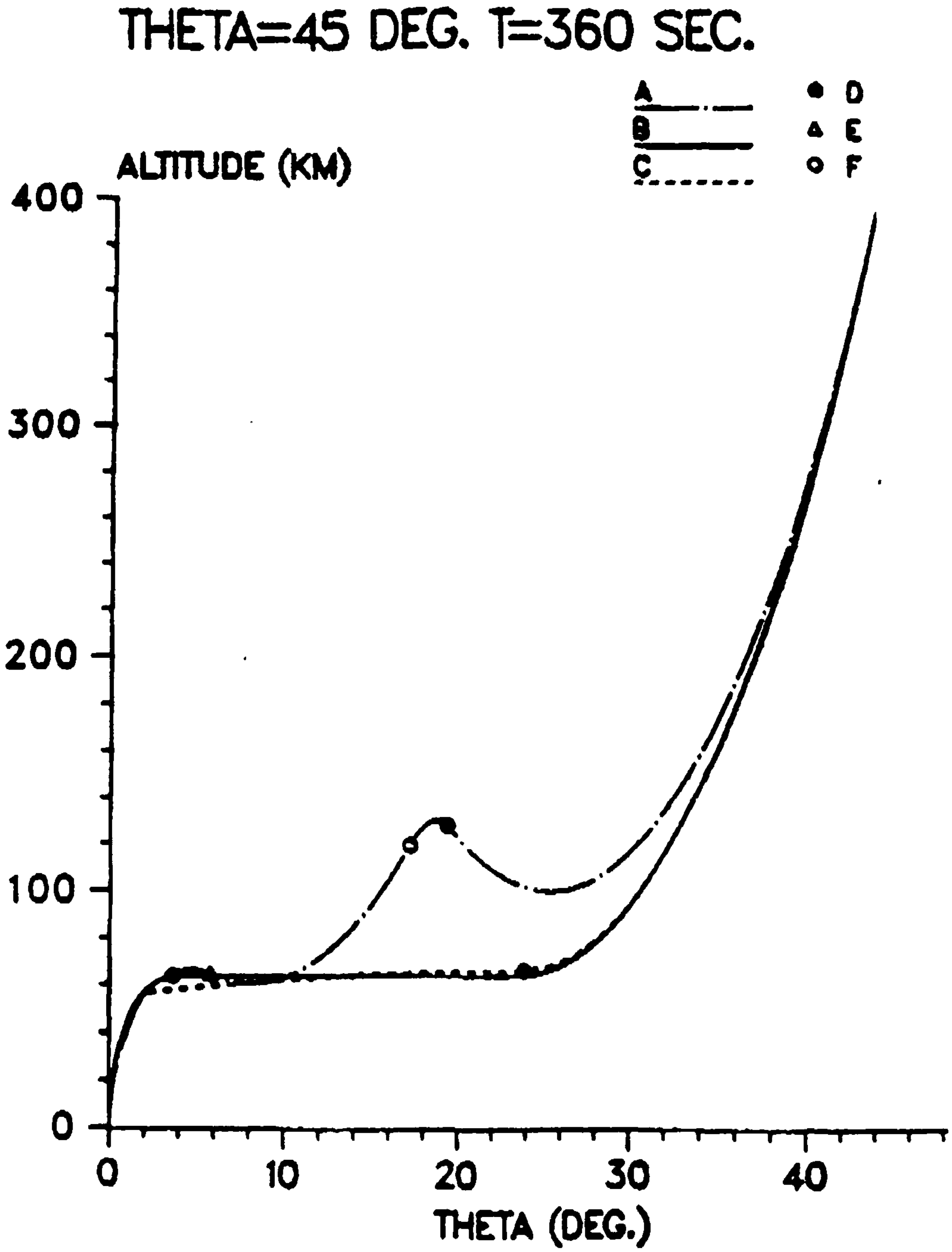
THETA=45 DEG. T=360 SEC.
A
B
C
● D
▲ E
○ F
ALTITUDE (KM)
400
300
200
100
0
0
10
20
30
40
THETA (DEG.)

Figure 1

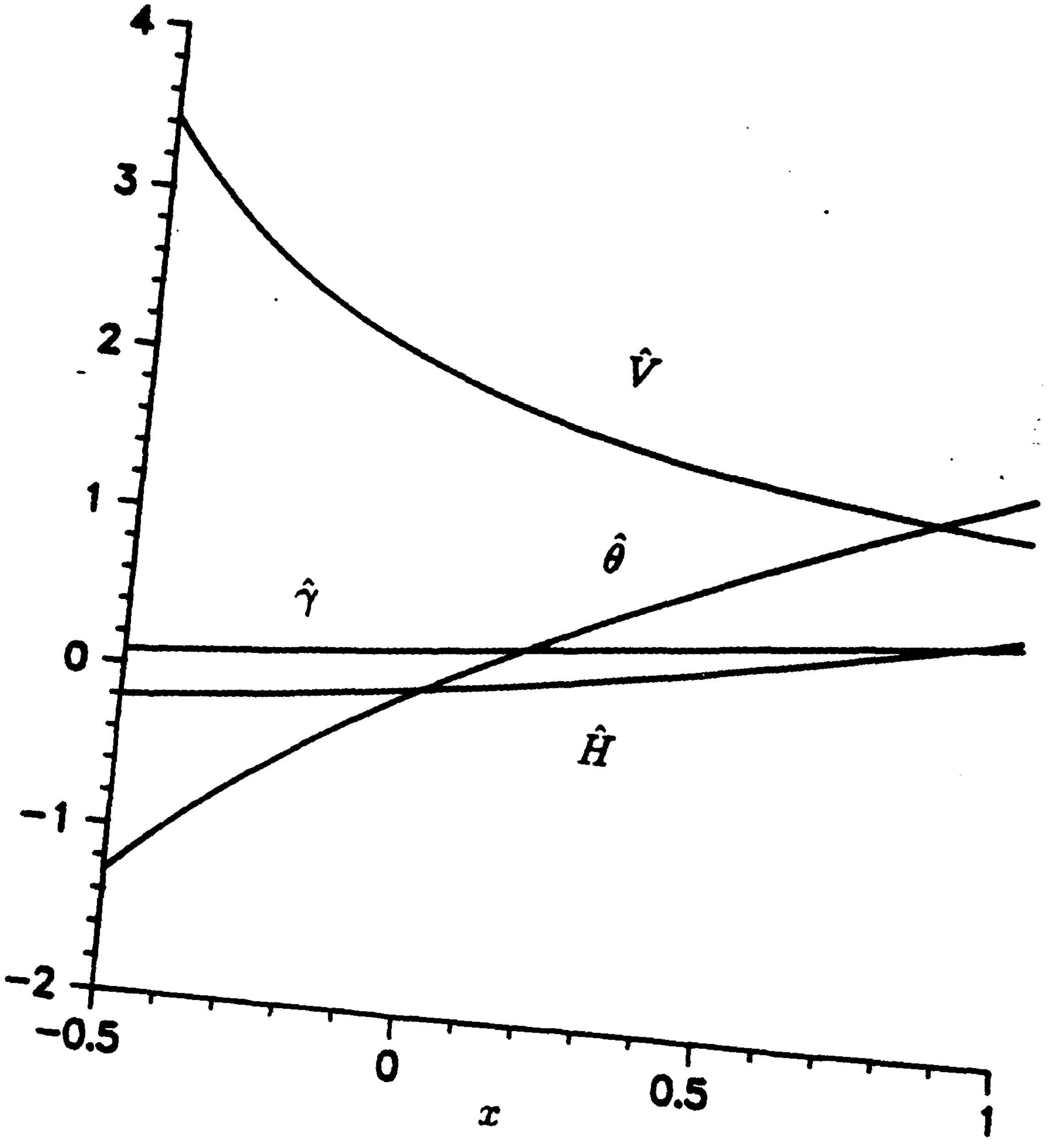

Figure 2

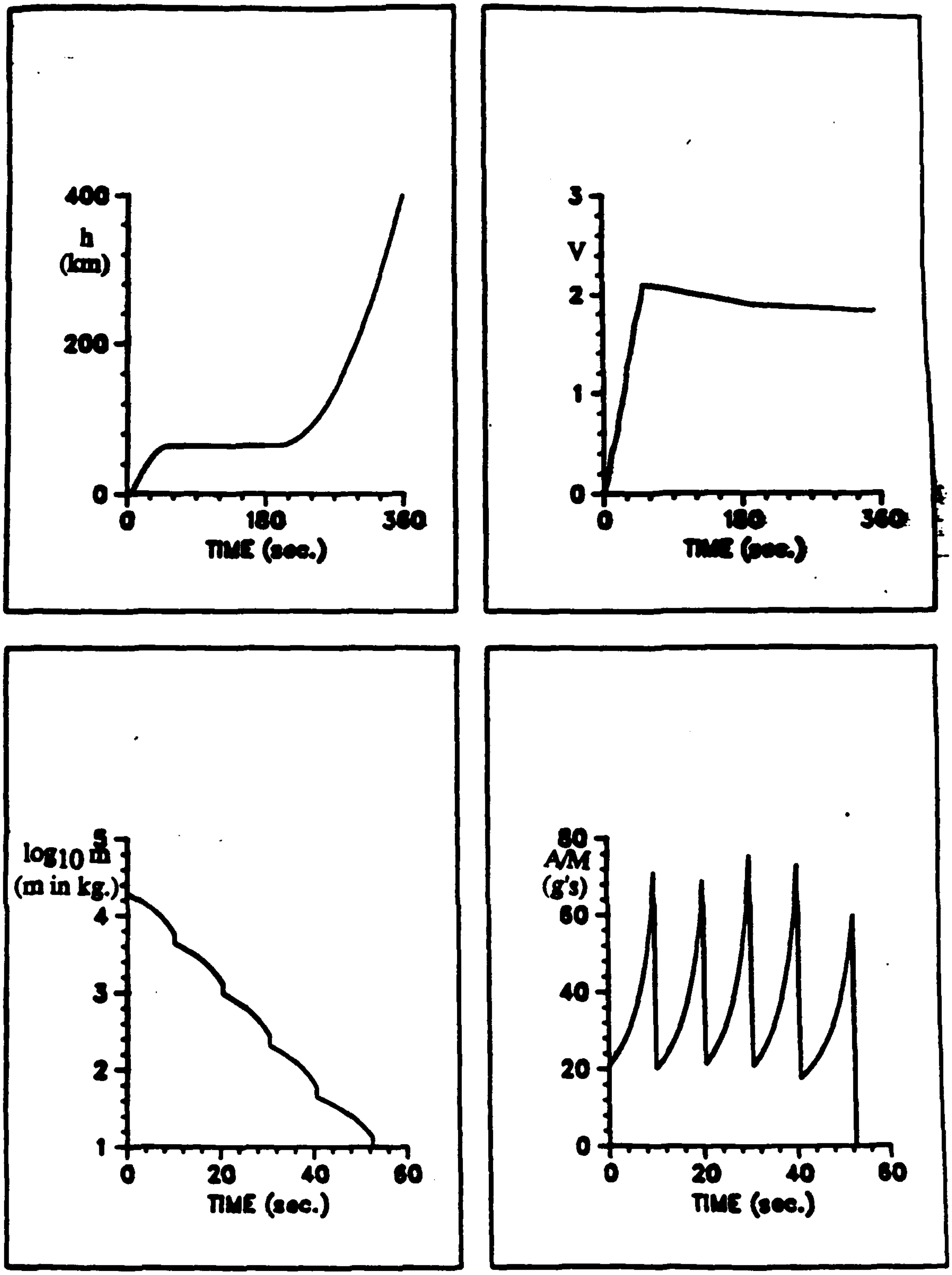

Figure 3 (Parts 1-4 & 8)

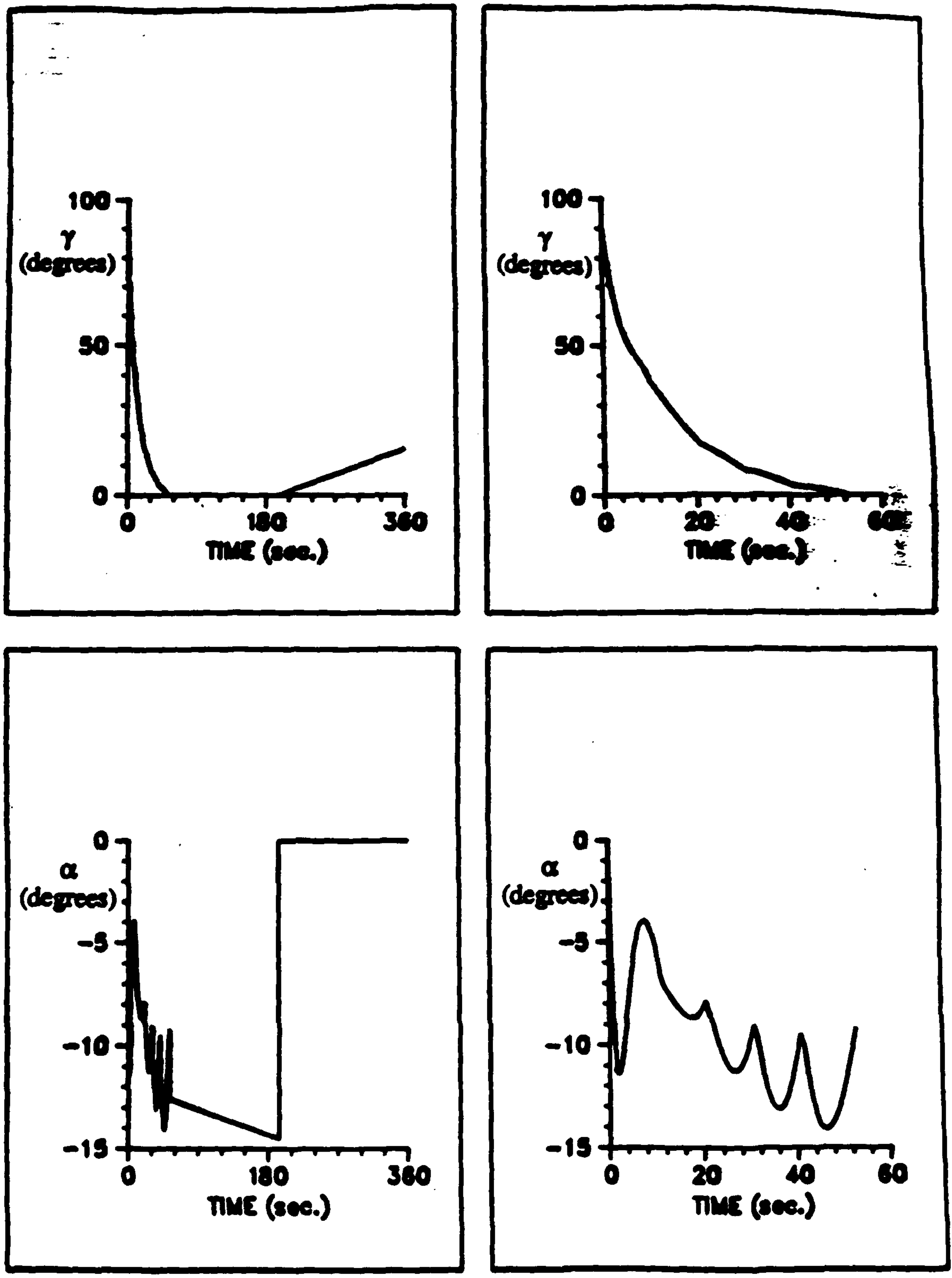

Figure 3 (parts 5-8 of 8)

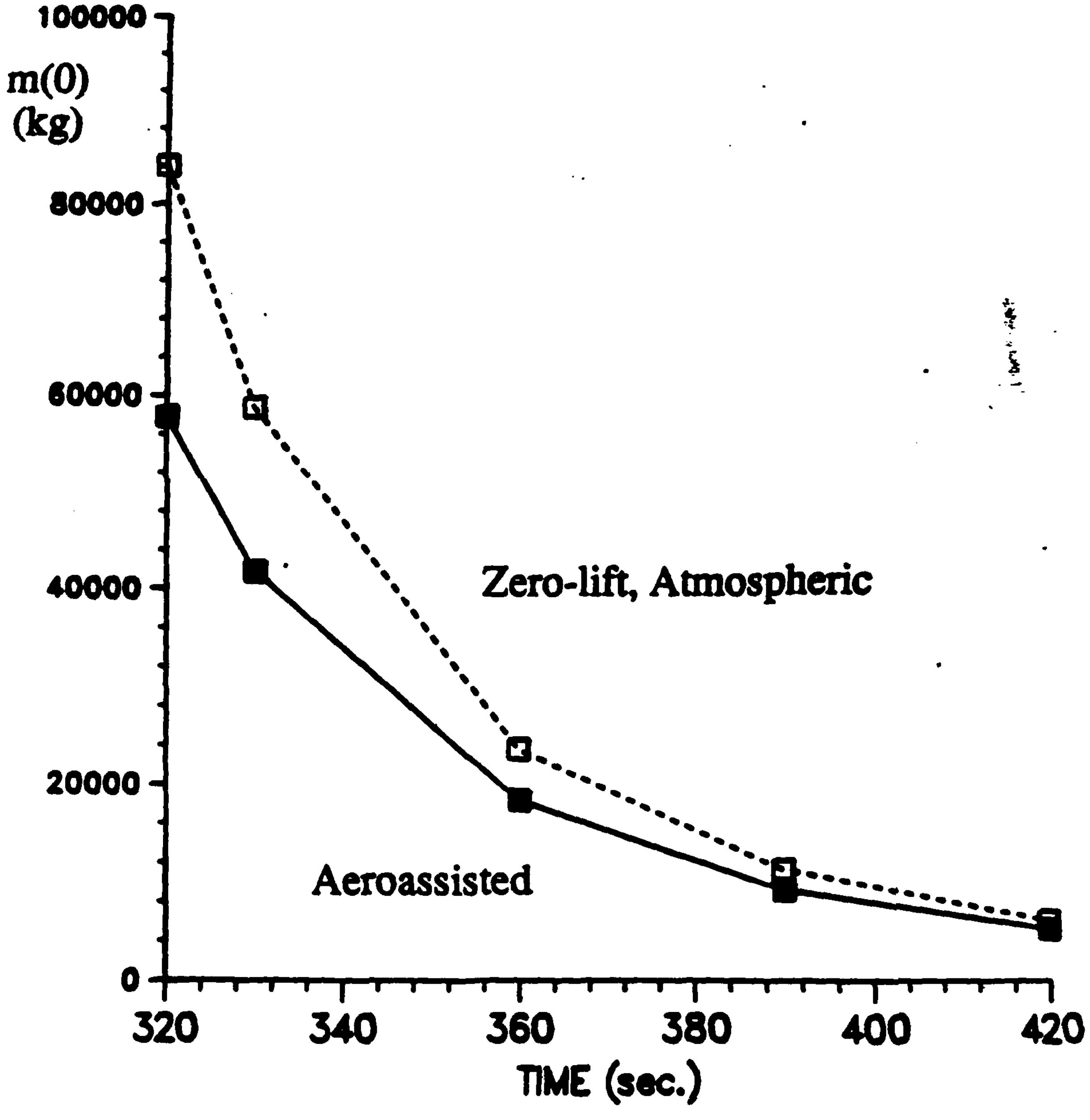
100000
m(0)
(kg)
80000
60000
40000
20000
0
320
340
360
380
400
420
TIME (sec.)
Zero-lift, Atmospheric
Aeroassisted

Figure 4

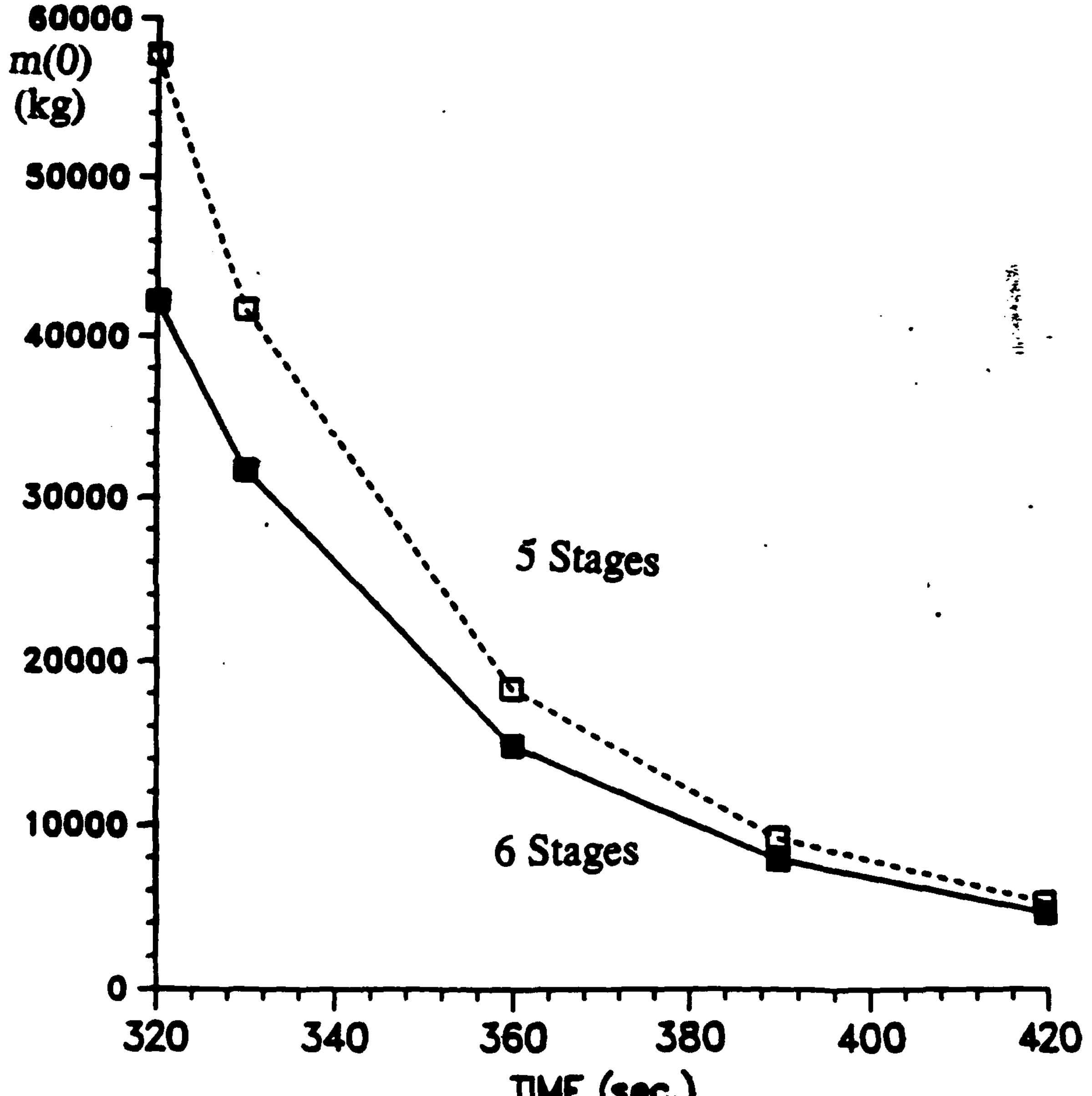

60000
m(0)
(kg)
50000
40000
30000
20000
10000
0
320
340
360
380
400
420
TIME (sec.)
5 Stages
6 Stages

Figure 5

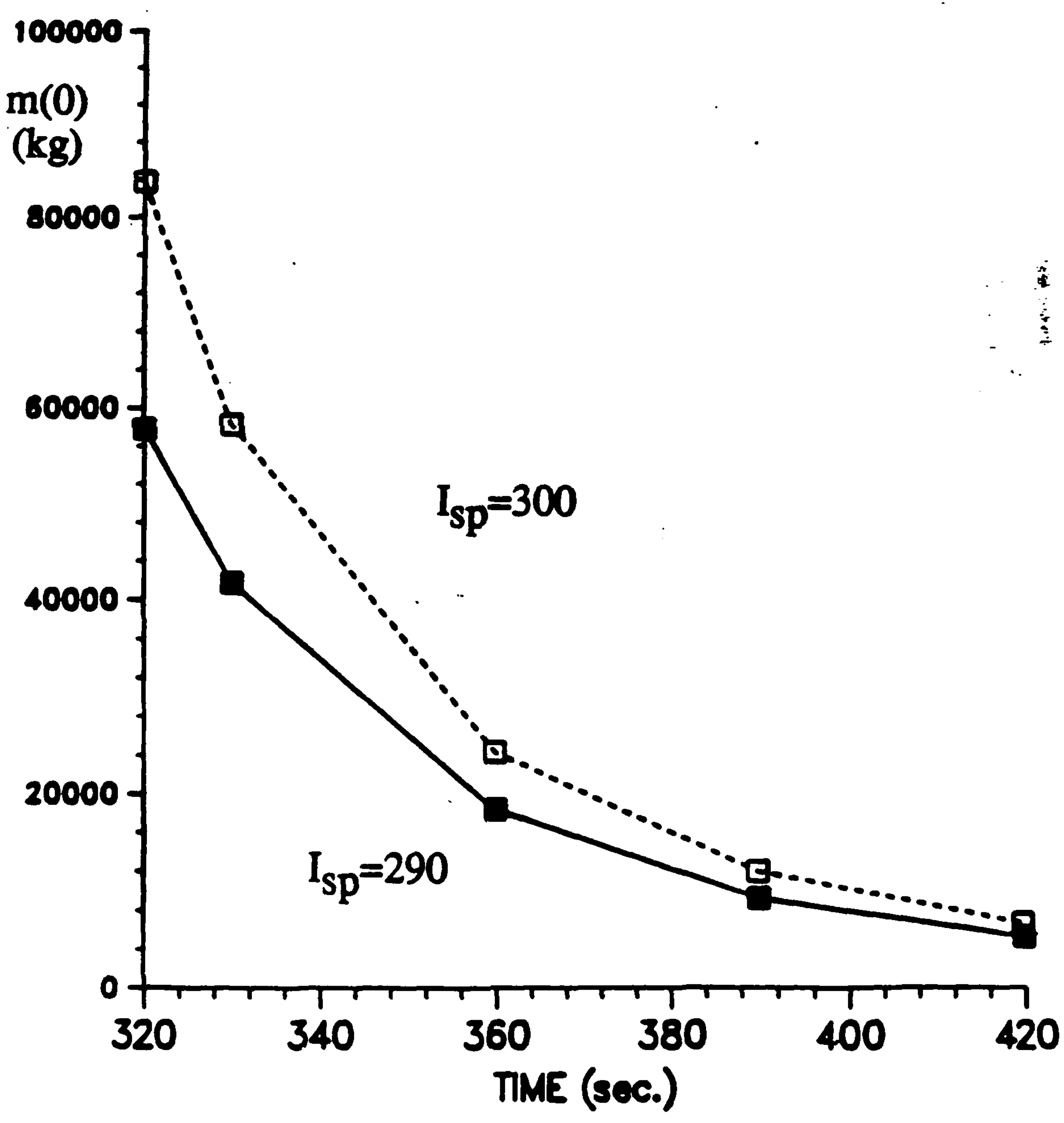

100000
m(0)
(kg)
80000
60000
40000
20000
0
I_{sp}=300
I_{sp}=290
320
340
360
380
400
420
TIME (sec.)

Figure 6

TIME-OPTIMAL ATTITUDE CONTROL OF A SPINNING MISSILE

by
Ebad Jahangir

A dissertation submitted in partial fulfillment
of the requirements for the degree of
Doctor of Philosophy
(Aerospace Engineering)
in The University of Michigan
1990

Doctoral Committee:
- Professor Robert M. Howe, Chairman
- Professor Elmer G. Gilbert
- Professor Donald T. Greenwood
- Associate Professor Pierre T. Kabamba
- Assistant Professor Costas Kravaris

(Title page only.)

A TWO-PULSE SCHEME FOR THE TIME-OPTIMAL ATTITUDE CONTROL OF A SPINNING MISSILE

E. Jahangir* and R. M. Howe**
University of Michigan
Ann Arbor, MI 48109-2140

Abstract

The problem of minimum-time attitude control of a spinning missile is addressed. The missile is modeled as a rigid body which is symmetric about one axis. The missile is assumed to have a large roll rate about this axis of symmetry. Control is achieved by a single reaction jet which, when fired, provides a constant moment about a transverse axis. Disturbance torques are assumed to be zero. The equations of motion are written under these assumptions. The missile is assumed to have some arbitrary initial transverse angular velocity and it is desired to take it to some final attitude in minimum time while reducing the transverse angular velocity to zero. This problem is formulated as an optimal control problem. Instead of taking the conventional approach of solving a two point boundary value problem, we consider an alternative approach. This approach deals with the specific case where only two thruster firings are sufficient to change the attitude of the missile in minimum time. By iterating on the switch times and integrating the state equations, we can compute the thruster firing times for a given set of boundary conditions. Some examples are included to illustrate the application of the concepts presented. We conclude by proposing a mechanization of this control scheme and pointing out some further research directions.

1. Introduction

Over the past three decades many papers and reports have treated various aspects of homing schemes and trajectory control associated with these schemes. Most of these papers consider surface-to-air or air-to-air missiles which use aerodynamic forces for trajectory control. With the advent of SDI, much attention has been focused on the interception of satellites or ICBM's outside the sensible atmosphere. Hence, aerodynamic forces cannot be generated for vehicle control. Instead, the thrust of a rocket engine is used to provide the necessary maneuver forces, with vehicle attitude control employed to point the thrust in the desired direction. Conventional thrust vector control systems tend to add both weight and complexity, and as a result counter the objective of minimizing the weight of the guided warhead. The simplest control involves a single thruster at right angles to the spin axis of the missile. In this scheme, the missile is given a large roll rate and the thruster is turned on for a fraction of each revolution in roll and at the right time during each roll cycle so that the desired attitude changes are achieved. Meanwhile the main thruster, by producing a thrust component perpendicular to the flight path, provides the necessary trajectory changes.

The problem of attitude control of spinning rigid bodies has not received much attention recently, although some research has been reported on this topic in the 1960's. The reorientation problem of a spinning rigid body is conceptually different than the simple rest-to-rest maneuver of a non-spinning rigid body. Because of the spin of the body, application of any moment about the transverse axes generates a precessional motion. If the initial transverse angular velocity is not zero, the problem becomes even more difficult because the problem loses its symmetry.

Athans and Falb[2] consider the problem of time-optimal velocity control of a rotating body with a single axis of symmetry. They show that for a single fixed control jet, the system has the properties of a harmonic oscillator. Thus, a switching curve can be derived to implement the control scheme. The cases of a gimballed control jet and two control jets are also considered. No mention is made of the complete attitude reorientation problem, however. Howe[3] proposes an attitude control scheme for sounding rockets. The main feature of this scheme is that it uses a single control jet. The control jet is fired for a fixed duration whenever certain conditions on direction cosines or transverse angular velocity are satisfied.

---

*Ph.D. Candidate in Aerospace Engineering Student Member, AIAA

**Professor of Aerospace Engineering Associate Fellow, AIAA

This results in the alternate reduction of attitude error and transverse angular velocity, finally ending in a limit cycle. Some other references[16,4,1,6,7,8,12,15,13] discuss the problem of reorienting a rotating rigid body which has no initial transverse angular velocity. Windenknecht[16] proposes a simple system for sun orientation of spinning satellites. In this scheme, the desired attitude is achieved by a succession of 180° precessional motions, each resulting in a small attitude change (small-angle approximations assumed valid), until the spin axis arrives at an attitude corresponding to the dead zone of the sun sensors. Cole *et al.*[4] prescribe the desired attitude change and solve for the necessary torques but give no details on mechanization. Other papers which propose active attitude control systems for spin stabilized vehicles have been published by Adams[1], Freed[6], and Grasshoff[7], but none of these explicitly discusses the reorientation problem. Grubin[8] uses the concept of finite rotations to mechanize a two-impulse scheme for reorienting the spin axis of a vehicle. If the torques are ideally impulsive, then the scheme is theoretically perfect. But in the case of finite-duration torquing, considerable errors can result. Wheeler[15] extends Grubin's work to include asymmetric spinning satellites, but the underlying philosophy is the same. Porcelli and Connolly[13] use a graphical approach to obtain control laws for the reorientation of a spinning body. Their results are only valid for small angles and small angular velocities. For this linearized case they prove that a two-impulse control scheme is fuel-optimal. Two sub-optimal control laws are then derived for the case of limited thrust based on the two-impulse solution.

None of the above papers consider time-optimal reorientation of a spinning space body. The control laws derived are based on small angle and/or impulsive torque approximations. For large angle maneuvers with limited thrust, sizeable errors can result because of these approximations. In the present work we examine a practical scheme for the attitude control of a spinning missile. The control scheme proposed is not limited to small angles and small angular velocities and the initial transverse angular velocity can be arbitrary, *i.e.*, it is not assumed to be zero. We have assumed no disturbances such as aerodynamic forces, gravity, solar radiation pressures, or structural damping. Because of the short flight times, these disturbances have negligible effect on the dynamics of the missile. These assumptions yield a simple mathematical model described by five state equations, *viz.*, two dynamical equations involving the transverse angular velocities and three kinematical equations giving the rates of change of Euler angles. The theory of optimal control is used to find a minimum-time control law.

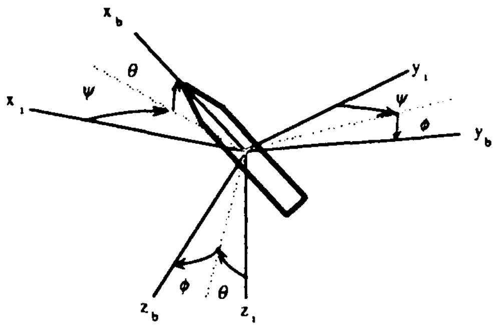

Figure 1: Axes systems.

2. Equations of Motion

Figure 1 shows the orientation of the moving body axes x_b, y_b, z_b relative to the inertial reference axes x_i, y_i, z_i, and also the Euler angles ψ, θ, ϕ relating the two axis systems. The body axes origin is at the missile c.g. with the x_b-axis assumed to be the axis of symmetry; the y_b- and z_b-axes lie in a plane perpendicular to the longitudinal axis, x_b. The missile is modeled as a rigid cylindrical body. We also assume that the control jet is located in the x_b-z_b plane and pointed in the direction of the z_b-axis. When fired, the control jet generates a constant positive moment about the y_b-axis.

Since no moment is applied about the x_b-axis, and since $I_y = I_z$ (the moments of inertia about the y_b- and z_b-axes are equal for a missile that is axially symmetric about its x_b-axis), it turns out that ω_x, the missile angular velocity component along the x_b-axis, is a constant equal to the initial spin velocity of the missile. We then obtain a set of five state equations: two dynamical equations involving the transverse angular velocities and three kinematical equations giving the rates of change of Euler angles. Thus

$$\dot{\omega}_y = \left(1 - \frac{I_x}{I_y}\right)\omega_x\omega_z + \frac{M_y}{I_y} \tag{1}$$

$$\dot{\omega}_z = -\left(1 - \frac{I_x}{I_y}\right)\omega_x\omega_y \tag{2}$$

$$\dot{\psi} = (\omega_y \sin\phi + \omega_z \cos\phi)\sec\theta \tag{3}$$

$$\dot{\theta} = \omega_y \cos\phi - \omega_z \sin\phi \tag{4}$$

$$\dot{\phi} = \omega_x + (\omega_y \sin\phi + \omega_z \cos\phi)\tan\theta \tag{5}$$

where

ω_y, ω_z = trasverse angular velocity components along the y- and z-axes, respectively,

ψ, θ, ϕ = Euler angles corresponding to yaw, pitch and roll, respectively,

I_x, I_y = the moments of inertia about the longitudinal and transverse axes, respectively,

M_y = the thruster torque about the y-axis.

For convenience we choose to write Eqs. (1)-(5) in terms of dimensionless variables and parameters in accordance with the following definitions:

$$\Omega_y = \frac{\omega_y}{\omega_x},\ \Omega_z = \frac{\omega_z}{\omega_x}$$
$$A = 1 - \frac{I_x}{I_y},\ \lambda_y = \frac{M_y}{I_y\omega_x^2}$$
$$\text{dimensionless time } T = \omega_x t$$

Now, if we redefine the $\dot{-}$ operator as differentiation with respect to the dimensionless time T, the equations become

$$\dot{\Omega}_y = A\Omega_z + \lambda_y \tag{6}$$

$$\dot{\Omega}_z = -A\Omega_y \tag{7}$$

$$\dot{\psi} = (\Omega_y \sin\phi + \Omega_z \cos\phi)\sec\theta \tag{8}$$

$$\dot{\theta} = \Omega_y \cos\phi - \Omega_z \sin\phi \tag{9}$$

$$\dot{\phi} = 1 + (\Omega_y \sin\phi + \Omega_z \cos\phi)\tan\theta \tag{10}$$

We assume that at the initial time, the missile body axis system coincides with the inertial axis system. The initial transverse angular velocity of the missile, however, is non-zero. We thus obtain the following initial conditions:

$$\Omega_z(T_0) = \Omega_{z0},\ \Omega_y(T_0) = \Omega_{y0}$$
$$\psi(T_0) = 0,\ \theta(T_0) = 0,\ \phi(T_0) = 0$$

The desired final conditions on the state variables are given by:

$$\Omega_z(T_f) = 0,\ \Omega_y(T_f) = 0$$
$$\psi(T_f) = \psi_d,\ \theta(T_f) = \theta_d,\ \phi(T_f) = \text{free}$$

The numerical values for the two parameters, A and λ_y, which will be used later in examples, are

$$A = 0.9,\ \lambda_y = 0.02$$

This value of A corresponds to a length to diameter ratio of 3.775 for a cylindrical body of uniform density. A missile weighing 10 lbs. and having a uniform mass density of aluminum would have the following dimensions:

length = 12.30 in., diameter = 3.26 in.

If the moment arm is half the length and the spin velocity is 50 rad/sec., $\lambda_y = 0.02$ corresponds to a thrust of 2.79 lbs.

3. Solution for the Linearized System

The equations of motion given by Eqs. (6)-(10) are nonlinear and no analytic solution can be found for the general case of arbitrary angles and angular velocities. Considerable simplification can be achieved, however, by assuming small angles and small transverse angular velocity compared to the axial spin velocity. For this linearized case, the equations of motion can be analytically integrated. These assumptions also yield some analytic results for the time history of the time-optimal control.

3.1. System Equations and Optimal Control Description

In order to get a simplified set of equations which can be easily integrated and which yield analytic solutions for the time optimal control, we assume that Ω_y, Ω_z and θ remain small during the attitude change maneuver. Eqs. (8)-(10) can then be written as

$$\dot{\psi} = \Omega_y \sin\phi + \Omega_z \cos\phi \tag{11}$$

$$\dot{\theta} = \Omega_y \cos\phi - \Omega_z \sin\phi \tag{12}$$

$$\dot{\phi} = 1 \tag{13}$$

Note that no assumption has been made on the magnitude of ψ or ϕ. Eq. (13) can be integrated with the initial condition $\phi(T_0) = 0$ to give

$$\phi = T - T_0 \tag{14}$$

We assume $T_0 = 0$ without loss of generality. Substituting this into Eqs. (11) and (12) we obtain the linearized equations of motion for the four state variables Ω_y, Ω_z, ψ, and θ as

$$\dot{\Omega}_y = A\Omega_z + \lambda_y \tag{15}$$

$$\dot{\Omega}_z = -A\Omega_y \tag{16}$$

$$\dot{\psi} = \Omega_y \sin T + \Omega_z \cos T \tag{17}$$

$$\dot{\theta} = \Omega_y \cos T - \Omega_z \sin T \tag{18}$$

These four equations can be written in the standard state-space form by defining the state vector $\mathbf{x}$ as

$$\mathbf{x} = \begin{bmatrix} \Omega_y & \Omega_z & \psi & \theta \end{bmatrix}^T$$

and the control u as

$$u = \lambda_y$$

The standard form for the equations is

$$\dot{\mathbf{x}} = \mathbf{A}\mathbf{x} + \mathbf{b}u \tag{19}$$

where

$$\mathbf{A} = \begin{bmatrix} 0 & A & 0 & 0 \\ -A & 0 & 0 & 0 \\ \sin T & \cos T & 0 & 0 \\ \cos T & -\sin T & 0 & 0 \end{bmatrix} \tag{20}$$

$$\mathbf{b} = \begin{bmatrix} 1 & 0 & 0 & 0 \end{bmatrix}^T \tag{21}$$

The initial state $\mathbf{x}_0$ is given by

$$\mathbf{x}_0 = \left[\begin{array}{cccc} x_{1,0} & x_{2,0} & 0 & 0 \end{array}\right]^T$$

We want to find a control which will take this initial state to the desired state $\mathbf{x}_d$

$$\mathbf{x}_d = \left[\begin{array}{cccc} 0 & 0 & x_{3,d} & x_{4,d} \end{array}\right]^T$$

while minimizing the time.

The question of existence of an optimal control for this class of problems is discussed by Cesari[3]. It is proven that a bang-bang optimal solution exists for the system described by $\dot{\mathbf{x}} = \mathbf{A}(t)\mathbf{x}(t)+\mathbf{B}(t)u(t)$ for a class of performance indices and constraints. He also shows that there may well be optimal solutions which are not bang-bang. However, if the opimal solution is unique, it must be bang-bang (under certain conditions on the states and constraints). At this time no general theorems are available on the uniqueness of optimal solutions for the one-sided controls, *i.e.*, $0 \leq u \leq u_{max}$. Therefore, we can only give necessary conditions for u^* to be an optimal control.

Proceeding with the derivation of the necessary conditions on the time-optimal control, we write the performance index

$$J = \int_{T_0}^{T_f} 1dt \qquad (22)$$

with the given constraints

$$\dot{\mathbf{x}} = \mathbf{A}\mathbf{x} + \mathbf{b}u \qquad (23)$$

$$0 \leq u \leq u_{max} \qquad (24)$$

The Hamiltonian can be written as

$$H = \mathbf{p}^T\dot{\mathbf{x}} - 1 \qquad (25)$$

where $\mathbf{p}$ is the costate vector. The necessary conditions for u^* to be an optimal control are

$$\dot{\mathbf{x}}^* = \frac{\partial H}{\partial \mathbf{p}} = \mathbf{A}\mathbf{x}^* + \mathbf{b}u^* \qquad (26)$$

$$\dot{\mathbf{p}}^* = -\frac{\partial H}{\partial \mathbf{x}} = -\mathbf{A}^T\mathbf{p}^* \qquad (27)$$

$$u^* = \begin{cases} u_{max} & \text{if } p_1^* > 0 \\ 0 & \text{if } p_1^* < 0 \end{cases} \qquad (28)$$

and

$$\mathbf{x}(T_0) = \mathbf{x}_0 \qquad (29)$$

$$\mathbf{x}(T_f) = \mathbf{x}_d \qquad (30)$$

$$\mathbf{p}(T_0) = \text{free} \qquad (31)$$

$$\mathbf{p}(T_f) = \text{free} \qquad (32)$$

$$H(T_f) = 0 \qquad (33)$$

Eqs. (26) and (27) are the differential equations for the state and costate vector. Eq. (28) is derived from the optimality condition *i.e.* maximizing the Hamiltonian H. Eqs. (29) and (30) are the given boundary conditions and Eqs. (31) and (32) are derived from the transversality conditions. Hence, in the problem we have 8 differential equations (Eqs. (26)-(27)) with 8 boundary conditions (Eqs. (29)-(30)) constituting a TPBVP (two point boundary value problem). Eq. (33) is used to determine T_f.

Eq. (27) can be solved analytically to obtain $\mathbf{p}$ as an analytical function of the dimensionless time, T and the initial condition, $\mathbf{p}(0)$. The expression for the switching function p_1 is

$$\begin{aligned} p_1 \;&=\; \rho_1 \cos AT + \rho_2 \sin AT - \frac{\rho_3}{1-A}(\cos AT \\ &\quad - \cos T) + \frac{\rho_4}{1-A}(\sin AT - \sin T) \qquad (34) \end{aligned}$$

where the initial conditions $\rho_1 = p_1(0)$, $\rho_2 = p_2(0)$, $\rho_3 = p_3(0)$, and $\rho_4 = p_4(0)$ are constants to be determined.

The expression for the control u^* can now be written as

$$u^* = \begin{cases} u_{max} & \text{if } S > 0 \\ 0 & \text{if } S < 0 \end{cases} \qquad (35)$$

where for convenience we have defined $S = p_1$. Eq. (35) states that the optimal control is a bang-bang type. A singular solution is not possible because if $S \equiv 0$ over some interval, that implies that $\rho_1 = \rho_2 = \rho_3 = \rho_4 = 0$. This means that $H \equiv -1$ for all T. This contradicts the transversality condition $H(T_f) = 0$.

The switching function S will be periodic if A is a rational number. However, it does not go through zero at regular intervals, *i.e.*, the intervals between successive times when $S = 0$ are not uniform. Thus, depending on the boundary conditions, the constants ρ_1, ρ_2, ρ_3 and ρ_4 will be different and each turn-on and turn-off interval may be of a different duration. Figure 2 shows the switching curve for $A = 0.9$, for some values of the costate initial conditions ρ_1, ρ_2, ρ_3 and ρ_4.

3.2. Two-pulse Solution

Starting at $T_0 = 0$, typical time history curves for the control u and the transverse angular velocity components x_1 and x_2, are shown in Figure 3 for the case where the final target state is reached with two thruster firings. The switch times, T_1, T_2, T_3 and T_f, are the four unknowns. The thruster is fired from T_1 to T_2 and then from T_3 to T_f.

The equations for $\dot{x}_1$ and $\dot{x}_2$, which are exact, can be integrated starting from any arbitrary initial conditions at T_i to obtain

$$x_1(T) \;=\; x_{1,i} \cos A(T - T_i)$$

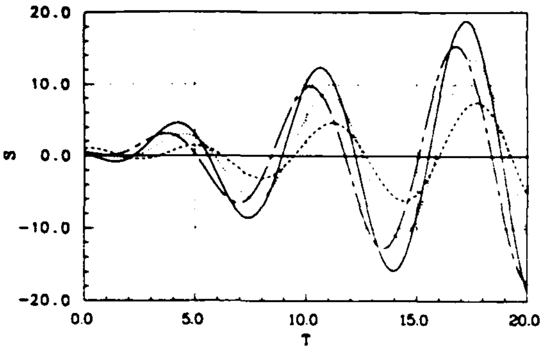

Figure 2: Switching function S for four different sets of costate initial conditions.

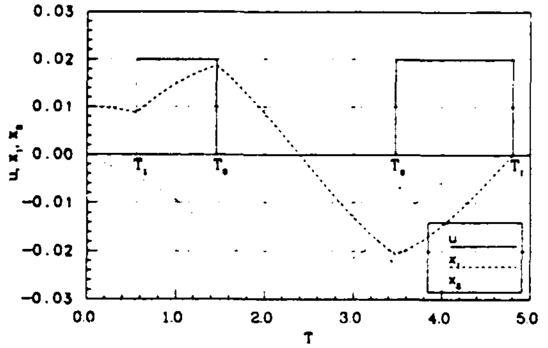

Figure 3: u, x_1 and x_2 vs. T.

$$+\left(x_{2,i}+\frac{u}{A}\right)\sin A(T-T_i) \quad (36)$$

$$\begin{aligned} x_2(T) &= \left(x_{2,i}+\frac{u}{A}\right)\cos A(T-T_i) \\ &\quad -x_{1,i}\sin A(T-T_i)-\frac{u}{A} \end{aligned} \quad (37)$$

The subscript i refers to arbitrary initial conditions. Substituting Eqs. (36) and (37) into the equations for $\dot{x}_3$ and $\dot{x}_4$ in Eq. (20), we obtain

$$\begin{aligned} \dot{x}_3 &= x_{1,i}\sin((1-A)T+AT_i) \\ &\quad +x_{2,i}\cos((1-A)T+AT_i) \\ &\quad +\frac{u}{A}(\cos((1-A)T+AT_i)-\cos T) \end{aligned} \quad (38)$$

$$\begin{aligned} \dot{x}_4 &= x_{1,i}\cos((1-A)T+AT_i) \\ &\quad -x_{2,i}\sin((1-A)T+AT_i) \\ &\quad +\frac{u}{A}(-\sin((1-A)T+AT_i)+\sin T) \end{aligned} \quad (39)$$

These can be easily integrated with the given initial conditions on x_3 and x_4. Thus we obtain

$$\begin{aligned} x_3(T) &= x_{3,i}+\frac{2}{1-A}\sin a(1-A) \\ &\quad [x_{1,i}\sin(b-aA)+x_{2,i}\cos(b-aA)] \\ &\quad +\frac{2u}{A}\left[\frac{1}{1-A}\cos(b-aA)\sin a(1-A)\right. \\ &\quad \left.-\cos b\sin a\right] \end{aligned} \quad (40)$$

$$\begin{aligned} x_4(T) &= x_{4,i}+\frac{2}{1-A}\sin a(1-A) \\ &\quad [x_{1,i}\cos(b-aA)-x_{2,i}\sin(b-aA)] \\ &\quad +\frac{2u}{A}\left[\frac{-1}{1-A}\sin(b-aA)\sin a(1-A)\right. \\ &\quad \left.+\sin b\sin a\right] \end{aligned} \quad (41)$$

where

$$a=\frac{T-T_i}{2} \qquad b=\frac{T+T_i}{2}$$

Since we now have expressions for x_1, x_2, x_3, and x_4 as functions of the running time T and the given initial conditions, we can obtain expressions for these variables at $T=T_f$. The procedure is to use Eqs. (36)-(37) and (40)-(41) with $T_i=T_0$ and $u=0$ to obtain the state variables at $T=T_1$. Then we let $T_i=T_1$ and use the associated initial conditions with $u=u_{max}$ to obtain the new conditions at $T=T_2$, and so on. Finally, we end up with $x_1(T_f)$, $x_2(T_f)$, $x_3(T_f)$, and $x_4(T_f)$ as functions of the boundary conditions and T_1, T_2, T_3 and T_f. Since the boundary conditions at $T=T_0$ and $T=T_f$ are known, this procedure yields four equations in four unknowns, T_1, T_2, T_3 and T_f. The problem can be simplified, however, by noting that T_3 and T_f can be chosen such that $x_1(T_f)=x_2(T_f)=0$. In this way T_3 and T_f can be expressed as functions of T_1 and T_2 and the problem is reduced to finding T_1 and T_2 such that $x_3(T_f)=x_{3,d}$ and $x_4(T_f)=x_{4,d}$. Since T_1 and T_2 cannot be expressed as explicit functions of the initial conditions, the problem must be solved iteratively.

This procedure of writing the nonlinear equations $\mathbf{x}(T_f)=\mathbf{f}(\mathbf{x}_0,T_1,T_2,T_3,T_f)$ can be thought of as a numerical integration method which uses the state transition matrix of the system to integrate the state from $\mathbf{x}(T_0)$ to $\mathbf{x}(T_f)$ in four time intervals of variable duration, where over each interval the control u remains constant. The state transition method to simulate linear systems is discussed by Howe[10].

In Eqs. (36) and (37) we let $T_i=T_2$, $T=T_3$ and $u=0$ and obtain

$$x_{1,3}=x_{1,2}\cos A(T_3-T_2)+x_{2,2}\sin A(T_3-T_2) \quad (42)$$

$$x_{2,3}=-x_{1,2}\sin A(T_3-T_2)+x_{2,2}\cos A(T_3-T_2) \quad (43)$$

Now letting $T_i=T_3$, $T=T_f$ and $u=u_{max}$, we obtain

$$\begin{aligned} x_1(T_f) &= x_{1,2}\cos A(T_f-T_2)+x_{2,2}\sin A(T_f-T_2) \\ &\quad +\frac{u_{max}}{A}\sin A(T_f-T_3) \end{aligned} \quad (44)$$

$$
\begin{aligned}
x_2(T_f) &= x_{2,2}\cos A(T_f-T_2) - x_{1,2}\sin A(T_f-T_2) \\
&\quad + \frac{u_{max}}{A}\left(\cos A(T_f-T_3)-1\right) \qquad (45)
\end{aligned}
$$

Setting $x_1(T_f) = x_2(T_f) = 0$ and using simple trignometric relationships, we finally obtain

$$
\begin{aligned}
T_3 &= T_2 + \frac{1}{A}\left(\tan^{-1}\left(\frac{-x_{2,2}}{-x_{1,2}}\right)\right. \\
&\quad \left. - \sin^{-1}\left(\frac{A\sqrt{x_{1,2}^2+x_{2,2}^2}}{2u_{max}}\right)\right) \qquad (46)
\end{aligned}
$$

$$
\begin{aligned}
T_f &= T_2 + \frac{1}{A}\left(\tan^{-1}\left(\frac{-x_{2,2}}{-x_{1,2}}\right)\right. \\
&\quad \left. + \sin^{-1}\left(\frac{A\sqrt{x_{1,2}^2+x_{2,2}^2}}{2u_{max}}\right)\right) \qquad (47)
\end{aligned}
$$

Clearly, adding $\frac{2n\pi}{A}$ to T_3 and T_f would still make $x_1(T_f) = x_2(T_f) = 0$. However, from Eq. (35) and Figure 2, we observe that the intervals between switches are never more than one period, *i.e.*, $\frac{2\pi}{A}$. Hence, we limit $T_1 \in (0, \frac{2\pi}{A})$ and $T_3 - T_2 \in (0, \frac{2\pi}{A})$. In the next section a condition is derived which provides a check for the time-optimality of a two-pulse solution.

3.3. Optimality of the Two-pulse Solution

Figure 3 shows the time history of the control for the two-pulse solution. Again, T_1 and T_3 represent the first and second turn-on times, and T_2 and T_f represent the first and second turn-off times, respectively. From Eq. (35) (the necessary condition on control), we know that

$$
u^* = \begin{cases} u_{max} & \text{if } S > 0 \\ 0 & \text{if } S < 0 \end{cases}
$$

Since the boundary conditions are satisfied by the two-pulse solution, we only have to check for the above necessary condition. Thus, in order for the two-pulse solution to be time-optimal, it should satisfy the following condition on S.

$$
S\begin{cases} < 0 & \text{if } T \in (T_0, T_1) \text{ or } T \in (T_2, T_3) \\ > 0 & \text{if } T \in (T_1, T_2) \text{ or } T \in (T_3, T_f) \end{cases} \qquad (48)
$$

Eq. (48) gives the necessary condition for the time-optimality of a given two-pulse solution. We now present a procedure to determine if the switching times obtained satisfy the necessary condition on the optimal control. We compute $S(T)$ such that $S(T_1) = S(T_2) = S(T_3) = 0$. Then $S(T)$ is plotted to see whether $S(T)$ goes through zero at only $T = T_1, T_2$ or T_3 or whether there are other $T \in [T_0, T_f]$ such that $S(T) = 0$.

		Example 1	Example 2
Boundary Conditions	$x_{1,0}$	0.0666666701	0.0282842708
	$x_{2,0}$	−0.0222222235	0.0282842708
	$x_{3,d}$	−0.0041141893	0.3913032919
	$x_{4,d}$	0.4101158694	0.1566834726
Turn-on and Turn-off Times	T_1	1.72042500	5.46257075
	T_2	5.27150921	6.28533040
	T_3	8.71603244	9.65781759
	T_f	10.47287320	12.13034180

Table 1: Examples for the optimality test.

From Eq. (48) we know that $S(T_1) = S(T_2) = S(T_3) = 0$. Thus, we can write

$$
\begin{bmatrix}
\cos AT_1 & \sin AT_1 & \frac{\cos T_1 - \cos AT_1}{1-A} & \frac{\sin AT_1 - \sin T_1}{1-A} \\
\cos AT_2 & \sin AT_2 & \frac{\cos T_2 - \cos AT_2}{1-A} & \frac{\sin AT_2 - \sin T_2}{1-A} \\
\cos AT_3 & \sin AT_3 & \frac{\cos T_3 - \cos AT_3}{1-A} & \frac{\sin AT_3 - \sin T_3}{1-A}
\end{bmatrix}
\begin{bmatrix} \rho_1 \\ \rho_2 \\ \rho_3 \\ \rho_4 \end{bmatrix}
= \begin{bmatrix} 0 \\ 0 \\ 0 \end{bmatrix} \qquad (49)
$$

One alternative way of writing this equation is

$$
\begin{bmatrix}
\cos AT_1 & \sin AT_1 & \frac{\cos T_1 - \cos AT_1}{1-A} \\
\cos AT_2 & \sin AT_2 & \frac{\cos T_2 - \cos AT_2}{1-A} \\
\cos AT_3 & \sin AT_3 & \frac{\cos T_3 - \cos AT_3}{1-A}
\end{bmatrix}
\begin{bmatrix} \frac{\rho_1}{\rho_4} \\ \frac{\rho_2}{\rho_4} \\ \frac{\rho_3}{\rho_4} \end{bmatrix}
= \begin{bmatrix} \frac{\sin T_1 - \sin AT_1}{1-A} \\ \frac{\sin T_2 - \sin AT_2}{1-A} \\ \frac{\sin T_3 - \sin AT_3}{1-A} \end{bmatrix} \qquad (50)
$$

This equation can be solved for $\frac{\rho_1}{\rho_4}$, $\frac{\rho_2}{\rho_4}$ and $\frac{\rho_3}{\rho_4}$ if the 3×3 matrix on the left hand side is non-singular. Once ρ_1, ρ_2, ρ_3 and ρ_4 are known, S can be plotted as a function of the dimensionless time T and the two-pulse solution can be checked to see if it satisfies the necessary conditions on the optimal control. If $S = 0$ for some $T \in [T_0, T_f], T \neq T_1, T_2, T_3$ then the necessary condition is violated and we can reject the switch times as non-optimal. However, if $S = 0$ only for $T = T_1, T_2, T_3$ and $T \in [T_0, T_f]$ then the switch times obtained remain candidates for being time-optimal.

Two examples are presented here. The initial and the desired final conditions and the corresponding switch times for the two examples are given in Table 1. The first example is shown as the solid curve in Figure 4. It can be seen from this plot that $S = 0$ only at the switch times T_1, T_2 and T_3 given in Table 1 for Example 1. Therefore, the solution is time-optimal. The dashed line in Figure 4 shows the second example, where the two-pulse solution obtained results in $S(T) = 0$ when $T \in [T_0, T_1)$. Therefore, this solution is not time-optimal.

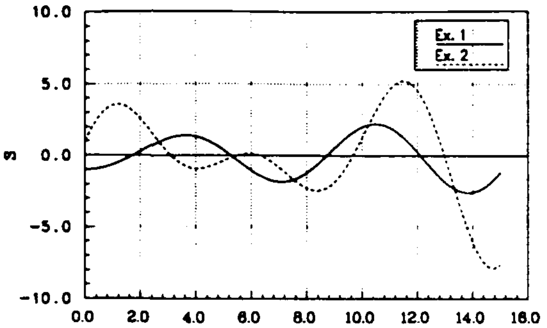

Figure 4: Switching function S vs. T.

4. Solution for the Nonlinear System

In the previous section we linearized the system equations and obtained some simple expressions for the time-optimal control. A two-pulse solution, based on analytic integration of state equations, was derived. These analytic expressions are only valid for transverse angular velocities much smaller than the axial spin velocity, and for small Euler angles. When the transverse angular velocity is not of negligible magnitude compared to the axial spin velocity or the angles get relatively large, the analytic solutions of Section 3 yield poor results. We consider the complete nonlinear equations of motion in this section and derive the necessary conditions for u^* to be an optimal control.

4.1. System Equations and Optimal Control Description

We wish to find the time history of the control u which takes our initial state to the desired state in minimum time. In order to write a state variable description of the system, we define the state $\mathbf{x}$ of the system as

$$\mathbf{x} = [\ \Omega_y \quad \Omega_z \quad \psi \quad \theta \quad \phi\ ]^T$$

and the control u as

$$u = \lambda_y$$

Eqs. (6)-(10) can now be written in the standard form.

$$\dot{\mathbf{x}} = \mathbf{f}(\mathbf{x}) + \mathbf{g}u \tag{51}$$

where

$$\mathbf{f}(\mathbf{x}) = \begin{bmatrix} Ax_2 \\ -Ax_1 \\ (x_1 \sin x_5 + x_2 \cos x_5) \sec x_4 \\ x_1 \cos x_5 - x_2 \sin x_5 \\ 1 + (x_1 \sin x_5 + x_2 \cos x_5) \tan x_4 \end{bmatrix} \tag{52}$$

$$\mathbf{g} = [\ 1 \quad 0 \quad 0 \quad 0 \quad 0\ ]^T \tag{53}$$

The initial state $\mathbf{x}_0$ is given by

$$\mathbf{x}_0 = [\ x_{1,0} \quad x_{2,0} \quad 0 \quad 0 \quad 0\ ]^T$$

We want to find a control which will take this initial state to the desired state $\mathbf{x}_d$

$$\mathbf{x}_d = [\ 0 \quad 0 \quad x_{3,d} \quad x_{4,d} \quad \text{free}\ ]^T$$

while minimizing the total maneuver time.

Filippov[5] gives a theorem and proves the existence of an optimal control for a Mayer problem. This theorem covers the more specific case of time-optimal control of Eq. (4.1) under the given constraints and the boundary conditions. We note that the existence of an optimal control for the linearized system discussed in Chapter 3 can also be proven using the more general Filippov's theorem.

In order to derive an expression for the time-optimal control, we write the performance index as

$$J = \int_{T_0}^{T_f} 1 dt \tag{54}$$

with the given constraints

$$\dot{\mathbf{x}} = \mathbf{f}(\mathbf{x}) + \mathbf{g}u \tag{55}$$

$$0 \le u \le u_{max} \tag{56}$$

We can also write the Hamiltonian

$$H = \mathbf{p}^T \dot{\mathbf{x}} - 1 \tag{57}$$

where $\mathbf{p}$ is the costate vector. The necessary conditions for u^* to be an optimal control are

$$\dot{\mathbf{x}}^* = \frac{\partial H}{\partial \mathbf{p}} = \mathbf{f}(\mathbf{x}^*) + \mathbf{g}u^* \tag{58}$$

$$\dot{\mathbf{p}}^* = -\frac{\partial H}{\partial \mathbf{x}} = \mathbf{H}(\mathbf{x}^*)\mathbf{p}^* \tag{59}$$

$$u^* = \begin{cases} u_{max} & \text{if } p_1^* > 0 \\ 0 & \text{if } p_1^* < 0 \end{cases} \tag{60}$$

and

$$\mathbf{x}(T_0) = \mathbf{x}_0 \tag{61}$$

$$x_1(T_f) = 0, x_2(T_f) = 0, x_3(T_f) = x_{3,d}, x_4(T_f) = x_{4,d} \tag{62}$$

$$p_5(T_f) = 0 \tag{63}$$

$$H(T_f) = 0 \tag{64}$$

Eqs. (58) and (59) are the differential equations for the state and costate vector. Eq. (60) is derived from the optimality condition, *i.e.*, maximizing the Hamiltonian H. Eqs. (61) and (62) are the given boundary conditions and Eqs. (63) and (64) are derived from the transversality conditions. Furthermore, we note from the theory of necessary conditions that

$$\frac{\partial H(\mathbf{x}^*, \mathbf{p}^*, T)}{\partial T} = \frac{dH(\mathbf{x}^*, \mathbf{p}^*, T)}{dT} = 0$$

This, in addition to Eq. (64), shows that

$$H(\mathbf{x}^*, \mathbf{p}^*, T) = 0 \text{ for all } T \in [T_0, T_f]$$

Hence, the time-optimal control problem is described by 10 scalar differential equations given by Eqs. (58) and (59). The boundary conditions on the state and costate variables are given by Eqs. (61)-(63). This constitutes a TPBVP (two point boundary value problem). Eq. (64) is used to determine T_f. We compare the results obtained in this section with the results that were obtained for the linearized equations of motion in Section 3.1. The control obtained in both cases is bang-bang and the switching is determined by the costate variable corresponding to $x_1 (= \Omega_y)$. However, the expression for the derivative of the costate vector in the nonlinear case cannot be integrated analytically. For this reason, no simple test for the optimality of the two-pulse solution for the nonlinear case (to be discussed in Section 4.2) analogous to Section 3.2 can be devised. Also, unlike the linearized system where the Hamiltonian was a function of time, $\frac{\partial H}{\partial T} = 0$ and therefore $H \equiv 0$.

4.2. Two-pulse Solution

In Section 4.1 the necessary conditions for u^* to be an optimal control are derived. We find that the solution to the time-optimal problem involves integrating 10 differential equations with split boundary conditions and an unknown T_f. Instead of trying to solve this complex TPBVP (two point boundary value problem), we propose a method which requires integration of only the state equations with the unknown switch times.

In this section we follow the same procedure used previously in Section 3.2 to obtain the optimal switch times T_1, T_2, T_3, and T_f, except here we integrate the state equations numerically instead of analytically. This removes the required assumption of small angles and small transverse angular rates and still leads to the calculation of the two-pulse switch times T_1, T_2, T_3, and T_f. However, no optimality test, analogous to the one in Section 3.3, can easily be devised because of our inability to integrate the costate equations analytically. Nevertheless, if the solution to the nonlinear problem is close to the solution of the time-optimal linearized problem, it is likely that the solution will be time-optimal. To verify this hypothesis, we generated several optimal trajectories by varying the initial costate variables. By comparing these trajectories with the trajectories generated by the two-pulse solution, it is verified that this hypothesis, *i.e.*, the two-pulse solution to the control of the nonlinear problem is time-optimal if it is close to the time-optimal solution of the linearized system, is indeed true.

4.2.1. Algorithm to Compute the Two-pulse Solution

The procedure used here is basically the same as in Section 3.2. However, instead of working with linearized equations by assuming small angles and small transverse angular velocities, we will employ here the complete nonlinear equations of motion and integrate them numerically. We can solve this problem by assuming initial trial values for T_1, T_2, T_3 and T_f, integrating Eq. (51) numerically from T_0 to T_f, and then updating the four time parameters T_1 through T_f based on the difference of the desired final conditions and the computed final conditions, *viz.*, $x_1(T_f) - x_{1,d}$, $x_2(T_f) - x_{3,d}$, $x_3(T_f) - x_{3,d}$ and $x_4(T_f) - x_{4,d}$. However, as in Section 3.2, we can separate the problem into two parts. The parameters T_1 and T_2 affect only the final Euler angles $x_3(T_f)$ and $x_4(T_f)$, whereas T_3 and T_f are chosen such that the final transverse angular velocity components $x_1(T_f)$ and $x_2(T_f)$ are zero. The parameters T_3 and T_f, as given by Eqs. (46) and (47), are simple analytic functions of T_1 and T_2. It should be noted that these equations involve no approximations. These have been obtained by integrating the transverse angular velocity equations, which are unaffected by small angle and small transverse angular velocity assumption. The algorithm to find T_1, T_2, T_3 and T_f is the following:

1. Assume T_1 and T_2
2. Integrate Eq. (51) from T_0 to T_1 with $u = 0$ and from T_1 to T_2 with $u = u_{max}$ (In order to avoid discontinuities in the middle of an integration step, integration is carried out in patched intervals with an integer number of steps in each interval)
3. Calculate T_3 and T_f from Eqs. (46) and (47)
4. Integrate Eq. (51) from T_2 to T_3 with $u = 0$ and from T_3 to T_f with $u = u_{max}$
5. If $|x_3(T_f) - x_{3,d}| < \epsilon$ and $|x_4(T_f) - x_{4,d}| < \epsilon$ then stop. Else
6. Update T_1 and T_2 (For simplicity, the Newton-Raphson update scheme is used)
7. Goto 2

		Example 3	Example 4
Boundary Conditions	$x_{1,0}$	0.0666666701	-0.0209311595
	$x_{2,0}$	-0.0222222235	-0.0651306177
	$x_{3,d}$	-0.0041141893	-0.2981263563
	$x_{4,d}$	0.4101158694	-0.0595274245
Linearized System	T_1	1.72042500	0.34050073
	T_2	5.27150921	3.44888255
	T_3	8.71603244	6.75078968
	T_f	10.47287320	8.72622400
Nonlinear System	T_1	1.74532925	0.29424471
	T_2	5.23598775	3.54733834
	T_3	8.72664626	6.69524732
	T_f	10.47197550	8.72664626

Table 2: Comparison of linearized and nonlinear systems.

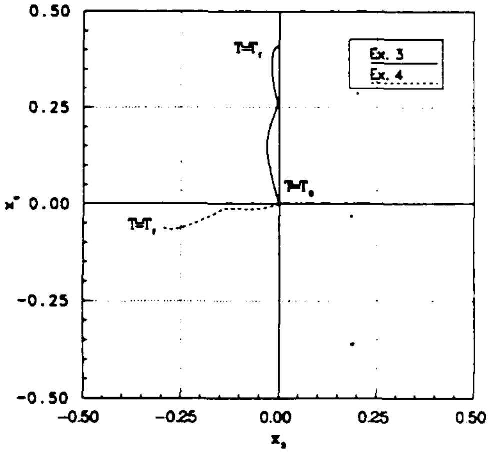

Figure 5: The path of x_b-axis in the x_3-x_4 plane.

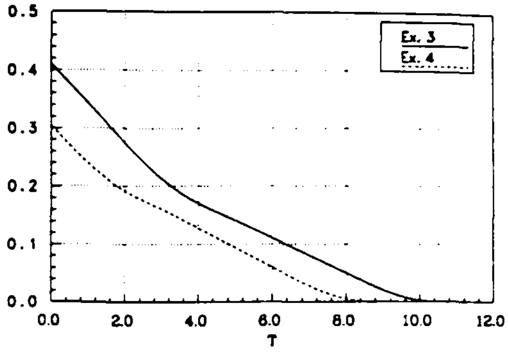

Figure 6: Total angle α vs. T.

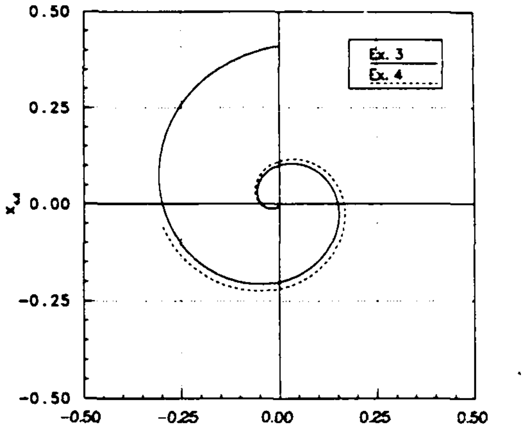

Figure 7: Path of the target in the $x_{3,d}$-$x_{4,d}$ plane.

5. Examples

We consider two examples here. The given initial conditions and the desired final conditions for the two examples are listed in Table 2. Also shown are the thruster turn-on and turn-off times obtained from the solution of both the linearized and the nonlinear problem for the two examples. It can be seen that the results for the nonlinear system are close to the results for the linearized system. Since we know that the results for the linearized system minimize the maneuver time, we conclude that the results for the nonlinear system also minimize T_f.

Figure 5 shows the path of the tip of a unit vector along the missile x_b-axis in the x_3-x_4 space, where x_3 and x_4 are the yaw and pitch angles measured with respect to the missile body axes at the start of the maneuver. The position of the target with respect to the moving missile body axis system can also be shown. As the missile x_b-axis moves toward the target direction, the angles $x_{3,d}$ and $x_{4,d}$ change with time. We define $\alpha = \cos^{-1}(\cos x_{3,d} \cos x_{4,d})$. In other words, α is the total angular distance of the target direction with respect to the missile x_b-axis. Figure 6 shows the angle α as a function of the dimensionless time T. We see that the attitude change maneuver is completed in about 1.5 roll revolutions. In Figure 7 the position of the target direction relative to the moving missile body axis system, given by the yaw angle $x_{3,d}$ and the pitch angle $x_{4,d}$, is plotted as the maneuver proceeds. An observer fixed in the missile body will see the target move in this fashion. The attitude change maneuver is completed when $x_{3,d} = x_{4,d} = 0$.

The total transverse angular velocity $\Omega = \sqrt{x_1^2 + x_2^2}$ is plotted as a function of the dimensionless time T in Figure 8, where we recall $x_1 = \Omega_y$ and $x_2 = \Omega_z$. As expected, Ω becomes zero at the same time $\alpha = 0$. Figure 9 shows the time history of x_1 and x_2 in the x_1-x_2 plane. When the x_1, x_2 trajectory radius, given by Ω, is constant in Figure 9, the missile coasts. Conversely, when the radius Ω changes, it means that the thruster is on.

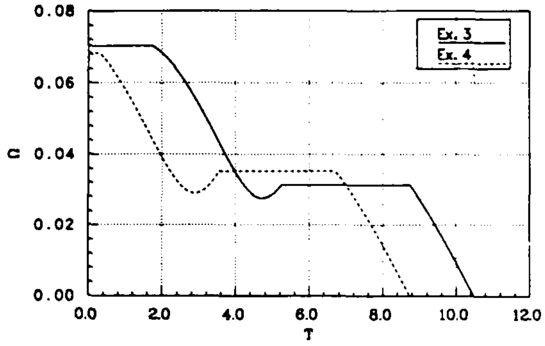

Figure 8: Total transverse angular velocity Ω vs. T.

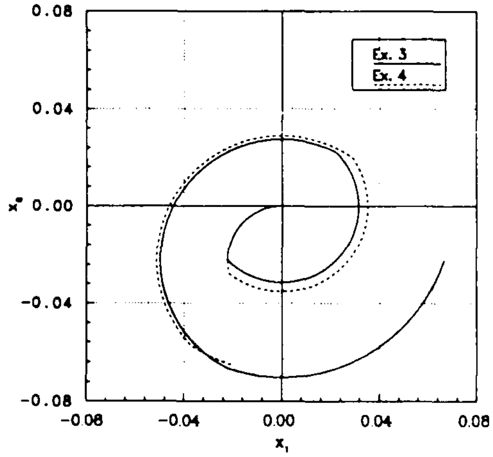

Figure 9: Trajectories of transverse angular velocity components x_1 and x_2.

6. Mechanization of the Control Scheme

The algorithm to find the thruster switch times which minimize the total maneuver time requires iterations. These iterations can be costly in terms of the time required for the solution to converge and also in terms of the complexity of the iterative procedure. Hence, this procedure cannot be used in real-time situations. The switch times can be stored on an on-board computer as functions of the boundary conditions. Table look-up and interpolation can then be used to compute the switch times and implement the attitude change maneuver.

In the exact solution, we compute T_1, T_2, T_3 and T_f as functions of the initial angular velocities and the desired Euler angles. A control law, however, can be devised based on T_1 and T_2 only. After the first thruster firing has been completed, we can measure the state variables at T_2. The switch times T_1 and T_2 can now be recomputed based on this measured state. These new T_1 and T_2 correspond to T_3 and T_f, respectively, for the previous T_1 and T_2. Thus for the new T_3 and T_f, $T_f - T_3 = 0$. In the presence of interpolation, numerical, or measurement errors this will not be quite true. Nevertheless, in reality this scheme would probably be superior because it can correct for system and measurement errors by introducing a feedback based on the latest state information.

7. Future Research

If the boundary conditions happen to lie outside the subset of the state space within which a two-pulse solution is time-optimal, the scheme given in Section 6 cannot be used. We can, however, use the geometric properties of the optimal control to generate a table of switch times as functions of boundary conditions over the desired range of the state space. This approach involves redefining the Euler angles such that $\psi(T_f) = \theta(T_f) = 0$. The roll angle $\phi(T_f)$ remains free as before. The state and costate equations can now be integrated backwards in time starting at $T = T_f$, with specified $\phi(T_f)$ and costate vector $\mathbf{p}(T_f)$. By varying these initial conditions over the range of their possible values, we can generate a table of thruster turn-on and turn-off times which spans the entire subset of state variables for which time-optimal solutions are desired. By storing this table in an on-board computer and using table look-up and interpolation to compute the firing times, this scheme can be implemented in real time. Current research focuses on creating this table and implementing the control law using function generation. The results of this approach will appear in a Ph.D.

dissertation[11] as well as in other future research papers.

Acknowledgements

The research reported in this paper has been supported by the U.S. Army Strategic Defense Command under contract number DASG60-88-C-0037 and by AFOSR under contract number F49620-86-C-0138.

References

[1] Adams, J. J., "Study of an Active Control System for a Spinning Body", NASA TN D-905, Langley Research Center, Langley Field, VA, June 1961.

[2] Athans, M. and Falb, P. L., *Optimal Control*, McGraw-Hill Inc., 1966.

[3] Cesari, L., *Optimization - Theory and Applications*, Springer-Verlag, 1983.

[4] Cole, R. D., Ekstrand, M. E. and O'Neil, M. R., "Attitude Control of Rotating Satellites", *ARS Journal*, Vol. 31, 1961, pp. 1446-1447.

[5] Filippov, A. F., "On Certain Qustions in the Theory of Optimal Control", *SIAM J. Control*, 1962, pp. 76-84.

[6] Freed, L. E., "Attitude Control System for a Spinning Body", *National IAS-ARS Joint Meeting, Los Angeles*, Paper 61-207-1901, June 13-16, 1961.

[7] Grasshoff, L. H., "A Method for Controlling the Attitude of a Spin-Stabilized Satellite", *ARS Journal*, Vol. 31, 1961, pp. 646-649.

[8] Grubin, C., "Generalized Two-Impulse Scheme for Reorienting a spin stabilized Vehicle", *ARS Guidance, Control, and Navigation Conference, Stanford, CA*, Aug 7-9, 1961.

[9] Howe, R. M., "Attitude Control of Rockets Using a Single Axis Control Jet", *XIth International Astronautical Congress, Stockholm*, 1960.

[10] Howe, R. M., "Dynamic Accuracy of the State Transition Method in Simulating Linear Systems", *Transactions of The Society for Computer Simulation*, Jan. 1988, pp. 27-41.

[11] Jahangir, E., *Time-optimal Attitude Control of a Spinning Missile*, Ph.D. Dissertation, University of Michigan, 1990.

[12] Patapoff, H., "Bank Angle Control System for a Spinning Satellite", AIAA Paper No. 63-339, August 1963.

[13] Porcelli, G. and Connolly, A., "Optimal Attitude Control of a Spinning Space-Body - A Graphical Approach", *IEEE Transactions on Automatic Control*, Vol. AC-12, No. 3, June 1967, pp. 241-249.

[14] Roberson, R. E., "Attitude Control of a Satellite Vehicle - An Outline of the Problems", *Proc. VIII International Astronautical Congress, Barcelona*, 1957, pp. 317-339.

[15] Wheeler, P. C., "Two-Pulse Attitude Control of an Asymmetric Spinning Satellite", *Progress in Aeronautics and Astronautics*, Vol. 13, 1964.

[16] Windenknecht, T. G., "A Simple System for Sun Orientation of a Spinning Satellite", *National IAS-ARS Joint Meeting, Los Angeles*, Paper 61-204-1898, June 13-16, 1961.

REACHABLE DOMAIN FOR INTERCEPTION AT HYPERBOLIC SPEEDS

Nguyen X. Vinh*, Elmer G. Gilbert*, Robert M. Howe**, Donglong Sheu†
The University of Michigan
Ann Arbor, Michigan

and

Ping Lu‡
Iowa State University
Ames, Iowa

Abstract

The interception of an ICBM at low altitude and in a short time requires hyperbolic speeds. At the acquisition time t_0, if updated information about the trajectory of the target dictates a velocity correction for the interceptor, then it is of interest to assess the potential for interception. The reachable surface is defined as the boundary of the set of all attainable points at a given time t, for a fuel potential, conveniently expressed in terms of the Δv available. Properties of this surface are derived and its mathematical characterization is obtained. As an application of the concept, a necessary condition for a successful interception of a target given in terms of a capture function is explicitly derived.

Nomenclature

$A, \cdots, E$	=coefficients as defined in Eq. (18)
a	=semi major axis
$\mathbf{e}$	=eccentricity vector
e	=eccentricity
e_x, e_y, e_z	=components of $\mathbf{e}$
f, g	=components defined by $\mathbf{r} = f\mathbf{r}_0 + g\mathbf{v}_0$
H	=hyperbolic eccentric anomaly at time t
$\mathbf{h}$	=angular momentum
h	=magnitude of $\mathbf{h}$
h_x, h_y, h_z	=components of $\mathbf{h}$
i	=inclination angle
k	$\triangleq v_0/v_c$
p	=semi-latus rectum
R_{ij}	=elements of the propagation matrix as given in Eq. (10)
$\mathbf{r}$	=position vector at time t
r	=magnitude of $\mathbf{r}$
$S(\eta, t)$	=reachable surface for impulse η at time t
t	=time
t'	=dimensionless time of flight defined in Eq. (8)
$\mathbf{v}$	=velocity vector at time t
v_c	=local circular speed at time t_0
v_x, v_y, v_z	=components of $\mathbf{v}$
x, y, z	=components of position vector $\mathbf{r}$
γ	=flight path angle at time t
$\Delta(\ )$	=variation of ( )
δ	=elevation angle of $\Delta\mathbf{v}_0$
ϵ	=azimuth of $\Delta\mathbf{v}_0$
η	$\triangleq \Delta v/v_c$
ν	=true anomaly at time t

Subscripts

0	=at the initial time t_0
1	=for the velocity, denotes the condition after the impulse at t_0
P_0	=position on nominal trajectory
P	=actual position of the interceptor
T	=position of the target

Introduction

The ultilization of satellite-based missiles for intercepting ICBM's during their ascent constitutes one of the major efforts in building a defense program. An alternative approach is to use high performance, multistage, earth-based interceptors. The very short flight times and long ranges require hyperbolic speeds and a high ratio of the take-off mass to payload mass.

In practice, precise information about the motion of the target is only known during the last phase of the interception. Thus the final interceptor stage for the earth-based missile needs to be maneuverable so that corrections in the interception can be made. This is conveniently expressed in terms of the potential characteristic velocity, Δv, which can be produced by the rocket engine of the interceptor. Considering its relatively small size, it is important to fully assess the maneuverability of the interceptor.

---

* Professor of Aerospace Engineering. Member AIAA.

** Professor of Aerospace Engineering. Associate Fellow AIAA.

† Research Assistant. Student Member AIAA.

‡ Assistant Professor of Aerospace Engineering. Associate Member AIAA.

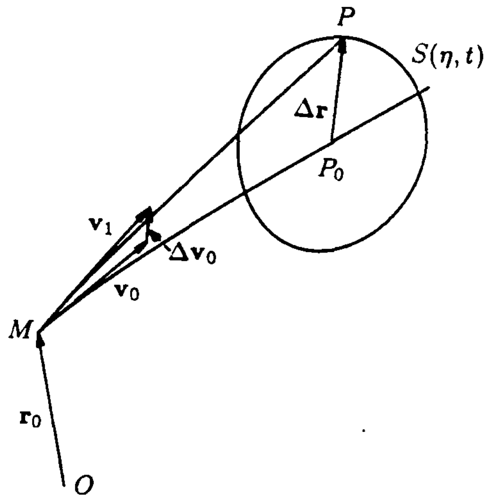

Fig. 1 Geometry of the problem.

Suppose at the time t_0, when we start the velocity correction, the position vector $\mathbf{r}_0$ and the velocity vector $\mathbf{v}_0$ of the interceptor are known (Fig. 1). For earth-based interceptor, the speed is hyperbolic and the position is lower than the intended interception point. For satellite-based interceptor, the speed is elliptic and the starting position is higher. But, it is also possible that after the initial correction, the interceptor accelerates to hyperbolic speed. With this in mind, the exact formulas presented in this paper, except as indicated for the series expansions, concern the motion in this speed range. But the discussion and the characteristic properties obtained are general. The time t_0 is the time when information about the trajectory of the target has been updated to warrant changing the course of the interceptor. Without correction, the interceptor continues to move on its Keplerian trajectory since we consider that the interception is achieved in the vacuum. For each admissible velocity correction, the position of the interceptor for flight in the vacuum is known for each $t > t_0$. For a given fuel potential Δv, let the set of all positions admissible at time t in three dimensional space be denoted by $D(t)$, which is called the reachable domain at time t. Note that it is not necessary to specify either the velocity of the target, or of the interceptor to characterize an interception. Hence, if a target position belongs to the reachable domain at t, it may be intercepted by a suitable admissible velocity correction at t_0. It is the purpose of this paper to obtain a mathematical characterization of the surface $S(t)$ which bounds the reachable domain $D(t)$.

Exact Calculation

If $\mathbf{r}_0$ and $\mathbf{v}_0$ are specified at t_0, then the position of the interceptor at any time t is given by

$$\mathbf{r} = f\mathbf{r}_0 + g\mathbf{v}_0 \tag{1}$$

where f and g are function of the time and they can be calculated by the formulas in Appendix A. They are given in the exact and explicit form and the only numerical iteration involved is the solution of the Kepler's equation to obtain the hyperbolic anomaly H for each given time t. We notice that the f and g functions can also be computed using Taylor's series expansions as given in Ref. 1. Since the time of flight $\Delta t = t - t_0$ is usually short, the use of these series, up to $(\Delta t)^6$ is accurate. If an impulse $\Delta\mathbf{v}_0$ is applied at time t_0 to change the velocity to $\mathbf{v}_1 = \mathbf{v}_0 + \Delta\mathbf{v}_0$, the new position vector as function of t, can be obtained by the same formulas by changing $\mathbf{v}_0$ into $\mathbf{v}_1$. For a given magnitude Δv, with all possible directions, the increment $\Delta\mathbf{r}$, from the nominal position P_0 (with $\Delta\mathbf{v}_0 = 0$) to the actual position P (with $\Delta\mathbf{v}_0$) describes the surface $S(t)$ which is the boundary of the reachable domain. An example of the surface is shown in Fig. 2. For the numerical computation we have taken the gravitational constant as unity and the initial distance r_0 as the unit distance.

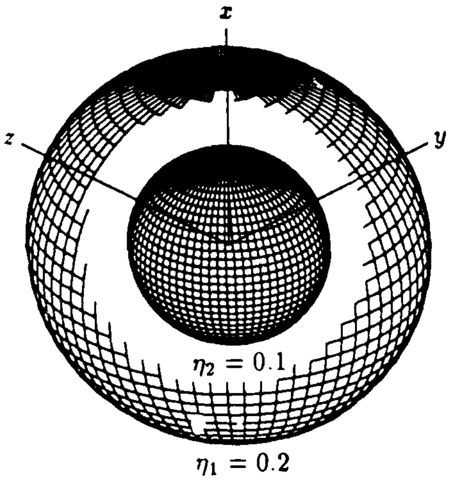

Fig. 2 The reachable surface with $\eta_1 > \eta_2$.

Properties of the Reachable Domain

The potential for maneuverability of the interceptor, in terms of the fuel consumption, is characterized by the total characteristic velocity Δv which can be fractioned into several impulses Δv_i, applied at the different times t_i. By definition, the reachable domain is the largest domain obtained at the time t and this involves an optimization process using many impulses. Optimal interception for this type of high thrust propulsion system has been discussed in Ref. 2 using the primer vector theory and it has been shown that for minimum fuel interception with time constraint, we have the following possibilities:

1. One impulse applied immediately at the time t_0.
2. One impulse applied at a later time $t_1 > t_0$.
3. One impulse applied at the time t_0, followed by another impulse at mid-course at the time t_m.

If very short time is required, that is if $\Delta t < \Delta t_{max}$ where Δt_{max} is relatively small, then a unique impulse applied at t_0 is optimal. We assume that the necessary condition for this case is satisfied and denote the strength of the impulse by the fraction η such that $\Delta v = \eta v_c$, where v_c is the circular speed at the distance r_0, that is $v_c = \sqrt{\mu / r_0} = 1$. The boundary $S(\eta, t)$ of the reachable domain at the time t, using the impulse with magnitude η will be referred to as the reachable surface.

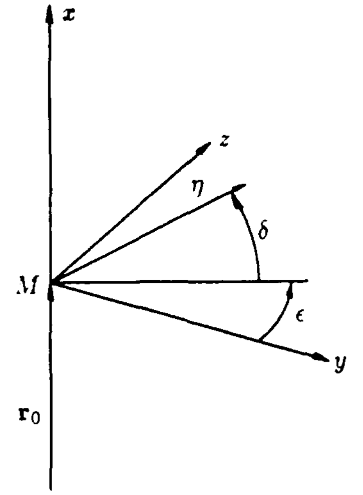

Fig. 3 Coordinate system.

If we use the coordinate system $Mxyz$ with M located at the initial point, and Mx along the vector $\mathbf{r}_0$, My orthogonal to it and in the initial plane of motion, and Mz completing a right-handed orthogonal system as shown in Fig. 3, then, the direction of the vector impulse η is defined by the azimuth ϵ and the elevation angle δ. Then, we first observe that, for finite t, S is a surface, with curvilinear coordinates ϵ and δ, periodic in ϵ and δ and has finite dimension. By continuity, it is a closed surface.

We shall give some properties of this surface:

Two surfaces $S(\eta_1, t)$ and $S(\eta_2, t)$ for the same t with $\eta_1 \neq \eta_2$ and $\eta_1 \eta_2 > 0$ have no common point. First, for any given vector η, the resulting point P at the time t is uniquely defined. This is from the uniqueness of the trajectory generated by the differential equation of motion with prescribed initial condition. Conversely, for any point P at time t, by Lambert theorem, the orbit is uniquely determined and hence $\mathbf{v}_1$ at time t_0 and consequently $\Delta \mathbf{v}_0$ is uniquely determined. The correspondance is one to one. Now, if two surface $S(\eta_1, t)$ and $S(\eta_2, t)$ have a common point, from one to one correspondance, we must have $\eta_1 = \eta_2$ which contradicts the assumption.

We now prove

Lemma *If $\eta_1 > \eta_2$ at the time t, the closed surface $S(\eta_2, t)$ is enclosed by the closed surface $S(\eta_1, t)$.*

First, they can only be in a position such that one encloses the other. Otherwise, let η approach η_2 from η_1 continuously. There must exist some η_3, $\eta_2 < \eta_3 < \eta_1$ such that $S(\eta_3, t)$ and $S(\eta_2, t)$ have a common point and this is not true.

Next, suppose that the opposite is true, that is $S(\eta_2, t)$ encloses $S(\eta_1, t)$. Then, for any $\eta \leq \eta_2$ the surface $S(\eta, t)$ will also enclose the surface $S(\eta_1, t)$ since if there exists $0 < \eta_3 < \eta_2 < \eta_1$ such that $S(\eta_3, t)$ is inside $S(\eta_1, t)$, there must exist some $\eta_3 < \eta_4 < \eta_2 < \eta_1$ such that $S(\eta_4, t)$ has a common point with $S(\eta_1, t)$. On the other hand, since $S(0, t)$ is a point, $S(\eta, t)$ should approach this point when $\eta \to 0$. This cannot happen if $S(\eta, t)$ for all $\eta \leq \eta_2$ encloses the finite surface $S(\eta_1, t)$. Hence, the *lemma* is proved by contradiction. With this *lemma*, we have the following property.

Theorem *Given $\eta_{max} > 0$. For any point P inside the closed surface $S(\eta_{max}, t)$, there exists a unique control vector η, with $0 \leq \eta < \eta_{max}$, such that the transfer leads to P at time t.*

For any point P inside the given closed surface, by Lambert theorem, there exists a unique control vector η leading to the point $P \in S(\eta, t)$. If $\eta > \eta_{max}$, by the *lemma* $S(\eta, t)$ encloses $S(\eta_{max}, t)$ which contradicts the assumption.

With the previous analysis, we now see that the potential for interception is dictated by the reachable surface $S(\eta_{max}, t)$, at maximum strength $\eta = \eta_{max}$ for the impulse. To have a mathematical characterization of this surface, simply denoted by $S(t)$ for each η, we use a moving coordinates system, parallel to the initial system but centered at the nominal point P_0. Although exact computation of $\Delta\mathbf{r}$ is available, for small values of η as in the present case of small velocity correction, it is convenient and accurate to compute its linearized expression. From Eq. (1), we have

$$\Delta\mathbf{r} = \frac{\partial\mathbf{r}}{\partial\mathbf{v}_0}\Delta\mathbf{v}_0 \tag{2}$$

where $\Delta\mathbf{v}_0$ is the velocity increment at $t = t_0$. The matrix $\partial\mathbf{r}/\partial\mathbf{v}_0$ is the propagation matrix. It is a function of the time and is completely determined in terms of the initial condition on $\mathbf{r}_0$ and $\mathbf{v}_0$. It is calculated according to

$$\frac{\partial\mathbf{r}}{\partial\mathbf{v}_0} = \mathbf{r}_0\left(\frac{\partial f}{\partial\mathbf{v}_0}\right)^T + \mathbf{v}_0\left(\frac{\partial g}{\partial\mathbf{v}_0}\right)^T + g\mathbf{I} \tag{3}$$

where $\mathbf{I}$ is the unity matrix and the partial derivatives are given in Appendix B. Again, the formulas presented are general. They are not restricted to small time interval Δt, and furthermore they can be used with any orthogonal inertial system. Therefore, by repeated application of the same program of calculation, we can obtain the reachable surface for the case of multiple-impulse interception.

By the transformation (2), it is clear that the reachable surface $S(t)$ is an ellipsoid whose principal axes are proportional to the magnitude η of the impulse applied. If the $Mxyz$ system as shown is Fig. 3 is used, then we have

$$\mathbf{r}_0 = r_0\,\mathbf{i} \tag{4}$$

and

$$\mathbf{v}_0 = kv_c(\sin\gamma_0\,\mathbf{i} + \cos\gamma_0\,\mathbf{j}) \tag{5}$$

where γ_0 is the initial flight path angle and k is the ratio specifying the initial speed in terms of the circular speed v_c at distance r_0. In this case, it is easy to verify that the two vectors $\partial f/\partial\mathbf{v}_0$ and $\partial g/\partial\mathbf{v}_0$ in Eq. (3) are lying in the Mxy plane and the propagation matrix is of the form

$$\frac{\partial\mathbf{r}}{\partial\mathbf{v}_0} = R(t) = \begin{bmatrix} R_{11} & R_{12} & 0 \\ R_{21} & R_{22} & 0 \\ 0 & 0 & g \end{bmatrix} \tag{6}$$

Let

$$\Delta\mathbf{v}_0 = \eta v_c(\sin\delta\,\mathbf{i} + \cos\delta\cos\epsilon\,\mathbf{j} + \cos\delta\sin\epsilon\,\mathbf{k}) \tag{7}$$

Then, by using a dimensionless time of flight t' such that

$$t' = \sqrt{\frac{\mu}{r_0^3}}(t - t_0) \tag{8}$$

we have the equations of the reachable ellipsoidal surface as defined by $\Delta\mathbf{r}/r_0$, in the form

$$\begin{aligned} \Delta\bar{x} &= \frac{\Delta x}{r_0} = \eta R_{11}\sin\delta + \eta R_{12}\cos\delta\cos\epsilon \\ \Delta\bar{y} &= \frac{\Delta y}{r_0} = \eta R_{21}\sin\delta + \eta R_{22}\cos\delta\cos\epsilon \\ \Delta\bar{z} &= \frac{\Delta z}{r_0} = \eta g\cos\delta\sin\epsilon \end{aligned} \tag{9}$$

It is clear that this surface is symmetric with respect to the initial plane defined by $\mathbf{r}_0$ and $\mathbf{v}_0$. If the reference orbital radius r_0 corresponds to a circular orbit period of 90 minutes, a flying time of 3 minutes is $t' = \pi/15$ and we can use Taylor's series expansion of up to the order of t'^6 to have an explicit and accurate representation of $R(t)$. The series apply to both the elliptic and the hyperbolic range. We have then

$$\begin{aligned} R_{11} &= t' + \frac{1}{3}t'^3 - \frac{1}{2}k\sin\gamma_0 t'^4 \\ &\quad - \frac{1}{60}(18k^2 - 11 - 54k^2\sin^2\gamma_0)t'^5 \\ &\quad + \frac{1}{90}k\sin\gamma_0(90k^2 - 51 - 150k^2\sin^2\gamma_0)t'^6 \\ R_{12} &= k\cos\gamma_0\Big[\frac{1}{4}t'^4 - \frac{3}{5}k\sin\gamma_0 t'^5 \\ &\quad - \frac{1}{180}(45k^2 - 33 - 225k^2\sin^2\gamma_0)t'^6\Big] \\ R_{21} &= k\cos\gamma_0\Big[\frac{1}{4}t'^4 - \frac{3}{5}k\sin\gamma_0 t'^5 \\ &\quad - \frac{1}{24}(6k^2 - 5 - 30k^2\sin^2\gamma_0)t'^6\Big] \\ R_{22} &= t' - \frac{1}{6}t'^3 + \frac{1}{4}k\sin\gamma_0 t'^4 \\ &\quad + \frac{1}{120}(27k^2 - 8 - 63k^2\sin^2\gamma_0)t'^5 \\ &\quad - \frac{1}{24}k\sin\gamma_0(18k^2 - 5 - 26k^2\sin^2\gamma_0)t'^6 \\ R_{33} &= g = t' - \frac{1}{6}t'^3 + \frac{1}{4}k\sin\gamma_0 t'^4 \\ &\quad + \frac{1}{120}(9k^2 - 8 - 45k^2\sin^2\gamma_0)t'^5 \\ &\quad - \frac{1}{24}k\sin\gamma_0(6k^2 - 5 - 14k^2\sin^2\gamma_0)t'^6 \end{aligned} \tag{10}$$

We notice that for very short time of flight, if we neglect terms of order of t'^4 and higher, the propagation matrix $R(t)$ is a diagonal matrix. The principal axes of the ellipsoid are parallel to the initial axes.

Furthermore, since $R_{22} = R_{33} = g$, it is of revolution about the x-axis.--

For an initial velocity $\mathbf{v}_0$ such that $k = 2$ and $\gamma_0 = 30°$, we have generated the reachable surface $S(\eta, t)$ at the time $t' = \pi/10$, for the values of speed correction $\eta_1 = 0.2$ and $\eta_2 = 0.1$. As expected, the surface $S(\eta_2, t)$ is inside the surface $S(\eta_1, t)$ and they have no common point. This is shown in Fig. 2. The computation has been done using the exact formulas in Appendix A, and then the linearized version with respect to $\Delta\mathbf{v}_0$ as given in Appendix B, and finally the explicit series as given in Eqs. (10). For small η, the propagation matrix $R(t')$ computed from Eq. (10) and the values from Appendix B have excellent agreement. The relative errors in terms of the order of t'^n, for $n = 3, 4, 5, 6$ are shown in Fig. 4 where we have defined

$$\%\text{error} = \max_{||\Delta\mathbf{r}||=1} ||\Delta\mathbf{r}_n - \Delta\mathbf{r}|| \times 100 \qquad (11)$$

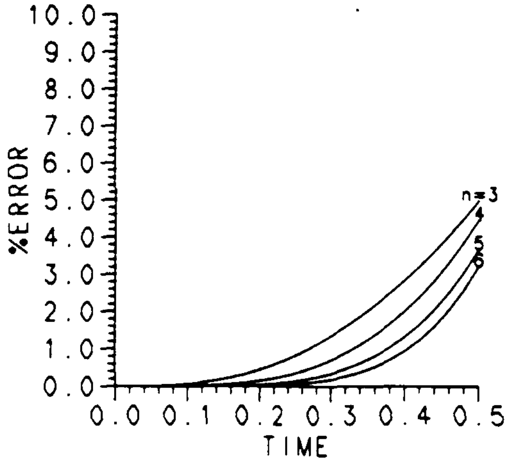

Fig. 4 Error percentage with Taylor's series expansion.

In the following, the computation is done with the series expansions.

As the reachable surface is propagated as function of t, at each value of t, there exists a maximum distance r_{max} and a minimum distance r_{min} for the interceptor. By symmetry, it is obtained for $\epsilon = 0$ and a certain value of δ which can be easily computed by solving a quartic equation. Of global interest is the domain which cannot be reached by the interceptor for any value of t less than a prescribed t_{max}. This domain is outside of a cone, with vertex at the initial point M, which is the envelope of the reachable surface $S(t)$. This envelope is also symmetric with respect to the initial plane $(\mathbf{r}_0, \mathbf{v}_0)$.

Mathematically, for given η, we consider the equation of the reachable surface $S(t)$, locus of all points P,

$$\mathbf{r}_p = \mathbf{r}_p(\delta, \epsilon, t). \qquad (12)$$

For each t, considered as a parameter, this is a parametric representation with curvilinear coordinates δ and ϵ. The equation of the envelope is obtained by eliminating t between this equation and the equation

$$\frac{\partial \mathbf{r}_p}{\partial t} \cdot \left(\frac{\partial \mathbf{r}_p}{\partial \delta} \times \frac{\partial \mathbf{r}_p}{\partial \epsilon} \right) = 0 \qquad (13)$$

With $\mathbf{v}_1 = \mathbf{v}_0 + \Delta\mathbf{v}_0$ and $\Delta\mathbf{v}_0$ given in Eq. (7), and $\mathbf{r}_p$ as given in Eq. (1) with $\mathbf{v}_0$ changed into $\mathbf{v}_1$, we have

$$\begin{aligned} \frac{\partial \mathbf{r}_p}{\partial t} &= \dot{f}_p \mathbf{r}_0 + \dot{g}_p(\mathbf{v}_0 + \Delta\mathbf{v}_0) \\ \frac{\partial \mathbf{r}_p}{\partial \delta} &= \frac{\partial \mathbf{r}_p}{\partial \mathbf{v}_1} \frac{\partial \Delta\mathbf{v}_0}{\partial \delta} \\ \frac{\partial \mathbf{r}_p}{\partial \epsilon} &= \frac{\partial \mathbf{r}_p}{\partial \mathbf{v}_1} \frac{\partial \Delta\mathbf{v}_0}{\partial \epsilon} \end{aligned} \qquad (14)$$

We can then perform the exact computation of the envelope using the formulas in the Appendices A and B. Figure 5 shows the envelope for the case where $k = 2$, $\gamma_0 = 30°$ and $\eta = 0.1$. With small speed correction, the cone envelope is near the nominal trajectory and for clarity the plot is expanded for the time interval $.07\pi \le t' \le .10\pi$.

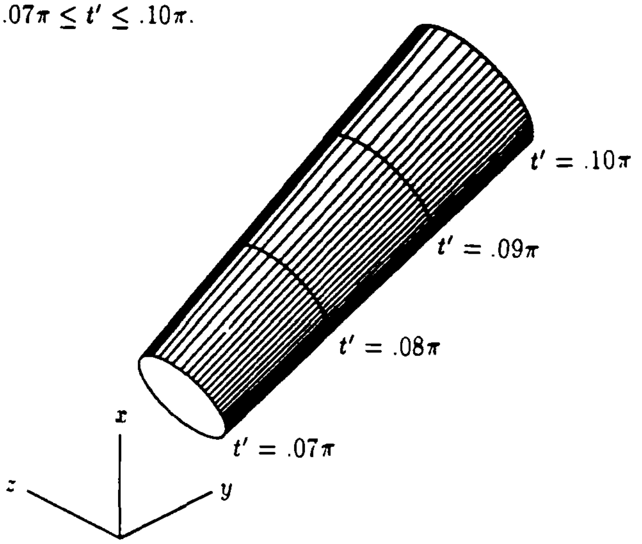

Fig. 5 The cone envelope of the reachable surface.

For small velocity change, if the linearized equations are used, then

$$\frac{\mathbf{r}_p}{r_0} = \frac{\mathbf{r}_{p_0}}{r_0} + R(t')\Delta\mathbf{v}_0 \qquad (15)$$

where with the dimensionless time of flight t', and by Taylor's series, the propagation matrix $R(t')$ is given in Eq. (10), and $\Delta \mathbf{v}_0$ in Eq. (7) with $v_c = 1$, and with the coordinates of the reference point P_0 being

$$\begin{aligned}
\frac{x_{P_0}}{r_0} = \bar{x}_{P_0} &= 1 + k \sin\gamma_0 t' - \frac{1}{2}t'^2 + \frac{1}{3}k\sin\gamma_0 t'^3 \\
&+ \frac{1}{24}(3k^2 - 2 - 9k^2\sin^2\gamma_0)t'^4 \\
&+ \frac{1}{60}k\sin\gamma_0(-18k^2 + 11 \\
&+ 30k^2\sin^2\gamma_0)t'^5 + \frac{1}{720}\{5(90k^2 - 54 \\
&\quad - 105k^2\sin^2\gamma_0)k^2\sin^2\gamma_0 \\
&\quad - (22 - 66k^2 + 45k^4)\}t'^6 \qquad (16) \\
\frac{y_{P_0}}{r_0} = \bar{y}_{P_0} &= k\cos\gamma_0\{t' - \frac{1}{6}t'^3 + \frac{1}{4}k\sin\gamma_0 t'^4 \\
&+ \frac{1}{120}(9k^2 - 8 - 45k^2\sin^2\gamma_0)t'^5 \\
&- \frac{1}{24}k\sin\gamma_0(6k^2 - 5 - 14k^2\sin^2\gamma_0)t'^6\} \\
\frac{z_{P_0}}{r_0} = \bar{z}_{P_0} &= 0
\end{aligned}$$

With the series solution, simple computation of the envelope can be done by considering its intersection with the plane making an inclination angle i with the initial reference plane. First for $i = 0$, we have $\epsilon = 0$ and Eq. (13) becomes

$$\begin{aligned}
A\sin^2\delta + B\cos^2\delta + C\sin\delta\cos\delta& \\
+ D\sin\delta + E\cos\delta = 0& \qquad (17)
\end{aligned}$$

where

$$\begin{aligned}
A &= \eta(R_{12}\dot{R}_{21} - R_{22}\dot{R}_{11}) \\
B &= \eta(R_{21}\dot{R}_{12} - R_{11}\dot{R}_{22}) \\
C &= \eta(R_{12}\dot{R}_{22} - R_{22}\dot{R}_{12} + R_{21}\dot{R}_{11} - R_{11}\dot{R}_{21}) \qquad (18) \\
D &= -\dot{x}_{P_0}R_{22} + \dot{y}_{P_0}R_{12} \\
E &= \dot{x}_{P_0}R_{21} - \dot{y}_{P_0}R_{11}
\end{aligned}$$

with the R_{ij} given by Eq. (10) and x_{P_0} and y_{P_0} by Eq. (16). Equation (17) can be transformed into a quartic equation in $\tan\delta/2$. After solving for δ, we substitute into Eq. (15) to have the equations of the envelope.

If we intersect the cone by a plane, making an angle i with the initial plane, then by simple geometry, it appears that it behaves like that in the new plane, the initial velocity has components $k\sin\gamma_0$ and $k\cos\gamma_0\cos i$ and the planar impulse has the elevation angle δ' with magnitude

$$\eta' = \sqrt{\eta^2 - k^2\cos^2\gamma_0\sin^2 i} \qquad (19)$$

Hence, in the computation of the intersection of the cone envelope by this plane, it suffices to replace in Eqs. (15) and (18) η by η' and in the functions R_{ij} and x_{P_0} and y_{P_0} we leave $k\sin\gamma_0$ the same but replace $k\cos\gamma_0$ by $k\cos\gamma_0\cos i$ and consequently we replace k^2 by $k^2(\sin^2\gamma_0 + \cos^2\gamma_0\cos^2 i)$. For each value of i we have two intersecting curves and at the maximum inclination

$$\sin i_{max} = \frac{\eta}{k\cos\gamma_0} \qquad (20)$$

the two lines concide, being the contact line between the envelope and the plane i_{max}. This line is the trajectory in the plane i_{max} with initial velocity component $k\sin\gamma_0$ and $k\cos\gamma_0\cos i$ and zero velocity change. Hence, it is given explicitly by the equations (16) with the necessary change for the terms $k\cos\gamma_0$ and k^2.

Condition for Interception

At this point, it is relevant to specify the problem. The interceptor is launched on its nominal trajectory only after some preliminary information about the target motion is acquired. The problem of minimum fuel intercepting an ICBM at low altitude using a multi-stage earth-launched rocket has been discussed in detail in Ref. 3. For long range and short time interception at low altitude the interceptor must accelerate to hyperbolic speed and use aerodynamic lifting force generated by its last stage to follow the curvature of the earth. The last phase is the ascent in the vacuum for interception with the initial condition such that $v_0 \approx 2v_c$, $\gamma_0 \approx 0$ and r_0 at near the top of the atmosphere. The duration of this last phase is between 2 and 3 minutes. If at the beginning of this phase, at $t = t_0$, updated information about the trajectory of the target is received, correction should be made. Let $\mathbf{r}_T(t)$ be the newly revised position vector of the target whose position is denoted by T. We can evaluate the relative position from the nominal point P_0 of the interceptor to the target T

$$P_0T = \Delta\mathbf{r}_T \qquad (21)$$

as function of t near the intended interception time t_f. If there exists a value of t such that the target is inside the reachable surface, then certainly, interception can be achieved. Mathematically we define a capture function using normalized variables

$$\begin{aligned}
F(\Delta\bar{x}, \Delta\bar{y}, \Delta\bar{z}, t') &= \frac{(R_{21}\Delta\bar{x} - R_{11}\Delta\bar{y})^2}{(R_{11}R_{22} - R_{12}R_{21})^2} \\
&+ \frac{(R_{22}\Delta\bar{x} - R_{12}\Delta\bar{y})^2}{(R_{11}R_{22} - R_{12}R_{21})^2} + \frac{\Delta\bar{z}^2}{R_{33}^2} \qquad (22)
\end{aligned}$$

We notice that, by setting $F = \eta^2$, we have the equation in Cartesian coordinates of the reachable surface at the time t'. Then, let $\Delta\bar{x}_T$, $\Delta\bar{y}_T$, and $\Delta\bar{z}_T$ be the components of the relative position vector $\Delta\mathbf{r}_T/r_0$. The condition for capture is then

$$F(\Delta\bar{x}_T, \Delta\bar{y}_T, \Delta\bar{z}_T, t') \le \eta^2 \tag{23}$$

As a simple illustration, consider the function to the order of t'^3. The equation for the reachable ellipsoid is

$$\frac{\Delta\bar{x}^2}{t'^2(1+t'^2/3)^2} + \frac{\Delta\bar{y}^2}{t'^2(1-t'^2/6)^2} + \frac{\Delta\bar{z}^2}{t'^2(1-t'^2/6)^2} - \eta^2 = 0 \tag{24}$$

It is interesting to notice that although the propagation matrix $R(t')$ depends on the initial speed $v_0 = kv_c$ and flight path angle γ_0, to the order of t'^3 included, it is independent of $\mathbf{v}_0$. This can be explained that although the reachable domain $D(t')$ as it moves away from the initial point depends, on any order in t', on k and γ_0, because the nominal position P_0 depends on $\mathbf{v}_0$, the deviation of the actual position P of the interceptor from P_0 for short time interval is mainly influenced by the impulse $\Delta\mathbf{v}_0$. The coordinates of the nominal position P_0 can be computed by either using the exact formulas in Appendix A, or more conveniently by the Taylor's series (16) valid for the whole range of speed.

The actual position P of the interceptor is $\mathbf{r}_p = (x_p, y_p, z_p)$. Its coordinates can be obtained using the same series with the following change

$$k\sin\gamma_0 \rightarrow k\sin\gamma_0 + \eta\sin\delta = (v_{x_1}/v_c)$$

$$k^2\sin^2\gamma_0 \rightarrow (k\sin\gamma_0 + \eta\sin\delta)^2 = (v_{x_1}/v_c)^2$$

$$k\cos\gamma_0 \rightarrow k\cos\gamma_0 + \eta\cos\delta\cos\epsilon = (v_{y_1}/v_c)$$

$$k^2 \rightarrow [k^2 + \eta^2 + 2k\eta(\sin\gamma_0\sin\delta + \cos\gamma_0\cos\delta\cos\epsilon)] = (v_1/v_c)^2$$

Notice that, this is simply a change of definition of the various terms. The new velocity $\mathbf{v}_1$ has a lateral component $\eta v_c\cos\delta\sin\epsilon$. This gives the lateral coordinates

$$\frac{z_p}{r_0} = g\eta\cos\delta\sin\epsilon \tag{25}$$

where the function $g(t')$ is calculated from the last equation (10) with the change in $k\sin\gamma_0$, $k^2\sin^2\gamma_0$ and k^2 as above. By linearizing with respect to η and evaluating the difference $\Delta\mathbf{r}/r_0$, we have the equations (9).

Returning to Eq. (24), for a time interval of $t' = \pi/15$ (about 3 minutes), the principal axes of the ellipsoid are $\Delta\bar{x}_{max} = 0.2125\eta$, $\Delta\bar{y}_{max} = \Delta\bar{z}_{max} = 0.2079\eta$. It is nearly a sphere. With a maximum velocity correction of 600 m/sec, we have $\eta = 0.0759$. The capture radius is $\Delta r = 0.0158r_0$ and it is about 100 km.

Conclusions

In this paper we have introduced the concept of the reachable domain, which is the set of points attainable at the time t by an interceptor flying in the vacuum about a spherical earth and using a fuel potential represented by a total characteristic velocity Δv. We notice the fact that at high orbital speed and for a relatively short time duration from an initial time t_0, the largest domain is obtained by using the total impulse applied at the time t_0. This domain can be exactly calculated using the classical equations in astrodynamics. General properties of the reachable surface which is the boundary of the reachable domain were derived. To have a mathematical characterization of the reachable surface, for small velocity change, we use a linearized version and derive the partial derivatives to calculate the propagation matrix $R(t)$, which is the mapping of the velocity change $\Delta\mathbf{v}_0$ into the position change $\Delta\mathbf{r}$. With this linearization, it is seen that the reachable surface is an ellipsoid and it is approximately a sphere for small time interval. As the time varies, the ellipsoid generates a cone which contains the totality of the trajectories of the interceptor.

As an application of the reachable domain, we have considered the case of interception of a target during its last phase. If the revised information on the trajectory of the target, obtained at the acquisition time t_0, dictates a change of the course of the interceptor, then a capture function derived in explicit form can be used to assess the feasibility of the interception for any given Δv.

Another possible application of this concept is in the case of several space launching bases either on the same orbit or on a system of orbits. Then, with the knowledge of the possible launch site of the ICBM, and its typical trajectory, we can compute the intended landing area and evaluate the requirement for its defense in terms of the number of the space launching bases and their orbital characteristics.

This paper discusses the case of impulsive change in the velocity. The case of continuous thrusting is obviously of interest and is currently under study by the authors.

Appendix A Nominal Trajectory Equations

Given at t_0,

$$\mathbf{r}_0 = x_0\,\mathbf{i} + y_0\,\mathbf{j} + z_0\,\mathbf{k},$$
$$\mathbf{v}_0 = v_{x_0}\,\mathbf{i} + v_{y_0}\,\mathbf{j} + v_{z_0}\,\mathbf{k}.$$

Then with $\mu = 1$ the *nominal* trajectory can be computed by the following procedure,[4]

$$\begin{aligned}
\mathbf{h} &= h_x\,\mathbf{i} + h_y\,\mathbf{j} + h_z\,\mathbf{k} = \mathbf{r}_0 \times \mathbf{v}_0 \\
\mathbf{e} &= e_x\,\mathbf{i} + e_y\,\mathbf{j} + e_z\,\mathbf{k} = -\mathbf{h} \times \mathbf{v}_0 - \mathbf{r}_0/r_0 \\
p &= h^2 \\
a &= \frac{p}{e^2-1} \qquad \text{(for } e > 1) \\
\sin\nu_0 &= \frac{h}{r_0 e}\mathbf{r}_0 \cdot \mathbf{v}_0 \\
\cos\nu_0 &= \frac{\mathbf{r}_0 \cdot \mathbf{e}}{r_0 e} \\
\tan\frac{\nu_0}{2} &= \frac{\sin\nu_0}{1+\cos\nu_0} \\
\tanh\frac{H_0}{2} &= \sqrt{\frac{e-1}{e+1}}\tan\frac{\nu_0}{2} \\
(t-t_0)a^{-3/2} &= e(\sinh H - \sinh H_0) - (H - H_0)
\end{aligned}$$

(H can be computed for a given t)

$$\begin{aligned}
\tan\frac{\nu}{2} &= \sqrt{\frac{e+1}{e-1}}\tanh\frac{H}{2} \\
r &= \frac{p}{1+e\cos\nu} \\
f &= 1 - \frac{r}{p}[1-\cos(\nu-\nu_0)] \\
g &= \frac{r r_0}{h}\sin(\nu-\nu_0) \\
\dot{f} &= \frac{1}{h}\tan\frac{(\nu-\nu_0)}{2}\Big[\frac{1-\cos(\nu-\nu_0)}{p} \\
&\quad - \frac{1}{r} - \frac{1}{r_0}\Big] \\
\dot{g} &= 1 - \frac{r_0}{p}[1-\cos(\nu-\nu_0)] \\
\mathbf{r} &= f\mathbf{r}_0 + g\mathbf{v}_0 \\
\dot{\mathbf{r}} &= \dot{f}\mathbf{r}_0 + \dot{g}\mathbf{v}_0
\end{aligned}$$

Appendix B Variational Trajectory Equations

Upon the application of a small impulse $\Delta\mathbf{v}_0$ at t_0, the *variation* of the trajectory can be computed by the following prodedure

$$\begin{aligned}
\frac{\partial\mathbf{h}}{\partial\mathbf{v}_0} &= \begin{bmatrix} 0 & -z_0 & y_0 \\ z_0 & 0 & -x_0 \\ -y_0 & x_0 & 0 \end{bmatrix} \\
\frac{\partial h}{\partial\mathbf{v}_0} &= \frac{1}{h}\Big(\frac{\partial\mathbf{h}}{\partial\mathbf{v}_0}\Big)^T\mathbf{h} \\
\frac{\partial p}{\partial\mathbf{v}_0} &= 2h\frac{\partial h}{\partial\mathbf{v}_0} \\
\frac{\partial\mathbf{e}}{\partial\mathbf{v}_0} &= \begin{bmatrix} 0 & h_z & -h_y \\ -h_z & 0 & h_x \\ h_y & -h_x & 0 \end{bmatrix} \\
&\quad + \begin{bmatrix} 0 & -v_{z_0} & v_{y_0} \\ v_{z_0} & 0 & -v_{x_0} \\ -v_{y_0} & v_{x_0} & 0 \end{bmatrix}\frac{\partial\mathbf{h}}{\partial\mathbf{v}_0} \\
\frac{\partial e}{\partial\mathbf{v}_0} &= \frac{1}{e}\Big(\frac{\partial\mathbf{e}}{\partial\mathbf{v}_0}\Big)^T\mathbf{e} \\
\frac{\partial a}{\partial\mathbf{v}_0} &= \frac{1}{e^2-1}\Big(\frac{\partial p}{\partial\mathbf{v}_0} - 2ea\frac{\partial e}{\partial\mathbf{v}_0}\Big) \\
\frac{\partial\sin\nu_0}{\partial\mathbf{v}_0} &= \Big(\frac{1}{h}\frac{\partial h}{\partial\mathbf{v}_0} - \frac{1}{e}\frac{\partial e}{\partial\mathbf{v}_0}\Big)\sin\nu_0 + \frac{h}{r_0 e}\mathbf{r}_0 \\
\frac{\partial\cos\nu_0}{\partial\mathbf{v}_0} &= -\frac{1}{e}\cos\nu_0\frac{\partial e}{\partial\mathbf{v}_0} + \frac{1}{r_0 e}\Big(\frac{\partial\mathbf{e}}{\partial\mathbf{v}_0}\Big)^T\mathbf{r}_0 \\
\frac{\partial\tan\nu_0/2}{\partial\mathbf{v}_0} &= \frac{1}{1+\cos\nu_0}\Big(\frac{\partial\sin\nu_0}{\partial\mathbf{v}_0} - \tan\frac{\nu_0}{2}\frac{\partial\cos\nu_0}{\partial\mathbf{v}_0}\Big) \\
\frac{\partial\tanh H_0/2}{\partial\mathbf{v}_0} &= \frac{\tan\nu_0/2}{(e+1)\sqrt{e^2-1}}\frac{\partial e}{\partial\mathbf{v}_0} \\
&\quad + \sqrt{\frac{e-1}{e+1}}\frac{\partial\tan\nu_0/2}{\partial\mathbf{v}_0} \\
\frac{\partial H_0}{\partial\mathbf{v}_0} &= (1+\cosh H_0)\frac{\partial\tanh H_0/2}{\partial\mathbf{v}_0} \\
\frac{\partial H}{\partial\mathbf{v}_0} &= -\frac{3(t-t_0)/2}{a^{5/2}(e\cosh H - 1)}\frac{\partial a}{\partial\mathbf{v}_0} \\
&\quad - \frac{\sinh H - \sinh H_0}{e\cosh H - 1}\frac{\partial e}{\partial\mathbf{v}_0} \\
&\quad + \frac{e\cosh H_0 - 1}{e\cosh H - 1}\frac{\partial H_0}{\partial\mathbf{v}_0} \\
\frac{\partial\tan\nu/2}{\partial\mathbf{v}_0} &= -\frac{\tan\nu/2}{(e^2-1)}\frac{\partial e}{\partial\mathbf{v}_0} \\
&\quad + \sqrt{\frac{e+1}{e-1}}\frac{1}{1+\cosh H}\frac{\partial H}{\partial\mathbf{v}_0} \\
\frac{\partial\sin\nu}{\partial\mathbf{v}_0} &= \cos\nu(1+\cos\nu)\frac{\partial\tan\nu/2}{\partial\mathbf{v}_0} \\
\frac{\partial\cos\nu}{\partial\mathbf{v}_0} &= -\sin\nu(1+\cos\nu)\frac{\partial\tan\nu/2}{\partial\mathbf{v}_0}
\end{aligned}$$

$$
\begin{aligned}
\frac{\partial r}{\partial \mathbf{v}_0} &= \frac{r}{p}\Big(\frac{\partial p}{\partial \mathbf{v}_0} - r\cos\nu\frac{\partial e}{\partial \mathbf{v}_0} - re\frac{\partial \cos\nu}{\partial \mathbf{v}_0}\Big) \\
\frac{\partial f}{\partial \mathbf{v}_0} &= \frac{1}{p}[1-\cos(\nu-\nu_0)]\Big(-\frac{\partial r}{\partial \mathbf{v}_0} + \frac{r}{p}\frac{\partial p}{\partial \mathbf{v}_0}\Big) \\
&\quad + \frac{r}{p}\Big(\cos\nu_0\frac{\partial \cos\nu}{\partial \mathbf{v}_0} + \cos\nu\frac{\partial \cos\nu_0}{\partial \mathbf{v}_0} \\
&\qquad\qquad + \sin\nu_0\frac{\partial \sin\nu}{\partial \mathbf{v}_0} + \sin\nu\frac{\partial \sin\nu_0}{\partial \mathbf{v}_0}\Big) \\
\frac{\partial g}{\partial \mathbf{v}_0} &= \frac{r_0}{h}\sin(\nu-\nu_0)\frac{\partial r}{\partial \mathbf{v}_0} \\
&\quad - \frac{rr_0}{p}\sin(\nu-\nu_0)\frac{\partial h}{\partial \mathbf{v}_0} \\
&\quad + \frac{rr_0}{h}\Big(\cos\nu_0\frac{\partial \sin\nu}{\partial \mathbf{v}_0} + \sin\nu\frac{\partial \cos\nu_0}{\partial \mathbf{v}_0} \\
&\qquad\qquad - \sin\nu_0\frac{\partial \cos\nu}{\partial \mathbf{v}_0} - \cos\nu\frac{\partial \sin\nu_0}{\partial \mathbf{v}_0}\Big) \\
\frac{\partial \mathbf{r}}{\partial \mathbf{v}_0} &= \mathbf{r}_0\Big(\frac{\partial f}{\partial \mathbf{v}_0}\Big)^T + \mathbf{v}_0\Big(\frac{\partial g}{\partial \mathbf{v}_0}\Big)^T + g\mathbf{I}
\end{aligned}
$$

The *variation* of trajectory is approximately computed by

$$\Delta\mathbf{r} = \frac{\partial \mathbf{r}}{\partial \mathbf{v}_0}\Delta\mathbf{v}_0.$$

Acknowledgement

This work was supported by the U.S. Army Strategic Defense Command under Contract No. DASG 60-88-C-0037.

References

1. Danby, J. M. A., *Fundamentals of Celestial Mechanics*, The MacMillan Co., New York, 1962.
2. Vinh, N. X., Lu, P., Howe, R. M. and Gilbert, E. G., "Optimal Interception with Time Constraint," *Journal of Optimization Theory and Applications*, to appear.
3. Gilbert, E. G., Howe, R. M., Vinh, N. X. and Lu, P., "Optimal Aeroassisted Intercept Trajectories at Hyperbolic Speeds," *AIAA Journal of Guidance, Control and Dynamics*, to appear.
4. Bate, R. R., Mueller, D. D. and White, J. E., *Fundamentals of Astrodynamics*, Dover Publications, Inc., New York, 1971.

A SCHEME TO GENERATE THRUSTER FIRING TIMES FOR THE TIME-OPTIMAL REORIENTATION OF A SPINNING MISSILE

E. Jahangir* and R. M. Howe**
University of Michigan
Ann Arbor, MI 48109-2140

Abstract

A scheme to generate thruster firing times as functions of the initial and the desired state of a spinning missile is described. The missile is modeled as a rigid body which is symmetric about one axis and which has a large roll rate about this axis of symmetry. Control is achieved by a single reaction jet which, when fired, provides a constant moment about a transverse axis. Disturbance torques are assumed to be zero. The missile is assumed to have some arbitrary initial transverse angular velocity and it is desired to take it to some final attitude in minimum time while reducing the transverse angular velocity to zero. This minimum-time reorientation problem is usually handled by solving a TPBVP (Two Point Boundary Value Problem). The control history thus obtained is stored in an on-board computer and implemented on-line by table look-up. We describe a scheme which does not need to solve a TPBVP. Instead, coordinate transformations are used such that each backwards integration of the transformed state and costate equations yields a unique time-optimal trajectory. By storing the state and the associated time-optimal control at discrete points in time, a set of boundary condition points can be generated for which the minimum-time control is known. This set of points can later be used to generate a table of thruster firing times as functions of the current and the desired state of the missile. Some examples are plotted to illustrate the application of the concepts presented.

1. Introduction

Over the past three decades many papers and reports have treated various aspects of homing schemes and trajectory control associated with these schemes. Most of these papers consider surface-to-air or air-to-air missiles which use aerodynamic forces for trajectory control. With the advent of SDI, much attention has been focused on the interception of satellites or ICBM's outside the sensible atmosphere. Hence, aerodynamic forces cannot be generated for vehicle control. Instead, the thrust of a rocket engine is used to provide the necessary maneuver forces, with vehicle attitude control employed to point the thrust in the desired direction. Conventional thrust vector control systems tend to add both weight and complexity, and as a result counter the objective of minimizing the weight of the guided warhead. The simplest control involves a single thruster at right angles to the spin axis of the missile. In this scheme the missile is given a large roll rate and the thruster is turned on for a fraction of each revolution in roll and at the right time during each roll cycle so that the desired attitude changes are achieved. Meanwhile the main thruster, by producing a thrust component perpendicular to the flight path, provides the necessary trajectory changes.

The problem of attitude control of spinning rigid bodies has not received much attention recently, although some research has been reported on this topic in the 1960's. The reorientation problem of a spinning rigid body is conceptually different than the simple rest-to-rest maneuver of a non-spinning rigid body. Because of the spin of the body about its symmetry axis, application of any moment about the transverse axes generates a precessional motion. If the initial transverse angular velocity is not zero, the problem becomes even more difficult because the problem loses its symmetry.

Athans and Falb[2] consider the problem of time-optimal velocity control of a rotating body with a single axis of symmetry. They show that for a single fixed control jet, the system has the properties of a harmonic oscillator. Thus, a switching curve can be derived to implement the control scheme. The cases of a gimballed control jet and two control jets are also considered. No mention is made of the complete attitude reorientation problem, however. Howe[8] pro-

---

*Ph.D. Candidate in Aerospace Engineering Student Member, AIAA

**Professor of Aerospace Engineering Associate Fellow, AIAA poses an attitude control scheme for sounding rockets. The main feature of this scheme is that it uses a single control jet. The control jet is fired for a fixed duration whenever certain conditions on direction cosines or transverse angular velocity are satisfied. This results in the alternate reduction of attitude error and transverse angular velocity, finally ending in a limit cycle. Some other references[16,3,1,5,6,7,12,15,13] discuss the problem of reorienting a rotating rigid body which has no initial transverse angular velocity. Windenknecht[16] proposes a simple system for sun orientation of spinning satellites. In this scheme the desired attitude is achieved by a succession of 180° precessional motions, each resulting in a small attitude change (small-angle approximations assumed valid), until the spin axis arrives at an attitude corresponding to the dead zone of the sun sensors. Cole *et al.*[3] prescribe the desired attitude change and solve for the necessary torques but give no details on mechanization. Other papers which propose active attitude control systems for spin stabilized vehicles have been published by Adams[1], Freed[5], and Grasshoff[6], but none of these explicitly discusses the reorientation problem. Grubin[7] uses the concept of finite rotations to mechanize a two-impulse scheme for reorienting the spin axis of a vehicle. If the torques are ideally impulsive, then the scheme is theoretically perfect. But in the case of finite-duration torquing, considerable errors can result. Wheeler[15] extends Grubin's work to include asymmetric spinning satellites, but the underlying philosophy is the same. Porcelli and Connolly[13] use a graphical approach to obtain control laws for the reorientation of a spinning body. Their results are only valid for small angles and small angular velocities. For this linearized case they prove that a two-impulse control scheme is fuel-optimal. Two sub-optimal control laws are then derived for the case of limited thrust based on the two-impulse solution. Most recently, Jahangir and Howe[11] have proposed a time-optimal scheme which does not require solving a TPBVP. This scheme can be used for the specific case when only two thruster firings are sufficient to complete the time-optimal attitude change maneuver. If the boundary conditions happen to lie outside this subset of the state space, the algorithm given by Jahangir and Howe fails to converge, since there does not exist a two-pulse time-optimal solution for such a case. If a control law is desired for boundary conditions which require more than two thruster pulses, we must solve a TPBVP involving ten nonlinear differential equations.

Both the two-pulse solution and the multiple-pulse solution require iterations and, therefore, can be costly in terms of the computer time required for the solution to converge and also in terms of the complexity of the iterative update scheme. Hence, an online iterative procedure does not appear to be practical for a real-time control algorithm. One possible alternative is to precompute the thruster firing times by solving a TPBVP for discrete values of the desired boundary conditions. These thruster firing times can then be stored as a table in an on-board computer and the control scheme can be implemented in real-time by table look-up and interpolation.

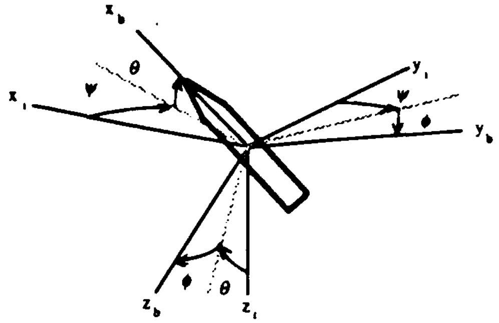

Figure 1: Axis systems.

Since we must store the control history as a function of the boundary conditions, we look for ways to generate a set of boundary condition points for which the thruster firing times are known without solving an iterative problem. To this end a new state vector is introduced in Section 4 which is related to the original state vector by a transformation. We will show in Sections 5 and 6 that we can generate a trajectory on the boundary of the set of reachable states by assuming a set of final conditions and integrating the transformed state and costate equations backwards in time. Since the boundary of the set of reachable states defines all the minimum-time trajectories, we can obtain all the desired boundary conditions and the associated time-optimal control histories by varying the final conditions over the range of their possible values. Finally, in Section 7 we illustrate the procedure by plotting some example time-optimal trajectories.

2. Equations of Motion

Figure 1 shows the orientation of the moving body axes x_b, y_b, z_b relative to the inertial reference axes x_i, y_i, z_i, and also the Euler angles ψ, θ, ϕ relating the two axis systems. The body axes origin is at the missile c.g. with the x_b-axis assumed to be the axis of symmetry; the y_b- and z_b-axes lie in a plane perpendicular to the longitudinal axis, x_b. The missile is modeled as a rigid cylindrical body. We also assume that the control jet is located in the x_b-z_b plane and pointed in the direction of the z_b-axis. When fired, the control jet generates a constant positive moment about the y_b-axis.

We have assumed no disturbances such as aerodynamic forces, gravity, solar radiation pressures, or structural damping. Because of the short flight times, these disturbances have negligible effect on the dynamics of the missile. Since no moment is applied about the x_b-axis, and since $I_y = I_z$ (the moments of inertia about the y_b- and z_b-axes are equal for a missile that is axially symmetric about its x_b-axis), it turns out that ω_x, the missile angular velocity component along the x_b-axis, is a constant equal to the initial spin velocity of the missile. We then obtain a set of five state equations: two dynamical equations involving the transverse angular velocities and three kinematical equations giving the rates of change of Euler angles. Thus

$$\dot{\omega}_y = \left(1 - \frac{I_x}{I_y}\right)\omega_x\omega_z + \frac{M_y}{I_y} \tag{1}$$

$$\dot{\omega}_z = -\left(1 - \frac{I_x}{I_y}\right)\omega_x\omega_y \tag{2}$$

$$\dot{\psi} = (\omega_y \sin\phi + \omega_z \cos\phi)\sec\theta \tag{3}$$

$$\dot{\theta} = \omega_y \cos\phi - \omega_z \sin\phi \tag{4}$$

$$\dot{\phi} = \omega_x + (\omega_y \sin\phi + \omega_z \cos\phi)\tan\theta \tag{5}$$

where

ω_y, ω_z = trasverse angular velocity components along the y- and z-axes, respectively,

ψ, θ, ϕ = Euler angles corresponding to yaw, pitch and roll, respectively,

I_x, I_y = the moments of inertia about the longitudinal and transverse axes, respectively,

M_y = the thruster torque about the y-axis.

For convenience we choose to write Eqs. (1)-(5) in terms of dimensionless variables and parameters in accordance with the following definitions:

$$\Omega_y = \frac{\omega_y}{\omega_x},\ \Omega_z = \frac{\omega_z}{\omega_x}$$
$$A = 1 - \frac{I_x}{I_y},\ \lambda_y = \frac{M_y}{I_y\omega_x^2}$$
$$\text{dimensionless time } T = \omega_x t$$

Now, if we redefine the $\dot{\ }$ operator as differentiation with respect to the dimensionless time T, the equations become

$$\dot{\Omega}_y = A\Omega_z + \lambda_y \tag{6}$$

$$\dot{\Omega}_z = -A\Omega_y \tag{7}$$

$$\dot{\psi} = (\Omega_y \sin\phi + \Omega_z \cos\phi)\sec\theta \tag{8}$$

$$\dot{\theta} = \Omega_y \cos\phi - \Omega_z \sin\phi \tag{9}$$

$$\dot{\phi} = 1 + (\Omega_y \sin\phi + \Omega_z \cos\phi)\tan\theta \tag{10}$$

In order to write a state variable description of the system, we define the state $\mathbf{x}$ of the system as

$$\mathbf{x} = \left[\ \Omega_y \quad \Omega_z \quad \psi \quad \theta \quad \phi\ \right]^T$$

and the control u as

$$u = \lambda_y$$

Eqs. (6)-(10) can now be written in the standard form.

$$\dot{\mathbf{x}} = \mathbf{f}(\mathbf{x}) + \mathbf{g}u \tag{11}$$

where

$$\mathbf{f}(\mathbf{x}) = \begin{bmatrix} Ax_2 \\ -Ax_1 \\ (x_1 \sin x_5 + x_2 \cos x_5)\sec x_4 \\ x_1 \cos x_5 - x_2 \sin x_5 \\ 1 + (x_1 \sin x_5 + x_2 \cos x_5)\tan x_4 \end{bmatrix} \tag{12}$$

$$\mathbf{g} = \left[\ 1 \quad 0 \quad 0 \quad 0 \quad 0\ \right]^T \tag{13}$$

We assume that at the initial time, the missile body axis system coincides with the inertial axis system. The initial transverse angular velocity of the missile, however, is non-zero. We thus obtain the following initial condition:

$$\mathbf{x}_0 = \left[\ x_{1,0} \quad x_{2,0} \quad 0 \quad 0 \quad 0\ \right]^T \tag{14}$$

We want to find a control which will take this initial state to a desired state, described by some non-zero desired yaw and pitch angles and zero final transverse angular velocity, in minimum time. The desired final state vector, $\mathbf{x}_d$, can be written as:

$$\mathbf{x}_d = \left[\ 0 \quad 0 \quad x_{3,d} \quad x_{4,d} \quad \text{free}\ \right]^T \tag{15}$$

We also assume an upper bound u_{max} on the control u. Thus, the constraint on the control can be written as:

$$0 \le u \le u_{max} \tag{16}$$

The numerical values for the two parameters, A and u_{max}, which will be used later in examples, are

$$A = 0.9,\ u_{max} = 0.02$$

This value of A corresponds to a length to diameter ratio of 3.775 for a cylindrical body of uniform density. A missile weighing 10 *lbs.* and having a uniform mass density of aluminum would have the following dimensions:

length = 12.30 *in.*, diameter = 3.26 *in.*

If the moment arm is half the length and the spin velocity is 50 *rad/sec*, $u_{max} = 0.02$ corresponds to a thrust of 2.79 *lbs.*

3. Time-Optimal Control Formulation

The problem, as stated in the previous section, is to find a control $u(T)$ which takes the initial state, $\mathbf{x}_0$, to the desired state, $\mathbf{x}_d$, in minimum time while satisfying the constraints $\dot{\mathbf{x}} = \mathbf{f}(\mathbf{x}) + \mathbf{g}u$ and $0 \leq u \leq u_{max}$. This is one specific case of a general Mayer problem. Filippov[4] gives a theorem and proves the existence of an optimal control for a Mayer problem. At this time no general theorems are available on the uniqueness of optimal solutions for the one-sided controls, *i.e.*, $0 \leq u \leq u_{max}$. Therefore, we can only give necessary conditions for u^* to be an optimal control.

In order to derive an expression for the time-optimal control, we write the performance index

$$J = \int_{T_0}^{T_f} 1 dt \tag{17}$$

We want to minimize the performance index J under the constraints of Eq. (11) and (16). Thus, we can write the Hamiltonian

$$H = \mathbf{p}^T \dot{\mathbf{x}} - 1 \tag{18}$$

where $\mathbf{p}$ is the costate vector. The necessary conditions for u^* to be an optimal control are

$$\dot{\mathbf{x}}^* = \frac{\partial H}{\partial \mathbf{p}} = \mathbf{f}(\mathbf{x}^*) + \mathbf{g}u^* \tag{19}$$

$$\dot{\mathbf{p}}^* = -\frac{\partial H}{\partial \mathbf{x}} = \mathrm{H}(\mathbf{x}^*)\mathbf{p}^* \tag{20}$$

$$u^* = \begin{cases} u_{max} & \text{if } p_1^* > 0 \\ 0 & \text{if } p_1^* < 0 \end{cases} \tag{21}$$

and

$$\mathbf{x}(T_0) = \mathbf{x}_0 \tag{22}$$

$$\mathbf{x}(T_f) = \mathbf{x}_d \tag{23}$$

$$\mathbf{p}(T_0) = [\ \text{free} \quad \text{free} \quad \text{free} \quad \text{free} \quad \text{free}\ ]^T \tag{24}$$

$$\mathbf{p}(T_f) = [\ \text{free} \quad \text{free} \quad \text{free} \quad \text{free} \quad 0\ ]^T \tag{25}$$

$$H(T_f) = 0 \tag{26}$$

where $\mathbf{H}(\mathbf{x}) = -\partial\mathbf{f}/\partial\mathbf{x}$. Eqs. (19) and (20) are the differential equations for the state and costate vector. Eq. (21) is derived from the optimality condition, *i.e.*, maximizing the Hamiltonian H. Eqs. (22) and (23) are the given boundary conditions and Eqs. (24)-(26) are derived from the transversality conditions. Furthermore, we note from the theory of necessary conditions that

$$\frac{\partial H(\mathbf{x}^*, \mathbf{p}^*, T)}{\partial T} = \frac{dH(\mathbf{x}^*, \mathbf{p}^*, T)}{dT} = 0$$

This, in addition to Eq. (26), shows that

$$H(\mathbf{x}^*, \mathbf{p}^*, T) = 0 \text{ for all } T \in [T_0, T_f]$$

Hence, in the problem we have 10 differential equations (Eqs. (19) and (20)) with 10 boundary conditions (Eqs. (22)-(25)) constituting a TPBVP. As mentioned earlier, the solution of this problem requires iterations and, therefore, is difficult to implement in real-time. In the actual missile, thruster firing times are computed off-line and are stored as a table in an on-board computer. Function generation is then used to compute the thruster turn-on and turn-off times as functions of the boundary conditions.

Instead of obtaining the thruster switch times by solving this iterative problem, we consider an alternative approach in the next section. An alternative optimal control formulation in terms of a new state vector is given. It is shown that, by assuming a set of final conditions and integrating backwards in time, we can generate time-optimal trajectories in the state space.

4. An Alternative Formulation of the Time-Optimal Control Problem

We define a new reference axis system. This axis system is fixed in the target and its x-axis points along the desired direction of the missile x_b-axis. The orientation of the missile with respect to an observer fixed in the target is given by the Euler angles, y_3, y_4, and y_5, where y_3, y_4, and y_5 correspond to yaw, pitch and roll, respectively. We also define $y_1 = x_1$ and $y_2 = x_2$. Thus, we can write a new state vector

$$\mathbf{y} = [\ y_1 \quad y_2 \quad y_3 \quad y_4 \quad y_5\ ]^T$$

The two state vectors $\mathbf{x}$ and $\mathbf{y}$ are related by a transformation (see Section 6.3 for the transformation relations). The equations of motion can be written in terms of this new state vector and are given by:

$$\dot{\mathbf{y}} = \mathbf{f}(\mathbf{y}) + \mathbf{g}u \tag{27}$$

We assume the initial and final conditions, respectively, to be

$$\mathbf{y}(T_0) = \mathbf{y}_0 = [\ y_{1,0} \quad y_{2,0} \quad y_{3,0} \quad y_{4,0} \quad y_{5,0}\ ]^T \tag{28}$$

$$\mathbf{y}(T_f) = \mathbf{y}_f = [\ 0 \quad 0 \quad 0 \quad 0 \quad \text{free}\ ]^T \tag{29}$$

A time-optimal control problem can be formulated for this system, similar to Section 3. We want to minimize the maneuver time, so we can again write the performance index as

$$J = \int_{T_0}^{T_f} 1 dt \tag{30}$$

under the constraints of Eqs. (23) and (16).

Proceeding with the derivation of the necessary conditions on the time-optimal control, we write the Hamiltonian

$$H = \mathbf{q}^T \dot{\mathbf{y}} - 1 \tag{31}$$

where $\mathbf{q}$ is the costate vector. The necessary conditions for u^* to be an optimal control are

$$\dot{\mathbf{y}}^* = \frac{\partial H}{\partial \mathbf{q}} = \mathbf{f}(\mathbf{y}^*) + \mathbf{g}u^* \tag{32}$$

$$\dot{\mathbf{q}}^* = -\frac{\partial H}{\partial \mathbf{y}} = \mathbf{H}(\mathbf{y}^*)\mathbf{q}^* \tag{33}$$

$$u^* = \begin{cases} u_{max} & \text{if } q_1^* > 0 \\ 0 & \text{if } q_1^* < 0 \end{cases} \tag{34}$$

The boundary conditions on the state variables are given by Eqs. (28) and (29). The boundary conditions on the Hamiltonian and the costate variables are derived from the transversality conditions:

$$H(T_f) = 0 \tag{35}$$

$$\mathbf{q}(T_0) = \mathbf{q}_0 = \left[\text{ free} \quad \text{free} \quad \text{free} \quad \text{free} \quad \text{free } \right]^T \tag{36}$$

$$\mathbf{q}(T_f) = \mathbf{q}_f = \left[\text{ free} \quad \text{free} \quad \text{free} \quad \text{free} \quad 0 \ \right]^T \tag{37}$$

We observe that this formulation still results in a TPBVP. If the initial state vector, $\mathbf{y}(T_0)$, is specified, an initial costate vector, $\mathbf{q}(T_0)$, must be determined which results in the desired final state and costate vectors. However, the state and costate vectors at the final time have some simple features. Each of the components of these vectors is either zero or free. Therefore, it is worthwhile to examine the system characteristics if the state and costate equations are integrated backwards in time starting at T_f.

In the next section we discuss a two dimensional system in terms of some simple sets in the state and costate space. By looking at the problem from a geometric point of view, we show for this 2-D system that the origin can be connected to all points in the set of reachable states in minimum time by varying the costate vector over $\mathcal{R}^2$ and integrating the system equations backwards in time. We note that this procedure of integrating the system backwards in time is fairly common. The most familiar example is the simple inertia system, $\ddot{x} = u$. In this system the state equations are integrated backwards in time, using the time-optimal control, to obtain a switching curve in the state space.

In Section 6 we apply this scheme to the complete nonlinear minimum-time attitude control problem of a spinning missile. Using the procedure analogous to Section 5, all mimimum-time trajectories can be generated. By storing the state vector at discrete points in time along the minimum-time trajectories, we are able to generate a set of points for which the thruster firing times are known.

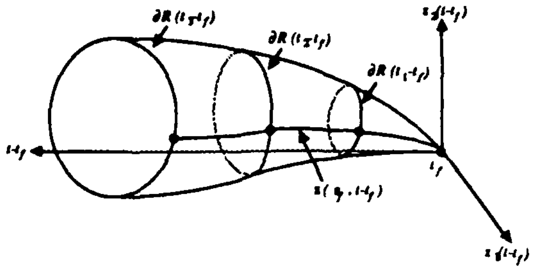

Figure 2: The set of reachable states for a 2-D system.

5. The Set of Reachable States for a 2-D System

In this section we examine the characteristics of the following 2-D system:

$$\dot{\mathbf{z}} = \mathbf{h}(\mathbf{z}, u)$$

where $\mathbf{z}$ is a 2×1 state vector and u is the scalar control. The desired final condition is assumed to be the origin, *i.e.*, $\mathbf{z}(t_f) = 0$. If we subject the system with final state $\mathbf{z}(t_f) = 0$ to all control histories and integrate the system backwards in time starting at t_f, we obtain a set of states that are reachable from the origin at time $t - t_f$, or simply the set of reachable states. We denote the set of reachable states simply as $R(t - t_f)$ in Figure 2. In the figure the boundary of the set of reachable states at time $t_i - t_f$ is denoted by $\partial R(t_i - t_f)$. It is well known from the geometric properties of the optimal control that the boundary of the set of reachable states defines all the minimum-time solutions. We, therefore, conduct the following experiment:

Let $u_{min}(\mathbf{z}, \mathbf{s})$ be the optimal control which is obtained by minimizing the Hamiltonian with respect to the control, where $\mathbf{s}$ is the 2×1 costate vector. Hence, if $\mathbf{z}^*$ is an optimal motion, it satisfies

$$\dot{\mathbf{z}}^* = \mathbf{h}(\mathbf{z}^*, u_{min}(\mathbf{z}^*, \mathbf{s}^*))$$

where $\mathbf{s}^*$ is a solution to the related costate equations. Clearly, $\mathbf{z}^*(t_f) = 0$.

In order to obtain a specific time-optimal trajectory, we need to assume some final conditions on the costate vector. We let $\mathbf{s}(t_f) = \mathbf{s}_f$, where $\mathbf{s}_f$ is an arbitrary constant vector. The system equations, $\dot{\mathbf{z}} = \mathbf{h}(\mathbf{z}, u_{min}(\mathbf{z}, \mathbf{s}))$, can now be integrated backwards in time starting from the final time t_f to obtain a trajectory $\mathbf{z}(\mathbf{s}_f, t - t_f)$ shown in the figure. The trajectory $\mathbf{z}(\mathbf{s}_f, t - t_f)$ represents the fact that it is a function of the specified final costate vector, $\mathbf{s}_f$, and the time parameter, $t - t_f$. This trajectory connects all points along its path to the origin in minimum time. Also, as mentioned earlier, this minimum-time trajectory lies on the boundary of the set of reachable states. By storing $\mathbf{z}(\mathbf{s}_f, t - t_f)$ at discrete points in time, we can obtain a set of points in the state space for which the time-optimal control history is known. If we assume a different initial $\mathbf{s}_f$, another time-optimal trajectory is obtained. By varying $\mathbf{s}_f$ over $\mathcal{R}^2$ and integrating the system for each $\mathbf{s}_f$ backwards in time, all trajectories on the boundary of the set of reachable states can be generated. In this way all the reachable states can be obtained at discrete intervals and the associated control history can be stored as a function of these states.

In the next section we employ the techniques described here to obtain a set of boundary condition points for which the control history is known for the case of minimum-time reorientation of a spinning missile.

6. An Examination of the "y" System

We use here the idea of backwards integration and examine the system behaviour. Similar to the previous section, we conduct the following experiment.

Four of the final state variables are zero, as given in Eq. (29). We assume that $y_5(T_f) = y_{5,f}$, where $y_{5,f}$ is an arbitrary constant. Similarly, we assume an arbitrary value for the final costate vector, $\mathbf{q}(T_f) = \mathbf{q}_f$, where $q_{5,f} = 0$. The expression for the time-optimal control is given in Eq. (34). Once all the final conditions on the state and costate variables are specified, we start the integration at T_f and integrate the state and costate equations backwards in time. At each numerical integration step, we obtain a $\mathbf{y}(T')$ where $T' = T - T_f$. This trajectory connects all points along its path to the specified final state in minimum time. By varying the first four components of the final costate vector $\mathbf{q}_f$ over $\mathcal{R}^4$ (the fifth component is zero as given in Eq. (37)), the entire boundary of the set of reachable states is generated starting from the specified $\mathbf{y}_f$. We note here that the only non-zero component of the state vector is $y_{5,f}$, which corresponds to the roll angle of the missile. This angle can take on values in the range $[-\pi, \pi]$. By varying $y_{5,f}$ in this range, and following the aforementioned procedure of generating the boundary of the set of reachable states, all the time-optimal solutions can be generated. During the integration, the state vector, $\mathbf{y}$, and the corresponding thruster switch times can be stored at discrete points in time. Hence, this procedure gives a set of $\mathbf{y}$ points for which the control history given in terms of the thruster firing times is known.

The control scheme can then be implemented in real-time by using the thruster switch times which are stored at discrete values of the transformed state vector, $\mathbf{y}$. However, in the actual missile the desired attitude is measured with respect to the moving missile frame, whereas the vector $\mathbf{y}$ gives the orientation of the missile with respect to an observer fixed in the target. Hence, it is desirable to store the boundary conditions in terms of the original state vector $\mathbf{x}$. The boundary conditions in terms of the $\mathbf{x}$ vector are given in Eq. (14) and (15). The state vector $\mathbf{y}(T')$ can be transformed back to our original system to obtain the corresponding boundary conditions $x_{1,0}$, $x_{2,0}$, $x_{3,d}$, and $x_{4,d}$.

The procedure to generate the control history as a function of the boundary conditions can be summarized in the following way:

1. Initialize $\mathbf{y}_f$ and $\mathbf{q}_f$.

2. Integrate the $\dot{\mathbf{y}}$ and $\dot{\mathbf{q}}$ equations backwards in time and at each $T'_n = n\Delta T$ obtain $\mathbf{y}(T'_n)$, where ΔT is the time interval chosen to give desired data-point spacing between $\mathbf{y}(T'_n)$ and $\mathbf{y}(T'_{n+1})$, and n is a positive integer. Note that the numerical integration step can be a submultiple of ΔT.

3. Transform $\mathbf{y}(T'_n)$ to get the boundary conditions in the original form, $x_{1,0}$, $x_{2,0}$, $x_{3,d}$, and $x_{4,d}$. Store the thruster switching times as functions of these four variables. Note that if $q_1 > 0$, then $T_1 = 0$, and similarly if, $q_1 < 0$ then $T_1 > 0$, where T_1 is the first turn-on time of the thruster.

Each of these steps is discussed in the following sections.

6.1. Initialization of $\mathbf{y}_f$ and $\mathbf{q}_f$

As indicated earlier, five of the variables at T_f are zero.

$$y_{1,f} = y_{2,f} = y_{3,f} = y_{4,f} = q_{5,f} = 0$$

The other five variables at T_f are free. These must be varied over all possible values to obtain the optimal control history as a function of the boundary conditions. The variable $y_{5,f}$ corresponds to the roll angle and, thus, is confined to

$$y_{5,f} \in [-\pi, \pi]$$

The space over which $q_{1,f}$, $q_{2,f}$, $q_{3,f}$, and $q_{4,f}$ must be varied is a subset of the costate space. We refer to this subspace as $\mathcal{Q}$.

Definition: The space $\mathcal{Q}$ is defined as

$$\mathcal{Q} = \{\mathbf{q}(T_f) : q_5(T_f) = 0, q_i(T_f) = \pm 1, \\ q_j(T_f) \in [-1, +1], i, j = 1, 2, 3, 4, j \neq i\}$$

An algorithm to vary these variables over the range of their possible values is given below:

```
do $y_{5,f} = -\pi, \pi, \delta$        where $\delta$ is the desired
                                  spacing between values
                                  of $y_{5,f}$
do $i = 1, 4$
    $q_{i,f} = \pm 1$
    do $q_{j,f} = -1, +1, \Delta$   where $j \neq i$ and $\Delta$ is the
                                  desired spacing between
                                  values of $q_{j,f}$
```

During the implementation of our scheme to generate time-optimal solutions, we observe that a constant Δ (uniform spacing in $q_{j,f}$'s) does not result in a uniform span of the entire desired space of time-optimal solutions. We find that when $q_{j,f}$ is close to zero, very small Δ is needed to span the set of desired time-optimal solutions. Conversely, when $q_{j,f}$ is not close to zero, Δ need not be small.

6.2. Integration of State and Costate Equations

A practical issue in the implementation of the scheme given in Section 6 is the choice of a numerical integration algorithm and the handling of discontinuities that occur when the control switches from on to off or *vice versa*.

The RK-4 fixed-step algorithm is used to integrate the state and costate equations. We utilize the fact that analytic solutions for y_1 and y_2 can be obtained from Eq. (11). Thus, the equations for $\dot{y}_1$ and $\dot{y}_2$ do not have to be integrated numerically. The analytical solutions for y_1 and y_2 are also used to obtain the half- and full-frame derivative estimates of the remaining state and costate variables, as required in the RK-4 integration algorithm.

There is a discontinuity in these derivatives when the application of the control u starts or stops. This switching time is a function of q_1, the first component of the costate vector, as given by Eq. (34). If this discontinuity occurs within an integration step, it can cause large errors in the numerical solution. To reduce these errors, the step size must be chosen small enough to meet some integration error criterion, which can result in excessive computational time. Several papers have been written suggesting special methods to circumvent this difficulty. We choose the method proposed by Howe, Ye and Li[9] for its accuracy and ease of implementation. In this scheme, at each successive time step, q_1 is tested to see whether it has switched sign. If it has not, the integration proceeds to the next step. If switching has occurred, the time of its occurrence is computed by combining a fixed-point simplified Hermite interpolation with a continued fraction formula. Hermite interpolation is also used to compute the state and costate variable values at the crossover time. The RK-4 algorithm is then used to integrate through the remainder of the fixed-time step.

We define the following notation:

$$T_i = ih, \qquad i = 0, 1, 2, \ldots$$

$$u_i = u(T_i); \qquad \mathbf{y}_i \approx \mathbf{y}(T_i); \qquad \mathbf{q}_i \approx \mathbf{q}(T_i)$$

where h is the integration step size and $\mathbf{y}_i$ and $\mathbf{q}_i$ are the numerical approximations to the exact solution $\mathbf{y}(T_i)$ and $\mathbf{q}(T_i)$. The following computational procedure is used at the ith step.

1. Integrate from T_i to T_{i+1} with the RK-4 algorithm. In this integration u_i is used for all derivative evaluations over the interval.

2. Determine if $q_{1,i+1}$ has changed sign with respect to $q_{1,i}$. If not, repeat 1 starting at T_{i+1}. If q_1 has changed sign ($q_{1,i+1}q_{1,i} < 0$), it means that q_1 has a zero over the interval $T_i \leq T \leq T_{i+1}$ and the discontinuity has been crossed. In that case, proceed to step 3.

3. Using a fixed-point simplified Hermite interpolation between T_i and T_{i+1} followed by the continued fraction zero-finder described by Howe, Ye and Li[9], determine the zero T_z of q_1. Again, using Hermite interpolation, determine $\mathbf{y}(T_z)$ and $\mathbf{q}(T_z)$.

4. Change the control u from 0 to u_{max} (or from u_{max} to 0, as appropriate) and integrate from T_z to T_{i+1} to recompute $\mathbf{y}_{i+1}$ and $\mathbf{q}_{i+1}$.

5. Return to step 1 and repeat the steps starting at T_{i+1}.

6.3. Transformation Relations Between x and y

Let us consider a vector $\mathbf{r}$ originating at the missile c.g. We let $\{r_m\}$ represent the components of the vector $\mathbf{r}$ in the missile body axis frame; $\{r_t\}$ represent the components of the same vector in the frame $\mathcal{T}$; and $\{r_f\}$ represent the components of the same vector in the frame $\mathcal{F}$. The frame of reference $\mathcal{T}$ is an arbitrary axis system whose x-axis coincides with the desired direction of the missile x_b-axis. The frame of reference $\mathcal{F}$ is defined to be the missile axis sytem at the end of the maneuver. Previously, we have defined $x_{3,d}$ and $x_{4,d}$ to be the yaw and pitch angles describing the orientation of the desired direction of the missile x_b-axis with respect to the missile body axis system. In addition, we define $x_{5,d}$ to be the roll angle of the frame $\mathcal{F}$ with respect to the missile body axis system. It should be borne in mind that $x_{5,d}$ is free in the formulation of the optimal control problem in Section 3. Thus, we can write.

$$\{r_f\} = [\mathrm{C}\,(x_{3,d}, x_{4,d}, x_{5,d})]\,\{r_m\} \qquad (38)$$

where [C] is the direction cosine matrix and is defined in the following way:

$$[\mathrm{C}\,(\psi,\theta,\phi)] = \begin{bmatrix} \cos\psi\cos\theta & \sin\psi\cos\theta & -\sin\theta \\ -\sin\psi\cos\phi + & \cos\psi\cos\phi + & \cos\theta\sin\phi \\ \cos\psi\sin\theta\sin\phi & \sin\psi\sin\theta\sin\phi & \\ \sin\psi\sin\phi + & -\cos\psi\sin\phi + & \cos\theta\cos\phi \\ \cos\psi\sin\theta\cos\phi & \sin\psi\sin\theta\cos\phi & \end{bmatrix} \tag{39}$$

We have already defined $y_3 = y_3(T - T_f)$, $y_4 = y_4(T - T_f)$, and $y_5 = y_5(T - T_f)$ to be the Euler angles describing the missile orientation relative to an observer fixed in the frame $\mathcal{T}$. Therefore, we can write

$$\{r_m\} = [\mathrm{C}\,(y_3, y_4, y_5)]\,\{r_t\} \tag{40}$$

Finally, the frame $\mathcal{F}$ is obtained by rotating the frame $\mathcal{T}$ about its x-axis. This rotation is given by the angle $y_{5,f} = y_5(T_f)$ and we get

$$\{r_f\} = [\Phi]\,\{r_t\} \tag{41}$$

where

$$[\Phi] = \begin{bmatrix} 1 & 0 & 0 \\ 0 & \cos y_{5,f} & \sin y_{5,f} \\ 0 & -\sin y_{5,f} & \cos y_{5,f} \end{bmatrix} \tag{42}$$

The matrices [C] and [Φ] are both direction cosine matrices; therefore, each is an orthogonal matrix. Hence, the inverse of these matrices is obtained by merely transposing them.

Eqs. (40) and (41) can be combined to write

$$\{r_f\} = [\Phi]\,[\mathrm{C}\,(y_3, y_4, y_5)]^T\,\{r_m\} \tag{43}$$

Comparing Eqs. (43) and (38), we finally get

$$[\mathrm{C}\,(x_{3,d}, x_{4,d}, x_{5,d})] = [\Phi]\,[\mathrm{C}\,(y_3, y_4, y_5)]^T \tag{44}$$

We let the entries in $[\mathrm{C}(x_{3,d}, x_{4,d}, x_{5,d})]$ be denoted by ζ_{ij} and the entries in $[\Phi][\mathrm{C}(y_3, y_4, y_5)]^T$ by η_{ij}, where i and j are the row and column indices respectively. Equating $\zeta_{13} = \eta_{13}$, we obtain

$$-\sin x_{4,d} = \sin y_3 \sin y_5 + \cos y_3 \sin y_4 \cos y_5 \tag{45}$$

Since $-\pi/2 < x_{4,d} < \pi/2$, the above equation gives a unique value for $x_{4,d}$.

$$x_{4,d} = -\sin^{-1}(\sin y_3 \sin y_5 + \cos y_3 \sin y_4 \cos y_5) \tag{46}$$

To get an expression for $x_{3,d}$, we equate $\zeta_{11} = \eta_{11}$ and $\zeta_{12} = \eta_{12}$ and obtain

$$\cos x_{3,d} \cos x_{4,d} = \cos y_3 \cos y_4 \tag{47}$$

$$\sin x_{3,d} \cos x_{4,d} = -\sin y_3 \cos y_5 + \cos y_3 \sin y_4 \sin y_5 \tag{48}$$

$\mathbf{x}$	$\varphi(\mathbf{y})$
$x_{1,0}$	y_1
$x_{2,0}$	y_2
$x_{3,d}$	$\tan^{-1}\left(\frac{-\sin y_3 \cos y_5 + \cos y_3 \sin y_4 \sin y_5}{\cos y_3 \cos y_4}\right)$
$x_{4,d}$	$-\sin^{-1}(\sin y_3 \sin y_5 + \cos y_3 \sin y_4 \cos y_5)$

Table 1: Transformation relations between **x** and **y**.

Dividing Eq. (48) by Eq. (47), we get the following expression for $x_{3,d}$ without an ambiguity in the quadrant:

$$x_{3,d} = \tan^{-1}\left(\frac{-\sin y_3 \cos y_5 + \cos y_3 \sin y_4 \sin y_5}{\cos y_3 \cos y_4}\right) \tag{49}$$

Similarly, by equating $\zeta_{23} = \eta_{23}$ and $\zeta_{33} = \eta_{33}$, we obtain

$$\begin{aligned} \cos x_{4,d} \sin x_{5,d} = {} & \cos y_{5,f}\,(-\cos y_3 \sin y_5 + \\ & \sin y_3 \sin y_4 \cos y_5) + \sin y_{5,f} \cos y_4 \cos y_5 \end{aligned} \tag{50}$$

$$\begin{aligned} \cos x_{4,d} \cos x_{5,d} = {} & -\sin y_{5,f}\,(-\cos y_3 \sin y_5 + \\ & \sin y_3 \sin y_4 \cos y_5) + \cos y_{5,f} \cos y_4 \cos y_5 \end{aligned} \tag{51}$$

Dividing Eq. (50) by Eq. (51), we get the following expression for $x_{5,d}$ without an ambiguity in the quadrant:

$$x_{5,d} = \tan^{-1}\left(\frac{(a+b)\cos y_{5,f} + c \sin y_{5,f}}{(-a+b)\sin y_{5,f} + c \cos y_{5,f}}\right) \tag{52}$$

where

$$a = \cos y_3 \sin y_5$$

$$b = \sin y_3 \sin y_4 \cos y_5$$

$$c = \cos y_4 \cos y_5$$

Table 1 summarizes the transformation relations between the boundary conditions, given in terms of the state vector **x**, and the new state vector **y** at time $T - T_f$.

7. Example Trajectories

Three sets of final conditions on the state and costate variables are given in Table 2. We only vary the final roll angle $y_{5,f}$ in these three examples. Starting with these final values, the state and costate equations are integrated backwards in time. Figure 3 shows the plot of y_3 vs. y_4, where y_3 and y_4 are the yaw and pitch angles of the missile with respect to a frame whose x-axis coincides with the desired direction of the missile x_b-axis. At each integration step the state vector **y** is transformed to obtain the boundary conditions $x_{3,d}$ and $x_{4,d}$. The total angle α between the initial and the desired direction of the missile is given

	Example 1	Example 2	Example 3
$q_{1,f}$	0.25	0.25	0.25
$q_{2,f}$	−0.50	−0.50	−0.50
$q_{3,f}$	0.75	0.75	0.75
$q_{4,f}$	1.00	1.00	1.00
$y_{5,f}$	0.00	$2\pi/3$	$4\pi/3$

Table 2: Final conditions to generate example control histories.

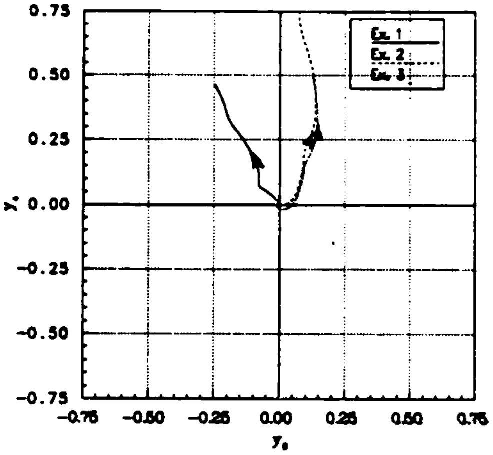

Figure 3: Path of the missile x_b-axis in the y_3-y_4 plane, where y_3 and y_4 are the yaw and pitch angles, respectively, of the x_b-axis with respect to the desired pointing direction.

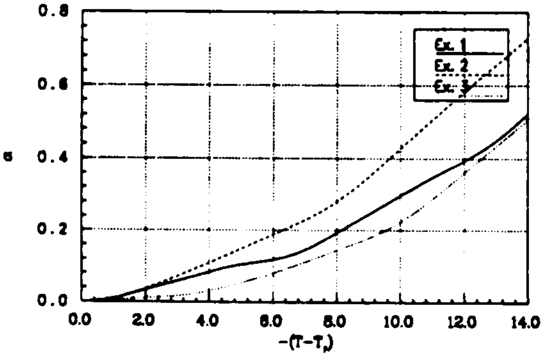

Figure 4: Total angle α vs. $-(T - T_f)$.

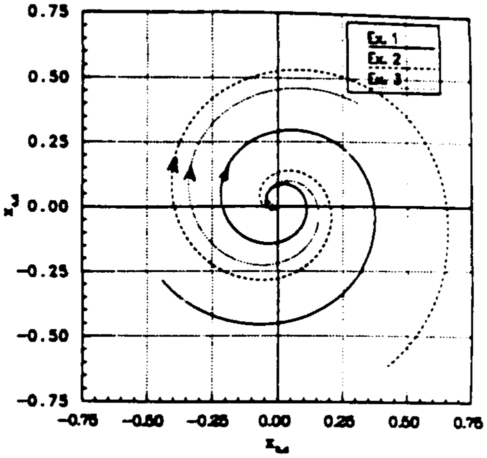

Figure 5: Path of the target in the $x_{3,d}$-$x_{4,d}$ plane, where $x_{3,d}$ and $x_{4,d}$ are the yaw and pitch angles, respectively, of the target direction with respect to the moving missile body-axis frame.

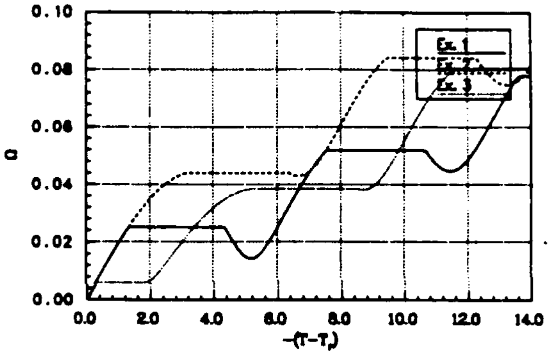

Figure 6: Total transverse angular velocity Ω vs. $-(T - T_f)$.

by $\alpha = \cos^{-1}(\cos x_{3,d} \cos x_{4,d})$. Figure 4 shows the angle α as a function of the dimensionless time T. The angles $x_{3,d}$ and $x_{4,d}$, which represent the target yaw and pitch angles, respectively, relative to the moving missile frame, are plotted in Figure 5.

The total transverse angular velocity $\Omega = \sqrt{y_1^2 + y_2^2}$ is plotted as a function of the dimensionless time T in Figure 6. We start at $\Omega = 0$ and, integrating backwards, obtain the time history of y_1 and y_2. Figure 7 shows the trajectory of transverse angular velocity components y_1-y_2 as the integration proceeds.

8. Mechanization of the Control Scheme

The thruster switch times $T_i, i = 1, 2, \ldots, n$ can be obtained from the approach given in Section 6 for the desired set of boundary conditions, where T_i is

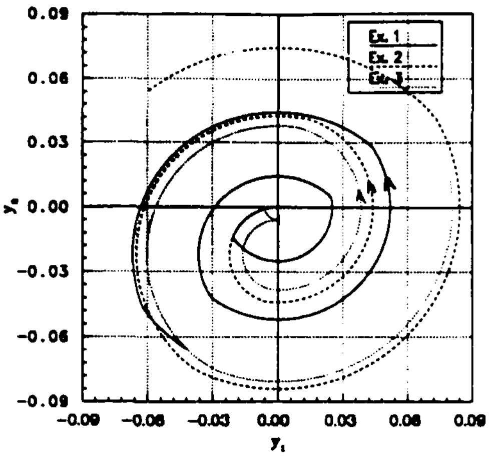

Figure 7: Trajectories of transverse angular velocity components y_1 and y_2.

the time when control switches and n is the total number of switches required to complete the attitude change maneuver. In order to implement this scheme in real-time, the switch times $T_i, i = 1, 2, \ldots, n$ must be stored in an on-board computer. We propose a control scheme which only needs to store T_1 and T_2, the first turn-on and turn-off times, respectively.

In this scheme table look-up followed by interpolation is used to compute T_1 and T_2. The thruster is then turned on from T_1 to T_2. After this first thruster firing has been completed, we can measure the state variables at T_2. The switch times T_1 and T_2 can now be recomputed based on this measured state. These new T_1 and T_2 correspond to T_3 and T_4, respectively, for the previous T_1 and T_2. Thus for the two-pulse case, the new T_3 and $T_4(= T_f)$ are such that $T_4 - T_3 = 0$. In the presence of interpolation, numerical, or measurement errors this will not be quite true. Nevertheless, in reality this scheme would probably be superior because it can correct for system and measurement errors by introducing feedback based on the latest state information.

When we store the thruster firing times at specified time intervals while integrating the state and costate equations backwards in time, a randomly spaced function is obtained. However, it is desirable for real-time function generation to have an equally spaced function. This table of equally spaced function values can be obtained by using linear interpolation across the randomly spaced function values. Once the equally spaced function to be used in real-time function generation is created, table search and interpolation can be carried out easily. Our recent research has focused on creating this table and implementing the control law using function generation. The results of this approach appear in a Ph.D. dissertation[10] and will also be published in future research papers.

Acknowledgements

The research reported in this paper has been supported by the U.S. Army Strategic Defense Command under contract number DASG60-88-C-0037 and by AFOSR under contract number F49620-86-C-0138.

References

[1] Adams, J. J., "Study of an Active Control System for a Spinning Body", NASA TN D-905, Langley Research Center, Langley Field, VA, June 1961.

[2] Athans, M. and Falb, P. L., *Optimal Control*, McGraw-Hill Inc., 1966.

[3] Cole, R. D., Ekstrand, M. E. and O'Neil, M. R., "Attitude Control of Rotating Satellites", *ARS Journal*, Vol. 31, 1961, pp. 1446-1447.

[4] Filippov, A. F., "On Certain Qustions in the Theory of Optimal Control", *SIAM J. Control*, 1962, pp. 76-84.

[5] Freed, L. E., "Attitude Control System for a Spinning Body", *National IAS-ARS Joint Meeting, Los Angeles*, Paper 61-207-1901, June 13-16, 1961.

[6] Grasshoff, L. H., "A Method for Controlling the Attitude of a Spin-Stabilized Satellite", *ARS Journal*, Vol. 31, 1961, pp. 646-649.

[7] Grubin, C., "Generalized Two-Impulse Scheme for Reorienting a spin stabilized Vehicle", *ARS Guidance, Control, and Navigation Conference, Stanford, CA*, Aug 7-9, 1961.

[8] Howe, R. M., "Attitude Control of Rockets Using a Single Axis Control Jet", *XIth International Astronautical Congress, Stockholm*, 1960.

[9] Howe, R. M., Ye, X. A. and Li, B. H., "An Improved Method for Simulation of Dynamic Systems with Discontinuous Nonlinearities", *Transactions of the Society for Computer Simulation*, Vol. 1, No. 1, Jan. 1984, pp.33-47.

[10] Jahangir, E., *Time-Optimal Attitude Control of a Spinning Missile*. Ph.D. Dissertation, University of Michigan, 1990.

[11] Jahangir, E. and Howe, R. M., "A Two-Pulse Scheme for the Time-Optimal Attitude Control of a Spinning Missile", *AIAA Guidance, Navigation and Control Conference, Portland, OR*, Aug 20-22, 1990.

[12] Patapoff, H., "Bank Angle Control System for a Spinning Satellite", AIAA Paper No. 63-339, August 1963.

[13] Porcelli, G. and Connolly, A., "Optimal Attitude Control of a Spinning Space-Body – A Graphical Approach", *IEEE Transactions on Automatic Control*, Vol. AC-12, No. 3, June 1967, pp. 241-249.

[14] Roberson, R. E., "Attitude Control of a Satellite Vehicle - An Outline of the Problems", *Proc. VIII International Astronautical Congress, Barcelona*, 1957, pp. 317-339.

[15] Wheeler, P. C., "Two-Pulse Attitude Control of an Asymmetric Spinning Satellite", *Progress in Aeronautics and Astronautics*, Vol. 13, 1964.

[16] Windenknecht, T. G., "A Simple System for Sun Orientation of a Spinning Satellite", *National IAS-ARS Joint Meeting, Los Angeles*, Paper 61-204-1898, June 13-16, 1961.

Appendix B

Bibliography of Papers Dealing with Boundary Layer Blowing

(Disregard numeric pagination)

Aroesty, J. & J. D. Cole, "Boundary-Layer Flows with Large Injection Rates," Rand Corp. Mem. RM-4620-ARPA, 1965.

Aroesty, J. & S. H. Davis, "Inviscid Cone Flows with Surface Mass Transfer," *AIAA J.* **4** (1966) 1830-1832.

Bott, J. F., "Massive Blowing Experiments," *AIAA J.* **6** (1968) 613-618.

Cole, J. D. & J. Aroesty, "The Blowhard Problem – Inviscid Flows with Surface Injection," *Int. J. Heat Mass Transf.* **11** (1968) 1167-1183; also, Rand Corp. Mem. RM-5196-ARPA, Santa Monica, CA, 1967.

Dershin, H., et. al., "Direct Measurement of Skin Friction on a Porous Flat Plate with Mass Injection," *AIAA J.* **5** (1967) 1934-1939.

El-Mistikawy, T. M. & M. J. Werle, "Numerical Method for Boundary Layers with Blowing – the Exponential Box Scheme," *AIAA J.* **16** (1978) 749-751.

Fernandez, F. L. & E. E. Zukoski, "Experiments in Supersonic Turbulent Flow with Large Distributed Surface Mass Injection," *AIAA J.* **7** (1969) 1759-1767.

Gupta, R. N., et. al., "Displacement-Thickness Induced Pressures on a Flat Plate with Homogeneous and Heterogeneous Vectored Injection," *Int. J. Heat Mass Transf.* **23** (1980) 405-408.

Gupta, R. N., et. al., " Hypersonic Interactions with Surface Mass Transfer – Part I: Steady Flow Over a Slender Wedge Wing," AIAA paper 82-0979; synoptic appears in *AIAA J.* **22** (1984) 449-450.

Gupta, R. N., et. al., " Hypersonic Interactions with Surface Mass Transfer – Part II: Flow with Impulsive Change in Angle of Attack of the Wing," AIAA paper 82-0979; synoptic appears in *AIAA J.* **22** (1984) 451-452.

Hartunian, R. A. & D. J. Spencer, "Visualization Techniques for Massive Blowing Studies," *AIAA J.* **4** (1966) 1305-1307.

Hartunian, R. A. & D. J. Spencer, "Experimental Results for Massive Blowing Studies," *AIAA J.* **5** (1967) 1397-1401.

Holden, M. S., et. al., "An Experimental Study of Transpiration Cooling on the Distribution of Heat Transfer and Skin Friction to a Sharp Slender Cone at Mach 11 and 13," AIAA paper 90-0308, 1990.

Hsia, H. T.-S., "Equivalence of Secondary Injection to a Blunt Body in Supersonic Flow," *AIAA J.* **4** (1966) 1832-1834.

Inger, G. R., "A Simple Model Shear Flow with Blowing," *AIAA J.* **4** (1966) 1834-1836.

Inger, G. R., "Laminar Boundary-Layer Solutions with Strong Blowing," *AIAA J.* **5** (1967) 1677-1678.

Inger, G. R., "An Integral-Method Solution for Massive Blowing on Slender Hypersonic Bodies," *AIAA J.* **5** (1967) 2068-2069.

Inger, G. R., "Strong Blowing Across a Couette-Poiseuille Shear Flow," *Phys. Fluids* **12** (1969) 1741-1746.

Inger, G. R. & G. A. Gaitatzes, "Strong Blowing into Supersonic Laminar Flows around Two-Dimensional and Axisymmetric Bodies," *AIAA J.* **9** (1971) 436-443.

Inger, G. R. & T. F. Swean, "Vectored Injection into Laminar Boundary Layers with Heat Transfer," *AIAA J.* **13** (1975) 616-622.

Inger, G. R. & T. F. Swean, "Hypersonic Viscous-Inviscid Interaction with Vectored Surface Mass Transfer," *AIAA J.* **14** (1976) 589-596.

Kang, S.-W., "Hypersonic Low-Reynolds-Number Flow over a Blunt Body with Mass Injection," *AIAA J.* **7** (1969) 1546-1552.

Kassoy, D. R., "On Laminar Boundary-Layer Blowoff. Part 2," *J. Fluid Mech.* **48** (1971) 209-228.

Kenworthy, M. & J. A. Schetz, "Experimental Study of Slot Injection into a Supersonic Stream," *AIAA J.* **11** (1973) 585-586.

King, H. H. & L. Talbot, "Effect of Mass Injection on the Drag of a Slender Cone in Hypersonic Flow," *AIAA J.* **2** (1964) 836-844.

Klemp, J. B. & A. Acrivos, "High Reynolds Number Flow Past a Flat Plate with Strong Blowing," *J. Fluid Mech.* **51** (1972) 337-356.

Kubota, T. & F. L. Fernandez, "Boundary Layer Flows with Large Injection and Heat Transfer," *AIAA J.* **6** (1968) 22-28.

Lee, G., "Hypersonic Flow Over a Blunt Flat Plate with Surface Mass Transfer," *AIAA J.* **4** (1966) 2049-2051.

Lees, L. & R. L. Chapkis, "Surface Mass Injection at Supersonic and Hypersonic Speeds as a Problem in Turbulent Mixing: Part I. Two-Dimensional Flow," *AIAA J.* **7** (1969) 671-680.

Lees, L. & R. L. Chapkis, "Surface Mass Injection at Supersonic and Hypersonic Speeds as a Problem in Turbulent Mixing. Part II: Axially Symmetric Flow," *AIAA J.* **9** (1971) 1067-1073.

Lewis, C. H., et. al., "Mass Transfer and First-Order Boundary-Layer Effects on Sharp Cone Drag. Part I: At Supersonic Conditions," *AIAA J.* **4** (1966) 1697-1703.

Li, T.-Y. & J. F. Gross, "Hypersonic Strong Viscous Interaction on a Flat Plate with Surface Mass Transfer," *Proc. 1961 Heat Transfer and Fluid Mech. Inst.*, pp. 146-160.

Liu, T. M. & P. R. Nachtsheim, "Numerical Stability of Boundary Layers with Massive Blowing," *AIAA J.* **11** (1973) 1197-1198.

Libby, P. A. & D. R. Kassoy, "Laminar Boundary Layer at an Infinite Swept Stagnation Line with Large Rates of Injection" *AIAA J.* **8** (1970) 1846-1851.

Libby, P. A., "Numerical Analysis of Stagnation Point Flows with Massive Blowing," *AIAA J.* **8** (1970) 2095-2096.

Libby, P. A., "Laminar Flow at a Three-Dimensional Stagnation Point with Large Rates of Injection," *AIAA J.* **14** (1976) 1273-1279.

Liu T.-M. & H. H. Chiu, "Fast and Stable Numerical Method for Boundary-Layer Flows with Massive Blowing," *AIAA J.* **14** (1976) 114-116.

Marvin, J. G. & Y. S. Shaeffer, "A Method for Solving the Nonsimilar Laminar Boundary-Layer Equations Including Foreign Gas Injection," NASA TN D-5516, 1969.

Nachtsheim, P. R. & M. J. Green, "Numerical Solution of Boundary-Layer Flows with Massive Blowing," *AIAA J.* **9** (1971) 533-535.

Napolitano, M., "Numerical Study of Strong Slot Injection into a Supersonic Laminar Boundary Layer," *AIAA J.* **18** (1980) 72-77.

Nath, G. & B. K. Meena, "Three-Dimensional Compressible Stagnation Point Boundary Layers with Large Rates of Injection," *AIAA J.* **15** (1977) 747-748.

Nilson, R. H. & Y. G. Tsuei, "Film Cooling by Oblique Slot Injection in High-Speed Laminar Flow," *AIAA J.* **13** (1975) 1199-1202.

Reinecke, W. G., "Penetration of a Lateral Sonic Gas Jet into a Hypersonic Stream," *AIAA J.* **13** (1975) 173-176.

Richards, B. E. & J. L. Stollery, "Laminar Film Cooling Experiments in Hypersonic Flow," *J. Aircraft* **16** (1979) 177-181.

Rosenbaum, H., et. al., "Flowfield Interactions Induced by Massive Lateral Injection," *AIAA J.* **13** (1975) 1441-1447.

Smith, F. T. & K. Stewartson, "On Slot Injection into a Supersonic Laminar Boundary Layer," *Proc. Roy. Soc.* A **332** (1973) 1-22.

Smith, F. T. & K. Stewartson, "Plate-Injection into a Separated Supersonic Boundary Layer," *J. Fluid Mech.* **58** (1973) 143-159.

Spaid, F. W., "Two-Dimensional Jet Interaction Studies at Large Values of Reynolds and Mach Numbers," *AIAA J.* **13** (1975) 1430-1434.

Stewartson, K., "Plate-Injection into a Separated Supersonic Boundary Layer. Part 2. The Transition Region," *J. Fluid Mech.* **62** (1974) 289-304.

Taylor, T. D.& B. S. Masson, "Supersonic Flow Past a Finite Cone with Large Surface Mass Injection," *AIAA J.* **7** (1969) 1268-1273.

Thomas, P. D., "Flow Over a Finite Plate with Massive Injection," *AIAA J.* **7** (1969) 681-687.

Wallace, J. & N. Kemp, "Similarity Solutions to the Massive Blowing Problem," *AIAA J.* **7** (1969) 1517-1523.

Werle, M. J., "Supersonic Laminar Boundary-Layer Separation by Slot Injection," *AIAA J.* **17** (1979) 160-167.

Yasuhara, M., "On the Hypersonic Viscous Flow Past a Flat Plate with Suction or Injection," *J. Phys. Soc. Japan* **12** (1957) 177-182.

Zukoski, E. E. & F. W. Spaid, "Secondary Injection of Gases into Supersonic Flow," *AIAA J.* **2** (1964) 1689-1696.

For additional (mostly earlier) references, see:
Schlichting, H., *Boundary Layer Theory,* 7 ed., McGraw-Hill, 1979, pp. 403-407.